Measuring Rate Constants and Product Branching for Reactions Relevant to Combustion and Atmospheric Chemistry

by

Zachary J. Buras

B.S. in Chemical Engineering, UC Santa Barbara, 2011
M.S. Chemical Engineering Practice, Massachusetts Institute of Technology, 2014

Submitted to the Department of Chemical Engineering
in Partial Fulfillment of the Requirements for the Degree of

Doctor of Philosophy in Chemical Engineering

at the

MASSACHUSETTS INSTITUTE OF TECHNOLOGY

February 2018

Signature redacted

Author...
Department of Chemical Engineering
December 15, 2017

Signature redacted

Certified by...
William H. Green
Hoyt C. Hottel Professor in Chemical Engineering
Thesis Supervisor

Signature redacted

Accepted by...
Patrick S. Doyle
Robert T. Haslam (1911) Professor of Chemical Engineering, Graduate Officer
Committee for Graduate Students

Measuring Rate Constants and Product Branching for Reactions Relevant to Combustion and Atmospheric Chemistry

by

Zachary J. Buras

Abstract

Over the last century there have been countless experimental measurements of the overall reaction kinetics of gas-phase radicals, often with the aid of lasers. In more recent decades, *ab initio* predictions of product branching using quantum chemical calculations combined with modern rate theories have become common. However, there are few experimental measurements against which to validate predicted product branching, even for an important reaction system such as hydroxyl radical addition to acetylene that is critical to oxidation chemistry both in the atmosphere and in combustion. As a result, many of the kinetic parameters that appear in commonly used combustion mechanisms are based purely on predictions. The few experiments that do attempt to quantify product branching generally fall into two categories, each with unique advantages/disadvantages: crossed molecular beams (CMB) that simulate single collision conditions, or end-product analysis of a complex, thermalized process, such as pyrolysis. Laser flash photolysis (LFP) with molecular beam mass spectrometry (MBMS) offers a compromise between CMB and end-product experiments: the reaction conditions are thermalized but still simple enough that primary products can be quantified with confidence.

This thesis describes a unique apparatus, and the improvements made to it, that combines LFP and MBMS for primary product branching quantification, as well as multiple-pass laser absorbance spectrometry (LAS) for accurate measurements of overall kinetics. The full capability of this LFP/MBMS/LAS apparatus is demonstrated for the chemically interesting phenyl radical + propene reaction system, which has been implicated as a potential source of second aromatic ring formation under combustion conditions. Overall kinetic measurements are also reported in this work either for systems that involve a newly discovered reactive species (various cycloaddition reactions of the simplest Criegee Intermediate formed in atmospheric ozonolysis) or that was disputed in the literature (vinyl radical + 1,3-butadiene, which has been implicated as a potential source of benzene in combustion). Finally, this thesis shows how detailed chemical insights made either experimentally or theoretically can be translated into applications *via* the Reaction Mechanism Generator (RMG). The application discussed is natural gas high temperature pyrolysis for the production of C2 commodity chemicals.

Thesis Supervisor: William H. Green
Title: Hoyt C. Hottel Professor in Chemical Engineering

Acknowledgements

First, I would like to express gratitude to my thesis advisor, Professor William Green, who trusted me with a lot of freedom and was incredibly patient as this thesis gradually took shape. As just one example of his graciousness, he once met me at his home on a Sunday in order to find a factor of two error in one of my calculations. I learned a lot from him not just about science but also about treating everyone with respect.

My thesis committee members, Professors Robert Field and William Tisdale, always brought helpful, unexpected insights into our annual meetings, and provided a much-needed dose of pragmatism and experience whenever I proposed an unrealistic timeline or research direction.

I was very fortunately early on to have two excellent graduate mentors at MIT: Drs. Joshua Middaugh and Amrit Jalan. During his PhD Josh did the vast majority of the work upgrading the LAS apparatus to incorporate PI TOF-MS, a job that was largely thankless at the time, but that was ultimately the right choice for the long-term prospects of this project. For the 1.5 years that Josh and I overlapped I was able to see firsthand the habits of an exemplary engineer to which I should aspire. Similarly, Amrit was a research role model with whom I had the pleasure to closely collaborate for half of a year. During that short time, Amrit handed to me my first research project that I felt complete ownership of (reactions of Criegee Intermediates), an experience that was crucial to my development as a confident, independent researcher.

I had the opportunity to work closely in the laser lab with several post-docs, visiting scholars and graduate students, each of whom brought with them their own unique assets: Dr. Mickael Matrat, Prof. Angayle (AJ) Vasiliou, Prof. Andrew Cooksy, Prof. Rehab Elsamra, Prof. Guozhu Liu, Zehao Gou and Te-Chun (Jim) Chu. Mickael was already working in the lab when I first joined, and without his intense drive it probably would have taken much longer to get the PI TOF-MS working. Mickael also wrote the MATLAB analysis scripts that I have subsequently used or adapted throughout my thesis work. AJ joined the lab at the same time as me as a post-doc, and brought experience and perspective that I could only fully appreciate later. Andrew was instrumental during the lab move from Building 6 to E18 and had no qualms whatsoever about doing necessary work that was well below his stature (aligning lasers, wiring safety interlocks, etc.). Rehab came to MIT on a year-long Fulbright scholarship and thanks to her determination that year was the most productive of my PhD. Guozhu brought with him many ideas both for improvements to the experimental apparatus (such as how we might reach higher reaction

temperatures) and chemical systems to study (such as molecular weight growth reactions of phenyl and naphthyl radcials, as well as reactions of resonance stabilized radicals). Although he was unable to see them come to fruition during the short one year that he was at MIT, his ideas most certainly took hold and could provide the basis for many more years-worth of research. Zehao was Guozhu's student at Tianjin University, and he impressed me with his eagerness to try new things and challenge assumptions. Finally, Jim is another MIT graduate student who is inheriting the laser lab project (and other projects). I have worked with Jim the longest out of anyone else in the laser lab, and during that time we have encountered many unanticipated difficulties while changing reactor designs. Through it all Jim has stayed optimistic and maintained a forward-looking, problem-solving attitude, which I needed to stay grounded.

Towards the tail end of my graduate career I had the opportunity to become a user and then a contributor to the signature product of the Green group: RMG. I was only able to do this, however, thanks to the shared, accumulated knowledge of several dedicated RMG developers: Dr. Nathan Yee, Mengjie (Max) Liu, Kehang Han, Dr. Connie Gao, Dr. Pierre Bhoorasingh and Matt Johnson. Nathan was my go-to RMG guy (as he was for most of the group) thanks both to his broad experience and approachability. Nathan was also a classmate and a good friend throughout our years at MIT. Our morning workouts, afternoon coffee breaks and evening trivia domination prevented me from becoming totally consumed by research. Max has provided critical RMG support for several of my projects, especially related to aromatics. I have learned to be careful what half-formed ideas I mention to him even in passing because usually the next day he will have written some script to try it. Kehang's work on cheap heuristics for polycyclic thermochemistry estimation was crucial to the success of the high temperature pyrolysis modeling project. When I had enough of a grasp on RMG to make cogent suggestions for improvement Kehang was willing to rewrite his algorithms to implement them. Connie answered a lot of my RMG questions when I was really a novice and patiently outlined all of the challenges ahead for aromatic chemistry in RMG. Pierre was a student in Prof. Richard West's group at Northeastern who spent a day getting Jim and me set up to use his mechanism importer tool, which was the spark that initiated the high temperature pyrolysis modeling project. Finally, Matt and I worked together to improve RMG's rate-calculation software, Cantherm, and as one of the newest graduate students in the group Matt has given guidance regarding how he thinks RMG's database should be structured to facilitate more efficient use of the data in the future.

Besides the RMG developers mentioned specifically above, many others including Dr. Nick Vandewiele, Dr. Shamel Merchant, Dr. Alon Dana and Mark Goldman provided help at various times and generally fostered an environment of open collaboration in the Green group.

I enjoyed collaborating with three post-docs on different projects: Drs. Enoch Dames, Soumya Gudiyella and Adeel Jamal. Although they each had unique personalities and backgrounds, the similarity among them that struck and inspired me the most was their uniform optimism, which made collaboration very smooth. Enoch provided computational support for our vinyl radical + 1,3-butadiene work and was an excellent resource for information on many topics. Soumya and I worked closely on modeling of high temperature pyrolysis, where her background in shock tube pyrolysis, chemical mechanism development and gas turbine modeling were instrumental in getting that project off of the ground. Finally, Adeel is a computational chemist who brought his expertise to our phenyl radical + propene and hydroxyl radical + phenylacetylene work, and whose company I enjoyed during our late-night discussions.

I also had help from two UROP's: Isabel Plana and Kristopher Wiggins. Isabel helped to analyze some old data and also conducted a thorough literature review of Criegee Intermediate chemistry that subsequently guided my research direction. Kris wrote a custom MATLAB script to model and optimize different waveguide designs for focusing the output of an atomic resonance lamp in the ionization region of the PI TOF-MS. He also initiated a LabView script to enable continuous TOF-MS data acquisition up to 50 kHz.

Although the majority of the Green group does computational work, I would also like to acknowledge a couple of the other experimentalists in the group who worked on crude oil desulfurization/upgrading: Dr. Yuko Kida, Dr. Caleb Class and Lawrence Lai. Despite the fact that their experiments are conducted at much different conditions than mine they were able and willing to provide general experimental advice and equipment support. They all also took seriously their roles as the main EHS representatives, which helped to maintain a safe lab environment despite the use of many toxic gases and the high turnover of people working in the lab.

Professor Field's students, Dr. David Grimes and Timothy Barnum, were my liaisons to the chemistry department. Given that my experimental research is more similar to what would be encountered in a physical chemistry lab than in a chemical engineering lab, having David and

Tim to talk to about topics such as vacuum hardware, lasers and molecular beams (and also to borrow equipment from) was a godsend in some situations.

I also benefited from some excellent MIT staff members: Dr. Gang Liu in the chemistry electronics shop, Dennis Nagle and Anthony Caravaggio in the chemistry machine shop, Mark Belanger in the Edgerton student machine shop and Andrew Gallant in the central machine shop. Gang and Andrew especially went above and beyond what their jobs required of them on a consistent basis and were always solicitous towards students.

Our group administrator, Gwen Wilcox, has kept both daily and long-term operations running smoothly, as she manages complicated problems such as the move from Building 6/66, expensive purchases and Professor Green's schedule.

As our contacts at SABIC, Drs. Istvan Lengyel and Sreekanth Pannala, shared pilot plant data with us and provided valuable input, guidance and conversation whenever we met.

I received some advice regarding apparatus design from Prof. Vadim Knyazev at Catholic University and Dr. Mark Blitz at University of Leeds. I visited Prof. Knyazev's lab for a day and afterwards maintained a steady stream of questioning *via* e-mail for the next couple of years, which he readily answered. Similarly, I had intermittent correspondence with Dr. Blitz over the last five years, and although we never met in person he was always open and responsive.

My roommates for the last several years, Eric Anderson and Yuqing Cui, were both very kind and understanding as my schedule for graduation kept shifting.

I would like to thank my Practice School group for an unforgettable learning experience, especially Joel and Yoyo Paulson who know how to work hard and also how to have fun. Also our station director Bob Hanlon imparted a lot of wisdom to us that I still recall frequently

Thank you to friends outside of the MIT cohort, especially Tim Wall and Chas Mitchell, who checked in every once in a while to remind me of the wider world outside of academia.

I would have never made it to MIT, much less finished a PhD, if it weren't for the support of both my parents, Joe and Linda, and my grandparents, Sam and Barbara. From the beginning they all invested heavily in my education and I am very grateful to have always had their strong backing.

My girlfriend, Lisi Xie, served many roles: she was a constant source of support, a technical sounding board and my main confidant. The last five years are unimaginable without her.

Contents

List of Figures

List of Tables

Chapter 1

Introduction

Over the last 100 years there have been many experimental measurements of the overall decay kinetics of gas-phase radicals important to combustion and atmospheric chemistry,[1] often with the aid of lasers. In more recent decades, *ab initio* or DFT quantum calculations of the potential energy surfaces (PES's) of radical reactions have become commonplace, which are then combined with modern rate theory to obtain the predicted product distribution or branching as a function of both temperature, T, and pressure, P.[2] However, until recently there were few experimental measurements of the product branching against which to validate predictions. Even for a reaction such as hydroxyl radical + acetylene (OH + C_2H_2) that is critical to oxidation in both the atmosphere and combustion, there are still no measurements against which to validate the complicated T,P-dependent product branching predicted by Senosiain et al.,[3] which has subsequently been incorporated into many widely-used combustion mechanisms.[4] The main goal of this thesis is to partially fill the large knowledge gap between experimental and theoretical product branching using a new experimental technique.

The experiments that do attempt to quantify product branching generally fall into just a few categories, which will be described shortly. First, however, it is helpful to define terms. Scheme 1-1 uses the example reaction system of phenyl radical + propene (C_6H_5 + C_3H_6, C_9H_{11} PES) to illustrate what is meant by "overall kinetics" and "primary products" as opposed to secondary or side products.
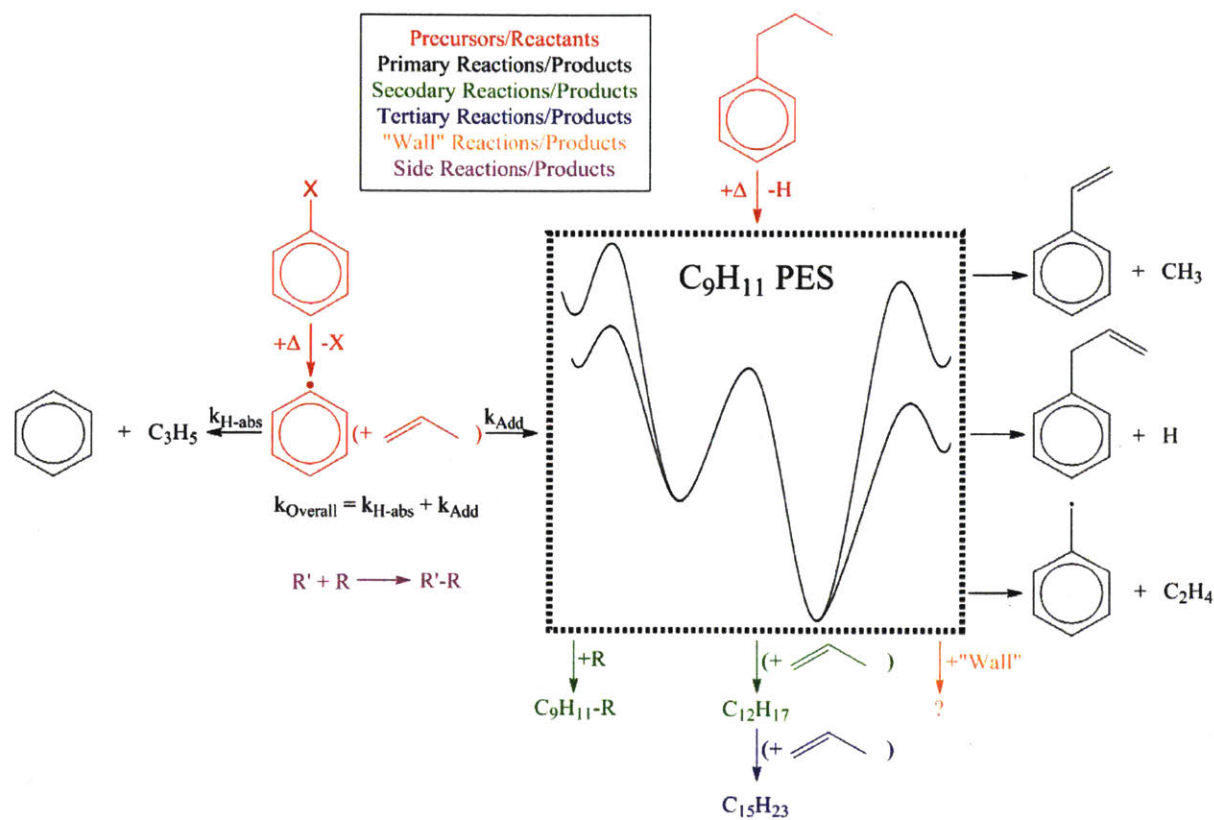
Scheme 1-1: Definition of primary, secondary, etc. reactions/products using phenyl radical + propene as an example.

In an experiment aimed at quantifying products, the first objective is to somehow access the PES of interest (often a doublet, or radical, PES) and then see what products come off of it. Once a PES is identified for experimental exploration, the experimentalist must make two decisions: first, will the PES be accessed unimolecularly (e.g., propylbenzene, C_9H_{12}, decomposition to C_9H_{11}) or bimolecularly ($C_6H_5 + C_3H_6$), and second, where will the energy, Δ, come from to make the initial radical. The most common energy sources for gas-phase radical generation are either thermal or photolytic. All four combinations of experimental choices can be visualized in Scheme 1-1. For the bimolecular option, the radical precursor will often have one weak bond that will break preferentially upon heating or laser excitation. For example, the X in the C_6H_5X precursor could be either nitrogen monoxide, NO, or iodine atom, I, both of which make a weak single-bond with carbon that is known to photodissociate following 266 nm laser excitation.[5-6] For the unimolecular option, a precursor could also be chosen that exploits the weakness of one particular bond, or a conventional hydrocarbon, such as C_9H_{12} shown in

Scheme 1-1 could simply be pyrolyzed at high enough temperatures to break C-H bonds. Also worth considering is that depending on how the PES is accessed and the conditions of the experiment (temperature, pressure and composition) there might be an excess of internal energy initially, which can facilitate unimolecular reactions *via* chemical activation.[7]

Any products formed through unimolecular reactions (including isomerizations, β-scissions and dissociations) on the PES are considered primary products. For the C_9H_{11} PES, there are several feasible primary products, including styrene from β-scission of a methyl radical, CH_3, and benzyl radical + ethene (C_2H_4) from a new unimolecular pathway described in section 4.2. If the C_9H_{11} PES is accessed *via* C_6H_5 + C_3H_6, then benzene (C_6H_6) and a C_3H_5 isomer might also be considered primary products as they are directly formed from the reactants through hydrogen-abstraction. The overall kinetics of C_6H_5 + C_3H_6 can then be defined as the sum of all rate coefficients consuming C_6H_5: $k_{Overall} = k_{Add} + k_{H-abs}$. This is the effective rate coefficient that will be observed if only C_6H_5 decay is monitored, as in the case of direct absorbance experiments.[8]

Secondary reactions are bimolecular reactions between an isomer on the PES of interest and something else also present in the reactor. For example, one of the C_9H_{11} isomers could recombine with another radical, R, such as CH_3 or X. Another kind of secondary reaction might be radical addition of a C_9H_{11} isomer to a closed-shell molecule present in excess, such as C_3H_6. The secondary product formed would be another radical, which could then undergo a tertiary reaction, and so on. "Wall" reactions are really a catchall for unobserved loss processes, many of which might actually involve the reactor wall. Finally, side reactions don't involve any of the isomers on the PES of interest, and nominally should not affect quantification of the primary product branching. For example: $CH_3 + X \rightarrow CH_3X$.

Figure 1-1 shows the actual C_9H_{11} PES, calculated by Kislov et al.,[9] to illustrate the complexity of a real PES. In reality, even this PES is not "complete", but it does show most of the energetically favorable reactions relevant to C_6H_5 + C_3H_6.
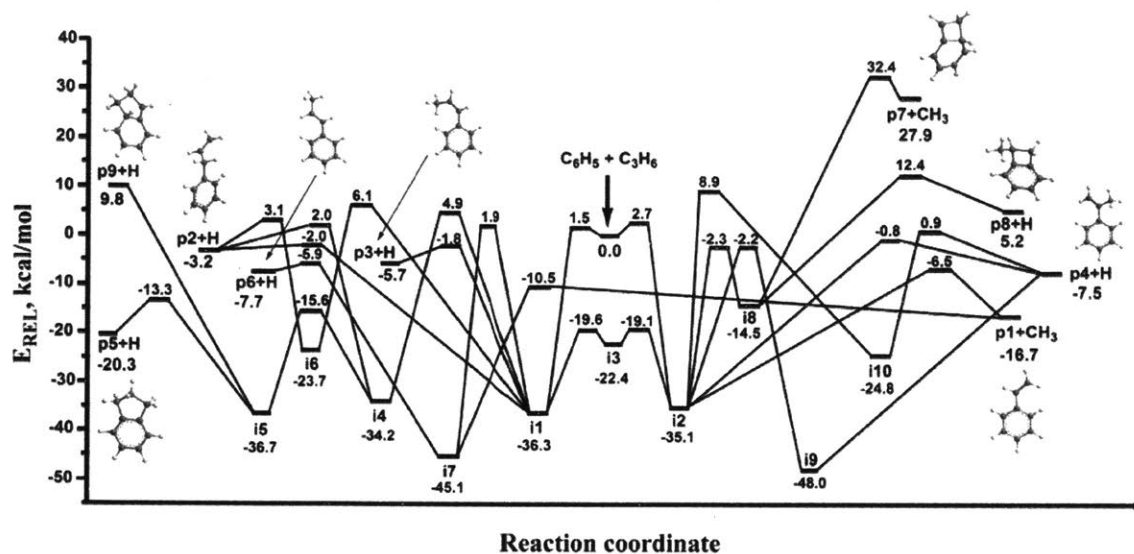
Figure 1-1: Example of a potential energy surface (PES): C_9H_{11}. Taken from Kislov et al.[9]

As mentioned earlier, experiments aimed at primary product quantification of a particular PES can usually be grouped into a handful of categories, shown in Figure 1-2. Literature examples of each type of experiment are also provided, and are mostly taken from work published within the last ten years. Note that Figure 1-2 is not meant to be exhaustive in terms of the types of experiments listed or the literature examples given, nor does it consider combustion experiments aimed at measuring macroscopic properties (e.g., ignition delay, laminar flame speed, extinction strain rate). Rather, Figure 1-2 is meant to summarize some of the most common experimental techniques in use currently for quantifying products of a specific PES.

Collision Frequency in Reactor

10^9 s^{-1} → Combustion

	CMB + MS CLMB + MS	LFP+ GC/MS Discharge Flow Reactor + MBMS	Flow Pyrolysis + GC/MS Flow Pyrolysis + MBMS **Flash Pyrolysis + MBMS**
None			
10 μs		**LFP + MBMS**	Shock Tube + HRR-TOF-MS
		LFP + Absorbance/LIF	Shock Tube + Absorbance/LIF

Time Resolution of Product Detection
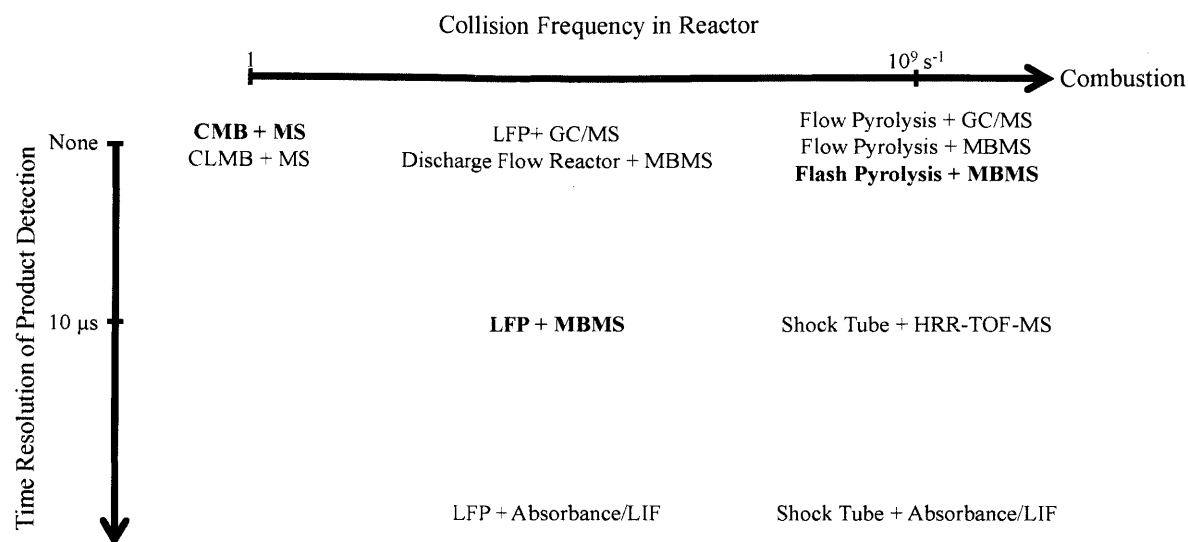
Figure 1-2: Summary of experimental techniques in literature for quantifying product branching, organized according to collision frequency in reactor (how closely the experiment mimics combustion conditions) and time resolution of product detection. The three bolded techniques are discussed in detail in the text. Abbreviations have the following meaning: CMB = Crossed Molecular Beams, CLMB = Crossed Laser Molecular Beam, MS = Mass Spectrometry, LFP = Laser Flash Photolysis, MB = Molecular Beam, GC = Gas Chromatography, HRR-TOF = High Repetition Rate Time-of-Flight, LIF = Laser Induced Fluorescence. Examples of each technique: CMB + MS,[10-20] CLMB + MS,[21] LFP + GC/MS,[22-24] Discharge Flow Reactor + MBMS,[25] Flow Pyrolysis + GC/MS,[26] Flow Pyrolysis + MBMS,[27-29] Flash Pyrolysis + MBMS,[30-42] LFP + MBMS,[43-50] Shock Tube + HRR-TOF-MS,[51-52] LFP + Absorbance/LIF,[53-56] Shock Tube + Absorbance/LIF.[57-59]

Fundamentally, every experiment that measures products from a chemical reaction consists of two parts: a reactor and a detector. As shown, there is a wide diversity of reactors employed throughout the literature, ranging from crossed molecular beams (CMB's) that simulate single-collision conditions, to pyrolysis reactors where each molecule experiences around a billion collisions per second. The type of reactor combined with the detection technique determines the time resolution for product detection, which is another important experimental variable. For example, if a laser flash photolysis (LFP) reactor is used with molecular beam mass spectrometry (MBMS) detection, time zero for reaction is well defined by the time of the laser flash, and mass spectra can be recorded in ~10 μs intervals. In that case (LFP + MBMS) the time resolution is actually determined by the time scale of transport in the MB (~10-100 μs). In contrast, if LFP is used with GC/MS there is essentially no time resolution because running a

chromatogram requires ~10 minutes, during which time any reactive products will be converted to more stable forms. Nonetheless, useful information can be gained from LFP + GC/MS experiments, especially considering the isomer selectivity of GC, which is why end product analysis more generally is still used. Of course, there are many other experimental variables besides collision frequency and time resolution to consider, such as sensitivity, selectivity, T,P-range, etc, that would allow further subdivision of the experimental techniques listed in Figure 1-2. However, for the purpose of this discussion, which is to illustrate experimental trends in gas-phase kinetics research, the two variables chosen in Figure 1-2 are sufficient.

Three specific experimental techniques in Figure 1-2 have come to dominate the recent literature on product branching, and will be discussed in more detail: CMB + MS, Flash Pyrolysis + MBMS and LFP + MBMS. These three examples also make nice case studies, as each one has its own unique advantages and disadvantages.

Figure 1-3 shows a CMB "reactor" with quadrupole MS (QMS) detection. Briefly, two pulsed molecular beams with well-defined velocity profiles collide in a vacuum chamber. One beam might be photolytically generated C_6H_5, for example, and the other might be C_3H_6. The molecules in the intersecting beams undergo a single-collision with a partner, forming a radical adduct in some cases with a large excess of internal energy due to the exothermicity of the radical addition reaction. Because there are no further collisions after the first one (collisionless environment) the internal energy of the adduct can only be channeled into unimolecular rearrangement and decomposition. The bimolecular products are detected by QMS on a rotatable stage, such that for a given collision energy, E_{col}, QMS signal can be measured as a function of three variables: mass-to-charge ratio of the product's cation (m/z), angle of the QMS (θ), and translational energy of the product (E_t, quantified by the flight-time of the cation). From this multivariate measurement, insights can be made into the relative product branching, the dynamics of the chemistry (e.g., did the adduct survive multiple rotational periods) and the energetics. Specifically, the heat of reaction, ΔH_{rxn}, for a particular bimolecular product channel can be calculated by an energy balance:

$$E_{T,max} = -\Delta H_{rxn} + E_{col} \qquad (1\text{-}1)$$

where $E_{T,max}$ is the maximum translation energy observed for the product. In other words, the maximum translation energy that a given product can have is the sum of the exothermicity of the reaction and the collision energy. Being able to quantify ΔH_{rxn} allows for reasonable guesses of

the product's isomeric identity to be made. For example, Kaiser et al. were able to conclude that indane was not the major $C_6H_5 + C_3H_6$ product at m/z=118 amu because the measured ΔH_{rxn} was not nearly exothermic enough.[13]
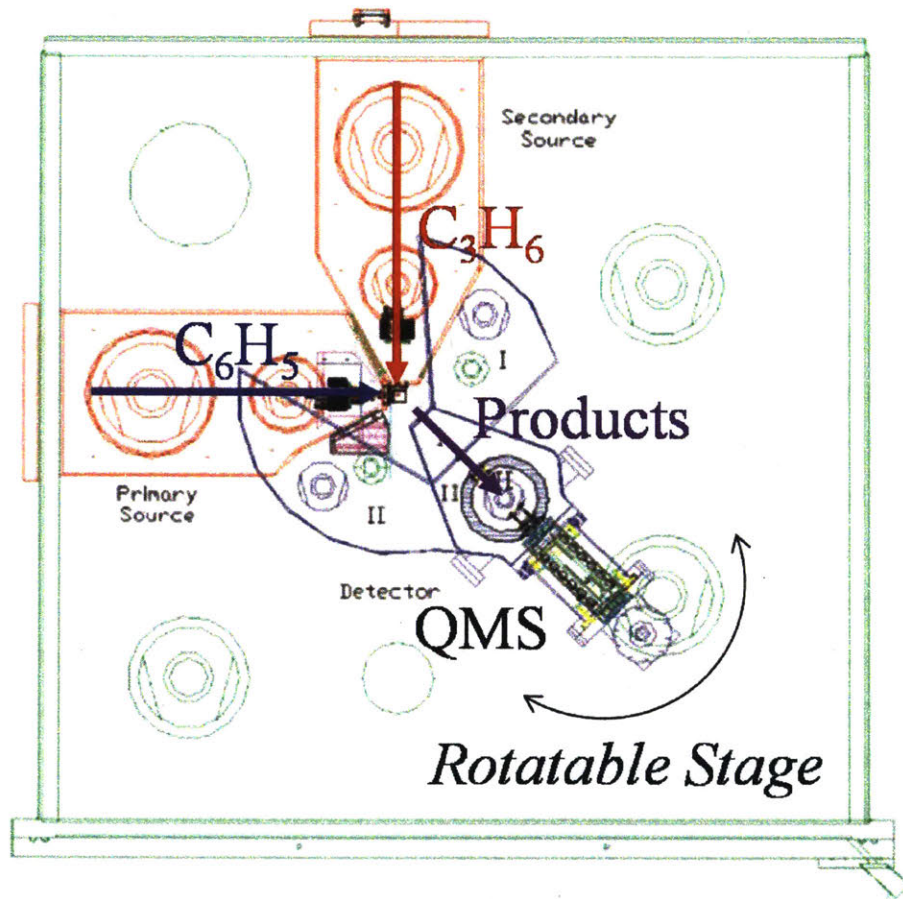
Figure 1-3: Schematic of a Crossed Molecular Beam (CMB) apparatus with quadrupole mass spectrometry (QMS) product detection. Taken from Gu et al.[60]

There are two major advantages of CMB + MS over some of the other experimental techniques listed in Figure 1-2. First is the exquisite detail that can be obtained for a given PES, examples of which were provided in the preceding paragraph. The second is the lack of either secondary or wall reactions, owing to the collisionless environment. Therefore, one can be confident that all of the measured products are coming from the PES of interest. The main disadvantage is that measurements made with CMB, such as product branching fractions, cannot be directly applied to the thermalized conditions of most applications. Instead, the CMB results must first be rationalized by a theoretically calculated PES, which can then be used to extrapolate

the CMB findings to a thermal environment. Of course, relying on theoretical calculations introduces additional uncertainty to any subsequent thermal prediction. The other disadvantage is that it may not be possible to observe all of the major primary products with CMB + MS. For example, none of the three CMB experiments looking at C_6H_5 + C_3H_6 were able to observe C_6H_6 from H-abstraction, even though it should be a major product, because of overlap with the ^{13}C isotopologue of scattered C_6H_5.[18] Another reason that a product might not be observed is sensitivity, even if that product accounts for up to 10% of the branching.[11] As will be shown in section 4.2, it is likely that an important product of C_6H_5 + C_3H_6 was missed by all three CMB experiments due to the latter issue.

The second experimental technique for product quantification that has come to prominence is at the opposite collision frequency extreme as CMB: flash pyrolysis + MBMS (Figure 1-4). In fact, the two techniques are often regarded as complementary, such that theoretical calculations are often validated at both extremes.[61] As shown, the flash pyrolysis reactor is a short silicon carbide flow reactor (either pulsed or continuous depending on downstream pumping capacity) that can be heated up to 1700 K with pressures ~100 Torr and very short residence times of ~10-100 μs (hence they are often referred to as microreactors). The effluent of the reactor is directly sampled for MBMS detection of products. Although only MBMS detection is shown in Figure 1-4, other detection techniques have also been coupled with flash pyrolysis that allow more isomeric specificity to product measurements, such as matrix infrared (IR)[36] or IR/UV ion dip spectroscopy.[39-40]
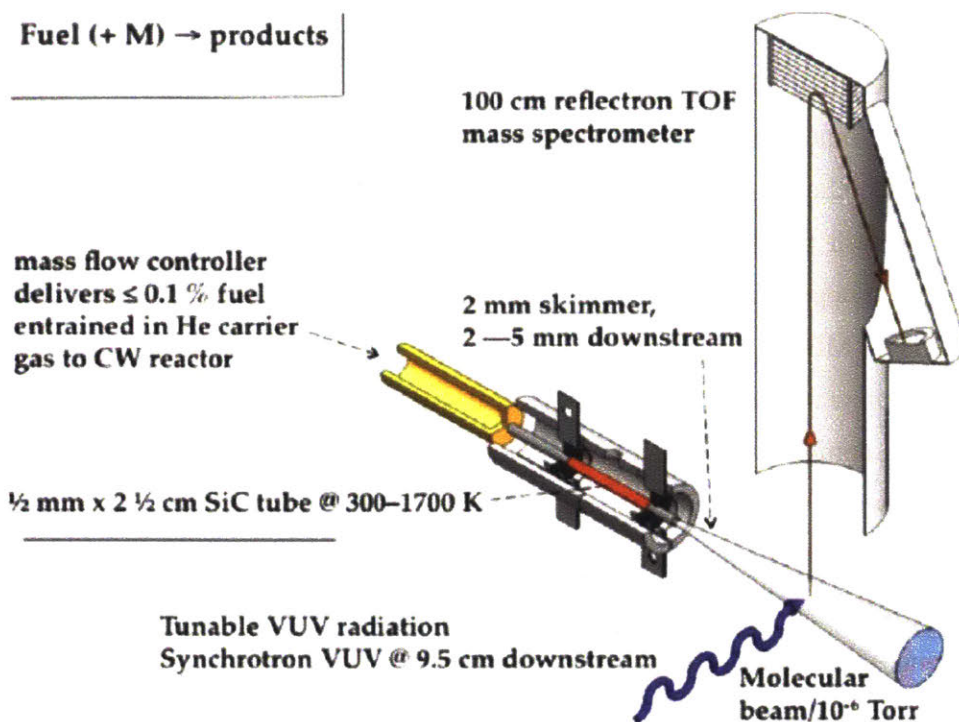
Figure 1-4: Schematic of flash pyrolysis reactor with molecular beam mass spectrometry (MBMS) product detection. Taken from Guan et al.[62]

The advantage of flash pyrolysis, and of pyrolysis generally, is that it can more closely mimic the real conditions of combustion (high T and P) especially compared to CMB experiments. Unlike regular pyrolysis, however, flash pyrolysis offers a unique advantage in that the short residence time should make primary product detection possible before secondary and higher generation reactions become important. The main disadvantage is that the complicated flow, temperature and pressure profiles inside of the microreactor make it difficult to extract quantitative kinetic and product branching measurements to compare against predictions. Instead, flash pyrolysis is mostly useful for qualitative insights currently, such as what are the major products of $C_6H_5 + C_3H_6$ at ~1200 K and ~300 Torr and what isomers dominate,[31] rather than exactly how much of each is made. However, efforts are being made to build models for flash pyrolysis,[62] so as to enable quantitative comparisons with theory.[36] Another disadvantage is the lack of time-resolution, as indicated by Figure 1-2, which is common among all pyrolysis reactors. This is due to the lack of a clearly defined time zero for reaction, in contrast to an LFP reactor or shock tube where t=0 corresponds to the photolysis flash and shock, respectively.

Instead, pyrolysis reactors have a residence time, τ, that can be adjusted, but given the aforementioned complexities of transport in the microreactor, adjusting the residence time will only add another dimension to the problem. In other words, the T,P conditions at one τ will not be the same as another τ, even if everything else is kept fixed. Finally, secondary reactions do still occur in a flash pyrolysis reactor, even if they are less than in regular pyrolysis, and can become important depending on the reactor conditions. Returning to the example of $C_6H_5 + C_3H_6$, flash pyrolysis + MBMS experiments were also unable to observe either benzene from H-abstraction or benzyl radical/C_2H_4 from the new pathway, likely due to secondary reactions.

The last common technique for product branching quantification is somewhat of a compromise between CMB and flash pyrolysis: LFP + MBMS. Figure 1-5 shows the original apparatus of Slagle and Gutman that popularized this technique. A laser flashes the otherwise inert contents of a flow reactor, such that a weak bond in a chemical precursor breaks (the C-I bond in iodobenzene, C_6H_5I, for example) forming a reactive radical (C_6H_5) and a (hopefully) less-reactive co-product (I atom). The laser flash defines t=0, and the evolution of the gas mixture is monitored relative to that point by time-resolved MBMS.
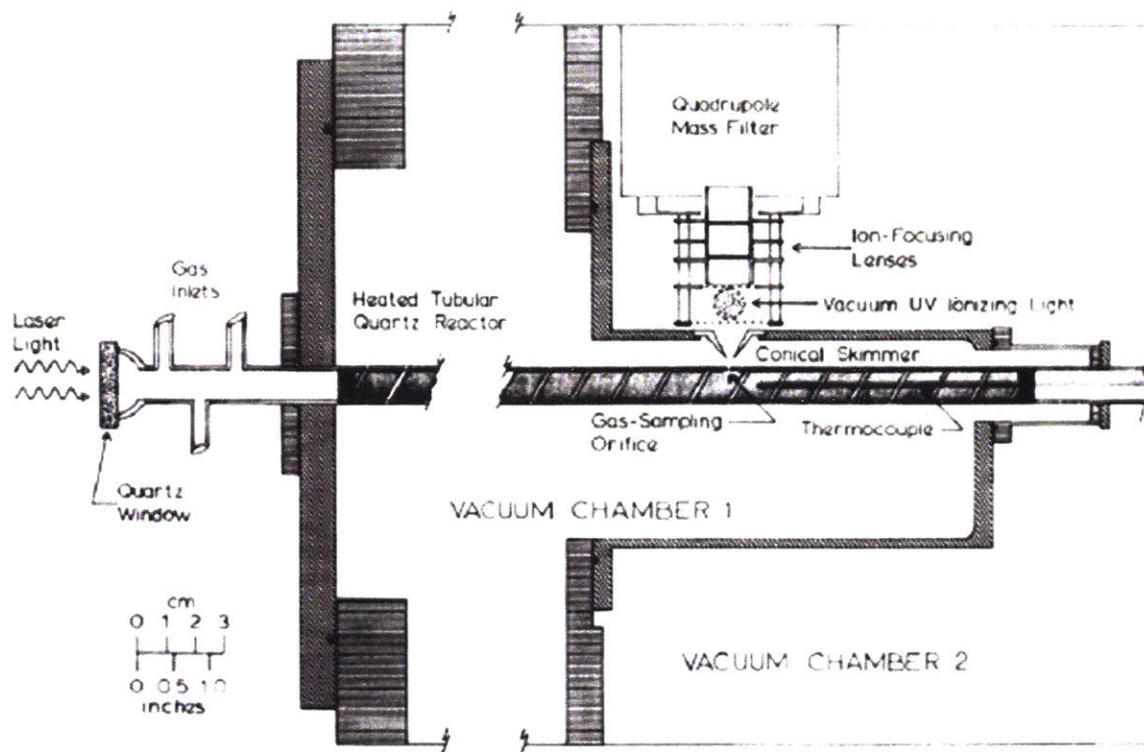
Figure 1-5: Schematic of original Laser Flash Photolysis (LFP) reactor with molecular beam mass spectrometry (MBMS) product detection. Taken from Slagle et al.[63]

Unlike either CMB or flash pyrolysis, not only does LFP + MBMS have time-resolution, it offers *high* time-resolution down to ~10-100 μs at which point transport of the MB becomes rate-limiting.[64-65] This is useful for discerning primary products from secondary products from tertiary products, etc, based on their respective growth time scales. Furthermore, instead of only measuring product branching, LFP + MBMS has sufficient time resolution to accurately measure kinetics (time-dependence) as well, which has been utilized throughout the literature. The contents of the LFP reactor are also thermalized, which makes it easier to connect laboratory measurements with applications, although theoretical calculations are still generally needed. It should be noted, that although historically the collision frequency in LFP reactors has been ~2 orders of magnitude lower than pyrolysis reactors (as indicated in Figure 1-2) due to pumping requirements and inhomogeneous initial radical concentrations following photolysis, this is not a fundamental limitation. For example, Krasnoperov and co-workers have repeatedly used LFP up to 1 atm (using absorbance for detection) by carefully maintaining a uniform photolysis beam

profile ($\pm$7% radial intensity).[56] Another example of using LFP at high collision frequency (high P) is with on-axis MBMS, where pressures up to ~3 atm were explored.[48] The final advantage of LFP is that the reactor has a well-defined T and P, unlike in flash-pyrolysis. There are two major disadvantages. The first is that LFP is not immune to side, secondary and wall reactions. In fact, as will be most clearly demonstrated for the C_6H_5+ C_3H_6 system in section 4.2, the presence of a photolytic co-product, X (I atom for example), can make secondary reactions even more important than they would be in a flash pyrolysis reactor with only hydrocarbons. Second, LFP is limited to temperatures <~1000 K, because above that point photolytic precursors with intrinsically weak bonds will start to thermally dissociate, at which point the LFP reactor begins to resemble a flow pyrolysis reactor.

As can be surmised from this brief overview of the literature, none of the common experimental techniques for product branching quantification is perfect, but as a suite of techniques they offer a stringent litmus test for any theoretical predictions. Using C_6H_5 + C_3H_6 as a chemically-interesting test system (section 4.2), this thesis demonstrates the additional knowledge that can be gained by applying LFP + MBMS to a system that has already been studied extensively by both CMB[11, 13, 18] and flash pyrolysis experiments,[31] as well as theory.[9, 66]

Although the discussion so far has focused solely on product branching, measurements of overall kinetics are also still needed in some cases. For example, when a new reactive intermediate with unknown kinetics is discovered, as discussed in Chapter 3 for the atmospherically important Criegee Intermediate, or when theoretical kinetics predictions are in dispute, as discussed in section 4.1 for vinyl radical + 1,3-butadiene.

Finally, Chapter 5 will demonstrate how the detailed chemical knowledge gained either from experiments or predictions can be applied to applications *via* RMG. The application that will be discussed is natural gas high temperature pyrolysis for production of C2 commodity chemicals.

Before delving into the detailed chemistry that comprises the core of this thesis, however, the experimental apparatus used throughout must first be described, which is done in the following chapter.

Chapter 2

Improvements to LAS and PI TOF-MS Experimental Apparatus

2.1 Overview of Apparatus

The experimental apparatus used in this work combines laser flash photolysis (LFP) for radical generation, laser absorbance spectrometry (LAS) for fast kinetics measurements, and time-resolved photoionization (PI) time-of-flight mass spectrometry (TOF-MS) for quantitative product branching measurements. The LAS and time-resolved PI TOF-MS portions of the apparatus were designed, built, characterized and tested mostly by Dr. Huzeifa Ismail and Dr. Joshua Middaugh, respectively, and are described in detail in their theses.[67][68] Most of what they describe still applies, thus only a brief overview of the apparatus is provided in this section. Later sections will describe in detail the improvements made to the apparatus as part of my thesis work. The final section of this chapter will summarize the characterization of the modified apparatus.

Figure 2-1 to Figure 2-3 show the apparatus from different angles and cross-sectional views. The apparatus consists of a "bow-tie-shaped" custom quartz flow reactor housed in a custom vacuum chamber (Figure 2-2). The reactor is ~1 m long (99.0 cm) and has a 1.6 cm ID (2.5 mm wall thickness) in its central 40 cm and a 3.6 cm ID (2.0 mm wall thickness) everywhere else. The narrow ID at the center of the reactor is matched by the diameter of the photolysis laser used to generate radicals. As a result, radial diffusion of photolytically-generated radicals and subsequent products is eliminated as a loss process in the center of the reactor where sampling for TOF-MS occurs. The larger diameter at the edges of the reactor is necessary to accommodate the Herriott cell for LAS.[69-71] The reactor shown in Figure 2-2 is different than the ones used by either Ismail or Middaugh, both in terms of construction material and geometry, and the reasons for these changes are discussed in detail in section 2.2.2
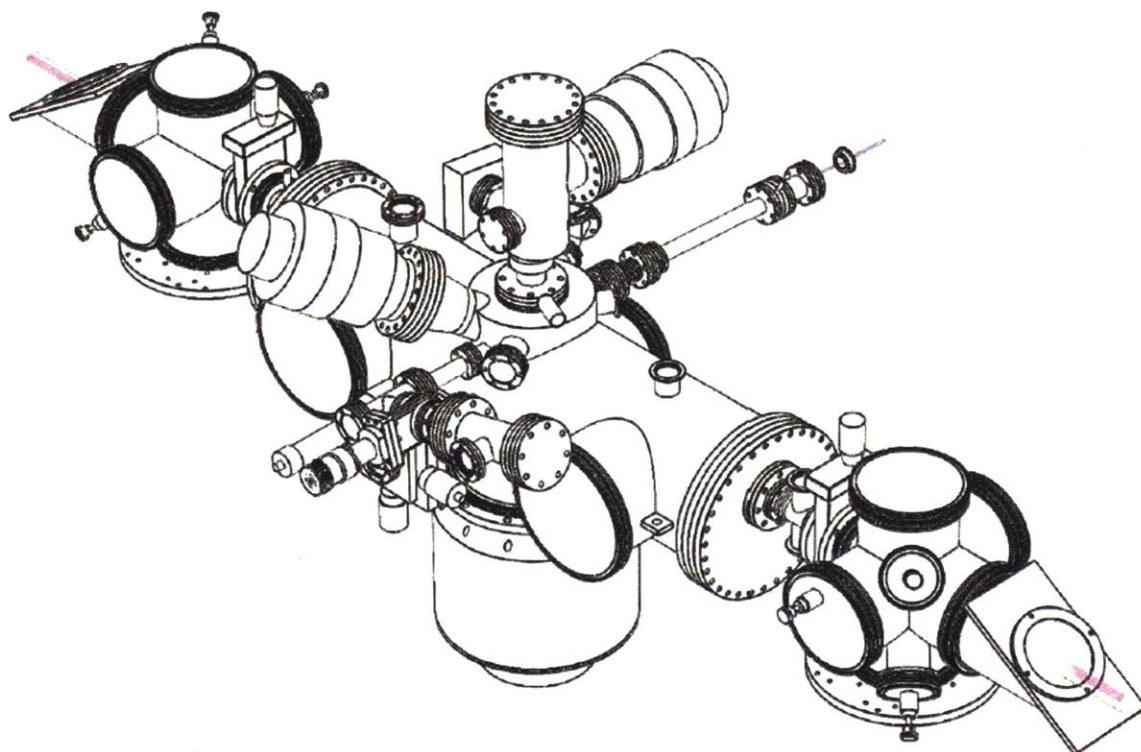
Figure 2-1: 3-D isometric view of LAS and PI TOF-MS apparatus. Photolysis beam is shown in pink, probe beam is green and 355 nm beam used to generate VUV is purple. Courtesy of Dr. Joshua Middaugh.
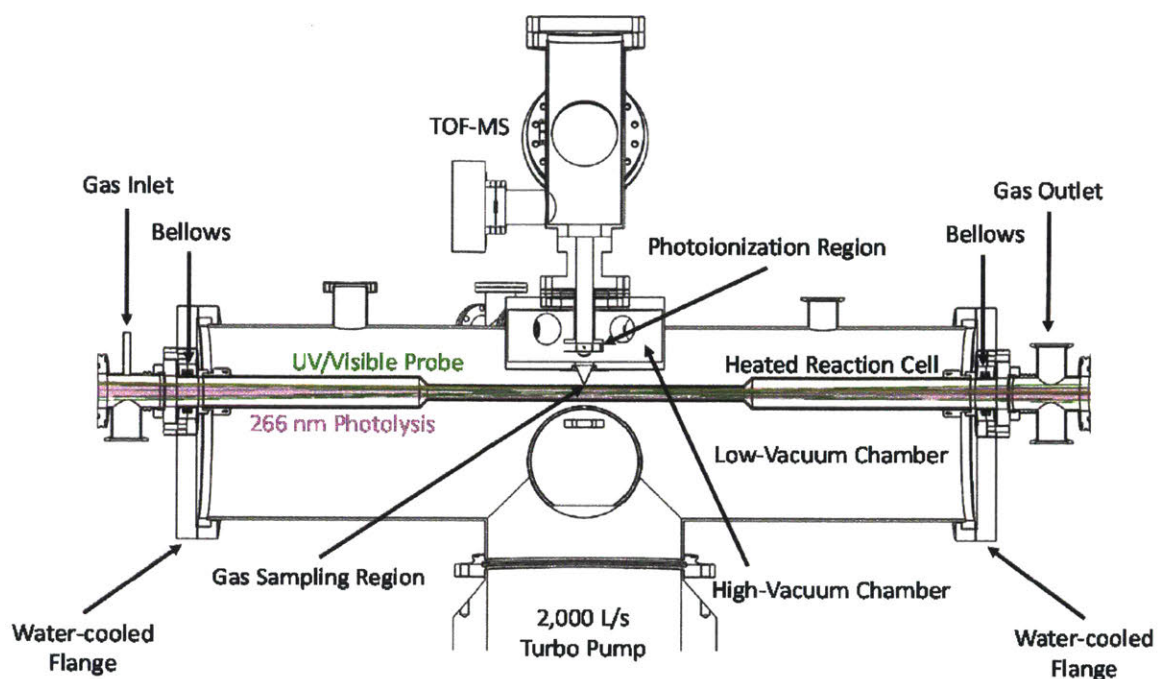
Figure 2-2: Front cross-sectional view of LAS and PI TOF-MS apparatus, showing reaction cell.
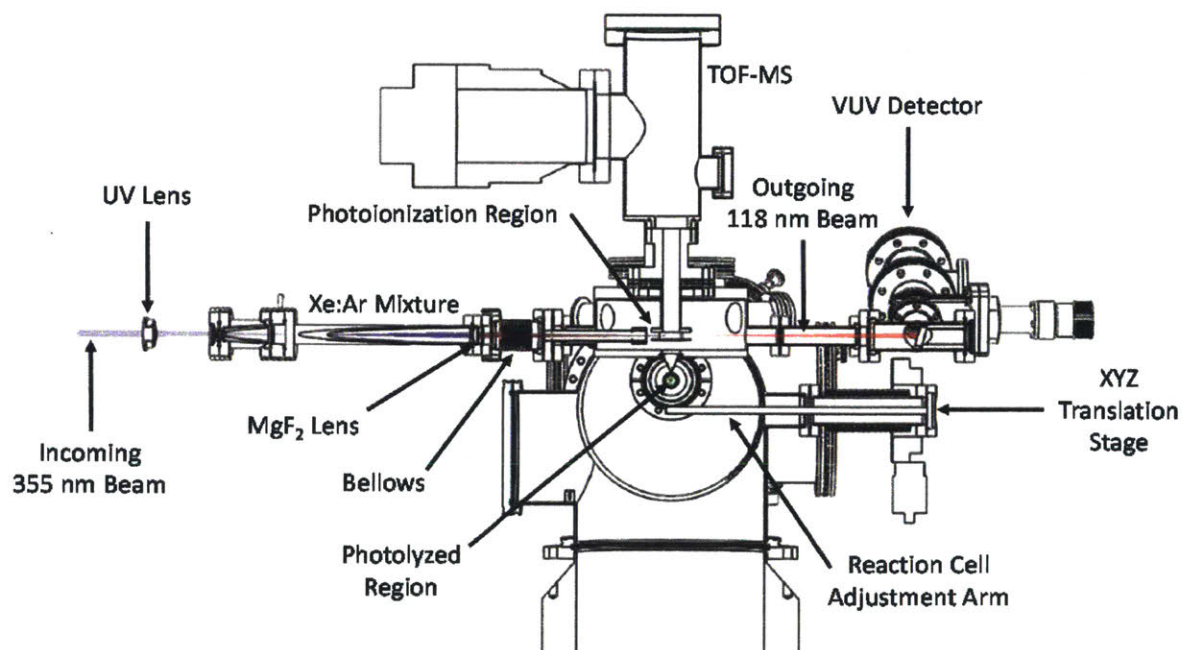
Figure 2-3: Side cross-sectional view of LAS and PI TOF-MS apparatus, showing VUV generation.

Gases are mixed upstream and pumped through the reactor by a roots blower. Pressure is controlled in the reactor by throttling a butterfly valve at the exit. The contents of the flow reactor are coaxially flashed by a collimated laser beam (usually either the fourth, 266 nm, or third, 355 nm, harmonic frequency of an Nd:YAG laser) at a set repetition rate (usually 1 Hz). The total gas flow through the reactor is set such that one flash per refresh (FPR) conditions are maintained. The photolysis beam is expanded by a set of telescoping lenses, and clipped by an adjustable iris to the same diameter as the narrow section of the reactor (16 mm). This approach to setting the photolysis beam diameter (expand and then clip) is intended to reduce radial inhomogeneities at the edges of the beam. A "funnel-shaped" pinhole, similar to that used by Wyatt et al.,[72] is drilled in the center of the reactor with a 275 μm diameter at the narrowest point. A small portion of the reactor contents are sampled through the pinhole, and the center of the resulting gas expansion is skimmed by a Beam Dynamics skimmer (Model 16.3, 1.0 mm orifice diameter), forming a molecular beam. After traversing ~50 mm, the molecular beam intersects with a focused 118 nm (10.5 eV) vacuum ultraviolet (VUV) laser beam (ninth harmonic frequency of an Nd:YAG laser) inducing PI. The VUV generation setup is shown in Figure 2-3. Cations formed in the ionization region are accelerated, focused, and guided to the detector of the Kore TOF-MS (ETP electron multiplier, model AF824) by a set of ion optics. Residual 355 nm radiation from VUV generation is dispersed by an off-axis MgF$_2$ lens and beam dumped in order to prevent undesired multi-photon or light-induced electron ionization. This improvement to the VUV generation setup is discussed in detail in section 2.2.1

The reactor is heated by nichrome ribbon wire in two zones. First, there is a 5 cm pre-heat zone slightly upstream of where the Herrott cell and photolysis laser overlap (referred to as the Herriott Cell Overlap region) that rapidly brings the room temperature flowing gas mixture to the desired temperature. Then there is a reaction zone that maintains the gas at near isothermal conditions for almost the entire remaining length of the reactor (up to the last 20 cm). The temperature of the gas leaving each zone is measured by a thermocouple inside the reactor and out of the path of the photolysis laser and Herriott cell. The thermocouple reading is used to control the power provided to each heated zone. Using this scheme, the temperature in the central 0.6 m corresponding to the Herriott Cell Overlap region only varies up to ±3% (2 standard deviations) of the full scale (Figure 2-4). The variance is even less for the 0.2 m region upstream of the reactor center, where products are sampled for TOF-MS (referred to as the MS

Sampling region). Temperature profiles were measured for nominal temperatures of 300-800 K, and 10-50 Torr of flowing helium with a 1 s residence time from gas inlet to outlet. All of the measured profiles were of similar quality as those in Figure 2-4.
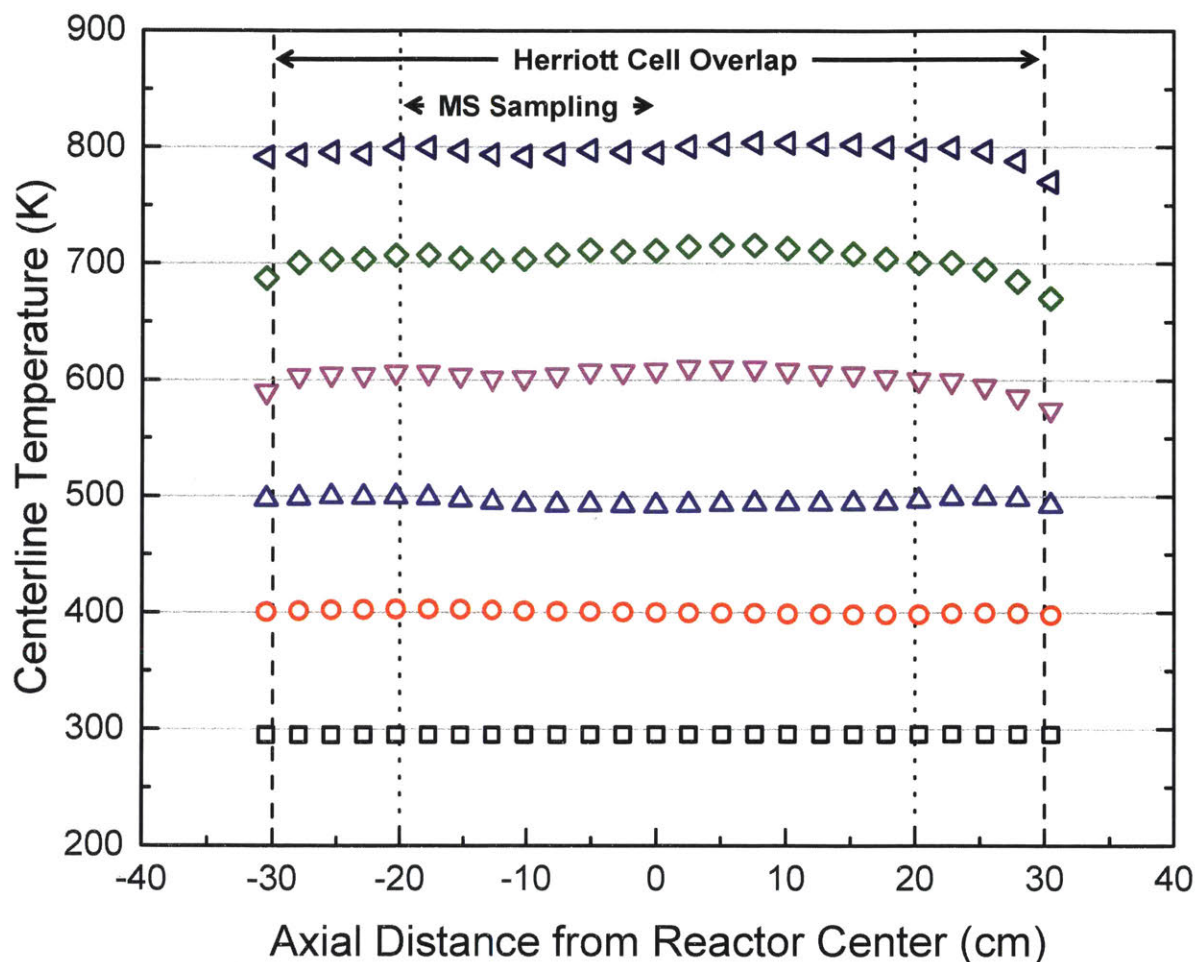
Figure 2-4: Representative axial centerline temperature profiles.

The current accessible T,P-range of this apparatus is 300-800 K and 1-50 Torr. The lower bound for T is set by room temperature (no controlled cooling capability yet) and for P the lower bound is set by the accuracy of the pressure gauge controlling the butterfly valve. Of course, a different P-gauge could be used with a lower range, so the real limit is set by the density of gas needed to observe the chemistry of interest. The high-T and high-P limits are closely related, as they are currently set by the maximum power output of the short pre-heater before it burns out. Both upper bounds have additional constraints as well. For T, many of the chemical precursors

that will photodissociate at 266 or 355 nm such as iodobenzene, C_6H_5I, will also start to thermally dissociate significantly on a 1 s time scale (residence time of reactor) as T approaches 1000 K.[73] For P, as discussed by Osborn et al., less than 10 Torr is desirable to allow fast (<1 ms) radial diffusion to "smooth out" any non-uniformity in photolytically-generated radical concentration due to a non-uniform beam profile.[64] However, this is mainly a concern if kinetics (i.e., time-dependence) are to be measured by time-resolved MS, in which case transport delays (including diffusion to the MS sampling region within the reactor) can and should be minimized to 10-100 μs.[64][65] In our case, however, kinetics are measured by LAS, which does not require any physical sampling of the reactive mixture (hence no transport delays) and which is also mostly insensitive to local concentration variations under pseudo-first-order conditions. Therefore, as long as the primary reaction products can be clearly resolved by TOF-MS before secondary reactions take over, a lower time resolution is acceptable, allowing both LAS and PI TOF-MS measurements up to 50 Torr in the current apparatus.

The Herriott cell consists of a UV/visible probe laser beam that passes through the photolyzed region of the reactor ~40 times by reflecting between a pair of mirrors on opposite sides of the reactor. The overall overlap pathlength between the Herriott cell and the photolyzed region is typically ~30 m. The probe beam is currently generated by a Spectra Physics Tsunami Ti:Sapphire laser (pumped by a Millennia Xs diode laser) with a GWU doubler/tripler module. Using this laser combination, reactive species have been probed at 375 nm (simplest Criegee intermediate[74-76]), 408.4 nm (allyl radical), 423.2 nm (vinyl radical[77]), 447.7 nm (benzyl radical) and 505.3 nm (phenyl radical). The reference and signal intensity, I_0 and I, of the probe beam are measured at the entrance and exit of the reactor by a pair of Thorlabs DET110 Silicon detectors and subtracted from one another to achieve a large reduction in noise.[67] Absorbance is calculated by the Beer-Lambert law, which is proportional to the concentration of the reactive species being probed (or mixture of species).

A fourth laser (New Focus Vortex TLB-6025 CW diode laser) outputs a beam centered at 1315.28 nm to quantitatively probe iodine (I) atom by its $^2P_{3/2} \rightarrow {}^2P_{1/2}$ hyperfine transitions.[78] This is useful for quantifying initial radical concentrations when an iodinated photolytic precursor is used, such as diiodomethane (CH_2I_2), vinyl iodide (C_2H_3I) or iodobenzene (C_6H_5I). The "I atom laser" beam passes through slits in the Herriott mirrors, counter to the probe laser, in

a single pass (~70 cm overlap with photolyzed region) and is focused on a Thorlabs DET10C InGaAs detector.

Absorbance traces (both from UV/visible probe and I atom lasers) are measured and averaged using a 1 GHz oscilloscope (Lecroy 6100A Waverunner), while mass spectra are measured and averaged using a 2.5 GHz oscilloscope (Tektronix DPO7254). Both oscilloscopes are triggered by a photodiode signal: for absorbance the trigger is the photolysis flash defining t=0 for reaction, and for mass spectra the trigger is the VUV PI laser flash defining t=0 for flight time in the TOF-MS. The timing of the experiment (firing of pulsed lasers) is controlled by a BNC 575 digital delay generator, which is used to scan the delay time between the photolysis and PI laser flashes. The entire experiment, including the temperature and pressure of the reaction cell, gas flows, timing and data acquisition/storage, is controlled by a custom LabView program. The data recorded is further analyzed by a custom MATLAB program that can automatically integrate MS peak areas at specified m/z's, and fit absorbance traces to common kinetic models such as pseudo-first-order and second-order decays.

2.2   Improvements to Apparatus

Two major improvements were made to the LAS and PI TOF-MS apparatus over the course of this thesis work: dissociative ionization in the TOF-MS was minimized by modifying the VUV generation setup, and the reactor material/geometry was changed for a number of reasons. Both improvements are discussed in the following two sections.

2.2.1   Minimizing Dissociative Ionization

Dissociative ionization, also referred to as fragmentation, is an unavoidable feature of MS detection. If a pure sample is being analyzed, fragmentation is desirable because it provides a unique fingerprint of the molecule with isomeric detail. For a mixture of chemical species, however, overlapping fragmentation patterns are difficult to disentangle and it is preferable for each species to produce one signal at their respective parent m/z. This is especially true for a mixture that is evolving with time, such as in a post-flash photolysis reactor, which is why "soft" photoionization (PI) is the ionization method of choice for time-resolved TOF-MS.[64, 79-82] The PI source used in our TOF-MS, as well as in many others, is the ninth harmonic frequency of a 1064 nm Nd:YAG laser, which generates 118.2 nm (10.487 eV) radiation, abbreviated as 118 nm (and 10.5 eV).[83] While providing an intense and convenient source of vacuum ultraviolet (VUV)

radiation suitable for ionizing most organic molecules,[84] the overall "up-conversion" of 1064 to 118 nm light is a very inefficient process and the wasted light must be dealt with in some way.

In the first step of the overall VUV-generation process, 1064 nm is frequency tripled to 355 nm in a solid crystal and the two wavelengths are separated by a set of coated dichroic mirrors such that the excess 1064 nm radiation can be beam-dumped inside of the laser housing. In the second step, 355 nm is frequency tripled to 118 nm in a mixture of xenon (Xe) and argon (Ar) gas under vacuum with an efficiency of ~0.0001%.[85] Various research groups have taken different approaches to handling the residual UV radiation: simply allow it to pass into the ionization region with the VUV and accept the consequences,[86] use a "waveguide" to direct the VUV to the ionization region while simultaneously attenuating the UV,[82] or separate the wavelengths with a grating[87] or some kind of prism.[88] [89] We have undertaken three of these approaches at different times (ignoring, waveguide and prism) and the results are discussed below.

Figure 2-5 shows results from a ray tracing simulation for both the 355 and 118 nm radiation during VUV generation if both wavelengths are permitted into the ionization region unperturbed (no waveguide or prism). The simulations were conducted using custom MATLAB scripts assuming:

1. Geometrical optics (diffraction not considered) because both wavelengths are much smaller than any physical feature of the system.
2. Paraxial approximation (refraction angles are small).
3. Perfectly thin lenses (thickness ignored).
4. Cylindrical symmetry (input 355 nm beam is perfectly aligned with optical system).

The 355 nm beam is focused close to the center of the Xe/Ar mixture (referred to as the Xe cell) by a UV fused SiO_2 lens where frequency tripling to 118 nm occurs. Both beams are then focused by an MgF_2 lens (suitable for VUV wavelengths), but due to their markedly different indices of refraction in MgF_2[90] the 118 nm beam is focused close to ionization region of the TOF-MS, whereas the 355 nm beam is focused much further away. In these simulations, the input 355 beam is assumed to have a "flat-top" intensity profile, although a Gaussian profile was also considered and gave similar results.
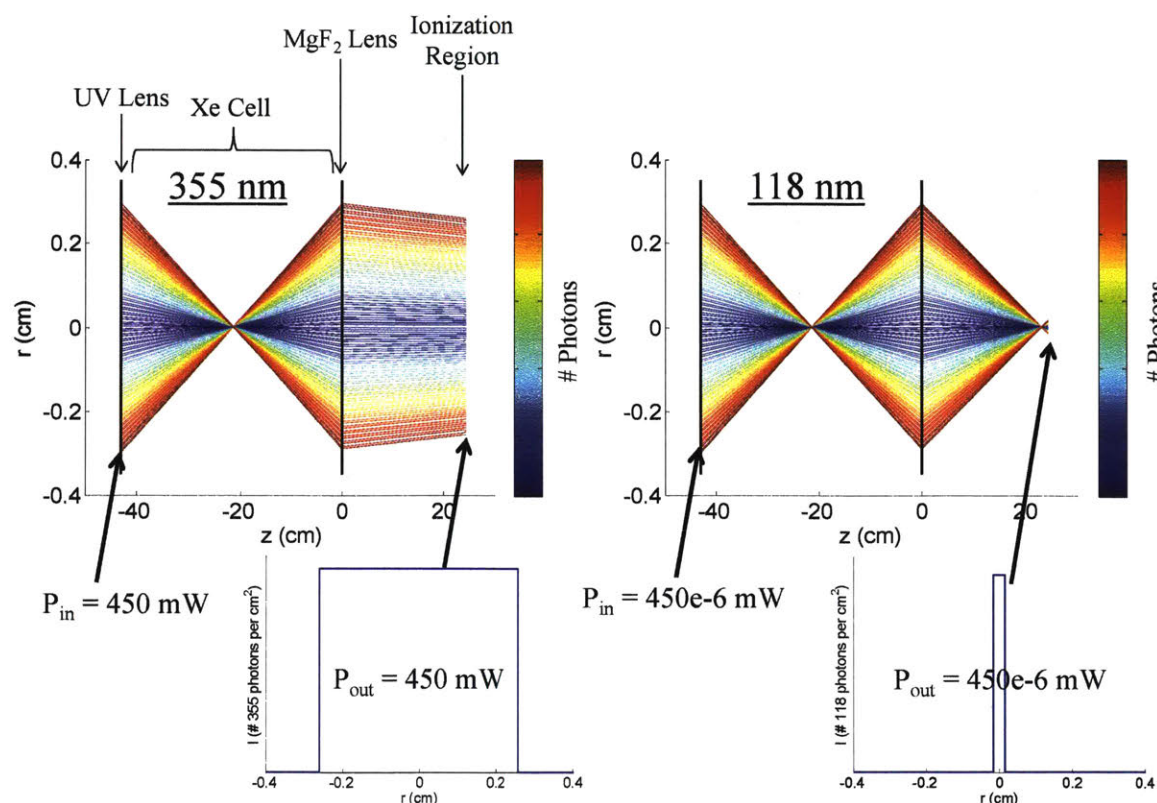
Figure 2-5: Ray tracing simulation results for VUV generation without a waveguide.

The blue mass spectra in Figure 2-6 demonstrate the two main issues that arise when nothing is done to attenuate, divert or dump the residual 355 nm radiation, as in the simulation of Figure 2-5. The first is that species with ionization energies (IE's) above 10.5 eV are observed in the MS. This is most clearly observed for helium, which is present in high concentration in the reactor as a bath gas but has an IE of 24.6 eV.[91] The second issue is unexpected fragmentation, such as C_2H_3I fragmenting to $C_2H_3^+$, which has an appearance energy (AE) of 11.3 eV.[92] Evidence of excessive fragmentation is also observed in the mass spectrum of the calibration gas mixture, which should only have peaks at nine m/z's corresponding to the parent masses of the nine species in the mixture (labelled in Figure 2-6). Many unidentified smaller peaks are clustered around the C2 (27-30 amu), C3 (39-43) and C4 (50-58) m/z's, indicative of fragmentation of larger species. Fragmentation is particularly problematic if time-resolved mass spectra are desired. For example, C_2H_3I is a common photolytic precursor of vinyl radical, C_2H_3, that has frequently been utilized by this lab for LAS experiments.[77, 93-96] However, its prospects as a photolytic precursor in time-resolved PI TOF-MS experiments are greatly diminished if it

always fragments substantially to C_2H_3, thereby obscuring any small, transient signals at the same m/z due to C_2H_3 chemistry. Based on the simulations of Figure 2-5, the large excess of 355 nm radiation in the ionization region is the prime suspect for both issues, either due to multiphoton ionization (MPI)[97] or light-induced electron impact ionization (LEI).[89] In either case, it was concluded that for our application it is not sufficient to simply allow the UV radiation through.
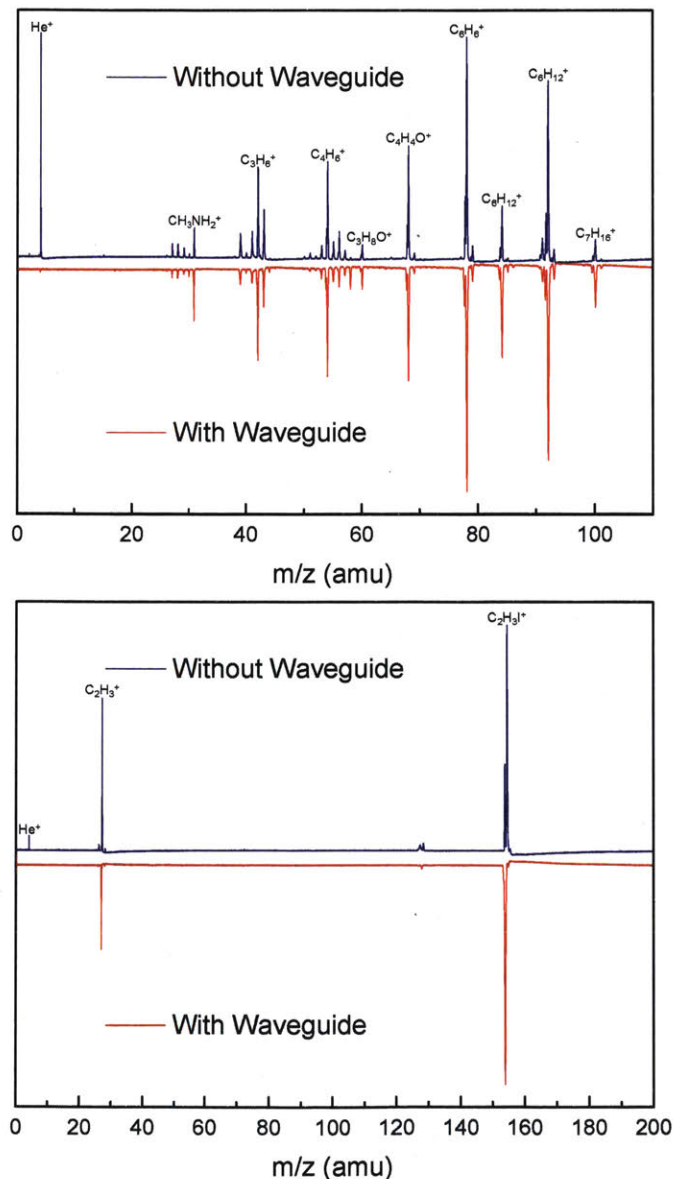
Figure 2-6: Mass spectra of calibration gas (top) and vinyl iodide, C_2H_3I (bottom), with and without a waveguide for the PI laser.

The first approach taken to reducing the overall UV radiation in the ionization region was to couple the immediate output of the MgF$_2$ lens with a hollow, glass "waveguide" that terminates near the ionization region. This design was taken from Blitz et al., where unexpected ionization of He was also observed initially.[82] Figure 2-6 shows mass spectra recorded with the waveguide, wherein He$^+$ was eliminated but excessive fragmentation of both the calibration gas and C$_2$H$_3$I persisted (also analogous to what was observed by Blitz et al.[82]). In order to gain further insight, Figure 2-7 shows the results of a ray-tracing simulation for VUV generation with a waveguide. The overall power in the ionization region, P$_{out}$, of both the 355 and 118 nm radiation are attenuated by absorbance of the waveguide glass (by factors of ~2 × for 355 nm and ~4 × for 118 nm), while the intensity of both wavelengths at the same axial point is predicted to sharpen (compared to the case without a waveguide, Figure 2-5). While it is expected that the waveguide will lower P$_{out}$, the second prediction is an artifact of the assumption of perfectly cylindrical symmetry (assumption #4 in the list above). If He ionization is a multi-photon process that requires x 355 nm photons, then the rate of He (non-resonant) MPI will depend on the intensity of 355 nm radiation, I$_{355}$, to the x power (MPI$\propto$I$_{355}^x$).[97] In contrast, the desired 118 nm single photon ionization (SPI) will depend linearly on I$_{118}$. Therefore, the attenuation of 118 nm power by the waveguide will result in a linear decrease in SPI, whereas the attenuation of 355 nm will result in a superlinear decrease in MPI (and possibly the elimination of observable He$^+$). Attenuating 355 nm P$_{out}$ will also reduce He ionization by LEI, wherein electrons are ejected by the photoelectric effect *via* 355 nm photons striking the metal walls and are subsequently accelerated by the ion optics. While this experimental and simulation exercise was illuminating in that it highlighted the importance of the residual UV radiation, it did not solve the main issue of excessive fragmentation. Furthermore, parameters of the waveguide (e.g., diameter, shape, material) could be optimized to attenuate more 355 nm without sacrificing 118 nm P$_{out}$, but fundamentally there will always be some residual UV in the ionization region if a waveguide is used. Therefore a fundamentally different approach was sought and implemented.
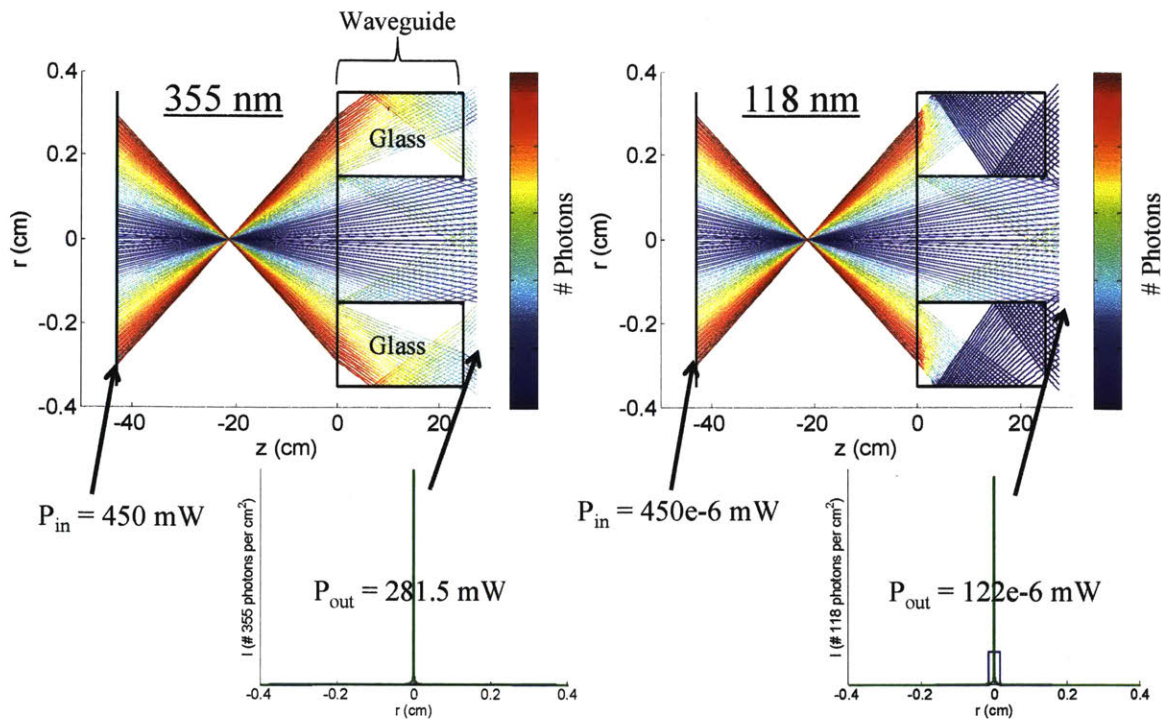
Figure 2-7: Ray tracing simulation results for VUV generation with a waveguide.

Before moving on, another interesting aspect of the waveguide design is worth mentioning: while the 355 nm radiation undergoes total internal reflection (TIR) inside of the glass where the index of refraction, n, is higher compared to vacuum, 118 nm TIR occurs inside the hollow vacuum core of the waveguide due to n being less than one for VUV wavelengths in glass.[98] This property of VUV radiation has previously been utilized for fiber optic applications,[99] and could perhaps be utilized in future applications to focus the divergent output of atomic resonance lamps.[100]

If leftover 355 nm radiation is the fundamental problem, as the previous results suggest, then the logical solution is to prevent it from ever reaching the ionization region. This can be accomplished by dispersing the two wavelengths and selectively permitting one into the ionization region. The dispersal can be accomplished with a grating,[87] a prism[88] or an off-axis lens.[89, 101] The latter, elegant solution, adapted from Tonokura et al.,[89] was used here and is summarized by the ray-tracing simulation in Figure 2-8 and the CAD drawing in Figure 2-9. In this design the MgF$_2$ lens both focuses the VUV in the ionization region and acts as a prism to separate the residual UV. After propagating a distance past the MgF$_2$ lens that is sufficient for

the two beams to completely separate (l_2), the VUV is aligned so as to pass through a small pinhole into the ionization region, while the UV is not and is blocked as a result. The dimensions in Figure 2-8 were roughly optimized for our apparatus considering the two goals (focusing of 118 in ionization region and blocking of 355) and constraints imposed by the stock vacuum parts and optics available. Figure 2-9 shows the physical VUV generation setup that was eventually used.
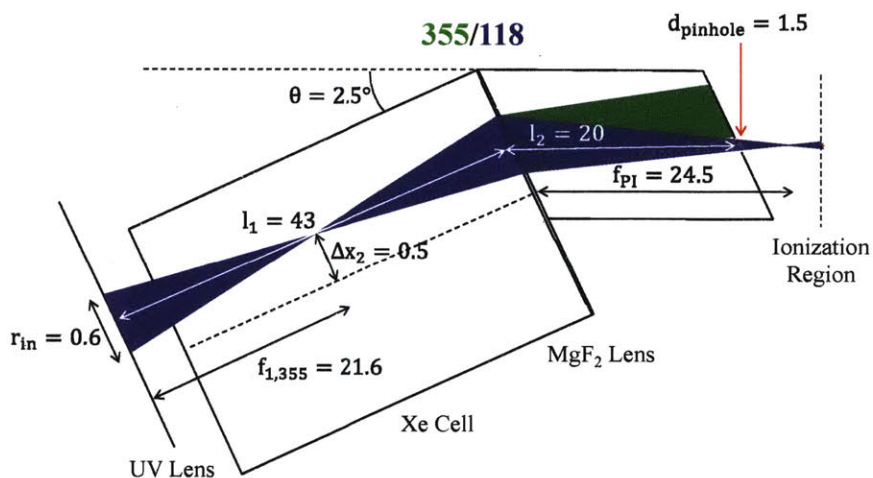
Figure 2-8: Ray tracing simulation results for VUV generation using MgF$_2$ lens as a prism to separate 355 and 118 nm radiation. All lengths are in cm.
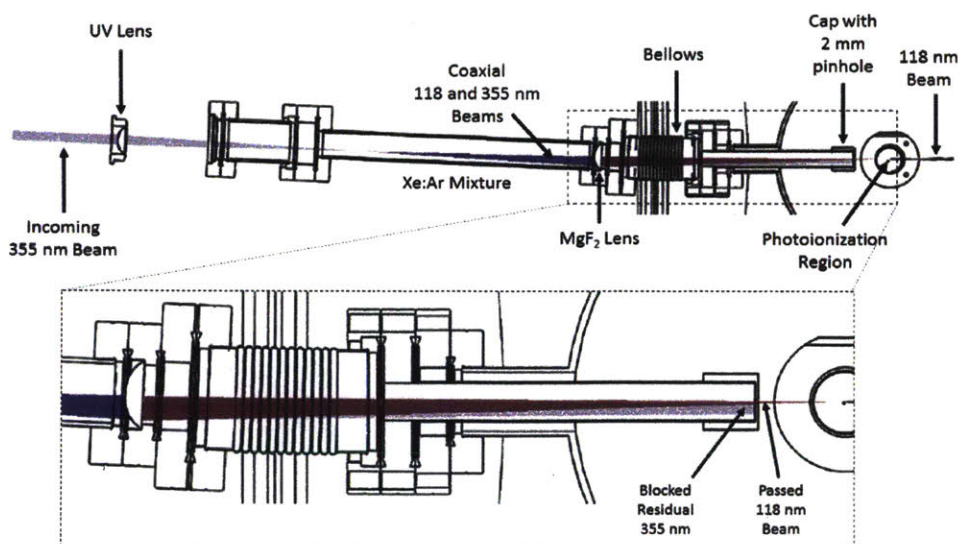
Figure 2-9: Top cross-sectional view of VUV generation using MgF$_2$ lens as a prism to separate 355 and 118 nm radiation.

As expected, once 355 nm radiation was eliminated from the ionization region, all irregular cation signals disappeared from the TOF-MS (Figure 2-10): He^+, C2, C3 and C4 fragments of the calibration gas, and $C_2H_3^+$ from C_2H_3I fragmentation. The lack of a giant $C_2H_3^+$ fragment allowed transient C_2H_3 to be observed with TOF-MS following C_2H_3I photodissociation. Similarly, it also became possible to measure transient C_6H_5 (phenyl radical) from C_6H_5I (iodobenzene) photodissociation with time-resolved PI TOF-MS, which was previously impossible due to fragmentation. More generally, the reduction in fragmentation greatly "cleaned up" the mass spectra, regardless of what was being sampled from the reactor. This was essential for interpreting the chemistry occurring during flash photolysis, which turned out to be more complicated than we initially assumed (e.g., wall catalysis and secondary reactions with I atom), as discussed in detail in section 4.2.
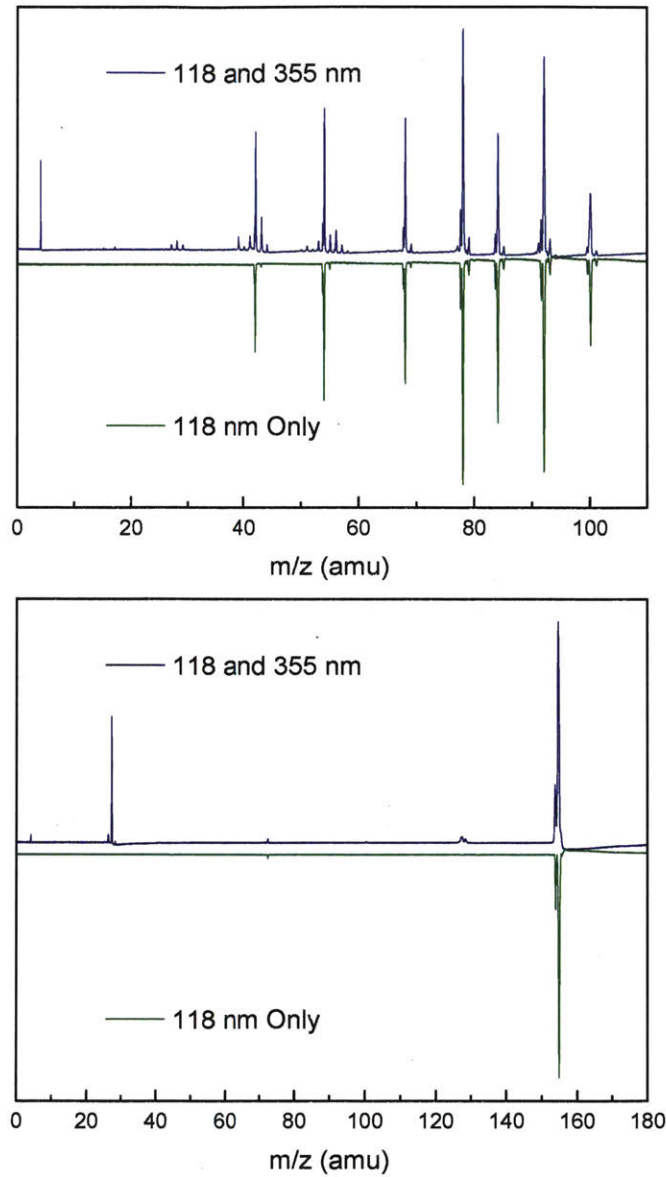
Figure 2-10: Mass spectra of calibration gas (top) and vinyl iodide, C_2H_3I (bottom), with and without residual 355 nm radiation in the photoionization region.

The following design equations can be used in lieu of a ray-tracing simulation (Figure 2-8) should modification or adaptation of the VUV generation setup be needed in the future:

$$f_{i,\lambda} = \frac{R_i}{n_{i,\lambda}-1} \tag{2-1}$$

$$f_{PI} = f_{2,118}\left(\frac{f_{1,355}-l_1}{f_{1,355}+f_{2,118}-l_1}\right) \tag{2-2}$$

$$\Theta = \text{atan}\left(-\frac{\Delta x_2}{f_{2,118}}\right) \tag{2-3}$$

$$l_2 = \frac{2r_{in}\left(1-\frac{l_1}{f_{1,355}}\right)}{r_{in}\left[\frac{2}{f_{1,355}}+\left(\frac{1}{f_{2,118}}+\frac{1}{f_{2,355}}\right)\left(1-\frac{l_1}{f_{1,355}}\right)\right]+\Delta x_2\left(\frac{1}{f_{2,355}}-\frac{1}{f_{2,118}}\right)} \times \left(\frac{1}{\cos\Theta}\right) \tag{2-4}$$

$$d_{pinhole} = \left(\left[\frac{l_2\frac{\cos\Theta}{\tan\Theta}-\Delta x_2\frac{l_2}{f_{2,118}}\cos\Theta-r_{in}\left(1-\frac{l_1}{f_{1,355}}\right)}{\frac{1}{\tan\Theta}-\frac{r_{in}}{f_{1,355}}-\frac{r_{in}}{f_{2,118}}\left(1-\frac{l_1}{f_{1,355}}\right)-\frac{\Delta x_2}{f_{2,118}}}\right] - \left[\frac{l_2\frac{\cos\Theta}{\tan\Theta}-\Delta x_2\frac{l_2}{f_{2,118}}\cos\Theta}{\frac{1}{\tan\Theta}-\frac{\Delta x_2}{f_{2,118}}}\right]\right)\times\left(\frac{1}{\sin\Theta}\right) \tag{2-5}$$

Many of the variables in Eq. 2-1 to 2-5 are shown pictorially in Figure 2-8. Equation 2-1 is the generic formula for calculating the focal length, $f_{i,\lambda}$, of a given lens i, at a wavelength λ, provided the lens's radius of curvature, R_i, and the index of refraction of λ in the lens material, $n_{i,\lambda}$. For the optical setup used here, there are only two lenses: the UV fused SiO_2 lens for focusing 355 nm in the Xe cell (i=1), and the MgF_2 lens used for focusing 118 nm in the ionization region and dispersing residual 355 nm to the wall (i=2). Equation 2-2 can be used to calculate the focus of the 118 nm beam, f_{PI}, relative to the MgF_2 lens, where l_1 is the distance between lens 1 and 2. Equation 2-3 gives the angle of the Xe cell relative to the normal of the apparatus, θ, such that for a given radial shift of the 118/355 nm beam from the centerline axis of the MgF_2 lens, Δx_2, the VUV beam will still be on-axis with the ionization region. Equation 2-4 gives the axial distance after which the 118 and 355 nm beams are perfectly separated, l_2, relative to the MgF_2 lens, where r_{in} is the initial radius of the 355 nm beam before it is focused by lens 1. Finally, Eq. 2-5 gives the diameter of the pinhole at l_2 that will allow all of the 118 nm radiation to escape, $d_{pinhole}$.

As an example of how they can be used, Eq. 2-1 to 2-5 are applied to the current setup. The focal length of the UV lens, and the distance between it and the MgF_2 lens should be chosen to maximize frequency tripling of the 355 nm beam. In our case, $f_{1,355}$ = 21.6 cm (R_1 = 10.3 cm, CVI Laser Optics PN: PLCX-25.4-64.4-UV-355) and l_1 = 43 cm were empirically found to maximize VUV generation. In other words, the 355 nm beam is focused roughly in the center of a long Xe cell. A suitable MgF_2 lens should then be chosen that will roughly focus the VUV in the photoionization region and allow sufficient 118/355 nm separation. In our case, a Thorlabs LA6007 MgF_2 lens with R_2 = 7.54 cm was used. Based on the different $n_{2,\lambda}$ for λ = 118 and 355 nm (1.66 and 1.39, respectively[90]) $f_{2,118}$ = 11.4 and $f_{2,355}$ = 19.3 cm, and according to Eq. 2-2 f_{PI} = 24.5 cm. Δx_2 should be as large as possible to maximize 118/355 nm separation. In our case, Δx_2 = 0.5 cm such that the off-axis 355/118 beam is still entirely within the 1.25 cm radius of the

MgF$_2$ lens. The necessary angular shift of the entire Xe cell assembly can then be calculated by Eq. 2-3 as 2.5°. For the actual set-up, there is a flexible bellows between the MgF$_2$ lens and the rest of the vacuum chamber that allows θ to be easily adjusted (Figure 2-9). Finally, the axial position of the pinhole relative to the MgF$_2$ lens and its diameter can be calculated by Eq. 2-4 and 2-5. For our case r_{in} = 0.3 cm, therefore l_2 = 18.9 cm and $d_{pinhole}$ = 0.14 cm. These values don't exactly match the dimensions in Figure 2-8 because other considerations were made in the ray-tracing simulations (i.e., what vacuum parts were available). The equations above also don't consider the thickness of the MgF$_2$ lens (thin lens approximation), while the ray-tracing simulations did with negligible effect.

2.2.2 Compact Quartz Reactor

Figure 2-11 shows the "compact quartz reactor" that was designed, installed, characterized and tested in this work. As suggested by its name, this reactor is both smaller (1.6-3.6 cm ID) and constructed of a different material (quartz) than the previous reactor.[68] In particular, the previous reactor was essentially a ~6 cm ID stainless steel tube with a pinhole-tipped cone protruding into the photolyzed region through which gases were sampled for PI TOF-MS. Both reactors have the same length (~1 m) because the same vacuum chamber with fixed dimensions was used to house both (Figure 2-2). The main motivation for changing the reactor material was to minimize catalysis of undesired reactions by the walls, which was only discovered after the TOF-MS was rid of excessive fragmentation as described in the previous section. The motivation for tightening the ID was to eliminate radial diffusion as a loss process in the MS Sampling region, so as to extend the longest chemical time scale that could be probed reliably with PI TOF-MS.
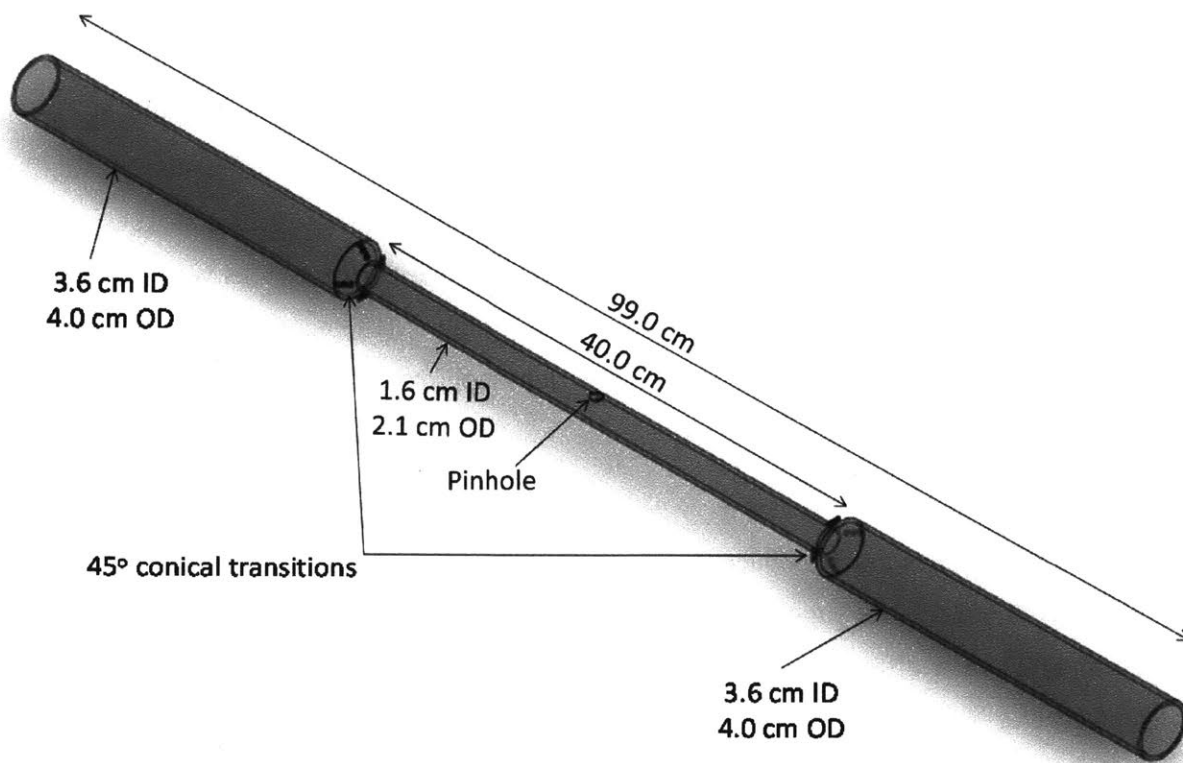
Figure 2-11: 3-D isometric view of compact quartz reactor with dimension.

Figure 2-12 provides two examples of wall catalysis in the compact quartz reactor from the same experiment. Following iodobenzene (C_6H_5I) photodissociation both phenyl radical (C_6H_5, m/z=77 amu) and I atom (127 amu) are promptly formed as expected. Unexpectedly, benzene (C_6H_6, 78 amu) is also formed promptly, and HI (128 amu) is formed gradually. The appearance of C_6H_6 and HI is surprising because it suggests both C_6H_5 and I are taking hydrogens, H, from somewhere, but in the gas-phase the only sources of H are C_6H_5I and C_6H_5 itself. Control experiments with varying [C_6H_5I] and [C_6H_5] verified that neither of these species is providing H to C_6H_5 or I. The same conclusion can be drawn by comparing the growth time scales of biphenyl (C_6H_5-C_6H_5, 154 amu) and C_6H_6 in Figure 2-12. Biphenyl appears on the same time scale as C_6H_5 is decaying (characteristic time ~10 ms), consistent with gas-phase recombination of C_6H_5. If C_6H_6 were also forming in the gas-phase through some direct reaction involving C_6H_5, then it should also appear on the same ~10 ms time scale, which it clearly does not. Although HI does appear to form at the same rate that I atom is decaying, the source of H is still mystifying.
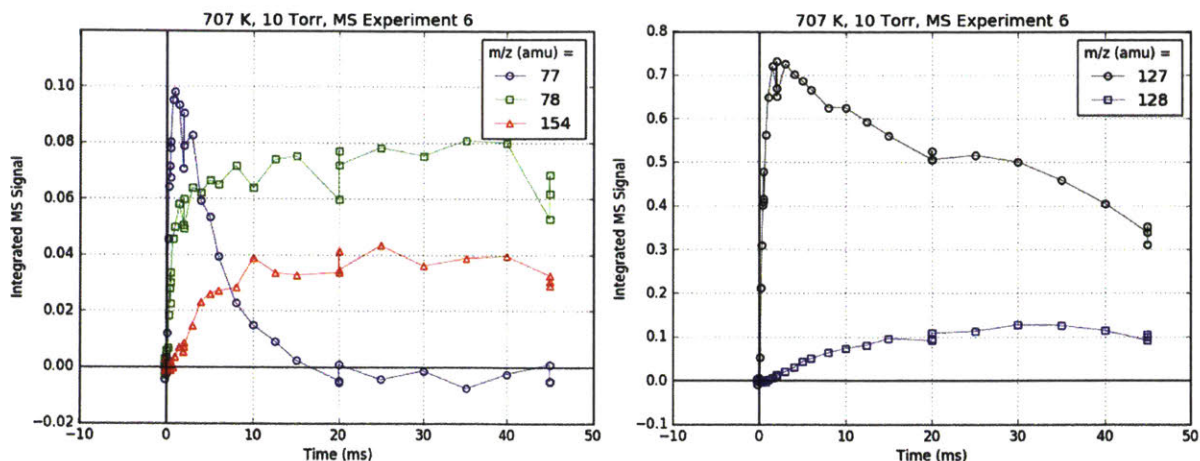
Figure 2-12: Examples of wall catalysis in compact quartz reactor following iodobenzene photodissociation: prompt benzene (78 amu) formation (left) and gradual HI (128 amu) formation (right). Refer to section 4.2 for complete experimental details.

If H is not coming from the gas phase, then it must be from an outside source, namely the walls. For example, H-atoms that are generated from gas-phase chemistry following photolysis might adsorb on and eventually saturate the walls (denoted H-wall). C_6H_5 that is formed in the gas-phase could then quickly abstract one of these weakly wall-bound H's *via* Eley-Rideal heterogeneous kinetics: $C_6H_5(g) + H\text{-wall} \rightarrow C_6H_6$. This kind of H-abstraction reaction on a surface has been observed previously between gas-phase fluorine atom, F, and deuterium, D, adsorbed on various surfaces, including quartz.[102]

From a bond-energy perspective, the ideal reactor surface would have only strong R-F bonds exposed, where R could be carbon, C, or silicon, Si. For example, halocarbon wax, which contains a mixture of C-F and C-Chlorine bonds, is commonly used to coat the inner surfaces of photolysis reactors for low-T kinetic studies.[81] More commonly, Teflon, or polytetrafluoroethylene (PTFE), has become a household name over the last century because of its "non-stick" (low reactivity) property. Unfortunately, neither halocarbon wax nor Teflon are suitable for the highest temperatures of interest in this work (800 K), therefore quartz is still the standard reactor material in the field of high-temperature gas-phase kinetics. In particular, the use of boric-acid treated quartz, which has an inert layer of boron oxide, B_2O_3, was first proposed by Krasnoperov et al.[103] and has been successfully applied to many other high temperature kinetic studies since then. However, the MS time profiles shown in Figure 2-12 were

obtained using a boric-acid treated quartz reactor, which was clearly not sufficient to reduce wall catalysis below the detection limit.

The extent of wall catalysis (quantified by the ratio of maximum C_6H_6 to C_6H_5, which is ~1:1 in Figure 2-12) observed in the compact quartz reactor is about the same as what was observed in the previous stainless steel reactor, suggesting that perhaps it is not the actual reactor walls that are catalyzing H-abstractions, but whatever has accumulated on them over the course of experiments. Given that the inner walls of the quartz reactor exhibit a yellow/brown tint even after only a few flash photolysis experiments with phenyl radical (~10k flashes total), it seems likely that heavy aromatic or iodinated molecules are condensing on the surface, which could certainly have consequences for the gas-phase chemistry of interest. If this is the case, lower radical concentrations could be used to keep the reactor clean for longer, but as shown in the following section we are already operating at the optimal initial radical concentration of ~10^{12} cm^{-3}. Lowering the radical concentration further would bring both the LAS and PI TOF-MS measurements close to their respective detection limits, especially if a heavy excess reagent such as propene, C_3H_6, is also present in high concentration.

As shown later using C_6H_5 + C_3H_6 as an example (section 4.2) the most practical approach to extracting reliable product branching information from the time-resolved PI TOF-MS experiments, even with wall catalysis, is through control experiments. Specifically, if enough excess reagent is added (C_3H_6 in the example) C_6H_5 will react faster in the gas-phase than it can abstract an H from the walls. By varying [C_3H_6] we can verify that this limit has been reached. Of course, the radical products of C_6H_5 + C_3H_6 might also undergo wall catalysis, thereby confusing the product distribution further. For example, the radical adduct of C_6H_5 + C_3H_6 might also abstract an H from the wall to make propylbenzene. This kind of secondary wall effect can also be accounted for with control experiments, specifically at higher temperatures, the radical adduct will unimolecularly isomerize and decompose faster than it can react on the walls.

Because a lot of the chemistry of interest to us is inherently "dirty" (e.g., molecular weight growth to PAH), accumulation of heavy products in the reactor and subsequent wall catalysis is an inevitable consequence of using flash photolysis with an intrusive detection technique such as time-resolved PI TOF-MS. This would explain the proliferation of recent literature on molecular weight growth chemistry under single-collision conditions (no walls),[10][20] or qualitative end-product analysis (no time dimension) of a high-temperature reactor.[35][41]

Conversely, other than the work of Park and Lin,[43] there is a dearth of thermalized flash photolysis experiments with time-resolved product detection studying the same chemistry. Nonetheless, there are advantages to conducting such experiments, as will be demonstrated for $C_6H_5 + C_3H_6$, if one is willing to wade through the associated challenges (e.g., wall catalysis).

As a final note regarding wall catalysis, although the C_6H_6:C_6H_5 ratio in Figure 2-12 is not significantly better than what was obtained in the previous stainless steel reactor, it could be demonstrably worse. Specifically, it was observed that with a constricted sampling pinhole (essentially a 300 μm tube through the 2.5 mm thick quartz reactor wall) C_6H_6:C_6H_5 was as high as ~10:1, depending on the reactor pressure, due to wall catalysis within the long and narrow pinhole. This situation was remedied, and the ratio brought down to the more manageable 1:1 seen in Figure 2-12 by adopting the "funnel-shaped" pinhole geometry of Wyatt et al.[72] and Park and Lin,[43] shown in Figure 2-13. Essentially, the narrow section of the pinhole should be as short as possible to minimize the residence time of reactive species during sampling. The funnel-shaped geometry can be achieved either by mechanical or laser drilling.
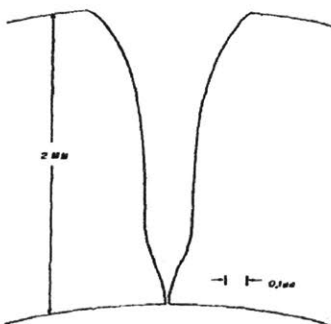
Figure 2-13: "Funnel-shaped" pinhole geometry used to minimize wall reactions. Taken from Wyatt et al.[72]

Besides wall catalysis, the compact quartz reactor design was also intended to eliminate radial diffusion loss from the MS Sampling region. Figure 2-14 shows snapshots of a COMSOL simulation conducted by Te-Chun Chu of the transport processes (no chemistry) occurring in the large-ID (6 cm) reactor. When the photolysis laser is fired at t=0 ms, a concentrated, 1.3 cm diameter core of radicals (I atom in the simulation) is created near the sampling pinhole. Within 8 ms the concentration of I atom in the core has dropped by about an order of magnitude due to fast radial diffusion at the relatively low pressure of the reactor (10 Torr, 500 K), and within 16 ms the I atom has a uniformly low concentration throughout the reactor. Experimentally, at the

same conditions, PI TOF-MS signal at 127 amu from photolytically generated I atom was also found to decay to a constant level (~10% of peak value) within ~15 ms. While fast radial diffusion is not a problem for a high time-resolution detection technique like LAS that can measure processes down to ~1 μs, for PI TOF-MS, which will be shown in the next section to have ~1 ms time resolution, this leaves a very narrow time window (if any) during which product branching can be quantified before all of the stable products diffuse out of the MS sampling region. Of course, the reactor pressure could simply be increased, which according to the correlation of Fuller et al. would linearly increase the diffusion time scale.[104] However, the simulation of Figure 2-14 assumes that the photolysis laser intensity is radially uniform, which in reality it is not. Therefore, as discussed by Osborn et al.,[64] radial diffusion is actually desirable to "smooth out" initial non-uniformity *within* the concentrated core of radicals created at t=0. The conundrum is then the following: radial diffusion should be fast *within* the core of radicals (<1 ms) but slow outside of it. The obvious solution used throughout the field is to restrict radial diffusion outwards by matching the reactor ID with the photolysis laser diameter, which was the same approach taken here with some modification.
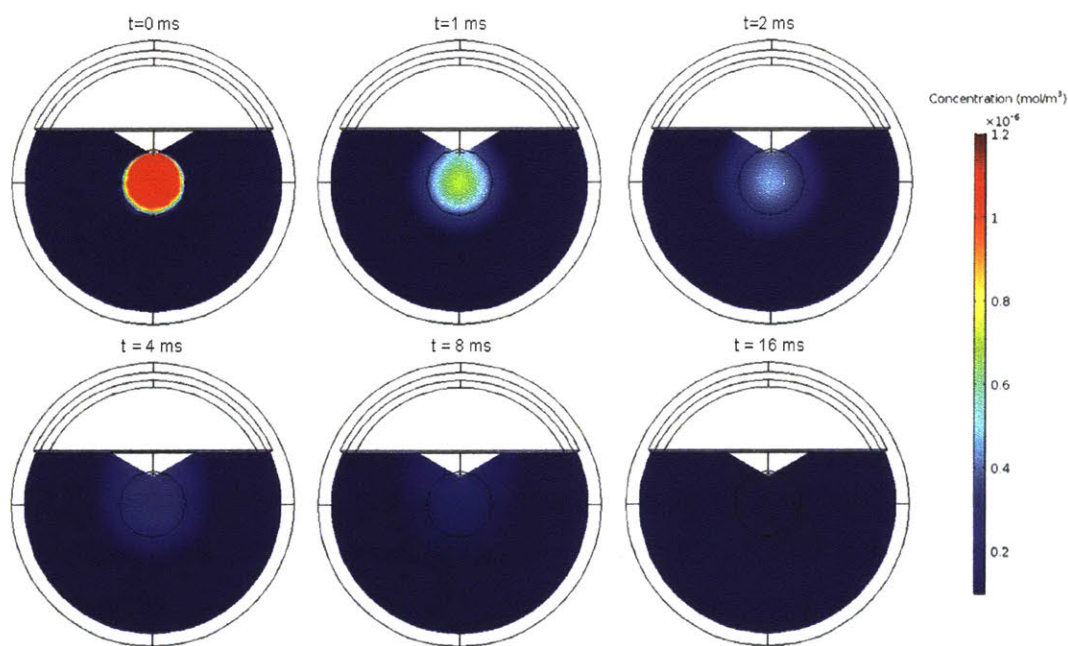
Figure 2-14: COMSOL-simulated cross-sectional concentration profiles of photolytically-generated I atom in the large-ID (~6 cm) stainless steel reactor. Cross sections are shown at the axial center of the reactor (where sampling for MS occurs). Photolysis beam diameter is 1.3 cm and reactor conditions are 500 K and 10 Torr. Courtesy of Te-Chun Chu.

The challenge for our apparatus is to design a reactor that will restrict radial diffusion loss in the MS Sampling region while still accommodating the Herriott Cell for LAS. With the aid of some COMSOL simulations, the compact reactor geometry shown in Figure 2-2, Figure 2-11 and Figure 2-15 was chosen because it could meet both criteria. Figure 2-15 compares radial profiles of the compact quartz reactor with the photolysis laser and Herriott cell that must fit inside of it. The radius of the Herriott cell, $r_{Herriott}$, was calculated as a function of axial distance, z, according to the following equation[69]:

$$r_{Herriott} = r_{in}\left[1 + 2\frac{L}{R_{mirror}}\left(\left[\frac{z}{L}\right]^2 - \left[\frac{z}{L}\right]\right)\right]^{\frac{1}{2}} \qquad (2\text{-}6)$$

where r_{in} is the radius of the Herriott cell at the mirrors (usually ~1.6 cm), L is the distance between mirrors (~150 cm) and R_{mirror} is the radius of curvature of the mirrors (80.0 cm for the current pair). As shown, the Herriott cell was calculated to fit inside of the compact quartz reactor (central 100 cm) and associated vacuum hardware (everything outside of the central 100 cm), which was later verified experimentally.
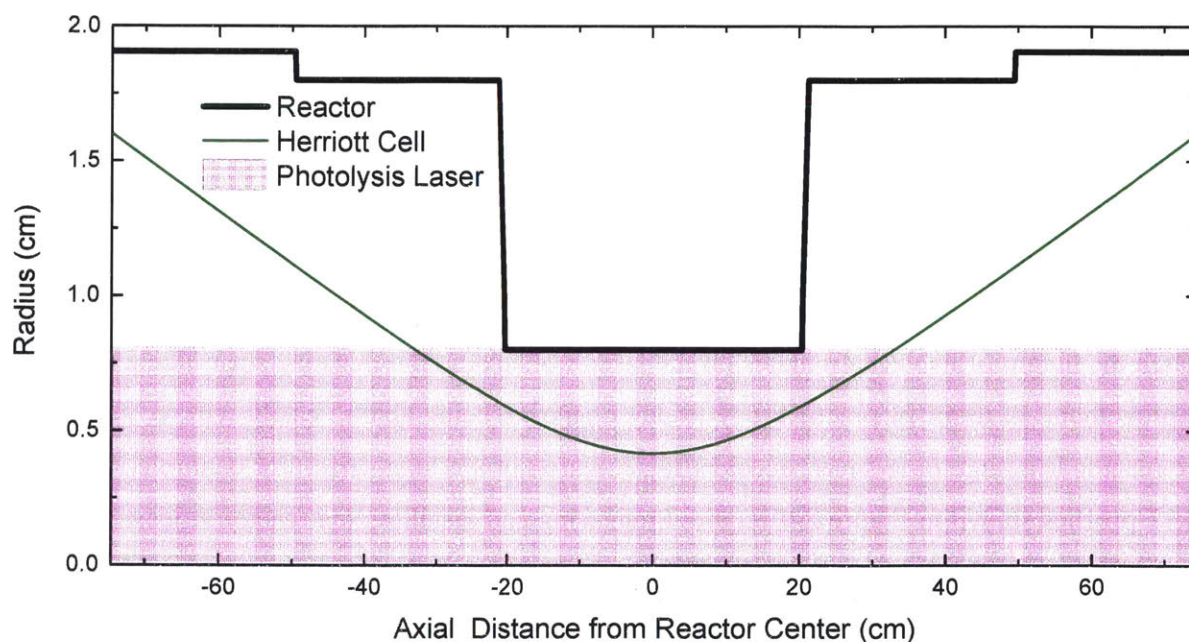
Figure 2-15: Axial profiles of compact quartz reactor and lasers that must fit inside of it.

Most importantly, for an overall residence time of 1 s (gas inlet to outlet, Figure 2-2) corresponding to a 1 Hz experiment, the residence time in the MS Sampling region (20 cm of narrow, central section upstream of pinhole) of the compact quartz reactor is ~50 ms. After 50

ms the TOF-MS signal will start to decrease due to dilution by upstream gas, but up until that point there should be no decrease in TOF-MS signal due to transport effects (i.e., no radial diffusion out of the MS Sampling volume). This can be seen in Figure 2-12, where the 127 amu signal from I atom has only decreased by ~50% after 45 ms (likely due to I atom abstracting an H from the wall to make HI) and all of the stable products (benzene, biphenyl and HI) stay at their steady state concentrations for the full 45 ms. Eliminating transport losses for time-resolved PI TOF-MS, even for only ~50 ms, widened the window of time during which stable product branching could be measured and even enabled the observation of secondary products at later times that might not have been possible to see before (see C_6H_5 + C_3H_6 example in section 4.2).

There are three other benefits to the compact quartz reactor design. The first is that because of its narrow diameter (4.0 cm OD at most) and because it is held in place by hand-tightened Ultra-Torr fittings (Figure 2-2), the entire reactor (including the Ultra-Torr fitting) can simply slide out of the side of the vacuum chamber. Although this process does require removing one of the Herriott crosses, it only takes one person about an hour to go from doing an experiment with the reactor under high vacuum to having the reactor out of the chamber and in his or her hands. Re-installing the reactor in the vacuum chamber is just as easy and can also be done in about an hour. In contrast, to remove the larger diameter stainless steel reactor from the vacuum chamber required about a day's worth of work, mostly because the entire apparatus had to be rolled out of its niche in the laser table. Re-installing the previous reactor would take even longer, because once the apparatus was back in place its height had to be carefully adjusted to match the height of its vacuum mates on the laser table. Although this may seem like a mundane improvement, in terms of practical day-to-day operation being able to easily remove and install the reactor is a huge time-saver, accelerating research in the long–term. For example, obtaining the T profiles shown in Figure 2-4 required removing and installing the reactor at least ten times in order to try different heater patterns. The reactor can also be cleaned/coated more frequently, which as mentioned earlier might help with some of the wall catalysis issues. Finally, if the Herriott cell alignment is lost then the reactor can be pulled out and the Herriott cell easily realigned in the open without the reactor walls imposing an additional constraint.

The second additional benefit is that because the overall inlet to outlet volume of the reactor has been reduced by about half, the amount of gas needed per photolysis flash (assuming one flash per refresh) is also cut in half. Less gas use is a boon both economically (some of the

chemical precursors like vinyl iodide are quite expensive) and environmentally ("use only what you need").

The final benefit is that due to the lower thermal conductivity of quartz compared to stainless steel, higher T's can be reached without overheating the vacuum seals or the flexible bellows on either the inlet or outlet side of the reactor. In fact, other research groups that use quartz reactors for time-resolved TOF-MS routinely reach T's of ~1000 K,[64] a limit that we hope to approach eventually. Before the new reactor design was finalized, COMSOL simulations were conducted to confirm the T,P-range over which we could reasonably expect to operate (Figure 2-16). The main constraints considered were the melting point of the Kalrez o-rings (600 K) making the vacuum seal between the reactor and the rest of the chamber, and the strain point of quartz (1170 K). The simulations were also helpful in sizing the pre-heater, i.e., choosing what length and what kind of nichrome ribbon wire to use. At lower pressure, less power is needed to bring the lower-density gas to the desired temperature, and all of the constraints are satisfied. Even up to 50 Torr and 700 K none of the constraints are exceeded, but at 100 Torr the outer wall T starts to exceed the quartz softening point. In reality, we found that if the pre-heater was worked too hard, it would simply burn out, which empirically allowed us to estimate the current T,P-limit as 300-800 K and 1-50 Torr (900 K has not been attempted yet). Most importantly, as shown in Figure 2-4, temperatures up to 800 K have been reached with the compact quartz rector without incident, whereas the only attempt to reach 800 K with the stainless steel reactor resulted in overheating and warping of the flexible bellows that then required replacement.
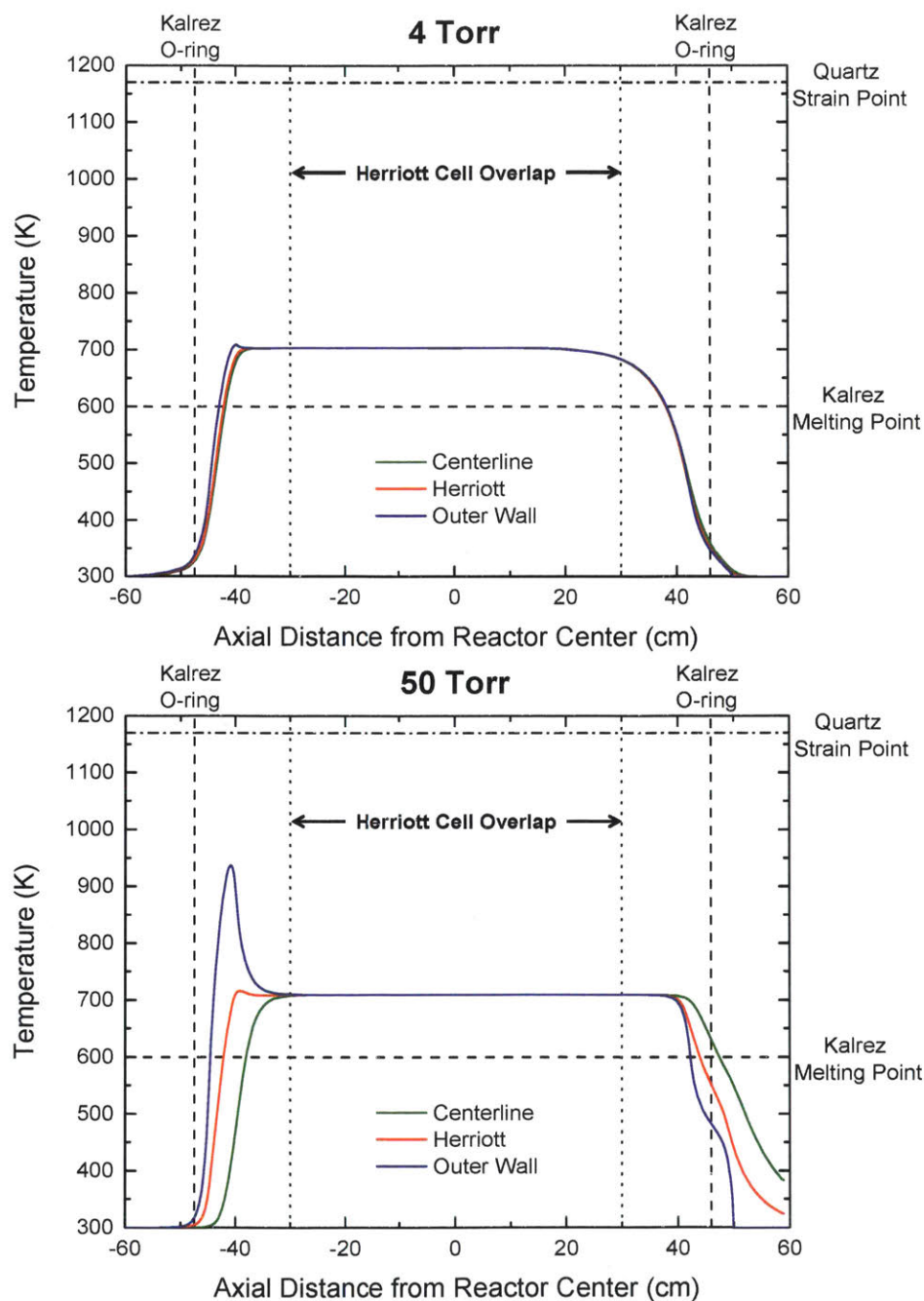
Figure 2-16: COMSOL-simulated temperature profiles in compact quartz reactor at 4 (top) and 50 Torr (bottom) for ~0.5 s residence time (2 Hz flash photolysis experiment). Important design constraints are also shown.

To summarize, tightening the diameter of the flash-photolysis reactor has three clear benefits:

1.) The longest chemical time scales that can be measured with time-resolved PI TOF-MS before

transport effects become competitive was extended from <10 ms to ~50 ms. 2.) The reactor is now easy to remove from and install in the vacuum chamber. 3.) Less gas is needed for the same experiment. In contrast, switching the reactor material from stainless steel to quartz had only one clear benefit: experiments can be conducted at 800 K, with the possibility of extending this limit up to 1000 K. Wall catalysis is still an issue, but it is at least no worse than before, and its effect on product branching can be checked by control experiments. Given the number of quartz reactors that were broken in this process (at least five) future consideration should be given to using the same compact reactor geometry of Figure 2-11, but fabricated out of a material stronger than quartz.

2.3   Characterization of Modified Apparatus

All of the characterization below applies to the apparatus after implementing the improvements described in section 2.2 (only 118 nm single photon ionization used to create cations for TOF-MS, and compact quartz reactor). Estimates for both LAS and PI TOF-MS sensitivity are discussed in section 2.3.1, the time-resolution for both detection techniques is discussed in section 2.3.2 (as well as the mass-resolution for PI TOF-MS) and the expected precision and accuracy of overall kinetics and product branching measurements made with this apparatus are discussed in section 2.3.3.

Although this characterization is helpful for clearly defining the current limitations of the apparatus and brainstorming future improvements, the real test for the modified apparatus is if it can be used for its original intended purpose: simultaneous measurements of overall kinetics with high time-resolution by LAS and quantitative product branching with time-resolved PI TOF-MS. This capability is demonstrated for the chemically-interesting phenyl radical + propene $(C_6H_5 + C_3H_6)$ system in section 4.2. Note that all of the other chemical systems experimentally studied in this thesis (1,3-cycloadditions of the simplest Criegee Intermediate in Chapter 3, and vinyl radical + 1,3-butadiene in Chapter 4) were probed using the original LAS and PI TOF-MS apparatus described by Middaugh.[68] However, for those systems the main contribution was accurate quantification of overall consumption kinetics (not product branching) using LAS. Because the LAS portion of the apparatus was largely unaffected by the improvements described above (by design), it is unimportant which iteration of the apparatus was used for LAS

experiments. If anything, LAS was easier to do in the larger-ID reactor because there was much more space for the Herriott alignment (in contrast to the tight alignment of Figure 2-15).

2.3.1   Sensitivity

As already mentioned, the LAS portion of the apparatus was unaffected by the improvements discussed in section 2.2. Therefore, the same cross section weighted detection limit for LAS estimated by Ismail still applies: $\sigma_i C_i = 3.3 \times 10^{-8}$ cm^{-1}.[67] For phenyl or vinyl radical, both of which have visible absorption cross sections $\sim 10^{-19}$ cm^2,[96, 105] this corresponds to a minimum detectable concentration of $\sim 10^{11}$ cm^{-3}. The main sources of noise are the Millennia Xs pump laser and thermal lensing of the Herriott cell within the heated reactor.

Before reporting measurements of the PI TOF-MS sensitivity, it is helpful to estimate the expected detection limit using simple calculations. To begin, the detection limit for TOF-MS detection is defined as the point at which only one ion is generated per photoionization laser shot (single ion counting limit). Several assumptions are then made. First, typical 355 to 118 nm conversion efficiency are only 0.0001%,[83] such that for 50 mJ pulse^{-1} of 355 nm input energy, $\sim 10^{11}$ photons of VUV should be generated. Second, it is assumed that the free jet density drops by two orders of magnitude relative to the reactor density before being skimmed 2 mm from the reactor pinhole, after which the molecular beam has minimal spread in the transverse direction.[106] Finally, a typical photoionization cross section of 10^{-17} cm^2 (10 MB) is assumed, which gives a detection limit of 10^9 cm^{-3} in excellent agreement with our measured detection limit below. Typically we operate at conditions such that the TOF-MS signals for important products of a photolytically initiated reaction are 1-2 orders of magnitude above the detection limit, and are therefore well above the single ion counting regime.

The sensitivity of the PI TOF-MS portion of the apparatus was measured using a custom calibration gas mixture. The mixture, which contained seven species diluted in helium (propene, 1,3-butadiene, furan, benzene, cyclohexane, toluene and heptane) with known concentrations and known photoionization cross sections, was also used to calibrate the conversion of time-of-flight to m/z in the TOF-MS.

The signal for any given species i in the TOF-MS is given by Eq. 2-7:

$$S_i = \sigma_i R_i C_i \tag{2-7}$$

where S is the signal (integrated m/z peak area), σ is the photoionization cross section at 10.487 eV, R is the mass discrimination factor, and C is the concentration in the reaction cell. Equation

2-7 is a simplification of the complete relationship between S and C,[64] but will suffice for our purposes. The mass discrimination factor is an instrument-dependent conversion factor that accounts for any systematic differences in signal due to differences in the gas sampling and the detection efficiencies for each species. Technically, every species has its own mass discrimination factor, but typically this parameter is mostly a function of mass-to-charge ratio (m/z) and is not strongly dependent on the exact identity and features of the species being detected. The mass discrimination factor for the PI TOF-MS was measured by the calibration gas signal during an experiment (phenyl radical + propene at 707 K and 10 Torr) and is shown in Figure 2-17. Note that of the seven calibration gas species, only four could be used in this analysis because the remaining three (propene, benzene and toluene) overlapped with some other species or precursor impurity in the reactor during that particular experiment. The mass discrimination factor was fit to a power law:

$$R_i = A \left[\frac{m}{z}\right]^b \tag{2-8}$$

which is the functional form typically used to match R. The fit in Figure 2-17 uses b=0.57, similar to the square root dependence on m/z empirically observed before.[64] Interestingly, without excess propene present in the reactor no dependence of R_i on m/z was observed across the entire calibration gas range (42-100 amu). Nonetheless, for the combustion applications of current interest to us, a heavy hydrocarbon like propene will often be present in the reaction mixture. Therefore, the best approach to quantifying R_i (needed for subsequent product quantification) is to fit the measured signals *in situ* of a small known concentration of calibration gas, such as in Figure 2-17.
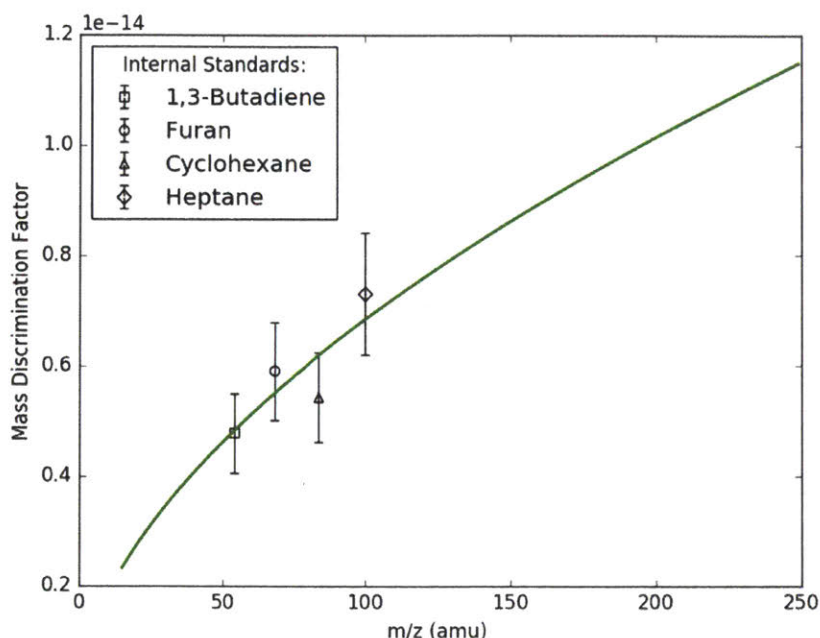
Figure 2-17: Mass discrimination factors measured (markers) at 707 K, 10 Torr during a phenyl radical + propene experiment. Error bars are from 15% uncertainty in photoionization cross sections and line is a power law fit.

The detection limit for the PI TOF-MS was estimated by measuring signals from the species in the calibration gas mixture using various levels of dilution, and comparing them to the noise in the baseline of the mass spectra after averaging 100 times. To account for the fact that each species has a different photoionization cross section, and thus gives a different signal for the same concentration, the signal-to-noise ratio (S_i/N) is plotted versus the cross section weighted concentration ($\sigma_i C_i$, Figure 2-18). Plotting versus $\sigma_i C_i$ effectively collapses all of the data onto a single line (accounting for at least 15% cross section uncertainty), which was fit using the least-squares method. Defining the minimum discernable signal to correspond to $S_i/N = 3$, the detection limit for the PI TOF-MS is estimated to be $\sigma_i C_i = 2 \times 10^{-8}$ cm^{-1}. In terms of a typical organic molecule such as propene (~10 MB photoionization cross section[84]) or a radical such as phenyl (~17 MB[107]) this detection limit corresponds to ~10^9 cm^{-3}, identical to the single ion counting limit estimated above, and about two orders of magnitude lower than the LAS detection limit. However, this detection limit is an optimistic estimate because it was measured with only helium bath gas. In a real experiment, there will often be a large organic molecule (e.g. propene) also present in high concentration that tends to lower the S/N for a given $\sigma_i C_i$ due to both

attenuation of VUV photons and a decrease in the molecular beam density for a heavier carrier gas.[108] Therefore, initial radical concentrations during actual experiments were typically $\sim 10^{12}$ cm^{-3} such that the various stable products formed have concentrations $\sim 10^{11}$ and give MS S/N's of at least 10 (above single ion counting limit) even in the presence of a heavy excess reagent. This initial radical concentration is also ideal for LAS as it is 10× that detection limit, but not so high that radical-radical recombination will become a significant problem (typical high-pressure bimolecular rate coefficients of $\sim 1 \times 10^{-10}$ cm^3 molecule^{-1} s^{-1} for vinyl[96] and phenyl radicals[109]).

Another feature of Figure 2-18 worth commenting on is the linear dependence of S/N on C_i for a given species, such as benzene or toluene. It is reassuring that in the S/N range of 10-100 where most products were quantified the MS detector is within its linear response regime.
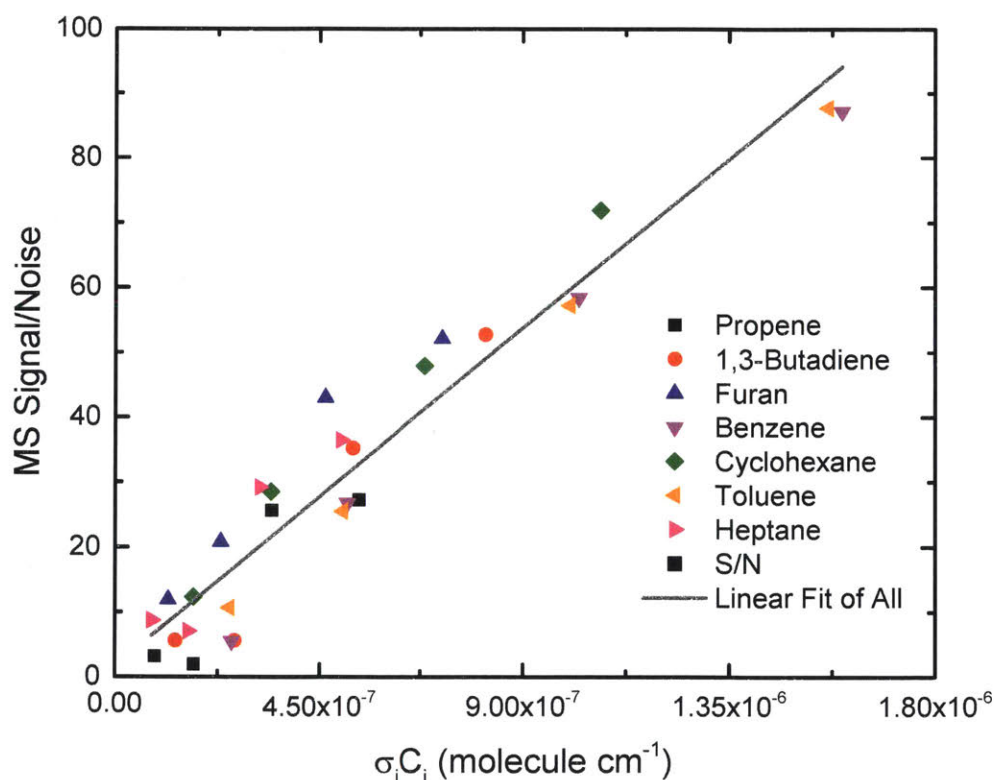
Figure 2-18: Calibration gas measurements used to determine detection limit of PI TOF-MS. Courtesy of Te-Chun Chu.

2.3.2 Time and Mass Resolution

Because the Ti:Sapphire laser is actually pulsed at 80 MHz, or every 12.5 ns, the fastest possible reaction timescale that can be measured by LAS is limited to 10× this value in order to

have at least 10 points to fit during the decay. For a pseudo-first order system, this timescale corresponds to a maximum reaction rate of $k' = 8 \times 10^6 \, \text{s}^{-1}$. However, this upper-limit is constrained further by considering the effect of RC electronics on the signal during data acquisition. Specifically, the Stanford Research System SR560 pre-amplifier used to take the difference between the laser intensity before and after the reaction cell (increasing the sensitivity of the LAS experiment by orders of magnitude, as discussed by Ismail[67]) has a maximum 1 MHz bandwidth. Therefore, the fastest measurable k' for the LAS experiment is $1 \times 10^6 \, \text{s}^{-1}$, as we have previously noted.[75] Similarly, the slowest radical decay that we have managed to observe with LAS, that of I atom with $k' = 50 \, \text{s}^{-1}$, also exhibited signal distortion due to the electronic data acquisition process.[75] In that case, the pre-amplifier, which had a high-pass filter of 0.03 Hz, was not the problem, but rather the oscilloscope to which the signal was AC coupled also acted as a high pass filter with an RC time constant of 65 ms. Therefore, we estimate the slowest measurable k' without significant electronic signal distortion as 50 s⁻¹. For transient species that are smaller or more reactive than I atom, their slowest decays will likely be limited by some other physical process, such as diffusion out of the LAS probe volume or wall reaction, before this limit is reached. Thus, the absolute greatest range of first order rate coefficients that can be measured using the LAS method is estimated as the following.

$$50 \, \text{s}^{-1} < k' < 1 \times 10^6 \, \text{s}^{-1}$$

The range of kinetic timescales that can currently be measured using the time-resolved PI TOF-MS technique are very limited compared to the LAS technique. Although the BNC 575 delay generator has sub-nanosecond time resolution and can control the relative timing of the photolysis and the photoionization lasers to well within their ~10 ns pulse durations, the time resolution of the PI TOF-MS measurements is constrained to much longer timescales by other factors. In particular, the fastest possible measurement timescales are limited by transport delays during molecular beam sampling that include diffusion to the sampling pinhole, flow through the pinhole and transport *via* the supersonic expansion to the ionization region of the TOF-MS. The effect of effusive and supersonic sampling on kinetic measurements has been extensively characterized theoretically by Moore and Carr[110] and Taatjes,[111] and experimentally it has been verified that processes as fast as 100 μs can be resolved by both effusive[65] and supersonic[64] expansions. In our case, the rate-limiting transport step is actually diffusion within the reactor due to radial inhomogeneities in the photolysis beam, a delay that becomes more acute at higher

pressure. In order to estimate the overall effect of all transport processes on the observed PI TOF-MS time-resolution, the simple, one-parameter model of Baeza-Romero et al. for transport of species i from the reactor to the ionization region was adapted[65]:

$$\frac{dS_i}{dt} = k_{sampling}(R_i \sigma_i C_i(t) - S_i) \qquad (2-9)$$

where $k_{sampling}$ is a first order rate-coefficient used as a fit parameter to describe the rate of transport both to and from the ionization region, and S_i, R_i, σ_i and C_i have the same definitions as before (MS signal, mass discrimination factor, photoionization cross section and concentration in the reactor). Baeza-Romero et al. showed for a variety of $C_i(t)$ functional forms that Eq. 2-9 can be used to accurately fit for kinetic processes with pseudo-first-order rate coefficients, k', up to half of $k_{sampling}$. For example, If $C_i(t)$ is a step function at t = 0 that changes by $\Delta C_{i,0}$ (can be either positive or negative) to a constant value, then Eq. 2-9 can be solved to give an analytical equation for the change in $S_i(t)$, $\Delta S_i(t)$:

$$\Delta S_i(t) = R_i \sigma_i \Delta C_{i,0}\left(1 - e^{-k_{sampling}t}\right) \qquad (2-10)$$

Therefore, if we photolytically generate some species in the reaction cell that has a step concentration profile, $k_{sampling}$ can be determined by fitting the TOF-MS signal observed for this species to Eq. 2-10. The positive jump in I atom MS signal (m/z=127 amu) following photodissociation of C_6H_5I was used for this purpose (Figure 2-19), although a more complicated form of $C_I(t)$ was used that accounts for subsequent reactions of I atom necessitating numerical solution of Eq. 2-9.

Figure 2-19 compares two different models of sampling: instantaneous ($k_{sampling} \rightarrow \infty$) and fit ($k_{sampling}$ = 750 s^{-1}). Clearly the instantaneous model is not suitable, but it is helpful for visualizing what the profile should look like (what it *does* look like inside of the reactor) and how sampling effects distort that behavior. Over the course of conducting experiments on the phenyl radical + propene system (section 4.2), $k_{sampling}$ was fit over a range of T, P and reactor gas composition, from which it was observed that $k_{sampling}$ is typically ~1000 s^{-1} (such as in Figure 2-19) and decreases with increasing pressure and propene concentration, C_{C3H6}. The last two observations are consistent with diffusion within the reactor being the rate-limiting transport step, as both increasing P and C_{C3H6} will inhibit diffusion. From this analysis, the fastest process that could be measured reliably with time-resolved TOF-MS is ~500 s^{-1} (half of $k_{sampling}$) giving a time-resolution of ~1 ms. Of course this resolution can and should be improved down to a 10-100 μs time scale, for instance by using a reactor P < 10 Torr or working to improve the radial

uniformity of the photolysis beam. Nonetheless, for the purpose of primary product branching quantification, a 1 ms time resolution is sufficient so long as primary products can still be distinguished from later generation products, which was found to be the case for the phenyl radical + propene system. This is especially true considering that the LAS portion of the apparatus already has μs time resolution and as a non-intrusive detection technique is preferable for kinetic measurements.
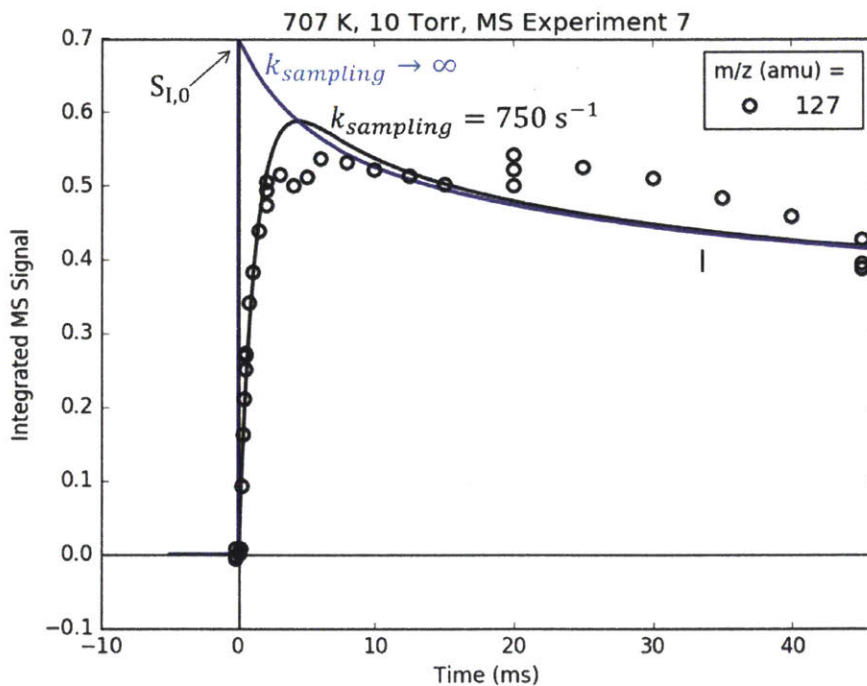
Figure 2-19: Measured (markers) time-resolved PI TOF-MS profile of I atom at 127 amu following 266 nm photodissociation of iodobenzene in the presence of C_3H_6 at 707 K, 10 Torr. Lines are two different models of MB sampling: instantaneous (blue) and delayed by fitting a $k_{sampling}$ of 750 s^{-1} (black). Back-extrapolation of $S_{I,0}$ for initial radical concentration quantification is also shown.

The slowest k' that can be measured with TOF-MS is limited by convective transport of the reactive gas out of the MS Sampling region (Figure 2-4). For a typical total residence time of 1 s the residence time in the MS Sampling region is ~50 ms. Therefore, the range of pseudo-first-order rate coefficients that can be measured using the PI TOF-MS method is as follows:

$$20 < k' < 500s^{-1}$$

Depending on the identity of the species being sampled for PI TOF-MS, the lower bound on k' could be higher due to wall reaction loss. Clearly this is a very restrictive range, but it is sufficient for extracting quantitative product branching by PI TOF-MS.

The mass resolution of the PI TOF-MS, $m/\Delta m$, is ~400 as measured by fitting a gaussian to each of the seven peaks in the calibration gas mass spectrum and taking the full width at half maximum, FWHM, of the fit as Δm (see Figure 2-20). This resolution is more than sufficient to distinguish chemical species with m/z values separated by 1 amu over the m/z range of interest, 1-200 amu. For example, in Figure 2-20 the ^{13}C isotopologue for each species is clearly resolvable. The current cation flight time is relatively short (~20 µs for m/z = 200 amu), therefore it is certainly possible to achieve higher mass resolution by extending the length of the flight path.
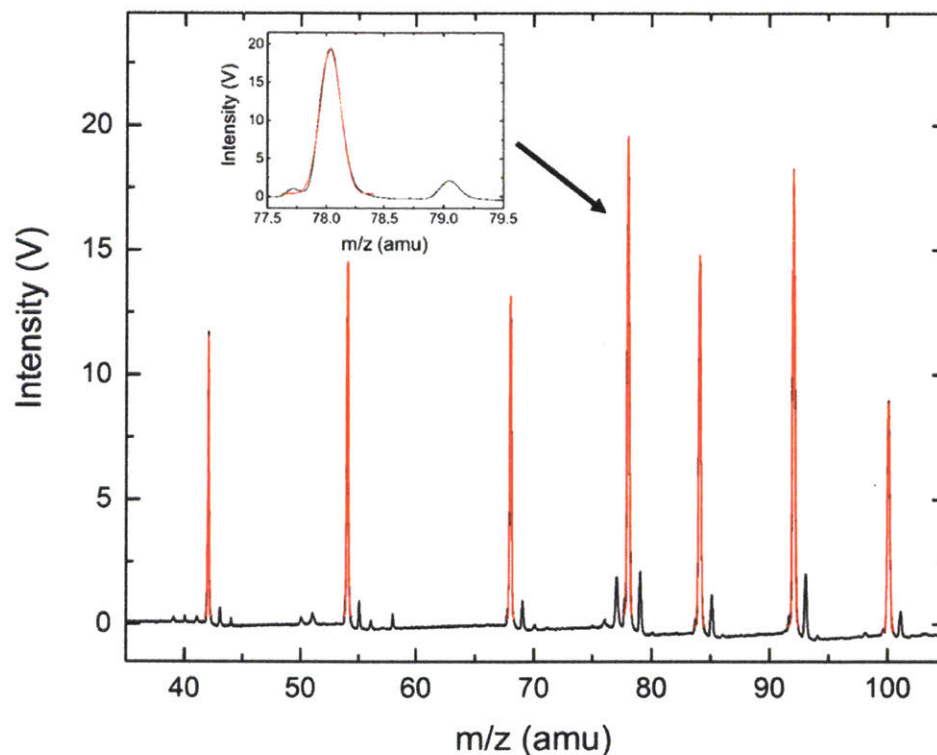
Figure 2-20: Representative mass spectrum of calibration gas with gaussian fits to each peak in order to estimate Δm. Calibration gas consists of propene (m/z=42 amu), 1,3-butadiene (54), furan (68), benzene (78), cyclohexane (84), toluene (92) and n-heptane (100). There is a fragment of an iodobenzene impurity (C_6H_5I) at 77 amu and an acetone impurity at 58 amu. Other unidentified peaks are likely accumulated impurities in the reactor. Courtesy of Te-Chun Chu.

Table 2-1 summarizes the sensitivity and resolution of both parts of the apparatus. Using the phenyl radical as an example, the PI TOF-MS detection limit is ~2 orders of magnitude lower than it is for LAS. As already mentioned, for a typical initial radical concentration of 1×10^{12} molecules cm^{-3}, the LAS S/N will be ~10, and the various products that are subsequently formed with concentrations of ~1×10^{11} molecules cm^{-3} will appear in the TOF-MS with S/N up to ~100. Despite its lower sensitivity (currently), LAS can measure much faster values of k'. The advantage of combining both experiments is clear: while PI TOF-MS can only be used to accurately measure k' values up to 500 s^{-1}, LAS can extend that range to 1×10^{6} s^{-1}. Furthermore, even if the time resolution of the PI TOF-MS experiment is too slow to resolve k', it can still be used to accurately quantify product branching fractions down to ~10%. Finally, other than wall reactions, all of the limitations in Table 2-1 are technical rather than fundamental, therefore they all have technical solutions. As an example, routes to improve the fastest TOF-MS k' have already been discussed, while the slowest TOF-MS k' (due to convection out of the MS-sampling region) could be doubled by shifting the entire TOF-MS sampling assembly (pinhole, skimmer, TOF-MS, PI laser) to the exit of the narrow reactor region (or simply decreasing the gas residence time). As another example, the detection limit of LAS could drop by an order of magnitude by increasing the number of probe laser passes accordingly, such as in cavity ringdown spectrometry,[8] or with an astigmatic Herriott cell.[112] It also bears mentioning that although LAS in this apparatus currently uses a picosecond Ti:Sapphire laser, there is no reason that another UV/visible laser with a narrower bandwidth could not be directly used instead to allow more selective radical detection. For example, a dye laser tuned to the 308 nm absorbance band of hydroxyl radical, OH, an important oxidant in atmospheric and combustion chemistry.[54] [58] Despite all of the dimensions in which this complex apparatus could improve even further, the current iteration is perfectly capable of achieving the original goal: simultaneous measurements of overall kinetics with high time-resolution and quantitative primary product branching (see section 4.2).

Table 2-1: Summary of LAS and PI TOF-MS apparatus characterization.

Detection Technique	Detection Limit		Slowest Measurable k'		Fastest Measurable k'		Mass Resolution
	$\sigma_i C_i$ (cm^{-1})	[Phenyl Radical] (cm^{-3})[a]	Value (s^{-1})	Cause	Value (s^{-1})	Cause	
LAS	3×10^{-8}	1×10^{11}	50	High-Pass RC Filter of Oscilloscope	1×10^6	Low-Pass RC Filter of Differential Pre-Amplifier	-
PI TOF-MS	2×10^{-8}	1×10^9	20	Convection/ Wall Reactions	500	Diffusion to Pinhole/ MB Sampling	400

[a]Absorption and photoionization cross sections of phenyl radical at 504.8 nm and 10.5 eV taken from Tonokura et al.[105] and Sveum et al.,[107] respectively.

2.3.3 Precision and Accuracy

Besides verifying that the LAS and PI TOF-MS apparatus *can* be used to measure overall kinetics and product branching, it is equally important to know *how precisely* and *accurately* those quantities can be measured and *why*. Table 2-2 summarizes the answers to these questions.

Table 2-2: Summary of precision and accuracy for both overall kinetics and product branching measurements using LAS and PI TOF-MS, respectively.

Measurement	Precision		Accuracy	
	Value ($\pm$%, 1σ)	Cause	Value ($\pm$%)	Cause
Overall Kinetics by LAS	<1	Fitting k'	10	Mass Flow Controller Calibrations
Product Branching by PI TOF-MS	10	Fluctuations in PI Laser/VUV Generation	15	Photoionization Cross Sections

For overall kinetics measured by LAS, the precision is very high, <$\pm$1% uncertainty in fitting k', due to the high density of data points for a given absorbance decay. However, the accuracy is limited by $\pm$5% systematic uncertainty in the mass flow controller (MFC) calibrations used to control gas flow rates, which translates into $\pm$10% systematic uncertainty in the excess reagent concentrations needed to convert k' into the bimolecular rate coefficient of interest, k. If each MFC was specifically calibrated for the gas that is used to flow during an experiment, then the accuracy would improve to $\pm$1%.

For product branching measured by PI TOF-MS, the precision is $\pm$10% due to fluctuations in the 118 nm photoionization laser energy. This was determined by comparing replicate measurements of both photolysis-dependent and independent MS signals, both of which have one standard deviation uncertainties of 10%, suggesting that it is fluctuations in the PI Laser/VUV generation and not the photolysis laser that mostly contributes to the random

uncertainty in the signal. The accuracy is limited to ±15% due to systematic uncertainties in photoionization cross sections (PICS) needed for quantification. This is a well-known limitation of MS-based quantification techniques, but perhaps if relative PICS were measured with the same instrument and then applied to a measured product signal ratio the resulting product branching ratio would be known with much greater accuracy because of a large cancellation of systematic uncertainties.

Chapter 3

Kinetics of Atmospheric Reactions

All of the atmospheric reactions discussed below involve some kind of cycloaddition reaction of the simplest Criegee intermediate: either a dipolar 1,3-cycloaddition across an unsaturated alkene (section 3.1) or carbonyl (section 3.3) bond, or a head-to-tail cycloaddition to itself (section 3.2). Sections 3.1 and 3.2 adapted with permission from Buras et al.[74] and Buras et al.[75] Copyright 2014 American Chemical Society. Section 3.3 adapted with permission from Elsamra et al.[76] Copyright 2016 John Wiley & Sons.

3.1   Kinetics of CH_2OO + Alkenes

3.1.1   Introduction

Carbonyl oxide biradicals are an important class of atmospheric species formed as intermediates during alkene ozonolysis.[113] Once formed in the atmosphere, carbonyl oxides can impact the budgets of many important atmospheric species, such as OH,[114] organic acids,[115] and SO_2[116] with far reaching implications. The simplest carbonyl oxide, CH_2OO, is commonly referred to as the simplest Criegee Intermediate (CI) after Rudolf Criegee, who first proposed their formation in 1949.[117]

Despite the prediction of these species for decades, carbonyl oxides such as CH_2OO were not directly measured experimentally until 2012 when Welz et al. demonstrated reliable and stable production of CH_2OO *via* the first two steps of Scheme 3-1 below (248 nm rather than 355 nm photolysis was used by Welz et al.).[118]

$$CH_2I_2 \xrightarrow{\ 355\,nm\ } CH_2I + I$$

$$CH_2I + O_2 \xrightarrow{\ \alpha k_1\ } CH_2OO + I$$

$$\xrightarrow{\ (1-\alpha)k_1\ } Other(CH_2IO_2, IO, CH_2O)$$

$$CH_2OO + Alkene \xrightarrow{\ k_2\ } Products$$

$$CH_2OO \xrightarrow{\ k_3\ } Products$$

$$I \xrightarrow{\ k_4\ } Products$$

$$[CH_2I]_0 = [I]_0$$

$$[CH_2OO]_0 = 0$$
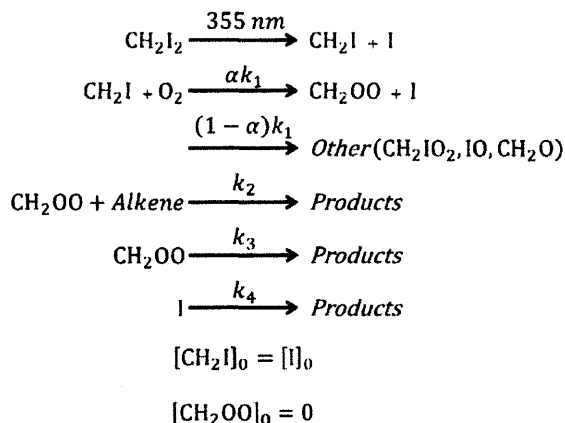
Scheme 3-1: Kinetic model used to fit CH_2OO and I Atom absorbance traces

This discovery has enabled many subsequent experimental studies on both the spectroscopy and kinetics of CH_2OO as summarized in a recent review by Taatjes.[119] This method for forming CH_2OO was employed to measure the kinetics of CH_2OO reacting with SO_2, NO_2, NO, H_2O, CH_3CHO and CH_3COCH_3 using photoionization mass spectrometry and laser-induced fluorescence of both HCHO and OH.[55, 118, 120-121] Sheps has also measured the reaction of CH_2OO with SO_2 using cavity-enhanced absorption[122] by probing the broad absorption feature from 250-450 nm assigned to the B $^1A' \leftarrow X\ ^1A'$ transition in CH_2OO by Beames et al.[123] and Lee et al.[124] Criegee Intermediates are commonly formed by reactions of ozone with alkenes, so the rate of CI reacting with alkenes is of considerable interest. Until recently, however, there were no experiments and only one theoretical study on the reaction of CH_2OO with alkenes, with no predicted reaction rates.[125] Very recently Vereecken et al. predicted the first rate coefficients for CH_2OO + alkenes using quantum calculations and transition state theory (TST).[126] Here we report the first experimental measurement of the kinetics of CH_2OO reacting with various alkenes using multiple-pass ultraviolet absorption at 375 nm and report additional quantum chemical calculations on these reactions.

3.1.2 Experimental Methods

All experiments were conducted on a modified version of the MIT laser-photolysis/Herriott multiple-pass laser-absorption apparatus described by Ismail et al.[96] This apparatus was modified to incorporate a time of flight mass spectrometer (TOF-MS) with supersonic molecular beam sampling from the center of the reactor and is described in detail by Middaugh.[68] For the purpose

of this work, where only the absorption capability of the apparatus was utilized, Ismail's description is still mostly accurate. The only relevant changes pertain to the dimensions of the reactor and the manner in which it is heated. The new reactor is 86 cm long, 6 cm in diameter and resistively heated by four heaters wrapped along the length of the reactor to create a uniform temperature profile ($\pm 2\%$ standard deviation) through the overlap region of the absorption and photolysis lasers. In order to minimize excited I atom formation and eliminate the possibility of CH_2 formation via a single-photon process[127] the third harmonic output of an Nd:YAG laser (355 nm) operated at a 2 Hz repetition rate was used to photolyze CH_2I_2 instead of a shorter wavelength such as the fourth harmonic of an Nd:YAG laser (266 nm). The frequency-doubled output of a mode-locked Ti:Sapphire laser (80 MHz pulsed laser with 1.2 ps FWHM wide pulses) was used to generate the ultraviolet probe beam, and the fundamental wavelength was measured before each experiment using a recently calibrated Ocean Optics USB2000 spectrometer. A narrow linewidth low-noise continuous-wave diode laser was used to generate an infrared beam tuned to the ($F = 3\ ^2P_{1/2} \leftarrow F = 4\ ^2P_{3/2}$) I atom atomic transition. Multiple-pass ultraviolet probe laser path lengths were in the range of $10 - 15$ m and infrared path lengths for I atom absorption, which were only single-pass, were in the range of $50 - 70$ cm. Both ultraviolet and infrared absorbance traces were averaged over 500 acquisitions. 375 nm was chosen as the ultraviolet probe wavelength because this was the closest wavelength to the peak of the B $^1A' \leftarrow$ X $^1A'$ transition at ~350 nm[122] that could be used with the available Herriott mirrors. Using 375 nm rather than shorter wavelengths also made it easier to reduce the interference from scattered 355 nm photolysis light. Helium was used as the bath gas in all experiments, which minimizes thermal lensing of the probe beam. CH_2I_2 was purchased from Sigma-Aldrich at 99% purity and was further purified by successive freeze-pump-thaw cycles. CH_2I_2 was introduced into the reactor by a helium flow through a room temperature bubbler maintained at 750 Torr. Helium (Airgas, 99.999%), oxygen (BOC, 99.999%), ethene (Airgas, 99.5%), propene (Airgas, 99.95%), iso-butene (Airgas, 99%), 1-butene (Airgas, 99%) and 2-butenes (Airgas, 99%) were all used directly from their cylinders without further purification.

3.1.3   Computational Methods

The electronic structure and rate coefficient estimation methods employed were identical to those used recently by Jalan et al. to study chemically activated reactions between CH_2OO and

HCHO, CH$_3$CHO and CH$_3$COCH$_3$.[128] All stationary points reported here were optimized using restricted Kohn-Sham calculations with the B3LYP density functional and the MG3S basis set,[129] equivalent to 6-311+G(2df,2p) for systems containing only H, C, and O.[130-131] All B3LYP/MG3S calculations employed an ultrafine density-functional integration grid (using *Int=Ultrafine* in *Gaussian 03*).[132] Zero-point energies were computed using the same DFT model chemistry and scaled by a factor of 0.99 before use in TST calculations. Electronic energies were computed using the RCCSD(T)-F12a[133-139] method with the VTZ-F12 basis[140] using the *Molpro* program suite[141] at geometries optimized using the B3LYP/MG3S electronic model chemistry. Conventional TST calculations for rate coefficients were performed using the CanTherm computer code.[142] Eckart tunneling corrections were used where applicable. One-dimensional hindered rotor corrections were applied to the partition functions using relaxed scans along torsional degrees of freedom.[128] The relaxed scans were performed at 10° intervals using the B3LYP/MG3S model chemistry.

3.1.4   Results and Discussion

3.1.4.1   Probing CH$_2$OO at 375 nm

To first verify CH$_2$OO was being probed in our apparatus at 375 nm, CH$_2$I$_2$ was photolyzed at 355 nm in the presence of eight different oxygen concentrations ranging from 0.10×10^{15} to 49.3×10^{15} molecules cm^{-3} (detailed experimental conditions given in Appendix A). Both ultraviolet absorption at 375 nm and single-pass infrared absorption tuned to the ($F = 3$ ^{2}P$_{1/2}$ ← $F = 4$ ^{2}P$_{3/2}$) I atom atomic transition[78] were simultaneously recorded as shown in Figure 3-1.
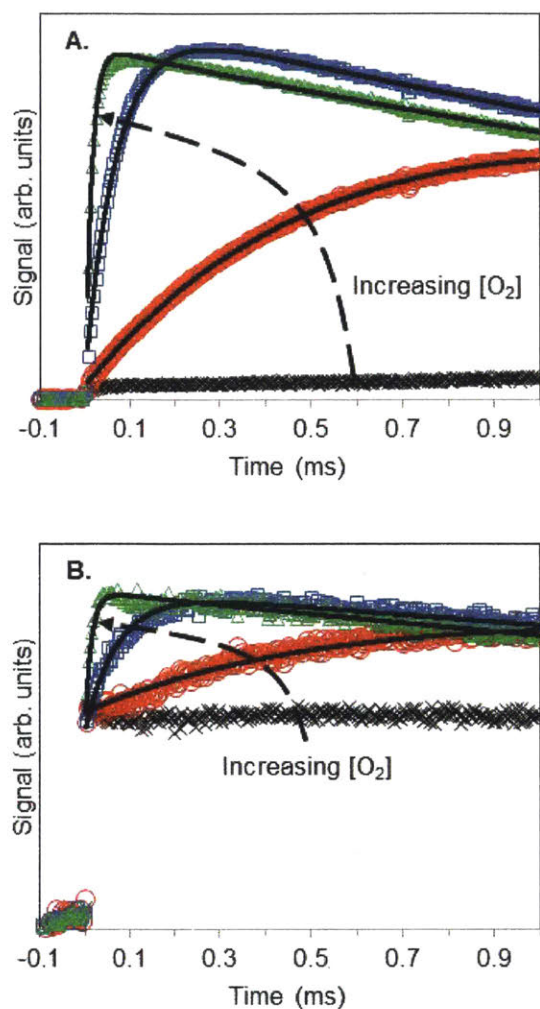
Figure 3-1: Measurement of CH_2OO formation at 298 K and 25 Torr using ultraviolet absorption of CH_2OO at $\lambda = 375$ nm (Panel A) and infrared absorption of I atom at $\lambda = 1315.246$ nm (Panel B) over the following range of O_2 concentrations (units of molecules cm^{-3}): $[O_2] = 0$ (black), 0.10×10^{15} (red), 9.7×10^{15} (blue) and 49.3×10^{15} (green). The infrared absorbance trace with no O_2 is shifted up for visual comparison and is not included in the model fit. Every 200th point is shown for clarity. Solid black lines are model fit.

The model fits shown in Figure 3-1 represent the analytical solutions (shown below) to the kinetic model given in Scheme 3-1. These were obtained assuming excess O_2 and alkene and also that ultraviolet (375 nm) absorption is mostly attributable to CH_2OO.

$$[CH_2OO](t) = \frac{\alpha k_1[O_2][CH_2I]_0}{k_1[O_2] - k_2[\text{Alkene}] - k_3} \left(e^{-(k_2[\text{Alkene}]+k_3)t} - e^{-k_1[O_2]t} \right) \tag{3-1}$$

$$[I](t) = \frac{[CH_2I]_0}{k_1[O_2] - k_4} \left([(1+\alpha)k_1[O_2] - k_4]e^{-k_4t} - \alpha k_1[O_2]e^{-k_1[O_2]t} \right) \tag{3-2}$$

$$A_{375}(t) = \sigma_{CH_2OO}(\lambda = 375 \text{ nm}) l_{375}[CH_2OO](t) + \text{shift} \qquad (3\text{-}3)$$

$$A_I(t) = \sigma_I(\lambda = 1315.246 \text{ nm}) l_I[I](t) \qquad (3\text{-}4)$$

where A is absorbance, σ is absorption cross section and l is path length. The global fit parameters in this model are α, k_1 and $\sigma_{CH_2OO}(\lambda = 375 \text{ nm})$. Different values for $[CH_2I]_0$, k_3, and k_4 were fit for each experiment. No alkene was present during these experiments so those terms do not affect the inferred reaction rate of interest, k_1. A baseline offset, with parameter name "shift", was also fit for each ultraviolet absorbance trace to account for any small contributions by other species. $\sigma_I(\lambda = 1315.246 \text{ nm})$ was computed for each reactor condition using the integrated cross section given by Ha et al.[78] and the approximation of the Voigt profile given by Whiting[143] to account for Doppler and collisional broadening. Both path lengths are also known, albeit with 20-25% uncertainty due to imprecise knowledge of exactly where the probe beams intersect the photolysis beam. The full results from this fit are presented in Appendix A along with comparison to literature. The value obtained for k_1 is $(1.4 \pm 0.1) \times 10^{-12} \text{ cm}^3 \text{ molecule}^{-1}\text{s}^{-1}$, in good agreement with Huang et al.[144] $[(1.58 \pm 0.22) \times 10^{-12} \text{ cm}^3 \text{ molecule}^{-1}\text{s}^{-1}]$, Stone et al.[145] $[(1.67 \pm 0.04) \times 10^{-12} \text{ cm}^3 \text{ molecule}^{-1}\text{s}^{-1}]$ and Eskola et al.[146] $[(1.39 \pm 0.01) \times 10^{-12} \text{ cm}^3 \text{ molecule}^{-1}\text{s}^{-1}]$. We also measured k_1 at 700 K following the same procedure as above in order to confirm that the same species was observable at high temperatures (see Appendix A). We found $k_1(700 \text{ K}) = (1.0 \pm 0.1) \times 10^{-13} \text{cm}^3 \text{ molecule}^{-1}\text{s}^{-1}$, which is qualitatively consistent with the negative temperature dependence observed by Eskola et al.[146]

The results above demonstrate that the species absorbing strongly at 375 nm is a product of $CH_2I + O_2$. Both Huang et al.[144] and Stone et al.[145] concluded that at 25 Torr (the pressure used in all experiments reported here unless otherwise noted) CH_2OO should be the major species, with $\alpha \approx 0.90$. Furthermore, we measured that at 298 K and 4 Torr the 375 nm absorbing species reacts with acetone at a rate of $(2.03 \pm 0.15) \times 10^{-13} \text{cm}^3\text{molecule}^{-1}\text{s}^{-1}$ (see section 3.3 for details), in good agreement with the measured CH_2OO + acetone rate of $(2.3 \pm 0.3) \times 10^{-13} \text{cm}^3\text{molecule}^{-1}\text{s}^{-1}$ from Taatjes et al.[120]

As shown in Scheme 3-1, CH_2IOO, CH_2O and IO are all other possible products of CH_2I + O_2 and therefore could be contributors to the ultraviolet absorbance signal observed above. CH_2IOO and CH_2O are both known to absorb only weakly at this wavelength[124, 147] and therefore will make negligible contributions to the absorbance. IO, however, does absorb strongly in this

range, particularly at wavelengths longer than 375 nm.[148] Nonetheless, the following evidence indicates that the contribution of IO is also negligible at our conditions. First, there is the agreement of the measured rate above with literature for CH_2OO + acetone. Second, as shown in Figure A 6, the transient absorption was found to decrease with increasing λ between 370 and 385 nm, consistent with the spectrum of CH_2OO[122] and inconsistent with IO.[148] Third, the literature values for α and the IO cross section at 375 nm[148] would give an absorption an order of magnitude smaller than the transient absorption we observe. Finally, the probe wavelength was moved from 375 to 427.2 nm where IO is known to absorb strongly due to the 4,0 band of its $A^2\Pi \leftarrow X^2\Pi$ transition.[149] Figure 3-2 compares the measured pseudo-first-order decay rates of the absorbance traces observed for λ = 375 nm and λ = 427.2 nm taken at the same conditions as a function of propene concentration. The decay rate measured at λ = 375 nm is clearly dependent on $[C_3H_6]$, whereas at λ = 427.2 nm it is not. This demonstrates that two different species are being predominantly probed at 375 and 427.2 nm, which we attribute to CH_2OO and IO, respectively. Details of the experiment to probe IO at λ = 427.2 nm can be found in Appendix A.
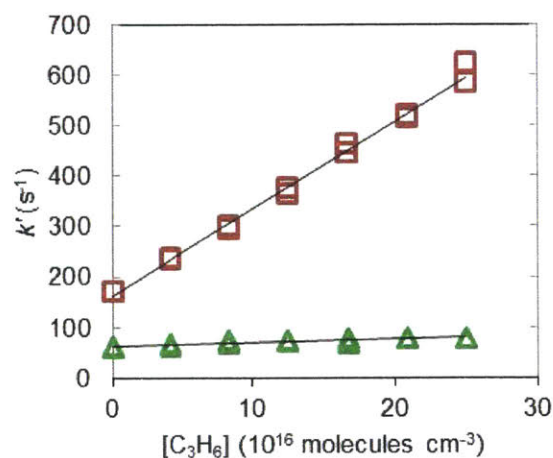
Figure 3-2: Comparison of pseudo-first-order decay rates k' vs. propene concentration for species measured at λ = 375 nm (CH_2OO, □) and λ = 427.2 nm (IO, △) at T = 298 K and P = 25 Torr.

Taken together, this evidence suggests that whatever contribution IO makes to the absorbance signal at 375 nm is small compared to CH_2OO and independent of alkene concentration, and should therefore not affect the k_2 values reported here. At the high

temperature extreme of 700 K the fit value obtained for σ_{CH_2OO} decreases only slightly from the 300 K measurements, suggesting that the same species is still predominantly being probed. Hence, we assume this species is still CH_2OO at 700 K.

3.1.4.2   Experimental Measurements of CH_2OO + Alkene Rates

At alkene concentrations $> 10^{16}$ molecules cm^{-3} a noticeable increase in the decay rate of CH_2OO was observed, as shown in Figure 3-3.
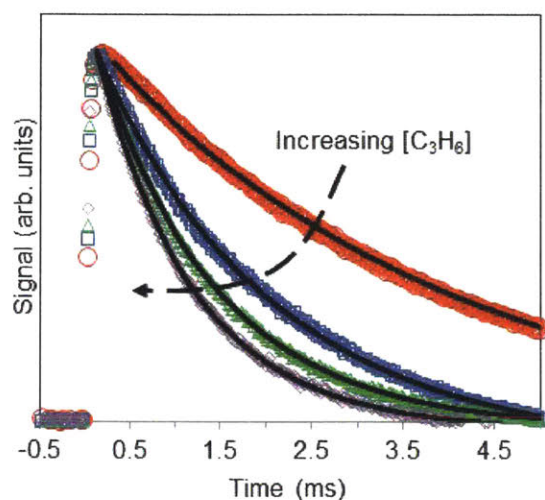
Figure 3-3: Representative decays of CH_2OO absorbance ($\lambda = 375$ nm) at 494 K and 25 Torr over the following range of C_3H_6 concentrations (units of molecules cm^{-3}):$[C_3H_6] = 0$ (red), 6.5×10^{16} (blue), 13.0×10^{16}(green) and 19.5×10^{16} (purple). Every 200th point is shown for clarity. Single-exponential fits are shown as solid black lines.

Care was taken to ensure that the time scale of CH_2OO formation was at least an order of magnitude faster than CH_2OO decay so that the decay portion could be fit to a single exponential and a simple pseudo-first-order analysis could be conducted. The decay of CH_2OO in the absence of any alkene was also described adequately by a single exponential fit, suggesting a first order loss process. Control experiments were conducted to ensure that substantially increasing photolysis power or precursor concentration did not increase the measured second order rate constants above their error bounds, and all measurements were conducted such that the reaction cell contents were totally refreshed between photolysis shots. A full description of the

experimental conditions and error analysis is given in the Appendix A. Sample linear fits of k' versus [Alkene] for ethene and propene at 298 K are shown in Figure 3-4.
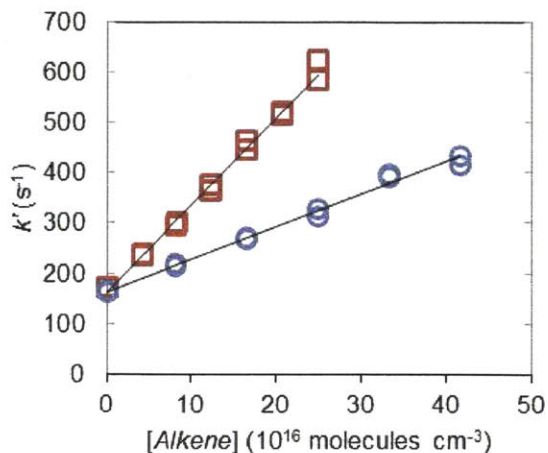
Figure 3-4: Pseudo-first-order CH_2OO decay rate k' vs. alkene concentration for propene ($\square$) and ethene ($\bigcirc$) at T = 298 K and P = 25 Torr. Error bars are not given for individual k' values because the uncertainty due to fitting a single exponential to a measured decay was very small (< 0.1%).

The rate of CH_2OO reacting with ethene, propene and the three butene isomers (iso-butene, 1-butene and a mixture of cis- and trans-2-butene) at 298 K was measured from 10 to 50 Torr as shown in Figure 3-5. The pressure dependence appears flat over this range for all of the CH_2OO + alkenes rates, especially considering the uncertainty of the measurements. From these results, k_2 appears to be pressure independent over this range using helium as a bath gas. For atmospheric models, however, where nitrogen acts as a more efficient stabilizer, we recommend using the rates reported here at low pressures as reasonable lower bounds.
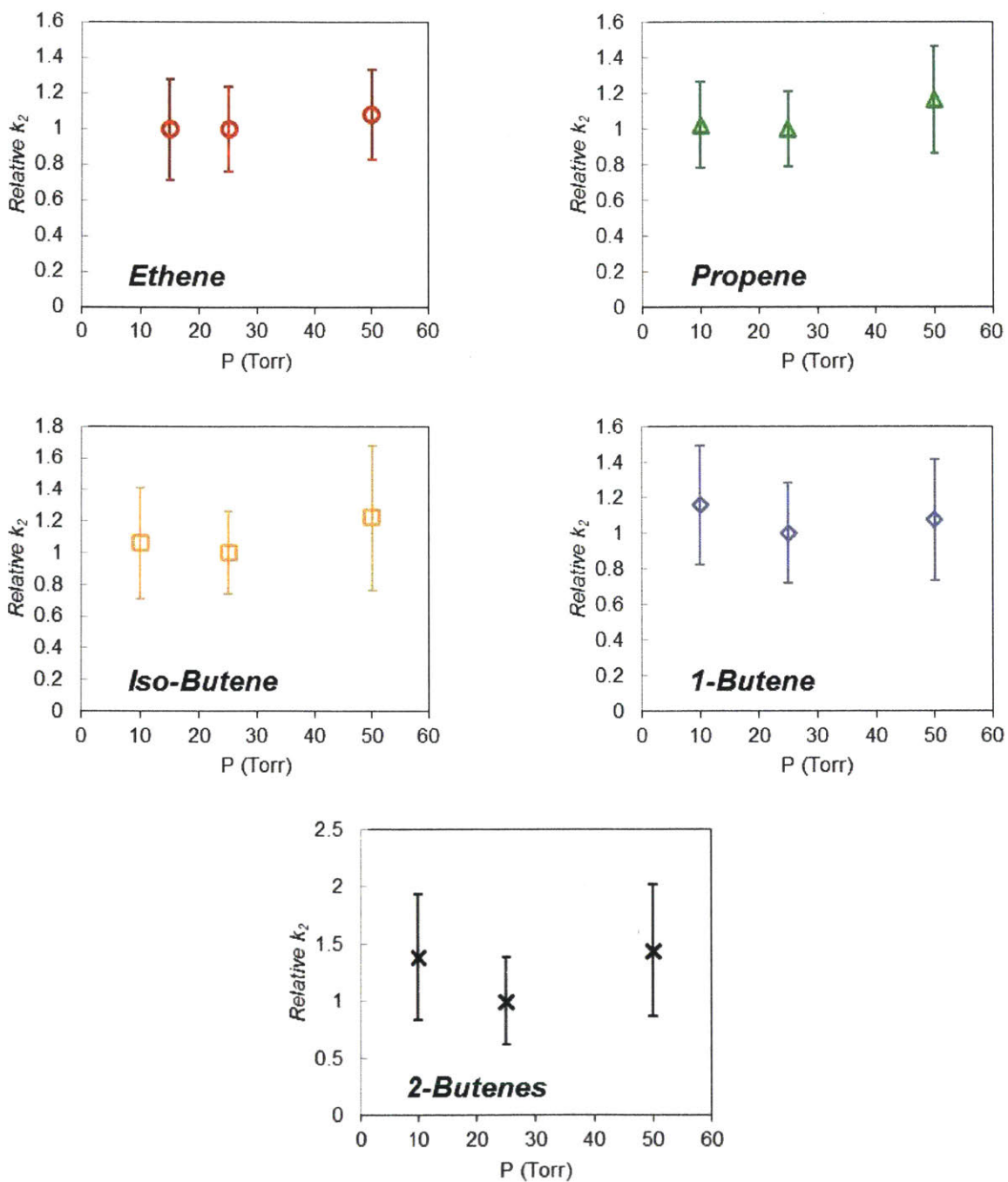
Figure 3-5: Experimental CH_2OO + Alkenes rates at 298 K as a function of pressure, normalized to 25 Torr measurement.

CH$_2$OO + alkenes rates were also measured at 298, 390 and 494 K (all at 25 Torr). Attempts were made to measure the rate at 600 K as well, but at this temperature CH$_2$OO decayed very rapidly even in the absence of any excess reagent (k$_3$ ≈ 2000 s^{-1} as opposed to 100 − 300 s^{-1} at the lower temperatures) possibly due to unimolecular decomposition of CH$_2$OO. There was also a reproducible baseline offset in the 375 nm absorption at 600 K that was not observed at lower temperatures possibly due to absorption by an unknown product (see Figure A 4). For these reasons the temperature dependence of CH$_2$OO + alkenes was only measured up to 494 K. Figure 3-6 shows the measured temperature dependence of all five alkenes and Table 3-1 summarizes the Arrhenius fit parameters obtained. The theoretical predictions (also shown in Figure 3-6) are discussed in the following section.
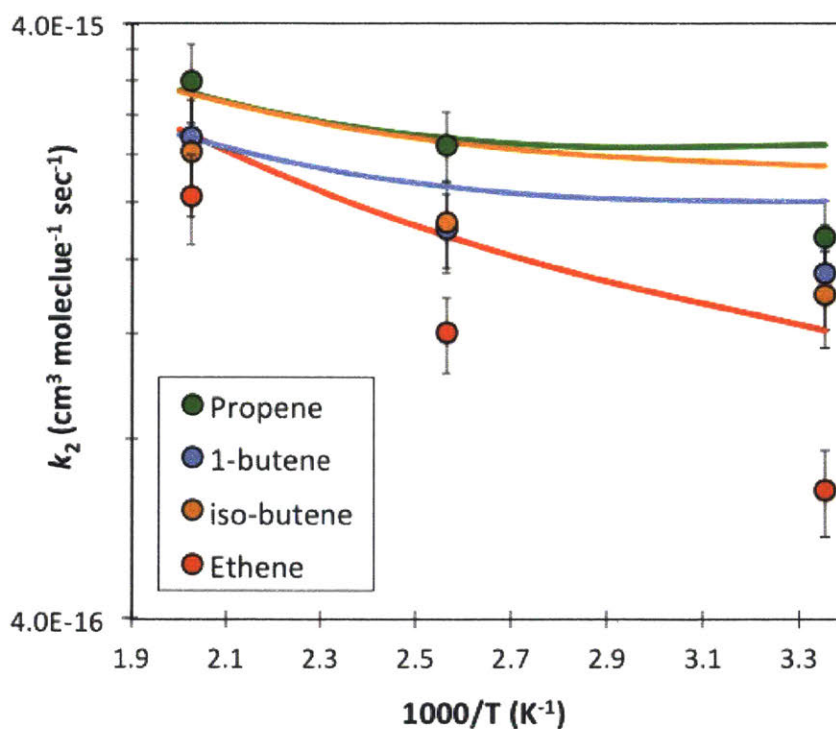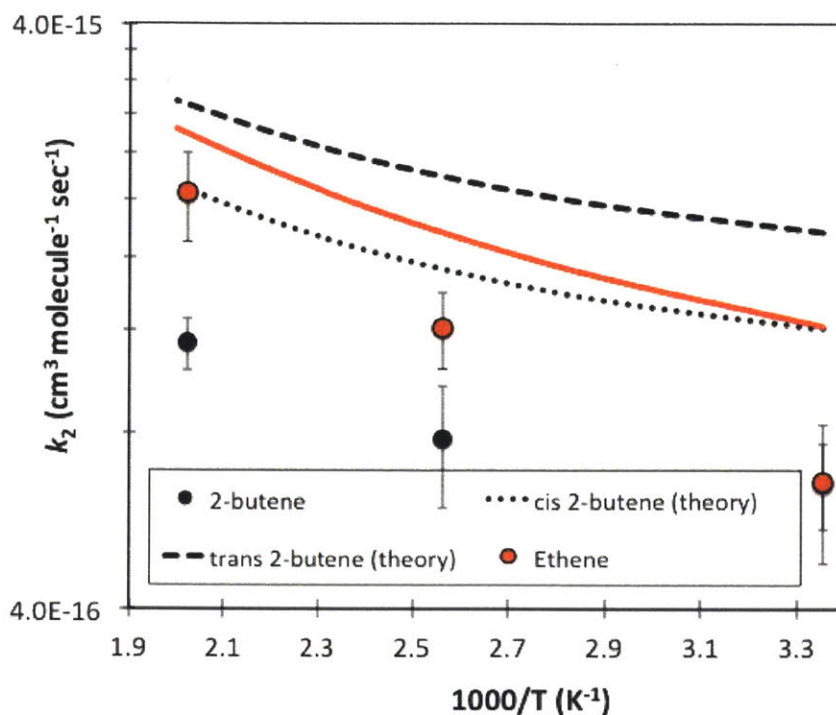
Figure 3-6: Comparison of experimental and theoretical rate coefficients for $CH_2OO + C_2H_4$, C_3H_6, 1-C_4H_8, iso-C_4H_8 (top) and $CH_2OO + C_2H_4$ and 2-C_4H_8 (bottom). Theoretical predictions are represented by the curves and have all been scaled down by a factor of 5. Experimental rate coefficients are represented by filled circles and correspond to measurements at 298 K, 390 K and 494 K and P = 25 Torr.

Table 3-1: Arrhenius fit parameters and experimental rate constants at 298 K for the reaction of CH_2OO with alkenes at 25 Torr. The uncertainty of the rate constants reported here includes both random and systematic uncertainty contributions as detailed in Appendix A. The form of the Arrhenius equation is $k(T) = A\,e^{-\frac{E_a}{RT}}$.

	A (10^{-15} cm^3 molecule^{-1} s^{-1})	**E_a** (J mol^{-1})	**k_2 (298 K)** (10^{-15} cm^3 molecule^{-1} s^{-1})
Ethene	11 ± 3	7000 ± 900	0.7 ± 0.1
Propene	8 ± 2	3700 ± 600	1.8 ± 0.3
Iso-Butene	5 ± 2	3400 ± 1300	1.4 ± 0.3
1-Butene	5 ± 2	3200 ± 1400	1.5 ± 0.3
2-Butene	2 ± 1	3500 ± 1700	0.7 ± 0.2

The measured rate coefficients reported here for CH_2OO + alkenes at 298 K and 25 Torr (see Table 3-1) are 1-4 orders of magnitude slower than for the reactions of CH_2OO with SO_2, NO_2, ketones and aldehydes at similar pressures[118, 120] but an order of magnitude faster than the upper

limit rate for reaction with H_2O.[55] The possible impact of the CH_2OO + alkenes reaction in the atmosphere is discussed in more detail in a later section. Also interesting to note is that ethene, as the only alkene without any alkyl substitution, has an apparent activation energy (E_a) almost twice that of the other substituted alkenes studied here, consistent with the trend computed by Vereecken et al.[126]

3.1.4.3   Theoretical Predictions of CH_2OO + Alkene Rates
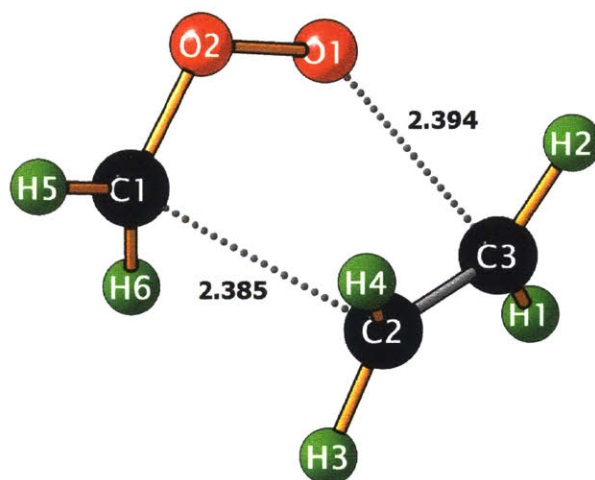
Figure 3-7: DFT optimized saddle point for the CH_2OO + C_2H_4 cycloaddition reaction. Bond lengths shown in Å.

1,3-dipolar cycloaddition is expected to be the dominant mode of reaction between CH_2OO and alkenes.[125] Several 1,3-dipolar cycloaddition reactions (especially those of O_3) have been studied previously using quantum chemical methods.[150-151] Like O_3, the reaction between CH_2OO and alkenes involves formation of a weak Van der Waals complex before the cycloaddition saddle point.[125] For this study, we assume any pre-reaction complex formation to have little effect on the overall kinetics and use conventional transition state theory (TST) along with *ab initio* calculations[152] for the concerted cycloaddition reactions between CH_2OO and ethene (C_2H_4), propene (C_3H_6) and butene isomers (iso-C_4H_8, 1-C_4H_8, 2-C_4H_8) to understand the experimentally observed difference in reactivity.

Because of symmetry numbers and optical isomers (or "reaction path degeneracy") the actual reaction rate coefficient is 4 times larger than the calculated value for the unique CH_2OO + C_2H_4 saddle point (Figure 3-7). An important feature of the CH_2OO + C_2H_4 saddle point is the

central O (O2 in Figure 3-7) which puckers out of the C1-C2-C3-O1 'ring' plane. Using conventional TST, the overall rate of $CH_2OO + C_2H_4$ (accounting for symmetry and optical isomers) was fit to a simple Arrhenius expression (neglecting the curvature of the predictions) with A = 3.8E-14 cm^3/molecule-sec and E_a = 4600 J mol^{-1} (1.1 kcal/mol). The highest-level calculations of Vereecken et al.[126] on this reaction agree very closely with our calculations, even though somewhat different electronic structure methods were used. The quantum calculations predict E_a within ~1 kcal/mole and the A factor within a factor of ~4, about as well as one could expect for conventional TST for such low-barrier reactions.
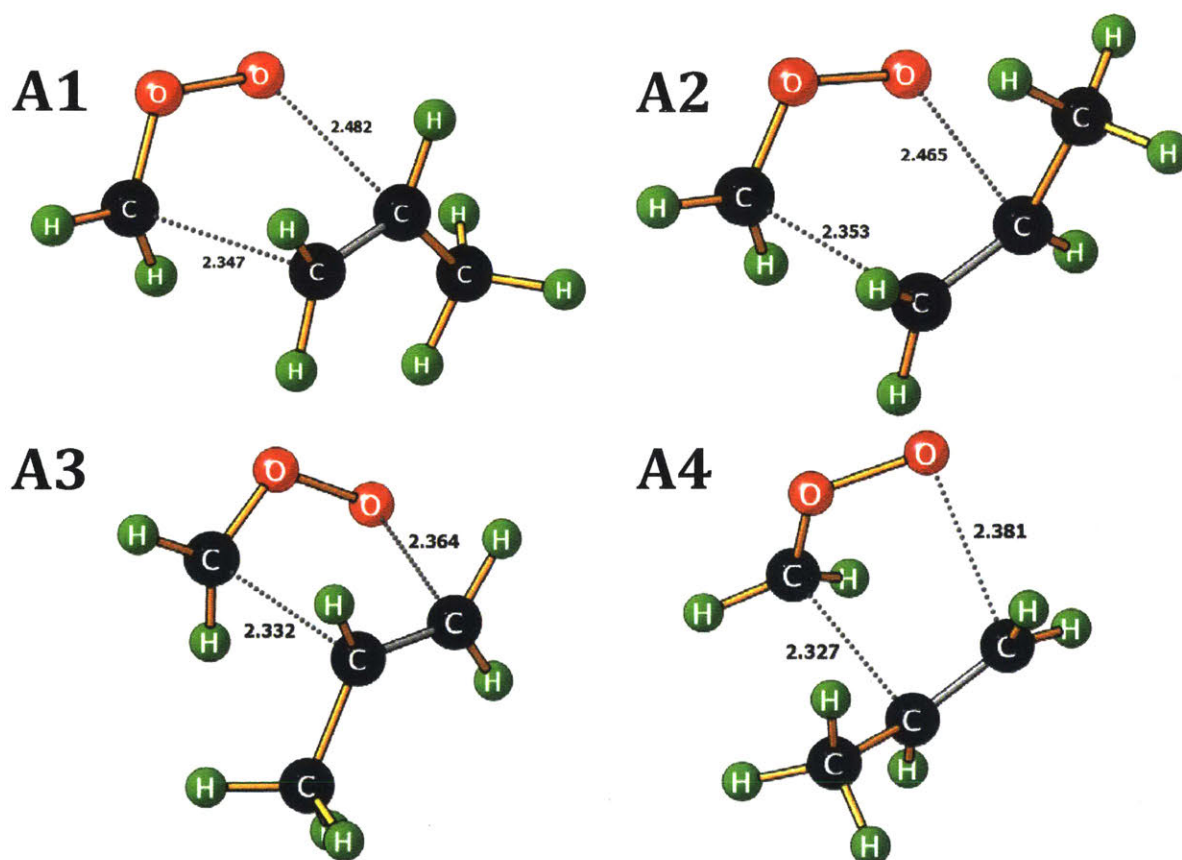
Figure 3-8: DFT optimized saddle points for the $CH_2OO + C_3H_6$ cycloaddition reaction. Bond lengths shown in Å.

However, for $CH_2OO + C_3H_6$, there are four distinct cycloaddition channels (Figure 3-8) corresponding to methyl substitution at each vinylic H atom in the $CH_2OO + C_2H_4$ saddle point. A comparison of our computed ZPE inclusive reaction barriers (E_0) for the four $CH_2OO + C_3H_6$

cycloaddition channels is shown in Table 3-2. Vereecken et al.[126] used lower level theory for this reaction than for the CH_2OO + ethene reaction, and with that lower level of theory they obtained lower E_0's (by a few kJ/mole), but qualitatively similar results: both calculations agree that saddle point A1 is "submerged", i.e. has an energy lower than that of the reactants.

Table 3-2: Comparison of ZPE inclusive barrier heights (E_0) for the four CH_2OO + C_3H_6 cyclo-addition channels. The E_0 value of CH_2OO + C_2H_4 was calculated to be 2930 J mol^{-1}.

Reaction	Site of –CH$_3$ substitution	E_0 (J mol^{-1})
Channel A1	H1	-3340
Channel A2	H2	840
Channel A3	H3	6690
Channel A4	H4	7520

Both channels A1 and A2 have E_0 lower than the barrier for CH_2OO + C_2H_4 and are characterized by methyl substitution on the C atom (C3 in Figure 3-7) under attack by the O end of CH_2OO (O1 in Figure 3-7). Channel A1 has –CH$_3$ and the puckered O atom (similar to O2 in Figure 3-7) on opposite sides of the forming C-C-C-O plane while Channel A2 has them on the same side. It is possible that steric repulsion between the –CH$_3$ group and puckered O atom leads to the higher barrier for channel A2. Methyl substitution on C2 (Channels A3 and A4) appears to have the opposite effect leading to an increase in the reaction barrier compared to CH_2OO + C_2H_4. The position of the –CH$_3$ group above or below the ring plane has a very small effect on the barrier height in these cases.[152]

Similar to CH_2OO + C_3H_6, the reactivity of CH_2OO towards 1-C_4H_8 depends on the position of the –C_2H_5 substituent on the CH_2OO+C_2H_4 saddle point in Figure 3-7. The resulting barrier heights follow similar relative trends and are summarized in Table 3-3. It is interesting to note that with the exception of Channel A1, barrier heights for all other saddle points decrease by 1800-2000 J mol^{-1} in going from –CH$_3$ to –C_2H_5 as the substituent. The barrier height for Channel A1 also goes down but only by ~500 J mol^{-1}.

Table 3-3: Comparison of ZPE inclusive barrier heights (E_0) for the four CH_2OO + 1-C_4H_8 cyclo-addition channels. The E_0 value of CH_2OO + C_2H_4 was calculated to be 2930 J mol^{-1}.

Reaction	Site of –C_2H_5 substitution	E_0 (J mol^{-1})
Channel A1	H1	-3800
Channel A2	H2	-1650
Channel A3	H3	4720
Channel A4	H4	5710

Table 3-4: Comparison of ZPE inclusive barrier heights (E_0) for the CH_2OO + iso-C_4H_8 and CH_2OO + 2-C_4H_8 cyclo-addition channels. The E_0 value of CH_2OO + C_2H_4 was calculated to be 2930 J mol^{-1}.

Reaction	Site of –CH_3 substitutions	E_0 (J mol^{-1})
CH_2OO + iso-C_4H_8		
Channel A1	H1, H2	-2440
Channel A2	H3, H4	12080
CH_2OO + 2-C_4H_8		
Channel A1[a]	H1, H3	-950
Channel A2[b]	H1, H4	-1250
Channel A3[b]	H2, H3	2830
Channel A4[a]	H2, H4	3200

[a] Calculated with respect to cis-2-C_4H_8
[b] Calculated with respect to trans-2-C_4H_8

Unlike 1-C_4H_8, both 2-C_4H_8 and iso-C_4H_8 are characterized by two –CH_3 substitutions compared to C_2H_4. They can proceed through several different transition states as seen in Table 3-4. As seen in Table 3-4, the barrier heights for these reactions are bounded by the CH_2OO+iso-C_4H_8 system while the CH_2OO+2-C_4H_8 reactions lie in between. The upper bound on these barrier heights corresponds to both –CH_3 groups on C3 (Channel A2 for iso-C_4H_8) while the lower bound has both –CH_3 groups on C2 (Channel A1 for iso-C_4H_8). For CH_2OO+2-C_4H_8, all saddle points with a –CH_3 substitution at H1 (Channels A1, A2) have a negative barrier similar to CH_2OO + C_3H_6. Both Channels A3 and A4 have a –CH_3 substitution at H2 and have barrier heights comparable to or slightly higher than CH_2OO + C_2H_4. For 2-C_4H_8, it is not surprising that the highest barrier channel corresponds to both –CH_3 substituents on the same side of the plane as the puckered O atom.

A comparison of predicted absolute rate coefficients for CH_2OO + C_2H_4, C_3H_6, 1-C_4H_8 and iso-C_4H_8 is shown in Figure 3-6. Our computed TST (high-pressure-limit) rates at 298 K

agree very closely with Vereecken et al.'s highest level calculation for $CH_2OO + C_2H_4$, but less well with their lower-level calculations for CH_2OO + propene and CH_2OO + 2-butene. Our calculations consistently overestimate the rate coefficient by factors varying between 5 and 10 depending on the alkene type and temperature. In general, the discrepancy is highest at low temperatures. The calculated rates for C_3H_6 and 1-C_4H_8 give curved Arrhenius plots due to the contributions of distinct saddle points, and flatten out at lower temperatures because of the submerged saddle points. Even though current calculations overestimate the absolute rate coefficients in the 300-500 K temperature range, they capture qualitative trends in relative reactivity between the alkenes. As seen in Figure 3-6, the reaction with C_3H_6 is faster at lower temperatures but because of the relatively stronger temperature dependence of $CH_2OO + C_2H_4$, the difference in reactivity decreases as temperature increases. Both experiments and calculations agree that the rate coefficients for CH_2OO reacting with propene, 1-butene, and isobutene are very similar (within 40% at all temperatures), but do not agree on the details. The comparison is more complicated for 2-C_4H_8 as it is the sum of the rates for the *cis* and *trans* isomers weighted by their respective equilibrium distribution at the temperature of interest. For simplicity, the calculated values for *cis* and *trans* isomers are shown separately in Figure 3-6 (bottom) along with the experimental measurements. As expected the *trans* isomer is relatively more reactive and the corresponding rates are upper bounds for the overall CH_2OO+2-C_4H_8 rate. Similarly, the rates for the *cis* isomer represent lower bounds on the calculated overall 2-C_4H_8 rate coefficients. The *trans* isomer is thermodynamically favored and should be more representative of the overall behavior of 2-C_4H_8. Similar to C_3H_6, the lowest barrier heights for CH_2OO + *cis*-2-C_4H_8 and CH_2OO + *trans*-2-C_4H_8 computed by Vereecken et al.[126] are systematically lower compared to corresponding values obtained here using higher level calculations.

More accurate estimation of the flux through shallow/submerged saddle points like those discussed here requires a two-bottlenecks-in-series variational TST treatment,[153-154] which is beyond the scope of the present work. The rate coefficients for CH_2OO + alkenes reported here are almost 2 orders of magnitude smaller than the corresponding measurements for addition to carbonyl compounds[120] indicating a shift from a very loose TS to a tight TS. This is because the saddle point for addition to carbonyls is deeply submerged ($E_0 \sim$ -21000 J mol^{-1}), while E_0 for alkenes was found to be much higher varying between -4000 J mol^{-1} and 12000 J mol^{-1}.

3.1.4.4   Impact of CH₂OO + Alkene Measurements on Atmospheric Models

Alkenes are an important constituent of the atmosphere. They are emitted as products of combustion[155-156] and also as chemical intermediates in the manufacturing of plastic and other industrial and agricultural processes.[157] Natural sources of alkenes include emissions from vegetation, soils and the oceans.[158] As such, it is worthwhile to investigate what impact alkenes may have on CH_2OO chemistry in the atmosphere.

The recent study of Percival et al.[159] on atmospheric sulfuric acid concentrations concluded that three reactions - with H_2O, SO_2 and NO_2 – can have a comparable effects on atmospheric CH_2OO levels, combining to give CI removal rates of 20 s^{-1} or faster by bimolecular reaction. They did not consider possible reactions of CI with alkenes, though of course they noted that reaction of alkenes with ozone is a major source of CI in the environment.

Recent measurement of the concentration of a small subset of alkenes (C2-C6) in polluted urban areas was found to exceed 100 ppb.[160] Combining this concentration with our newly measured CH_2OO rate coefficient at 298 K results in a relatively small CI removal rate of ~ 2-5×10^{-3} s^{-1}. We expect alkenes to compete with H_2O, SO_2 and NO_2 in the removal of CI only if alkene concentrations reach 400 ppm (1×10^{16} molecule cm^{-3}), which is possible in alkene rich environments such as emission plumes, polymer melts, rubber, etc.[161-162] Since the CI formation rate is highest in alkene-rich environments, the reactions of CI with alkenes may be significantly more important than one would compute from atmospheric averages which implicitly assume CI formation and CI destruction to be uncorrelated. Our measurements also reveal that the reaction of alkenes with CH_2OO is faster than the reaction of alkenes with the CI's parent molecule O_3, ~5×10^{-17} cm^3 molecule^{-1} s^{-1}.[159]

3.1.5   Conclusions

Using Herriott multiple-pass laser-absorption we have probed the B $^1A' \leftarrow$ X $^1A'$ transition in the simplest Criegee Intermediate, CH_2OO. The identity of CH_2OO is confirmed by room temperature measurement of the $CH_2I + O_2$ reaction rate as well as the reaction rate of CH_2OO + acetone, both of which agree well with previous measurements. We then measured kinetics of CH_2OO reacting with C2-C4 alkenes at 25 Torr and temperatures ranging from 298 K – 494 K. The Arrhenius fits from these measurements are given below.

Ethene: $k_2 = (11 \pm 3) \times 10^{-15} cm^3 molecule^{-1}s^{-1} \exp[-(7000 \pm 900)J\ mol^{-1}/RT]$

Propene: $k_2 = (8 \pm 2) \times 10^{-15} cm^3 molecule^{-1}s^{-1} \exp[-(3700 \pm 600)J\ mol^{-1}/RT]$

Iso − Butene: $k_2 = (5 \pm 2) \times 10^{-15} cm^3 molecule^{-1} s^{-1} \exp[-(3400 \pm 1300)J\, mol^{-1}/RT]$

1 − Butene: $k_2 = (5 \pm 2) \times 10^{-15} cm^3 molecule^{-1} s^{-1} \exp[-(3200 \pm 1400)J\, mol^{-1}/RT]$

2 − Butene: $k_2 = (2 \pm 1) \times 10^{-15} cm^3 molecule^{-1} s^{-1} \exp[-(3500 \pm 1700)J\, mol^{-1}/RT]$

We recommend using the above rates as reasonable lower bounds for atmospheric rates. Theory predicts some of the Arrhenius plots are significantly curved, consistent with the experiments, and the error bars are significant, so caution is recommended when extrapolating these fits outside of the experimental temperature range. For all alkyl substituted alkenes $E_a \approx 3500 \pm 1000\, J\, mol^{-1}$, whereas for ethene $E_a \approx 7000 \pm 900\, J\, mol^{-1}$. Ab initio calculations for the concerted cycloaddition reactions between CH_2OO and the various alkenes combined with conventional TST calculations qualitatively capture reactivity trends between C_2H_4, C_3H_6, 1-C_4H_8 and iso-C_4H_8 although the absolute rate coefficients are all overestimated. The reactivity of 2-C_4H_8 depends on the cis-trans distribution with the trans isomer expected to dominate. Interestingly, the reaction of Criegee Intermediate with alkenes is at least an order of magnitude slower than the analogous reaction with carbonyl compounds, due to the significantly different submerged barrier height. In normal atmospheres where the concentration of alkenes is less than 100 ppb, Criegee Intermediates are expected to react with other species (e.g. H_2O, NO_2, SO_2) much faster than they react with alkenes, but the reactions of Criegee Intermediates with C=C double bonds could be important in environments with higher concentrations of alkenes, such as in emission plumes or in rubber exposed to ozone. These high-alkene environments are the locations where Criegee Intermediates are also formed the fastest.

3.2   Kinetics of CH_2OO Self-Reaction

3.2.1   Introduction

Following the discovery of an efficient route to produce the simplest Criegee Intermediate, CH_2OO, by photolysis of diiodomethane, CH_2I_2, in the presence of O_2,[118] there has been a tremendous amount of experimental work done on this species as summarized in a recent review by Taatjes et al.[163] Many of these experiments involve such high concentrations of CH_2OO that self-reaction needs to be taken into account. As such, it is important to have an accurate rate coefficient for this reaction, k_{self}. Vereecken et al. recently predicted a rate coefficient for this reaction at 300 K of $\sim 4 \times 10^{-11} cm^3\, molecule^{-1}\, s^{-1}$ (factor of five uncertainty) using variational Transition State Theory.[126] Even more recently, using FTIR, Su et al. recommended a

value approaching the collision limit, $k_{self} = 40 \pm 20 \times 10^{-11} cm^3$ molecule^{-1} s^{-1} near room temperature in 20-100 Torr of N_2 bath gas.[164]

We have shown that CH_2OO can be selectively probed using UV absorbance at $\lambda = 375$ nm (section 3.1.4.1). It is often difficult to determine absolute concentrations of reactive intermediates, which is needed to determine self-reaction rate coefficients, but we are able to quantify absolute concentrations by probing the 1315.246 nm F = 3 $^2P_{1/2} \leftarrow$ F = 4 $^2P_{3/2}$ atomic transition of I atom formed as the co-product of CH_2OO formation. This provides a very direct way of accurately determining the absolute concentration of CH_2OO. In this work we combine both of these measurements with laser flash photolysis to measure k_{self}. By simultaneously measuring the absolute CH_2OO and I atom concentrations, which have very different time-dependences, we have also put an upper bound on the rate coefficient for CH_2OO + I. Finally, we have determined an absolute absorption cross-section for CH_2OO at our ultraviolet probe wavelength in good agreement with a recent measurement by Ting et al.[165] but in disagreement with the measurement of Sheps.[122] Accurate quantification of the absolute absorption spectrum of CH_2OO in this ultraviolet range is necessary in order to predict the true fate of CH_2OO in the troposphere.

3.2.2   Experimental Methods

The relevant aspects of the apparatus were described in section 3.1.2 so only a few details are noted here. All measurements were conducted at 297 K. The fourth harmonic output of an Nd:YAG laser (266 nm) operated at either a 0.5, 0.91 or 2 Hz repetition rate was used to photolyze CH_2I_2. Different pairs of convex and concave lenses were used to collimate the photolysis beam to various diameters. For all experiments, except for the single UV pass control, the UV probe beam was in a Herriott multiple-pass configuration giving effective path lengths in the range of 10 − 15 m. The I atom laser was single-pass for all experiments (45 − 60 cm path length). Both UV and infrared absorbance traces were averaged over 500 acquisitions. CH_2I_2 was purchased from Sigma-Aldrich at 99% purity and was further purified by successive freeze-pump-thaw cycles. CH_2I_2 was introduced into the reactor by flowing bath gas (either He or N_2, depending on the experiment) through a room temperature bubbler maintained at 750 Torr. Helium (Airgas, 99.999%), nitrogen (Airgas, 99.99%) and oxygen (Airgas, 99.999%) were all used directly from their cylinders without further purification.

3.2.3   Results and Discussion

3.2.3.1   Quantifying $[CH_2OO]_0$ using I Atom Absorbance

In order to determine self-reaction rate coefficients, it is necessary to quantify the initial concentration of the species of interest. We are able to quantify $[CH_2OO]_0$ by fitting simultaneously recorded absorbance traces of co-produced I atom (Figure 3-9).
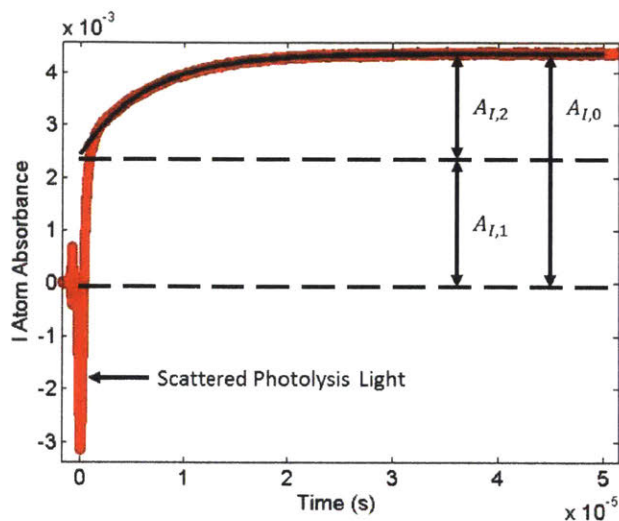
Figure 3-9: Representative I atom absorbance trace at 297 K, in 50 Torr He and $[O_2] = 1.1 \times 10^{17}$ cm^{-3} with model fit (black line) to extract value of $[CH_2OO]_0$.

We have previously shown (section 3.1.4.1) that the growth and decay of I atom for this system can be captured by the simple kinetic model in **Scheme 3-2**, which has the biexponential analytical solution shown below.

$$CH_2I_2 \xrightarrow{266\ nm} I + CH_2I$$

$$CH_2I + O_2 \xrightarrow{\alpha k_{growth}} I + CH_2OO$$

$$\xrightarrow{\beta k_{growth}} I + \begin{array}{l}\text{Products other than } CH_2OO \\ (e.g., HCOOH,\ dioxirane, CH_2O + O)\end{array}$$

$$\xrightarrow{\gamma k_{growth}} \begin{array}{l}\text{Non-I atom forming channels} \\ (CH_2IO_2, IO + CH_2O)\end{array}$$

$$I \xrightarrow{k_{uni,I}} \text{Products}$$

$$[I]_0 = \frac{A_{I,1}}{\sigma_I(\lambda = 1315.246\ nm)l_I}$$

$$[CH_2OO](t = 0) = 0$$

$$\alpha + \beta + \gamma = 1$$

Scheme 3-2: Kinetic model for I atom growth

$$[I](t) = \left(\frac{1}{k_{growth}[O_2] - k_{uni,I}}\right)\left([([I]_0 + [CH_2OO]_0)k_{growth}[O_2] - [I]_0 k_{uni,I}]e^{-k_{uni,I}t} - \right.$$

$$\left. [CH_2OO]_0 k_{growth}[O_2]e^{-k_{growth}[O_2]t}\right) \tag{3-5}$$

$$A_I(t) = \sigma_I(\lambda = 1315.246\ nm)l_I[I](t) \tag{3-6}$$

Note that $[CH_2OO]_0 \neq [CH_2OO](t = 0)$ in this model. The initial jump in I atom absorbance shown in Figure 3-9, $A_{I,1}$, corresponds to the initial photolytic production of $CH_2I + I$, while the second rise, $A_{I,2}$, corresponds to production of I atom by the reaction $CH_2I + O_2 \rightarrow CH_2OO + I$ with rate coefficient $k_{growth}(= 1.4 \pm 0.1 \times 10^{-12}\ cm^3\ molecule^{-1}\ s^{-1})$.[74, 144-146] Here we assume that the amount of I atom produced by this second process, $[I]_{0,2}$, is equal to the maximum amount of $[CH_2OO]$ formed, $[CH_2OO]_0$ (i.e., branching of $CH_2I + O_2$ to other CH_2OO isomers or their fragments is negligible, $\beta \ll \alpha$). With this assumption $[CH_2OO]_0$ can be calculated using Beer's Law.

$$[I]_{0,2} = [CH_2OO]_0 = \frac{A_{I,2}}{\sigma_I(\lambda = 1315.246\ nm)l_I} \tag{3-6}$$

More details of calculating $[CH_2OO]_0$ using this procedure, including a propagation of uncertainty, are included in Appendix B. From this analysis, the overall uncertainty in our determination of $[CH_2OO]_0$ is 35%. Assuming $\beta \ll \alpha$ is partially justified by the 10% upper bound on the branching fraction of $CH_2I + O_2$ to formic acid determined by Welz et al.[118] (the same limit can be placed on dioxirane formation, assuming it has a comparable photoionization

cross section as formic acid). Several researchers have also measured CH_2O in similar reaction conditions,[118, 145] and found that most of it is formed by secondary chemistry (presumably from CH_2OO) on a much longer timescale than that shown in Figure 3-9, again consistent with $\beta \ll \alpha$. Furthermore, one would expect any channel of $CH_2I + O_2$ that produces I atom and decomposition products of CH_2OO (e.g., $CH_2O + O$) to be pressure dependent, but as shown below our results are insensitive to pressure and bath gas, lending further credence to the assumption that $\beta \ll \alpha$.

Several prior researchers have measured the ratio of $\frac{A_{I,2}}{A_{I,1}}$ (this ratio is often assumed to equal α in the literature).[144-145] Our measurements are consistent with the prior work, though our error bar is higher: literature values of this ratio at our conditions are about 0.8, and our measurements range from 0.6-1.0 with an error bar of about 0.2 (Appendix B). We note that some assumptions are required to equate $\alpha = \frac{A_{I,2}}{A_{I,1}}$: first that β is negligible ($\beta \ll \alpha$), and second that the $CH_2I + I$ producing channel dominates over any other photolysis channel producing I atoms. For the analysis in this paper, we do not need to know the ratio $\frac{A_{I,2}}{A_{I,1}}$, only the value of $A_{I,2}$, which appears in Eq. 3-6, nor do we need to know the value of α or γ, but only that $\beta \ll \alpha$ (i.e., that the reaction of $CH_2I + O_2$ forms I atoms and CH_2OO in a 1:1 ratio).

3.2.3.2   Measured CH_2OO self-reaction

The decays of both CH_2OO and I atom were recorded simultaneously by UV and IR absorbance respectively, for a range of experimental conditions as summarized in Table 3-5.

Table 3-5: Summary of experimental conditions (T = 297 K for all experiments and $[O_2]$ = 0.55 and 1.1×10^{17} cm^{-3} for all 25 and 50/100 Torr experiments, respectively)

Experiment Title	Photolysis beam iameter (cm)	l_l^a (cm)	FPR^b	Bath gas	P (Torr)	$[CH_2I_2]$ (10^{14} molecule/ cm^3)^c	Photolysis power (mJ/pulse)	$[CH_2OO]_0^d$ (10^{12} molecule/cm^3)	Number Of traces
25 Torr N$_2$	1.15	55	1.5	N$_2$	25	2	15 – 65	2 – 8	6
	1.15	55	1.5	N$_2$	25	1.5	65	6	1
	1.15	55	1.5	N$_2$	25	1	65	4	1
50 Torr N$_2$	1.5	55	1.65	N$_2$	50	4	15 – 65	2 – 11	6
	1.15	55	1.65	N$_2$	50	3	65	9	1
	1.15	55	1.65	N$_2$	50	2	65	6	1
100 Torr N$_2$	1.3	64	1.51	N$_2$	100	4	15 – 65	3-9	6
25 Torr He	1.15	55	1.5	He	25	3	15 – 65	2 – 9	6
50 Torr He	1.15	55	1.65	He	50	6	15 – 65	5 – 18	6
Double FPR Control	1.15	55	3.3	N$_2$	50	4	15 – 65	3-11	6
Half FPR Control	1.3	64	0.85	He	50	6	15 – 65	4-13	6
Smaller Photolysis Beam Control	1	47	1.65	N$_2$	50	4	15 – 65	2 – 13	6
Larger Photolysis Beam Control	1.3	58	1.65	N$_2$	50	4	15 – 65	3 – 9	6
Single UV Pass Control	1.3	60	1.65	N$_2$	50	4	15 – 65	3 – 10	6

^{a}25% relative uncertainty in all l_l values reported

^{b}FPR = Flashes per Refresh

^{c} $[CH_2I_2]$ was estimated by using the vapor pressure of CH_2I_2 at 298 K[166] and assuming that after passing through the bubbler the gas was saturated with $[CH_2I_2]$. Therefore, these values represent upper bound estimates of the true $[CH_2I_2]$.

^{d}Determined from simultaneously recorded I atom absorbance at short times. All $[CH_2OO]_0$ values reported have 35% relative uncertainty.

[CH$_2$OO](t) and [I](t) were first fit to the "complex" kinetic model shown in Scheme 3-3, which requires numerical integration.

$$CH_2OO \xrightarrow{\;k_{uni}\;} \text{Products}$$

$$2\,CH_2OO \xrightarrow{\;k_{self}\;} \text{Products}$$

$$CH_2OO + I \xrightarrow{\;k_{CH_2OO+I}\;} \text{Products}$$

$$I \xrightarrow{\;k_{uni,I}\;} \text{Products}$$

$$2I + M \xrightarrow{\;k_{self,I}\;} I_2 + M$$

$$[CH_2OO]_0 = \frac{A_{I,2}}{\sigma_I(\lambda = 1315.246 \text{ nm})l_I}$$

$$[I]_0 = \frac{A_{I,0}}{\sigma_I(\lambda = 1315.246 \text{ nm})l_I}$$
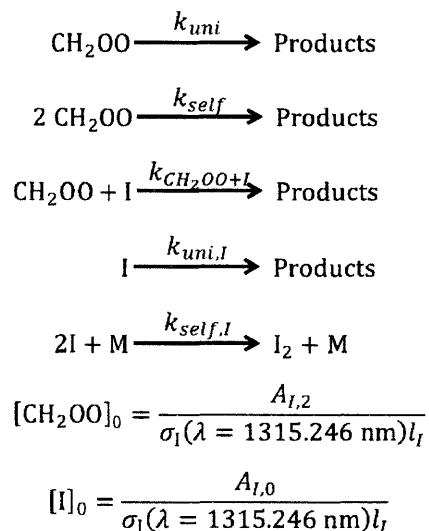
Scheme 3-3: "Complex" kinetic model for simultaneous CH$_2$OO and I atom decay

$$\frac{A_{375}(t)}{A_{375,0}} = (1 + b)\frac{[CH_2OO](t)}{[CH_2OO]_0} - b \qquad (3\text{-}7)$$

$$\frac{A_I(t)}{A_{I,0}} = (1 + c)\frac{[I](t)}{[I]_0} - c \qquad (3\text{-}8)$$

Following the recommendation of Su et al.,[164] we have included CH$_2$OO + I in this model. We have also included self-reaction of I atom using the recommended overall third order rate coefficients of Baulch et al. based on extensive literature review for different bath gases, M.[167] Note that in this model, t = 0 is defined as the time at which both CH$_2$OO and I atom are at their maximum concentrations. Because the growth of both CH$_2$OO and I atom occur on a time scale at least two orders of magnitude faster than their respective decays, we found it was unnecessary to include the formation step (Appendix B). We have previously shown at similar conditions that IO does not make a noticeable contribution to the observed absorbance at 375 nm (section 3.1.4.1), therefore we assume A$_{375}$(t) $\propto$ [CH$_2$OO](t) only. This assumption is most readily validated using the present data by the fact that A$_{375}$(t) returns to baseline at timescales ($\sim$10 ms) where [IO] would still be near its maximum.

[CH$_2$OO]$_0$ and [I]$_0$ are both obtained by fitting the I atom absorbance trace at short times when formation occurs as discussed in the previous section. The global fit parameters (constant for a given experiment) in this model are k_{uni}, k_{self}, k_{CH_2OO+I} and $k_{uni,I}$. Local fit parameters

(allowed to vary from trace to trace) are b and c, which are included to take into account the fact that the oscilloscope signal sometimes goes below baseline, and the value of $[CH_2OO]_0$, which was allowed to vary within its $\pm 35\%$ relative uncertainty. Representative decays and fits of the "complex" model are shown in Figure 3-10.
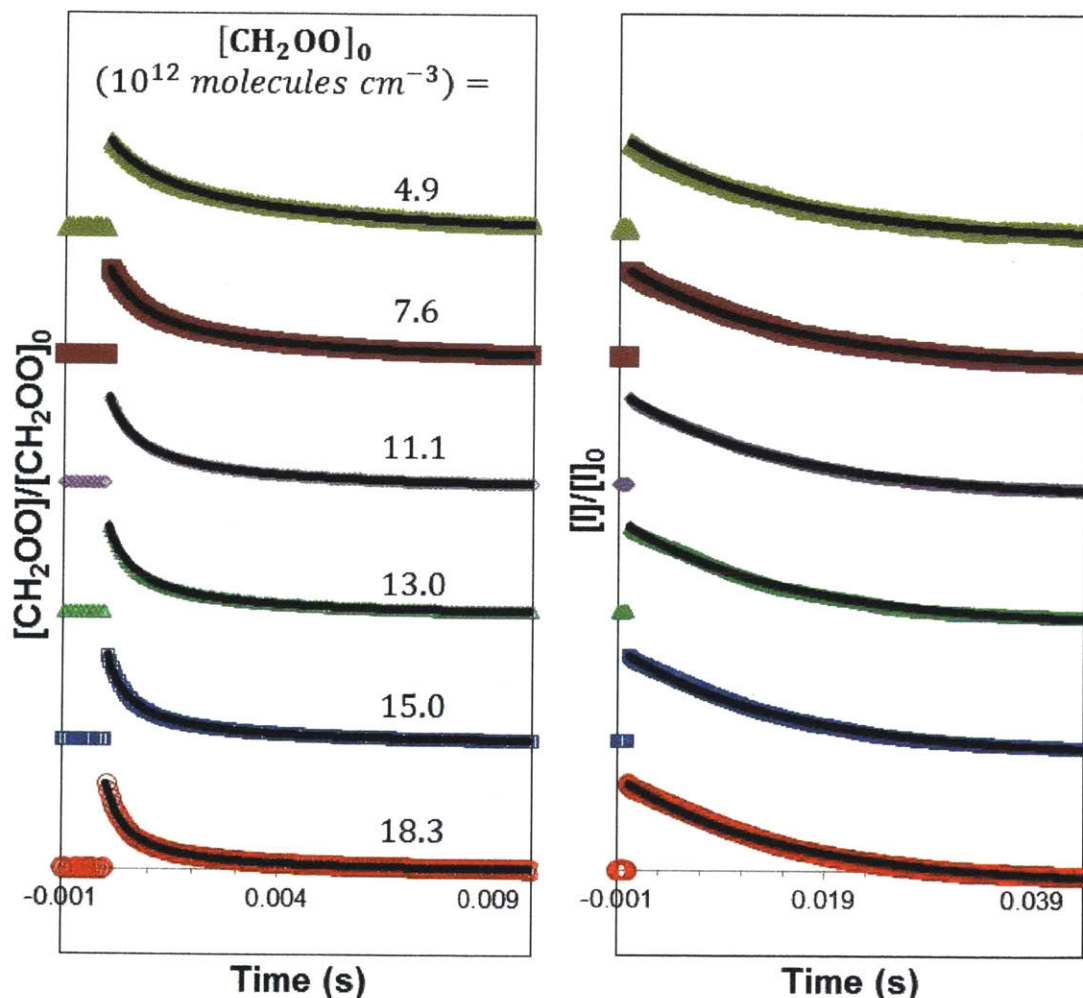
Figure 3-10: Measured decays of CH_2OO (left) and I atom (right) at 297 K and 50 Torr He over a range of $[CH_2OO]_0$ values. Solid black lines are fits of the "complex" model. Only every 100th data point is shown for clarity.

The fit parameters obtained by fitting this model to all of the experiments in Table 3-5 are summarized in Table B 1. Interestingly, while the decay of CH_2OO becomes faster and appears more second-order for higher $[CH_2OO]_0$ values as expected, the decay of I atom is completely insensitive to $[CH_2OO]_0$ and $[I]_0$. From the experiments where the diiodomethane concentration

was also varied we found that the I atom decay is insensitive to $[CH_2I_2]$. A separate experiment was conducted at varying O_2 concentrations to show that oxygen also has no effect (Figure B 6). This leaves diffusion out of the beam as the dominant loss process for I atom, which is corroborated by the fact that the only experimental parameter that significantly decreased the time constant of the decay of I atom signal was switching the bath gas from N_2 to He (Appendix B). Furthermore, at these low pressures and for our photolysis beam diameters, diffusion is expected to occur on a time scale of $10 - 100$ ms, consistent with the ~15 ms timescale for I atom decay observed here.[104]

This suggests that $CH_2OO + I$ is not significant, and indeed if k_{CH_2OO+I} is unconstrained during the fitting procedure very good fits are obtained with $k_{CH_2OO+I} \approx 0$ (Appendix B). Furthermore, if k_{CH_2OO+I} is constrained to equal $5 \times 10^{-11} cm^3$ molecule$^{-1}s^{-1}$, the theoretically predicted value by Su et al.,[164] the model is not able to simultaneously fit the decay of both CH_2OO and I atom well. Only for $k_{CH_2OO+I} < 1.0 \times 10^{-11} cm^3$ molecule$^{-1}s^{-1}$ is the model able to adequately fit the data (Figure B 2). Therefore we conclude that $1.0 \times 10^{-11} cm^3$ molecule$^{-1}s^{-1}$ is a conservative upper bound on the rate coefficient for $CH_2OO + I$ at 297 K.

If $CH_2OO + I$ is removed from the kinetic model, it is no longer necessary to fit the decays of CH_2OO and I together and a "simplified" kinetic model, shown in Scheme 3-4, for the decay of CH_2OO only can be fit to the data.

$$CH_2OO \xrightarrow{k_{uni}} Products$$

$$2\ CH_2OO \xrightarrow{k_{self}} Products$$

$$[CH_2OO]_0 = \frac{A_{I,2}}{\sigma_I(\lambda = 1315.246\ nm)l_I}$$
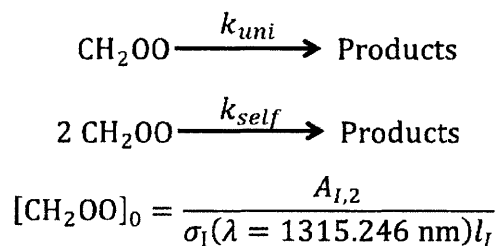
Scheme 3-4: "Simplified" kinetic model for CH_2OO decay

The analytical solution to this "simplified" model is shown below.

$$\frac{A_{375}(t)}{A_{375,0}} = (1 + b)\frac{[CH_2OO](t)}{[CH_2OO]_0} - b = (1 + b)\frac{k_{uni}}{(k_{uni} + 2k_{self}[CH_2OO]_0)e^{k_{uni}t} - 2k_{self}[CH_2OO]_0} - b \quad (3\text{-}9)$$

Unlike the "complex" model, in this model $[CH_2OO]_0$ is fixed at the value determined by the simultaneous I atom measurement for a given trace (not allowed to vary $\pm 35\%$) and k_{uni} is a

local fit parameter. k_{uni} captures the contributions of $CH_2OO + I$ as well as other first order loss processes such as unimolecular decay of CH_2OO and diffusion out of the beam. (Because the concentration of I atom drops by at most 20%, and in most cases less than 10%, over the ~2 ms time scale that CH_2OO decays, the $CH_2OO + I$ reaction can be treated as pseudo-first-order. This provides another way to estimate k_{CH_2OO+I} as discussed in Appendix B). Representative fits of this "simplified" model are shown in Figure 3-11 and Table 3-6 summarizes the fit values of k_{self} and k_{uni} obtained. Because k_{self} and $[CH_2OO]_0$ are always multiplying each other in this "simplified" model, the 35% relative uncertainty in $[CH_2OO]_0$ causes k_{self} to also be uncertain by at least $\pm 35\%$.
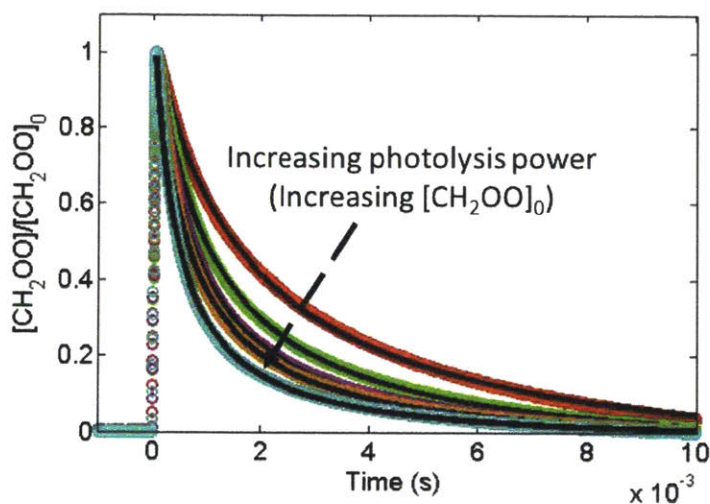
Figure 3-11: Representative decays of normalized CH_2OO absorbance ($\lambda = 375$ nm) at 297 K and 50 Torr He over a range of $[CH_2OO]_0$ values ($5 - 18 \times 10^{12}$ molecules cm^{-3}). Solid black lines are fits of the "simplified" model.

Table 3-6: Fit CH_2OO self-reaction rate coefficient, k_{self}, and first order decay, k_{uni}, from "simplified" model for all experiments (T=297 K)

Base Case Experiments	k_{self} [b] $(10^{-11} cm^3$ $molecule^{-1} s^{-1})$	Range of k_{uni} (s^{-1})
P = 25 Torr He	4.7 ± 1.6	69 - 146
P = 25 Torr N_2	4.2 ± 1.5	96 - 246
P = 50 Torr He	5.4 ± 1.9	34 - 228
P = 50 Torr N_2	6.8 ± 2.4	8 - 249
P = 100 Torr N_2	5.9 ± 2.1	73 - 283
Control Experiments[a]		
Larger Photolysis Beam (1.3 cm)	4.7 ± 1.6	91 - 401
Smaller Photolysis Beam (1 cm)	7.7 ± 2.7	0 - 304
Single UV Pass	4.5 ± 1.6	206 - 490
Double Flashes per Refresh (3)	7.4 ± 2.6	24 - 155
Half Flashes per Refresh (0.9)	5.9 ± 2.1	2 - 270

[a]Control experiments were at a total pressure of 50 Torr N_2, except for "Half Flashes per Refresh" experiment, which was in 50 Torr He
[b]Uncertainty in k_{self} reflects 35% uncertainty in $[CH_2OO]_0$

As shown, the fit k_{self} values range from $4.2 - 7.7 \times 10^{-11} cm^3$ $molecule^{-1} s^{-1}$ and are all within each other's uncertainty. Because of the large calculated exothermicity of this reaction and the relatively small predicted barrier to chemically activated products,[126, 164] the rate coefficients we measure here should not depend on either pressure or bath gas. Therefore, rather than being representative of any real trend, the k_{self} values measured at different pressures and bath gases are representative of our overall uncertainty in k_{self}.

Of course, it is important to also note that all of the control experiments give k_{self} values in reasonable agreement. The control experiment with a single pass of the UV probe beam is particularly important. In this experiment the UV and I atom probe beams followed the same single-pass path through the reactor. The fact that the k_{self} value obtained from this experiment is in good agreement with those measured using a very different multiple-pass geometry strongly suggests that any spatial inhomogeneity in the photolysis beam is small such that a nearly homogenous cylinder of radicals is generated at each photolysis flash. As expected, diffusion out

of the single-pass beam is much faster than diffusion out of the large region covered by the Herriott multiple pass geometry, resulting in the consistently higher k_{uni} values for this experiment.

Furthermore, the absorption cross section of CH_2OO at the UV probe wavelength ($\lambda = 375$ nm) was measured as $6.2 \pm 2.2 \times 10^{-18}$ cm^2 molecule^{-1} for the single UV pass experiment (Figure B 5) in good agreement with our previous measurement (Figure A 1) as well as the recent measurement of Ting et al. ($7.7 \pm 0.385 \times 10^{-18}$ cm^2 molecule^{-1} at 375 nm), who used a different method to determine $[CH_2OO]_0$.[165] We note that our values and those of Ting et al. are significantly lower than the absolute cross section measured by Sheps ($25 \pm 6 \times 10^{-18}$ cm^2 molecule^{-1}), who in addition to using a different method to estimate $[CH_2OO]_0$ also had a different multiple-pass reactor geometry.[122] This agreement of $\sigma_{CH_2OO}(\lambda = 375$ nm) values between us and Ting et al. provides evidence that the way in which we are quantifying $[CH_2OO]_0$ using the I atom absorbance is accurate.

Finally, based on the range of values we have measured we recommend using $k_{self} = 6.0 \pm 2.1 \times 10^{-11} cm^3$ molecule^{-1} s^{-1}. This value is within the large uncertainty of the theoretical prediction of Vereecken et al.[126] but much smaller than the experimentally and theoretically determined estimate of Su et al.[164] The authors of that previous work later revised their recommended k_{self} to $8 \pm 4 \times 10^{-11} cm^3$ molecule^{-1} s^{-1} based on subsequent ultraviolet absorption experiments,[168] in much better agreement with our measurements. Chhantyal-Pun et al. also later measured $k_{self} = 7.3 \pm 0.6 \times 10^{-11} cm^3$ molecule^{-1} s^{-1} using cavity ring down spectroscopy,[169] again in good accord with the measurements reported here.

Using this newly measured self-reaction rate-coefficient we can estimate at what $[CH_2OO]_0$ this sink of CH_2OO will compete with other loss processes, $[CH_2OO]_{0,min}$. Typically in both the atmosphere and in laboratory experiments, $k_{uni} \approx 100$ s^{-1}.[118] Therefore $[CH_2OO]_{0,min} = \frac{k_{uni}}{k_{self}} \approx 2 \times 10^{12}$ molecules cm^3, which is unlikely to be reached in the atmosphere[170] but is certainly typical in many laboratory experiments including alkene ozonolysis.[171]

3.2.4   Conclusions

The rate of self-reaction of the simplest Criegee Intermediate, CH_2OO, is of importance in many current laboratory experiments where CH_2OO concentrations are high, such as flash photolysis and alkene ozonolysis. Using laser flash photolysis while simultaneously probing both

CH_2OO and I atom by direct absorption we can accurately determine absolute CH_2OO concentrations as well as the UV absorption cross section of CH_2OO at our probe wavelength ($\lambda = 375$ nm), which is in agreement with a recently published value. Knowing absolute concentrations we can accurately measure $k_{self} = 6.0 \pm 2.1 \times 10^{-11} cm^3$ molecule^{-1} s^{-1} at 297 K. We are also able to put an upper bound on the rate coefficient for CH_2OO + I of $1.0 \times 10^{-11} cm^3$ molecule^{-1} s^{-1}.

3.3   Kinetics of CH_2OO + Carbonyls

3.3.1   Introduction

Criegee Intermediates (CI) were postulated many years ago as important biradicals in atmospheric alkene ozonolysis[117] where they are likely to be formed with high internal energy and can initiate tropospheric oxidation reactions.[113] They also impact the atmospheric budgets of SO_2[116] and NO_X[118, 172] and are linked to the formation of H_2SO_4.[173] Reaction of CI with water dimer is by far the major bimolecular loss for this intermediate, which is based on the high concentration of H_2O in the troposphere and the moderate rate constant of the reaction of CI with water dimer.[174] For its potential importance in the atmosphere, reactions of CI with neutral atmospheric molecules have been of interest to many experimentalists and theoreticians.[55, 74, 113, 116, 118, 120, 172-176] However, direct kinetic measurements were only accessible recently, after Welz et al. demonstrated an efficient route for the formation of the simplest CI (CH_2OO) through the reaction of CH_2I + O_2.[118] Reactions with carbonyl compounds have received special attention as the highly exothermic and barrierless cycloaddition of CI to the C=O bond makes them efficient CI scavengers. In the present work, we report the temperature dependent rate coefficients for reactions of CH_2OO with acetone (CH_3COCH_3) and acetaldehyde (CH_3CHO) and compare these with similar studies on C2-C4 alkenes (ethene, propene and butenes).[74] Existing literature on the carbonyl reactions has been limited to room temperature.[55, 120, 175-177] Taatjes et al.[120] used Photo-Ionization Mass Spectrometry (PIMS) and found the reaction with CH_3CHO to be 4 times faster than with CH_3COCH_3 at P = 4 Torr. In the case of CH_3COCH_3 they observed products at two masses: m/z =104 amu, which they assigned to the secondary ozonide (SOZ) and m/z = 89 amu, which they hypothesized was the daughter ion of another 104 amu isomer. Acetic

acid (CH₃COOH), formaldehyde (HCHO) and formic acid (HCOOH) were all detected as products in the reaction between CH_2OO and CH_3CHO. Stone et al.[55] investigated the reaction of CH_2OO with CH_3CHO at pressures between 25 Torr and 300 Torr. They monitored HCHO using LIF and found the HCHO yield from the reaction to decrease with pressure, implying that the reaction is pressure dependent. Horie et al.[175] used FT-IR to measure the rate of CH_2OO reaction with CH_3CHO relative to CF_3COCF_3 in the solution phase and observed SOZ formation in both reactions. Berndt et al.[176] measured the room temperature rate coefficient for the reactions of CH_2OO with CH_3CHO and CH_3COCH_3. In their work, CH_2OO radicals were generated from the reaction of ozone with C_2H_4 at atmospheric pressure and the rate coefficient was indirectly measured by detecting H_2SO_4 after titration with SO_2. Several ab initio calculations have been performed on CH_2OO + carbonyls.[128, 177-178] Recently Jalan et al.[128] used electronic structure and RRKM calculations to determine both the rates and the product branching of the title reactions. We previously reported rates for reactions of CH_2OO with alkenes (section 3.1) and found the kinetics to be slow relative to carbonyl compounds with small positive experimental Ea's. The main interest of this work is to measure and understand the T-dependence of CH_2OO + C=O bonds in CH_3CHO and CH_3COCH_3 and compare these with similar results for CH_2OO + C=C bonds obtained earlier. We also report the effect of pressure on the kinetics of the title reactions at 298 K and 444 K. The products of the reactions were measured at 298 K and 10, 25 and 50 Torr by Photo-Ionization Time-of-Flight Mass Spectrometry (PI TOF-MS). The MS study was limited to products with ionization energy ≤ 10.5 eV. Finally, our measurements were compared against theoretical predictions using the molecular geometries and energies computed by Jalan et al. (RCCSD(T)-F12a/cc-pVTZ-F12//B3LYP/MG3S level of theory).[128]

3.3.2   Experimental Methods

All experiments were conducted on a modified version of the MIT laser-photolysis/Herriott multiple-pass laser-absorption apparatus described by Ismail et al.[96] This apparatus was modified to incorporate a PI TOF-MS with supersonic molecular beam sampling from the center of the reactor. Detailed descriptions of the apparatus are available in a published MIT Ph.D. thesis[68] and only the essential details are included here. The stainless steel reactor is 86 cm long, 6 cm in diameter and resistively heated by four heaters wrapped along the length of the reactor to create a

uniform temperature profile (standard deviation $\pm 2\%$ of average) through the overlap region of the absorption laser. The heaters enable the gas mixture to be heated up to 700 K, though in the present work, measurements were limited to 500 K to avoid secondary chemistry that could arise from the thermal decomposition of CH_2OO at high temperatures. The internal pressure of the reactor was monitored by a capacitance manometer and controlled via an automated butterfly valve. In order to minimize the possibility of CH_2 formation (via a single-photon process[127]) or photolytic fragmentation of either CH_3CHO or CH_3COCH_3, the third harmonic output of an Nd:YAG laser (355 nm) operated at a repetition rate of 2 Hz was used to photolyze CH_2I_2 instead of a shorter wavelength such as the fourth harmonic of an Nd:YAG laser (266 nm). The frequency-doubled output of a Ti:Sapphire laser (80 MHz pulsed laser with 1.2 ps full width at half maximum, FWHM, pulses) was used to generate the 375 nm probe beam. The fundamental wavelength of the Ti:Sapphire laser was measured before each experiment using a recently calibrated Ocean Optics USB2000 spectrometer. Multiple-pass probe laser path lengths were in the range of 10–15 m. Because the probe laser generates a continuous pulse train, a complete transient absorption trace is recorded for each photolysis flash. Transient absorbance traces were averaged over 500 acquisitions. Helium was used as a balance gas. The flow of this gas was varied to adjust the total gas mixture flow and maintain the same number of photolysis flashes per refresh. All experiments were operated at one flash per refresh to avoid secondary chemistry.

The relative time-dependent product concentrations were determined using the PI TOF MS method. A small amount of the reactive gas mixture was continuously sampled via a small pinhole at the tip of a cone that juts slightly into cross section of the photolysis beam at the center of the reaction cell. The sampled gas was supersonically expanded, and the center of the resultant free jet was passed through a Beam Dynamics skimmer to form a collimated molecular beam. The gas in the molecular beam was effectively "frozen" in composition by cooling while in transit to the ionization region of the PI TOF-MS, where it was photo-ionized using 118.2 nm (10.487 eV) light. The 118.2 nm light was generated by focusing the third harmonic (355 nm) output of a pulsed Nd:YAG laser (<12 ns FWHM wide pulses at 2Hz) in a 1:10 Xe:Ar gas cell at a total pressure of 90–100 Torr. The relative abundance of ions at different mass-to-charge ratios (m/z) were analyzed using a Kore Time-of-Flight mass spectrometer and detected using the Kore-supplied discrete dynode electron multiplier detector and analog pre-amplifier. The correspondence between time-of-flight and m/z was determined by calibration with a mixture of

known stable species. Control experiments were conducted with and without acetone, O_2 or CH_2I_2.

CH_2I_2 was purchased from Sigma-Aldrich at 99% purity and was further purified by successive freeze-pump-thaw cycles. CH_2I_2 was introduced into the reactor by a helium flow through a room temperature bubbler maintained at 750 Torr. CH_3COCH_3 (Sigma Aldrich, $\geq$ 99.9%) and CH_3CHO (Sigma Aldrich, $\geq$ 99.5%) were used after purification by freeze-pump-thaw cycles using liquid nitrogen. During use, the carbonyl compounds were maintained at constant temperatures such that their respective vapor pressures were sufficient to drive the flow through an MKS mass flow controller (MFC). Because the MFC's have been calibrated with N2, the uncertainty in the concentration of CH_3CHO and CH_3COCH_3 in the reactor is 10%, as we have previously explained,[74] which is the dominant contribution to the uncertainty in our measurements of overall rate coefficients. In the TOF-MS experiments a small flow of calibration gas, consisting of 100 ppm each of nine species with known photoionization cross sections diluted in helium, was simultaneously introduced as an internal standard. The uncertainty in the concentration of the calibration gas is also 10% for the same reasons, which has been accounted for in the final reported uncertainty of our TOF-MS results. Helium (Airgas, 99.999%) and oxygen (BOC, 99.999%) were used directly without further purification.

3.3.3   Results and Discussion

3.3.3.1   Generation of CH$_2$OO

CH_2OO radicals were generated utilizing the method demonstrated by Welz et al., (but using 355 nm instead of 248 nm photolysis)[118]

$$CH_2I_2 \xrightarrow{355\,nm} CH_2I + I$$

$$CH_2I + O_2 \xrightarrow{k_1} CH_2OO + I$$
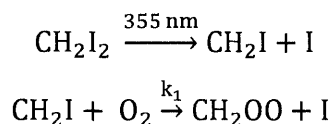
Figure 3-12 shows the CH_2OO 375 nm absorption following 355 nm photolysis of CH_2I_2 in the presence of O_2. Flat signal was observed in the absence of either CH_2I_2 or O_2. Previous work in our laboratory has demonstrated that CH_2OO is the dominant radical being probed at 375 nm (section 3.1.4.1).This was verified by measuring the formation rate of CH_2OO by simultaneously recording the UV absorption at 375 nm and the infrared absorption of the co-produced I atom (probing the F= 3 $^2P_{1/2}\leftarrow$ F=4 $^2P_{3/2}$ hyprefine atomic

transition)[127] at different concentrations of O_2. The resulting rate coefficient (k_1) agreed well with literature confirming that the species being monitored is a product of CH_2I + O_2. Furthermore, the room temperature reaction rate of this species with CH_3COCH_3 agreed well with Taatjes's value[120] for CH_2OO + CH_3COCH_3 at the same temperature and pressure. As a result we think the change in the absorption intensity of the probe, $A_{375nm}(t)$, in our system is representative of the concentration of CH_2OO as a function of time:

$$A_{375\,nm}(t) \propto [CH_2OO](t)$$

From our previous study on CH_2OO self-reaction (section 3.2), the absorption cross section of CH_2OO at 375 nm, $\sigma_{CH_2OO}(375\,nm)$, is $(6.2 \pm 2.2) \times 10^{-18}$ cm^2 molecule^{-1}. For further discussion of the absorption spectrum of CH_2OO see Ting et al.[165]

Once generated, CH_2OO radicals undergo reactions with the co-reactants CH_3COCH_3/CH_3CHO (k_2, k_3) and are also removed from the center of the reactor by other processes. Possible removal processes of CH_2OO in our system include:

$$CH_2OO + CH_3COCH_3 \xrightarrow{k_2} Product$$

$$CH_2OO + CH_3CHO \xrightarrow{k_3} Product$$

$$CH_2OO + CH_2OO \xrightarrow{k_{self}} Products$$

$$CH_2OO + I \xrightarrow{k_{CH2OO+I}} Products$$

$$CH_2OO \xrightarrow{k_4} Products$$
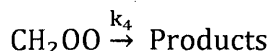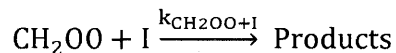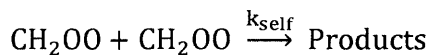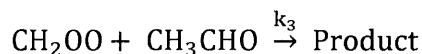
Reactions are carried out under pseudo first order conditions, where the co-reactant, CH_3COCH_3 or CH_3CHO, is in great excess over the initial concentration of CH_2OO and I, so the first-order processes dominate. Most of the radicals react with the species which is in excess. This simplifies the analysis of the transient concentration data greatly, as the kinetics can be accurately fitted by a single exponential function of the form a exp(-k't) + c, black dashed line in Figure 3-12.

In most of our absorption experiments, the maximum [CH_2OO] is small enough, 4.9×10^{11} molecule cm^{-3}, that the second-order reaction is negligible. The rate constant for the self-reaction of CH_2OO was reported recently by Buras et al.,[75] Ting et al.,[168] and Pun et al.[169] Employing an average value of $k_{self}= 7 \times 10^{-11}$ cm^3 molecule^{-1} s^{-1} and the

upper bound rate coefficient for $CH_2OO + I$ of 1×10^{-11} cm^3 molecule^{-1} s^{-1},[19] the computed removal by second order processes is always less than 35 s^{-1}, at least an order of magnitude slower than the first-order processes. Therefore once the CH_2OO formation process is complete, the measured exponential decay of the signal due to CH_2OO absorption in our system can be described by a simple equation:

$$A_{375}(t) = a \exp(-k'_{total}t) + c \tag{3-10}$$

$$k'_{total} = k_{co-reactant}[co-reactant] + k'_4 \tag{3-11}$$

where k'_4 is a catch-all rate that captures effects such as diffusion out of the probe beam, reaction with contaminants and unimolecular decomposition of CH_2OO, a is a scaling factor and c is a vertical offset.
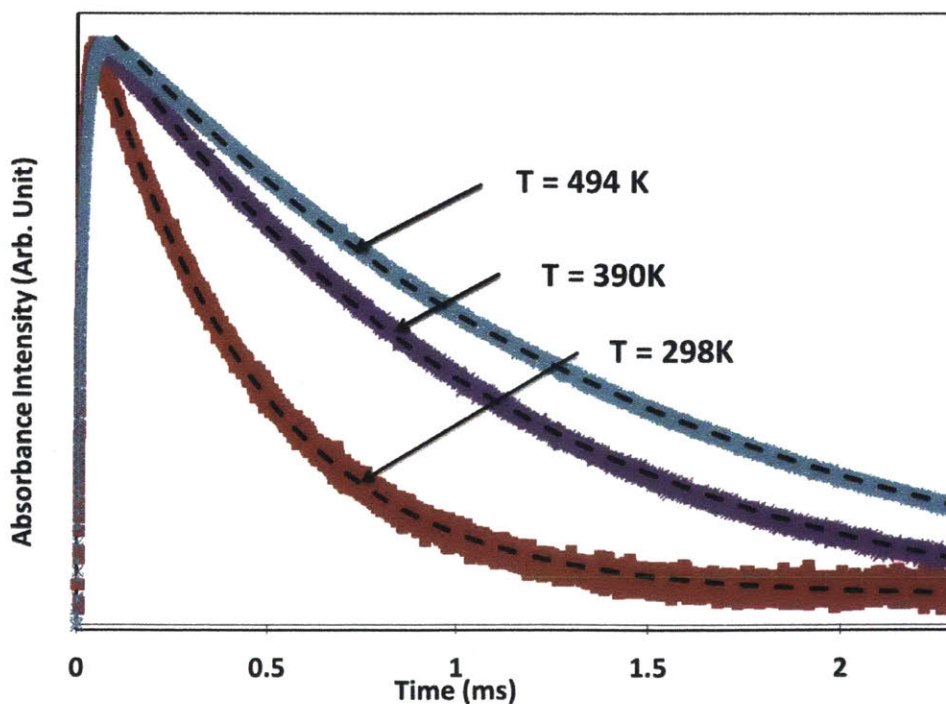
Figure 3-12: Time resolved CH_2OO absorption signal at 3 temperatures for P = 25 Torr, $[O_2]$ = 6×10^{16} molecules cm^{-3}, $[CH_2I_2]$ = 1.4×10^{14} molecules cm^{-3} and $[CH_3CHO]$ = 1.0×10^{15} molecules cm^{-3}. The dashed lines are single exponential fits. The reaction is fastest at low T.

A single exponential function was able to fit the absorption traces well at all temperatures less than 500 K. The resultant pseudo-first order plots at 298 K, as shown in Figure 3-13,

squares, have a relatively small intercept, k'_4, compared to the total removal rate in the presence of the maximum concentration of the co-reactant. This observation demonstrates that reactions with CH_3COCH_3/CH_3CHO are the dominant consumption routes for CH_2OO radicals at room temperature. However, as the temperature increases, triangles and circles in Figure 3-13, the title reactions become slower, and the secondary chemistry becomes competitive. Attempts to measure the rate of the title reactions at temperatures above 500 K were made, but, as we have previously shown,[74] even at low photolysis energy (50 mJ/pulse) and low CH_2I_2 concentration, the decay of the CH2OO absorption was fast ($\sim$2000 s^{-1}) and not very sensitive to the concentration of the co-reactant, so we could not accurately determine k_2 or k_3. We hypothesize that this is due to the onset of fast unimolecular decomposition at T>500 K.

Control experiments were carried out at different experimental conditions of $[CH_2I_2]$ and photolysis energy. The results are consistent with the base condition ($[CH_2I_2] = 1.4 \times 10^{14}$ molecules cm^{-3} and 50 mJ/pulse), implying that the effect of laser energy and precursor concentration on the measured rate coefficients is negligible. The conditions and results of the control experiment are shown in Appendix C.

3.3.3.2   T-dependence of CH_2OO + CH_3COCH_3 and CH_2OO + CH_3CHO

A series of 375 nm absorption decay profiles were collected at P = 25 Torr under identical O_2 and CH_2I_2 concentrations at different temperatures between 298 K and 500 K. The decay constants, k'_{total}, extracted from each absorption signal were then plotted against the co-reactant concentration at a given temperature. Sample kinetic plots for $CH_2OO+CH_3COCH_3$ and CH_2OO+CH_3CHO at T = 298 K, 390 K and 494 K are shown in Figure 3-13.
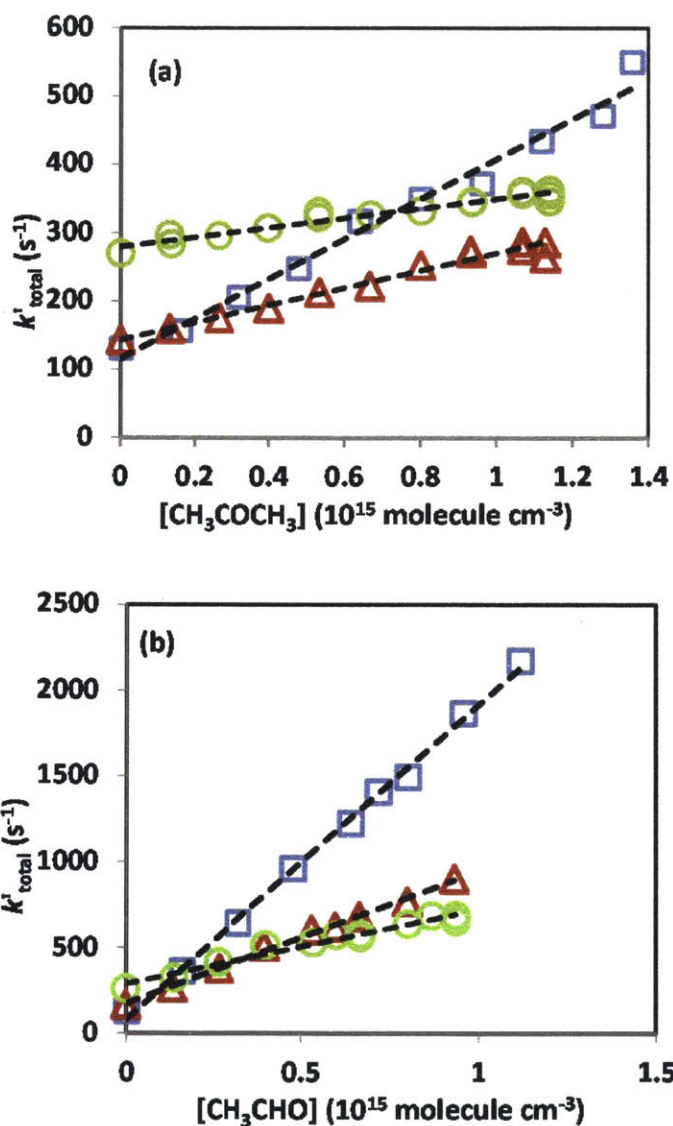
Figure 3-13: Pseudo-first-order rate coefficient of CH_2OO decay as a function of (a) $[CH_3COCH_3]$ and (b) $[CH_3CHO]$ at P=25 torr and T = 298 K (squares), 390 K (triangles) and 494 K (circles). For discussion of uncertainties, see the text.

Bimolecular rate coefficients for the title reactions (k_2 and k_3) at any given temperature were obtained from the slopes of the k'_{total} vs. $[CH_3COCH_3]$ and $[CH_3CHO]$ plots respectively, Table 3-7. The decrease in the rate coefficients with temperature reflects the slower removal of CH_2OO by the co-reactant.

Table 3-7: Bimolecular rate coefficients[a] for the reaction of CH_2OO + CH_3COCH_3, k_2, and CH_2OO + CH_3CHO, k_3, as a function of temperature at P = 25 Torr.

Temperature (K)	k_2 (cm^3 molecule^{-1} s^{-1})	k_3 (cm^3 molecule^{-1} s^{-1})
298	$(3.0 \pm 0.6) \times 10^{-13}$	$(1.2 \pm 0.2) \times 10^{-12}$
340	$(1.9 \pm 0.3) \times 10^{-13}$	$(8.0 \pm 1.1) \times 10^{-13}$
390	$(1.3 \pm 0.3) \times 10^{-13}$	$(4.9 \pm 0.8) \times 10^{-13}$
444	$(7.9 \pm 1.9) \times 10^{-14}$	$(3.6 \pm 0.5) \times 10^{-13}$
494	$(7 \pm 2) \times 10^{-14}$	$(2.7 \pm 0.6) \times 10^{-13}$

[a]reported uncertainty includes statistical and systematic errors.

The errors resulting from fitting a single exponential to the measured decay profile are very small ($< 0.1\%$); therefore, error bars are not given for individual k' values, Figure 3-13. The main uncertainty in our experiments is due to the imperfect control of the concentrations. We expect maximum systematic errors of ~10% in the reported concentrations due to the uncertainties in the flow controller calibration. As a result, we assumed errors of ±10% for every concentration of the co-reactant to calculate the upper and lower limits of the corresponding rate constants. The reported uncertainties in Table 3-7, Table 3-8, Figure 3-14 and Figure 3-15 include statistical fitting errors as well as our estimates of the maximum systematic error over the T and P range of interest.

Our measured rate coefficients are largely consistent with prior room temperature measurements. At 298 K and 25 torr, our measurement for CH_2OO + CH_3CHO $(1.2 \pm 0.2) \times 10^{-12}$ cm^3 molecule^{-1} s^{-1} is consistent within the uncertainties with the indirect measurement by Berndt et al. $(1.7 \pm 0.5) \times 10^{-12}$ cm^3 molecule^{-1} s^{-1} and in slight disagreement with Stone et al.'s indirect measurement of $(1.48 \pm 0.04) \times 10^{-12}$ cm^3 molecule^{-1} s^{-1}.[55, 176] The kinetics of CH_2OO +CH_3CHO was found to be ~4 times faster than CH_2OO +CH_3COCH_3 across all the temperature range studied here. At 4 torr, our rate coefficients for both reactions are consistent with the room temperature values reported by Taatjes et al.[120]

The temperature dependence of both reactions follows simple Arrhenius kinetics with distinct negative temperature dependence:

$$k_2(T) = (7 \pm 2.5) \times 10^{-15} \text{ cm}^3 \text{ molecule}^{-1} \text{ s}^{-1} \exp[+(9251 \pm 2918) \text{ J mol}^{-1}/RT]$$

$$k_3(T) = (3 \pm 0.8) \times 10^{-14} \text{ cm}^3 \text{ molecule}^{-1} \text{ s}^{-1} \exp[+(9076 \pm 2652) \text{ J mol}^{-1}/RT]$$

The variations in k_2 and k_3 with temperature are shown in Figure 3-14. Also shown are the rate coefficients for CH_2OO + alkenes measured in section 3.1. Such negative temperature dependencies are common for reactions that have a long-range attraction between the reactants and low or submerged reaction barriers.[179] When comparing the reactivity of CH_3CHO and CH_3COCH_3 with our previous data for alkenes (Figure 3-14), the differences are obvious. At room temperature, rate coefficients for CH_2OO + carbonyl compounds were found to be two orders of magnitude higher than with alkenes. Considering that reactions of CH_2OO with double bonds are expected to proceed mainly via 1,3 dipolar cycloaddition,[126] then the increase in the rate coefficients in going from alkenes to carbonyl compounds is likely due to the differences in the nature of the corresponding double bonds. The C=O bond is expected to be more reactive towards CH_2OO on account of its higher dipolar character compared to the C=C bonds in alkenes. The reported pre-exponential factor for the reaction of CH_2OO with alkenes is similar to that reported here for the reaction with carbonyl compounds, CH_3COCH_3 and CH_3CHO, implying that the differences in their reactivity towards CH_2OO is due primarily to the depth of the submerged transition state. Further explanation is given in the theory section below (section 3.3.3.5).
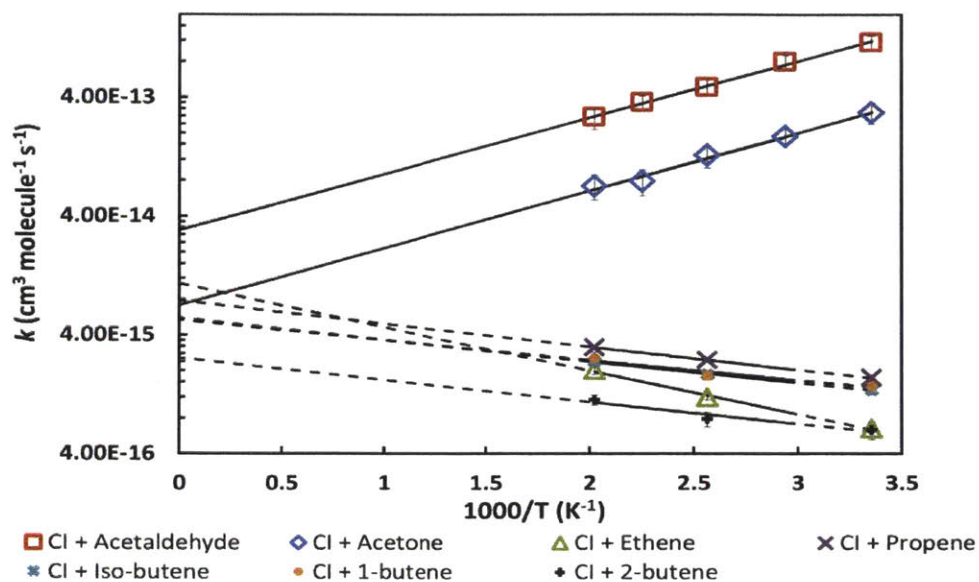
Figure 3-14: Arrhenius plot of the experimentally determined rate constants for CH_2OO + CH_3COCH_3, k_2, and CH_2OO + CH_3CHO, k_3, together with the best fit to $k = A\exp(-E/RT)$, solid line, and statistical and systematic errors. Also included are data for CH_2OO + alkenes.[74]

3.3.3.3   P-Dependence of CH_2OO + CH_3COCH_3 and CH_2OO + CH_3CHO

Experiments were done at P = 4, 25 and 50 Torr. The corresponding rate coefficients are presented in Figure 3-15 and Table 3-8. Within the uncertainty of our measurements, weak pressure dependence was observed for both reactions at 298 K. Any pressure dependence in the rate coefficients is even harder to discern at 444 K. The difference between the rate coefficients across the measured pressure range of interest is comparable to the uncertainty associated with the individual measurements.
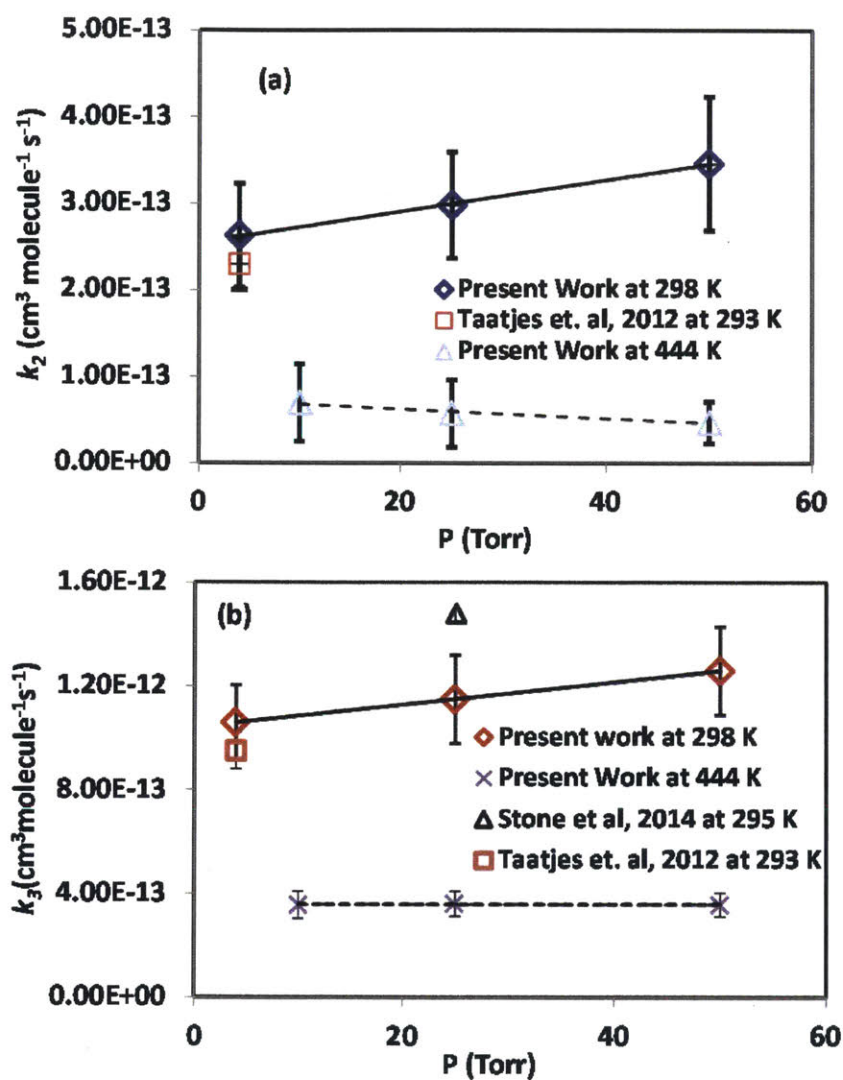
Figure 3-15: Plot of the pressure-dependence of the rate coefficients for the reactions (a) $CH_2OO + CH_3COCH_3$, k_2, and (b) $CH_2OO + CH_3CHO$, k_3. Both statistical (fitting) and systematic errors have been incorporated in the error bars.

Table 3-8: Bimolecular rate coefficients[a] for the reaction of CH_2OO + CH_3COCH_3, k_2, and CH_2OO + CH_3CHO, k_3, as a function of pressure at 298 K and 444 K.

Pressure (Torr)	k_2 (cm^3 molecule^{-1} s^{-1})	k_3 (cm^3 molecule^{-1} s^{-1})
T = 298 K		
4	$(2.6 \pm 0.6) \times 10^{-13}$	$(1.1 \pm 0.1) \times 10^{-12}$
25	$(3.0 \pm 0.6) \times 10^{-13}$	$(1.2 \pm 0.2) \times 10^{-12}$
50	$(3.5 \pm 0.8) \times 10^{-13}$	$(1.3 \pm 0.2) \times 10^{-12}$
T = 444 K		
10	$(8.5 \pm 2.2) \times 10^{-14}$	$(3.6 \pm 0.5) \times 10^{-13}$
25	$(7.9 \pm 1.9) \times 10^{-14}$	$(3.6 \pm 0.5) \times 10^{-13}$
50	$(7.4 \pm 1.2) \times 10^{-14}$	$(3.6 \pm 0.5) \times 10^{-13}$

[a]reported uncertainty includes statistical and systematic errors.

3.3.3.4   TOF-MS Results

Because we were not able to detect any products in the PI TOF-MS for the CH_2OO + CH_3CHO system at 25 Torr using 10.5 eV photoionization, the results in this section focus exclusively on CH_2OO + CH_3COCH_3. The time resolved mass spectra for CH_2OO + CH_3COCH_3 were recorded at three different pressures 10, 25 and 50 Torr. In all cases the CH_2OO reactant was observed at m/z = 46 amu. Figure 3-16 shows a section of our measured mass spectra for CH_2OO + CH_3COCH_3 as a function of reaction time. Two cations from products were observed, at m/z = 104 amu and 89 amu. The m/z = 104 amu channel is attributed[120] to the parent ion of the secondary ozonide (SOZ), an expected major product. The m/z=89 amu channel was assigned as a daughter ion of another mass 104 species that fragments upon photo-ionization; Taatjes et al. proposed that this easily fragmented, mass 104 species is methoxymethyl acetate.[120]
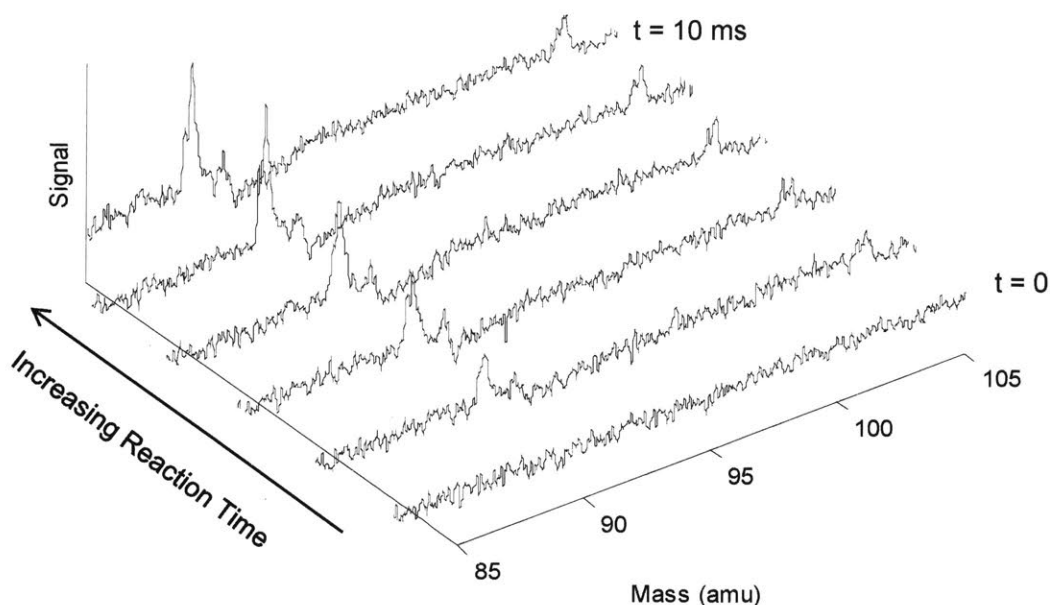
Figure 3-16: Section of mass spectrum at 298 K, 10 Torr, $[O_2] = 6 \times 10^{16} cm^{-3}$, $[CH_2I_2] = 2.44 \times 10^{14} cm^{-3}$ and $[CH_3COCH_3] = 1.24 \times 10^{15} cm^{-3}$ showing time dependence of two product peaks of $CH_2OO + CH_3COCH_3$: $\frac{m}{z} = 89$ and 104 amu. The spectrum at $t = -0.2$ ms has been subtracted so that only species formed following the photolysis flash at t=0 are evident.

To achieve sufficient signal-to-noise ratio, a higher $[CH_2OO]$ was used in the mass spectrometry experiments than in the absorbance experiments reported above, increasing the contribution from the self-reaction of CH_2OO (k_{self}). Therefore, the self-reaction of CH_2OO is included in the kinetic model for $CH_2OO + CH_3COCH_3$, as shown in Scheme 3-5. Once formed in the presence of acetone, CH_3COCH_3, we assume that CH_2OO can react with $CH_3COCH_3 (k_2)$, react with itself (k_{self}), or unimolecularly decompose/diffuse out of the sampling volume (k_4). The product branching fractions to SOZ, methoxymethyl acetate, and formic acid are represented by β_{104}, β_{89} and β_{46}. Formic acid is expected to be a major product,[128] but we cannot observe this channel because the ionization energy (IE) of formic acid is larger than 10.5 eV.[180]

$$CH_2OO + CH_3COCH_3 \xrightarrow{k_2} \text{Products} \xrightarrow{\beta_{89}} \text{Product which forms } \frac{m}{z} = 89$$

$$\xrightarrow{\beta_{104}} \frac{m}{z} = 104 \text{ Product (SOZ)}$$

$$\xrightarrow{\beta_{46}} HCOOH + CH_3COCH_3$$

$$CH_2OO \xrightarrow{k_4} \text{Products}$$

$$2\, CH_2OO \xrightarrow{k_{self}} \text{Products}$$
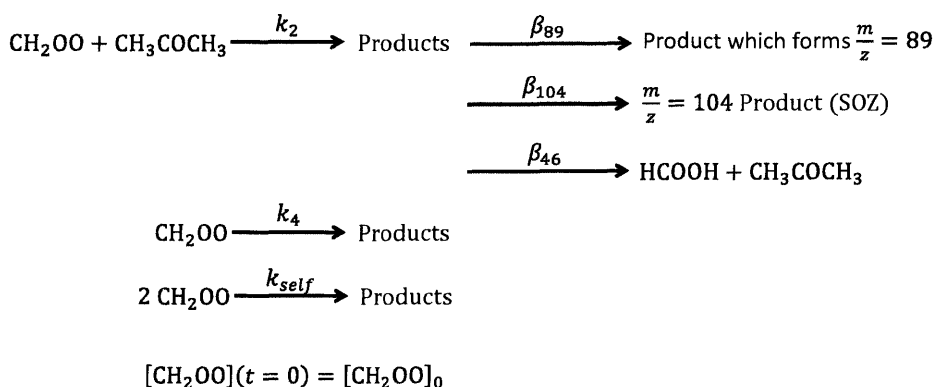
$$[CH_2OO](t = 0) = [CH_2OO]_0$$

Scheme 3-5: General kinetic model for $CH_2OO + CH_3COCH_3$.

This kinetic model is consistent with the measured time-dependence, Figure 3-17, though at long times the stable product signals decline, presumably due to diffusion out of the volume illuminated by the photolysis laser.

We couldn't determine absolute product branching fractions of the $CH_2OO + CH_3COCH_3$ reaction, β_i (where i = 89 or 104), as the photoionization cross section for the products, σ_{89} and σ_{104}, are not known. However, we can ratio the measured value of $\sigma_i\beta_i$ at one pressure to another pressure. Assuming σ_i is pressure-independent, then the relative pressure dependent yield of product i is given by the following expression:

$$\frac{(\beta_i)_{P1}}{(\beta_i)_{P2}} = \frac{\left(\frac{S_i(t\to\infty)}{\overline{S}_{calmix,j}} \frac{[calmix,j]}{[Products_{(CI+Acetone)}](t\to\infty)} \right)_{P1}}{\left(\frac{S_i(t\to\infty)}{\overline{S}_{calmix,j}} \frac{[calmix,j]}{[Products_{(CI+Acetone)}](t\to\infty)} \right)_{P2}} \tag{3-12}$$

Where S_i is the integrated MS peak area for the species i, $\overline{S}_{calmix,j}$ is the average value of the integrated peak area of MS signals for one of the calibration mixture species used as internal standards, j, $\sigma_i(E)$ is the photoionization cross-section of species i at energy E, [calmix, j] is the concentration of calibration species j, and $[Products]_{CI+Acetone}$ (t → ∞) is the steady state concentration of all CH_2OO + Acetone products. An analytical expression for $[Products]_{CI+Acetone}$ (t → ∞) obtained by solving the kinetic model represented by Scheme 3-5 is given in Appendix C along with details of how it is quantified. A full derivation of Eq. 5 is also provided in the Appendix C.

$S_i(t \to \infty)$ and $\overline{S}_{calmix,j}$ are determined from the PI TOF-MS data as shown in Figure 3-17 and Figure C 4. If the product species concentration was constant after being formed, then the value of $S_i(t \to \infty)$ would simply be the TOF-MS signal at long times. However, the

products do undergo subsequent reactions and they also diffuse out of the sampling volume as manifested by a slow, but noticeable decay in signal. Therefore, $S_i(t \to \infty)$ is obtained by first fitting $S_{46}(t)$, $S_{89}(t)$ and $S_{104}(t)$ to the kinetic model shown in Scheme 3-5 with the addition of a first-order loss term for the 89 and 104 amu producs (solid lines in Figure 3-17). The fit model is then simulated without the first order loss-terms for 89 and 104 amu (dashed lines in Figure 3-17) and $S_i(t \to \infty)$ is taken as the values of these simulations at long time. $S_{calmix,j}(t)$ was recorded simultaneously as $S_i(t)$ and averaged over all of the time points to obtain $\bar{S}_{calmix,j}(t)$ as indicated by the line in Figure C 4. Control experiments were conducted at the same conditions as the experiment in Figure 3-17, but without CH_3COCH_3, O_2 or the calibration mixture to support the identification of the $\frac{m}{z} = 89$ amu and $\frac{m}{z} = 104$ amu species as products of $CH_2OO +$ CH_3COCH_3 and not as products of something else. Details of the control experiments are in Appendix C.
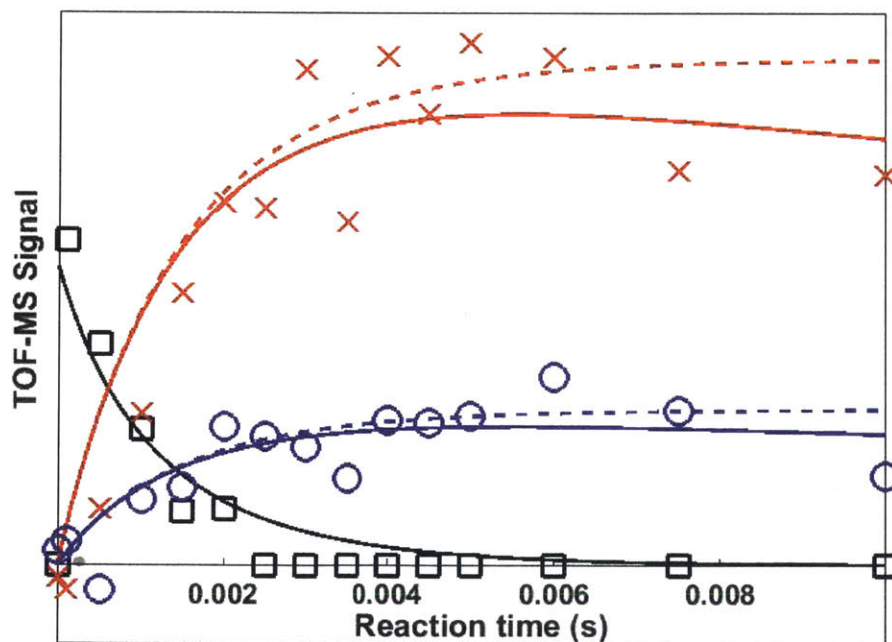
Figure 3-17: Measured TOF-MS signals at 298 K, 10 Torr, $[O_2] = 5.95 \times 10^{16} cm^{-3}$ and $[CH_3COCH_3] = 1.24 \times 10^{15} cm^{-3}$ for $\frac{m}{z} = 46$ amu (black squares), $\frac{m}{z} = 89$ amu (red crosses) and $\frac{m}{z} = 104$ amu (blue circles) recorded simultaneously as the benzene internal standard signal shown in Figure C 4. The lines are fits to the kinetic model described by Scheme 3-5 with (solid) and without (dashed) the addition of first-order loss terms for the 89 and 104 amu products. $S_i(t \to \infty)$ is taken as the maximum value of the dashed lines. Note that the signal at $t = -0.20$ ms was subtracted from all subsequent time points so that the signal is roughly zero at $t = 0$.

Figure 3-18 shows the measured values of $\frac{(\beta_i)_{P1}}{(\beta_i)_{P2}}$ for $\frac{m}{z}$ = 89 amu. The error bars are from

propagation of uncertainty. The yield of the species leading to the $\frac{m}{z}$ = 89 amu signal increases

by about a factor of 2 as the pressure is increased from 10 torr to 25 torr and then stabilizes. For

$\frac{m}{z}$ = 104 amu, however, the TOF-MS signal was too low to discern a trend with respect to

pressure (see Figure C 5). The relative pressure dependent yield of SOZ in a He bath gas

predicted by Jalan et al.[128] is also shown in Figure 3-18 for comparison. The measured P-

dependence of the 89 amu signal is quite different from the P-dependence predicted for SOZ,

supporting the hypothesis that the 89 amu signal is coming from a different species, not SOZ.
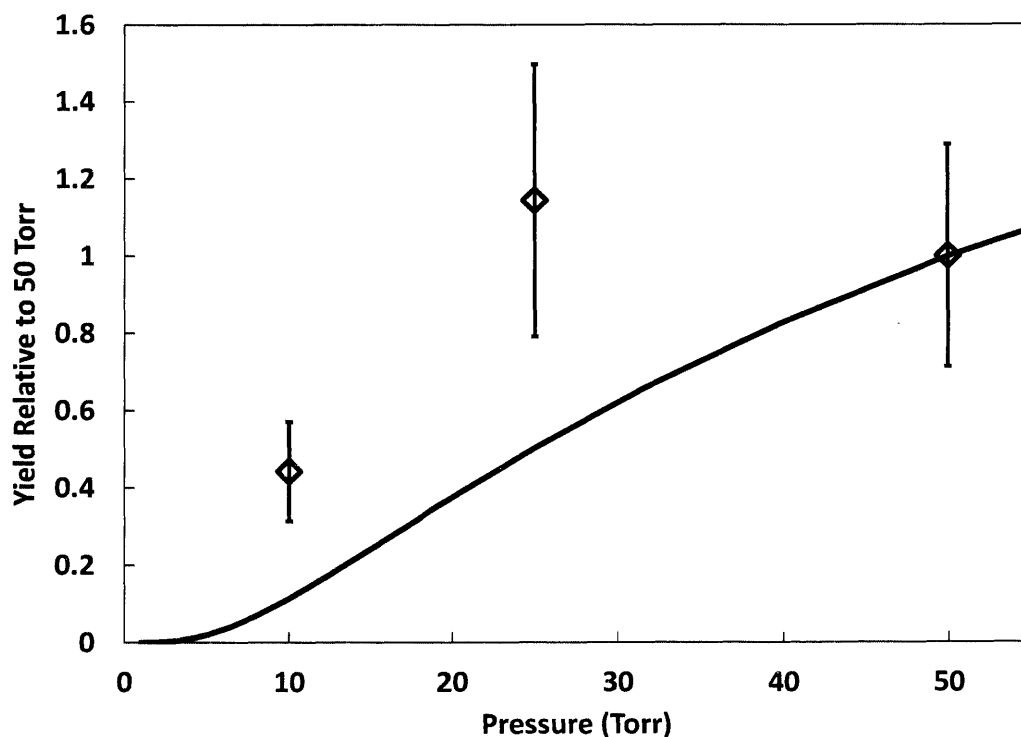
Figure 3-18: Relative yield of $\frac{m}{z}$ = 89 amu product from CH_2OO + CH_3COCH_3 normalized to

the 50 Torr measurement $\left(\frac{(\beta_{89})_{P=X\ Torr}}{(\beta_{89})_{P=50\ Torr}}\right)$ at 298 K (markers) compared to predicted relative yield

of SOZ at the same conditions from Jalan et al.[128] (line).

The relative ratio of $\frac{\beta_{89}}{\beta_{104}}$ can be determined by the following equation.

$$\frac{\left(\frac{\beta_{89}}{\beta_{104}}\right)_{P1}}{\left(\frac{\beta_{89}}{\beta_{104}}\right)_{P2}} = \frac{\left(\frac{S_{89(t\to\infty)}}{S_{104(t\to\infty)}}\right)_{P1}}{\left(\frac{S_{89(t\to\infty)}}{S_{104(t\to\infty)}}\right)_{P2}} \tag{3-13}$$

The results are shown in Figure 3-19 below. Because of the weakness of the $\frac{m}{z} = 104$ amu signal the error bars are large and we cannot determine conclusively if the ratio is P-dependent.
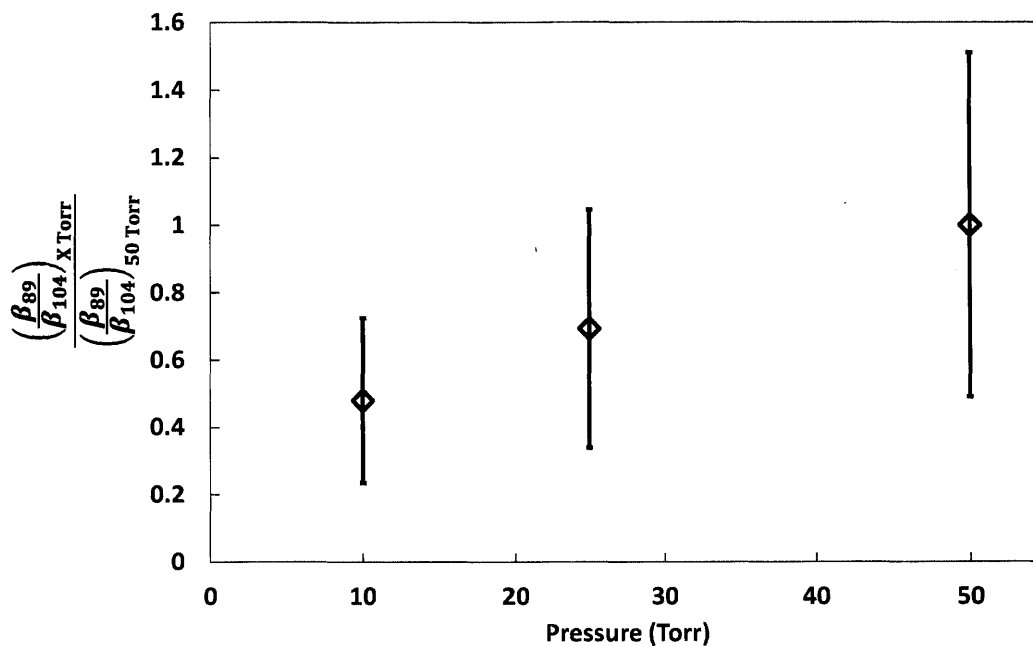
Figure 3-19: Ratio of $\frac{m}{z} = 89$ to $\frac{m}{z} = 104$ amu product yield from CH_2OO + CH_3COCH_3 normalized to the 50 Torr measurement $\left(\frac{\left(\frac{\beta_{89}}{\beta_{104}}\right)_{X\,Torr}}{\left(\frac{\beta_{89}}{\beta_{104}}\right)_{50\,Torr}}\right)$.

The results of our MS experiments agree qualitatively with the previous results of Taatjes et al.,[120] in that the only products observed from the reaction CH_2OO + CH_3COCH_3 are at m/z = 104 and m/z = 89 (they also did not go to high enough ionization energies to see formic acid) and the MS signal for the latter is about 5 times more intense than that of the former. All of our results are discussed in the context of Jalan et al.'s predictions of the overall rate coefficient and the product branching in the following section.[128]

3.3.3.5 Theoretical Analysis of Temperature Dependence and Product Branching

As shown by Jalan et al.,[128] the entrance channels for the title reactions are characterized by two transition states: a loose outer transition state (TS_{outer}) leading to the formation of the Van der Waals (VdW) complex and an inner 1,3-cycloaddition transition state (TS_{inner}) leading to the secondary ozonide (SOZ). Either of these transition states can be rate-limiting depending on the temperature and pressure of interest. Figure 3-20 depicts the entrance channel for both reactions and the simple phenomenological mechanism employed to model this process.
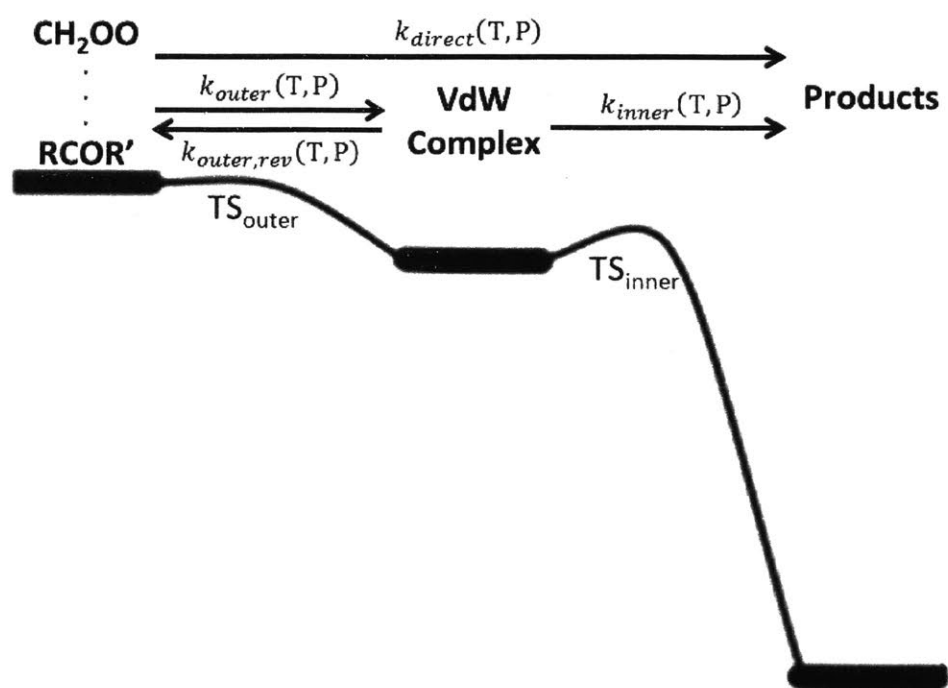
Figure 3-20: Schematic of entrance channel PES for CH_2OO + CH_3CHO/CH_3COCH_3. Relative energies for VdW and TS_{inner} are -7.3 kcal/mol and -5.3 kcal/mol for the CH_2OO + CH_3CHO system respectively and are -7.6 kcal/mol and -4.9 kcal/mol for the CH_2OO + CH_3COCH_3 system (including zero point energy corrections).[128]

As shown, the reactants may either skip directly to the SOZ and other products via a chemically activated process with T,P-dependent rate coefficient k_{direct}, or they may be stabilized in the VdW complex well with a rate coefficient k_{outer}. However, owing to its shallow well, even the stabilized VdW complex has a very short lifetime, and it will either redissociate to the reactants, $k_{outer,rev}$, or cross TS_{inner}, k_{inner}. Applying the pseudo-steady-state approximation

(PSSA) to the VdW complex and assuming pseudo-first-order conditions with respect to the carbonyl, one arrives at the following equation for the experimentally observable second-order rate coefficient for the decay of CH_2OO, $k_{observable}$.

$$k_{observable}(T, P) = k_{direct}(T, P) + k_{outer}(T, P)\left(\frac{k_{inner}(T,P)}{k_{outer,rev}(T,P)+k_{inner}(T,P)}\right) \qquad (3\text{-}14)$$

Cantherm, a computer code developed as part of the RMG-Py software package,[181] was used to obtain values for all of the T,P-dependent k's in Eq. 3-14 by solving the 1-D master equation using the Reservoir State approximation (the same results are obtained in the low- and high-pressure limits using the Modified Strong Collision approximation). All inputs to Cantherm (electronic energies, vibrational frequencies, rotational constants and hindered rotor scans for all stationary points, as well as the collisional energy transfer model) were supplied by the calculations of Jalan et al.[128] The only remaining input left to be specified is k_{outer} in the high-pressure limit, $k_{outer}^{P=\infty}(T)$. This is because TS_{outer}, as a loose barrierless transition state, would require a variable reaction coordinate (VRC-TST) treatment to be located accurately. Instead, by supplying an estimate of $k_{outer}^{P=\infty}(T)$, microcanonical rate coefficients, $k_{outer}(E)$, can be obtained from the inverse Laplace transform of $k_{outer}^{P=\infty}(T)$.[7]

A reasonably accurate estimate of $k_{outer}^{P=\infty}(T)$ can be obtained using analytical expressions from Georgievski and Klippenstein[182] for typical long-range interactions between reacting fragments. These analytical expressions rely on estimates of the dipole moment, quadrupole moment and polarizability of the reacting fragments in addition to the masses. For the systems of interest here, these properties were estimated using the B3LYP density functional with the MG3S basis set used by Jalan et al. for the CH_2OO + CH_3CHO and CH_2OO + CH_3COCH_3 potential energy surfaces.[128] Ionization energies (required for estimating the contribution from dispersion interactions) for CH_3CHO and CH_3COCH_3 were obtained from the NIST Chemistry Webbook while the value for CH_2OO was obtained from the work of Lee et al.[124] The contributions from each of the long-range interactions for CH_2OO + CH_3CHO and CH_2OO + CH_3COCH_3 are shown in Table 3-9.

Table 3-9: Contributions from various long-range interactions to the overall capture rate $k_{outer}^{P=\infty}(T)$ for $CH_2OO + CH_3CHO$ and $CH_2OO + CH_3COCH_3$. All rate expressions in units of $(10^{-10}$ cm^3 molecule^{-1} sec$^{-1})$ and temperatures in K.

Interaction	$CH_2OO + CH_3CHO$ $(10^{-10}$ cm^3 molecule^{-1} sec$^{-1})$	$CH_2OO + CH_3COCH_3$ $(10^{-10}$ cm^3 molecule^{-1} sec$^{-1})$
Dipole-dipole	$21.39\ T^{-\frac{1}{6}}$	$20.17\ T^{-\frac{1}{6}}$
Dipole-induced dipole	7.17	6.80
Induced dipole – induced dipole	$1.42\ T^{\frac{1}{6}}$	$1.45\ T^{\frac{1}{6}}$
Dispersion	$1.88\ T^{\frac{1}{6}}$	$1.89\ T^{\frac{1}{6}}$

For the purpose of our master equation calculations, only the most significant long-range interaction (the dipole-dipole interaction) was used for $k_{outer}^{P=\infty}(T)$ because the various contributions cannot simply be summed together. Furthermore, as will be shown later, our results are largely insensitive to the absolute value of $k_{outer}^{P=\infty}(T)$ in our T and P range.

Figure 3-21 compares our calculation of $k_{observable}$ for both reactions at 298 and 444 K as a function of pressure with the experimental measurements. Also shown is the predicted branching to the major products, computed using a modified version of Eq. 3-14 where k_{direct} and k_{inner} are for specific products rather than the sum of all products. Clearly there are low and high-P limits to $k_{observable}$ in all cases, although the difference becomes less pronounced at higher temperatures. The difference between $k_{observable}^{P=0}$ and $k_{observable}^{P=\infty}$ is due to the states of TS_{inner} below the energy of the separated reactants being inaccessible in the collisionless low-P limit. In the high-P limit, these submerged states are populated and $k_{observable}$ increases correspondingly. At higher temperatures, the inclusion or exclusion of the submerged TS_{inner} states matters less, as more of the higher energy states are populated, and these dominate the rate.
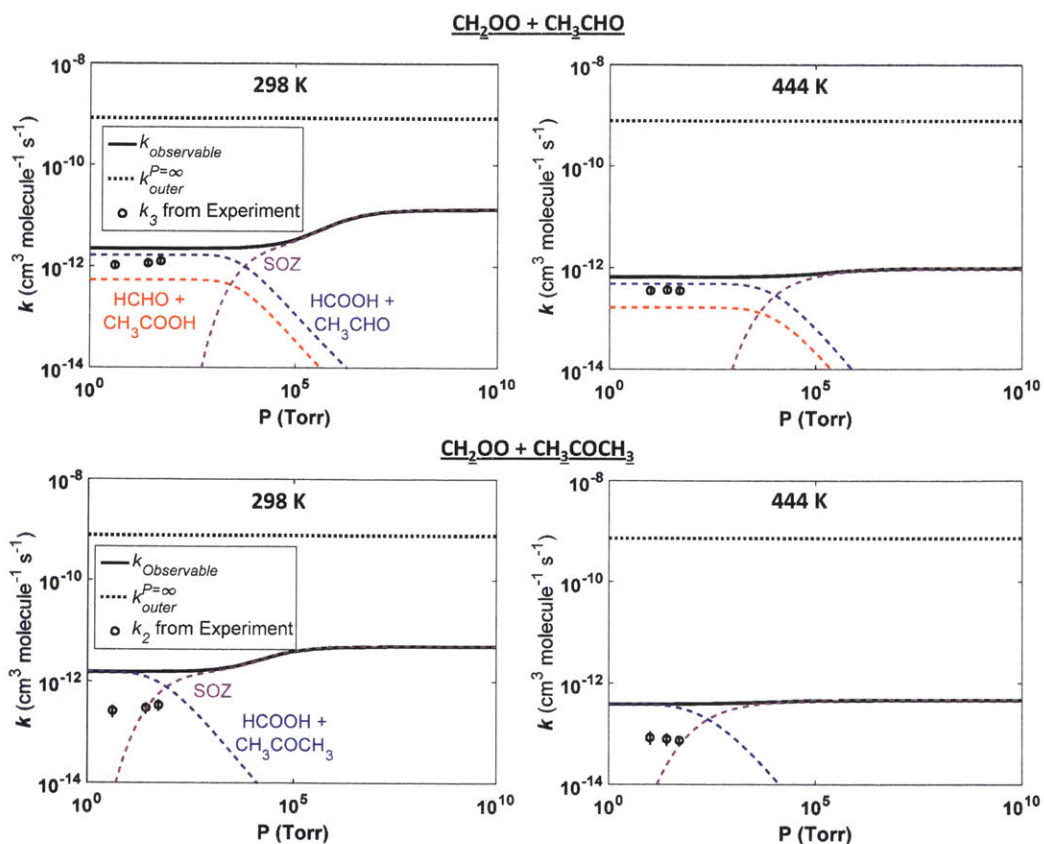
Figure 3-21: Predicted P-dependence for CH_2OO + CH_3CHO (upper)/CH_3COCH_3 (lower). Black dots represent experimental measurements for overall CH_2OO + CH_3CHO and CH_2OO + $CH3COCH_3$ rate coefficients, k_3 and k_2, respectively.

The bottleneck to $k_{observable}$ in both the low and high-P limits over the temperature range of interest to us (298-500 K) is TS_{inner}. This is demonstrated for $k_{observable}^{P=0}$ by varying $k_{outer}^{P=\infty}(T)$ over two orders of magnitude (Figure C 6). As shown, increasing $k_{outer}^{P=\infty}(T)$ by a factor of ten has a negligible effect on $k_{observable}^{P=0}$, while decreasing it by a factor of ten has a more noticeable, but still small impact on $k_{observable}^{P=0}$.

In the high-P limit, $k_{direct}(T, P) = 0$ and Eq. 3-14 simplifies to the following.

$$k_{observable}^{P=\infty}(T) = k_{outer}^{P=\infty}(T) \left(\frac{k_{inner}^{P=\infty}(T)}{k_{outer,rev}^{P=\infty}(T) + k_{inner}^{P=\infty}(T)} \right) \tag{3-15}$$

If $k_{outer}^{P=\infty}(T)$ was rate-limiting, then $k_{outer,rev}^{P=\infty}(T) \ll k_{inner}^{P=\infty}(T)$ and Eq. 3-15 would simplify to $k_{outer}^{P=\infty}(T)$. This is clearly not the case, because, as shown in Figure 3-21, in the high-P limit $k_{observable}^{P=\infty}(T)$ is three orders of magnitude smaller than $k_{outer}^{P=\infty}(T)$ (shown by the dotted black

line). Furthermore, if $k_{inner}^{P=\infty}(T)$ is indeed rate-limiting in the high-P limit, $k_{outer,rev}^{P=\infty}(T) \gg k_{inner}^{P=\infty}(T)$ and Eq. 3-15 simplifies further.

$$k_{observable}^{P=\infty}(T) = \frac{k_{outer}^{P=\infty}(T)}{k_{outer,rev}^{P=\infty}(T)} k_{inner}^{P=\infty}(T) \tag{3-16}$$

Using canonical TST expressions for the three high-P k's above results in a simple expression for $k_{observable}^{P=\infty}(T)$:

$$k_{observable}^{P=\infty}(T) = \frac{k_B T}{h} \frac{\left(\frac{Q_{TS,outer}}{Q_{reactants}}\right)\left(\frac{Q_{TS,inner}}{Q_{VdW\,complex}}\right)}{\left(\frac{Q_{TS,outer}}{Q_{VdW\,complex}}\right)} \times$$

$$\exp\left(-\frac{\left[\left(E_0^{TS,outer}-E_0^{reactants}\right)+\left(E_0^{TS,inner}-E_0^{VdW}\right)-\left(E_0^{TS,outer}-E_0^{VdW}\right)\right]}{RT}\right) \tag{3-17}$$

$$k_{observable}^{P=\infty}(T) = \frac{k_B T}{h}\left(\frac{Q_{TS,inner}}{Q_{reactants}}\right) \times \exp\left(-\frac{\left[E_0^{TS,inner}-E_0^{reactants}\right]}{RT}\right) \tag{3-18}$$

where E is the zero-point inclusive energy and Q is the partition function per unit volume for a given species. Equation 3-18 is the canonical TST equation one would obtain by simply ignoring TS_{outer} and the VdW complex and is therefore denoted k_{TST}. Figure 3-22 compares $k_{observable}^{P=0}(T)$, $k_{observable}^{P=\infty}(T)$ from Eq. (3-15), and $k_{TST}(T)$ along with our experimental measurements. $k_{TST}(T)$ is virtually indistinguishable from $k_{observable}^{P=\infty}(T)$, because the inner transition state is rate-limiting, as expected.
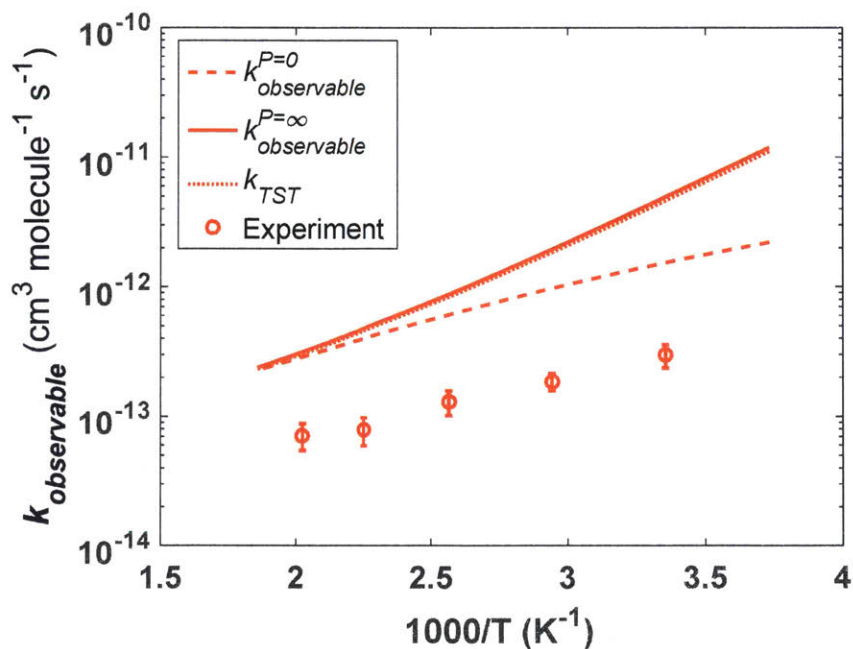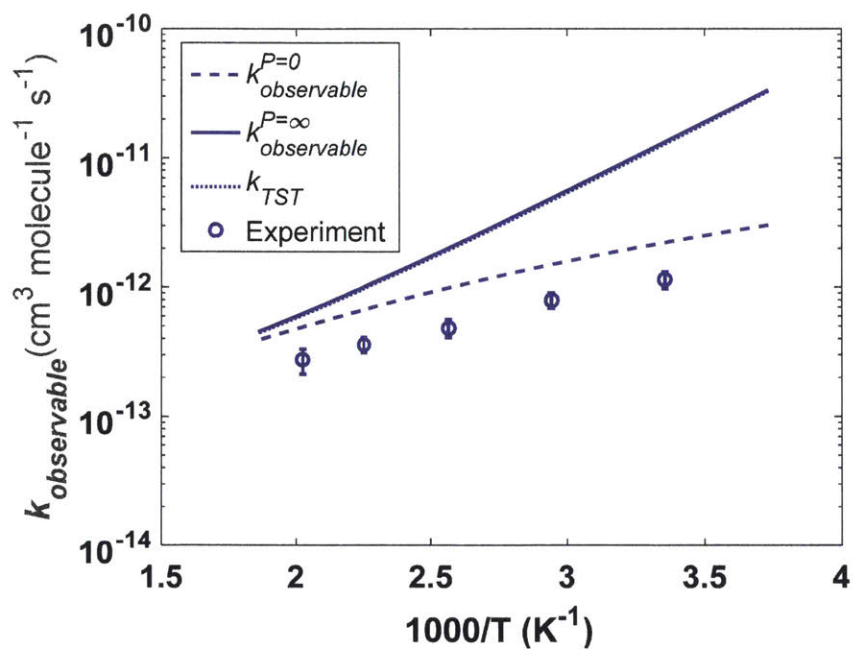
Figure 3-22: Predicted T-dependence for $CH_2OO + CH_3CHO$ (upper)/CH_3COCH_3 (lower) in the low- and high-pressure limits, $k_{observable}^{P=0}(T)$ and $k_{observable}^{P=\infty}(T)$, respectively. Predictions of simple TST calculations are also shown, $k_{TST}(T)$. Blue and red dots represent experimental measurements for $CH_2OO + CH_3CHO$ and $CH_2OO + CH3COCH_3$, respectively (P = 25 Torr in Helium).

For both $CH_2OO + CH_3CHO$ and $CH_2OO + CH3COCH_3$, Figure 3-21 suggests that our experimental measurements were conducted in the low-P limit with respect to $k_{observable}$, which is consistent with the lack of P-dependence observed for either k_2 or k_3. In the case of $CH_2OO +$ CH_3CHO, $k_{observable}^{P=0}(T)$ is within a factor of two of experiment, whereas for $CH_2OO +$ $CH3COCH_3$ $k_{observable}^{P=0}(T)$ is higher by about a factor of five. We observed a similar order of magnitude discrepancy between predictions and measurements for the case of $CH_2OO +$ alkenes (section 3.1.4.3), which we attribute mostly to uncertainty in the PES. Table 3-10 compares simple Arrhenius fits between the predictions (P=0) and experiment. It appears from the discrepancy between the model predictions and the experimental data that the theoretically calculated A-factors are mostly at fault, whereas the computed submerged barrier heights give E_a's in remarkable agreement with experiment.

Table 3-10: Theoretical Arrhenius parameters in the low-pressure limits (in units of A: cm^3/molecule/sec and E_a: kcal/mole) for the $CH_2OO + CH_3CHO$ and $CH_2OO + CH_3COCH_3$ systems for T in the 300-500 K range. Experimentally determined values shown for comparison.

System		Theory	Experiment
		P = 0	**(P = 25 Torr in He)**
$CH_2OO + CH_3CHO$	A	6.6×10^{-14}	$(3 \pm 0.8) \times 10^{-14}$
	E_a	-2.1	-2.2 ± 0.6
$CH_2OO + CH_3COCH_3$	A	2.8×10^{-14}	$(7 \pm 2.5) \times 10^{-15}$
	E_a	-2.4	-2.2 ± 0.7

Product branching from $CH_2OO + CH_3CHO$ and $CH_2OO + CH_3COCH_3$ has already been discussed in detail by Jalan et al.[128] who used detailed RRKM/Master equation calculations to provide evidence for organic acid formation at low-pressures. Similar calculations of the product distribution, shown in Figure 3-21, suggest that the acetaldehyde system is in the low-pressure limit for the product distribution under the current experimental conditions (P = 4 to 50 Torr in Helium). In contrast, the acetone system is predicted to exhibit notable pressure dependence in the product branching over the same pressure range, which is qualitatively consistent with the P-dependence of the m/z = 89 isomer yield shown in Figure 3-18. However, the $CH_2OO +$ CH_3COCH_3 PES used does not include a m/z = 104 isomer other than SOZ that is produced in significant quantities. Our TOF-MS results and prior work by Taatjes et al.[120] strongly suggests

another m/z =104 adduct is formed, probably in higher concentration than the SOZ. Our work (Figure 3-18) even suggests that this adduct might be in its high-P limit in 50 Torr He. Further investigation of this PES would be most beneficial to understanding these experimental results.

The high yield of 88% HCHO from CH_2OO+CH_3CHO in 4 Torr N_2 estimated by Stone et. al.,[55] appears to be in disagreement with our predicted low-pressure product distribution in Figure 3-21, where HCHO accounts for only ~25% of the yield. However, this discrepancy can be explained by taking into consideration the uncertainties in both the measurements and predictions, as detailed in Appendix C. Qualitatively, their measured decrease in HCHO yield with pressure is consistent with our predictions.

Calculations of k_{TST} were also conducted up to 2000 K and compared to identical calculations for CH_2OO + alkenes (section 3.1.4.3) in order to evaluate the real A factors as $T \rightarrow \infty$. Similar to Figure 3-14, Figure 3-23 shows that although values of k for CH_2OO + carbonyls are 2-3 orders of magnitude higher than for CH_2OO + alkenes at room T, as T increases the two sets of k values merge to within a factor of two of each other. This demonstrates that the A factor (entropic term) is similar for CH_2OO + C=O and C=C cycloadditions and the large difference in k's at room temperature is almost entirely due to the energetic difference of the reaction barrier. The strong curvature of the carbonyl predictions at high T is due to the emerging dominance of the entropic term. Specifically, the positive temperature dependence of the ratio of inner TS to reactant vibrational partition functions dominates over other contributions at high T (Figure C 7). The larger k for the acetaldehyde reaction as compared to acetone over the entire T range is attributable partly to the 0.4 kcal/mol difference in submerged TS_{inner} barrier heights and partly to the larger A-factor for the former.
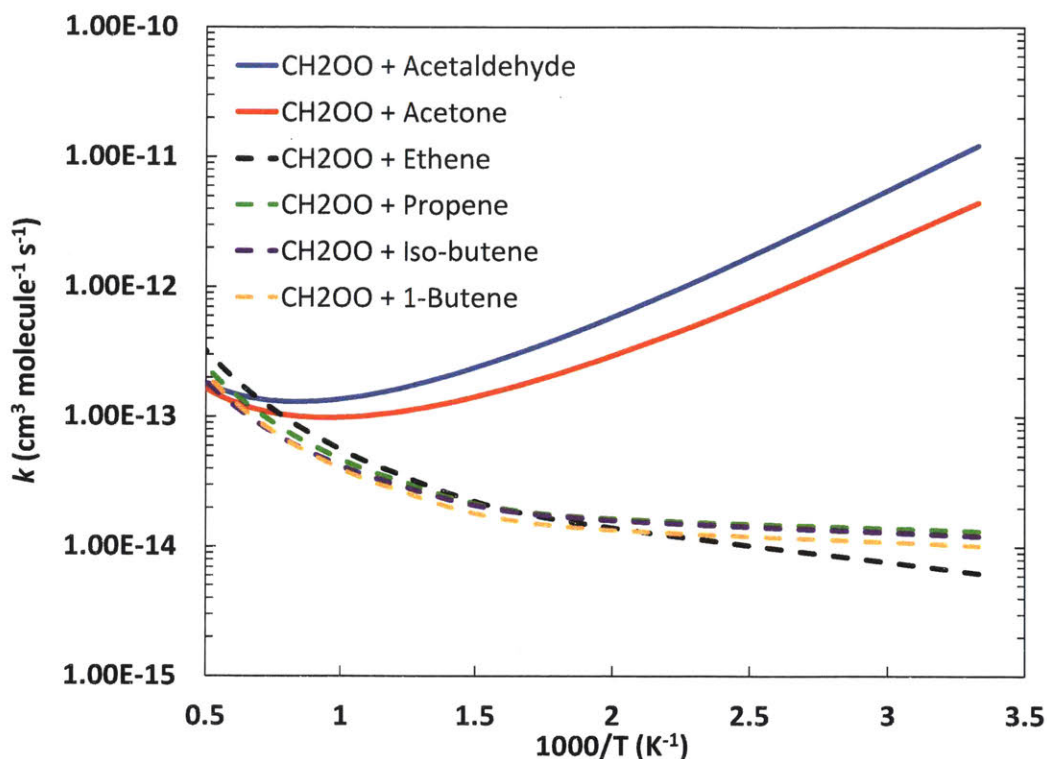
Figure 3-23: Predicted T-dependence for CH_2OO + carbonyls/alkenes in the high-pressure limit up to 2000 K demonstrating similar A factors.

3.3.4 Conclusions

We have determined the temperature dependence of the rate constants, k_2, and k_3 for the CH_2OO + CH_3COCH_3 and CH_2OO + CH_3CHO reactions over the temperature range 298-500 K. The results show a decrease in k_2 and k_3 of a factor of 4 over this temperature range. Theoretical analysis suggests that the overall kinetics are determined mainly by the tight 1,3-cycloaddition saddle point. The computed high- and low-pressure rate-coefficients both show negative temperature dependence although the experimentally determined slope is in much better agreement with the low-pressure estimates. Weak pressure dependence is observed for both reactions at 298 K over the pressure range 10 to 50 Torr He. Under our experimental conditions, no pressure effect could be discerned at 444 K. These findings are supported by the theoretical calculations, which predict that the

variation of the overall rate coefficients for both reactions are negligible as a function of pressure in the pressure range of interest. Previous work on these systems has shown that organic acids, HCOOH and CH_3COOH are the dominant products for the CH_2OO + CH_3CHO reaction at low pressures.[120, 128] HCOOH formation was predicted to be dominant for the CH_2OO + CH_3COCH_3 reaction. The yield of SOZ is relatively small compared to organic acids at the pressure range studied. Using PI TOF-MS, two product masses were observed; m/z = 89 and m/z = 104 for the reaction of CH_2OO + CH_3COCH_3, which have been tentatively assigned[120] to a daughter ion of methoxy methyl acetate and SOZ, respectively. The relative yield of these products was found to have zero-to-weak pressure dependence at 298 K while the yield of m/z = 89 increases with pressure over the same range. Both of these experimental results are consistent with the previous conclusions of Taatjes et al.[120] regarding the identity of the m/z = 89 species, but there are many unknowns in the chemistry of chemically-activated SOZ, and further theoretical exploration of the CH_2OO + CH_3COCH_3 PES would be most helpful.

Chapter 4

Kinetics and Product Branching of Combustion Reactions

Two reaction systems relevant to polycyclic aromatic hydrocarbon (PAH) formation under combustion conditions were studied: vinyl radical + 1,3-butadiene in section 4.1, which can affect formation of the first aromatic ring (benzene), and phenyl radical + propene in section 4.2, which can affect second-ring formation (indene). The phenyl radical + propene work is especially important as it is the only chemical system reported in this thesis that used the improved version of the LAS/PI TOF-MS apparatus described in Chapter 2. As such, the phenyl radical + propene work is the best guide for future experiments/modeling. Section 4.1 is adapted with permission from Buras et al.[77] Copyright 2015 American Chemical Society.

4.1   Vinyl Radical + 1,3-Butadiene

4.1.1   Introduction

Soot is an undesirable by-product of hydrocarbon combustion that is primarily composed of polycyclic aromatic hydrocarbons (PAH).[183] Besides being deleterious to human health[184] and the environment,[185-187] soot formation also represents an inefficient use of hydrocarbon fuel. For all of these reasons, it is important to understand the physical and chemical processes leading to soot formation so that these pathways can be minimized.

As described in detail in the reviews of Richter and Howard,[183] McEnally et al.[188] and Wang,[189] formation of the first aromatic ring is a crucial step in the path to PAH and eventually soot. For many flames it is thought to be the rate limiting step.[190-192] Benzene is the prototypical first aromatic ring, although others such as toluene, styrene, phenylacetylene, indene and naphthalene are certainly possible and have been considered in the literature. Several reactions that have received special attention over the last 30 years as potential sources of benzene in

various flames are the following: 1. $n - C_4H_3/n - C_4H_5 + C_2H_2$,[193-197] 2. $C_2H_3 + 1,3 - C_4H_6$,[193-194, 198-205] and 3. $C_3H_3 + C_3H_3$.[195, 206-208] Chemistry of five carbon rings (i.e., cyclopentadienyl, cyclopentadiene and fulvene) is also thought to lead to larger aromatic rings.[206, 209-210] With the exception of propargyl radical recombination, $C_3H_3 + C_3H_3$, there is a dearth of direct experimental measurements of the reactions listed above.

Scheme 4-1 summarizes the currently accepted pathways for the reaction of vinyl radical with 1,3-butadiene, $C_2H_3 + 1,3 - C_4H_6$. There are several pathways leading to cyclic species that could conceivably undergo subsequent reactions to form benzene or other aromatics. Specifically, the cyclohexadiene isomers ($c - C_6H_8$) could lose two hydrogen atoms, either by H_2 elimination or H-abstraction followed by spontaneous H emission, to form benzene.[211-217] Cavallotti et al. computed the pathway to cyclopentadiene ($c - C_5H_6$) that could also lead to aromatic ring formation.[202]
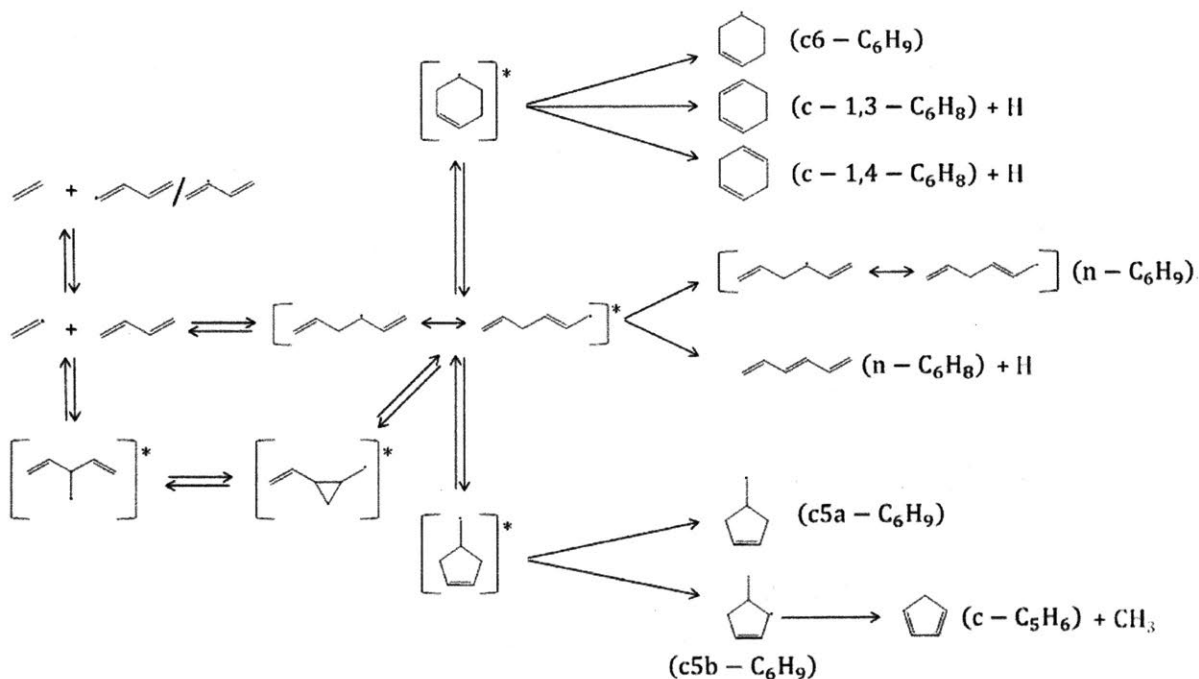
Scheme 4-1: Proposed reaction network for $C_2H_3 + 1,3 - C_4H_6$ (modified from Cavallotti et al.[202]), with nomenclature used in this work. Asterisks denote ro-vibrationally excited isomers.

As early as 1984, Cole et al. considered the role of $C_2H_3 + 1,3 - C_4H_6$ in a 1,3-butadiene flame, but they concluded that this reaction did not produce sufficient cyclohexadiene to explain

the amount of benzene formed.[193] Weissman and Benson reached a similar conclusion when studying methyl chloride pyrolysis.[199] However, others have concluded that $C_2H_3 + 1,3 - C_4H_6$ is a significant pathway to benzene formation in 1,3-butadiene flames,[194, 200-201] hexane pyrolysis,[198] a 1,3-butadiene doped methane flame[204] and ethane pyrolysis.[205]

Of course, whether a certain reaction is important in a given system depends on a host of system variables, which are myriad for something as complex as a flame. For example, temperature, pressure, equivalence ratio and chemical identity of the fuel are all sensitive variables. So the lack of consensus in the literature with respect to the importance of $C_2H_3 + 1,3 - C_4H_6$ to benzene formation in different environments is not surprising. What is concerning, however, is the large disagreement in the literature with respect to the overall rate coefficient for the title reaction. In particular, the overall rate coefficient predictions of Westmoreland et al.,[194] Cavallotti et al.[202] and Xu et al.[205] disagree by more than two orders of magnitude at some conditions and display strikingly different temperature and pressure dependence. While they differ on the rate, all three predictions agree that at atmospheric pressure and below ~ 1000 K the dominant product is the linear adduct $(n - C_6H_9)$. Above this temperature, however, Westmoreland et al. predict the linear C_6H_8 isomer $(n - C_6H_8)$ to dominate, whereas Cavallotti et al. and Xu et al. predict cyclic species $(c - C_6H_8$ or $c - C_5H_6)$ to eventually dominate. In at least one recent case, this disagreement has prevented the inclusion of the $C_2H_3 + 1,3 - C_4H_6$ reaction in a model of a 1,3-butadiene flame.[218]

Despite these clear discrepancies for a reaction that is of known importance, to our knowledge there has not yet been any direct experimental measurement of either the overall rate of $C_2H_3 + 1,3 - C_4H_6$, nor the product branching. In this work, we report the first such experiment over a relatively limited temperature and pressure range of $297 - 700$ K and $4 - 100$ Torr. Coupled with theoretical predictions, however, these results can be extrapolated to combustion temperatures for direct use in modeling. Discrepancies between our results and the literature are discussed, along with possible implications for soot formation.

4.1.2   Experimental Methods

All experiments were conducted on a modified version of the MIT laser-photolysis/Herriott multiple-pass laser-absorption apparatus described by Ismail et al.[93] This apparatus was modified to incorporate a photoionization time-of-flight mass spectrometer (PI

TOF-MS) with supersonic molecular beam sampling from the center of the reactor. A detailed description of this apparatus was given by Middaugh[68] and only the essential details are included here. The reactor is 86 cm long, 6 cm in diameter, constructed of stainless steel and resistively heated by four heaters wrapped along the length of the reactor to create a uniform temperature profile (standard deviation $\pm 2\%$) through the overlap region of the absorption laser. The heaters enable the gas mixture to be heated up to 700 K. The internal pressure of the reactor was monitored by a capacitance manometer and controlled via an automated butterfly valve. For some control experiments the inside of the reactor was coated with polydimethylsiloxane (PDMS), which has previously been used to minimize wall reactions in both a stainless steel[146] and Pyrex reactor[219] up to 750 K. The fourth harmonic output of a Nd:YAG laser (266 nm) operated at a repetition rate of 0.91, 2 or 5 Hz was used to photolyze vinyl iodide, C_2H_3I, and produce $C_2H_3 + I$. Unless noted otherwise, the repetition rate of the photolysis laser was such that the contents of the reaction cell were completely refreshed between photolysis flashes (Flashes per Refresh, FPR, < 1). The frequency-doubled output of a Ti:Sapphire laser (80 MHz pulsed laser with 1.2 ps full width at half maximum, FWHM, pulses) was used to generate the visible probe beam. The fundamental wavelength was measured before each experiment using a recently calibrated Ocean Optics HR2000+ spectrometer. The wavelength, λ, of the probe beam was 423.2 nm for all experiments reported here due to the strong absorption of C_2H_3 at this wavelength as we have previously observed[93-96] and the lack of interference by other absorbing species (i.e., allylic species) at least at low temperatures (T < 400 K). The path length of the multiple-pass visible probe laser was ~20 m, allowing sensitive detection of C_2H_3 at concentrations as low as $\sim 10^{12}$ molecules cm^{-3} as used here. Absorbance traces were averaged over 500 flashes.

A small amount of the reactive gas was continuously sampled via a small pinhole at the tip of a cone that juts slightly into the photolysis beam at the center of the reaction cell. The sampled gas was supersonically expanded, and the center of the resultant free jet passed through a Beam Dynamics skimmer to form a collimated molecular beam. The gas in the molecular beam was effectively "frozen" in composition by cooling while in transit to the ionization region of the PI TOF-MS, where it was photoionized using 118.2 nm (10.487 eV) light. The 118.2 nm light was generated by focusing the third harmonic (355 nm) output of a pulsed Nd:YAG laser (<12 ns FWHM pulses, repetition rate set to match the photolysis laser) in a 1:10 Xe:Ar gas cell at a total

pressure of 90-100 Torr. The relative abundance of ions at different mass-to-charge ratios (m/z) were analyzed using a Kore TOF-MS and detected using the Kore supplied discrete dynode electron multiplier detector and analog pre-amplifier. Mass spectra were also averaged over 500 acquisitions. The correspondence between time-of-flight and $\frac{m}{z}$ was determined by calibration with a mixture of stable species.

Helium was used as the bath gas in all of the experiments reported here. C_2H_3I was purchased from Oakwood Chemicals at $\geq$ 95% purity and was further purified by successive freeze-pump-thaw cycles. Helium (Airgas, 99.999%) and 1,3-butadiene (Sigma-Aldrich, $\geq$ 99%) were used directly without further purification. Although the purchased 1,3-butadiene contains p-tert-butylcatechol as an inhibitor, PI TOF-MS analysis revealed no signal at the parent mass of this species or its fragment (m/z =166 and 151 amu, respectively). The largest observable impurity in the 1,3-butadiene was its dimer (4-vinylcyclohexene), which from Gas Chromatography analysis is only ~0.1%. PDMS (MW = 70,000 − 80,000) was purchased from Spectrum Chemical.

4.1.3   Computational Methods

Electronic energies of all species studied in this work were determined at the CCSD(T)-F12a/cc-pVTZ-F12[133-135, 138] level of theory using Molpro,[220] and are shown in Figure 4-1 below. Molecular geometries and force constants for species and saddle points were determined at the M08SO/MG3S[129, 221] level of theory, utilizing QChem 4.1.[222] A computational grid with 75 radial points and 434 angular points per radial point was used in the calculations for all species. Frequencies were scaled by the recommended value of 0.983.[223] Loose internal degrees of freedom for relevant adducts and transition states (i.e., hindered rotors) were treated separately by performing relaxed potential energy scans about the bond defining the internal rotor; these calculations were performed in Gaussian 03[132] at the BMK/6-311+G(d,p) level of theory.[224] Reduced internal moments of inertia for all internal rotors were estimated at the $I^{(2,3)}$ level as defined by East and Radom.[225] Cantherm[142] was used for all TST and RRKM/Master Equation calculations, which were performed in the regions of 300-2000 K, and 1 Torr − 7.6×10^4 Torr (or 100 atm) in both Helium and Nitrogen bath gases. The master equation for energy transfer was solved using the modified strong collision (MSC) method, which is documented elsewhere.[7] Eckart[226] tunneling corrections were applied to all relevant reactions.

The exponential down model for collisional energy transfer was adopted in this work. A temperature dependent formulation was used for the average downward energy transferred per collision,

$$\langle \Delta E_d \rangle = \langle \Delta E_d \rangle_{300} \left(\frac{T}{300\,K} \right)^n \; cm^{-1} \qquad (4\text{-}1)$$

With $\langle \Delta E_d \rangle_{300} = 175.5$ and $400\ cm^{-1}$, and $n = 0.95$ and 0.7 for He and N_2 respectively. Values for Nitrogen were adopted based on toluene energy collision parameters,[197, 207] while those for Helium were adopted from recent calculations of Jasper and Miller,[227] with $\langle \Delta E_d \rangle_{300}$ increased by 50%. Lennard Jones collision diameters and well depths were estimated via the Joback[228] method, which is based on the critical temperature and pressure of parent compounds. The method of corresponding states was subsequently used to estimate the LJ parameters[229] and is described in the context of RMG elsewhere.[230]

4.1.4   Results and Discussion

4.1.4.1   Potential Energy Surface for $C_2H_3 + 1,3\text{-}C_4H_6$

Regarding the terminal addition of vinyl to 1,3-butadiene, a Gaussian 03 IRC calculation at the CBS-QB3 level of theory followed by single point electronic calculations at the CCSD(T)-F12a/cc-pVTZ-F12 indicated the presence of a van der Waals complex stabilized by -1.0 kcal/mol relative to the reactants, and a 0 K barrier height of 0.14 kcal/mol (not including ZPE, 0.3 with ZPE). A stable transition state could not be located for the entrance channel at the M08SO/MG3S level of theory; transition state searches repeatedly resulted in multiple imaginary frequencies. Thus, CBS-QB3 (B3LYP/CBSB7) geometries and frequencies were used for computing the high pressure limit rate of the entrance channel.

We note that the uncertainty in the present addition barrier height (1 kcal/mol for CCSD(T)-F12a/cc-pVTZ-F12) exceeds the barrier height itself. Thus, a high level variational TST or variable reaction coordinate approach would be more appropriate for this reaction, and is recommended as future work. However, because the predicted entrance channel rate is in good agreement with the experimental values obtained in this work, a higher level rate theory calculation for the entrance channel was not conducted. The potential energy surface relevant to the ME/RRKM calculations discussed below is illustrated in Figure 4-1. A sensitivity analysis of the predicted entrance channel rate constant to a $\pm 1.0\ kcal\ mol^{-1}$ change in entrance barrier height demonstrates that the contributions to overall rate uncertainties at 300, 500, and 1000 K

are a factor of 5.4, 2.7, and 1.7, respectively. The overall estimated uncertainty in the high pressure limit entrance channel rate is further discussed below.

In this work, vinyl addition to the secondary carbon of 1,3-butadiene, forming 2-methylene-3-butenyl, was not considered in the ME/RRKM simulations because this slower channel does not contribute significantly to the overall rate of vinyl + 1,3-butadiene under the conditions of this study. This was confirmed through a calculation at the CCSD(T)-F12a/cc-pVTZ-F12 level of theory, with a computed barrier of 4.9 kcal/mol (at 0 K, including ZPE). Thus, the corresponding high-pressure limit rate relative to the preferred terminal addition reaction is negligible (less than 0.02% at 300 K, rising to 2% at 1000 K, and 5% at 2000 K). Similarly, the two possible H-abstraction channels were also not included in the ME simulations because the barriers for H-abstraction from the 1- and 2- sites of 1,3-butadiene were calculated to be 11.5 and 9.4 kcal/mol, respectively (at 0 K, including ZPE). Thus, they are not competitive with the addition reactions under the conditions of this work.
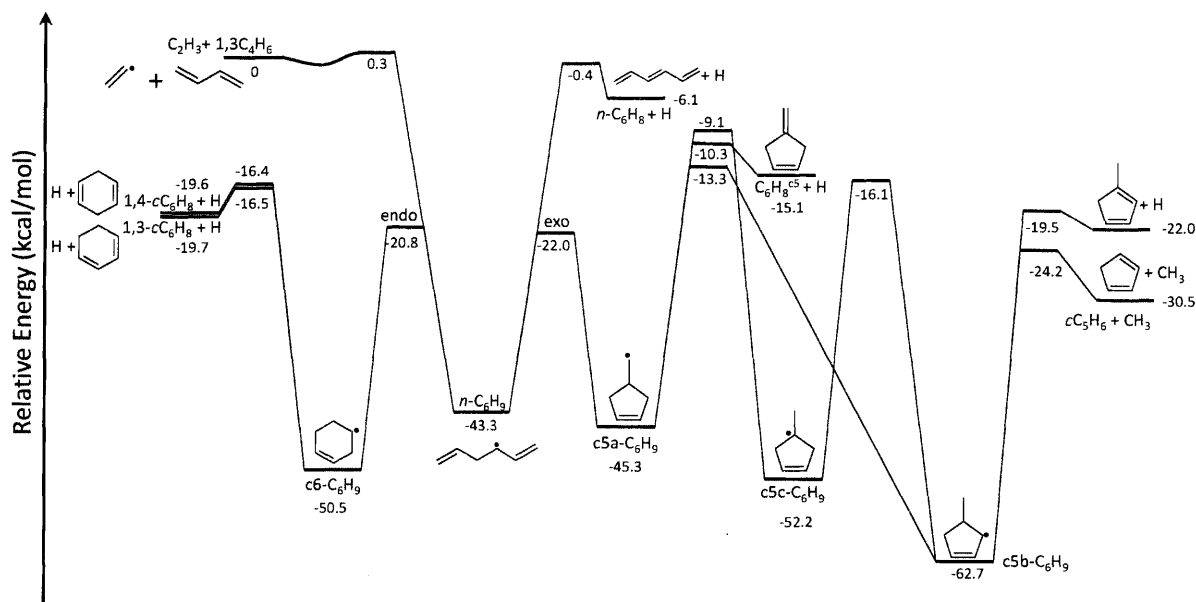
Figure 4-1: Zero Kelvin relative energy diagram (ZPE included) for the reaction of vinyl + 1,3-butadiene, with selected channels shown. All energies other than the entrance barrier height calculated at the CCSD(T)-F12a/cc-pVTZ-F12 level of theory. See text for discussion.

4.1.4.2   Overall Rate of C_2H_3 + 1,3-C_4H_6

In order to measure the overall reaction rate of C_2H_3 + 1,3 − C_4H_6, k_1, several kinetic models described below and in Appendix D were developed and fit to the absorbance data. k_1

can be apportioned into the fraction, α, that forms the linear adduct isomer, $n - C_6H_9$, and the remaining fraction, $1 - \alpha_{n-C_6H_9}$, that forms all of the other products.

$$C_2H_3 + 1,3 - C_4H_6 \xrightarrow{\alpha_{n-C_6H_9}k_1} n - C_6H_9 \tag{R1a}$$

$$C_2H_3 + 1,3 - C_4H_6 \xrightarrow{(1-\alpha_{n-C_6H_9})k_1} \text{Other Products} \tag{R1b}$$
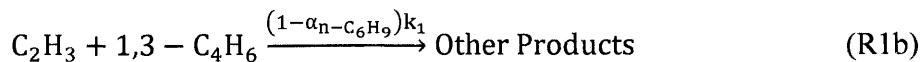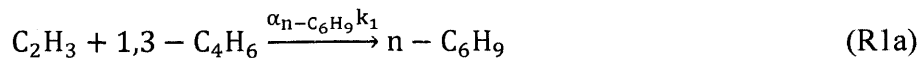
The reason for this distinction will become clear in coming paragraphs. In addition to undergoing bimolecular reaction with $1,3 - C_4H_6$, C_2H_3 can also undergo a number of other first-order and pseudo-first-order processes such as diffusion out of the probe beam, unimolecular decay and reaction with the C_2H_3I precursor. The total first-order rate of all of these processes, k_2, should be constant for a given experiment where temperature (T), pressure (P), $[C_2H_3I]$ and the laser alignment are kept fixed, as was done here. Therefore, all of these processes may be adequately captured by a single pseudo-first-order reaction in our models.

$$C_2H_3 \xrightarrow{k_2} \text{Products} \tag{R2}$$

C_2H_3 can also undergo self-reaction with rate coefficient k_{self}. However, we have found that including k_{self} decreases k_2 from $\sim 250 \ s^{-1}$ to $\sim 150 \ s^{-1}$ with no impact on k_1 (Figure D 4 and Figure D 5). For the sake of simplicity and because the goal of this work is to measure k_1, the model presented here neglects k_{self}. This approximation is most convincingly justified by the observation that in the absence of $1,3 - C_4H_6$ the decay of C_2H_3 is fit well by a single-exponential decay with rate k_2, as shown for representative traces in Figure 4-2 and Figure 4-3.

A major challenge to measuring k_1 using laser flash photolysis is the well-known ultraviolet photodissociation of $1,3 - C_4H_6$.[231] The major products of this process are thought to be propargyl and methyl radicals $(C_3H_3 + CH_3)$ with measurable contributions of ethylene + acetylene $(C_2H_4 + C_2H_2)$ and vinylacetylene + H_2 $(C_4H_4 + H_2)$ as well. This complicating side-phenomenon is likely a major reason why there is currently no direct measurement of C_2H_3 + $1,3 - C_4H_6$. Recently, while measuring the branching fractions of ethynyl radical, C_2H, reacting with $1,3 - C_4H_6$, Lockyear et al. found that using 248 nm photolysis there is a noticeable amount of C_3H_3 and C_4H_4 formed from $1,3 - C_4H_6$ photodissociation.[232] We indeed observe transient absorbance of our visible probe laser light if a sufficiently high concentration of $1,3 - C_4H_6$ is photolyzed at 266 nm, which we attribute to C_3H_3. Although, to our knowledge, the visible absorption spectrum of C_3H_3 has not yet been measured, given the chemical similarity between C_3H_3 and the allyl radical, C_3H_5, which is known to absorb visible light,[233] it is

reasonable to assume that C_3H_3 can also absorb substantially around 400 nm. Photodissociation of $1,3-C_4H_6$ is therefore undesirable for our experiment for two reasons: 1. Visible absorbance of C_3H_3 will convolute the interpretation of our transient absorbance results, and 2. The additional radicals formed, i.e. C_3H_3 and CH_3, can react with C_2H_3 from C_2H_3I photolysis and make it difficult to extract the actual rate coefficient of interest, k_1. For both of these reasons, in all experiments reported here $[1,3-C_4H_6]$ and the 266 nm photolysis energy were kept sufficiently low ($< 5 \times 10^{16}$ molecules cm^{-3} and <30 mJ/pulse, respectively) such that no transient absorbance was detectable at $\lambda = 423.2$ nm when only $1,3-C_4H_6$ was photolyzed (Figure D 1). At these conditions CH_3 is also not observed using PI TOF-MS and we can therefore estimate $[CH_3]_0 < 0.3 \times 10^{12}$ molecules cm^{-3} based on the sensitivity of the TOF-MS. Only at 700 K is a measurable amount of CH_3 detected. While this constraint resolves the first issue mentioned above, it doesn't guarantee that side reactions involving C_3H_3 and CH_3 are not occurring. To address this concern we conducted control experiments to measure k_1 at different photolysis energies. If $1,3-C_4H_6$ photodissociation is affecting the measured kinetics via C_3H_3, CH_3 or some other channel, then by doubling the photolysis power the measured k_1 should also change substantially. As shown later, this is not what was observed and we therefore conclude that at our experimental conditions $1,3-C_4H_6$ photodissociation does not affect the main results presented here.

Table 4-1 summarizes the experimental conditions of this work. At each T, P, Photolysis Energy and $[C_2H_3I]$ condition, $\lambda = 423.2$ nm absorbance traces were recorded at 6-9 different $[1,3-C_4H_6]$ values ranging from $0 - 5 \times 10^{16}$ molecules cm^{-3}, in evenly spaced intervals. Note that in all but two experiments the photolysis energy was kept relatively low at 15 mJ/pulse to minimize $1,3-C_4H_6$ photodissociation. For the two experiments where the energy was doubled, $[C_2H_3I]$ was also halved in order to maintain close to the same $[C_2H_3]$ and therefore keep the effects of C_2H_3 self-reaction negligible on the obtained values of k_1. Attempts were also made to measure k_1 at 599 and 700 K, but unfortunately at these elevated temperatures $1,3-C_4H_6$ photodissociation significantly interfered with the measurements.

Table 4-1: Summary of experimental conditions for $\lambda = 423.2$ nm absorbance experiments. In all cases the number of Flashes per Refresh (FPR) was less than one and $[1,3 - C_4H_6]$ was varied from $0 - 5 \times 10^{16}$ molecules cm^{-3} for each experiment.

T (K)	P (Torr)	Photolysis Energy (mJ/pulse)	$[C_2H_3I]$ (10^{14} molecule/ cm^3)	$[C_2H_3]_0$ (10^{12} molecule/ cm^3)	A_0 (10^{-4})	Number of traces	Model Used
297	4	15	2.4	1.5 ± 0.5	9	9	
297	25	15	2.4	1.8 ± 0.9	10	9	
297	25	30	1.2	1.6 ± 0.8	9	6	Low-T
297	50	15	2.4	1.5 ± 0.8	10	9	
297	100	15	2.4	1.0 ± 0.6	10	9	
340	25	15	2.4	2.0 ± 1.1	11	9	Low-T
390	25	15	2.4	2.1 ± 1.2	11	9	High-T
444	25	15	2.4	1.7 ± 1.0	8	9	High-T
494	4	15	2.4	1.7 ± 0.9	7	8	
494	25	15	2.4	1.9 ± 1.1	8	9	
494	25	30	1.2	1.9 ± 1.1	8	6	High T
494	100	15	2.4	1.7 ± 1.1	10	9	

In these experiments, $[C_2H_3]_0$ was determined from the initial absorbance of the visible probe laser, A_0, its pathlength, $l_{probe}(= 2000 \pm 600$ cm), and the measured cross section of vinyl as a function of temperature and pressure at the probe wavelength, $\sigma_{C_2H_3}(\lambda = 423.2$ nm), according the following equation.

$$[C_2H_3]_0 = \frac{A_0}{\sigma_{C_2H_3}(\lambda=423.2 \text{ nm})l_{probe}} \qquad (4\text{-}2)$$

Using the values of A_0 in Table 4-1 and of $\sigma_{C_2H_3}(\lambda = 423.2$ nm) in Table D 3, it is straightforward to see how the values of $[C_2H_3]_0$ were calculated. Note that the measured fraction of C_2H_3I that photodissociates to C_2H_3 is ~0.7% (~1.4%), consistent with $\sigma_{C_2H_3I}(\lambda = 266$ nm) $\approx 5 \times 10^{-19}$ cm^2 molecule^{-1} reported in the literature,[234] and our photolysis diameter and energy of 1.2 cm and 15 mJ (30 mJ).

As shown in Table 4-1 a distinction is made between "Low-T" (T < 390 K) and "High-T" (T $\geq$ 390 K) data. For the Low-T data, only reactions R1 and R2 are necessary to completely describe the transient absorbance traces. This Low-T model emerges as the well-known pseudo-first-order model.

$$\frac{[C_2H_3](t)}{[C_2H_3]_0} = e^{-(k_1'+k_2)t} \qquad (4\text{-}3)$$

$$\frac{A(t)}{A_0} = (1 + a)\frac{[C_2H_3](t)}{[C_2H_3]_0} - a \qquad (4\text{-}4)$$

$$a = \frac{(k_1'+k_2)}{RC-(k_1'+k_2)} \qquad (4\text{-}5)$$

$[C_2H_3]_0$ is the initial concentration of C_2H_3, $k_1' = k_1[1,3 - C_4H_6]$, $A(t)$ is the time-dependent absorbance and RC is the time constant for our electronic data collection circuit that acts as a high-bandpass filter on the recorded decays (= 65 ms as we have shown previously[75]). Each Low-T experiment was fit to this model, where k_1 and k_2 are both global fit parameters (a single value of each was fit for all 6-9 traces of a given experiment). A more conventional pseudo-first-order analysis was also employed wherein a local k' value (= $k_1' + k_2$) was fit to each trace and k_1 was extracted from the slope of k' versus $[1,3 - C_4H_6]$ (Figure D 3). As shown in Figure D 4 and Figure D 5, the values of k_1 and k_2 obtained are the same in either case (global or local fit), but the uncertainty bounds are smaller when global values of k_1 and k_2 are fit to the whole body of data by virtue of parameter reduction. For this reason, we prefer the global model. For the chemical decays of this work that occur on timescales $\leq$ 10 ms, the effect of the RC electronics is adequately captured by including a without distorting the measured decay time constant (k_1 and k_2 in this case). Values of a are $\leq$ ~0.05. Figure 4-2 shows representative fits of the Low-T model to 300 K absorbance traces. Considering that only 2 parameters are used to fit 6-8 decays, the fits are in good agreement.
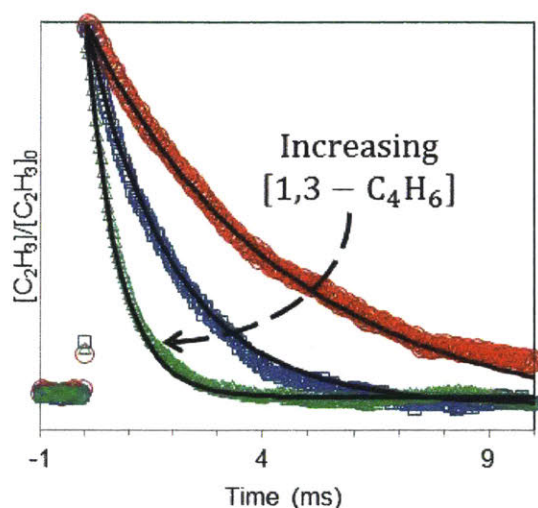
Figure 4-2: Representative measured decays of C_2H_3 using $\lambda = 423.2$ nm absorbance at relatively low-T (297 K, 100 Torr) and at the following $1,3 - C_4H_6$ concentrations (units of molecules cm^{-3}): 0 (red circles), 1.2×10^{16} (blue squares) and 5×10^{16} (green triangles). The experimental decays have been smoothed using a 200 point moving average. Solid black lines are fits of the low-T model (single-exponential).

Implicit in the Low-T model is the assumption that C_2H_3 is the sole contributor to the 423.2 nm absorbance. This assumption is justified for $T < 390$ K by the good fits of the single-exponential model to the data, but for $T \geq 390$ K this assumption breaks down because at these higher temperatures the allylic products of the title reaction also contribute to the absorbance. Two of the expected C_6H_9 products are allylic radicals so it is expected that like allyl, they also absorb visible light relatively strongly. However, from earlier predictions of the product branching,[194, 202, 205] as well as our predictions shown later, we can assume that at our experimental conditions only the $n - C_6H_9$ allylic radical was produced at concentrations sufficient to affect the measured absorbance. As mentioned earlier, $\lambda = 423.2$ nm was specifically chosen to avoid competing absorbance by allylic radicals. This approach was successful for $T < 390$ K, where the vibronic bands we are probing are defined relatively sharply.[233, 235] At higher temperatures, however, the bands broaden and merge due to population of higher vibrational states at the ground electronic energy. This makes it much more difficult, if not impossible, to find a wavelength to probe one species selectively in a mixture. Here, we have taken the approach of modelling the contributions of both C_2H_3 and $n - C_6H_9$ to the overall 423.2 nm absorbance. R1 and R2 serve as the basis for this model, which only needs to be expanded on by the addition of one reaction of the allylic product.

$$n - C_6H_9 \xrightarrow{k_3} \text{Products} \qquad\qquad (R3)$$
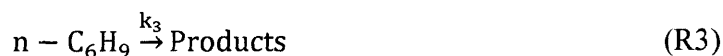
R3 is analogous to R2 already considered for C_2H_3. Initially, we also included a fourth reaction of $n - C_6H_9 + 1,3 - C_4H_6$, but found that this reaction was too slow for us to detect. Again we have neglected possible radical-radical reactions, i.e. self-reaction or cross reaction of $C_2H_3 + n - C_6H_9$, on the basis of low experimental radical concentrations; if these reactions were important exponentials would not fit the data. A straightforward analytical solution exists for this High-T model represented by R1-3. The solution for $[C_2H_3](t)$ is the same exponential decay function as in Eq. 4-3, whereas $[n - C_6H_9](t)$ is a biexponential function.

$$[n - C_6H_9](t) = \frac{\alpha_{n-C_6H_9} k_1' [C_2H_3]_0}{k_1' + k_2 - k_3} \left[1 - e^{-(k_1' + k_2 - k_3)t}\right] e^{-k_3 t} \qquad (4-6)$$

The expression for the overall $A(t)$ can then be determined by weighting the contributions of $[C_2H_3](t)$ and $[n - C_6H_9](t)$ by their respective absorption cross sections, $\sigma(423.2 \text{ nm})$. The normalized solution is shown below.

$$\frac{A(t)}{A_0} = e^{-(k_1'+k_2)t} + \frac{bk_1'}{k_1'+k_2-k_3}\left[1 - e^{-(k_1'+k_2-k_3)t}\right]e^{-k_3t} \tag{4-7}$$

$$b = \frac{\alpha_{n-C_6H_9}\sigma_{n-C_6H_9}(423.2\text{ nm})}{\sigma_{C_2H_3}(423.2\text{ nm})} \tag{4-8}$$

Equations 4-7 and 4-8 constitute the High-T model. k_1, k_2, k_3 and b are all global fit parameters. There is no a parameter as in the Low-T model because it is a small correction (typically <5% of the full scale as mentioned earlier) and Eqs. 4-4 and 4-5 were derived for the case of a simple exponential chemical decay. A benefit of this model is that there are a reasonable number of fit parameters (4 parameters to fit the entire transient behavior of 6-9 absorbance decays) each of which can be ascribed to an observable physical process. Furthermore, values of $[C_2H_3]_0$, $\sigma_{C_2H_3}$, $\sigma_{n-C_6H_9}$, $\alpha_{n-C_6H_9}$ and the probe laser pathlength don't need to be known in order to obtain accurate values of k_1, the quantity of interest. Note that if b = 0 (no contribution of $n - C_6H_9$ either because it is not being produced, $\alpha_{n-C_6H_9} = 0$, or its cross sections is small compared to that of C_2H_3) the pseudo-first-order model of Eq. 4-3 is recovered. Representative fits of 494 K absorbance traces to the high-T model are shown in Figure 4-3. Clearly the decays are not single exponential, this is most evident for high $[1,3 - C_4H_6]$. As shown, the High-T biexponential model describes this behavior very well, especially considering the use of only four fit parameters.
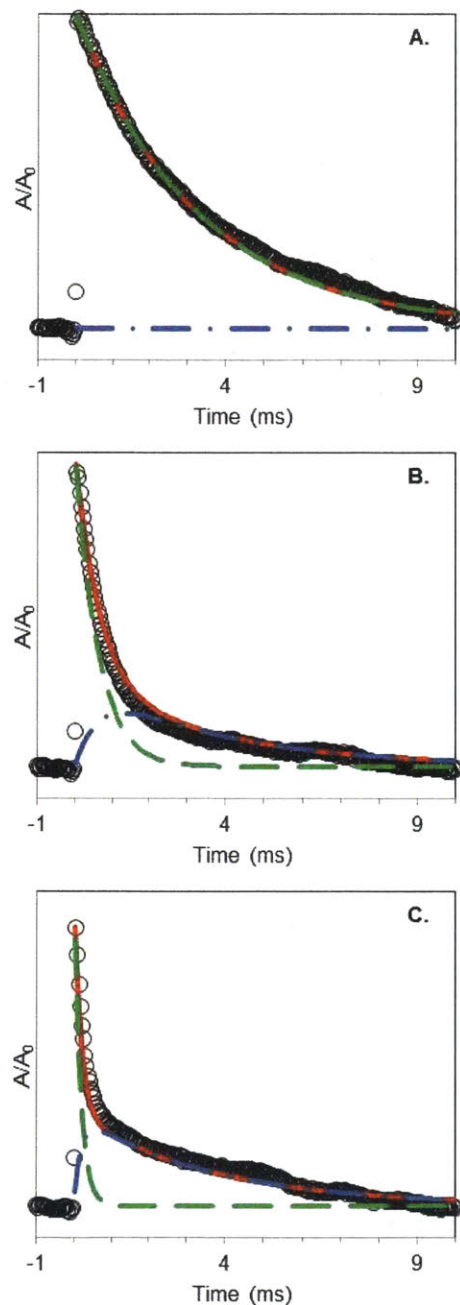
Figure 4-3: Representative measured absorbance decays using $\lambda = 423.2$ nm at relatively high-T (494 K, 100 Torr) and at the following $1,3 - C_4H_6$ concentrations (units of molecules cm^{-3}): 0 (Panel A), 1.2×10^{16} (Panel B) and 5×10^{16} (Panel C). The experimental decays have been smoothed using a 200 point moving average. Green dashed lines are the modeled C_2H_3 decay, blue dashed-dotted lines are the modeled n-C_6H_9 growth and decay and the solid red lines are the fits of the overall high-T model.

All of the fit parameter values for the High-T model are included in Table D 2. It is worth mentioning here that the fit values of b vary from ~0.25 − 0.40 and increase as a function of increasing T and decreasing P. Assuming that $\alpha_{n-C_6H_9} \approx 1$, which is predicted at our conditions as shown in the next section, these values of b simply represent the ratio of $n - C_6H_9$ to C_2H_3 cross sections. We have previously measured T- and P-dependent values of $\sigma_{C_2H_3}(\lambda)$ using the approach of Ismail et al.,[96] but currently we cannot measure $\sigma_{n-C_6H_9}(\lambda)$ without available $n - C_6H_9I$ or $n - C_6H_9Br$ precursors nor, to our knowledge, have these values been measured in the literature. Nonetheless, we have measured the T- and P-dependent cross section of the allyl radical, C_3H_5, which we expect to be similar to $\sigma_{n-C_6H_9}(\lambda)$. As shown in Figure D 2, our measured $\frac{\sigma_{C_3H_5}}{\sigma_{C_2H_3}}$ (423.2 nm) values are in excellent agreement with the fit b values mentioned above, lending credibility to our model, and supporting the conclusion made later that $n - C_6H_9$ is the dominant product at our conditions $\left(\alpha_{n-C_6H_9} \approx 1\right)$.

Figure 4-4 is an Arrhenius plot that summarizes our measured temperature dependence of k_1 with comparisons to literature. The error bars on individual k_1 measurements in Figure 4-4 and Figure 4-5 include fitting uncertainty as well as systematic uncertainty due to 10% uncertainty in $[1,3 - C_4H_6]$ as discussed previously.[74] Our experimental results are fit well by the simple Arrhenius expression $(1.1 \pm 0.2) \times 10^{-12}$ cm^3 molecule^{-1} s^{-1} $\times \exp\left(-\frac{9.9 \pm 0.6 \text{ kJ mol}^{-1}}{RT}\right)$, as shown by the dotted-dashed black line. The fact that k_1 values obtained from both the Low- and High-T models all lie along the same Arrhenius fit provides confidence in our interpretation of the absorbance results. The calculations of the total rate of vinyl + 1,3-butadiene performed in this work at 25 Torr He and 760 Torr N$_2$ are also shown in Figure 4-4 and are in good agreement with the current experimental data. From these predictions, k_1 in the high pressure limit can be expressed in modified Arrhenius form as 6.5×10^{-20} cm^3 molecule^{-1} s^{-1} $\times$ T$^{2.40}$ $\exp\left(-\frac{1.76 \text{ kJ mol}^{-1}}{RT}\right)$ from 300 to 2000 K. The slope of our measurements and predictions also agree well with the TST predictions of Cavallotti et al.[202-203] However, the absolute values of our measurements and predictions are significantly different from any of the predictions mentioned above. Most strikingly, our results disagree both quantitatively and qualitatively with the pressure dependent

predictions of Cavallotti et al and Xu et al.[205] These differences are discussed in more detail in the following section on product branching.
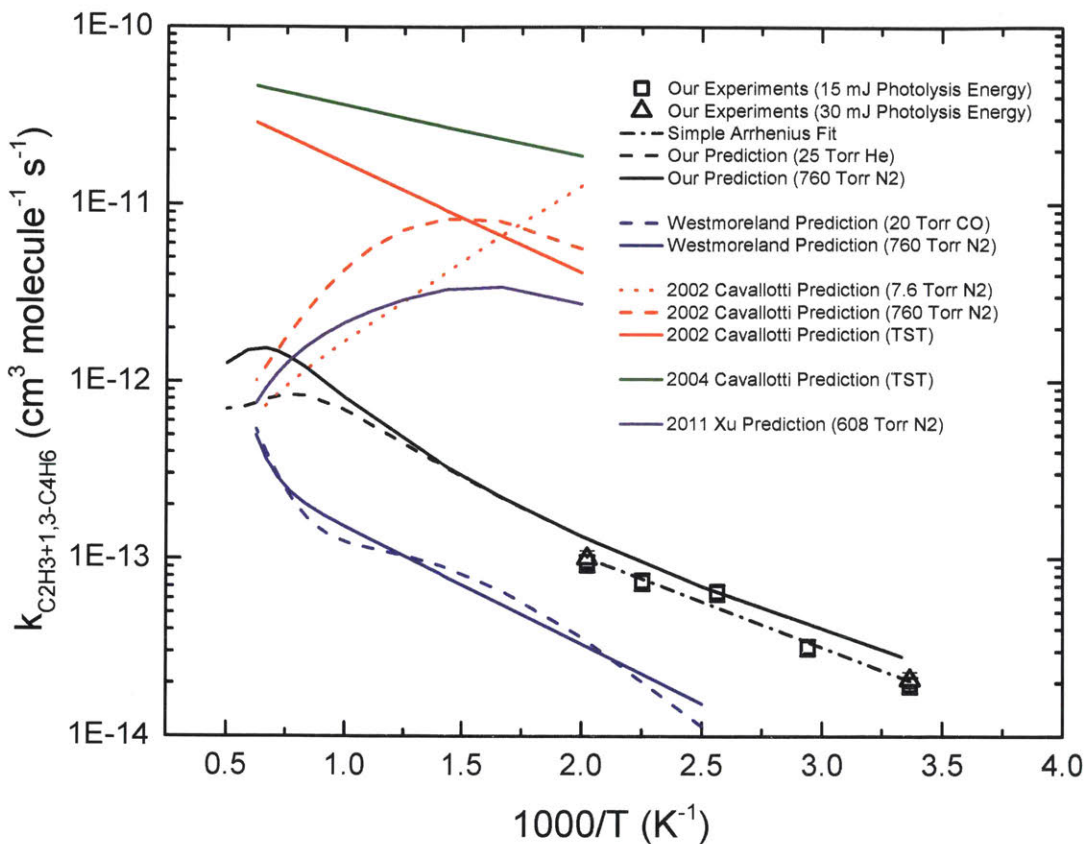
Figure 4-4: Arrhenius plot of our measured overall rate constant for $C_2H_3 + 1,3 - C_4H_6$ at 25 Torr (symbols) with a simple Arrhenius fit (dotted-dashed black line) and comparison to literature predictions: Westmoreland et al.[194] (blue lines), 2002 Cavallotti et al.[202] (red lines), 2004 Cavallotti et al.[203] (green line) and Xu et al.[205] (purple line). Also shown are the theoretical predictions of this work (black lines).

At the two temperature extremes of our experiments (297 and 494 K) we measured k_1 at both 15 and 30 mJ pulse^{-1} of photolysis energy and found the values to be within their error bars. These results justify our assumption that $1,3 - C_4H_6$ photodissociation is not affecting the measured kinetics as discussed earlier. The 494 K result is particularly convincing given that photodissociation is more likely to occur at higher temperature.

Figure 4-5 shows the measured pressure dependence of k_1 again at the temperature extremes of 297 and 494 K. Although some of the measurements at the same T are outside of the error bars of others, no consistent trend is discernible from these results. The outlying data points

are suggestive not that there is any pressure dependence at our conditions, but that our error bars are underestimated perhaps by a factor of two. The measured lack of pressure dependence is consistent with both our own predictions and those of Westmoreland et al.[194] (Figure 4-4) showing that even at the relative low P of this work ($\leq$ 100 Torr) we are already near the high-P limit (k_∞).

It is informative to compare our measured k_1 for vinyl radical addition to 1,3-butadiene with other radical additions to 1,3-butadiene. Phenyl + 1,3-butadiene provides a good comparison because its overall rate coefficient has been measured in an experimental study quite similar to this work.[236] Phenyl decay was measured by cavity ringdown spectrometry (CRDS) at $\lambda = 504.8$ nm from $298 - 450$ K at 40 Torr. At these conditions the authors also concluded they were already in the high-pressure limit and the dominant product was expected to be the radical adduct. The Arrhenius pre-exponential factor that they measured is around an order of magnitude higher than what we measured for vinyl + 1,3-butadiene in the same T,P-range, while the E_A values are nearly identical. A similar difference between vinyl and phenyl radical addition to the same unsaturated C-C bond has also been observed for vinyl/phenyl radical addition to acetylene.[196, 237] This comparison provides greater confidence in our measurement. Refer to Figure D 6 for Arrhenius comparison plots of vinyl/phenyl + 1,3-butadiene/acetylene.
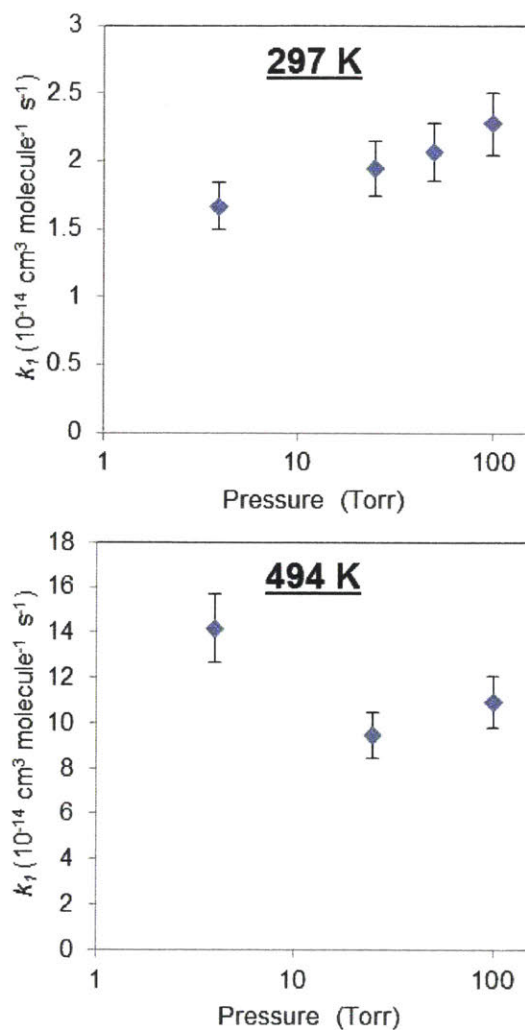
Figure 4-5: Measured pressure dependence of overall $C_2H_3 + 1,3 - C_4H_6$ rate constant at 297 K (upper panel) and 494 K (lower panel).

4.1.4.3   Product Branching of C_2H_3 + 1,3-C_4H_6

Experiments were conducted at both 4 and 25 Torr over a range of temperatures using PI TOF-MS in order to measure the products of $C_2H_3 + 1,3 - C_4H_6$, as summarized in Table 4-2. For the 4 Torr experiments, we were able to obtain useful results for $T \geq 494$ K despite significant $1,3 - C_4H_6$ photodissociation that prevented absorbance measurements at 599 and 700 K. At each T and P there is a "Base Case" experiment, and several control experiments to aid in interpreting the results.

Table 4-2: Summary of experimental conditions for PI TOF-MS experiments

Experiment Title	T (K)	P (Torr)	PDMS coated?	Photolysis Energy (mJ/pulse)	Photolysis Diameter (cm)	$[C_2H_3I]$ (10^{14} molecule/ cm^3)	$[1,3\text{-}C_4H_6]$ (10^{16} molecule/ cm^3)	FPR[1]
Base Case	297	25	No	50	1.2	2.5	1.2	0.94
C_2H_3 Only Control	297	25	No	50	1.2	2.5	0	0.94
1,3-C_4H_6 Control	297	25	No	50	1.2	0	1.2	0.94
Base Case	494	25	No	30	1.2	1.2	1.2	0.92
C_2H_3 Only Control	494	25	No	30	1.2	1.2	0	0.92
1,3-C_4H_6 Only Control	494	25	No	30	1.2	0	1.2	0.92
2x[C_2H_3I] Control	494	25	No	30	1.2	2.4	1.2	0.92
2x Photolysis Control	494	25	No	50	1.2	1.2	1.2	0.92
2x FPR Control	494	25	No	30	1.2	1.2	1.2	2.30
Base Case	494	4	No	30	1.2	1.2	1.2	0.92
1,3-C_4H_6 Only Control	494	4	No	30	1.2	0	1.2	0.92
No Cal Mix Control	494	4	No	30	1.2	1.2	1.2	0.92
PDMS Coated Control	494	4	Yes	30	1.2	1.2	1.2	0.92
1.5 cm Photolysis Diameter Control	494	4	Yes	30	1.5	1.2	1.2	0.92
Maximum Photolysis Power Control	494	4	Yes	80	1.2	1.2	1.2	0.92
Base Case	599	4	No	30	1.2	1.2	1.2	0.93
1,3-C_4H_6 Only Control	599	4	No	30	1.2	0	1.2	0.93
No Cal Mix Control	599	4	No	30	1.2	1.2	1.2	0.93
C_2H_3 Only Control	599	4	No	30	1.2	1.2	0	0.93
Base Case	700	4	No	30	1.2	1.2	1.2	0.93
1,3-C_4H_6 Only Control	700	4	No	30	1.2	0	1.2	0.93
No Cal Mix Control	700	4	No	30	1.2	1.2	1.2	0.93
Half 1,3-C_4H_6 Control	700	4	No	30	1.2	1.2	0.6	0.93

[1]FPR = Flashes per Refresh

Figure 4-6 shows a section of our measured transient mass spectra at both 25 and 4 Torr (494 K and 599 K, respectively) under conditions where $C_2H_3 + 1,3 - C_4H_6$ occurs. Other than the I Atom signal at 127 amu, transient behavior was not observed in any other region of the spectrum (due to significant dissociative ionization of C_2H_3I to C_2H_3, the transient behavior of C_2H_3 could not be discerned even after background subtraction). At both pressures, there is clearly growth occurring at m/z = 81 amu, which we tentatively assign to some mixture of C_6H_9 isomers produced by the title reaction (Scheme 4-1 and Figure 4-1). This assignment was confirmed by control experiments showing that the 81 amu species requires the simultaneous presence of C_2H_3 and $1,3 - C_4H_6$ to form. The mass spectra obtained at 297 K and 25 Torr exhibits identical behavior as at 494 K and 25 Torr (Figure D 8), although the signal-to-noise was lower due to the slower $C_2H_3 + 1,3 - C_4H_6$ reaction rate at this temperature, resulting in a lower product concentration.
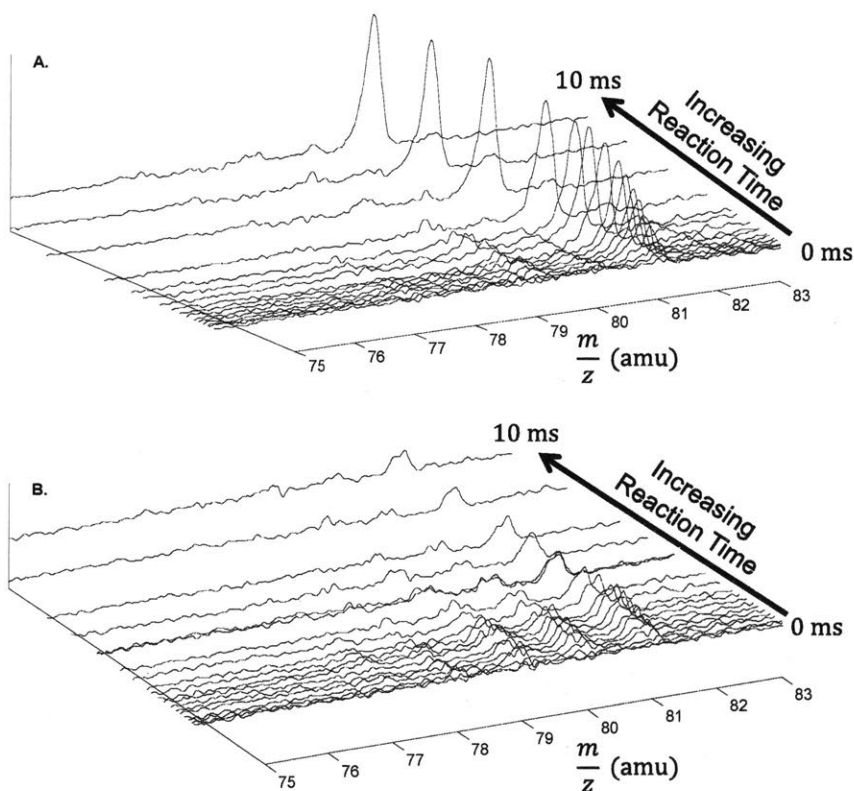
Figure 4-6: Transient mass spectra obtained under conditions where $C_2H_3 + 1,3 - C_4H_6$ can occur for **A.** 494 K and 25 Torr, and **B.** 599 K and 4 Torr. In both cases $[C_2H_3I] = 1.2 \times 10^{14}$ and $[1,3 - C_4H_6] = 1.2 \times 10^{16}$ molecules cm^{-3}. The spectrum acquired at a reaction time of -0.20 ms was subtracted from all subsequent spectra so that only transient changes are observed. The spectra were also smoothed and baseline corrected.

At 4 Torr, there is also a transient peak at 80 amu, which control experiments confirm as another product of $C_2H_3 + 1,3 - C_4H_6$. This species was not observable in any of the 25 Torr experiments. We assign this species to a mixture of 1,3- and 1,4-cyclohexadiene isomers $(c - C_6H_8)$, based on our predictions of the product branching shown in Figure 4-9 below.

There is one final peak at 79 amu that is present at both pressures and that does not correspond to an expected product of $C_2H_3 + 1,3 - C_4H_6$. In Appendix D we discuss control experiments aimed at identifying this species and ultimately conclude that it is likely not a product of $C_2H_3 + 1,3 - C_4H_6$. At 700 K there were also several other transient species besides 79, 80 and 81 amu, (e.g., 15 and 78 amu) but none of these species required the presence of C_2H_3 and are therefore attributed to $1,3 - C_4H_6$ photodissociation and subsequent reactions. Despite these complications, the transient signals at 80 and 81 amu were found to be the only species clearly attributable only to $C_2H_3 + 1,3 - C_4H_6$ at all of the T and P conditions of Table 4-2.

Unfortunately, we cannot discern among C_6H_9 isomers using our PI TOF-MS with fixed ionization energy. Neither can we provide an estimate of the quantitative branching fraction to this channel because the photoionization cross sections of the C_6H_9 isomers have not yet been measured. Nonetheless, our theoretical predictions below provide strong evidence that the 81 amu signal is solely due to $n - C_6H_9$ $\left(\alpha_{n-C_6H_9} \approx 1\right)$, which is also consistent with our interpretation of the fit b parameters in the previous section.

Similarly, we can't distinguish between 1,3- and 1,4-cyclohexadiene. However, the photoionization cross sections of both isomers are known at our ionization energy (10.5 eV).[238-239] Therefore we were able to quantify the total branching to both cyclohexadiene isomers at 4 Torr and relatively high temperature conditions (494, 599 and 700 K) where they become significant products (see Appendix D for details of quantification). Control experiments conducted after coating the inside of the stainless steel reactor with PDMS gave the same quantitative cyclohexadiene branching fractions as experiments without the coating. PDMS has previously been used in similar kinetic studies to render reactor walls inert up to 750 K.[146, 219] Therefore, we conclude that wall reactions do not consume a significant portion of the vinyl radical pool, possibly due to the unique geometry of our reactor.

Figure 4-7 compares our measurement of this branching with our predictions. In both cases, the branching fraction of total $C_6H_8 + H$ products increases with higher temperature, as expected for a chemically activated channel. However, the model greatly overpredicts the

branching. The large error bars on the experimental measurements are from propagation of uncertainty (see Appendix D for an account of the various contributors).
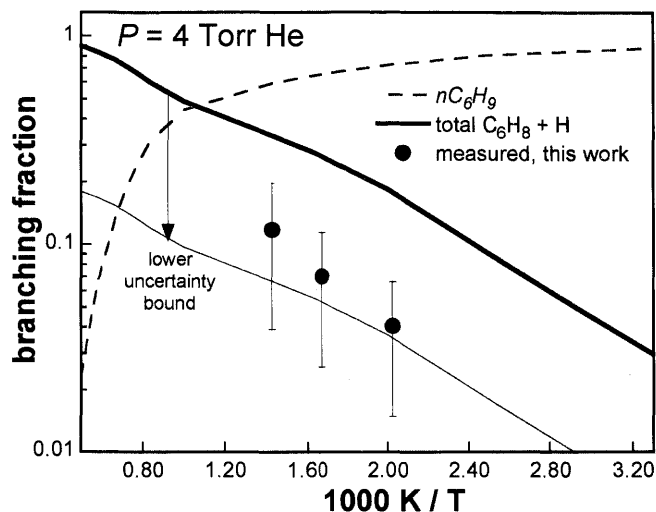
Figure 4-7: Branching fractions for major bimolecular product species (minor contributions not shown) of the reaction of vinyl + 1,3-butadiene at 4 Torr He. Predicted branching fractions of $n - C_6H_9$ (dashed line) and total $C_6H_8 + H$ (thick solid line), are compared with measured branching fractions (filled circles). Also depicted is an estimated uncertainty bound in the calculations of a factor of 5; see text for discussion.

Sensitivity analyses of the predicted total branching fraction for the C_6H_8 isomers [+ H] were performed with respect to several input parameters: relevant barrier heights, the average downward energy transferred upon collision with the He bath gas, and the influence of 1,3-butadiene as a colliding partner. The lower bound illustrated in Figure 4-7 represents a combined ±1 kcal/mol barrier uncertainty with a factor of two increase in $\langle \Delta E_d \rangle_{300}$ for Helium. Additional uncertainties arise from the use of Eckart tunneling corrections, the MSC solution to the master equation, and A-factors for reactions where hindered internal motions are important. Last, uncertainties also arise from the fact that gas mixtures for 4 Torr experiments contained up to 22% 1,3-butadiene (see Table D 5), which was not considered in the branching fractions predicted in Figure 4-7. The average downward energy transferred upon collision for 1-butene (a suitable analog to 1,3-butadiene) is a factor of eight larger than that for Helium in observations of excited toluene stabilization.[240] Simulations performed using weighted averages of energy transfer properties where the bath gas consists of 20% 1,3-butadiene and 80% Helium suggest branching to total C_6H_8 + H is twice as low between 500-700 K and at 4 Torr. Although the

current branching fractions are uncertain by at least a downward factor of five, it is expected that future high-accuracy rate calculations may reconcile predicted branching fractions with those observed in this work at 4 Torr in Helium. We also note that while uncertainties in predicted branching are high for simulations at low pressure and with Helium as a bath gas, the simulations in N_2 at and above 1 atm – combustion relevant conditions – are more reliable due to the larger $\langle \Delta E_d \rangle_{300}$ of N_2.

The product branching calculations performed here and shown in Figure 4-9 support the observation that the dominant product species at and above 25 Torr is $n - C_6H_9$, of mass 81 amu. Thus, at 1 atmosphere, the formation of $c - C_5H_6 + CH_3$ is negligible, in contrast to previous predictions by Cavallotti et al.[202-203] As noted in previous works and also illustrated in Figure 4-4, there remains a great deal of disparity between theoretical predictions of the total rate of vinyl + 1,3-butadiene. The two sets of computed results by Cavallotti et al.[202-203] and predictions of recent work by Xu et al.[205] are more than an order of magnitude faster than those predicted here and earlier by Westmoreland et al.[194] We note that the rate constant for the entrance channel computed by Cavallotti (private communications) used a 2-dimensional treatment of the hindered rotor that not only accounts for the rotation of the two moieties about the axis defining the forming bond, but also one of the rocking motions in the transition state. Cavallotti et al. employed the Unimol code originally developed by Gilbert and Smith.[241] Use of this code to treat a 2D internal rotor resulted in a factor of 400 increase in the pre-exponential factor compared with treating all internal degrees of freedom as harmonic oscillators. It was further noted by Cavallotti that this approach, as implemented in the Unimol code, can lead to substantial errors, thus explaining the large discrepancy between computed high pressure limit rate coefficients presented in this work and those of Cavallotti et al. (private communications).

The discrepancy between the high-pressure limit entrance channel rate computed in this work and that reported by Xu et al.[205] is primarily due to differences in predicted barrier heights (0.3 kcal/mol via the F12 method and -0.6 via CBSQB3) and in choice of rate parametrization (strict vs modified Arrhenius). Gaussian output files used for the TST calculation by Xu et al along with their corresponding TST-derived rates for the high pressure limit rate of the entrance channel were provided by means of personal communication. One can see that the RRHO rates computed using the Xu et al. geometry and frequencies (blue line of Figure 4-8), and the RRHO rate computed using the geometry and frequencies computed here using a different DFT

functional and basis set, are very similar after compensating for the 1 kcal/mole difference in computed barrier height (black dashed line), differing by less than a factor of 3 over the full T range. The strict Arrhenius fit used by Xu et al. (red line of Figure 4-8) differs significantly from the computed k(T) at some temperatures, since it does not allow for the strong curvature of k(T) on the Arrhenius plot. Considering all the calculations and the experimental data, it appears that the computed rates are all uncertain by a factor of 3 or more; the rates computed here are (perhaps fortuitously) close to the low temperature experimental measurements giving us a little more confidence in the predictions at higher temperatures. Thus, an overall factor of 3 uncertainty is recommended for the predicted high-pressure limit rate coefficient for the reaction of vinyl radical + 1,3-butadiene.
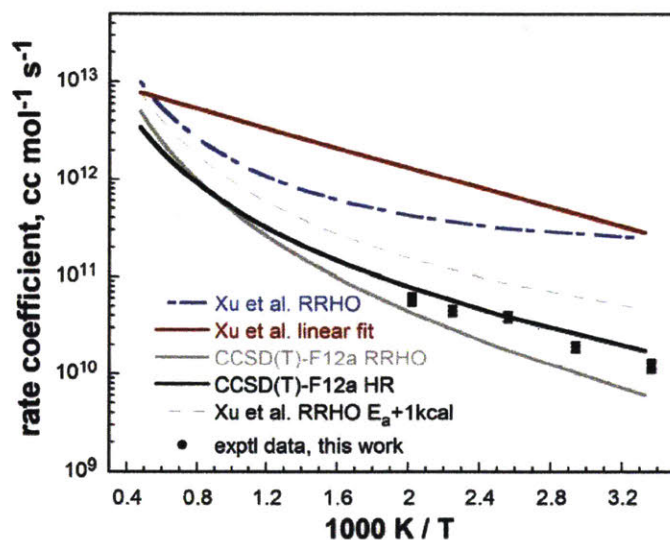
Figure 4-8: Comparisons of computed high pressure limit rates for the reaction of vinyl radical + 1,3-butadiene between experimental and computed values of this work, as well as those of Xu et al.[205]

In comparing predicted rates of individual product channels between this work and previous studies, the 25 Torr rates shown in Figure 4-9 are in good qualitative agreement with the corresponding lower pressure estimates of Westmoreland et al.,[194] albeit their simulations were performed in a CO bath gas. However, the aforementioned authors predict the formation of $n - C_6H_8 + H$ to dominate around 1250 K, while the current calculations suggest this channel to dominate at considerably higher temperatures.

A general observation made in this work and supported both by present experiments and computation is the negligible chemically activated well skipping to bimolecular product channels at temperatures below 500 K and pressures above 25 Torr. Clearly evident from Figure 4-9 is that $n - C_6H_9$ is the dominant product not just at 25 Torr, but also at 760 Torr. At 25 Torr and 300 K, 94% of the product is predicted to be the linear adduct, while at 1000 K, 71% of the product is $n - C_6H_9$, with the two $c - C_6H_8$ species representing the remaining product distribution. At 1000 K and 760 Torr, only 2% of the product species are predicted to be the two $c - C_6H_8$ species + H. This is in contrast to the recent work by Xu et al.,[205] who predict these channels to contribute more equally to the total product distribution at 0.8 atm and at 1000 K and above. Because the PES used here and the Master Equation solution method, MSC, are both similar to that employed by Xu et al., it is unclear why these differences exist. Higher level collisional energy transfer models may increase the total predicted branching to bimolecular products, further increasing the discrepancy in predicted and measured branching shown in Figure 4-7. Nonetheless, recommended future work entails a rate theory calculation more reliable than the MSC method.

The overall dominance of the $n - C_6H_9$ adduct suggests this species could persist long enough to undergo bimolecular reactions with other gas phase species at low enough temperatures, and of course where there is sufficient vinyl and 1,3-butadiene. If this is the case, care should be taken to ensure that the fate of $n - C_6H_9$ is properly accounted for. Compared to some previous kinetic models which use rates that predict a larger proportion of bimolecular c5- and c6-ring products, inclusion of the present rates in kinetic models may in fact decrease overall predicted benzene concentrations for relevant conditions.
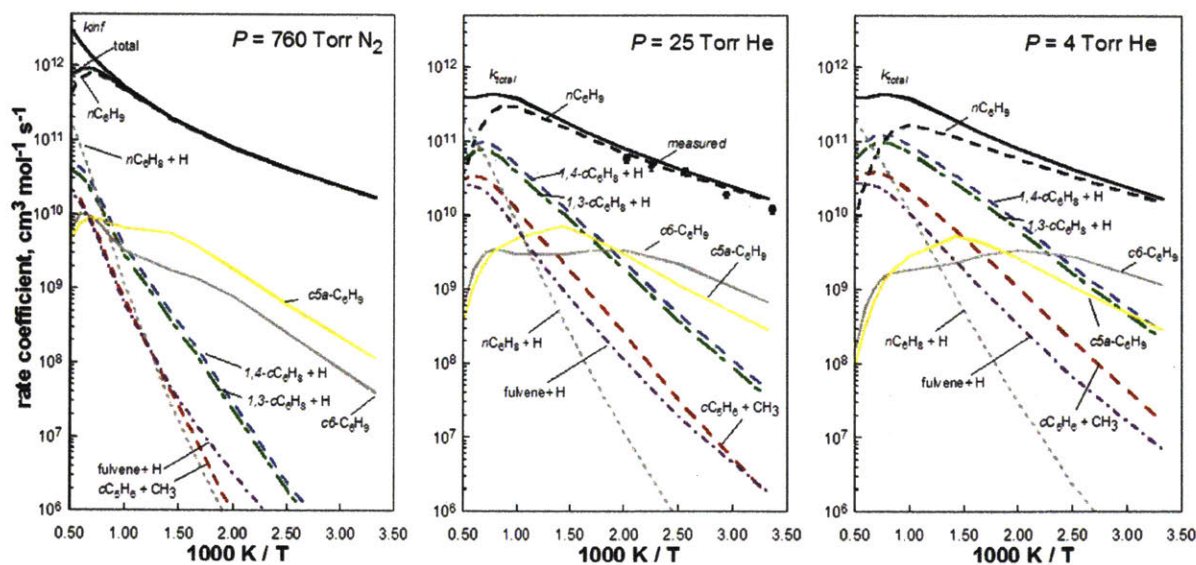
Figure 4-9: Predicted rates of major channels for the reaction of vinyl + 1,3-butadiene for 760 Torr N_2 (left), 25 Torr He (middle) and 4 Torr He (right). Measurements of the overall rate at 25 Torr He, are shown as black circles, and accompanied by an Arrhenius fit.

4.1.4.4 Implications for Soot Formation

The impact of our newly measured rate coefficient on pre-existing pyrolysis or combustion models will depend on the conditions of the system. For example, if $C_2H_3 + 1,3 - C_4H_6$ is already the dominant route for benzene production, then a larger k_1 will increase the predicted benzene formation if the addition step is rate-limiting. If, however, another route involving vinyl radicals dominates benzene formation, such as $C_2H_3 \xrightarrow{C_2H_2} n - C_4H_5 \xrightarrow{C_2H_2} C_6H_6 + H$ as suggested by Miller et al.,[196] it is conceivable that increasing k_1 will actually decrease benzene formation by converting reactive C_2H_3 to long-lived, resonantly-stabilized $n - C_6H_9$, acting effectively as a trap for vinyl radicals. Regardless of the overall effect, we recommend that future models incorporate the rates reported here to improve the accuracy of predictions and to assess the true role of $C_2H_3 + 1,3 - C_4H_6$.

4.1.5 Conclusions

We report the first direct rate coefficient measurement of $C_2H_3 + 1,3 - C_4H_6$, k_1, using laser flash-photolysis with visible probe absorbance. Photodissociation of $1,3 - C_4H_6$ is kept at an acceptable level by using relatively low $[1,3 - C_4H_6]$ and photolysis energy, as well as maintaining $297\ K \leq T \leq 494\ K$ for all absorbance experiments reported here. For $T < 390\ K$

the decay of C_2H_3 could be monitored selectively using $\lambda = 423.2$ nm as the probe wavelength, enabling a straightforward pseudo-first-order analysis of the results. For $T \geq 390$ K, however, the major allylic product, $n - C_6H_9$, makes a non-negligible contribution to the absorbance and a model that accounts for this behavior is used. Our interpretation of the absorbance traces at different temperatures is validated by the good fits of the model to the data, as well as the fact that a simple Arrhenius fit is able to capture the resulting temperature dependent k_1 measurements, shown below.

$$k_1 = (1.1 \pm 0.2) \times 10^{-12} \text{ cm}^3 \text{ molecule}^{-1} \text{ s}^{-1} \times \exp\left(-\frac{9.9 \pm 0.6 \text{ kJ mol}^{-1}}{RT}\right)$$

k_1 is pressure-independent at the conditions of our experiment $(4 - 100 \text{ Torr}, T \leq 494 \text{ K})$, leading us to conclude that we are already in the high-pressure limit, consistent with our predictions and others in literature.[194]

Analysis of the reaction products at $T \leq 494$ K and $P = 25$ Torr using photoionization time-of-flight mass spectrometry (PI TOF-MS) reveals only species with m/z = 81 amu, consistent with the molecular formula C_6H_9. Predictions of the product branching using quantum chemistry and pressure dependent rate calculations show the dominant product at almost all combustion relevant T and P (including our experimental conditions) to be the linear allylic species $n - C_6H_9$. This prediction is consistent both with the PI TOF-MS results cited above, and with the measured contribution of $n - C_6H_9$ to the absorbance traces at $T \geq 390$ K. Furthermore, the measured overall rate of $C_2H_3 + 1,3 - C_4H_6$ is in excellent agreement with the predictions. However, for $494 \leq T \leq 700$ K and $P = 4$ Torr we experimentally measured ~10% or less branching to the sum of 1,3- and 1,4-cyclohexadiene isomers, which was a factor of five lower than the predicted branching. We attribute this discrepancy to uncertainty in $\langle\Delta E_d\rangle_{300}$ and the computed barrier heights.

The predicted temperature and pressure dependent product branching rates are presented in a form that can be easily incorporated into combustion and pyrolysis models for $300 \leq T \leq 2000$ K and $P \geq 1$ Torr. We recommend that these rates be used in future detailed kinetic models so that the role of $C_2H_3 + 1,3 - C_4H_6$ in the formation of the first aromatic ring can finally be elucidated.

4.2   Phenyl Radical + Propene

4.2.1   Introduction

The addition of phenyl radical, C_6H_5, to the unsaturated C=C bond in propene, C_3H_6, produces two different propylbenzene radicals depending on the addition site, which are representative of a broader class of alkylaromatic radicals. As defined here, alkylaromatic radicals consist of an aromatic group, which can either be a single benzene ring or a polycyclic aromatic hydrocarbon (PAH) of arbitrary size, and at least one alkyl side chain of arbitrary length and branching on which the radical site resides. Alkylaromatic radicals can form either by "bottom-up" growth of smaller molecules, such as C_6H_5 + C_3H_6,[242] or by "top-down" decomposition of larger molecules, such as in the combustion or pyrolysis of gasoline, diesel and jet fuels which contain significant amounts of closed-shell alkylaromatic compounds like propylbenzene.[29] Once formed, the subsequent decomposition, growth or oxidation of alkylaromatic radicals can dictate the extent of PAH and soot formation, with potentially deleterious effects on climate[186] and human health.[184] Soot, or "coke", formation is also usually undesirable in industrial processes such as ethane steam cracking,[205] where fouling of the reactor can necessitate costly shutdowns for cleaning. Alkylaromatic linkages and radicals are also important in the chemistry of heavy oils, coal, kerogen, lignin and many polymers. Understanding all of the ways in which alkylaromatic radicals can react is therefore critical to a number of diverse applications including combustion, industrial cracking, organic geochemistry, and utilization of waste materials and biomass.

The two propylbenzene radicals directly formed by C_6H_5 + C_3H_6 have served as relatively simple surrogates for more complicated alkylaromatic radicals in many top-down experimental and theoretical studies of propylbenzene oxidation and pyrolysis, recently summarized by Yuan et al.,[29] and in nine bottom-up studies utilizing C_6H_5 + C_3H_6 (including this work) summarized in Table 4-3. From this large body of work on the C_9H_{11} potential energy surface (PES) a consensus has emerged (with some caveats discussed below) regarding the major expected reaction pathways of the C_6H_5 + C_3H_6 system, shown in Scheme 4-2. C_6H_5 mostly reacts with C_3H_6 by addition to the terminal and central C=C sites, and by hydrogen, H, abstraction from the allylic carbon in C_3H_6. The two propylbenzene radicals formed by addition can easily interconvert via a 1,2-phenyl-migration, and are usually assumed to be equilibrated at combustion-relevant

temperatures. The central-addition product will mostly β-scission a methyl radical, CH_3, to form styrene, whereas the terminal-addition product will β-scission an H on one of the two neighboring carbons to form 3- or 1-phenylpropene. Alternatively, if the radical site on the terminal addition product can shift to the end of the alkyl chain via a 1,2-H-migration, the resulting alkylaromatic radical can easily undergo a secondary ring-closure to form a five-membered ring. Subsequent β-scission of an H forms indane, which can make indene following loss of two more H atoms. Indene is a precursor to PAH and soot, and it is mostly because of this potential route to indene that $C_6H_5 + C_3H_6$ has been of such interest.[242] However, the 1,2-H-migration that enables indane formation has a barrier at least 6 kcal/mol higher than the various β-scissions mentioned above, rendering that pathway uncompetitive, even at combustion conditions.[9] The lack of indane formation from $C_6H_5 + C_3H_6$ and the dominance of styrene and phenylpropene isomers as products is supported both by calculations of the product branching,[9, 13] and by experiments conducted under single-collision[11, 13, 18] and thermal environments.[31]
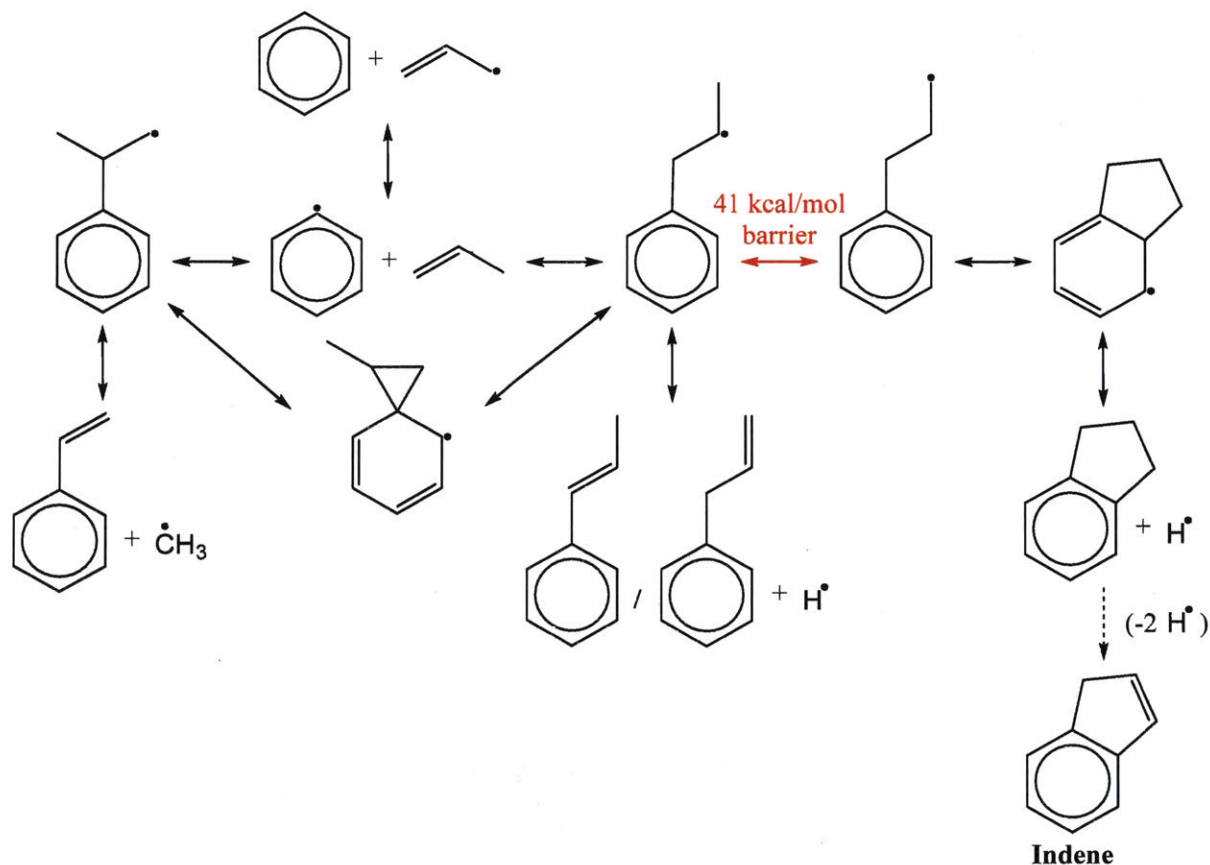
Scheme 4-2: Major expected reaction pathways of phenyl radical + propene

Table 4-3: Summary of literature on phenyl radical + propene system.

Publication	Experiment		Theory
	Reaction Conditions	*Detection Technique*	
1972 Hefter et al.[243]	Photolytically-generated C_6H_5 in liquid C_3H_6 (183-213 K)	Electron Spin Resonance of products	-
2006 Park et al.[8]	Photolytically-generated C_6H_5 in excess C_3H_6/Ar gas (296-496 K, 40 Torr)	Cavity Ring Down Specrometry (CRDS) of C_6H_5	G2M(RCC6)//B3LYP
2008 Zhang et al.[11]	Crossed Molecular Beams (CMB) of C_6H_5 and C_3H_6 (≥31 kcal/mol collision energy)	Electron Impact (EI) Quadrupole Mass Specrometry (QMS)	-
2012 Kaiser et al.[13]	CMB of C_6H_5 and C_3H_6 (~10 kcal/mol collision energy)	EI QMS	G3(MP2,CC)//B3LYP[a] + RRKM[b]
2012 Zhang et al.[31]	Pyrolytically-generated C_6H_5 in excess C_3H_6 gas (1200-1500 K, 300 Torr)	Tunable Vacuum Ultraviolet (VUV) Molecular Beam Mass Spectrometry (MBMS)	-
2012 Kislov et al.[9]	-	-	G3(MP2,CC)//B3LYP[a] + RRKM[b]/ME[c]/TST[d]
2013 Albert et al.[18]	CMB of C_6H_5 + C_3H_6 (≥20 kcal/mol collision energy)	VUV QMS	-
2014 Wang et al.[66]	-	-	CBS-QB3 + TST[d]
This Work	Photolytically-generated C_6H_5 in excess C_3H_6/He gas (295-707 K, 10-50 Torr)	Multiple-pass laser absorbance of C_6H_5, C_3H_5 and C_7H_7 + VUV Time-of-Flight (TOF) MBMS	G3(MP2,CC)//B3LYP[a] + RRKM[b]/ME[c]/TST[d]

[a]Same level of theory used in this work, which is described in Theoretical section. [b]RRKM = Rice-Ramsperger-Kassel-Marcus theory for k(E). [c]ME = Master Equation model of T,P-dependent kinetics. [d]TST = Transition State Theory for high-P, T-dependent kinetics.

The single-collision experiments, conducted in crossed molecular beam (CMB) apparatuses with Quadrupole Mass Spectrometry (QMS) detection, ruled out significant indane formation at collision energies, E_{col}, of ~10 kcal/mol[13] and ~30 kcal/mol[11] based on both the measured exoergicity of the H-loss channel and from experiments with deuterated C_3H_6. The thermal experiment, conducted in a fast pyrolysis reactor maintained at 1200-1500 K in 300 Torr of C_3H_6, ruled out indane formation based on the measured photoionization efficiency (PIE) curves of the product(s) at a mass-to-charge ratio, m/z, of 118 amu, corresponding to the mass of the various H-loss products with molecular formula C_9H_{10}.

Although there is qualitative agreement in the literature regarding what the major products of $C_6H_5 + C_3H_6$ should (styrene and phenylpropene isomers) and should not (indane) be, quantitatively there are three discrepancies. First, the extent of H-abstraction is predicted to be significant, increasing from ~10% of the product branching at 300 K to ~80% at 3000 K,[9] but this has never been quantified experimentally. Of the six previous experimental studies listed in

Table **4-3**, only the photolysis experiments of Hefter et al. in liquid C_3H_6 reported measurable products of H-abstraction: benzene, C_6H_6, and allyl radical, the most thermodynamically stable of the C_3H_5 isomers.[243] In that work, C_6H_5 was found to prefer radical addition to the terminal C=C carbon in propene over the other two major entrance reactions (Scheme 4-2), consistent with the low temperatures used (182-213 K). Of the two remaining experiments conducted in a thermal reactor, the fast pyrolysis experiment of Zhang et al. were done under aggressive conditions that would encourage many side, secondary, tertiary and higher reactions,[31] making it impossible to extract quantitative information about the underlying chemistry without a detailed kinetic mechanism. The Cavity Ring Down Spectrometry (CRDS) experiments of Park et al. were conducted under more controlled conditions, and the probe laser wavelength used, 504.8 nm, was tuned to a known absorbance feature of C_6H_5,[105] where few other radicals absorb, enabling selective detection of C_6H_5.[8] While convenient for accurate quantification of overall consumption rates, selective detection of a photolytically-generated radical reactant (C_6H_5 in this case) leaves the experimentalist blind to subsequent product formation, which was the case in Park et al.[8] Finally, all three of the CMB experiments with QMS detection were unable to detect C_6H_6, likely due to overlap with the large ^{13}C peak of scattered C_6H_5.[18]

The second quantitative discrepancy is the extent of CH_3-loss relative to H-loss. Kaiser et al. computed relative product yields under single-collision conditions by combining G3(MP2,CC)//B3LYP calculations of the C_9H_{11} PES with microcanonical Rice-Ramsperger-Kassel-Marcus (RRKM) theory for energy-dependent rate coefficients, k(E), and then applying the steady-state approximation to the set of differential equations describing the reaction network.[13] This calculation does not include the contribution of H-abstraction because as noted above it was not possible to observe products of H-abstraction in the CMB experiments. The single-collision product calculations of Kaiser et al. were quantitatively consistent with CMB experiment reported in that same work at $E_{col} \approx 10$ kcal/mol, where yields of CH_3- and H-loss products were measured as ~70% and ~30%, respectively. At higher E_{col} it was predicted that the yield of CH_3-loss would drop steadily to ~20% at ~45 kcal/mol to be replaced by various H-loss products (mostly 3-phenylpropene). This prediction was also consistent with earlier CMB experiments at $E_{col} > 30$ kcal/mol, where only H-loss products were observed, and the CH_3-loss yield was approximated as <10% due to the detection limit.[11] However, Albert et al. measured a much higher relative product yield of CH_3- to H-loss at intermediate E_{col}'s of ~20 and 25 kcal/mol than expected based on the calculations of Kaiser et al.: ~10:1 and ~3:1, respectively.[18] One proposed explanation for the experimental discrepancy between Albert et al. and Kaiser et al. is that the latter used 80 eV electron impact ionization, necessitating the deconvolution of fragments, whereas the former used 9.9 eV "soft" vacuum ultraviolet (VUV) photoionization (PI). Furthermore, the G3(MP2,CC)//B3LYP C_9H_{11} PES first reported by Kaiser et al. was later combined with RRKM theory to solve the Master Equation (ME) describing temperature- and pressure-dependent kinetics under thermal conditions.[9] These thermal calculations predict similar yields of CH_3 and H-loss products from 1200-1500 K and at 300 Torr, whereas Zhang et al. measured ~5× more styrene from CH_3-loss than the sum of all H-loss products at the same conditions. As mentioned earlier, however, this discrepancy could be due to secondary chemistry occurring during the pyrolysis.

Finally, there is disagreement regarding the identity of the dominant H-loss isomer. While there is wide agreement that styrene is the dominant CH_3-loss product, there are conflicting reports in the literature as to whether 3-phenylpropene or 1-phenylpropene dominates H-loss. The single-collision and thermal calculations of Kaiser et al.[13] and Kislov et al.,[9] respectively, both predict that 3-phenylpropene will have the highest yield of any H-loss product

by far over all conditions considered. This is in nominal agreement with the PIE curves measured at m/z=118 amu by Zhang et al., which could be fit by assuming almost 100% 3-phenylpropene, but given the number of potential 118 amu isomers (indane, both cis- and trans-1-phenylpropene, 2-phenylpropene and 3-phenylpropene) this fit is best considered as just one possible solution.[31] In contrast, the earlier CMB experiments of Zhang et al. identified 1-phenylpropene as the dominant H-loss isomer at $E_{col} \approx 45$ kcal/mol based on experiments with deuterated isotopologues of C_3H_6.[11] Albert et al. also tentatively assigned the H-loss product observed in ~20-25 kcal/mol CMB experiments to 1-phenylpropene, based on analogy to the products observed from C_6H_5 + 2-butene, 2-C_4H_8, in the same work.[18]

This work aims to alleviate the first two of the three discrepancies summarized above (extent of H-abstraction and the extent of CH_3- to H-loss) by applying a different detection technique to the problem: time-resolved molecular beam MS (MBMS) with VUV PI. The reaction conditions used here are most similar to those in the work of Park et al.[8] (photolytically generated C_6H_5 in a thermal environment), but the use of time-resolved MBMS for detection allows for quantification of all products as they are formed, including C_6H_6 from H-abstraction. Additionally, unlike the fast pyrolysis experiments of Zhang, which also used MBMS under thermal conditions, the primary products of C_6H_5 + C_3H_6 can be easily distinguished form later generation products based on their faster appearance, enabling more conclusive quantification of CH_3- to H-loss as a function of temperature and pressure. The experimental apparatus used in this work is also equipped to do multiple-pass laser absorbance measurements, allowing for precise quantification of the overall C_6H_5 consumption rate, which is compared to the CRDS measurements of Park et al.[8] Finally, benzyl radical was observed as an unexpected primary product of C_6H_5 + C_3H_6. This finding was rationalized by the inclusion of a new "aromatic-catalyzed" 1,2-hydrogen-migration pathway on the C_9H_{11} PES. All experimental measurements were quantitatively compared to the predictions of the Reaction Mechanism Generator (RMG), which was then used to predict the products of a slightly more complicated alkylaromatic system, 1-naphthyl + 2-butene, in order to demonstrate the general applicability of the insights made into the C_6H_5 + C_3H_6 system.

4.2.2   Experimental Methods

The modified LAS and PI TOF-MS apparatus used in this work was already described in Chapter 2. Both iodobenzene, C_6H_5I, (Sigma-Aldrich, 98%) and nitrosobenzene, C_6H_5NO

(Sigma-Aldrich, ≥97%) were used as photolytic precursors of C_6H_5 because both are known to almost entirely photodissociate to C_6H_5 + I/NO at 266 nm.[5-6] Iodobenzene was purged of oxygen by successive freeze-pump-thaw cycles, while nitrosobenzene, a powder at room temperature, was simply degassed. Both precursors were placed in air-tight bubblers and introduced into the reactor by flowing a controlled amount of helium through/over them. Because of the strong reactivity of C_6H_5 towards O_2,[105] even ~100 ppm of residual air in the reactor could have a measurable impact on the experiments. The clearest indicators of O_2 present somewhere in the reactor or associated gas lines are a strong visible absorbance signal from phenylperoxy radical, C_6H_5OO,[244] and a product at m/z=94 amu (likely phenol, C_6H_5OH, also seen by Zhang et al.[31]) in the MS following photolytic C_6H_5 generation. When C_6H_5I was used as the precursor, it was possible to eliminate all signs of O_2 from the experiment. With C_6H_5NO, however, there was always some residual O_2 in the precursor, manifested by both C_6H_5OO absorbance and C_6H_5OH MS signal. C_6H_5I can also be used up to 900 K before thermal decomposition on the residence time scale of this experiment (1 s) becomes important,[73] whereas for C_6H_5NO the limit is only 700 K.[5] I atom from C_6H_5I photolysis can also be quantified by IR absorbance, providing an estimate of the initial C_6H_5 concentration. For all of these reasons, C_6H_5I was the precursor of choice for almost all of the experiments reported here.

Helium, He, was used as the bath gas in all experiments reported here and was purchased from Airgas (UHP grade, 99.999%). C_3H_6 was also purchased from Airgas (CP grade, 99%) and used without further purification.

4.2.3 Computational Methods

The C_9H_{11} PES has already been exhaustively explored both by Park et al. using G2M(RCC6)//B3LYP[8] and Kislov et al. using G3(MP2, CC)//B3LYP.[9] Wang et al. reported CBS-QB3 calculations on a portion of the PES, focused on the 1,2-phenyl-migration connecting the terminal and central addition products.[66] This work took the C_9H_{11} PES calculated by Kislov et al., and added on one new C_9H_{11} isomer, three new transition states (TS's) and one new bimolecular product channel (benzyl radical, C_7H_7, + ethene, C_2H_4) that together comprise the newly discovered aromatic-catalyzed 1,2-H-migration and subsequent resonance stabilized radical (RSR) formation pathway. For consistency, the same level of theory was used. Briefly, geometries and frequencies of the new minima and saddle points were optimized using B3LYP/6-311G(d,p). Starting from the optimized geometries, relaxed potential energy scans

were performed (also using B3LYP/6-311G(d,p)) as a function of dihedral angle in 10° increments around all C-C and nascent C-C bonds that are likely to undergo internal rotation for all stationary points on the C_9H_{11} PES. In some cases the scan revealed that the starting geometry was not the conformational minimum and the geometry was re-optimized accordingly. The 0 K electronic energies of the optimized geometries were refined by using a simplified version of the composite G3(MP2, CC) method:

$$E_0[G3(MP2, CC)] = E[RCCSD(T)/6 - 311G(d, p)] + (E[MP2/G3large] - E[MP2/6 - 311G(d, p)]) + E(ZPE) \tag{4-9}$$

The first term on the right-hand side is the ground state electronic energy calculated with a high level of theory (spin-restricted coupled cluster) and a small basis set (6-311G(d,p)). The second term, in brackets, is an estimation of the error introduced by using a small basis set instead of a larger one (G3large, in this case). The last term is the zero point energy (ZPE) correction, calculated based on the B3LYP frequencies scaled by a recommended factor of 0.967.[245] The G3(MP2, CC)//B3LYP method has been applied to many aromatic-containing PES's because it offers a good compromise between accuracy and computational cost.[61, 242] Gaussian03[132] was used for all B3LYP calculations, and Molpro[220] was used for all coupled cluster calculations.

Both high-pressure (P) and P-dependent thermal rate coefficients, k(T) and k(T, P), were calculated on the G3(MP2, CC)//B3LYP C_9H_{11} PES using Cantherm, an open-source software included with RMG.[181] k(T)'s for every elementary chemical reaction were calculated by canonical transition state theory (TST) using the rigid-rotor harmonic oscillator (RRHO) approximation with low-energy (<10 kcal/mol barrier) internal rotations modelled as one-dimensional hindered rotors (1D-HR). Tunneling was modelled using the 1D-asymmetric Eckart correction.[226] Phenomelogical k(T,P)'s were fit by applying RRKM/ME under the modified strong collision (MSC) approximation (RRHO and 1D-HR approximations also used in calculating densities of states).[7] For the two barrierless exit channels found by Kislov et al., the high-P variational TST (VTST) k(T)'s calculated in that work were input to Cantherm and converted into k(E)'s for solution of the ME by inverse Laplace transform (ILT).[7] Lennard-Jones and collisional energy-transfer (CET) parameters were taken from Mebel et al. for an argon bath gas,[242] and scaled down for a helium bath gas using the calculations of Jasper et al.[246]

The same custom scripts used in Kaiser et al.[13] for simulating single-collision experiments on the C_9H_{11} PES were also used here on the expanded PES. k(E)'s were calculated

using RRKM at a fixed E corresponding to E_{col}. Using the calculated k(E) values, a system of ordinary differential equations (ODE's) was constructed that describes the connectivity of the PES. The initial composition was set to either 100% of the terminal or central addition adduct. The ODE's were solved under the steady-state approximation in order to determine predicted product branching as a function of E_{col} for comparison to CMB experiments. The product branching for the two different initial adducts were very similar, and a total product branching was estimated by summing the two sets of calculations weighted by the expected thermal branching between terminal and central addition. The temperature used to evaluate the thermal branching was calculated as 2/3 × E_{col}/R, or the temperature at which the average kinetic energy in a Boltzmann distribution is E_{col}.

Finally, all elementary reactions on the C_9H_{11} PES were added as training reactions to the RMG database.[181] Scheme 4-3 gives an example of one of the training reactions added in this work, and its position in the larger RMG database hierarchy. High-P kinetic data is provided with each training reaction, and in this case the TST calculated k(T)'s were used. The kinetic portion of the RMG database is currently divided into 53 reaction families common to gas-phase combustion chemistry, such as intramolecular H-migration (abbreviated as intra_H_migration). Each family uses reaction templates to describe the critical details for a given reaction. In the example given, the reaction template specifies a 1-4-H-migration from a carbon in a benzene ring (identified by the atom label "Cb") to a secondary carbon radical. The template can also provide information about atoms not directly involved in the reaction. For example, one of atoms between the two reacting ends is another Cb, and one of the atoms bonded to the radical carbon is a Cs (a carbon with only single bonds, i.e., an sp^3 carbon). Such details can have large impacts on the real kinetics, and it is critical for RMG to be aware of these details so that good estimates can be made for reactions with unknown kinetics. Training reactions are the most specific representations of a reaction in the RMG database. When RMG proposes a reaction with unknown kinetics during automatic mechanism generation, it will match the new reaction to similar training reactions based on their similar reaction templates, and utilize the kinetic parameters of the training reactions to estimate parameters for the new reaction. For example, this work is primarily concerned with C_6H_5 + C_3H_6, but any arbitrary alkylaromatic radical system, such as 1-naphtyl + 2-butene, 1-$C_{10}H_7$ + 2-C_4H_8, will undergo many of the same reactions with similar kinetics and heats of reaction. By training the RMG database on reliable

kinetics for the C_9H_{11} system, the knowledge gleaned from that specific system will automatically be applied to every analogous alkylaromatic system, including $1\text{-}C_{10}H_7 + 2\text{-}C_4H_8$. This analogy is explored in more detail in section 4.2.4.6.

Reaction Family: intra_H_Migration

Reaction Template

Training Reaction: i1 <=> i12 calculated using G3(MP2,CC)//B3LYP + TST
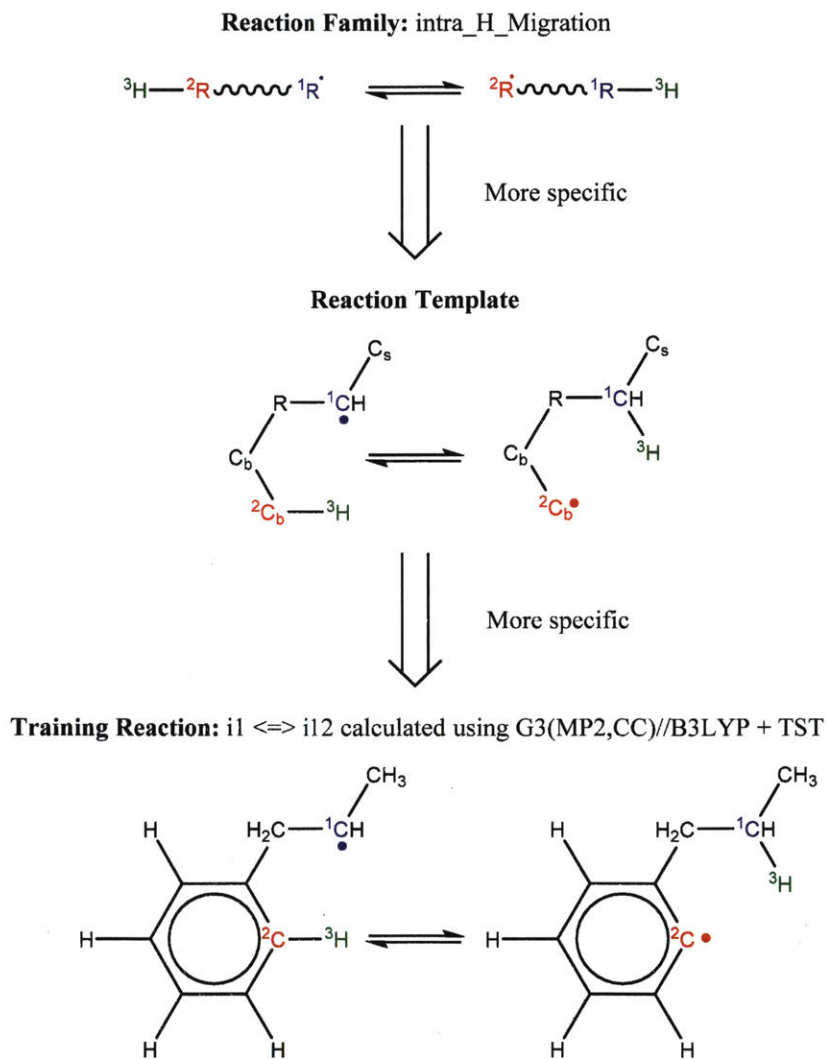
Scheme 4-3: Example of an RMG training reaction and its position in the hierarchy of the RMG database.

4.2.4   Results and Discussion

4.2.4.1   Calculated Energetics and Kinetics of C_9H_{11} PES

Figure 4-10 shows a reduced version of Kislov et al.'s G3(MP2,CC)//B3LYP C_9H_{11} PES[9] appended with the aromatic-catalyzed 1,2-H-migration and subsequent RSR formation pathway calculated in this work. For clarity, only the kinetically important features of the PES are shown,

and the same intermediate and product names are used as in the previous work (e.g., **i1** for intermediate 1 and **p1** for product 1, which is styrene). The major expected pathways of C_6H_5 + C_3H_6 forming styrene (**p1**), benzene (C_6H_6) and phenylpropene isomers (**p2-p4**) were already discussed in section 4.2.1 and will not be repeated here.
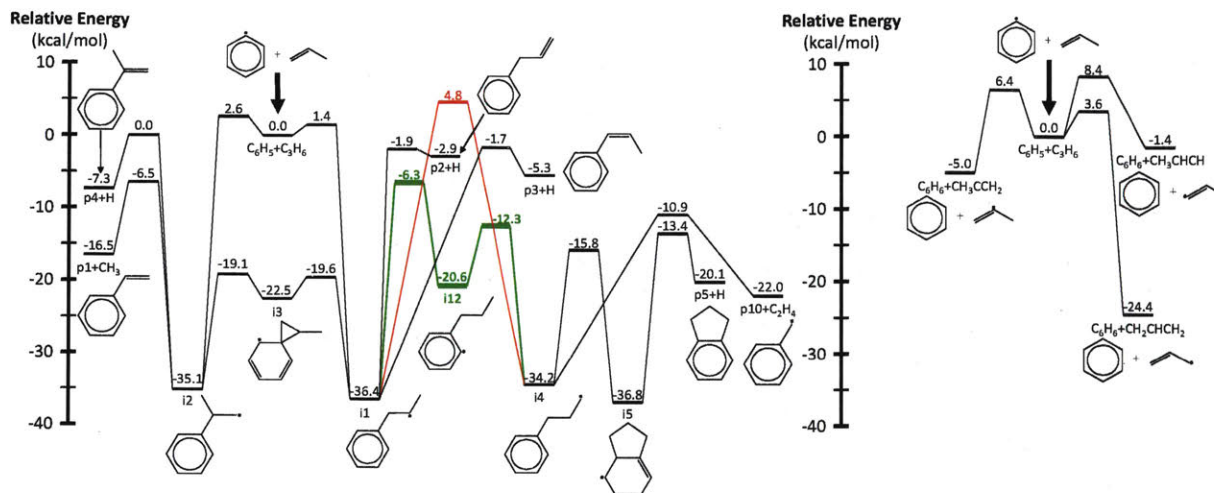
Figure 4-10: Simplified phenyl radical + propene PES calculated using G3(MP2, CC)//B3LYP/6-311G(d,p). Radical addition pathways are shown on the left and hydrogen abstraction on the right. The direct and aromatic-catalyzed 1,2-hydrogen-migrations are highlighted in red and green, respectively. Energies and geometries for all stationary points were calculated by Kislov et al.,[9] except for those in green and the β-scission of **i4** to **p10**+C_2H_4, which were calculated in this work.

The relatively high-energy (~40 kcal/mol) direct 1,2-H-shift from **i1** to **i4** is highlighted in red, and the lower-energy (~30 kcal/mol) aromatic-catalyzed 1,2-H-shift is highlighted in green. Once **i4** is formed, it can produce indane (**p5**) in two steps, as discussed in section 4.2.1, or it can simply β-scission a C-C bond to make benzyl radical, C_7H_7 (**p10**), and ethene, C_2H_4. It is because of the latter product channel, benzyl radical + C_2H_4, that the aromatic-catalyzed 1,2-H-migration was inferred from experiments described in the following sections.

The aromatic-catalyzed 1,2-H-migration proceeds in two steps. First **i1** undergoes a 1,4-H-migration, transferring one of the H's on an ortho-carbon to the secondary carbon radical on the alkyl side-chain *via* a 5-membered-ring TS (Figure 4-11). The barrier for this first, rate-limiting step in the aromatic-catalyzed 1,2-H-migration is energetically similar to the barrier for β-scission of CH_3 from **i2** (~30 kcal/mol), which is known to be a major loss channel for equilibrated **i1/i2**. The new intermediate formed (**i12**) has a radical site on an ortho-carbon and a

fully saturated propyl side-chain. **i12** can then undergo a 1,5-H-migration, transferring one of the H's on the primary carbon at the end of the alkyl side-chain *back* to the ortho-carbon *via* a low barrier (~8 kcal/mol) 6-membered-ring TS (Figure 4-11) forming **i4**. To summarize, an overall reaction (**i1**→**i4**) that has a high barrier as a one-step process (1,2-H-shift), is more energetically feasible as a two-step process (1,4-H-shift + 1,5-H-shift) enabled by the presence of a catalyst that is unaltered at the end of the process (the phenyl side group). Hence, the two-step **i1**→**i12**→**i4** process was given the name "aromatic-catalyzed" 1,2-H-shift in acknowledgement of the central role of the aromatic side group (phenyl in this case) as both a source and a sink of H-atom, much like a conventional Bronsted acid catalyst that acts as both source and sink of protons. This pathway is accessible to many radicals containing aromatic-groups as long as there is an H on at least one ortho-carbon site. The second step is fast if there is at least one H on a carbon in the chain in a β, γ or δ position relative to the aromatic group.
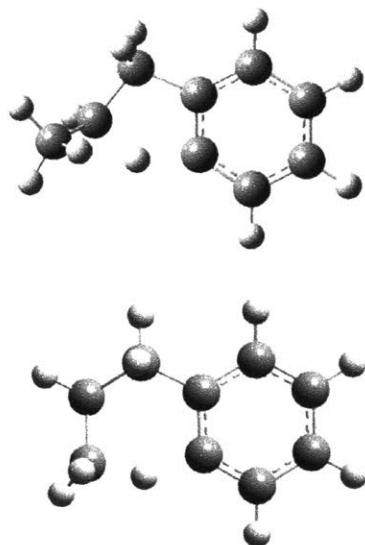
Figure 4-11: Optimized structures of transition states involved in aromatic-catalyzed 1,2-hydrogen-migration: 5-membered-ring intramolecular hydrogen-migration TS connecting **i1** and **i12** (top), and 6-membered-ring intramolecular hydrogen-migration TS connecting **i12** to **i4**.

Given the favorable energetics of the previously-unreported aromatic-catalyzed 1,2-H-shift, it was deemed worthwhile to revisit calculations of the $C_6H_5 + C_3H_6$ product branching

under both thermal (T, P, see Figure 4-12) and single-collision (E, see Figure 4-13) conditions, and to re-assess previous experimental results in this new context.
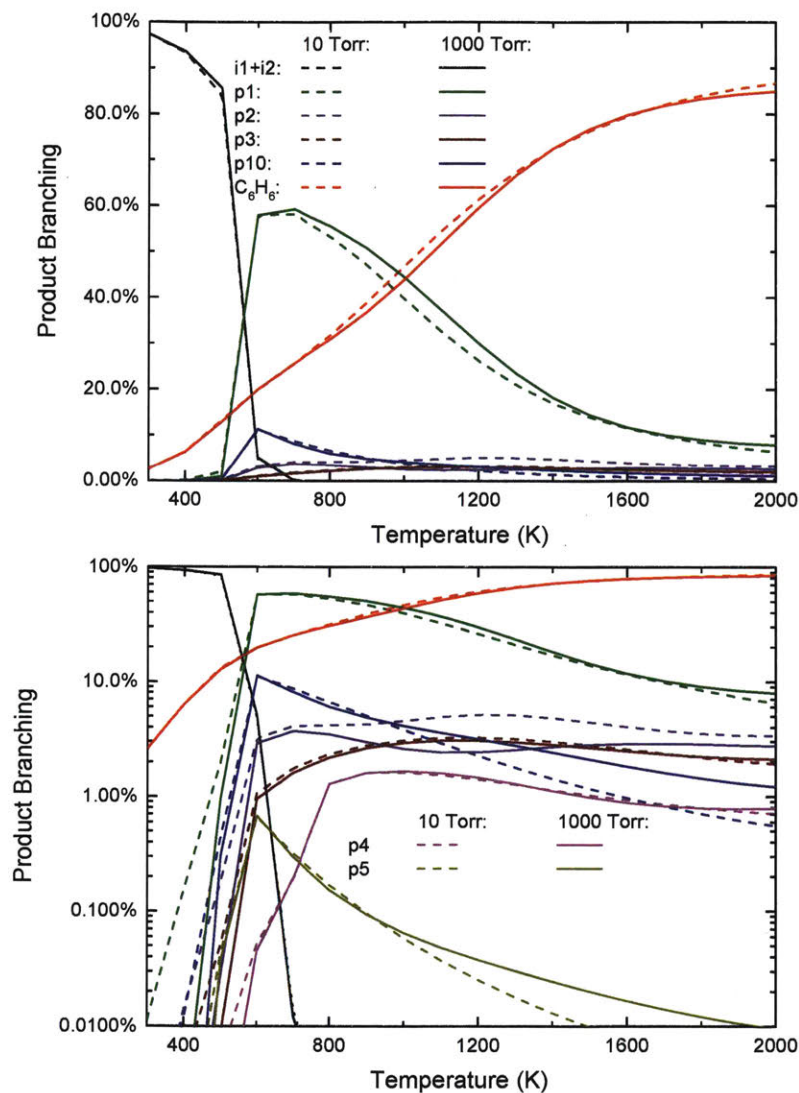
Figure 4-12: Predicted product branching of phenyl radical + propene on a linear (top) and logarithmic (bottom) scale as a function of T and P for otherwise fixed conditions: 50 millisecond reaction time, $[C_3H_6]$ = 5e16 cm^{-3} and $[C_6H_5]_0$ =3e12 cm^{-3} ([He] provides the balance of the gas density).

The thermal product branching was calculated by simulating the network of Cantherm-generated phenomelogical k(T,P)'s on the C_9H_{11} PES in an isothermal, isobaric, homogeneous batch reactor in CHEMKIN[247] for 50 milliseconds. The initial C_6H_5 and C_3H_6 concentrations were kept fixed at 3e12 and 5e16 cm^{-3}, respectively, for all T, P conditions, with the helium bath

gas providing the balance of the gas density. These specific reaction conditions were chosen to closely simulate the conditions of the experiment reported in this work in order to facilitate comparison. The k(T,P)'s taken from Cantherm include both thermal, well-to-well rates (i1→i3, for example) and chemically-activated, well-skipping rates (i1→p10 + C_2H_4, for example). When simulated together, the combined thermal and chemically-activated k(T, P)'s provide a complete picture of the chemical evolution of the thermal system in question, neglecting side and secondary reactions not on the same PES (considered later).

Qualitatively, the thermal product branching shown in Figure 4-12 is very similar to that calculated by Kislov et al.,[9] albeit their definition of product branching is slightly different. At low-T stabilized **i1** dominates the product distribution, but starting at 600 K styrene, **p1**, quickly comes to prominence. With further increase in T, branching to **p1** gradually decreases to be replaced mostly with C_6H_6 from the three H-abstraction channels. Of course unlike the predictions of Kislov et al., a peak branching of ~10% benzyl radical, **p10**, is predicted at ~600 K and diminishes with T like styrene. Given the chemical complexity of previous thermal experiments probing C_6H_5 + C_3H_6,[31, 243] the lack of observable benzyl radical in those works could easily be attributed to side reactions. However, in the product mass spectrum reported by Zhang et al. there is a peak at m/z=91 amu (mass of benzyl radical) though it is not discussed.[31]

Also unlike Kislov et al., the predicted pressure dependence from 10-1000 Torr over the whole T-range is negligible. This prediction was not sensitive to the choice of CET parameters or the method used to solve the ME.[7] The discrepancy with Kislov et al. is likely due to the difference in the definition of product branching, specifically the inclusion of both thermal and chemically-activated pathways in the simulation. The predicted lack of P-dependence is shown to be consistent with experiments in section 4.2.4.3.

Finally, although the branching to indane, **p5**, is about an order of magnitude higher than in Kislov et al. due to the aromatic-catalyzed 1,2-H-shift promoting isomerization to **i4**, the overall amount of **p5** formed is still small (~1% peak), consistent with the experiments of Zhang et al.[31] Overall, the predicted thermal product branching reported here does not alter the current understanding of C_6H_5 + C_3H_6 much (styrene, phenylpropene isomers and benzene are all still major products) other than the inclusion of a non-negligible, pressure-independent ~10% yield of benzyl radical and C_2H_4.

An identical approach to quantifying product branching under single-collision conditions was taken here as in Kaiser et al.,[13] and was already described in the section 4.1.3. Just as in the thermal case, the single-collision product branching shown in Figure 4-13 is very similar to what has previously been reported, this time by Kaiser et al., with some important exceptions. In terms of what is the same, **p1** dominates at low E_{col} and is gradually replaced by **p2** with increasing E_{col}. This was the same qualitative observation made by all three CMB experiments regarding the effect of E_{col} on the CH_3- to H-loss ratio.[11, 13, 18] What is different is up to ~15% branching to benzyl radical, **p10**, at the lowest E_{col}, followed by a steady decline. Considering that all of the CMB experiments were conducted at $E_{col} \geq 10$ kcal/mol, any **p10** formed in those experiments was likely below the detection limit. The other important difference is an increased yield of **p5** (up to 3%), but that would have also been too small to detect in the CMB experiments, consistent with the observations made therein.[11, 13]
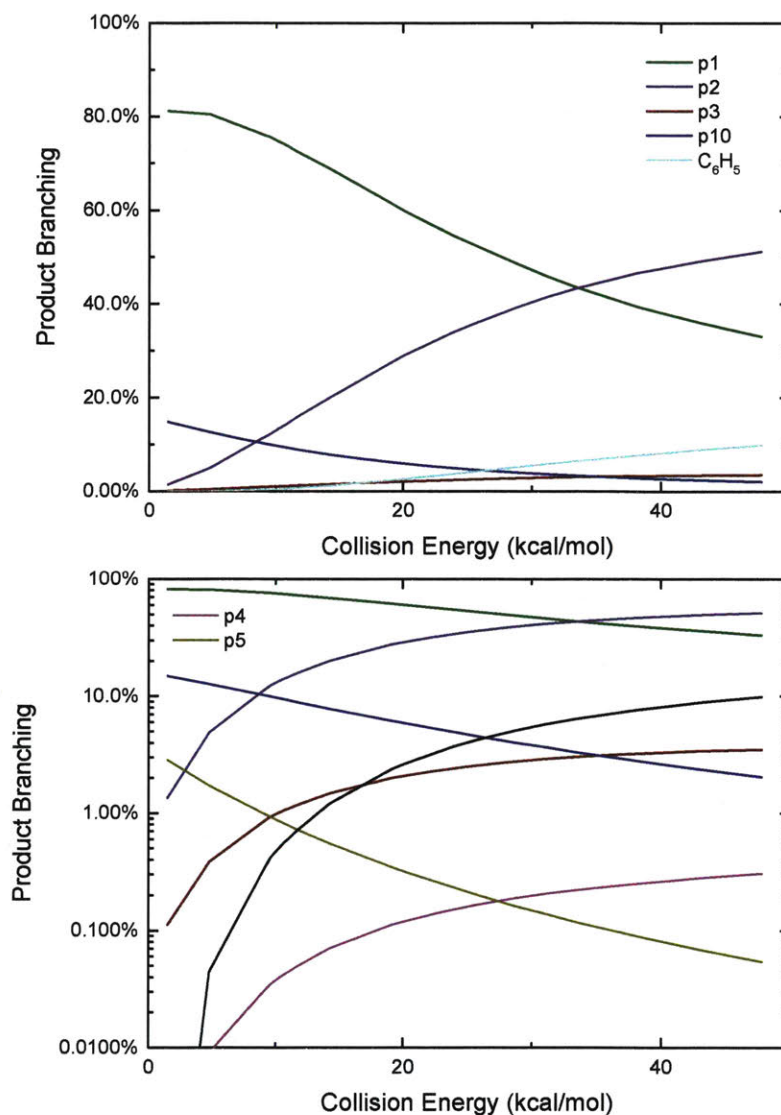
Figure 4-13: Predicted product branching of phenyl radical + propene on a linear (top) and logarithmic (bottom) scale as a function of collision energy under single-collision conditions.

To conclude this section, although the newly-discovered aromatic-catalyzed 1,2-H-migration is predicted to be both energetically and kinetically competitive with the other reactions on the C_9H_{11} PES available to C_6H_5 + C_3H_6, none of the six previously published experiments on this system have seen clear evidence for it. In the case of the thermal experiments this is either because of complex chemistry with side and secondary reactions,[31, 243] or because the detection technique was not intended for product measurements, as in the CRDS experiments of Park et al.[8] In the case of the CMB experiments, detection sensitivity is the issue.

Most of the remainder of this work will present experimental measurements coupled with detailed modelling that together quantitatively support the predictions above.

4.2.4.2   Overall k(T) Measured by 505.3 nm Absorbance

In addition to MBMS and laser absorbance experiments to quantify product branching, discussed in the following sections, 505.3 nm absorbance of C_6H_5 was also used to measure the total consumption rate coefficient, $k_{total}(T)$, of C_6H_5. These measurements of $k_{total}(T)$ are presented first because later results depend on them.

C_6H_5 is known to have a low-lying electronic transition at 504.8 nm at room temperature,[105] but in this work 505.3 nm was used to probe C_6H_5 at all T,P conditions due to slightly higher absorbance observed at that wavelength. The other radicals formed in the C_6H_5 + C_3H_6 system (CH_3,[56] C_3H_5[233] and C_7H_7[248]) are not expected to absorb significantly at such a relatively long wavelength. Therefore, C_6H_5 can be probed selectively at 505.3 nm. However, as mentioned earlier, if O_2 is present in the reactor at a similar concentration as C_6H_5, C_6H_5OO will also absorb strongly and broadly ~500 nm,[244] providing a convenient leak indicator.

$k_{total}(T)$ consists of contributions from five different C_6H_5 + C_3H_6 entrance channels (two radical additions and three H-abstractions):

$$C_6H_5 + C_3H_6 \rightarrow i1$$
$$\rightarrow i2$$
$$\rightarrow C_6H_6 + CH_2CHCH_2 \text{ (allyl radical, } C_3H_5)$$
$$\rightarrow C_6H_6 + CH_3CCH_2$$
$$\rightarrow C_6H_6 + CH_2CHCH$$
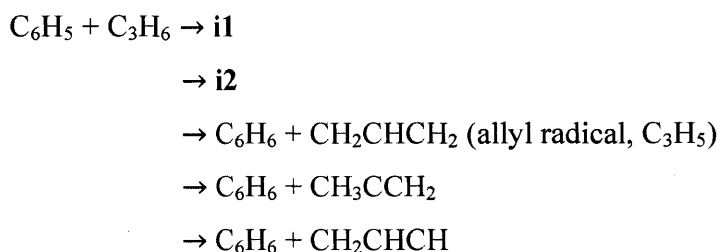
From calculations of the barrier heights for these five elementary reactions (Figure 4-10) it is expected that terminal radical addition to form i1 (1.4 kcal/mol barrier) will dominate C_6H_5 consumption, followed by central addition to i2 (2.6 kcal/mol) and H-abstraction from the allylic carbon (3.6 kcal/mol). The other two H-abstractions have higher barriers (6.4 and 8.4 kcal/mol) and are predicted to be negligible below 1000 K.

Background absorbance traces are recorded with He only (or He and C_3H_6 only) following photolysis to account for spurious absorbance, which is likely due to heating of the Herriott cell optics from scattered photolysis light and subsequent steering of the probe laser

beam slightly off of the signal photodiode. The background absorbance was subtracted from absorbance traces recorded with C_6H_5 present.

Each background-subtracted and normalized 505.3 nm absorbance trace was fit to an exponential decay assuming pseudo-first-order kinetics:

$$\frac{A}{A_0} = (1 - a)e^{-k't} + a \qquad (4\text{-}10)$$

$$k' = k_{total}[C_3H_6] + k_{wall} \qquad (4\text{-}11)$$

a is a vertical shift factor to account for slight offsets (usually ±10%) in the baseline due to noise, imperfect background subtraction and AC coupled detection electronics. k' is the pseudo-first-order decay rate, which consists of a contribution from $C_6H_5 + C_3H_6$ and from k_{wall}. k_{wall} is a fit parameter that accounts for all of the other C_6H_5 loss processes (wall reaction, self-reaction, reaction with impurities like O_2, reaction with the precursor, transport out of the sampling volume, etc.). Figure 4-14 shows representative 505.3 nm absorbance traces fit to exponential decays.
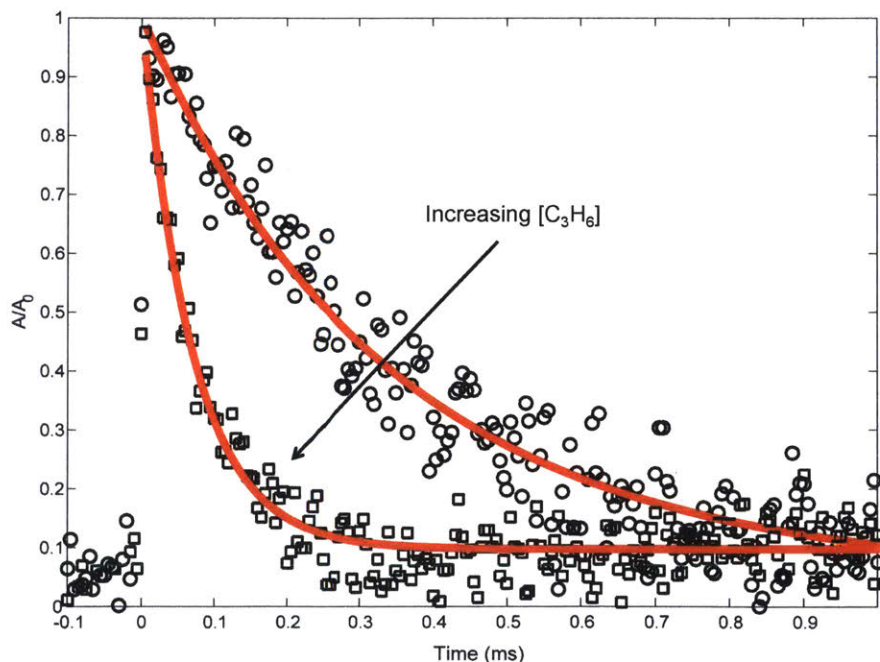
Figure 4-14: Representative 505.3 nm absorbance decays measured (markers) at 691 K, 10 Torr. Lines are exponential fits. Only every 10th point is shown for clarity.

Table 4-4 summarizes the conditions of the fourteen 505.3 nm absorbance experiments. Each experiment was conducted at a fixed T and P, and consisted of at least five absorbance traces at different [C_3H_6]. The nominal T was varied from 300 to 700 K, and P was mostly kept

at 10 Torr, except for one control experiment at 25 Torr to demonstrate the independence of $k_{total}(T)$ on P. C_6H_5I was used as the photolytic C_6H_5 precursor in all but two of the experiments for the three reasons mentioned in section 4.2.2. Initial radical concentrations were quantified by single-pass IR absorbance of I atom, following the same procedure described previously.[75, 96] For a given experiment, $[C_3H_6]$ was varied over a wide range to verify a linear relationship with k'. Some of the fit k_{wall} values are rather large (>1000 s^{-1}), likely due to a small air leak during those experiments that was later fixed (importantly, all of the MBMS results presented in the next section were obtained without the leak). However, in all experiments $[C_3H_6]$ was increased such that the decay of C_6H_5 due to $C_6H_5 + C_3H_6$ was 5-10× the contribution of k_{wall}. The vertical shift factor, a, was usually between -0.1 and 0.1, and in the worst case it was -0.25. Besides varying the precursor identity and P, control experiments were also conducted using different photolysis laser fluence, precursor concentration, radical concentration, and flashes per refresh (FPR), in order to verify the independence of a given $k_{total}(T)$ to all of these parameters. The reported uncertainty in $k_{total}(T)$ is at least 10% due to possible systematic uncertainty in $[C_3H_6]$, as well as fitting uncertainty.[74] For all experiments, the overlap pathlength between the Herriott cell and the photolysis laser was ~20 m. The absolute 505.3 nm absorbance signal observed for a given $[I]_0(=[C_6H_5]_0)$ was consistent with a C_6H_5 cross-section of ~2e-19 cm^2 at all conditions, similar to the measurement of Tonokura et al. (3.6±1.6e-19 cm^2 at 504.8 nm and 298 K).

Table 4-4: Summary of 505.3 nm absorbance experiments. Uncertainties represent two standard deviations.

Exp. #	Nominal T (K)	Real T (K)	P (Torr)	X^a	$[C_6H_5X]^{b,c}$ $(10^{13}\ cm^{-3})$	F^d $(mJ\ cm^{-2})$	$[C_3H_6]^b$ range $(10^{15}\ cm^{-3})$	IR $[I]_0$ $(10^{12}\ cm^{-3})$	# of Traces	k_{total}^c $(\times 10^{-14})$	k_{wall}^c	Range of a^f
1	300	295.3±0.4	10	I	6.5	15	26.8-215	3.5±1	7	1.1±0.1	550	-0.02 to 0.05
2	300	295.3±0.4	10	I	13.0	15	13.4-215	6±2	7	1.1±0.1	690	0.002 to 0.06
3	300	295.3±0.4	10	I	6.5	30	26.8-215	6±2	6	1.3±0.1	520	-0.09 to 0.10
4[g]	300	295.3±0.4	10	I	6.5	15	26.8-215	3±1	7	1.2±0.1	390	-0.09 to 0.04
5	400	394±4	10	I	6.1	15	25.4-152	3±1	6	3.0±0.3	720	-0.06 to 0.10
6	500	494±8	10	I	6.1	15	20.1-120	3±1	6	6.3±0.8	600	-0.11 to 0.10
7	600	589±14	10	I	5.6	15	11.5-69.0	2.5±1	6	13.3±1.6	400	-0.09 to 0.14
8	700	691±16	10	I	5.9	15	9.8-58.6	3±1	6	19.4±2.5	1700	-0.08 to 0.09
9	700	691±16	25	I	6.2	15	10.3-61.8	3±1	6	18.7±2.2	600	0.0 to 0.08
10	700	691±16	10	I	11.8	15	4.9-24.4	6±2	5	20.5±2.5	1700	-0.08 to 0.12
11	700	691±16	10	I	5.9	30	9.8-58.6	6±2	6	20.8±2.5	2000	-0.25 to 0.02
12[g]	700	691±16	10	I	5.9	15	9.8-58.6	4±2	6	18.0±2.1	1100	-0.12 to 0.12
13	300	295.3±0.4	10	NO	0.6	4	25.8-301	-	6	1.3±0.1	80	-0.03 to 0.13
14	500	494±8	10	NO	0.6	4	25.1-150	-	5	6.1±0.9	1600	0.03 to 0.11

[a]Identity of X in precursor, C_6H_5X. [b]10% uncertainty in all values due to systematic uncertainty in mass flow controller calibrations. [c]Precursor concentrations calculated assuming He exiting bubbler is saturated with C_6H_5X at its room T vapor pressure: 0.92 Torr for C_6H_5I[249] and 0.6 Torr for C_6H_5NO.[250] [d]Photolysis laser fluence. [e]Units are molecule, s, cm. [f]Vertical shift factor in fits to normalized absorbance traces. [g]Repetition rate of photolysis laser doubled to 2 Hz to check effect of Flashes per Refresh (FPR).

Figure 4-15 compares the fourteen measurements of $k_{total}(T)$ in this work against the previous measurements of Park et al. using CRDS.[8] The two sets of measurements agree well with each other, including the various control experiments. By using a different chemical precursor that does not significantly thermally decompose <900 K (C_6H_5I),[73] this work is able to extend the upper T at which $k_{total}(T)$ is measured by ~200 K compared to the previous work (C_6H_5NO, <700 K[5]).
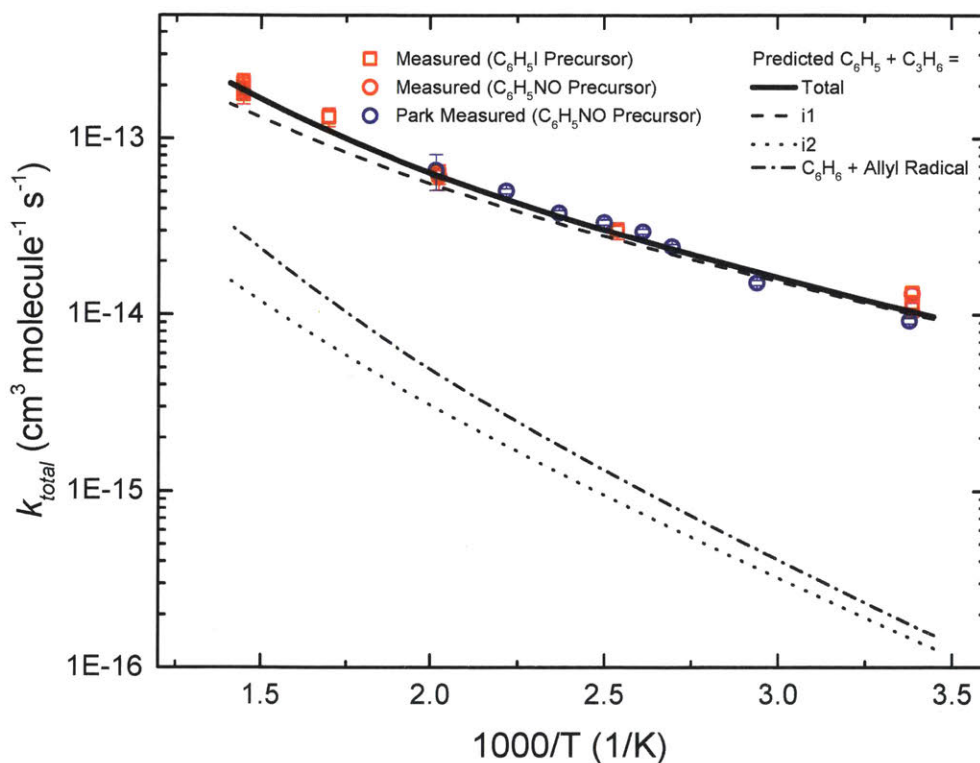
Figure 4-15: Measured (markers) and predicted (lines) kinetics of phenyl radical + propene entrance reactions.

Also shown is the predicted $k_{total}(T)$, obtained by summing the TST calculated rate coefficients for the five different entrance channels. The barrier for terminal addition had to be lowered by 0.75 kcal/mol in order to obtain the agreement between experiment and theory shown in Figure 4-15. As expected, terminal addition to **i1** is predicted to be the dominant entrance channel, especially at lower T, with central addition and allylic H-abstraction ~1-2 orders of magnitude slower over the experimental range. The calculated entrance rates in Figure 4-15

(including the adjusted rate for terminal addition) were used in all subsequent C_6H_5 + C_3H_6 models discussed in the following sections

4.2.4.3   Products Measured by MBMS

Table 4-5 summarizes the conditions of the 15 MBMS experiments. Only nominal temperatures of 600 and 700 K were explored because for T<600 K secondary reactions involving I atom will dominate the reaction flux (discussed later). Also, at lower T a higher $[C_3H_6]$ is needed to ensure fast and near-unity reaction of C_6H_5 with C_3H_6, but higher $[C_3H_6]$ tends to lower the MBMS sensitivity both due to attenuation of VUV photons and a decrease in the density of the molecular beam for a heavier carrier gas.[108] P was 10 Torr for all of the experiments except for two conducted at 25 Torr and another two conducted at 50 Torr to test the effect of pressure on the product distribution.

For a given T,P-condition, the time-dependent product branching was typically measured over four different $[C_3H_6]$, including an experiment without C_3H_6. Control experiments were also conducted at different photolysis laser fluence, precursor concentration and radical concentration to check the effect of these variables. Both 505.3 nm absorbance of C_6H_5 and IR absorance of I atom were measured simultaneously with all of the MBMS experiments.

Table 4-5: Conditions of MBMS experiments. Uncertainties represent two standard deviations.

Experiment #	Nominal T (K)	Real T (K)	P (Torr)	$[C_3H_6]^a$ (10^{15} cm^{-3})	$[C_6H_5I]^a$ (10^{13} cm^{-3})	IR $C_{I,0}$ (10^{12} cm^{-3})	MS $C_{I,0}$ (10^{12} cm^{-3})	Photolysis Laser Fluence (mJ cm^{-2})	$k_{sampling}^{b}$ (s^{-1})	c^c
1	600	605±4	10	0	6.1	2±0.8	1±0.5	14	1500	0
2	600	605±4	10	7.5	6.1	2±0.8	1±0.5	14	1000	0.32
3	600	605±4	10	15.0	6.1	2±0.8	1±0.5	14	1000	0.58
4	600	605±4	10	30.0	6.1	2±0.8	1±0.5	14	1000	0.69
5	600	605±4	10	15.0	12.1	3.5±1.2	1.5±0.75	14	1000	0.46
6	700	707±6	10	0	5.9	3±1.2	1±0.5	14	1500	0
7	700	707±6	10	7.4	5.9	3±1.2	1±0.5	14	750	0.57
8	700	707±6	10	15.0	5.9	3±1.2	1.5±0.75	14	750	0.74
9	700	707±6	10	29.0	4.1	3±1.2	1.5±0.75	20	750	0.86
10	700	707±6	10	15.0	11.9	3±1.2	1±0.5	7	750	0.53
11	700	707±6	10	15.0	11.9	5±1.7	2±1.0	14	750	0.51
12	700	700±6	25	0	5.9	2.5±1.0	1±0.5	14	750	0
13	700	700±6	25	7.2	5.9	2.5±1.0	1±0.5	14	600	0.3
14	700	687±5	50	0	6.1	2±1.0	1±0.5	14	800	0
15	700	687±5	50	7.7	6.1	2±1.0	1±0.5	14	600	0.68

[a]10% uncertainty in all values due to systematic uncertainty in mass flow controller calibrations. [b]Fit first-order rate of MB sampling (see section 4.2.4.4.5). [c]Exponent in power law fit to mass discrimination factor, $R = b(m/z)^c$ (see section 4.2.4.4.4).

Figure 4-16 shows representative, time-resolved mass spectra that have had the pre-photolysis background subtracted out so that only transient signals are observed. The spectra are divided into two m/z regions for clarity: a lower range from 70-125 amu where all of the primary C_6H_5 + C_3H_6 product signals appear, and a higher range from 125-250 amu where the side and secondary product signals appear, many of them corresponding to iodide-containing species. No transient signals were observed below 77 amu (C_6H_5) for any experiment. Qualitatively, all of the primary C_6H_5 + C_3H_6 products (see Figure 4-12 for prediction of product branching) are observed at their expected parent m/z: 78 amu for C_6H_6, 91 amu for **p10** (benzyl radical), 104 amu for **p1** (styrene), 118 amu for **p2-p4** (phenylpropene isomers) and 119 amu for **i1** and **i2**. It should be reiterated that initially the 91 amu product was unexpected based on the previous C_6H_5 + C_3H_6 literature, but can now be rationalized by the aromatic-catalyzed 1,2-H-migration that facilitates **p10** formation discussed in section 4.2.4.1. The side and secondary products can also be assigned intuitively: 127 and 128 amu correspond to I atom and HI, 134 amu is the recombination product of **i1** + CH_3 (named **i1-CH$_3$**), 142 amu is methyl iodide (CH_3I), 154 amu is biphenyl (C_6H_5-C_6H_5), 168 amu is allyl iodide (C_3H_5I) and 248 amu is the recombination product of **i1** + I (named **i1-I**). There is also a small transient signal at m/z=160 amu that is difficult to discern in Figure 4-16 corresponding to **i1** + allyl radical (named **i1-C$_3$H$_5$**).
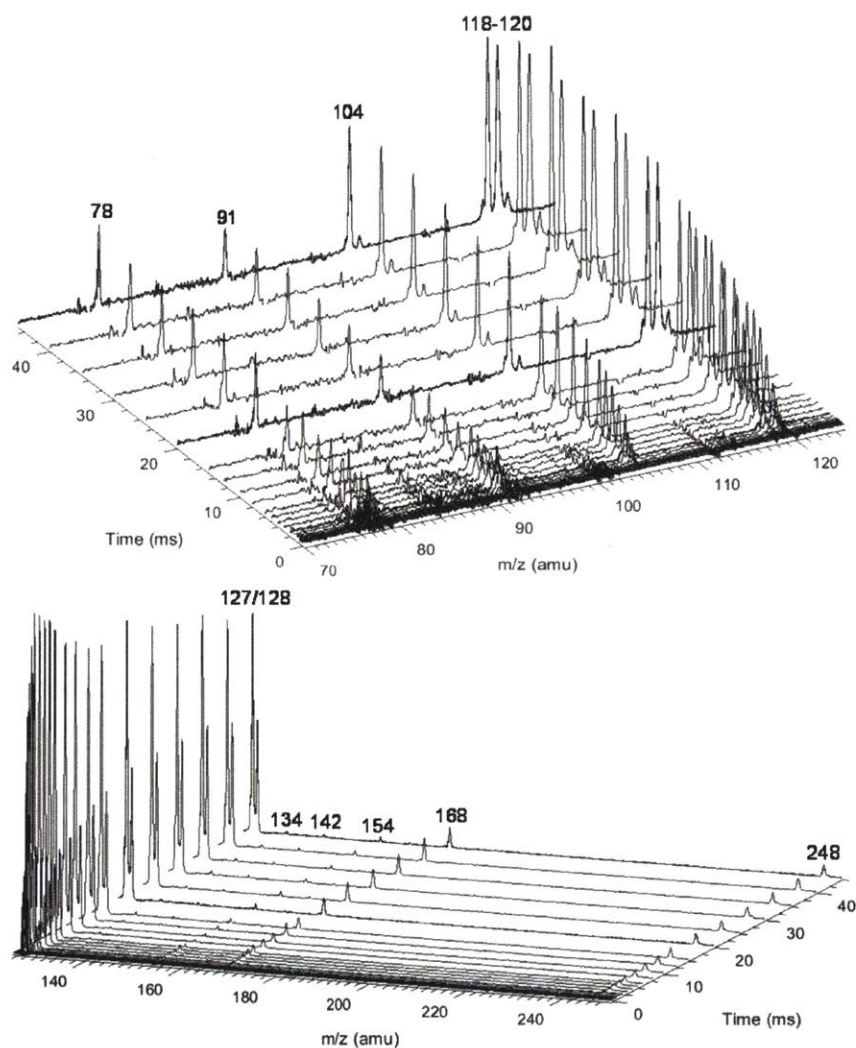
Figure 4-16: Representative background-subtracted, time-resolved mass spectra at m/z range where primary phenyl radical + propene products appear (70-125 amu, top) and higher m/z values where mostly the parent cations of iodide-containing species appear (125-250 amu, bottom). Measured at 605 K, 10 Torr (Experiment #2). Only positive changes shown.

All of the transient MBMS signals were integrated and plotted against reaction time, as shown for three representative experiments in Figure 4-17 (experiments #2, 7 and 15). The thick solid lines in those plots correspond to model predictions, which will be described in the following section. Qualitatively, there are several features of Figure 4-17 that are consistent with the product branching predictions of Figure 4-12. First, the product branching has a strong dependence on T, which can be seen by comparing experiments #2 and 7, conducted at nominal T's of 600 and 700 K, respectively, and 10 Torr. Second, **p1** (104 amu) is the dominant product

at 700 K, assuming similar photoionization cross sections (PICS) for all products. The 104 amu signal is 3-4× any of the other product signals, which is in nearly quantitative agreement with Figure 4-12. Third, C_6H_6 is clearly observed as a primary product. The importance of C_6H_6 with increasing T was predicted both here and in Kislov et al.,[9] but has never before been directly confirmed experimentally and was one of the main motivations for this work. Finally, the product branching has negligible P-dependence as seen by comparing experiments #7 and #15, both of which were nominally conducted at 700 K but at different P's (10 and 50 Torr, respectively). Although the time-dependence of the product growth is slower at higher-P, that is likely due to slower radial diffusion impeding the transport of transient species to the MBMS sampling volume rather than a chemistry effect (section 4.2.4.4.5). Disregarding the time-dependence, both experiments #7 and #15 reach nearly identical steady-state product distributions, in agreement with the lack of P-dependence exhibited in the predictions of Figure 4-12. The 25 Torr experiment (#13) exhibits behaviour intermediate to the 10 and 50 Torr experiments (Figure E 9 and Figure E 10). Figure E 11 and Figure E 14 show that the instantaneous primary product ratios (relative to styrene/104 amu) at 25 and 50 Torr are essentially time-independent and in agreement with the model, further supporting the claim that the distinct time-dependence of the absolute signal at higher-P is due to transport rather than chemistry effects.
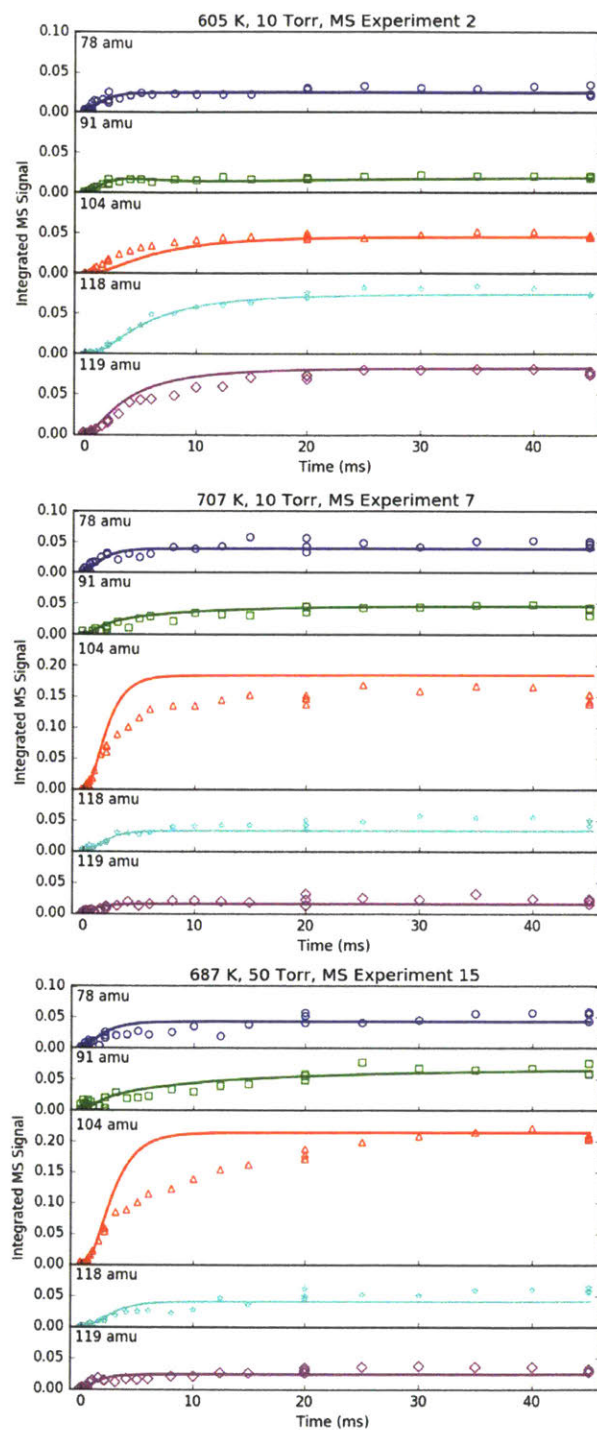
Figure 4-17: Time profiles of primary phenyl radical + propene products measured with MBMS at indicated conditions. Markers are experimental measurements and thick lines are model results.

Although there is great qualitative agreement between the measurements of Figure 4-17 and the predictions of Figure 4-12, there are some clear discrepancies. Most notably, at 600 K (experiment #2) the largest product signals are at m/z=118 and 119 amu, nominally corresponding to **p2-p4** and **i1**. The dominance of 119 amu at later times is especially unexpected given its assumed identity as a radical. Clearly there is more going on than suggested by Figure 4-12, and a more detailed model is needed. Specifically, a model that includes not just the major reactions on the C_9H_{11} PES, but also side and secondary reactions on other PES's, including those with I atom. Ideally, transport effects should also be accounted for in the model, as well as the weighting of each species' signal by its PICS, the contribution of ^{13}C isotopologues and dissociative ionization (fragmentation). Such a model was developed (model predictions shown as thick solid lines in Figure 4-17) and is described in detail in the following section. Another purpose behind constructing a model for this flash photolysis system with MBMS detection is to test if the current theoretical understanding of $C_6H_5 + C_3H_6$ is sufficient to quantitatively explain the experimental measurements. Of specific interest is whether the proposed aromatic-catalyzed 1,2-H-migration can really explain the 91 amu signal. After describing the development of the model, its predictions will be compared in detail to each transient MBMS signal in order to test this understanding (section 4.2.4.4.7).

Regarding the unexpected dominance of 118 and 119 amu at 600 K, careful modelling (and a critical experiment) revealed that both m/z's are actually mostly attributable to fragments of **i1-I**. At higher T's, **i1** undergoes unimolecular isomerization and decomposition reactions much faster than it can react with I atom, so the role of I atom is largely diminished at 700 K. At lower T's, the converse is true, hence MBMS experiments were not conducted below 600 K.

It should be mentioned that for the experiments without C_3H_6, evidence of catalysis by the walls was observed (Figure E 7 and Figure E 8). Specifically, fast hydrogenation of C_6H_5 to C_6H_6 was observed that was inexplicable by gas-phase chemistry (i.e., C_6H_5 self-reaction or reaction with the precursor). Slower, but still inexplicable, hydrogenation of I atom to HI was also observed. For this reason, MBMS experiments were conducted at various [C_3H_6] to confirm that sufficient C_3H_6 had been added such that C_6H_5 mostly reacted with C_3H_6 in the gas-phase, rather than abstracting an H-atom from the wall.

4.2.4.4 Modeling of Flash Photolysis with MBMS
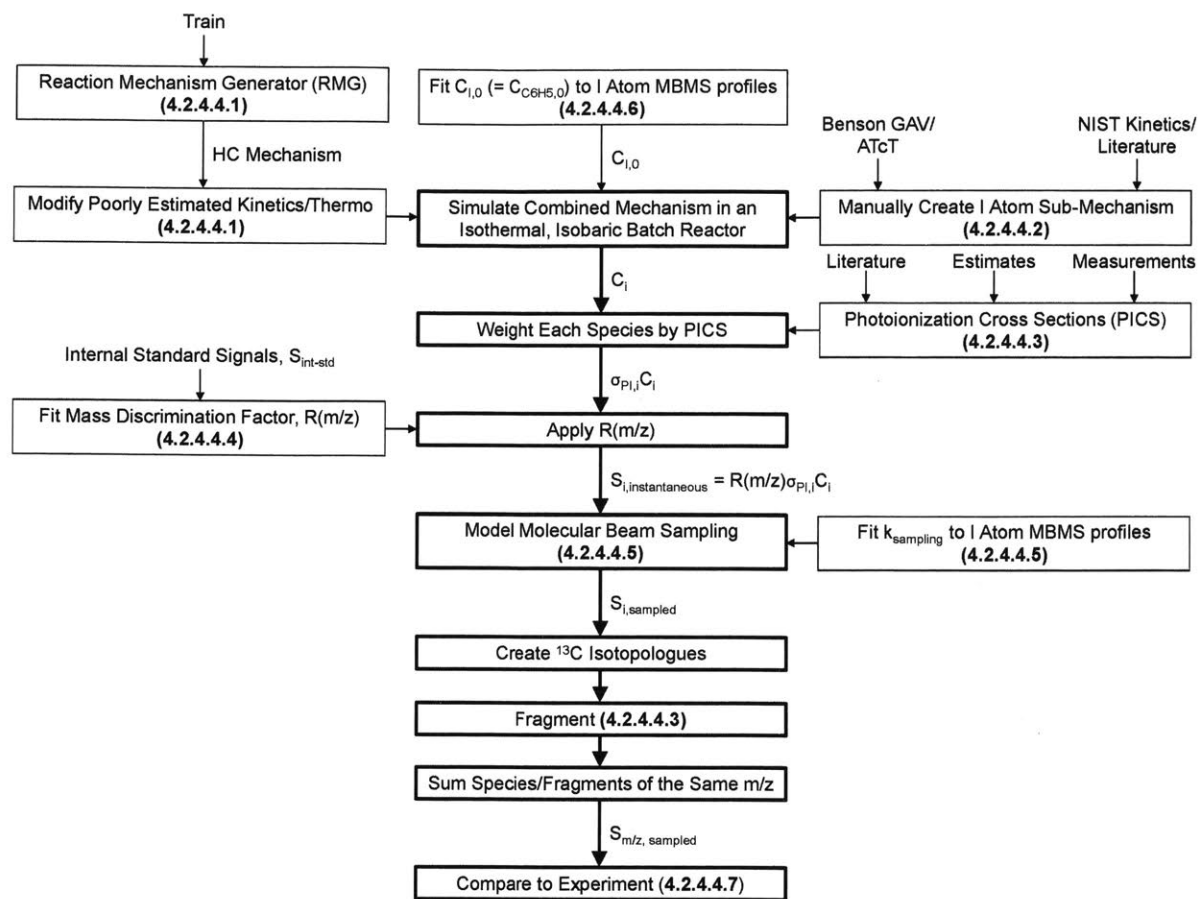
Figure 4-18: Overall approach to modeling MBMS experiments. Specific sub-sections where certain aspects of the model are discussed in more detail are given in parentheses.

The overall approach to modelling the MBMS experiments is summarized in Figure 4-18. Briefly, after being "trained" on the relevant alkylaromatic chemistry, RMG was used to automatically construct a chemical mechanism for the important hydrocarbon (HC) chemistry occurring in the flash photolysis experiment (see section 4.2.4.4.1 for details). A separate sub-mechanism for I atom chemistry was manually created (4.2.4.4.2), largely taking inspiration from recent work by Comandini et al.[251] and Tranter et al.,[109] and combined with the HC mechanism. The initial radical concentration was fit to MBMS time-profiles of photolytically produced I atom (4.2.4.4.6), and the combined HC + I atom mechanism was simulated in an isothermal, isobaric batch reactor in order to obtain concentration profiles for each species i, C_i. Each C_i is then weighted by the PICS for i, $\sigma_{PI,i}$, at 10.5 eV. PICS are mostly obtained from

literature, and for species where literature values are unavailable either estimates or measurements of the PICS were made (4.2.4.4.3). The PICS weighted C_i profiles were converted to simulated, instantaneous MBMS signals by applying the mass discrimination factor, R(m/z). R(m/z) was fit to the MBMS signals of internal standards, $S_{int\text{-}std}$, also present in the flash photolysis reactor during experiments at known, low concentrations (4.2.4.4.4). Transport effects were accounted for by a simple model adapted from Baeza-Romero et al.[65] that lumps all of the steps in MB sampling into a single first-order rate coefficient, $k_{sampling}$, which is fit to measured rise time of the I atom MBMS profile (4.2.4.4.5). Once, $S_{i,\ sampled}$ profiles had been calculated, ^{13}C isotopologues of major species were created assuming a natural abundance of 1.1%× # carbon atoms. Only isotopologues with zero or one ^{13}C are considered (or observed). Simulated species signals were then fragmented, again using either known, measured or estimated fragmentation patterns (4.2.4.4.3). Finally, species/fragments with the same m/z were summed and the total, simulated MBMS signal at a given m/z, $S_{m/z,\ sampled}$, was directly compared against experiments (4.2.4.4.7).

4.2.4.4.1. RMG Mechanism for Hydrocarbon Chemistry

RMG is an open-source tool for automatically generating detailed chemical mechanisms involving species that contain carbon, hydrogen, oxygen, nitrogen and sulfur (CHONS).[181] As mentioned in section 4.2.3, RMG relies on a kinetic database of training reactions, as well as rate rules, to estimate the kinetics of any CHONS reaction (provided the reaction falls under one of the 53 reaction families). Therefore, the accuracy of the kinetic estimates made by RMG, and the corresponding quality of the final model, largely depend on what is in the database. Initially, there were few training reactions and rate rules related to the alkylaromatic chemistry encountered in the C_6H_5 + C_3H_6 system, and the subsequent predictions of RMG related to C_6H_5 + C_3H_6 were demonstrably poor. To remedy this situation, the 28 elementary reactions calculated on the "complete" C_9H_{11} PES (Kislov et al.'s full PES[9] + the aromatic-catalyzed 1,2-H-migration and subsequent RSR formation from this work) were added as training reactions to the RMG database. Besides simply importing the kinetic calculations into the database, the suitability of the matching reaction template, which is meant to convey only the critical features of the reaction (see Scheme 4-3), was checked and in many cases modified. For example, if either the reactant or product has a radical in a benzylic position that fact should be captured in some way by the reaction template because the added resonance stabilization will have a large impact on

the overall kinetics. If each training reaction is matched by a suitable reaction template, then the training reaction data will be utilized as intended when RMG encounters an analogous reaction for a different system (e.g., 1-naphthyl radical + 2-butene compared to C_6H_5 + C_3H_6). Of the 28 training reactions added, 15 belonged to the reaction family for radical addition to an unsaturated bond (abbreviated as R_Addition_MultipleBond, the reverse reaction is a β-scission), 5 belonged to the intramolecular radical addition to an unsaturated bond family (Intra_R_Add_Exocyclic), 5 belonged to the intramolecular H-migration family (intra_H_migration), and 3 belonged to the H-abstraction family (H_Abstraction).

After training RMG on the relevant alkylaromatic chemistry, a hydrocarbon (HC only) mechanism was automatically generated that contained 69 species and 191 reactions. RMG was constrained to species with ≤ 18 carbon atoms in order to capture **i1** recombination with itself to make **i1**-dimer in the case that is important. Pressure-dependent kinetics were included up to PES's with 13 atoms total in order to capture the likely pressure dependence of CH_3 + C_3H_6. Pressure-dependence of the C_9H_{11} PES itself (20 atoms total) was neglected due to the predicted lack of P-dependence (Figure 4-12) and qualitatively confirmed by experiments (Figure 4-17).
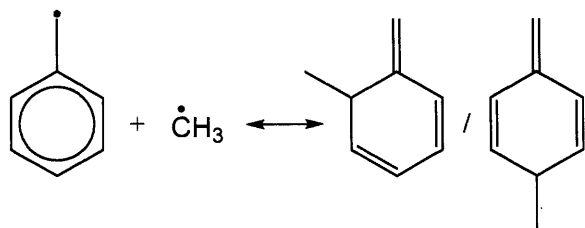
Scheme 4-4: Methyl + benzyl radical recombination reactions with overestimated kinetics in RMG.

In initial tests, the RMG HC mechanism captured most of the important C_6H_5 + C_3H_6 chemistry, but overestimated the extent of CH_3 recombination with **p10** (Scheme 4-4). CH_3 + **p10** recombination was deemed too fast because the unaltered HC mechanism was predicting substantial concentrations of the corresponding products at m/z=106 amu, which as shown in Figure 4-16 was clearly not observed at all (at any condition). This was because the training reaction used by RMG to estimate CH_3 + **p10** recombination was for CH_3 + cyclopentadienyl radical (CPD'yl). While not a bad estimate considering that both **p10** and CPD'yl have resonance stabilization, it failed to capture the full extent of **p10**'s stabilization, therefore the rate coefficient was slightly too fast. The HC mechanism was manually amended by replacing the

k(T)'s for the reactions in Scheme 4-4 with a new estimate: $1/2\times$ Troe et al.'s experimental measurement of CH_3 + **p1** → ethylbenzene,[252] by analogy to H + **p1** at various resonance sites.[253] The revised k(T)'s were slower than the previous estimates, and the overall model no longer predicted measurable MBMS signal at m/z=106 amu. More generally, the lack of kinetic data for the reactions in Scheme 4-4 highlight them as candidates for future theoretical and/or experimental investigation.

Estimates of k_{wall} for the two most important radicals in the system, C_6H_5 and **i1**, were also manually added to the HC mechanism. For C_6H_5, $k_{wall} = 100$ s^{-1}, which was fit to both 505.3 nm absorbance and 77 amu MBMS decays recorded simultaneously without C_3H_6 (Figure E 7 and Figure E 8). For **i1**, k_{wall} was estimated as half of the C_6H_5 value (50 s^{-1}), based on the lower expected reactivity of an alkyl radical compared to an aryl radical. Although other radicals in the system (e.g., H, CH_3, C_3H_5 and **p1**) should also have their own k_{wall} values, there was insufficient experimental information to obtain reliable estimates, and the main results presented in this work are insensitive to these parameters. For **i1**, although k_{wall} is a guess, at 700 K the model predictions are insensitive to it because unimolecular isomerization/decomposition occurs much faster. For C_6H_5, k_{wall} is important because it can alter the overall mass balance of the model, therefore it is reassuring that a relatively small value of 100 s^{-1} was sufficient to match experiments without C_3H_6. Note that this value of k_{wall} is much smaller than many of the values fit in the 505.3 nm absorbance experiments of section 4.1.4.2 (Table 4-4). As mentioned in that section, this was due to a small air leak during those experiments that was fixed prior to the current MBMS experiments. Also, the simple pseudo-first-order model used in section 4.1.4.2 does not account for self-reaction, whereas the current detailed model does, which would have the effect of decreasing k_{wall}. Finally, it is important to note that this fit value of k_{wall} is not meant to account for the fast wall catalysis of C_6H_5 to C_6H_6 observed in the absence of C_3H_6 (Figure E 7 and Figure E 8). Apparently this phenomenon is too complex to model as a first order rate and the current model does not attempt to describe it. Instead, as mentioned in section 4.2.4.3, wall catalysis was determined to be negligible by control MBMS experiments conducted at increasing $[C_3H_6]$, all of which the current gas-phase model was able to match sufficiently (including C_6H_6, most importantly). Similarly, wall catalysis of I to HI was not included in the model.

Other than the two modifications/additions mentioned above (and the barrier for C_6H_5 + C_3H_6 terminal addition being lowered by 0.75 kcal/mol to match the 505.3 nm absorbance

experiments), RMG's HC mechanism was used as is. By minimizing the amount of manual intervention in the HC mechanism construction the real accuracy of RMG can be gauged when comparing to experiments. If the comparison is satisfactory, then RMG can be confidently applied to analogous systems (e.g., 1-naphthyl radical + 2-butene). If the comparison is not satisfactory, sources of discrepancies can be easily identified and rectified (e.g., the overestimated CH_3 + **p1** reaction mentioned above).

4.2.4.4.2. Iodine Sub-Mechanism

As demonstrated by the various side and secondary products observed with MBMS in Figure 4-16, I atom is not merely an inert photolysis co-product of C_6H_5, but an active participant in much of the observed chemistry. In particular, I atom recombination with various radicals, R, to form iodide-containing species RI is prevalent. As such, any attempts at quantitatively modelling the MBMS experiments must include the contribution of I atom. Because RMG does not currently have the capability (or, more importantly, the data) to model halogen-containing species, the sub-mechanism of iodine chemistry had to be constructed manually. Fortunately, two recent mechanisms for shock tube pyrolysis of iodobenze under both neat[109] and acetylene-diluted conditions[251] provided a starting point for the current sub-mechanism.

Table 4-6: Thermochemistry and structures of iodide-containing species included in sub-mechanism.
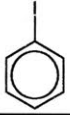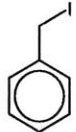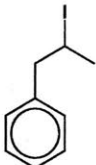
Species	Structure	$\Delta H_f°$ (298 K) (kcal mol^{-1})	$S_{int}°$ (298 K) (cal mol^{-1} K^{-1})	$C_P°$ (cal mol^{-1} K^{-1})						Reference
				300 K	400 K	500 K	600 K	800 K	1000 K	
I	-	25.5	43.2	5.0						251
HI	-	6.4	49.4	7.0	7.0	7.1	7.3	7.6	7.9	251
C_6H_5I		38.7	80.1	24.0	30.6	36.3	41.1	47.7	52.3	251
I_2	-	14.9	62.3	8.8	8.9	9.0	9.0	9.0	9.1	251
CH_3I	-	3.3	60.5	10.6	12.5	14.0	15.3	17.5	19.2	254
C_3H_5I		22.9	78.6	18.5	22.4	26.2	28.9	33.5	36.9	254
p10-I		30.0	93.0	28.1	36.3	43.9	49.6	58.5	64.7	254
i1-I		17.5	111.0	40.1	51.7	61.6	69.5	81.4	89.6	254

Table 4-7: Kinetics of reactions involving iodide-containing species included in sub-mechanism

Reaction #	Reaction	Arrhenius Parameters[a]			Reference
		A	n	E_A	
1	$I + i1 \leftrightarrow i1\text{-}I$	5.8×10^{-11}	0	0	255, b
2	$I + i1 \leftrightarrow HI + p2$	2.0×10^{-11}	0	0	256, c
3	$I + i1 \leftrightarrow HI + p3$	1.3×10^{-11}	0	0	256, c
4	$I + i2 \leftrightarrow HI + p4$	0.7×10^{-12}	0	0	256, c
5	$H + C_6H_5I \leftrightarrow HI + C_6H_5$	1.4×10^{-18}	2.5	-0.14	257
6	$C_6H_5 + C_6H_5I \leftrightarrow C_{12}H_{10} + I$	3.3×10^{-12}	0	11.0	251
7	$C_6H_5I \rightarrow C_6H_5 + I$	3.3×10^{-13}	0	45.9	73
8	$C_6H_5 + I \rightarrow C_6H_5I$	1.7×10^{-11}	0	0	251, d
9	$H + I + M \leftrightarrow HI + M$	1.3×10^{-31}	-1.87	0	258, e
10	$CH_3 + I \leftrightarrow CH_3I$	1.0×10^{-11}	0	0	259, f
11	$C_3H_5 + I \leftrightarrow C_3H_5I$	1.6×10^{-10}	0	0	260, g
12	$p10 + I \leftrightarrow p10\text{-}I$	8.3×10^{-11}	0	0	261, h
13	$I + I + M \leftrightarrow I_2 + M$	3.3×10^{-10}	0	-1.14	167, i
14	$I + C_3H_6 \leftrightarrow HI + C_3H_5$	3.0×10^{-11}	0	18.0	262
15	$H + HI \leftrightarrow H_2 + I$	6.6×10^{-11}	0	0	251
16	$C_6H_5 + HI \leftrightarrow C_6H_6 + I$	5.0×10^{-12}	0	0	251, d

[a]Modified Arrhenius expression used: $k(T) = AT^n e^{-\frac{E_A}{RT}}$. Units are kcal, molecule, s, cm. [b]Estimated by analogy to I + C2H5 → C2H5I measured at 298 K, 100 Torr Kr bath gas and increased by 5 × to match MBMS experiments. [c]Estimated as 0.3 × recombination rate (reaction #1) by analogy to $I + C_2H_5 \rightarrow HI + C_2H_4$ and adjusted for number of hydrogens. [d]Estimate. [e]Ar bath gas. [f]Measured at 400 K, 82 Torr CH3I bath gas. [g]Measured at 296 K, 750 Torr N2 bath gas. [h]Measured at 750-950 K, 190-1900 Torr Ar bath gas. [i]He bath gas.

Table 4-6 lists the eight iodide-containing species involved in the sub-mechanism and their thermochemical parameters. Four of the species were in the mechanism of Comandini et al. (I, HI, I_2 and C_6H_5I),[251] wherein the thermochemistry was obtained from the Active Thermochemical Tables (ATcT).[263] The thermochemistry of the remaining four species (CH_3I, C_3H_5I, p10-I and i1-I) was estimated by using Benson Group-Additivity Values (GAV).[254] Table 4-7 lists the 16 reactions in the sub-mechanism, seven of which are recombination reactions with I atom (reactions #1 and 8-13). Of these R + I → RI reactions, only two of them include pressure-dependence: R = H and I. Even then, as noted in the footnotes, only for R = I has a pressure-dependent rate coefficient been measured for the same bath gas used in this work (helium). Nonetheless, the literature recombination kinetics listed in Table 4-7 (with experimental conditions given in the footnotes) provide some reasonable estimate of the real kinetics at the conditions of this work, particularly for larger R's (such as p10), that are more likely to be in the high-P limit.

The most important reactions of the sub-mechanism are those involving **i1** (#1-4) because by diverting **i1** from unimolecular reaction, they affect the major product distribution of C_6H_5 + C_3H_6. Unfortunately, **i1** is far too specific of a radical for any previously published work to have studied the kinetics of its reaction with I atom. The closest analogue in the literature is ethyl radical, C_2H_5, + I, the recombination kinetics for which were measured at 300 K and 100 Torr Krypton,[255] and the corresponding disproportionation reactions which were measured as ~1/3× recombination.[256] In this work, it was found that a better match with the MBMS experiments could be obtained by increasing the recombination rate by 5×. The disproportionation rate was also increased accordingly, accounting for the different types and numbers of H-atoms on **i1** (and **i2**) compared to C_2H_5. Perhaps the ~5× difference between **i1** + I and C_2H_5 + I recombination is due to the latter, as a much smaller system, being further down the fall-off curve. Reassuringly, the fit **i1** + I → **i1**-I rate is actually slightly smaller than the literature rate for the similarly sized **p10** + I → **p10**-I rate (reaction #12). Other than for reactions #1-4, all of the rate coefficients in the sub-mechanism were taken directly from literature (usually an experiment) for the specific reaction of interest and used without further adjustment.

The remaining six reactions merit some discussion as well. Reaction #5 is fast, and could become problematic in the presence of a high H concentration where a cycle might be established between C_6H_5 and H. Fortunately at the conditions of the MBMS experiments in this work H concentration is low, and what little H that is formed preferentially reacts with C_3H_6 rather than C_6H_5I due to ~2 orders of magnitude difference in concentration. The possibility of other radicals besides H initiating the halogen-atom transfer reaction of #5 (i.e., R + C_6H_5I →RI + C_6H_5) was also considered, but due to the relatively high C-I bond energy in C_6H_5I (~67 kcal/mol[6]) such a reaction would be ≥ 10 kcal/mol endothermic for any R other than H in this system (e.g., CH_3, which is present in high concentration).[264]

Although S_N2 reactions such as #6 are highly favourable thermodynamically, kinetically they are slow. For C_6H_5 substituting for I in C_6H_5I the barrier is ~11.0 kcal/mol, and even if H is the nucleophile the barrier is still ~10 kcal/mol.[257] Therefore these types of reactions will not be important at the conditions of this work (≤700 K).

Thermal decomposition of C_6H_5I (#7) has already been mentioned several times as the reason for imposing a 900 K upper bound on flash photolysis experiments with that precursor. H-abstraction from C_3H_6 by I atom (#14) will not be important due to a high barrier (18 kcal/mol),

and reactions #15 and 16 are unimportant due to a low concentration of both H and HI. As mentioned in the previous section, catalytic hydrogenation of I to HI is not included in the sub-mechanism, although it is observed experimentally in the absence of C_3H_6 (Figure E 7 and Figure E 8). Therefore, this model is not expected to match experimental HI profiles well.

As a final note, although I atom chemistry is important to take into account when quantitatively analyzing product distributions, it has no effect on pseudo-first-order measurements of the total C_6H_5 consumption rate measured by direct absorption (section 4.2.4.2), which happen too quickly for I atom secondary reactions to play a role.

4.2.4.4.3. Photoionization Cross Sections (PICS)

The concentration of each species i in the combined HC and iodine chemical mechanism, C_i, is solved for using the design equations for an isothermal, isobaric, homogeneous batch reactor. C_i can then be related to the instantaneous MS signal, $S_{i,instantaneous}$, through a simple proportionality:

$$S_{i,instantaneous} = R(m/z)\sigma_{PI,i}C_i \qquad (4\text{-}12)$$
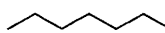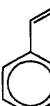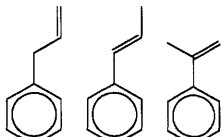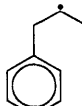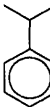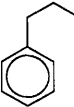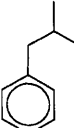
Where $R(m/z)$ is the mass discrimination factor discussed in section 4.2.4.4.4 and $\sigma_{PI,I}$ is the photoionization cross section (PICS) for species i discussed in this section. The subscript "instantaneous" indicates that transport delays during MB sampling are not taken into account yet (section 4.2.4.4.5). Although Eq. 4-12 is a drastic simplification of the complex relationship between concentration and MBMS signal,[64] it will suffice for the purposes here and is hopefully transparent.
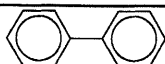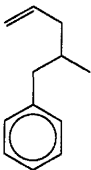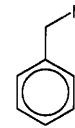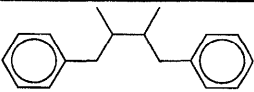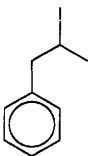
Any attempt to extract quantitative information from MS using PI must contend with the need for PICS. Although PICS have been measured for many common organic molecules[84, 265-267] and for a handful of common radicals,[107, 268-269] these measurements are a pittance compared to the number of possible organic molecules/radicals, even for a fixed molecular formula of reasonable size. Therefore, estimates of PICS are almost always needed. Fortunately, the ionization energy used for PI in this work (10.5 eV) is slightly above (~1 eV) the threshold ionization energy of many organic molecules in a region where PICS are often ~10 Megabarns (Mb).[40, 84, 267] Furthermore, from the sizable (but obviously finite) database of measured PICS in the literature, smart estimates can be made for analogous molecules with unknown PICS. As a last resort, experimental measurements of PICS can also be made for particularly important

molecules/radicals. All three approaches to obtaining PICS were taken here (literature, smart estimates and measurements).

Table 4-8 shows all of the important species (both molecules and radicals) in the C_6H_5 + C_3H_6 MBMS model for which PICS were needed. For most of the smaller species (parent m/z < 130 amu) literature PICS were available, but for almost all of the larger species there were no previously published measurements. The four internal standards (1,3-butadiene, furan, cyclohexane and heptane) are also included and noted in Table 4-8. Even for species with measured PICS (including the internal standards), there is $\pm 15\%$ uncertainty, which translates into at least $\pm 15\%$ uncertainty in all MBMS model versus data comparisons.

Table 4-8: Structures and photoionization cross sections, σ_{PI}, at 10.5 eV of all important species in model of MBMS experiments.

Species	Structure	Cation	m/z (amu)	σ_{PI} at 10.5 eV (Mb)[a]	Reference
CH$_3$	-	CH$_3^+$	15	$6.7^{+2.4}_{-1.8}$	268
C$_3$H$_5$		C$_3$H$_5^+$	41	6.1 ± 1.2	269
1,3-Butadiene[b]		C$_4$H$_6^+$	54	16.3 ± 3.3	267
Furan[b]		C$_4$H$_4$O$^+$	68	14.4 ± 3.0	267
C$_6$H$_5$		C$_6$H$_5^+$	77	17.0 ± 2.5	107
C$_6$H$_6$		C$_6$H$_6^+$	78	31.8 ± 6.4	84
Cyclohexane[b]		C$_6$H$_{12}^+$	84	21.3 ± 4.3	84
p10		C$_7$H$_7^+$	91	25.5 ± 4.0	270, c
Heptane[b]		C$_7$H$_{16}^+$	100	9.9 ± 1.5	266
p1		C$_8$H$_8^+$	104	42.9 ± 4.3	265
p2/p3/p4		C$_9$H$_{10}^+$	118	38.8 ± 7.0	This work, see text
i1		C$_7$H$_7^+$	91	5	Estimate, see text
		C$_9$H$_{11}^+$	119	5	
i2		C$_9$H$_{11}^+$	119	10	Estimate, see text
Propylbenzene		C$_9$H$_{12}^+$	120	30.0 ± 4.5	265
I	-	I$^+$	127	74^{+33}_{-23}	268, d
HI	-	HI$^+$	128	44 ± 7	268, 30
i1-CH$_3$		C$_{10}$H$_{14}^+$	134	30	Estimate[e]

Name	Structure	Ion	Mass	PICS	Note
CH_3I	-	CH_3I^+	142	48.2 ± 7.9	[268]
Biphenyl		$C_{12}H_{10}^+$	154	64	Estimate[f]
i1-C_3H_5		$C_{12}H_{16}^+$	160	40	Estimate[g]
C_3H_5I		$C_3H_5^+$	41	27.5	Estimate, see text
		$C_3H_5I^+$	168	22.5	
p10-I		$C_7H_7^+$	91	45.5	Estimate, see text
		$C_7H_7I^+$	218	4.5	
i1-dimer		$C_{18}H_{22}^+$	238	60	Estimate[h]
i1-I		$C_9H_{10}^+$	118	24	Estimate, see text
		$C_9H_{11}^+$	119	48	
		$C_9H_{11}I^+$	246	8	
I_2	-	I_2^+	254	50	Estimate[i]

[a]Uncertainty represents two standard deviations when applicable. Values without stated uncertainties are estimates. [b]Internal standard. [c]Inferred as $1.5 \times C_6H_5$ σ_{PI}. [d]PICS is for ground state ($^2P_{3/2}$) I atom. In this work, excited ($^2P_{1/2}$) I atom is assumed to be quenched to the ground state by C_3H_6 faster than the ~1 ms resolution of the MBMS experiment. [e]Estimated by analogy to σ_{PI} at 10.5 eV for the following series of alkylbenzene molecules: toluene (31.4 Mb), ethylbenzene (28.7 Mb) and propylbenzene (30.0 Mb). [f]Estimated as $2 \times C_6H_6$ σ_{PI} by applying bond-additive approach of Bobeldijk et al.[271] [g]Estimated as the sum of σ_{PI} for propylbenzene (30 Mb) and propene (10 Mb) by applying bond-additive approach of Bobeldijk et al.[271] [h]Estimated as $2 \times$ propylbenzene σ_{PI} by applying bond-additive approach of Bobeldijk et al.[271] [i]Estimated as at least 50 Mb by analogy to iodide-containing compounds with known σ_{PI}: HI and CH_3I.

Going down Table 4-8, the first species worth commenting on specifically are the phenylpropene isomers, p2-p4. None of these four isomers (trans-1-, cis-1-, 2- and 3-phenylpropene) have had their PICS quantified at any IE, although Zhang et al. measured the relative PIE curve for all of them.[31] Given that p2 and p3 are expected to be measurable primary products of $C_6H_5 + C_3H_6$ (Figure 4-12) it was deemed worthwhile to experimentally measure the PICS of at least one of the isomers. p2 was chosen because it was predicted to be the most important of the H-loss products. The procedure for measuring the PICS of p2 is provided in Appendix E (Figure E 3). The value measured and reported in Table 4-8 (38.8 ± 7.0 Mb) is

consistent with other alkenylaromatic molecules, like styrene (42.9$\pm$4.3 Mb). The same PICS was used for all phenylpropene isomers.

The overall PICS for i1, obtained by roughly fitting the 600 K MBMS experiments, is 10 Mb, which seems anomalously low when compared to the closed-shell aromatic compounds with PICS ~30-40 Mb. However, as discussed by Xu and Pratt it is not uncommon for radicals to have PICS 2-4$\times$ lower than their closed-shell analogues (propylbenzene in the case of i1 with a PICS of 30$\pm$4.5 Mb) due to a correspondingly lower occupancy of the HOMO from which the electron is ejected.[272] The fragmentation pattern of i1 was also roughly fit to the 600 K MBMS experiments. Specifically, a fast rise (~1 ms, at the time-resolution limit of the MBMS experiment as discussed in section 4.2.4.4.5) at m/z=91 amu could only be explained by a fragment of i1 that is 1:1 with the parent cation (5 Mb each). Although surprising initially, it is possible that the i1 parent cation undergoes a fast 1,2-H-migration to form the i4 parent cation, which can then easily fragment to $C_7H_7^+$ + ethene + e$^-$, where $C_7H_7^+$ could be either a benzyl or tropylium cation.[273] Such cation rearrangements have been observed before, particularly if the resulting fragments are thermodynamically favorable as in this case.[48] The same small total PICS (10 Mb, no fragmentation) was also used for i2, which is present in low concentration in the model anyway.

Of the six closed-shell iodide-containing species, only two have PICS measured in literature (HI and CH_3I), and both are ~50 Mb. Therefore, for the remaining four closed-shell iodide-containing species (C_3H_5I, p10-I, i1-I and I_2) it was assumed that each of their overall PICS are $\geq$50 Mb. In the case of all but i1-I, the overall PICS was simply set at 50 Mb and not adjusted any further.

Given the relatively low C-I bond energy compared to C-C and C-H bonds,[264] fragmentation of RI compounds to R$^+$ is facile, even at 10.5 eV, and must be taken into account. This is especially true for C_3H_5I and p10-I, for which the C-I bond in question is at a particularly vulnerable allylic and benzylic site, respectively. The R$^+$:RI$^+$ fragmentation pattern for C_3H_5I was measured by us as 55:45 (Figure E 4) and for C_7H_7I it was previously measured as ~10:1 close to 10.5 eV.[273] Both fragmentation patterns were applied to the 50 Mb total PICS estimate for C_3H_5I and p10-I.

Understanding the fragmentation pattern of i1-I was most crucial to interpreting the 600 K MBMS experiments. Although i1-I cannot be purchased commercially, the bromide, i1-Br,

can and the measured fragmentation pattern of **i1-Br** (Figure E 5) exhibited significant cations not only at the parent and $i1^+$ (119 amu) m/z, but also at 118 amu. This suggests a fragment channel to $p3^+$ + HBr + e^-, which seems reasonable given the weak benzylic C-H bond. **i1-I** is expected to form the same fragments as **i1-Br**, but to a greater extent due to the weaker C-I bond relative to C-Br. Attempts to synthesize **i1-I** via the Finkelstein reaction were mostly unsuccessful due to low conversion of **i1-Br** and thermal production of phenylpropene isomers.[274] Therefore, the only current recourse to quantifying **i1-I** and its fragments was to fit their PICS to the 600 K experiments while maintaining the constraint that the overall PICS $\geq$ 50 Mb. An overall PICS of 80 Mb and a 3:6:1 fragmentation pattern between $C_9H_{10}^+$:$C_9H_{11}^+$:$C_9H_{11}I$ was fit.

Finally, as noted in Table 4-8, several of the closed-shell hydrocarbons had their PICS estimated by applying the bond-additivity concept of Bobeldijk et al.[271] For example, the unknown PICS of biphenyl was estimated as 2× the PICS of C_6H_6 (2 × 32 = 64 Mb), and **i1-C_3H_5** was estimated as the sum of C_3H_6 and propylbenzene (10 + 30 = 40 Mb).

4.2.4.4.4. Mass Discrimination Factor, R(m/z)

As expressed in Eq. 4-12, R(m/z) is essentially a conversion factor between PICS-weighted concentration in the reactor and MBMS signal. Generally, R(m/z) increases monotonically as a function of m/z, and accounts for the greater radial spread of lighter species in the gas expansion (resulting in lower centerline concentrations and lower MBMS signals).[64] Individual values of R(m/z) are calculated for each of the four internal standards using their known concentrations (~1e-11 cm^{-3}) and PICS by rearranging Eq. 4-12:

$$R(int - std\ m/z) = \frac{S_{int-std}}{\sigma_{PI,int-std}C_{int-std}}$$ (4-13)

The four resulting R(m/z)'s are then fit to a power law:

$$R(m/z) = b(m/z)^c$$ (4-14)

A representative R(m/z) fit with C_3H_6 is shown in Figure 4-19. All 15 MBMS experiments were conducted with the internal standards present, therefore individual R(m/z)'s were fit to each experiment. Table 4-5 summarizes the fit values of the exponent, c, for each experiment, which is typically ~0.5.[64] Without C_3H_6, however, R(m/z) was essentially flat and a constant value was used. It should also be mentioned here that brief control experiments were conducted at each T,P

condition without the internal standards, to ensure that their presence was not altering the product distribution.

Once R(m/z) had been fit, all of the PICS-weighted concentration profiles in the model, $\sigma_{PI,i}C_i$, were multiplied by their corresponding R(m/z) according to Eq. 4-12, in order to obtain the simulated, instantaneous signal profiles, $S_{i,instantaneous}$, which are not yet comparable to experiments because transport delays still need to be accounted for (next section).
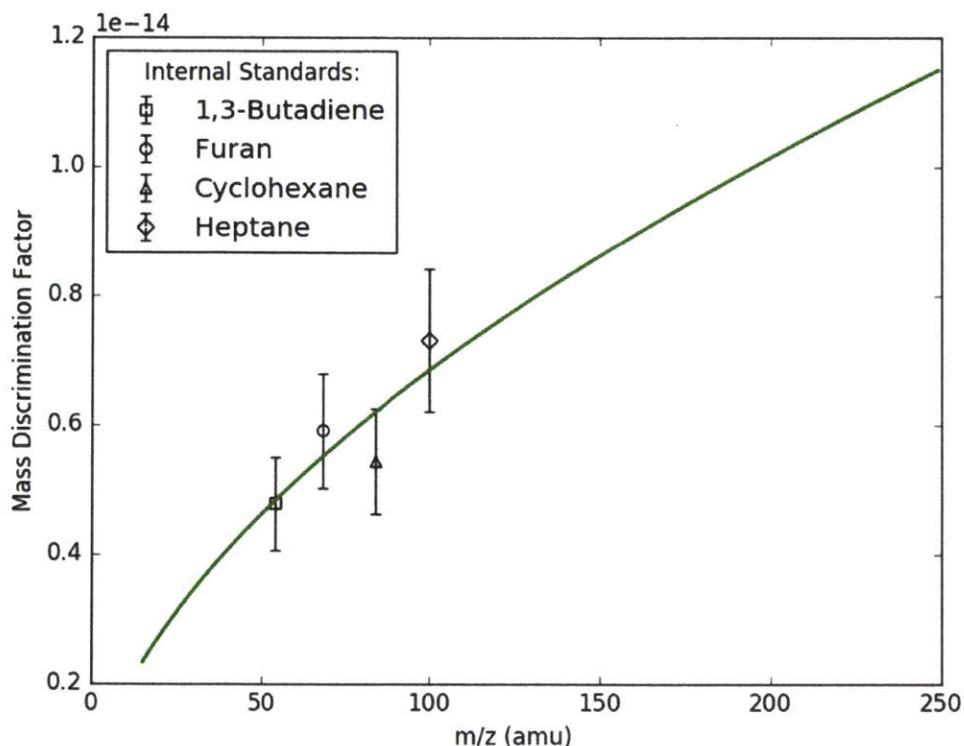
Figure 4-19: Representative mass discrimination factors (markers) and fit (line) at 707 K, 10 Torr (Experiment 7). Error bars are from $\pm 15\%$ uncertainty in internal standard PICS.

4.2.4.4.5.   Molecular Beam Sampling

The effect of effusive or molecular beam sampling on measured species profiles in kinetic studies has previously been described and quantified from a theoretical level.[110-111] Although it is feasible to apply such a rigorous sampling model to a simple chemistry mechanism, for a complex chemistry mechanism, such as the one used in this work consisting of almost 100 species, a simpler model for sampling (and transport more generally) is desired. Moreover, theoretical models for sampling do not take into account transport within the reactor, i.e., if radicals are not initially distributed uniformly in the radial dimension following photolysis

(usually due to a non-uniform photolysis beam profile) it will take some finite time for the non-uniformities to "smooth out" by diffusion. For the MBMS experiment reported here, diffusion within the reactor due to inhomogeneities does seem to be the rate-limiting transport step, as evidenced by the much slower appearance of products at 50 Torr compared to 10 Torr (Figure 4-17).

For these reasons, a simple model for transport that implicitly includes diffusion in the reactor was adapted from Baeza-Romero et al.[65] In their model, all of the steps involved in transporting a species i from somewhere inside the reactor to the ionization region of the MS (diffusion to the pinhole, flow through the pinhole and transport to the ionization region via an effusive or supersonic expansion, as well as transport out of the ionization region for neutral molecules) are lumped into a single first-order rate, $k_{sampling}$:

$$i \xrightarrow{k_{sampling}} i, sampled \xrightarrow{k_{sampling}} i, exit$$

Therefore, for any arbitrarily complex chemical mechanism a set of ODE's can be set up and numerically solved for the observed MBMS signal, $S_{i,sampled}$, after accounting for transport effects:

$$\frac{dS_{i,sampled}}{dt} = k_{sampling} \left(S_{i,instantaneous} - S_{i,sampled} \right) \tag{4-15}$$

The set of ODE's represented by Eq. 4-15 are only solved for dilute, time-dependent species. A new reactor type called "mbsampledReactor" was created in RMG to solve this set of ODE's. $S_{i,sampled}$ is directly comparable to experiments (section 4.2.4.4.7).

An advantage of this simple transport model is that $k_{sampling}$ is the only parameter that needs to be fit, which is done by comparison to the rise time of the I atom MBMS signal at 127 amu (Figure 4-20). I atom is used for fitting $k_{sampling}$ because it is formed in the reactor nearly instantaneously after photolysis and unlike C_6H_5 it has a long lifetime. In the limit of instantaneous sampling ($k_{sampling} \to \infty$) the model prediction is clearly not accurate, but after tuning $k_{sampling}$ to 750 s^{-1} the agreement is good in this case (especially for the rise time, which is chemistry-independent). The modelled I atom signal decreases at longer times due to the reactions in Table 4-7. Values of $k_{sampling}$ were fit to the I atom rise time in this manner for all 15 MBMS experiments, and are typically ~1000 s^{-1} (Table 4-5) although there is a trend toward slower sampling for higher P and with added C_3H_6, consistent with diffusion in the reactor being the rate-limiting transport step.
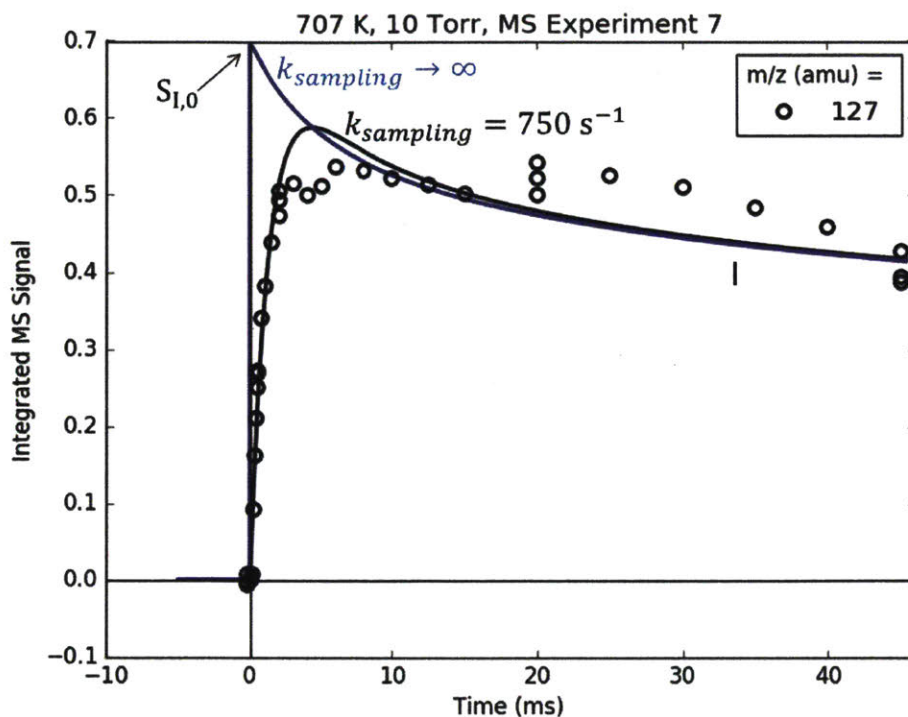
Figure 4-20: Representative measured iodine atom MS time-profile (markers) and comparison to two different models of MBMS sampling: $k_{sampling} \rightarrow \infty$ (blue) and $k_{sampling} = 750 \text{ s}^{-1}$ (black).

As shown for the 50 Torr MBMS experiments in Figure 4-17, this simple, one-parameter transport model is not sufficient to completely describe sampling at higher P's. In particular, the same $k_{sampling}$ that was fit to the MBMS rise time of I atom was used for all other species in the solution of Eq. 4-15, regardless of mass or size. If diffusion within the reactor is rate-limiting, then $k_{sampling}$ should decrease (get slower) with increasing species mass and collision diameter, σ. According to the Chapman-Enskog equation,[104] for a relatively heavy species in a He bath gas the mass of the heavy species will have little effect on the diffusion coefficient, D, whereas D $\propto \sigma^{-2}$. Therefore, although I atom has a similar mass as the major products of $C_6H_5 + C_3H_6$ (127 versus 78-119 amu), because its collision diameter is likely at least 2× smaller it will have a D ~4× faster. This would explain why the $C_6H_5 + C_3H_6$ products at 50 Torr (and 25 Torr) appear in the MS even slower than predicted by the model. Nonetheless, the higher-P experiments still quantitatively determine the product distributions after diffusion has homogenized the composition (or if instantaneous product ratios are used instead, Figure E 11 and Figure E 14).

Although faster time-resolution for the MBMS measurements is desirable and achievable down to 10-100's of microseconds,[64-65] with the current time-resolution of ~1 ms it is still possible to discern differences in chemical timescales. For example, as will be shown in section 4.2.4.4.7, it is possible to distinguish the faster growth time scale of C_6H_6 (direct H-abstraction) compared to **p1** (CH_3-loss through an intermediate, **i1**). Furthermore, high time resolution is achieved using the laser absorbance portion of the apparatus, which can easily measure processes as fast as 10's of microseconds.[75] For the purposes of this work (quantifying the primary products of $C_6H_5 + C_3H_6$), a 1 ms MBMS time resolution was deemed sufficient.

Finally, as discussed in more detail in the next section, the I Atom MBMS profile is also used to quantify the initial radical concentration by back-extrapolating the $k_{sampling} \to \infty$ simulation to t=0. The value obtained, $S_{I,0}$, indicated in Figure 4-20 is proportional to $C_{I,0}$ (and $C_{C6H5,0}$) according to Eq. 4-12.

4.2.4.4.6. Initial Radical Concentrations

As mentioned briefly in the previous section, $C_{I,0}$ (which is assumed $=C_{C6H5,0}$) is obtained from the following rearranged version of Eq. 4-12:

$$C_{I,0} = \frac{S_{I,0}}{\sigma_{PI,i} R(m/z=127 \text{ amu})} \qquad (4\text{-}16)$$

where $S_{I,0}$ is obtained by fitting and back-extrapolating the I atom MBMS profile (Figure 4-20). Values of $C_{I,0}$ obtained in this manner (labelled MS $C_{I,0}$) are summarized in Table 4-5. Compared to the $C_{I,0}$ values measured simultaneously by IR absorbance (labelled IR $C_{I,0}$), MS $C_{I,0}$ is typically ~2× lower, but still within their combined (large) uncertainties for most experiments. The systematic difference is likely due to an inhomogeneous photolysis beam profile, or a beam diameter that is slightly smaller than the reactor inner diameter where MBMS sampling occurs. In either case, MS $C_{I,0}$ should be (and was) used as the initial radical concentration in the model, because it is more representative of the local environment relevant to the MBMS experiments.

Another possible explanation for the systematic ~2× difference in IR and MS $C_{I,0}$ is the presence of excited ($^2P_{1/2}$) I atom, I*, which has been measured as ~30% of the total I atom yield immediately following 266 nm photodissociation of C_6H_5I.[6] Because the PICS of I* has been measured to be up to 7× lower than the PICS of I (ground state, $^2P_{3/2}$),[275] even a small amount of I* in the overall I atom mixture could substantially lower the 127 amu MBMS signal. However, it was assumed that I* was quenched to I by collision with C_3H_6 at a faster rate than the

resolution of the MBMS experiment (~1 ms).[96, 276] This assumption is supported by the independence of MS $C_{I,0}$ on [C_3H_6] shown in Table 4-5. Interestingly, even without C_3H_6 (no quenching gas) MS $C_{I,0}$ is still the same, perhaps suggesting quenching on the walls during sampling.

4.2.4.4.7. Model Comparison to MBMS Experiments

Before delving into comparisons between the flash photolysis/MBMS model and experiments it is helpful to recap exactly what has been fit to the 600 K MBMS data specifically:

1. The rate of reactions between **i1** and I atom (both recombination and disproportionations).

2. The total PICS (10 Mb) and fragmentation pattern (1:1 at m/z=91:119 amu) of **i1**.

3. The total PICS (80 Mb) and fragmentation pattern (3:6:1 at m/z=118:119:248 amu) of **i1-I**.

Therefore, good agreement between the 600 K model and experiments is mostly expected, especially for m/z=118, 119 and 248 amu, which are all almost entirely attributable to **i1-I**. However, nothing was fit to the 700 K MBMS experiments, except for $k_{sampling}$ and $C_{I,0}$, which had to be obtained from the I atom MBMS profiles. Therefore, the model should mostly be judged by its ability to simulate the 700 K experiments.

As already shown in Figure 4-17, the model described in detail from sections 4.2.4.4.1-4.2.4.4.6 matches the primary product profiles at 10 Torr and both 600 and 700 K. At 50 Torr and 700 K, although the simulated t-dependence is too fast because of inhibited diffusion as discussed in section 4.2.4.4.5, the final product distribution (and instantaneous product ratios in Figure E 11 and Figure E 14) is still matched well by the model. This section will focus on comparing every individual m/z with measured time-dependence against the model for both 600 and 700 K (10 Torr only), starting with the five primary products (m/z=78, 91, 104, 118 and 119 amu). Identical comparison plots are made for MBMS experiments at higher P (25 and 50 Torr) in Figure E 10 and Figure E 13.
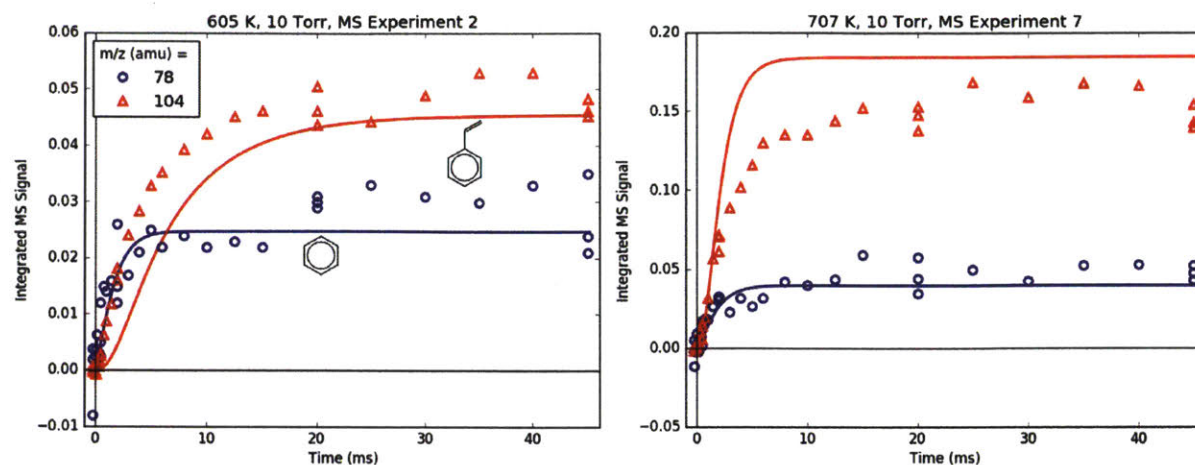
Figure 4-21: Measured (markers) and modeled (thick lines) 78 and 104 amu MBMS signal at indicated conditions. These are the only two primary phenyl radical + propene product m/z's that are entirely attributable to one species: benzene and styrene, respectively.

78 and 104 amu are compared together in Figure 4-21 because they are both unique in being the only major product signals entirely attributable to just one species: C_6H_6 and **p1** (styrene), respectively. As such, the 78:104 ratio is indicative of the competition between H-abstraction and radical addition in the reaction of C_6H_5 with C_3H_6, and the model could be fit to the measurements by adjusting the relative barrier heights of those two entrance channels. However, the measurements and the simulations already overlap considering the uncertainty in the model (at least ±15% due to the PICS), therefore it was deemed unnecessary (and essentially meaningless) to fit the barrier heights. Also, at 600 K, both the model and the experiment show a slower growth time scale for 104 amu (~10 ms), which is formed in two steps ($C_6H_5 + C_3H_6 \rightarrow$ **i1** $\rightarrow$ **p1** + CH_3), compared to 78 amu (~1 ms), which is formed in only one step ($C_6H_5 + C_3H_6 \rightarrow C_6H_6 + C_3H_5$). This demonstrates that although the time resolution of the current MBMS experiments is only ~1 ms, important differences in chemical time-scales can still be resolved.
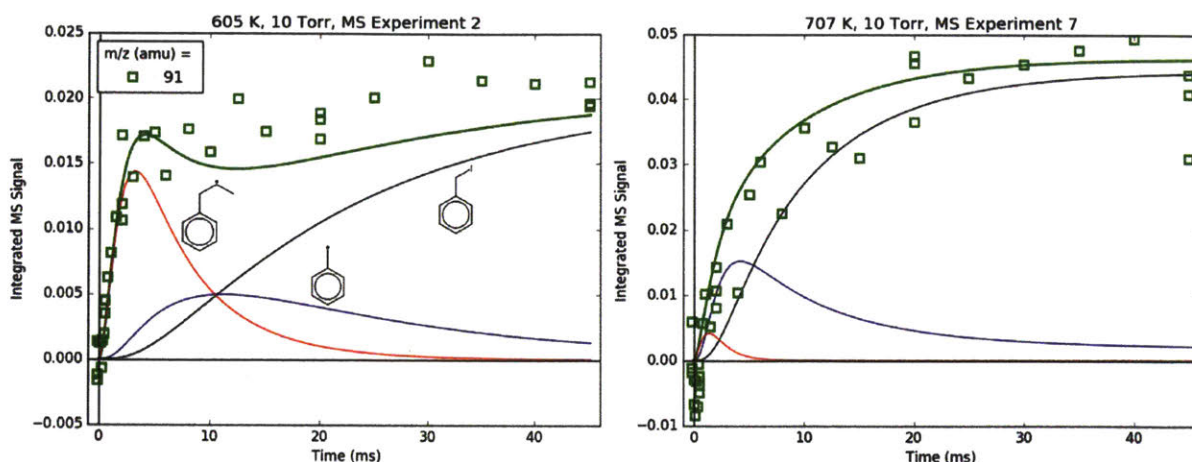
Figure 4-22: Measured (markers) and modeled (thick lines) 91 amu MBMS signal at indicated conditions. The thin lines correspond to different species contributing to the overall modeled 91 amu signal: the $C_7H_7^+$ fragments of **i1** (red) and benzyl iodide (black), and the parent cation of benzyl radical (blue).

91 amu, shown in Figure 4-22, is modelled as a complicated mixture of three different species signals all with distinct t- and T-dependence: **p10** (benzyl radical) and fragments of both **i1** and **p10**-I. For 600 K, the agreement at early times is due to fitting the extent of **i1** fragmentation to 91 amu. The measurements at later time were not fit, however, and are in excellent agreement with the model, which mostly consists of the **p10**-I contribution. Even more remarkable is that the model still performs well at 700 K, where nothing was fit, and the contribution of **i1** is greatly diminished because of its fast unimolecular isomerization/decomposition at that T. Once again, at later times the model is dominated by **p10**-I, in accord with the experiment. The measurements in Figure 4-22, and the ability of the model to quantitatively explain them, provides strong support for the never-before-seen aromatic-catalyzed 1,2-H-migration proposed in section 4.2.4.1. Without the addition of this pathway to Kislov et al.'s original PES,[9] virtually no **p10** or **p10**-I would be predicted, and the long-time 91 amu signal observed experimentally would be unaccounted for.
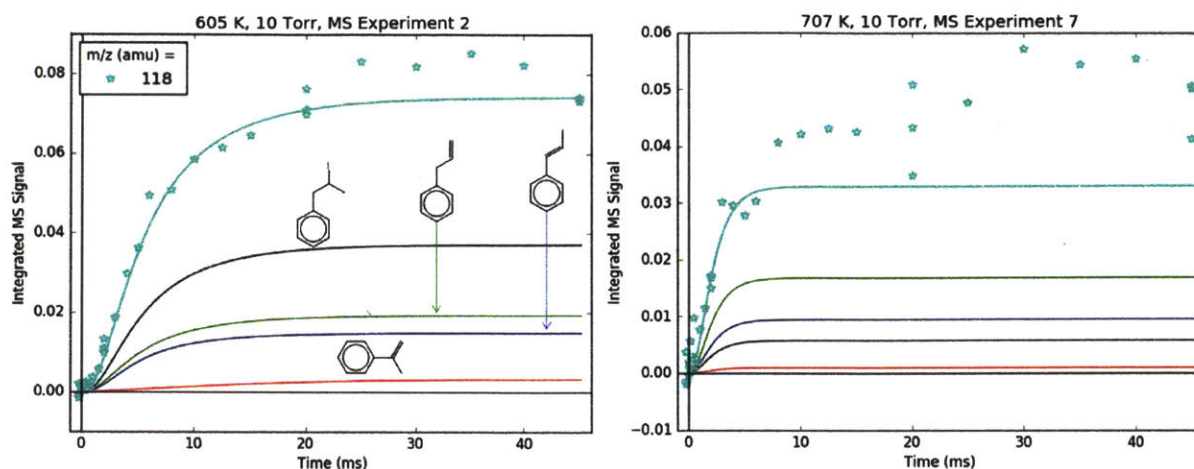
Figure 4-23: Measured (markers) and modeled (thick lines) 118 amu MBMS signal at indicated conditions. The thin lines correspond to different species contributing to the overall modelled 118 amu signal: the $C_9H_{10}^+$ fragment of **i1**-I (black) and the parent cations of 1-,2- and 3-phenylpropene (blue, red and green, respectively).
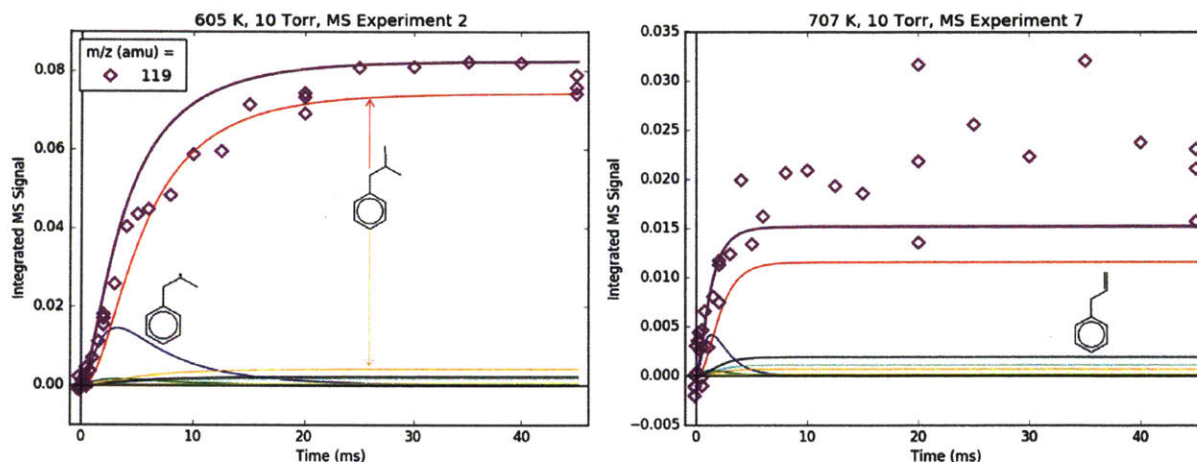
Figure 4-24: Measured (markers) and modeled (thick lines) 119 amu MBMS signal at indicated conditions. The thin lines correspond to different species contributing to the overall modelled 119 amu signal: the parent cations of **i1** and **i2** (blue and green, respectively), the $C_9H_{11}^+$ and ^{13}C-containing $C_9H_{10}^+$ fragments of **i1**-I (red and orange, respectively) and the parent cations of ^{13}C-containing 1-,2- and 3-phenylpropene (cyan, gold and black, respectively).

Both 118 and 119 amu, shown in Figure 4-23 and Figure 4-24, respectively, have large contributions from fragmentation of **i1**-I. 119 amu in particular is dominated by **i1**-I in the simulations at both 600 and 700 K, with a negligible contribution from the parent cation of **i1**. 118 amu exhibits a more diverse mix of simulated species: at 600 K **i1**-I is the largest contributor

to the 118 amu signal, but the phenylpropene isomers **p2** and **p3** also make a noticeable contribution. At 700 K, the roles are switched and **p2** and **p3** are dominant over **i1**-I. This is because **i1** is undergoing unimolecular reactions too quickly at higher T to participate in bimolecular recombination with I atom, hence the importance of **i1**-I is diminished at 700 K. It is important to reiterate that the good agreement at 600 K between the model and the experiments at 118 and 119 amu (and 246 amu shown later) is due to fitting of the unknown PICS and fragmentation pattern of **i1**-I. However, the fact that the same PICS and fragmentation pattern are used in the model at 700 K with satisfactory results gives credibility to the model.

Overall, all five of the primary C_6H_5 + C_3H_6 product m/z's are well-described by the model, imparting greater confidence to the predictions of section 4.2.4.1 upon which the model is based, and encouraging the extension of those predictions to analogous systems (section 4.2.4.6). The remainder of this section will compare the model simulations to the MBMS experiments for all of the other transient m/z's.
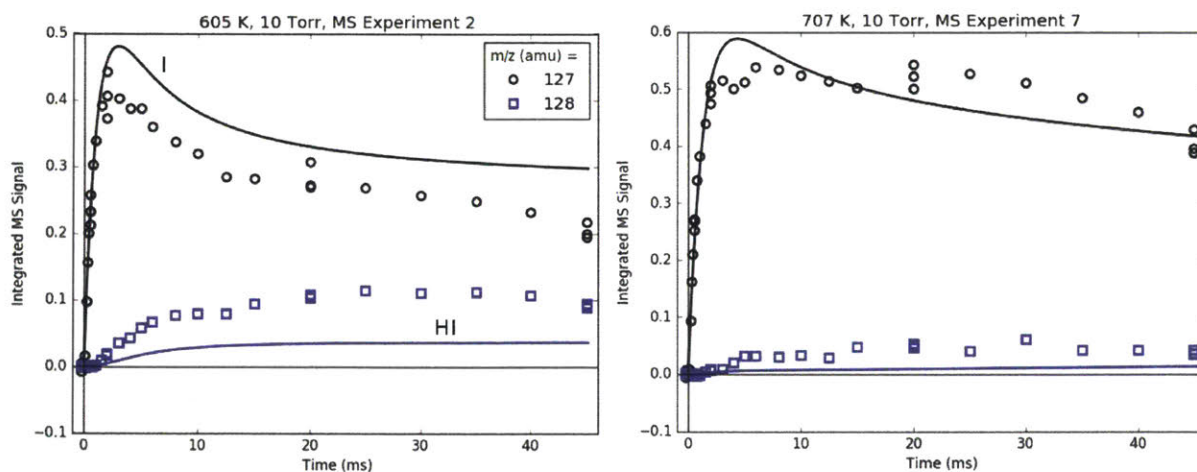
Figure 4-25: Measured (markers) and modeled (thick lines) 127 (black) and 128 (blue) amu MBMS signals at indicated conditions, which are exclusively attributable to I and HI.

Figure 4-25 compares I atom and HI at 127 and 128 amu, respectively. The rise time of the 127 amu signal was fit for $k_{sampling}$, and its absolute value was roughly fit for $[I]_0$. Therefore, the agreement between the modelled and measured I atom at early times is unremarkable. At longer times, however, the simulated decay of I atom was not fit, and generally follows the trend of the measured 127 amu signal, especially considering that the I atom PICS is ~35% uncertain (Table 4-8). Given the importance of **i1** recombination with I atom at 600 K in explaining many

of the observations made at that T, it is reassuring that the absolute I atom signal itself is also described well by the model over the entire measured time range.

As discussed earlier, HI is mostly formed through wall catalysis, which was not included in the model. Therefore, HI is underpredicted, especially at 600 K. At 700 K, the wall catalysis effect is reduced, probably because of less adsorption on the wall at higher T,[277] but HI is still underpredicted. Nonetheless, matching HI is not critical to the main goals and conclusions of this work, and is not discussed further.
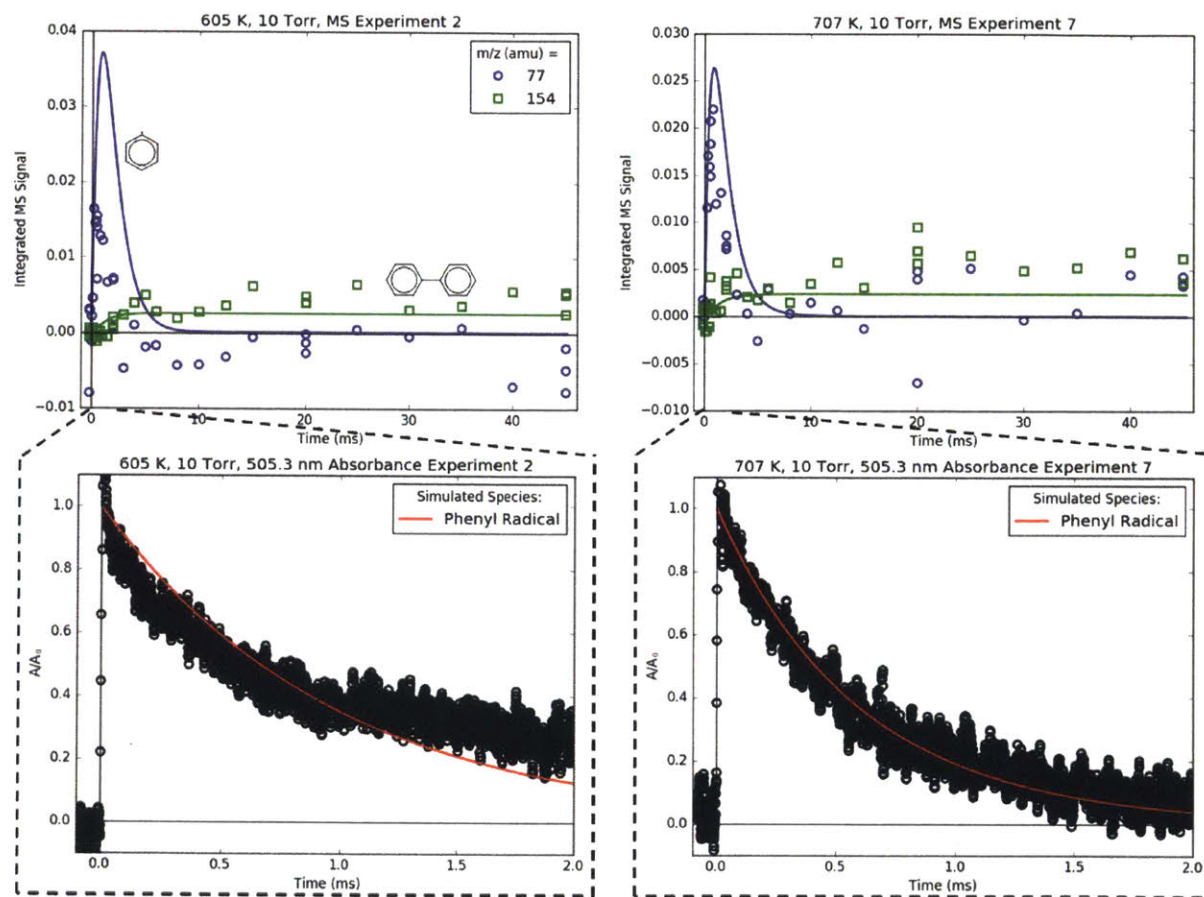
Figure 4-26: Top: Measured (markers) and modeled (thick lines) 77 (blue) and 154 (green) amu MBMS signals at indicated conditions, which are exclusively attributable to phenyl radical and biphenyl. Bottom: Measured (markers) and modeled (red line) 505.3 nm absorbance traces recorded simultaneously as MBMS plots on top.

Figure 4-26 compares the C_6H_5 signal measured both by MBMS at 77 amu and by simultaneously recorded 505.3 nm absorbance. As a short-lived species, C_6H_5 is difficult to resolve with MBMS, an issue that is compounded by the overlap of 77 amu with a fragment of

C_6H_5I, which is present in relatively high concentration. However, the decay of C_6H_5 was clearly resolved by 505.3 nm absorbance, which is a much faster and non-intrusive detection technique for measuring overall kinetics. The simulated C_6H_5 decay (without sampling effects, of course) is in good agreement with the 505.3 nm absorbance, which is expected given that the terminal addition rate of $C_6H_5 + C_3H_6$ was previously fit to absorbance measurements in section 4.2.4.2. Figure 4-26 and Figure 4-21 to Figure 4-24 illustrate the complementary nature of laser absorbance coupled with MBMS for kinetic studies: laser absorbance can resolve the time dependence of only one species (or at most a few species if there is spectral overlap that can be deconvoluted) with high t-resolution, whereas MBMS can resolve the time dependence of many species with lower t-resolution. Of course, the t-resolution of the MBMS measurements reported here can and should be improved in the future, but MBMS is unlikely to supplant laser absorbance as the preferred method for overall kinetics quantification.

Biphenyl, C_6H_5-C_6H_5, is also measured with MBMS at 154 amu (Figure 4-26), and the model is in near-quantitative agreement, especially considering that the PICS of C_6H_5-C_6H_5 was estimated by the method of Bobeldijk et al.[271] The C_6H_5 self-recombination rate ($C_6H_5 + C_6H_5 \rightarrow C_6H_5$-$C_6H_5$) used in the model is also an unadjusted estimate used directly from RMG.
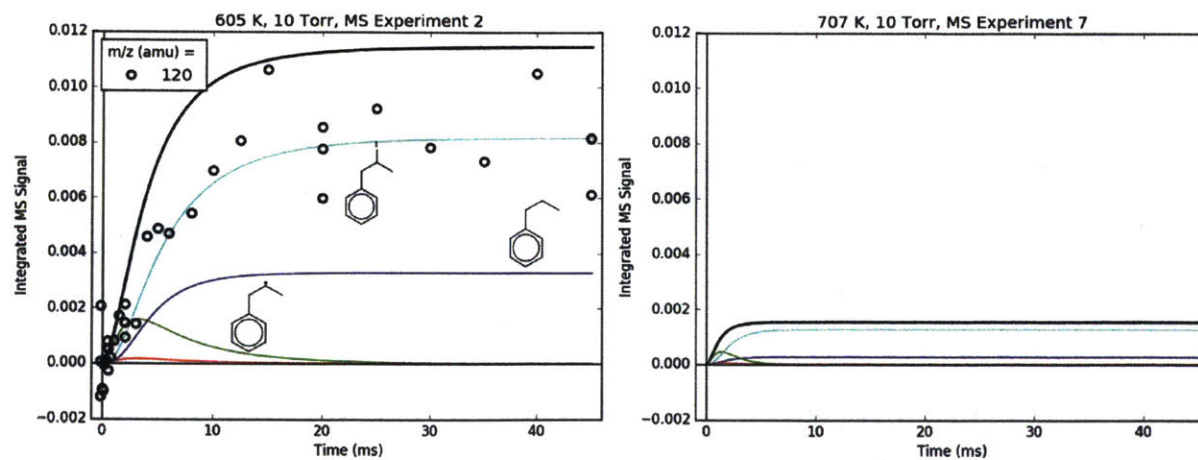
Figure 4-27: Measured (markers) and modeled (thick lines) 120 amu MBMS signal at indicated conditions. The thin lines correspond to different species contributing to the overall modelled 120 amu signal: the parent cation of propylbenzene (blue), the ^{13}C-containing $C_9H_{11}^+$ fragment of **i1**-I (cyan) and the parent cations of ^{13}C-containing **i1** and **i2** (green and red, respectively). The overall 120 amu signal at 707 K was too low to be detected, therefore only the modeled signal is shown at that condition.
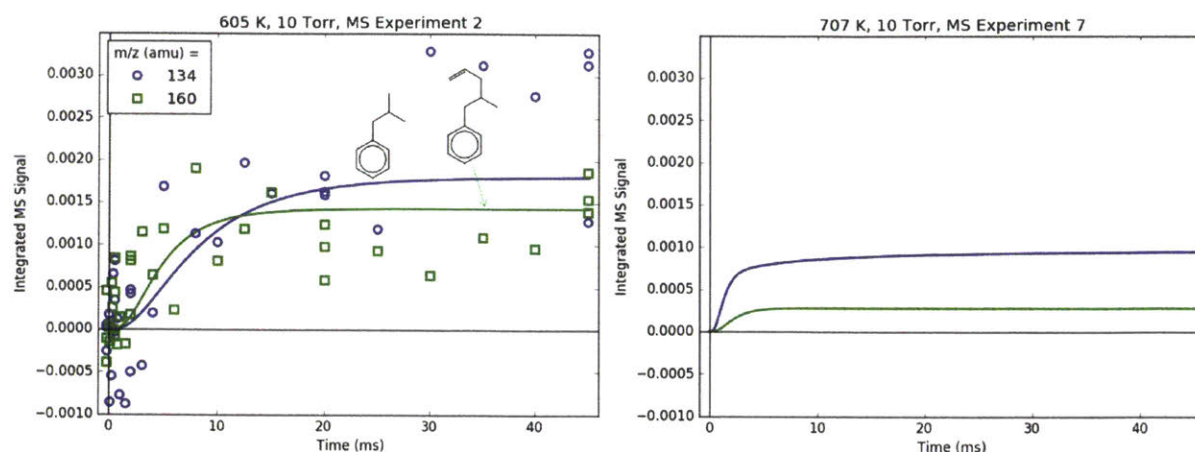
Figure 4-28: Measured (markers) and modeled (thick lines) 134 (blue) and 160 (green) amu MBMS signal at indicated conditions. Both signals are exclusively attributed to products of **i1** recombination with other radicals: methyl and allyl radical, respectively. Both signals were too low to be detected at 707 K, therefore only the modeled signal is shown at that condition.

Measured and modelled m/z signals corresponding to products of **i1** bimolecular recombination with H atom (120 amu), CH_3 (134 amu) and C_3H_5 (160 amu) are shown in Figure 4-27 and Figure 4-28. At 600 K, the signal at m/z=120 amu is actually mostly attributable to the ^{13}C isotopologues of various 119 amu species/fragments (specifically, the fragment of **i1**-I), with propylbenzene (from **i1** adding an H either by recombination, H-abstraction or disproportionation) contributing ~1/3 of the total modelled signal. At 700 K, the simulated signal is about an order of magnitude lower, below the detection limit of the MBMS, consistent with the lack of any measurable 120 amu signal. 134 and 160 amu are entirely attributable to the expected species: **i1**-CH_3 and **i1**-C_3H_5. At 600 K, the signal is discernible but near the detection limit, and by 700 K the simulated and measured signals have dropped below the detection limit. As mentioned before in a different context, this is because **i1** is too short-lived at higher T's to undergo bimolecular reactions (such as recombination with I, CH_3 or C_3H_5). Although not shown, in the model another secondary product of **i1** bimolecular reaction, **i1**-dimer, has a similar absolute signal and T-depedence as the species in Figure 4-28. However, no transient signal at the corresponding parent m/z (238 amu) was observed even at 600 K (Figure 4-16). Given that the PICS of **i1**-dimer was estimated as 2× the PICS of propylbenzene (2×30=60 MB),[271] its signal is probably slightly overpredicted, which so close to the detection limit can make the difference between seeing it and not seeing it experimentally.
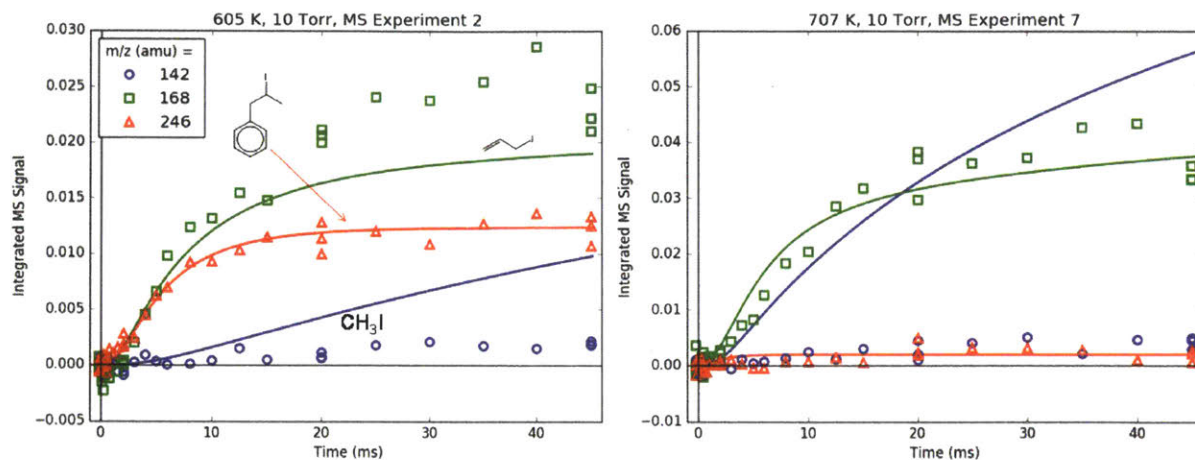
Figure 4-29: Measured (markers) and modeled (thick lines) 142 (blue), 168 (green) and 246 (red) amu MBMS signal at indicated conditions. All signals are exclusively attributed to the parent cation of an alkyl iodide: methyl, allyl and **i1** iodide, respectively.

Finally, Figure 4-29 shows the parent m/z's of all of the important iodide-containing species: 142 amu for CH_3I, 168 amu for C_3H_5I and 246 amu for **i1**-I. The parent m/z signal for **p10**-I at 218 amu is below the detection limit due to its severe (~10:1)[273] fragmentation to $C_7H_7^+$. The modeled C_3H_5I and **i1**-I both quantitatively match their respective m/z signal measurements at both T's (keeping in mind that the PICS and fragmentation pattern of **i1**-I was fit to the 600 K experiments). CH_3I, however, is overpredicted, especially at 700 K. As discussed in section 4.2.4.4.2, this is probably due to fall-off effects, not included in the I atom sub-mechanism, lowering the effective rate of $CH_3 + I \rightarrow CH_3I$ at higher T's and lower P's than where the original rate measurement was conducted (400 K, 82 Torr CH_3I).[259] Although the $CH_3 + I \rightarrow CH_3I$ rate could be fit to match the 142 amu MBMS signal, given the uncertainties in the many other CH_3 reactions and given that CH_3 was not observed with MBMS (discussed in following paragraph) it was decided that there were too many variables for too little data, and adjustment of one variable would have no physical significance.

Of equal importance as what was observed is what should have been observed but wasn't. Specifically, the model predicted significant concentrations of CH_3, methane (CH_4, from H-abstraction by CH_3), C_2H_4 (co-product of **p10**), ethane (C_2H_6, from self-recombination of CH_3) and C_3H_5 (co-product of C_6H_6 and general product of H-abstraction from C_3H_6), none of

which were observed experimentally by MBMS. There are three explanations for the lack of MBMS signal for these species:

1. The species ionization energy is > 10.5 eV, as in the case of CH_4 (12.6 eV^{278}), C_2H_4 (10.51 eV^{279}) and C_2H_6 (11.5 eV^{280}).

2. Although the simulated species concentration is high, once PICS and R(m/z) are taken into account the simulated signal is below the MBMS detection limit, as in the case of CH_3 at 600 K (CH_3 has a relatively small PICS and as a light species it is disfavored by R(m/z)).

3. The time-dependent species signal overlaps with some large time-independent signal, as in the case of CH_3 and C_3H_5, both of which overlap with a large C_3H_6-fragment.

As the co-product of **p1**, which is clearly observed as a dominant product at 700 K, CH_3 is the most glaringly absent signal in the MBMS. Besides the second and third experimental explanations above, the disparity between modelled and non-existent measured CH_3 could certainly be due to the model. Specifically, the model is overpredicting the concentration of CH_3 (Figure E 6) because as discussed in section 4.2.4.4.1 there is no k_{wall} for CH_3.

To conclude this lengthy section on quantitatively modelling the MBMS experiments, the intention of building a detailed model following the approach of Figure 4-18 was not to "perfectly" match experiments. Given the 100's of parameters in this model including rate coefficients, thermochemical parameters, PICS, $k_{sampling}$ and $C_{I,0}$, the relatively small experimental data set reported here (15 different conditions) could easily be fit perfectly and automatically. Rather, the goal was to build a model independent of the experiments that could quantitatively explain all of the major observations, using reasonable estimates. The model presented above has achieved this goal, and in the process has provided quantitative support for the predictions of section 4.2.4.1, which can now be confidently extended to other alkylaromatic systems using RMG (section 4.2.4.6).

4.2.4.5 Products Measured by Absorbance

Attempts were also made to quantify product branching by laser absorbance given that at room T three of the important radicals in the C_6H_5 + C_3H_6 system, C_6H_5, C_3H_5 and **p10**, are known to exhibit distinct visible absorbance features at 504.8,[105] 408.4[233] and 447.7 nm,[248] respectively (Figure 4-30). However, the strength of these features is expected to drop with increasing T due to line-broadening.[77] In particular, the peak absorbance cross section for **p10** at

447.7 nm is known to sharply decrease by ~1 order of magnitude when increasing T from 300 to 600 K,[281] such that at T ≥600 K all three radicals in Figure 4-30 will have similar absorbance cross sections of ~2e-19 cm^2.
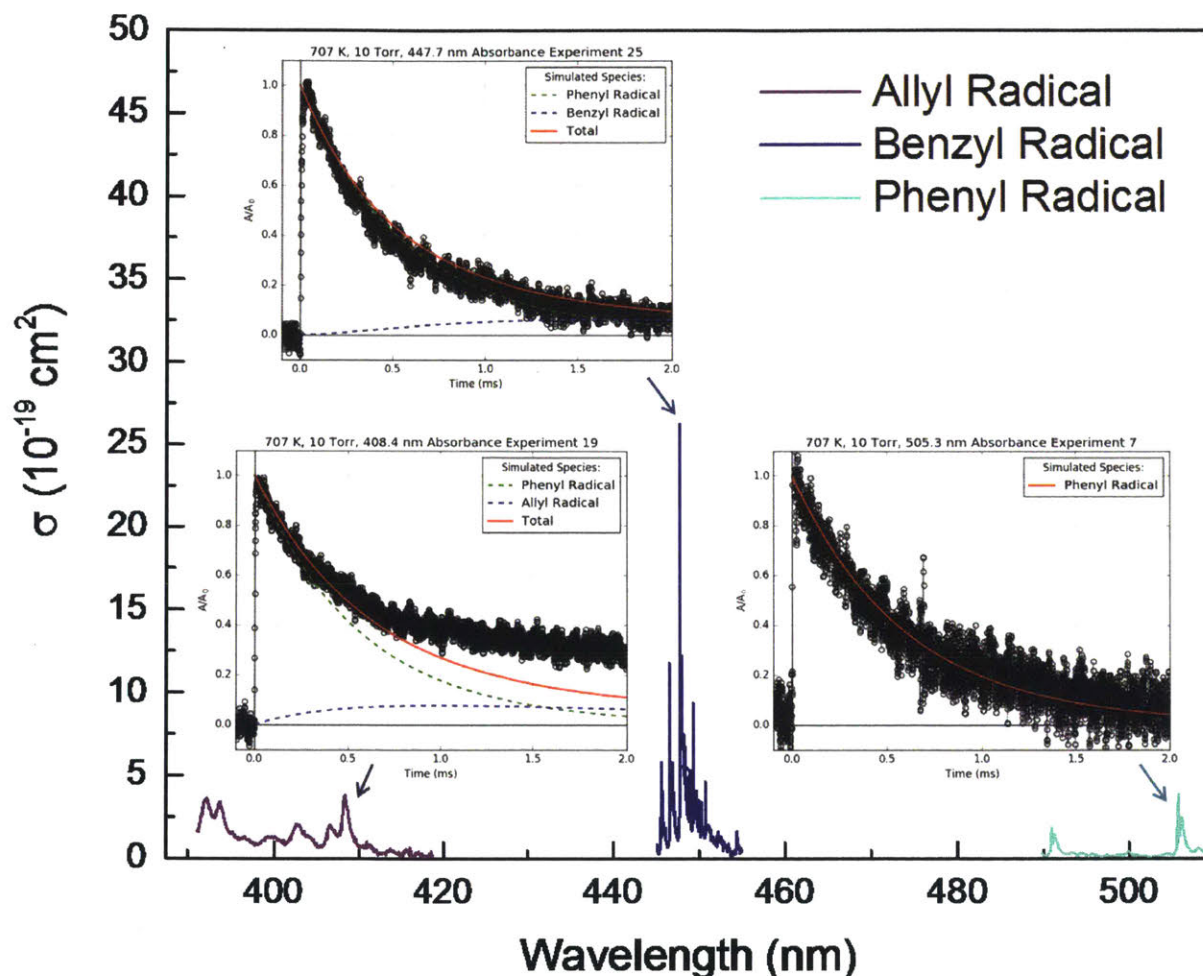
Figure 4-30: Room temperature visible absorbance spectra measured by Tonokura et al. for allyl,[233] benzyl[248] and phenyl[105] radicals. Insets show representative absorbance traces (markers are measured and lines are modeled) measured in this work at the different wavelengths indicated and otherwise identical conditions (707 K, 10 Torr, $[C_3H_6]$ = 7.5×10^{15} cm^{-3}).

Table 4-9 summarizes the conditions of the experiments to probe for products (C_3H_5 and **p10**) with laser absorbance. The experiment #'s are a continuation of those for the MBMS experiments. Experiments #2-4, 16-18 and 22-24 were conducted at nearly-identical conditions (nominally 600 K, 10 Torr and a range of $[C_3H_6]$, the radical concentration was slightly higher for the product probing experiments) but the probe laser wavelength was varied from 505.3,

404.8 and 447.7 nm, respectively. Similarly for experiments #7-9, 19-21 and 25-27, which were conducted at 700 K and 10 Torr.

Table 4-9: Conditions of laser absorbance experiments probing for products. Uncertainties represent two standard deviations

Exp. #	Probe Laser Wavelength (nm)	Nominal T (K)	Real T (K)	P (Torr)	$[C_3H_6]^a$ (10^{15} cm^{-3})	$[C_6H_5I]^a$ (10^{13} cm^{-3})	IR $[I]_0$ (10^{12} cm^{-3})	Photolysis Laser Fluence (mJ cm^{-2})
16	408.4	600	605±8	10	7.5	6.1	4.5±1.5	18
17	408.4	600	605±8	10	15.0	6.1	4.5±1.5	18
18	408.4	600	605±8	10	30.0	6.1	4.5±1.5	18
19	408.4	700	707±11	10	7.5	6.1	3.5±1.2	18
20	408.4	700	707±11	10	15.0	6.1	3.5±1.2	18
21	408.4	700	707±11	10	30.0	6.1	3.5±1.2	18
22	447.7	600	605±8	10	7.5	6.1	4.2±1.4	18
23	447.7	600	605±8	10	15.0	6.1	4.2±1.4	18
24	447.7	600	605±8	10	30.0	6.1	4.2±1.4	18
25	447.7	700	707±11	10	7.5	6.1	4.0±1.3	18
26	447.7	700	707±11	10	15.0	6.1	4.0±1.3	18
27	447.7	700	707±11	10	30.0	6.1	4.0±1.3	18

^{a}10% uncertainty in all values due to systematic uncertainty in mass flow controller calibrations.

The insets of Figure 4-30 compare the 700 K background-subtracted and normalized absorbance measurements at the three probe wavelengths. As already discussed (section 4.2.4.2) 505.3 nm absorbance of C_6H_5 typically returns to the baseline within ±10% due to noise and imperfect background subtraction (Table 4-4). C_6H_5 continues to contribute substantially to the absorbance at the lower wavelengths as well, similar to previous measurements of its UV-visible spectrum.[282] At 447.7 nm, the absorbance also essentially returns to baseline, but at 408.4 nm there is a clear, reproducible baseline-shift of ~30%, which exceeds the typical baseline shift fluctuations of ± 10%. Similar results were obtained at 600 K (no reliable baseline shift at 505.3 and 447.7 nm, and a possible baseline shift of ~10% at 408.4 nm). Once again, the model of section 4.2.4.4 was used to gain quantitative insight into what is happening.

The normalized absorbance traces at 408.4 and 447.7 nm were modelled as weighted sums of the simulated C_6H_5 and product concentration profiles in the reactor (unsampled):

$$\frac{A}{A_0} = \frac{c_{C6H5}}{c_{C6H5,0}} + \alpha \frac{c_{product}}{c_{C6H5,0}} \tag{4-17}$$

where product is either C_3H_5 or **p10**, $c_{C6H5,0}$ is the initial C_6H_5 concentration and α is the weighting factor that accounts for the ratio of product to C_6H_5 cross sections at the given visible wavelength. α was measured as ~1 for C_3H_5 at 408.4 nm (at both 600 and 700 K) by back-to-back flash-photolysis experiments with C_6H_5I and C_3H_5I. For **p10** at 447.7 nm, α was approximated as 1 at both 600 and 700 K based on the measured cross section of C_6H_5 in this

work ($\sim 2 \times 10^{-19}$ cm^2, largely independent of either T or wavelength) and the experiments of Matsugi et al. measuring the T-dependence of **p10**'s cross section.[281]

The model results are shown as thick red lines in the insets of Figure 4-30, where the individual contributions of $C_{C_6H_5}$ and $C_{product}$ are also shown as dashed lines. Although the model is in good quantitative agreement with the 447.7 and 505.3 nm measurements, at 408.4 nm the baseline shift in the model is only ~10% compared to ~30% measured experimentally. However, it was found that the predicted C_3H_5 yield (and the modelled baseline shift at 408.4 nm) was sensitive to the $C_3H_5 + I \rightarrow C_3H_5I$ rate coefficient. If this reaction was entirely removed, the C_3H_5 yield approximately doubled at short times, and the modelled 408.4 nm baseline shift increased to around 20% (Figure E 15), which is in reasonable agreement with the 30% measured experimentally considering the 10% baseline fluctuations regularly observed. Of course, $C_3H_5 + $ I recombination is occurring, because C_3H_5I was observed as an MBMS product. Perhaps C_3H_5 and I are recombining on the walls close to where MBMS sampling occurs, whereas in the gas-phase probed by absorbance little recombination occurs due to the pressure dependence of the reaction (which is not included in the model).

A different explanation for the poorly modelled 408.4 nm baseline shift is absorbance by something else entirely, especially given the relatively short wavelength. In any case, MBMS detection of stable products (C_6H_6 in the case of $C_6H_5 + C_3H_6$ H-abstraction) is a much preferred method for quantifying product branching than trying to probe for one radical product with laser absorbance in a "soup" of different radicals that might also absorb. It was demonstrated in the previous section that the model developed in this work could quantitatively explain all of the major product MBMS signals, including C_6H_6. The inability of the same model to quantitatively match all of the absorbance experiments should not detract from it significantly, especially considering the complications involved in quantitative absorbance measurements mentioned above.

4.2.4.6   Generalizing Aromatic-Catalyzed 1,2-Hydrogen Migration to Other Alkylaromatic Systems using RMG

The aromatic-catalyzed 1,2-H-migration proposed in section 4.2.4.1 and experimentally supported in section 4.2.4.4 is not limited to the $C_6H_5 + C_3H_6$ system, but will apply to any arbitrary alkylaromatic radical system with at least three carbons in a linear chain and at least one

H in an ortho-position. RMG, and other automatic mechanism generators like it, provides a convenient tool for generalizing new chemistry findings, such as the aromatic-catalyzed 1,2-H-migration, and exploring their implications for more complicated systems. In this case, the slightly more complicated alkylaromatic system considered is 1-naphthyl radical + 2-butene, $1\text{-}C_{10}H_7 + 2\text{-}C_4H_8$, the radical addition product for which is shown and labelled in Scheme 4-5. This particular system was chosen because both the number of aromatic rings and the length of the side chain have increased by one compared to $C_6H_5 + C_3H_6$. As will be shown, even these modest modifications to the original $C_6H_5 + C_3H_6$ framework will have consequential effects on the possible chemistry.
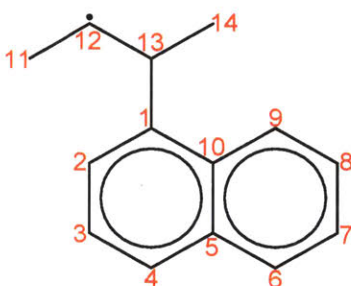
Scheme 4-5: Addition product of 1-napthyl radical + 2-butene with atom labels.

As already discussed in sections 4.2.3 and 4.2.4.4.1, RMG was "taught" the aromatic-catalyzed 1,2-H-migration (and alkylaromatic chemistry more generally) using training reactions. Scheme 4-6 shows the "aromatic-catalyzed pathways" found by RMG and included in the final, converged mechanism for $1\text{-}C_{10}H_7 + 2\text{-}C_4H_8$ at 600 K and 1 atm. Following aromatic-catalyzed 1,2-H-migration, the radical formed was actually predicted to react in two main ways: β-scission C_2H_4 to form an RSR directly (analogous to **p10** + C_2H_4 formation in $C_6H_5 + C_3H_6$, right branch of Scheme 4-6) or undergo a 1,3-phenyl shift and then β-scission C_3H_6 to form an RSR (left branch). Both RSR's are then predicted to recombine with CH_3 at various sites, although the extent of these reactions is overestimated by RMG as they were for CH_3 + **p10** recombination (Scheme 4-4).
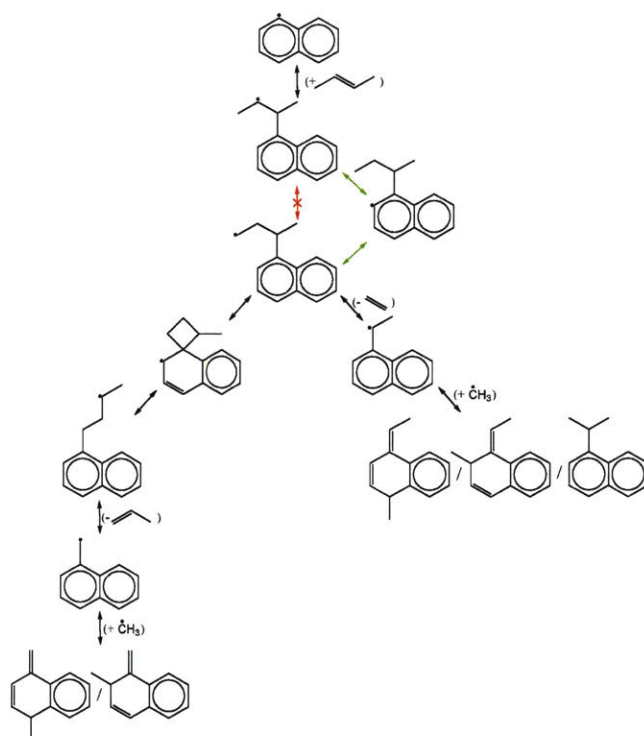
Scheme 4-6: Aromatic-catalyzed 1,2-hydrogen-migration for 1-napthyl radical + 2-butene and subsequent RMG-predicted pathways.

From Scheme 4-6 alone it can already be seen that simply adding one more carbon to the alkyl chain of **i1** opens up new chemistry (left branch). However, there are two more novel applications of the "aromatic-catalyzed" concept to the $1\text{-}C_{10}H_7 + 2\text{-}C_4H_8$ system that were not found by RMG. In the first, rather than the ortho-carbon, labelled 2 in Scheme 4-5, serving as the "active site" in the aromatic catalyst (source and sink of H), carbon 9 could instead. In fact, carbon 9 is probably a better active site than carbon 2 because in the rate-limiting step of the aromatic-catalyzed 1,2-H-migration carbon 2 loses its H in a 5-membered-ring TS (Figure 4-10 and Figure 4-11) whereas carbon 9 would form a more favourable 6-membered-ring TS. In the second application, carbon 2 could still be the active site, but instead of abstracting an H back from carbon 11 in the second step, as in Scheme 4-6, it could abstract an H from carbon 14. In this case, the net effect would be a 1,3-H-migration. The fact that RMG was unable to extrapolate the aromatic-catalyzed 1,2-H-migration that it was trained on to a different active site or to a 1,3-H-migration (or to a combination of both: a 1-3-H-migration using carbon 9 as the active site) points to areas of future work.
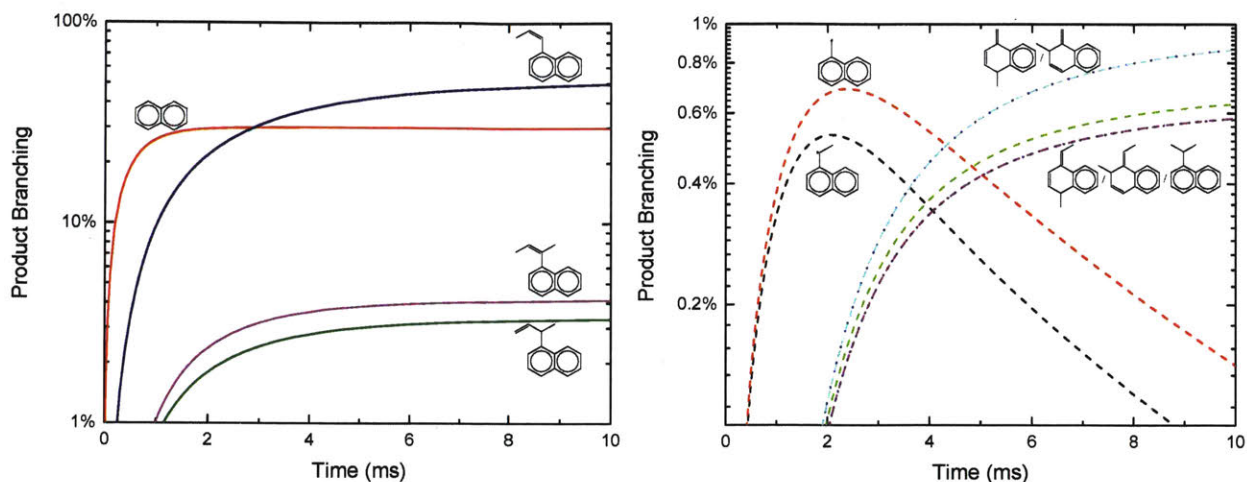
Figure 4-31: Major (left) and aromatic-catalyzed (right) products of 1-naphthyl radical + 2-butene predicted by RMG.

Figure 4-31 shows RMG's quantitative predictions of the product branching for $1\text{-}C_{10}H_7$ + $2\text{-}C_4H_8$ at 600 K and 1 atm. Just as in the case of $C_6H_5 + C_3H_6$, the major products are from H-abstraction (red line) and radical addition followed by CH_3 loss (black) or H loss (magenta and green). All of the "aromatic-catalyzed products" each have a yield of less than 1%, and in total they only account for ~4% of the product branching. However, if RMG had found the other three aromatic-catalyzed reactions described in the previous paragraph the branching would be higher. Nonetheless, the general applicability of aromatic-catalyzed reactions has been demonstrated and applied to the example $1\text{-}C_{10}H_7 + 2\text{-}C_4H_8$ system using RMG. Given the staggering number of different alkylaromatic structures that would be encountered in a real application (e.g., gasoline, kerogen) a tool like RMG is needed to extrapolate findings made for model systems (e.g., aromatic-catalyzed 1,2-H-migration in $C_6H_5 + C_3H_6$) to all possible analogous systems, even if the extrapolation is currently unsophisticated.

4.2.5   Conclusions

By applying a different experimental approach (flash photolysis with time-resolved MBMS) to a chemical system that has already been studied extensively both experimentally and computationally ($C_6H_5 + C_3H_6$) several new insights were made.

First, and most importantly, a previously-unreported aromatic-catalyzed 1,2-H-migration was proposed to explain unexpected benzyl radical formation observed experimentally from $C_6H_5 + C_3H_6$. Quantum calculations of the energetics and RRKM/ME calculations of the kinetics

for the new pathway were both favorable, predicting up to ~10 and 15% product branching to benzyl radical at thermal and single collision conditions, respectively. In order to gain further confidence in these predictions, a detailed model for the flash photolysis/MBMS experiment was developed that includes both hydrocarbon and iodine chemistry, as well a simple empirical model for transport. The model could quantitatively explain the complicated time- and temperature-dependence of the unexpected product (as well as the other four primary product m/z's) observed experimentally, providing strong support for the aromatic-catalyzed pathway as the main route to benzyl radical (and resonance stabilized radicals more generally).

Second, the extent of H-abstraction from $C_6H_5 + C_3H_6$ was quantified experimentally for the first time, using MBMS detection of the stable product (C_6H_6), and found to be in good agreement with the model described above (and the theoretical calculations upon which the chemistry portion of the model relies). Attempts to quantify H-abstraction by probing for the radical product (C_3H_5) with laser absorbance were less quantitatively successful, however, either due to poorly understood secondary chemistry involving I atom or spectral overlap of other radicals at the relatively short wavelength used (408.4 nm).

Finally, the competition between CH_3-loss and H-loss following radical addition of $C_6H_5 + C_3H_6$ was quantified experimentally and matched by the model. At the conditions of these experiments (600 and 700 K) CH_3-loss was dominant.

The only outstanding discrepancy in the $C_6H_5 + C_3H_6$ literature that this work did not address experimentally was the isomeric identity of the H-loss product. However, trapping of the effluent of the flash photolysis reactor followed by GC/MS detection of the stable $C_6H_5 + C_3H_6$ products might be a practical approach to addressing this issue in the future.

Given that the current theoretical understanding of $C_6H_5 + C_3H_6$ was sufficient to quantitatively explain the many experimental results of this work, this knowledge was "taught" to RMG using the language of training reactions. The ability of RMG to apply this knowledge to a slightly more complicated alkylaromatic system, $1-C_{10}H_7 + 2-C_4H_8$, was demonstrated, although areas for improvement were clearly identified. Specifically, RMG only applied the aromatic-catalyzed concept narrowly to the kind of 1,2-H-migration seen in the $C_6H_5 + C_3H_6$ system, instead of applying it more broadly to 1,3-H-migrations with different "active-sites" of the aromatic catalyst. Despite these shortcomings, RMG and similar automated tools are currently the best options for extrapolating detailed chemistry insights, such as the ones made in

this work, to real applications. Hopefully the overall framework presented here for translating fundamental experimental and theoretical insights into broader applications using RMG will serve as a guide for future fruitful work. For example, experiments with naphthyl radicals or butene isomers would be a logical extension of this work.

Chapter 5

RMG-Aided Modelling of Natural Gas High Temperature Pyrolysis

This chapter demonstrates how insights into detailed chemistry, made either experimentally or theoretically, can be used in an application *via* the Reaction Mechanism Generator (RMG). The application discussed is natural gas high temperature pyrolsysis (NG HTP) for the production of C2 commodity chemicals.

5.1   Introduction

Natural gas is a fossil fuel that is primarily composed of methane. Based on the origin of natural gas, it can also have varying amounts of heavier alkanes and minor amounts of species such as carbon dioxide, nitrogen, helium, hydrogen sulfide and water.[283] Natural gas is widely used around the world for a variety of applications pertaining to power generation, transportation, and residential usage and as a chemical industry feedstock.[284] Due to an increase in natural gas reserves around the world, it is expected that natural gas will become more important as a chemical feedstock.[285] As a result, it is of interest to convert natural gas to useful fuels and chemicals such as syngas and acetylene. Acetylene can be converted to ethylene through catalytic hydrogenation,[286] and ethylene is a building block for polymers and a number of chemical intermediates such as acetaldehyde, ethanol, ethylene glycol, etc.,[283] which can be used to make everyday products.

Non-catalytic, high-temperature pyrolysis (HTP) is commercially used to convert methane to acetylene.[286-287] In HTP, acetylene can be produced from methane/natural gas either through a one-step or a two-step process.[286] The well-known one-step process for acetylene production is the partial oxidation process (POX) developed by BASF.[286] In POX, methane and oxygen are premixed at an equivalence ratio greater than one in a mixing zone, ignited in a burner, combusted for milliseconds before quenching the products using water or heavy oil.[288] The two-

step process developed by Hoechst consists of two reaction zones, followed by a quenching zone.[286, 289] In the first reaction zone, a stoichiometric mixture of fuel and oxygen are combusted in the burner to provide the heat required for the pyrolysis reactions in the second reaction zone. A fresh hydrocarbon feed (cracking gas) is introduced in the second reaction zone. The cracking gas mixes with the hot effluent from the first reaction zone and pyrolyzes to form acetylene. The two-step process produces higher yields of acetylene when compared to the POX process, due to lower concentrations of oxidizing species such as OH, O and HO_2 in the second reaction zone.[290] However, the major drawback in non-catalytic HTP is the tendency of this process to produce soot.[291] Therefore, in this work, the two-step HTP process is modeled for natural gas and various cracking gas compositions, and the yield of acetylene, ethylene and soot-precursors (aromatic hydrocarbons up to 2-rings) are determined.

Partial oxidation processes has been extensively investigated, both experimentally and computationally in batch reactors,[285, 292-293] flow reactors[287, 294-297] and premixed flames.[298-301] However, limited studies are present in literature for the 2-step process. High temperature pyrolysis of hydrocarbons was investigated by Ktalkherman et al.,[302-304] where hydrogen and air were combusted in the first reaction zone, followed by addition of propane,[302] LPG[303] or naphtha[304] in the second reaction zone, to produce ethylene. The yield of ethylene was significantly higher when compared to the conventional steam cracking[302] and pyrolysis methods.[304] Recently, Zhang et al. numerically investigated the 2-step process using coke oven gas as primary feed, and methane as a secondary feed and optimized the design of a jet-in-cross flow reactor to maximize the acetylene production.[290]

A natural gas chemical kinetic mechanism is required to predict the yield of acetylene and other products from the HTP process. GRI-Mech 3.0[305] is a commonly used chemical kinetic mechanism for combustion of natural gas,[285, 290, 294] and consists of hydrocarbons up to propane. Other commonly used natural gas oxidation mechanisms are Glarborg,[295] Leeds,[306] Petersen,[307] Konnov[308] and Curran[309] mechanisms (to cite a few). The highest carbon number additive in the natural gas mechanisms in literature is n-pentane (C_5H_{12}).[309-310]

The natural gas and cracking gas compositions used in this study are shown in Table 5-1 and Table 5-2. Natural gas used in this study consists of heavy alkanes up to C_6 and cracking gas compositions range from C_1-C_6 hydrocarbons and also includes alcohols such as butanol and amyl alcohol. As per the authors' knowledge no natural gas mechanism exists in literature which

includes the reaction kinetics for all the species shown in Table 5-1 and Table 5-2. Therefore, the primary objective of this work is to develop a comprehensive mechanism for HTP of natural gas and all of the additives listed in **Table 5-2**, in order to predict the yield of acetylene, ethylene, aromatics (up to naphthalene) and other major intermediates formed in the 2-step HTP process.

Table 5-1: Natural gas composition used in this study

Species	Concentration (mol %)
Methane (CH_4)	91.612
Ethane (C_2H_6)	5.038
Nitrogen (N_2)	1.604
Carbon Dioxide (CO_2)	1.389
Propane (C_3H_8)	0.266
Allene (C_3H_4)	0.036
n-Butane (C_4H_{10})	0.027
Isopentane (C_5H_{12})	0.012
Hexane (C_6H_{14})	0.0075
Cyclohexane (C_6H_{12})	0.0075

Table 5-2: Cracking gas composition used in this study

#	Species	Concentration (mol %)
1	Natural gas (NG, composition shown in Table 1)	100
2	NG/Ethane (C_2H_6)	80/20 54/46 0/100
3	NG/Propane (C_3H_8)	87/13 64/36 6/94
4	NG/n-Butane (C_4H_{12})	89/11 70/30 25/75
5	NG/1-Butene (C_4H_{10})	59/41 68/32
6	NG/(Isopentane(iC_5H_{12},0.3)/n-Pentane (C_5H_{12},0.997))	86/14
7	n-Hexane (C_6H_{14})	100
8	NG/(n-Hexane (C_6H_{14}, 0.84)/Cyclohexane (C_6H_{12}, 0.16))	76/24
9	NG/Hexene (C_6H_{12})	77/23
10	NG/Butanol ($C_4H_{10}O$)	72/28
11	NG/Amyl alcohol ($C_5H_{12}O$)	77/23 87/13
12	NG/(n-Pentane(C_5H_{12},0.20)/Hexane(C_6H_{14}, 0.54)/Butanol($C_4H_{10}O$,0.26))	78/22

Another major contribution of this study is the development of a methodology for modeling the 2-step HTP process. The HTP reactor in this study was modeled using a chemical reactor network and a detailed natural gas mechanism, which includes elementary kinetics for all the species listed in Table 5-1 and Table 5-2. The natural gas mechanism was developed using the automated mechanism generation software, RMG (Reaction Mechanism Generator).[181] The results from the HTP reactor model were compared against pilot plant reactor data and the accuracy of the model in predicting the major products methane (CH_4), hydrogen (H_2), acetylene (C_2H_2), ethylene (C_2H_4), carbon monoxide (CO) and carbon dioxide (CO_2) is verified. The effect of cracking gas feed compositions and overall equivalence ratio, ϕ, on C2 (acetylene and ethylene) and aromatics yields is also investigated. Finally, the dominant decomposition and aromatic-forming pathways for the most highly-sooting pilot plant run are discussed.

5.2   Pilot Plant Data

The pilot plant data of the high temperature pyrolysis reactor was obtained from SABIC. The pilot plant data consisted of 71 runs. Natural gas was used as the fuel and oxygen was used as the oxidizer in the burner. The reactor heat duty was varied by changing the flow rates of the fuel and oxidizer while still maintaining stoichiometric conditions. The pressure in the burner section varied from 1.8-3.1 atm. The pressure in the cracking gas region varied from 1.2-1.5 atm. The overall equivalence ratio, ϕ, in the reactor ranged from 2-3.5. The cracking gas composition in the secondary reaction zone was also varied, as shown in Table 5-2. The dry product composition at the exit of the reactor was measured. The measured products included hydrogen (H_2), methane (CH_4), ethene (C_2H_4), acetylene (C_2H_2), carbon monoxide (CO) and carbon dioxide (CO_2). The inlet and outlet temperatures of cooling water in the burner and cracking gas regions were also measured.

5.3   Model Description

The model for NG HTP can be broken down into three components: 1.) A detailed chemical mechanism generated by RMG, 2.) A network of ideal reactors in series, and 3.) An approximation for heat loss along the length of the pilot plant reactor. Each component is discussed in detail below, with special emphasis on the chemical mechanism.

5.3.1   Mechanisms

RMG is an open-source tool for automatically generating gas-phase reaction mechanisms using a flux-based criterion.[181] RMG's kinetics database consists of 53 "reaction families" that describe how different functional groups can react. These families are populated with kinetic data in the form of general "rate rules", and specific "training reactions". Initially, RMG was not well-suited for predicting the chemistry of aromatic compounds because the rate rules and training reactions in the database were almost entirely for linear/branched hydrocarbons/oxygenates, which are oftentimes not extensible to cyclic or aromatic molecules. More fundamentally, the existing reaction families may not capture all of the ways in which aromatic molecules can react or form.

Due to these two initial limitations on RMG's aromatic prediction capability (lack of relevant kinetic data and non-exhaustive reaction families) it was necessary to rely on a "reaction library" of aromatic reactions at first. The chemical mechanism of Narayanaswamy et al.,[311] which was developed for high temperature combustion of gasoline surrogate mixtures, was converted into RMG reaction and thermochemistry libraries for this purpose. The Narayanaswamy mechanism was developed on top of a base mechanism from Blanquart et al.,[312] and the combined mechanism has been validated against an array of experimental data sets for the combustion of linear and branched alkanes, as well as substituted aromatics. Importantly, the Narayanaswamy mechanism includes PAH formation up to four aromatic rings, unlike other well-known combustion mechanisms such as GRI-Mech[305] and USC II.[313] Although many of the kinetic parameters in this mechanism are global (i.e., non-elementary) estimates, especially for reactions involving PAH, the sources of the estimates are well-documented and can usually be traced back to a quantum mechanical (QM) calculation of the potential energy surface (PES) consisting of elementary chemical reactions.

The overall strategy for obtaining a reliable, detailed chemical mechanism for NG HTP including PAH formation (at least up to indene/naphthalene) was therefore the following: 1.) Create an RMG mechanism for NG HTP, referred to hereafter as Mech v1, using the Narayanaswamy reaction library to capture PAH chemistry. 2.) Evaluate the performance of Mech v1 by combining it with the reactor network and heat loss model of the pilot plant, and compare the predictions and measurements. 3.) If Mech v1 performs satisfactorily, use it to identify the critical pathways to the following aromatics/aromatic precursors through sensitivity

analysis: 1, 3-cyclopentadiene (CPD), benzene, indene and naphthalene. 4.) Add the missing aromatic chemistry identified in step 3 to RMG's kinetic and thermochemistry databases in the form of new reaction families, training reactions and Benson-style group additivity values (GAV's) and corrections for thermochemistry.[314] 5.) Create an RMG mechanism for NG HTP, referred to hereafter as Mech v2, without relying on the Narayanaswamy reaction library, such that all PAH chemistry is derived from RMG's database. Mech v2 will then consist entirely of elementary steps for PAH formation, the predictions of which can be validated against the pilot plant measurements.

The main advantage of a chemical mechanism consisting of all elementary steps, as opposed to one containing non-elementary, empirically-fitted steps, is twofold. First, it is easier to extrapolate such a mechanism to other reaction conditions because the real temperature (and sometimes pressure) dependence of each elementary step is already accounted for. Second, improvement of the mechanism is straightforward. For example, if a sensitive reaction is identified that relies on a general rate rule, the modeler can easily improve upon this estimate by performing a QM calculation of the reactants and transition state (TS) involved in the elementary reaction, using transition state theory (TST) to predict the high-pressure limit kinetics, and adding the new kinetic parameters to the RMG database in the form of a training reaction. The new training reaction will then be used in subsequent RMG jobs not only to describe the kinetics of the sensitive reaction in question, but will also be applied to analogous reactions. In this manner, both the specific mechanism of interest to the modeler improves with time, as does the RMG database.

The following subsections describe the results obtained with Mech v1 and the improvements made to the RMG database as a result, specifically in relation to aromatic chemistry. The predictions of Mech v2 are then presented in the Results and Discussions section. It is the hope of the authors that the methodology presented here, which allowed us to go from limited, empirical knowledge of a type of chemistry (aromatic chemistry in this case) to a detailed, physics-based mechanism, can serve as an example to future mechanism developers.

Because the process being modeled consists of two distinct steps, burning of fuel for heat and cracking of hydrocarbons to produce C2's, both Mech v1 and v2 were also generated in a two-step process, Figure 5-1. The mechanisms were initiated with a "seed mechanism" consisting of H_2/O_2 chemistry.[315] The first RMG job was run using the conditions of the burner,

and relying on several libraries of small molecule thermochemistry that are not well-described by group-additivity estimates,[316] as well as a reaction library based on the Foundational Fuel Chemistry Model Version 1.0 (FFCM-1) for combustion of small hydrocarbon fuels (such as methane).[4] The RMG-predicted burner exit composition is then mixed with 12 different cracking gas mixtures, representative of the pilot plant runs, in different ratios ("Low" versus "High" heat duty). A total of 24 different RMG jobs are spawned, each for a different cracking gas mixture, to simulate the chemistry in the cracking section. The cracker simulations also use the same small-molecule thermochemistry and reaction libraries as the burner simulation. In the case of Mech v1, the Narayanaswamy reaction library is also used. Once all 25 jobs have converged, they are automatically merged such that overlapping reactions are not duplicated. Finally, if requested, libraries of aromatic reactions (or any reactions) can be appended onto the mechanism. This can be useful if the modeler wants to guarantee that certain chemistry is included in the mechanism that might have been overlooked by RMG's flux-based criterion. The final merged (and possibly appended) mechanisms can then be used to simulate both the burner and cracker sections, for a variety of cracking gas mixtures. More detailed versions of Figure 5-1 specific to Mech v1 and v2 are included in Appendix F.
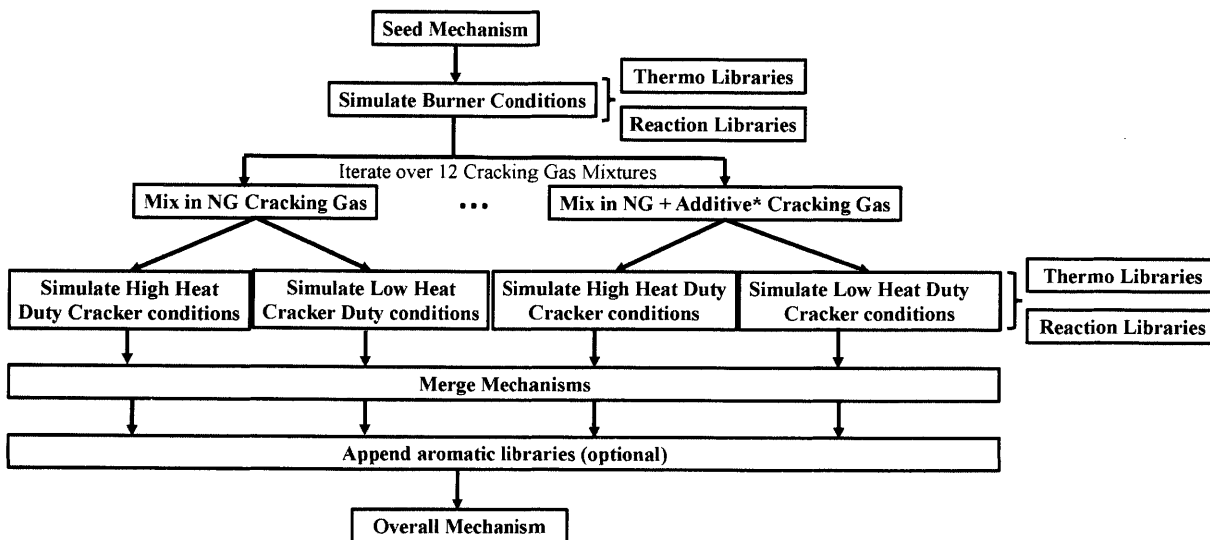
Figure 5-1: General flow diagram for development of RMG mechanisms for two-stage NG HTP. The composition of *additives are listed in Table 5-2.

5.3.1.1 Mech v1 (RMG + Narayanaswamy)

The agreement between the measurements and Mech v1 predictions of the pilot plant runs was deemed satisfactory and sensitivity analysis was performed, Table 5-3 (see section 5.4.3 for a detailed description of how sensitivity was quantified). Briefly, Table 5-3 shows the most sensitive reactions with respect to the composition of the six major species (C_2H_2, C_2H_4, CO, CO_2, CH_4 and H_2) and of four representative aromatics/aromatic precursors (CPD, benzene, indene and naphthalene), across all 71 simulated pilot plant runs. Remarkably, only 19 reactions (out of more than 10,000 reactions total in the mechanism) distinguish themselves as most sensitive across a wide range of pilot plant conditions. Importantly, 13 out of the 19 highly sensitive reactions are non-elementary. In various ways described below, previous mechanism developers have converted these complex, multi-step chemical processes into simple, single-step effective reactions that empirically match experiments.

For the small molecules, almost all of the sensitive reactions (#1-9) come from the FFCM-1 reaction library,[4] including the three non-elementary reactions: #1, 6 and 7. In turn, the authors of FFCM-1 obtained kinetic parameters for reactions #1, 6 and 7 from low-pressure limit calculations on each PES.[3, 317-318] As demonstrated by pressure-dependent calculations on these surfaces, for most combustion relevant pressures (<100 atm) assuming the kinetics to be in the low-pressure limit is entirely justifiable.

The 10 remaining reactions (#10-19) are all non-elementary and they all came from the Narayanaswamy library,[311] wherein different assumptions were made to obtain the simplified kinetics ultimately used. Reactions #10 and #12 were estimated based on experimental measurements.[319-320] For reactions #11, 13 and 14, phenomenological kinetics were used based on full RRKM/ME pressure-dependent calculations on the relevant surface.[207, 321] For reactions #15, 17 and 18, entrance onto the corresponding PES was assumed to be rate-limiting, and therefore was adopted as the overall rate coefficient.[322-324] #16 was estimated based on the analogous methyl radical + cyclopentadienyl radical system.[321] Finally, #19 was simply assumed to be in the collision limit.

Although most of the sensitive reactions in Mech v1 are based on estimates, this analysis illuminated what are expected to be the dominant pathways to aromatics, and therefore dictated what pathways should be added to the RMG database. Recombination of propargyl radical (C_3H_3) to form either fulvene or benzene (#13 and 14) was found to be particularly important,

because without this pathway benzene will not form, severely limiting PAH formation. However, this pathway involves some unusual singlet carbene chemistry that was not included in the RMG database. Therefore, an entire subsection (5.3.1.2) is dedicated to this one critical pathway, and the many additions to the RMG database needed to account for it. The remaining, more conventional, aromatic forming pathways added to the database are then discussed together in a single subsection (5.3.1.3). Finally, section 5.3.1.4 details another important improvement that had to be made to the database before Mech v2 could be created: a better algorithm for estimating thermochemistry of highly strained polycyclics.

Following all of the aforementioned changes to the RMG database, Mech v2 was generated in RMG following the general flow diagram in Figure 5-1 (specific flow diagram shown in Figure F 2). All of the model predictions in the Results and Discussions sections were obtained using Mech v2.

Table 5-3: Summary of most sensitive reactions for major species using Mech v1. + and − indicate net positive or negative sensitivity.

#	Sensitive Reactions	Sensitive for: C_2H_2	C_2H_4	CO	CO_2	H_2	CH_4	CPD	Ben-zene	Indene	Naph-thalene
1	$\dot{C}H_3 + \dot{C}H_3 \Longleftrightarrow H^\bullet + H_3C{-}\dot{C}H_2$	+	+	−	+	+	−		+		
2	$H^\bullet + HC{\equiv}CH \Longleftrightarrow H\dot{C}{=}CH_2$	+	−		−		−		−		
3	$H^\bullet + CH_4 \Longleftrightarrow H_2 + \dot{C}H_3$	+	+	−	+	+	−		+		
4	$H^\bullet + H_2C{=}CH_2 \Longleftrightarrow H_2 + H\dot{C}{=}CH_2$	+	−	−	+	+	+		+		
5	$H^\bullet + HC{\equiv}{-}OH \Longleftrightarrow H\dot{C}{\diagup}{\diagdown}OH$	−		+	−	+			−		
6	$\dot{O}H + HC{\equiv}CH \Longleftrightarrow H^\bullet + O{=}C{=}CH_2$	−		+	−	+	+		−	−	−
7	$\dot{O}H + CO \Longleftrightarrow H^\bullet + O{=}C{=}O$			+	−	−			+		
8	$H^\bullet + \dot{C}H_3 \Longleftrightarrow CH_4$						+				
9	$H^\bullet + H_2C{=}CH_2 \Longleftrightarrow H_2\dot{C}{-}CH_3$	+	+			+	−				
10	$H\dot{C}{=}C{=}CH_2 + HC{\equiv}CH \Longleftrightarrow$ (cyclopentadienyl radical)							+			
11	$\dot{C}H_3 +$ (cyclopentadiene) $\Longleftrightarrow 2H^\bullet +$ (fulvene)							−	+	+	
12	$H^\bullet +$ (cyclopentadienyl) $\Longleftrightarrow HC{\equiv}CH + H\dot{C}{\diagdown}$							−			
13	$H\dot{C}{=}C{=}CH_2 + H\dot{C}{=}C{=}CH_2 \Longleftrightarrow$ (fulvene)								+	+	
14	$H\dot{C}{=}C{=}CH_2 + H\dot{C}{=}C{=}CH_2 \Longleftrightarrow$ (benzene)								+	+	
15	(benzyl radical $\dot{C}H_2$) $+ HC{\equiv}CH \Longleftrightarrow H^\bullet +$ (indene radical)									+	+
16	$\dot{C}H_3 +$ (indene) $\Longleftrightarrow$ (naphthalene) $+ 2H^\bullet$									−	+

17	⇔ + H·										+
18	⇔										+
HC≡CH											
19	⇔									+	+
HC·=C=CH₂											

235

5.3.1.2 Improvements to RMG Database 1: Enable Propargyl Radical Recombination to Benzene

Scheme 5-1: Elementary steps from propargyl radical recombination to fulvene and benzene.

As shown in Scheme 5-1, the pathway from C_3H_3 recombination to fulvene/benzene involves two cyclic singlet carbenes as critical intermediates.[207] Therefore, RMG must first be able to accurately estimate singlet carbene thermochemistry using its group additivity approach[314] before any kinetic information can be imported. Fortunately, the thermochemistry of seven singlet carbenes containing a diversity of functional groups have already been calculated[7] (RQCISD(T)/cc-PV ∞ QZ//B3LYP/6-311++G(d,p) with bond additivity corrections) and are included in RMG's built-in "DFT_QCI" thermo library. These seven carbenes were used to fit seven new thermochemistry group corrections specifically for singlet carbenes, which were organized into a new branch of RMG's thermochemistry group correction tree (Figure 5-2 and Table 5-4). In addition, both the five- and six-membered cyclic singlet carbenes that appear on the C_3H_3 recombination PES have readily available thermochemistry from Miller et al.[207] (same level of theory as for the other carbenes), which were used to create thermochemistry group corrections specific to those critical intermediates (CsJ2_singlet-(Cds-Cds-Cds-Cds)Cs_5_ring and CsJ2_singlet-(Cds-Cds-Cds-Cds)Cs_6_ring, respectively). It is crucial that these two

intermediates have their own thermochemistry group correction(s) that captures the stabilizing, electron-donating effect of the doubly-conjugated π-bond network neighboring the vacant p-orbital of the singlet carbene, since it is the atypical stability of these carbenes that make the overall pathway to fulvene/benzene feasible.[325]
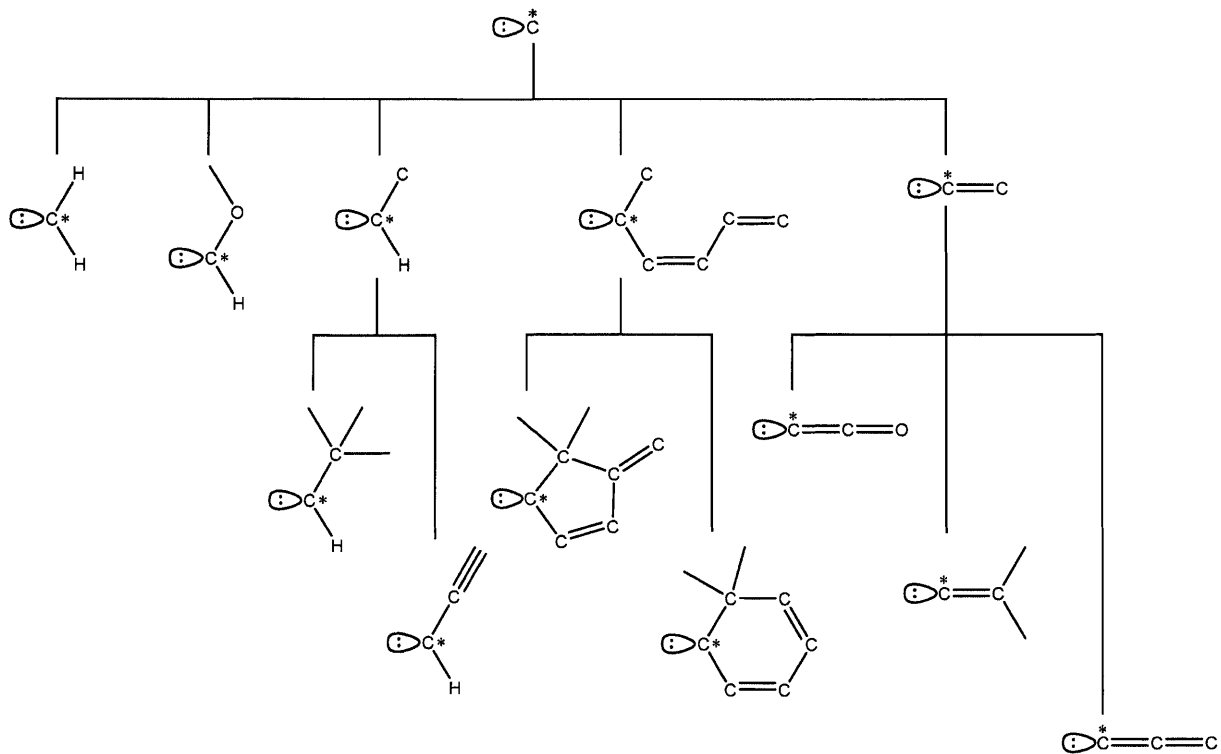
Figure 5-2: Organization of thermochemistry group corrections for singlet carbenes added to RMG database. Any unspecified ligand or valency is a wild card.

Table 5-4: Details of singlet carbene thermochemistry group corrections added to RMG database.
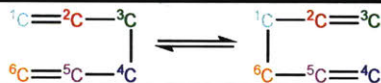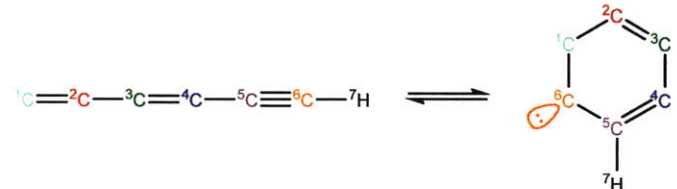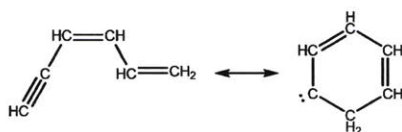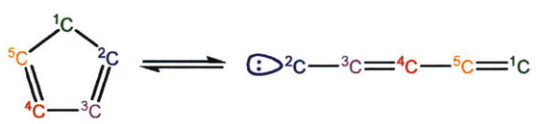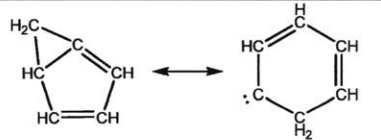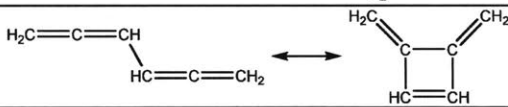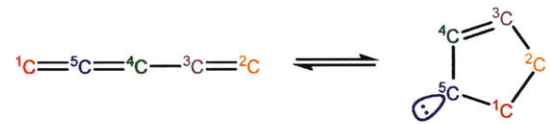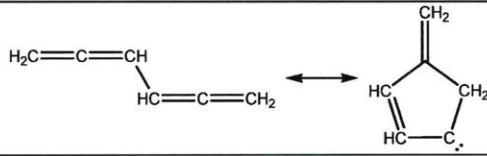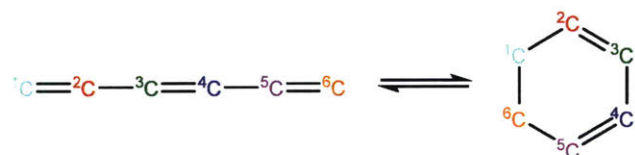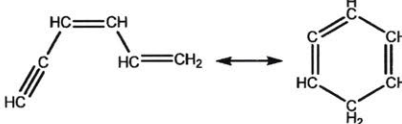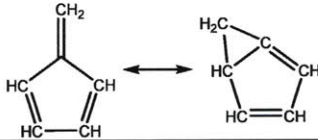
Group	Name	Source of Thermochemistry	Ref.
	CJ2_singlet	CsJ2_singlet-CsH	[316]
	CsJ2_singlet-HH	: CH$_2$	[316]
	CsJ2_singlet-OsH	HC——OH	[316]
	CsJ2_singlet-CH	CsJ2_singlet-CsH	[316]
	CsJ2_singlet-CsH	HC——CH$_3$	[316]
	CsJ2_singlet-CtH	HC——C≡CH	[316]
	CsJ2_singlet-(Cds-Cds-Cds-C)C	CsJ2_singlet-(Cds-Cds-Cds-Cds)Cs_6_ring	[207]
	CsJ2_singlet-(Cds-Cds-Cds-Cds)Cs_5_ring	: C	[207]

	CsJ2_singlet-(Cds-Cds-Cds-Cds)Cs_6_ring		207
	CdJ2_singlet-Cd	CdJ2_singlet-Cds	316
$:\overset{*}{C}=C=O$	CdJ2_singlet-(Cdd-Od)	$:C=C=O$	316
	CdJ2_singlet-Cds	$:C=CH_2$	316
$:\overset{*}{C}=C=C$	CdJ2_singlet-(Cdd-Cds)	$:C=C=CH_2$	316

Once the capability to accurately estimate singlet carbene thermochemistry was added to RMG, attention could be given to the kinetics aspect of C_3H_3 recombination. Of the 13 elementary steps in Scheme 5-1, only two belonged to an existing reaction family in RMG (both "tail-to-tail" and "head-to-head" recombination belong to the R_Recombination family; "tail-to-head" is not shown because it is essentially a dead-end). The remaining 11 elementary reactions were grouped into eight new reaction families and added as training reactions to the new families in the RMG database, Table 5-5.

At this point, it is worthwhile to mention the advantage of "teaching" RMG new chemistry using the approach presented here (thermochemistry group corrections, reaction families and training reactions) as opposed to simply creating a thermochemistry/reaction library for the relevant chemistry. By incorporating new chemistry into the RMG database, rather than circumventing it *via* libraries, this knowledge will automatically be applied to all analogous systems, whereas a library will not. Using C_3H_3 recombination as an example, if one of the hydrogens in propargyl radical was replaced with a methyl group, RMG would be able to apply the new reaction families and thermo group corrections to find an analogous pathway to a branched aromatic. The possibility of such pathways was proposed by Miller et al. when the original C_3H_3 recombination route to benzene was first fully elucidated,[207] but to our knowledge this chemistry has not been explored, likely due to the overwhelming number of possible radical recombination pairs. RMG can facilitate this exploration, but only if it is aware of the relevant chemistry, as it is now.

Table 5-5: New reaction families added to RMG database in order to capture elementary steps from propargyl radical recombination to benzene. All training reactions are from Miller and Klippenstein.[207]

Family	Name	Training Reactions
	6_membered_central _C-C_shift*	
	Concerted_Intra_ Diels_alder_ monocyclic_1,2_shiftH	
	Cyclopentadiene_ Scission	
	Intra_2+2_ cycloaddition_Cd	
	Intra_5_membered_ conjugated_ C=C_C=C_addition	
	Intra_Diels_alder_ Monocyclic	
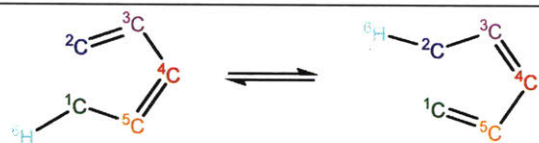
Intra_ene_reaction*
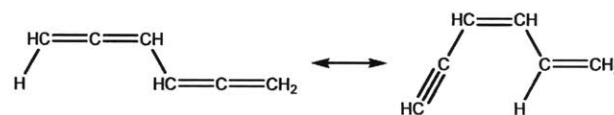
Singlet_Carbene_
Intra_Disproportionation
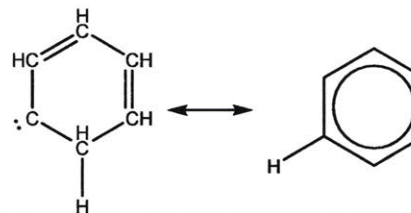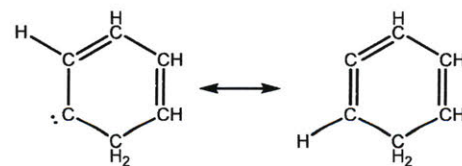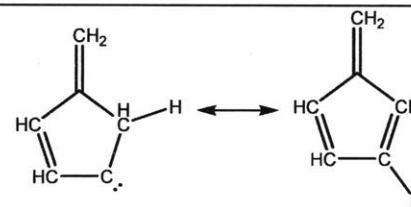
*Reaction family is its own reverse, therefore every training reaction appears twice in RMG database, in both forward and reverse directions.

Finally, as a check that all of the relevant aspects of the C_3H_3 recombination pathway to benzene were incorporated into the RMG database, RMG was used to reproduce the 1,5-hexadiyne pyrolysis experiments of Stein et al.[26] (Figure 5-3). This experiment was used by Miller et al. to validate their predictions,[207] which are also show for comparison. The slight disagreement in the transition from a 3,4-methylenecyclobutene dominated product distribution to a fulvene dominated distribution is likely due to subtle thermochemistry differences because the RMG predictions are relying on group additivity estimates for all species. Nonetheless, the agreement is satisfactory and provides confidence that RMG should now be able to accurately predict benzene formation through C_3H_3 recombination, which has long been considered the dominant path to benzene and higher aromatics starting from only small molecules (like those in NG).
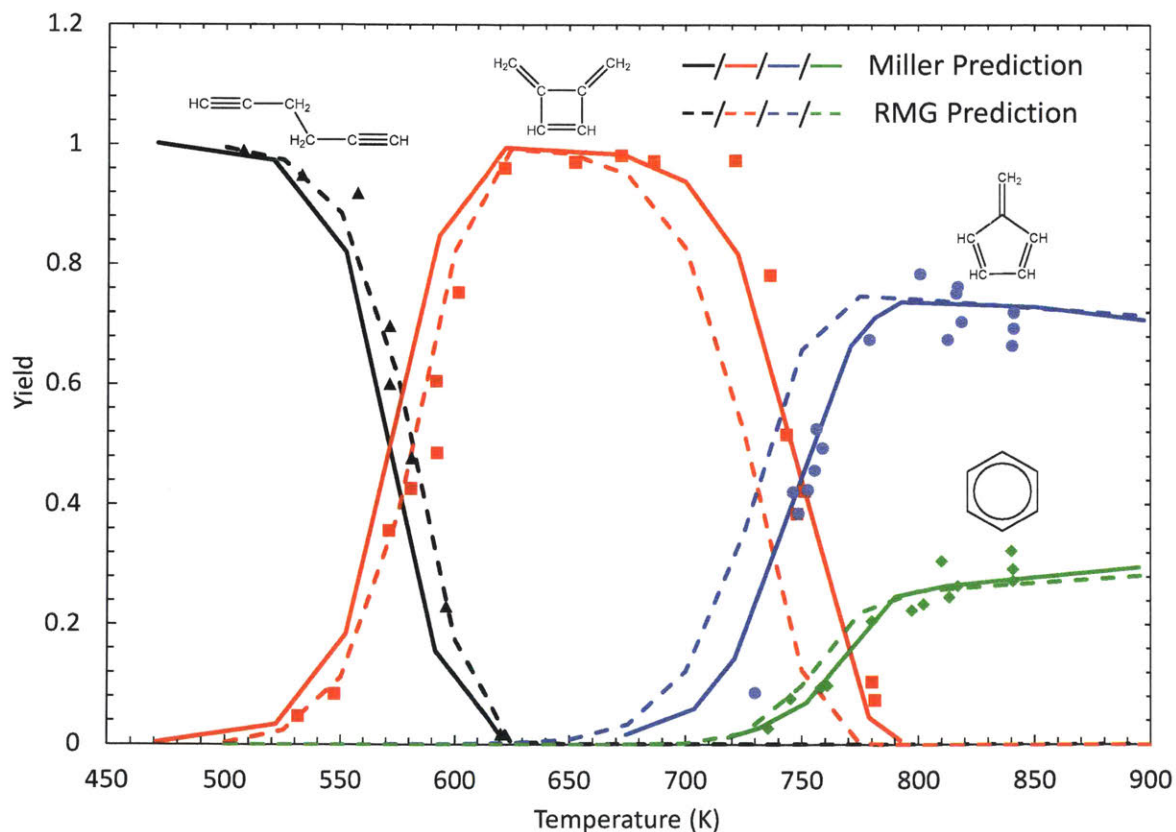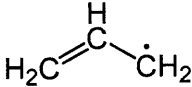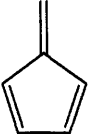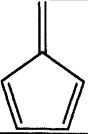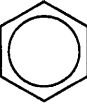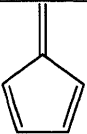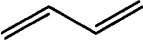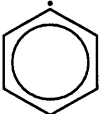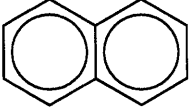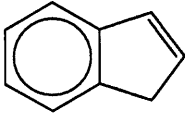
Figure 5-3: Comparison between predictions of Miller[207] and RMG, following database changes, and 1,5-hexadiyne pyrolysis experiments of Stein et al.[26] (symbols).

5.3.1.3   Improvements to RMG Database 2: Include Kinetics of Other Aromatic Forming/Consuming Pathways

In addition to the aromatic-forming/consuming pathways identified by the Mech v1 sensitivity analysis in section 5.3.1.1, Mebel et al. also identified a total of ten important pathways to naphthalene (six) and indene (four)[61] that were added in this work as elementary training reactions to the RMG database. Four of the pathways overlap between Mebel et al. and the sensitivity analysis on Mech v1 presented in Table 5-3 (reactions #15-18). In total, 15 different pathways to/from aromatics/aromatic precursors (CPD, fulvene, benzene, indene and napthalene) were added to the RMG database, Table 5-6. Many of the pathways involve steps on different sections of the same PES ($C_{10}H_9$ for example), and incorporating all of them into RMG's database helps a more complete understanding of each PES emerge.

The sources of the kinetic parameters are indicated, almost all of which are derived from calculations already available in literature. New calculations were needed only for the phenyl radical (C_6H_5) + propene (C_3H_6) pathway. For C_6H_5 + C_3H_6, Kislov et al.[9] covered all of the major pathways on their calculated PES except for the new "aromatic-catalyzed" 1,2-H-migration discussed in section 4.2. The aromatic-catalyzed pathway, which enables benzyl radical (C_7H_7) and C_2H_4 to appear as major products of C_6H_5 + C_3H_6, has been added as training reactions to RMG's database.

Table 5-6: Pathways to aromatics/aromatic precursors added as elementary training reactions to RMG database.

Route	Global Pathway to CPD/Fulvene/Benzene/Indene/Naphthalene	Molecular Formula of Relevant PES's	Refs.
A	$HC^\bullet{=}C{=}CH_2$ + $HC{\equiv}CH$ ⟶ (cyclopentadienyl)	C_5H_5	326
B	(H$_2$C=C(H)-$\dot{C}$H$_2$) + $HC{\equiv}CH$ ⟶ (cyclopentadiene) + $H^\bullet$	C_5H_7	326
C	$HC^\bullet{=}C{=}CH_2$ + $HC^\bullet{=}C{=}CH_2$ ⟶ (fulvene / benzene)	C_6H_6	207
D	$H^\bullet$ + (fulvene) ⟶ $H^\bullet$ + (benzene)	C_6H_7	326
E	$\dot{C}H_3$ + (cyclopentadienyl) ⟶ (fulvene) + $2H^\bullet$	C_6H_8	321
F	$HC^\bullet{=}CH_2$ + (1,3-butadiene) ⟶ (benzene) + $3H^\bullet$; (cyclopentadiene) + $\dot{C}H_3$	C_6H_9	77 327
G	(phenyl radical) + $2HC{\equiv}CH$ ⟶ (naphthalene) + $H^\bullet$	C_8H_7 $C_{10}H_7$	328
H	(phenyl radical) + $HC^\bullet{=}C{=}CH_2$ ⟶ (indene)	C_9H_8	322

CH₂ ... reaction diagrams

Label	Products formula	Ref.
I	C₉H₉	242
J	C₉H₁₁	9, Section 4.2
K	C₁₀H₉	61
L	C₁₀H₉ / C₁₀H₁₀	326
M	C₁₀H₉ / C₁₀H₁₀ / C₁₀H₁₁	242, 329
N	C₁₀H₁₁	326
O	C₁₀H₁₁	236

Besides simply inputting kinetic data as training reactions in the RMG database, it is equally important that that the new training reactions match sufficiently descriptive "reaction templates" for a given reaction family. Otherwise, distinguishing chemical features of the new
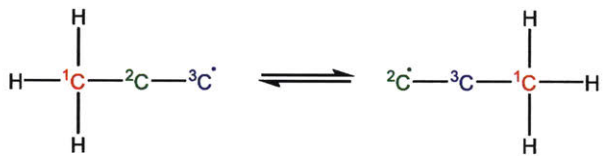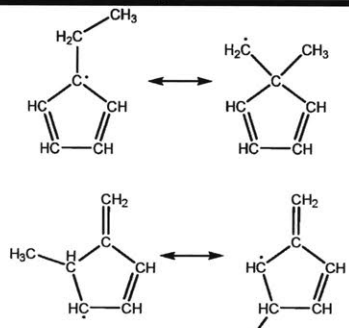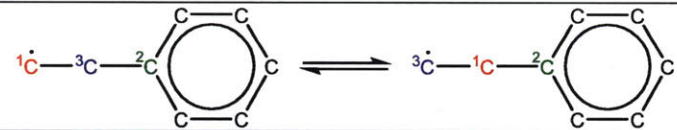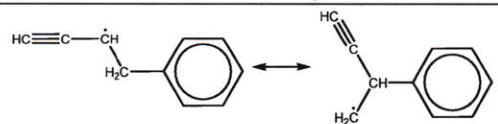
training reaction may go essentially unnoticed by RMG, representing an underutilization of the data. Therefore, care was taken to ensure that every training reaction added had its essential features captured by the matching reaction template of its reaction family. If a template was deemed insufficiently descriptive, more specific entries were added to that reaction family's hierarchical tree of functional groups that are used to construct the template. Scheme 5-2 summarizes the appropriate relationship between a reaction family, reaction template and training reaction. In this example (taken from the phenyl + vinylacetylene PES[61]), the reaction template captures the essential features of an intramolecular hydrogen migration from a benzene ring to a resonantly-stabilized radical site on an ortho-positioned chain. The position of the reaction template within the reaction family's hierarchical structure is also important, as it determines how training reactions are generalized to similar reactions. Consideration was also given to this point when adding the training reactions of Table 5-6.
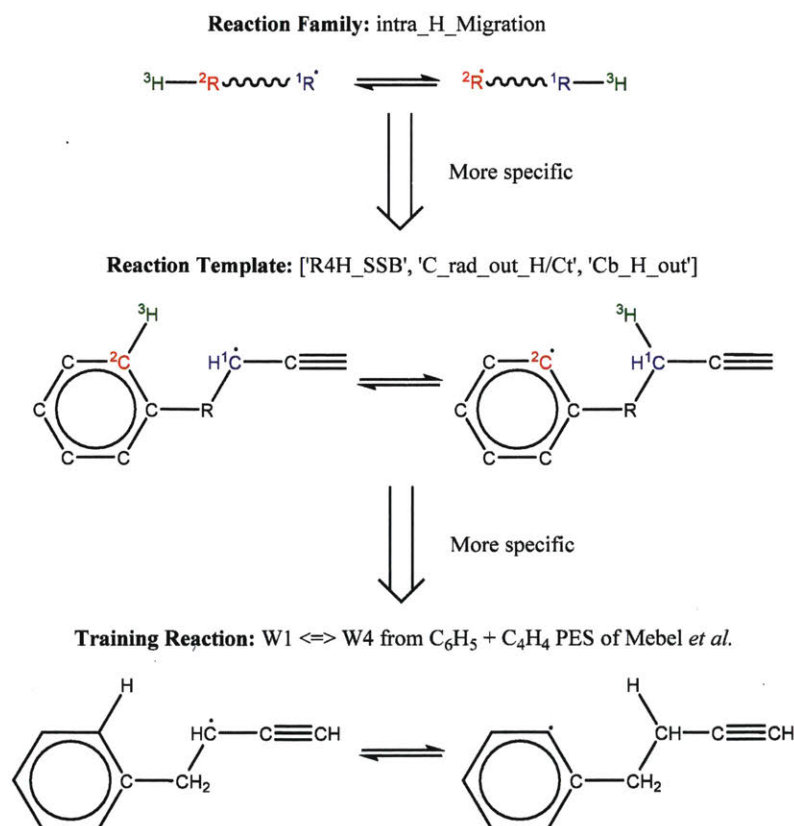
Scheme 5-2: Example of the relationship between a reaction family, reaction template and a training reaction in the RMG database. Any unspecified ligand or valency in the reaction family or template is a wild card.

Compared to C_3H_3 recombination to fulvene/benzene, the pathways in Table 5-6 are much more conventional. Almost all of the relevant elementary steps can be capture by five pre-existing RMG reaction families[181]: R_Addition_MultipleBond, intra_H_migration, R_Recombination and Intra_R_Add_Exocyclic/Endocyclic. As shown in Table 5-7, however, there were a few elementary reactions that needed new RMG reaction families. The Intra_R_Add_Exo_scission reaction family is particularly interesting because it raises the possibility of an aromatic group "walking" along the length of an alkyl radical chain, which could have a measurable impact on the final products of alkylbenzene pyrolysis, for example.[330] This new family was trained on an elementary reaction found by Mebel et al. on the phenyl + vinylacetylene (C_4H_4) PES.[61] By generalizing this specific training reaction to an entirely new reaction family, RMG is more likely to encounter new, unexplored chemistry.

Table 5-7: New reaction families added to RMG database in order to capture all known elementary steps involved in aromatic formation.

Family	Name	Training Reactions	Ref.
	1,2_shiftC[*]		326
	Intra_R_Add_Exo_scission[*]		61

[*]Reaction family is its own reverse, therefore every training reaction appears twice in RMG database, in both forward and reverse directions.

Most of the pathways to indene/naphthalene in Table 5-6 involve growth off of a phenyl radical substrate, largely through the straightforward 3-step process of C_6H_5 attack of an unsaturated hydrocarbon, cyclization and β-scission. The main exceptions are the pathways through CPD and 1,3-cyclopenatadienyl radical (CPD'yl), which, as detailed by Merchant,[326] go through a very different set of elementary steps, some involving tricyclic intermediates. As a means of validating RMG's ability to predict the unusual, but important, chemistry of CPD following the database additions above, an RMG-generated mechanism for CPD pyrolysis was compared to experimental measurements of the same process[331] (Figure 5-4). Only the six major species are shown (CPD, H_2, CH_4, benzene, indene and naphthalene), which together account for more than half of the mass balance at all temperatures (the remaining mass is mostly in larger PAH, which is not included in the RMG mechanism for reasons explained later). Although the predictions of RMG appear to be shifted to higher temperatures relative to the measurements, qualitatively all of the major species were found by RMG, and are predicted to have the correct relative abundance (mass fraction naphthalene > indene > benzene). As expected, indene is predicted to form mostly through the CPD + CPD'yl pathways, whereas naphthalene forms through CPD'yl + CPD'yl. Benzene forms through methyl radical (CH_3) addition to either CPD or CPD'yl (C_6H_9 and C_6H_8 PES's in Table 5-6), followed by H-loss and rearrangement on the H-assisted fulvene isomerization PES (C_6H_7 in Table 5-6). The qualitative agreement in Figure 5-4 and subsequent pathway analysis demonstrates that following the improvements to the RMG database outlined above (and an improvement to polycyclic thermochemistry estimation, discussed in the next section) it is possible for RMG to reasonably describe the unique chemistry of CPD.
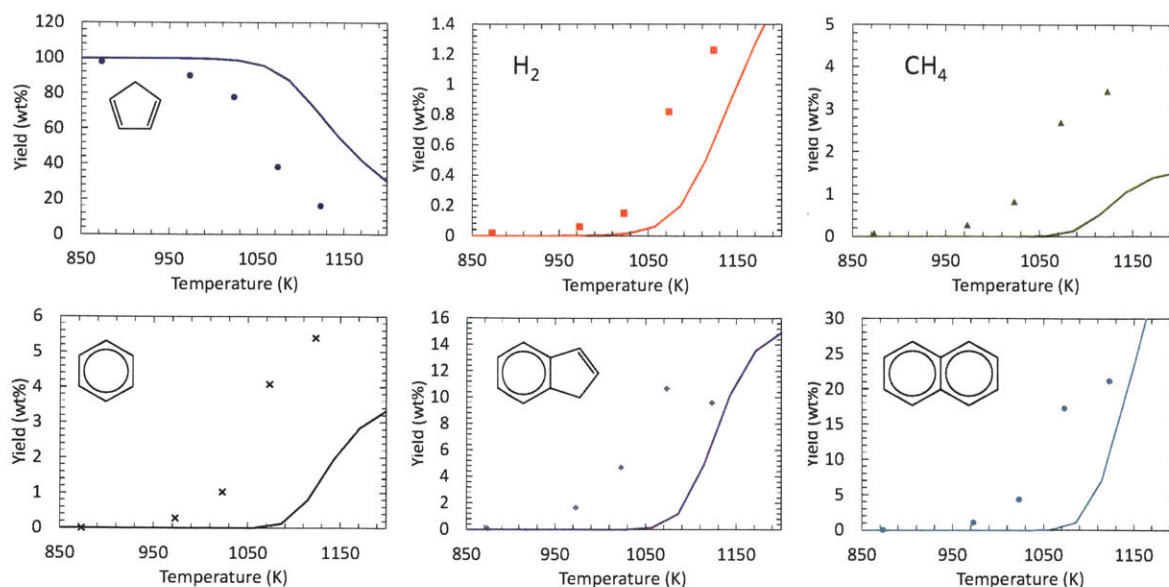
Figure 5-4: Comparison between predictions of RMG following database changes (lines), and 1,3-cyclopentadiene pyrolysis experiments of Djokic et al.[331] (symbols).

A key selling point of RMG is its potential to predict chemistry that might otherwise be overlooked, and indeed during initial attempts at generating Mech v2 for NG HTP, RMG proposed an unexpected pathway to naphthalene: phenyl radical + diacetylene (C_4H_2), Scheme 5-3. Largely drawing from training reactions on the $C_6H_5 + C_4H_4$ PES, superficially $C_6H_5 + C_4H_2$ seems like a reasonable route to 2-naphthyl radical (i3) as well as a radical precursor to benzofulvene (i4). However, CBS-QB3 QM calculations on the energetics of the RMG proposed pathway show that although the initial radical addition ($C_6H_5 + C_4H_2$ to i1), intramolecular H-migration (i1 to i2-trans) and ring-closing steps (i2-cis to i3 and i4) are all feasible (and estimated well by RMG's database), the step with the highest energy barrier is actually a trans-cis isomerization (i2-trans to cis). The CBS-QB3 calculated barrier is ~60 kcal, which is similar to what Kislov et al. calculated for the same high-energy isomerization.[332] The trans-cis isomerization is necessary to orient the triple bond on the alkene chain close enough to the radical site on the ring to initiate five- or six-membered ring closure. Unfortunately, RMG currently does not distinguish cis-trans isomers, the underlying assumption being that the energetic barrier to rotation around the double bond is small compared to other unimolecular isomerization barriers, such that equilibration of the cis-trans isomers is fast relative to everything else. Clearly the assumption of fast cis-trans equilibration is not valid in the case of

$C_6H_5 + C_4H_2$, and as a solution library reactions from i2-trans to i3 and i4 were created using the kinetics of i2-trans to i2-cis as the effective rate for the overall process. Including this effective library reaction in subsequent iterations of Mech v2 generation precluded naphthalene (and benzofulvene) production from $C_6H_5 + C_4H_2$.
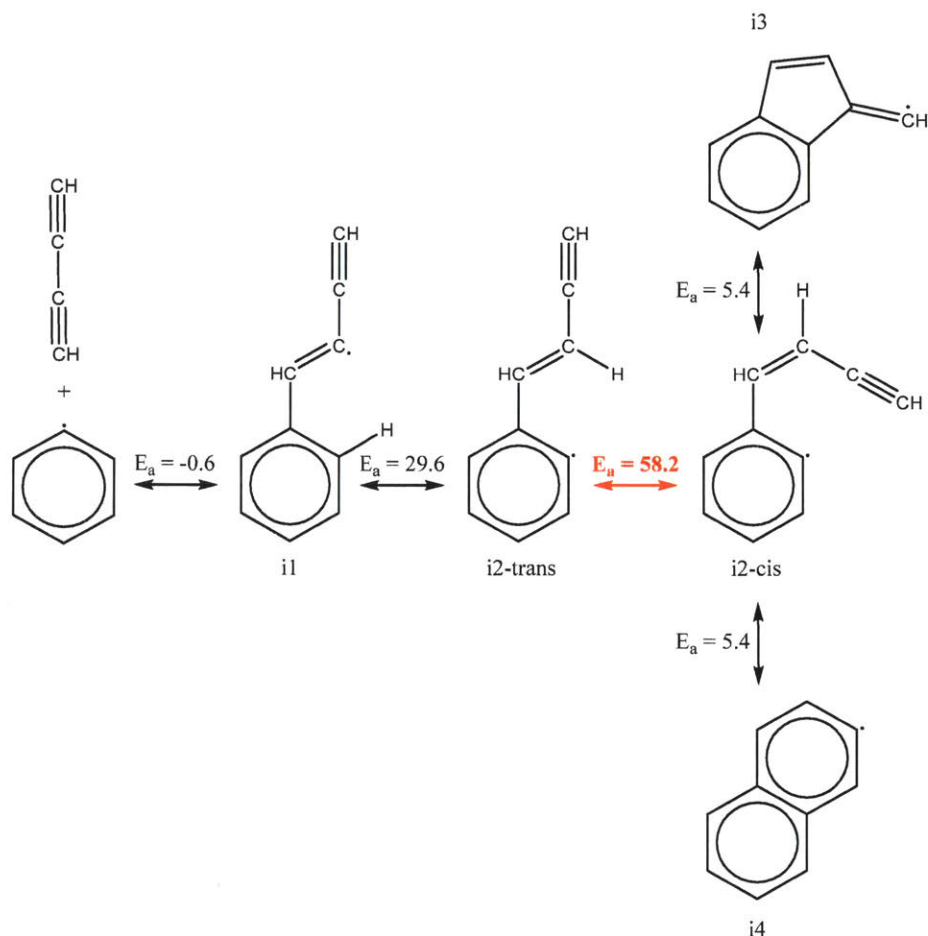
Scheme 5-3: RMG-proposed pathways from phenyl radical and diacetylene to naphthalene and benzofulvene precursors. Forward activation energies given in kcal/mol (ZPE-inclusive CBS-QB3), with rate-limiting step in red.

As a final note regarding the kinetics of aromatic-forming/consuming reactions, Table 5-6 is by no means an exhaustive list of important aromatic chemistry, especially if larger PAH is considered. In particular, phenyl addition/cyclization (PAC), wherein single aromatic rings can rapidly grow to many-ring PAH (see section 6.3.2),[27] will not be described well by the current RMG database. This is primarily due to a lack of RMG-friendly kinetic data for PAC in the literature. Nonetheless, the pathways listed in Table 5-6 (and C_3H_3 recombination discussed in

section 5.3.1.2) should be sufficient to describe the chemistry of CPD, fulvene, benzene, indene and naphthalene. Because RMG is not expected to know all of the chemistry of larger PAH, a constraint was placed on Mech v2 to only generate species with at most ten carbon atoms (like naphthalene). There is also another more fundamental reason for placing a cap on the largest species generated by RMG, as discussed in the next section.

5.3.1.4   Improvements to RMG Database 3: Polycyclic Thermochemistry Estimation

RMG estimates the thermochemistry of cyclic or polycyclic species by adding a ring strain correction (RSC) on top of the molecule's group-additivity predicted thermochemistry.[181] The RMG database contains a number of RSC's based on calculations for specific molecules, but it is impossible to have a specific pre-computed RSC for every possible cyclic/polycyclic. Therefore, empirical algorithms for estimating RSC's for any arbitrary ring structure have been developed and validated against a large data set of training molecules.[333] For polycyclic molecules with three or more rings, the algorithm for estimating RSC's is exemplified by Scheme 5-4. Essentially, the polycyclic is broken down into bicyclic components that have RSC entries in the RMG-database. The bicyclic RSC's are summed, and to prevent double-counting the RSC's of overlapping monocyclics, also in the database, are subtracted, in order to obtain the estimated polycyclic RSC.

Ring Strain Correction (kcal/mol):	45.6	33.9	37.9	26.2
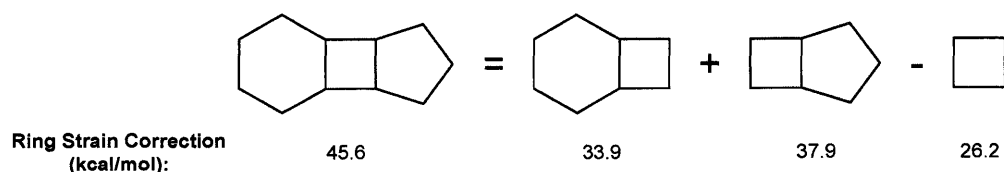
Scheme 5-4: Example of polycylic ring strain correction estimation algorithm.

The algorithm demonstrated in Scheme 5-4 works well provided the bicyclic and monocyclic components actually have RSC values in the database. However, compiling a complete database of RSC's just for bicyclic molecules is still combinatorically impractical, so another estimation algorithm was needed specifically for bicyclics, Scheme 5-5. As shown, the RSC of an unsaturated bicyclic is estimated by starting with the RSC of its saturated form, subtracting out the RSC of the saturated monocyclic components, and adding in the RSC of the true unsaturated monocyclic components. For the example below, it is clear that the majority of the ring strain comes from the unsaturated 1,2-cyclopentadiene unit.

| Ring Strain Correction (kcal/mol): | 74,5 | 14.9 | 6.3 | 65.9 |
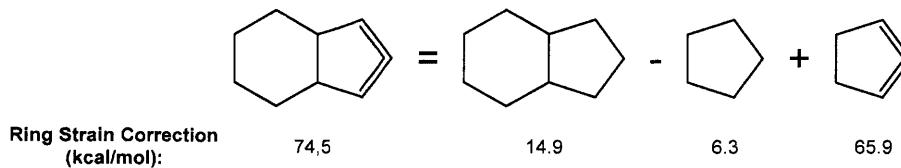
Scheme 5-5: Example of bicyclic ring strain correction estimation algorithm.

Without this bicyclic RSC estimation algorithm, if a highly strained bicylic such as the one in Scheme 5-5 does not have an exact match in RMG's RSC database, it will be approximated as the average RSC of similar molecules. The accuracy of the averaging approach is highly dependent on how well-populated the RSC database is and how "similar" is defined. Generally, the averaging approach largely underestimated RSC's of strained bicyclics, Figure 5-5, leading to an overprediction of such species in RMG, and diverting flux from more realistic species such as indene/naphthalene. The problem is compounded by the fact that the polycyclic RSC estimation algorithm in Scheme 5-4 relies on accurate bicyclic RSC's, so if a particular bicyclic RSC is underestimated, so will the RSC of many higher-order polycyclics and the RMG mechanisms will become crowded with many highly-strained polycyclics.

Figure 5-5 demonstrates for a small sample of 19 strained bicyclics (containing strained 1,2-CPD, cyclopentyne and cyclopropene monocyclic subunits) that the new bicyclic RSC algorithm matches their "true" (M06-2X calculations used as benchmark) thermochemistry much more accurately than the old averaging approach. A larger data set was later used to make this same point in Han et al.[333] Both the polycycic (Scheme 5-4) and bicyclic (Scheme 5-5) RSC estimation algorithms were implemented in creating Mech v2, which noticeably reduced the population of highly-strained polycyclics in the final mechanism.
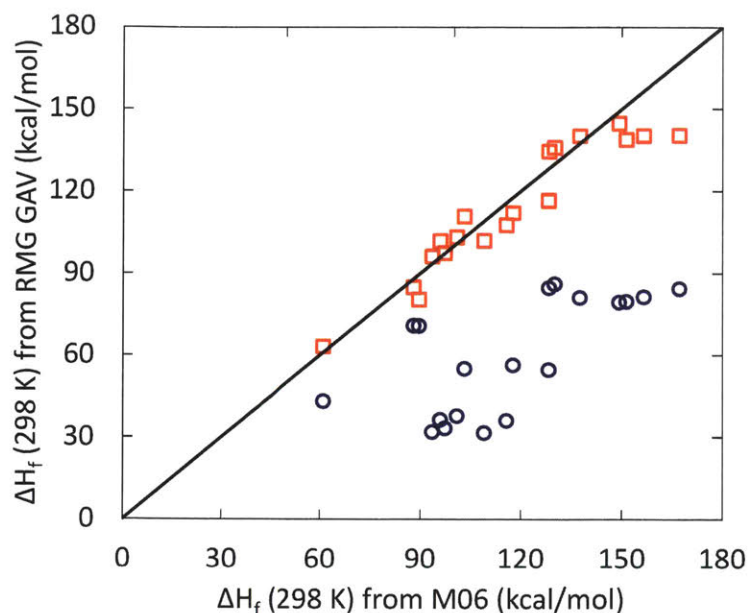
Figure 5-5: Performance of RMG's GAV thermochemistry estimates for 19 strained bicyclics without (blue circles) and with (red squares) the new bicyclic estimation algorithm.

Another limitation of the algorithm in Scheme 5-4 is that it works best for linear polycyclics, such as the one in the example given. It starts to break down for fused tricyclics, such as the indene derived molecule in Scheme 5-6. In this case, the RSC of the strained tricyclic is estimated using a linear combination of RSC's for bicyclics and monocyclics with little to moderate ring strain. Clearly, none of the constituents in Scheme 5-6 can accurately capture the strain experienced by the tricyclic. As a result, the tricyclic is estimated to be much more stable than it actually is, and appears as a major product of NG HTP. This is the main reason for limiting the maximum number of carbon atoms in any species to ten in Mech v2. Until RMG can predict RSC's for fused polycyclics more accurately, such a constraint on maximum species size will always need to be in place in order to obtain reasonable mechanisms.

Ring Strain Correction (kcal/mol): 9.2   2.1   2.1   17.0

0.0   6.0   6.0
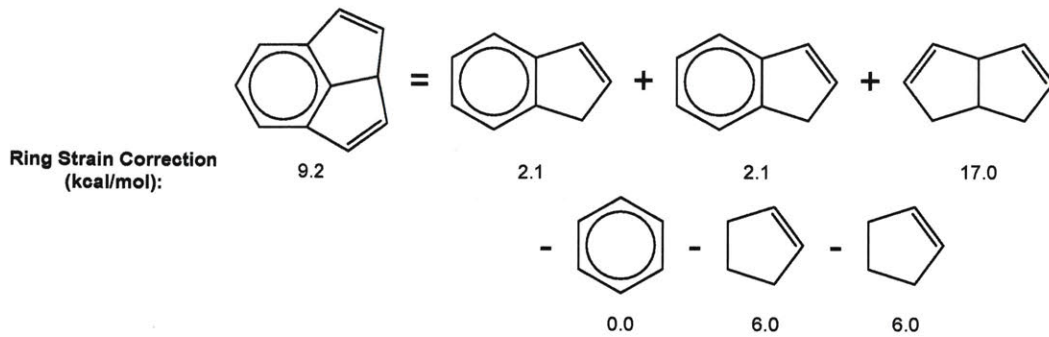
Scheme 5-6: Example of polycyclic thermochemistry estimation algorithm breaking down.

5.3.2   Reactor Network

The SABIC pilot plant HTP reactor was modeled as a series of ideal reactors, including a perfectly stirred reactor (PSR, also called CSTR in chemical engineering vernacular), plug flow reactors (PFR's) and a mixer (Figure 5-6). The simulations were performed using CHEMKIN 15151.[247] The burner section was simulated using a perfectly stirred reactor (PSR1) for the flame region and a short plug flow reactor (PFR1) for the post-flame region. The inlet streams to the PSR are a fuel (natural gas) and an oxidizer stream. The cracking gas is introduced after PFR1 and it instantaneously mixes with the effluent stream from PFR1 in a Mixer. The second reaction zone is simulated using two plug flow reactors with different diameters (PFR2 and PFR3). The exit composition from the last plug flow reactor (PFR3) was compared to the pilot plant data.
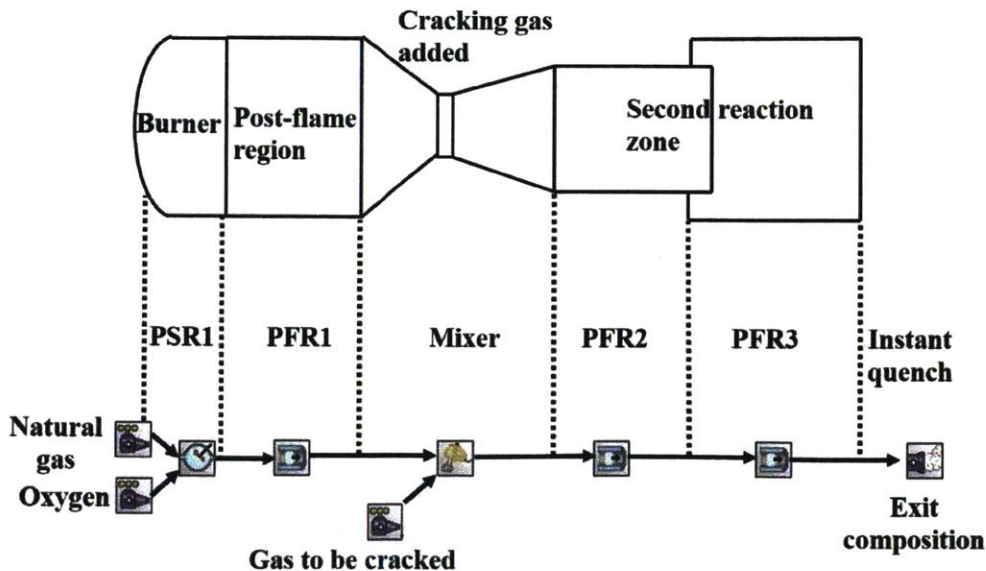
Figure 5-6: Reactor network for the High Temperature Pyrolysis (HTP) process.

A representative temperature profile from a reactor network simulation is shown in Figure 5-7. The temperature in the burner section is approximately 3100 K and it drops to 2800 K in the post-flame region. The addition of 'cold' cracking gas results in a temperature drop from 2800 to 1700 K. The temperature further decreases in the second reaction zone from 1600 K to 1200 K. The decrease in temperature along the axial length of the reactor is due to the addition of cracking gas at lower temperature, endothermic reactions and the use of a heat transfer coefficient which accounts for convective heat loss at the cooled walls of the reactor. More details about calculation of the heat transfer coefficient are provided in the next section.
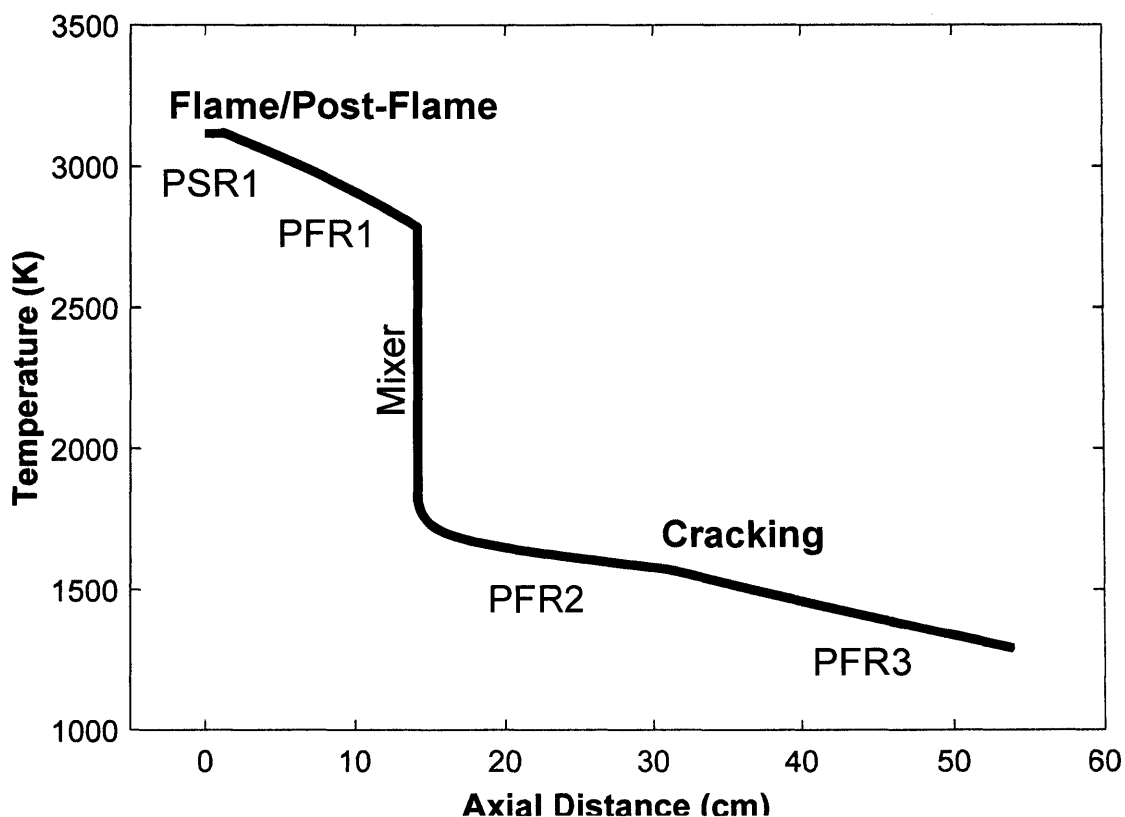
Figure 5-7: Representative axial temperature profile in the reactor network.

Figure 5-8 shows the dry mole fractions of the species measured at the pilot plant for a representative run: methane (CH_4), hydrogen (H_2), carbon monoxide (CO), carbon dioxide (CO_2), acetylene (C_2H_2) and ethene (C_2H_4). The stoichiometric ratio of fuel and oxidizer in the burner results in immediate consumption of methane in the flame region, and a negligible dry mole fraction of methane in the burner region. Introduction of natural gas as cracking gas results in an increase in mole fraction of methane followed by a rapid and then a slower

decrease as it is consumed to form H_2 and C2's. CO and CO_2 are diluted by the added cracking gas, and are also affected at very early residence times by the cracking chemistry.
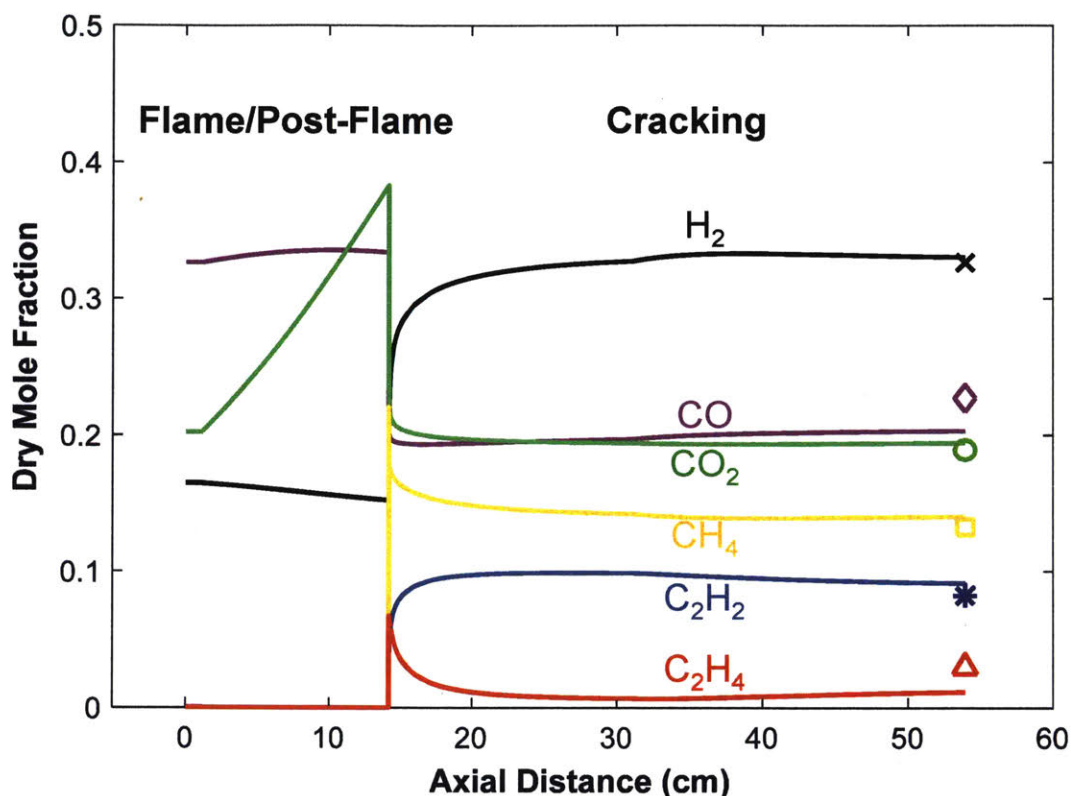
Figure 5-8: Representative dry mole fraction profiles of species measured at pilot plant vs. reactor axial distance. Lines are model predictions and symbols are measurements.

5.3.3 Heat Loss

The walls of the pilot plant reactor are water-cooled, necessitating a model for convective heat loss inside of the reactor. Without such a model, the predicted temperature profiles along the reactor length (Figure 5-7) are too high, resulting in accelerated chemistry that is not in agreement with the actual pilot plant measurements. Figure 5-9 shows the effect of heat loss on simulated temperature and major species profiles for a typical run. As shown, the major species concentrations are highly sensitive to heat loss. In particular, the temperature immediately after the cracking gas has been added is critical to the final composition because most of the cracking occurs at that location. Even a change of only ~60 K in this "critical temperature" has a substantial impact on the exit mole fractions of H_2, CO, CO_2 and CH_4. Therefore, it was necessary to accurately account for the convective heat loss within the reactor. Interestingly, the

exit mole fractions of C_2H_2 and C_2H_4 are predicted to be less impacted by such a variation in the critical temperature.
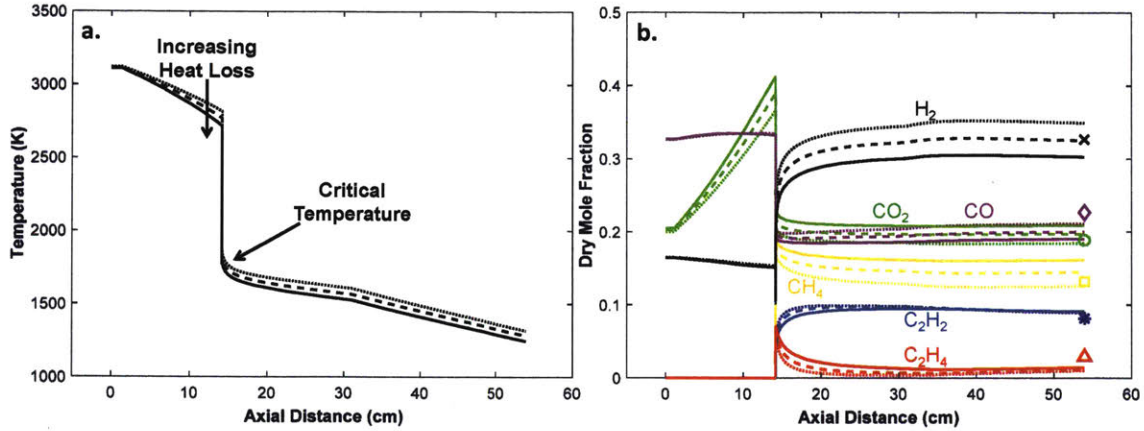
Figure 5-9: (a) Temperature profile and (b) species profiles for a range of heat loss values in the reactor. Lines are model predictions and markers are measurements.

CHEMKIN models heat loss along a PFR using the following equation (PSR uses integrated form), where either the heat transfer coefficient, h, or the heat flux per unit length, $\frac{dQ}{dz}$, must be specified by the user (alternatively a temperature profile can be input directly):

$$\frac{dQ}{dz} = \pi Dh[T(z) - T_0] \tag{5-1}$$

D is the PFR diameter, T is the gas temperature and T_0 is the wall temperature. For the model presented in this work h was specified and the reactor wall temperature was assumed to be 300 K. h was first estimated using the empirical correlation of Sieder and Tate for highly-turbulent forced convection in a tube[334]:

$$Nu = \frac{hd}{k} = 0.026 Re^{0.8} Pr^{\frac{1}{3}} \left(\frac{\mu_b}{\mu_0}\right)^{0.14} \tag{5-2}$$

Nu is the Nusselt number, D is the tube diameter, k is the gas thermal conductivity, Re is the Reynold's number, Pr is the Prandtl number, and $\left(\frac{\mu_b}{\mu_0}\right)$ is the ratio of gas viscosities at the bulk and wall temperatures. The gas properties necessary for Eq. 5-2 were estimated from Tables/equations in Bird, Stewart and Lightfoot[335] (viscosity, k and Pr) and RMG's database (heat capacity). For typical pilot plant conditions, Re > 20,000, satisfying the highly-turbulent criteria for Eq. 5-2. Note that because Re is proportional to linear flow velocity, U, which is in

turn proportional to the pilot plant heat duty (inlet flow of fuel and oxidizer and burner section), it is expected that h will roughly scale as (Heat Duty)$^{0.8}$.

Estimated values of h at different heat duties according to Eq. 5-2 were then tuned to match the measured pilot plant heat loss in the burner and cracker sections for 42 of the 71 runs (quantified by the temperature rise of the cooling water). For each heat duty, it was necessary to fit a separate h for the burner (PSR1 and PFR1) and cracker (PFR2 and PFR3) sections. The tuned cracker h was well within the uncertainty of the estimate, whereas the tuned burner h was typically ~3-4 times higher, possibly due to significant radiative heat loss at the burner temperature (~3000 K). Figure 5-10 compares the measured and predicted burner and overall (burner + cracker) heat loss after tuning h. As mentioned earlier, heat loss is shown to increase with heat duty. All subsequent predictions used this model for heat loss.
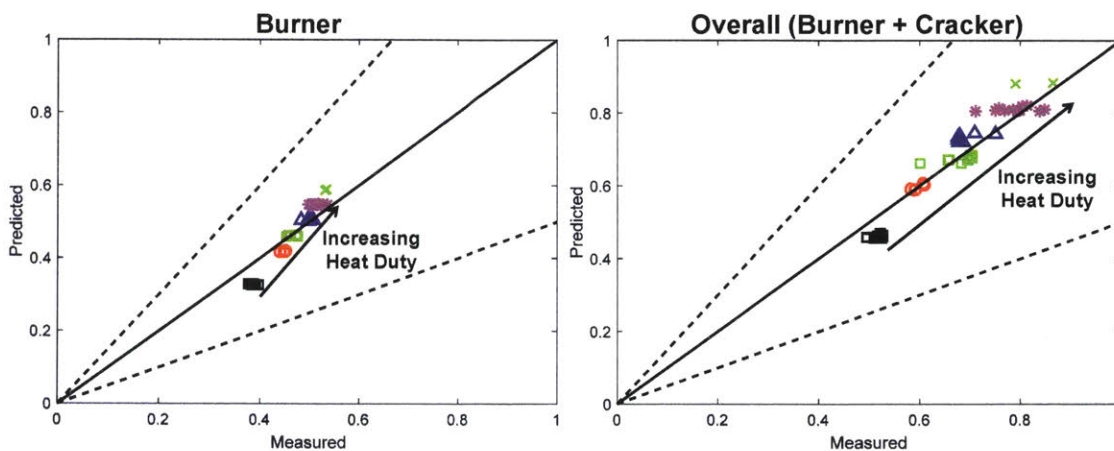
Figure 5-10: Parity plots of normalized heat loss along burner and overall length of pilot plant reactor.

5.4   Results and Discussion

All of the results below were generated using Mech v2 and the simple reactor network shown in Figure 5-6.

5.4.1   Model Comparison to Pilot Plant Data

The (dry) exit mole fractions of major species for 71 runs measured at the pilot plant are compared to our model predictions in Figure 5-11. The various symbols denote different cracking gas compositions. The predicted dry mole fractions of H_2, CO and CO_2 are in close agreement with the pilot plant measurements, whereas CH_4 is systematically underpredicted. This discrepancy could be resolved by adjusting the rate parameters of important reactions

within their uncertainty limits (#1, 2, 3, 6 or 8 shown in Table 5-8) or by tuning the heat transfer coefficient. However, because the predicted CH_4 concentration is still within a factor of 2 for most of the runs, such adjustments to the model were deemed unnecessary.
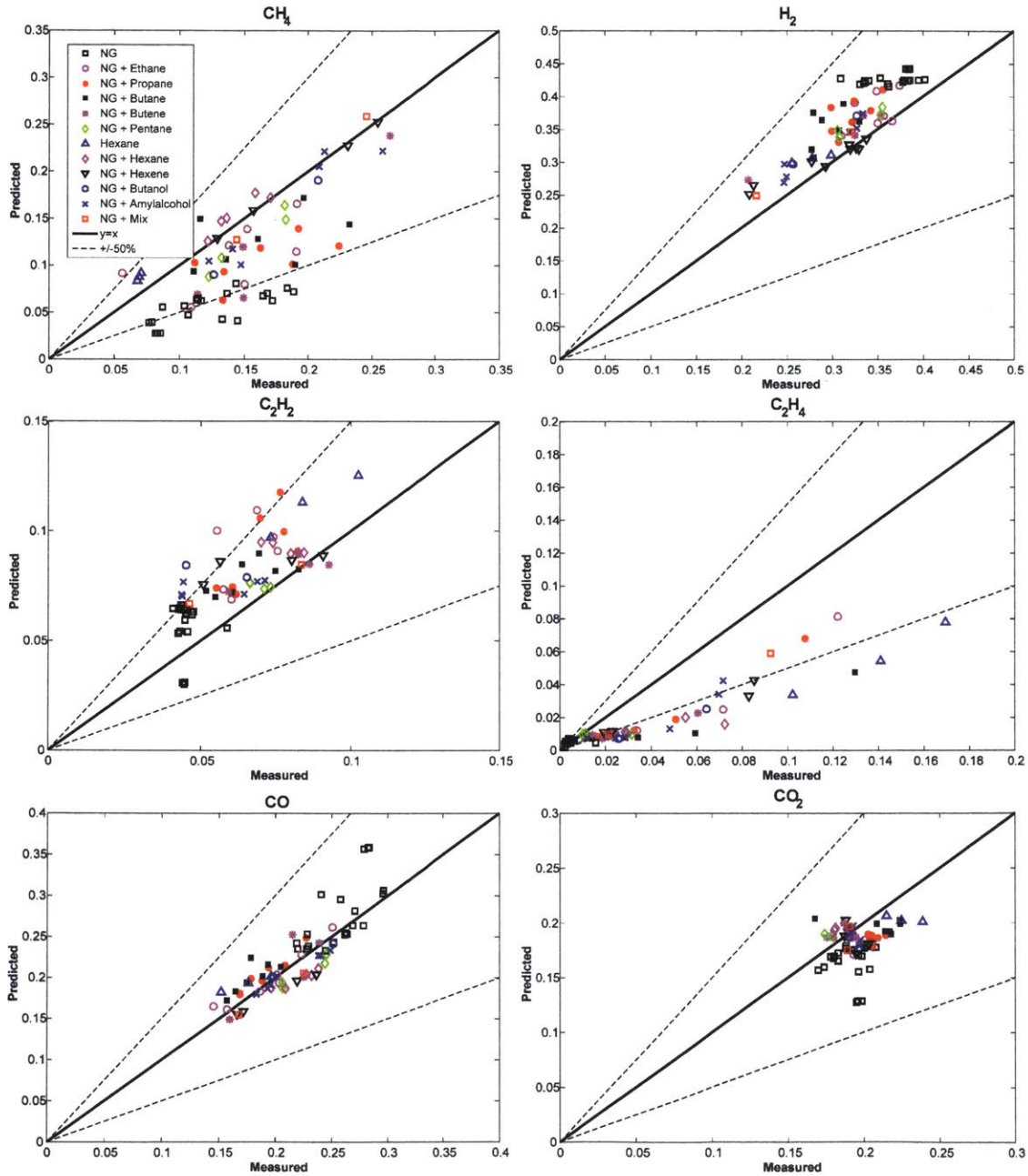
Figure 5-11: Parity plots of dry HTP reactor exit composition measured at the pilot plant and predicted by model.

Regarding the C2 products, while C_2H_2 is overpredicted for most of the runs and C_2H_4 is underpredicted, the combined yield of C_2H_2 and C_2H_4 is close to parity (Figure 5-12). Because C_2H_2 will be converted to C_2H_4 at a later stage in the process anyway,[286] the agreement between the model and pilot plant measurements for C2 yield was deemed satisfactory for the current purposes. More accurately describing the distribution of C2's between C_2H_2 and C_2H_4 will require a more detailed experimental data set against which to compare RMG's predictions, such as the CH_4 POX experiments of Kohler et al.[294] This will be one of the objectives of a forthcoming chemistry-oriented publication spearheaded by Te-Chun Chu.
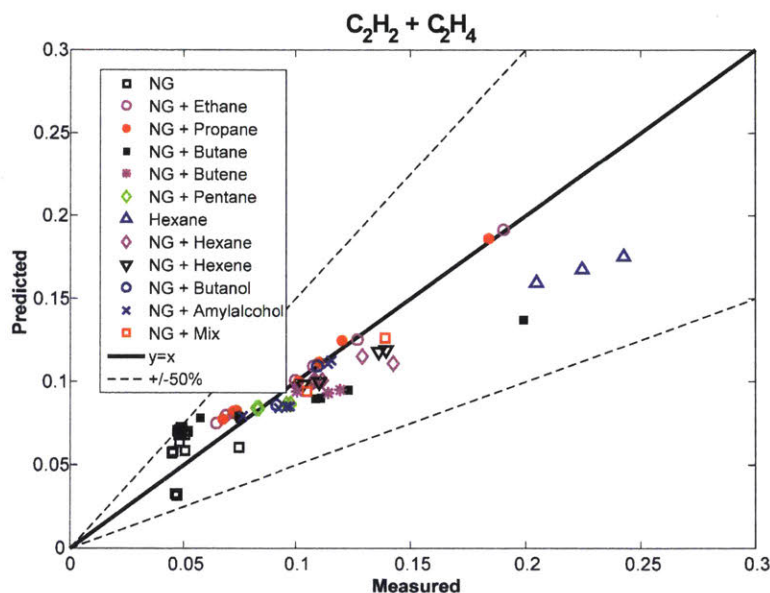
Figure 5-12: Parity plot of dry C2 exit composition (acetylene + ethylene) measured at the pilot plant and predicted by model.

5.4.2   Predicted C2 and Aromatic Yields

Both the predicted C2 and lumped aromatic yields at the exit of the HTP reactor for all 71 pilot plants runs are plotted as functions of overall equivalence ratio, ϕ, and cracking gas carbon number in Figure 5-13 and Figure 5-14, respectively. C2 yield is defined as the fraction of carbon atoms in the cracking gas that are incorporated into C2's (either C_2H_2 or C_2H_4) at the exit of the HTP reactor:

$$\text{C2 Yield} = \frac{\text{C atoms in } C_2H_2 \text{ at exit} + \text{C atoms in } C_2H_4 \text{ at exit}}{\text{Total C atoms in Cracking Gas}} \qquad (5\text{-}3)$$

The lumped aromatic yield is simply the summed mass fraction of all of the aromatic containing compounds at the exit of the reactor (mostly consisting of benzene, phenylacetylene,

phenyldiacetylene, styrene, indene and naphthalene). Overall ϕ is defined as the ratio of the stoichiometric amount of O_2 that would be needed to convert all of the hydrocarbons (both in the fuel and cracking gas) into CO_2 and H_2O, and the actual amount of O_2 fed into burner section:

$$\phi = \frac{\text{Stoichiometric } O_2 \text{ Input}}{\text{Actual } O_2 \text{ Input}} \qquad (5\text{-}4)$$

For all of the pilot plant runs, $\phi > 2.0$ in order to maintain fuel-rich conditions appropriate for pyrolysis. Finally, the cracking gas carbon number is defined as the moles of carbon atoms per mole of cracking gas:

$$\text{Cracking Gas Carbon Number} = \frac{\text{Moles of C atoms in Cracking Gas}}{\text{Moles of Cracking Gas}} \qquad (5\text{-}5)$$

For example, a pure NG cracking gas would have a carbon number ≈ 1 (almost pure CH_4), and a cracking gas consisting of an equimolar mixture of NG and propane would have a carbon number ≈ 2.
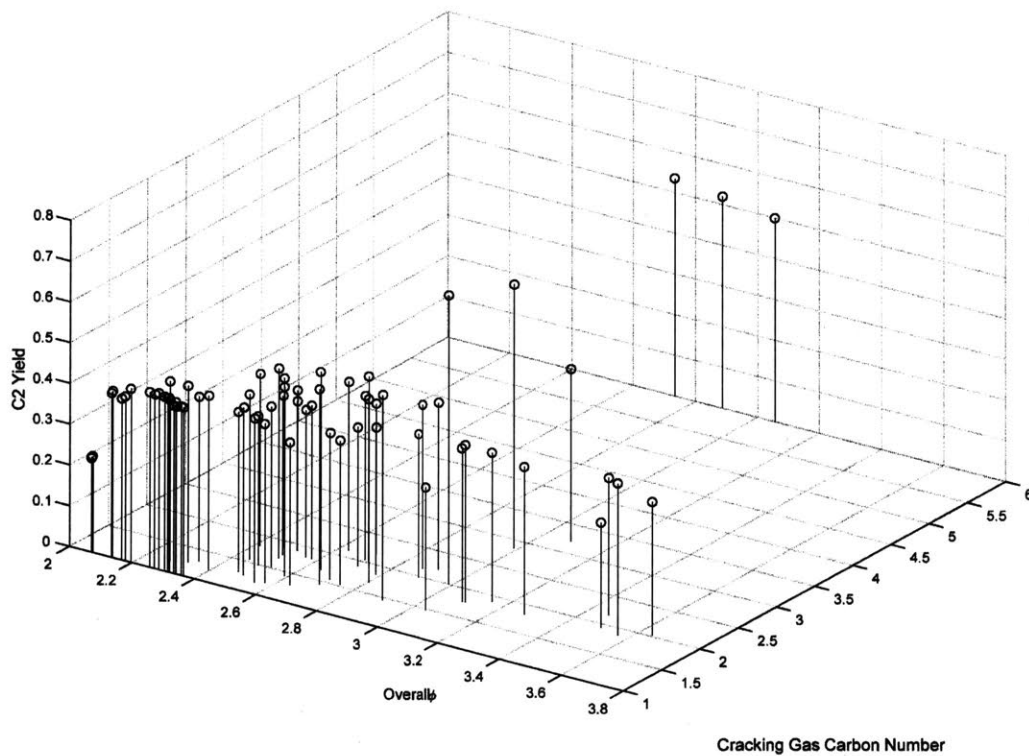
Figure 5-13: Predicted C2 yield for 71 pilot plant runs as a function of overall equivalence ratio, ϕ, and cracking gas carbon number.
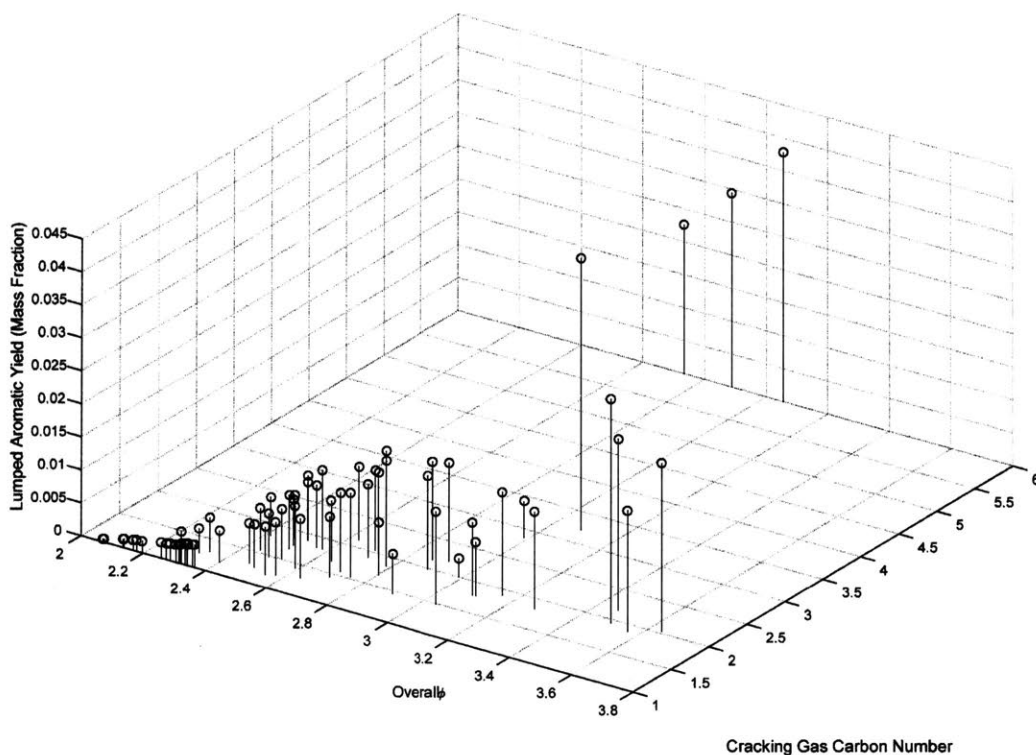
Figure 5-14: Predicted lumped aromatic yield for 71 pilot plant runs as a function of overall equivalence ratio, φ, and cracking gas carbon number.

The predicted C2 yield in Figure 5-13 has already been validated by comparisons to the actual pilot plant measurements in Figure 5-12. Interestingly, the C2 yield is always around 40-50%, largely independent of either overall φ or cracking gas carbon number. This observation might serve as a rule-of-thumb for future HTP reactor design. In contrast, there are no pilot plant measurements against which to validate the lumped aromatic yields predicted in Figure 5-14. Nonetheless, the trends exhibited by the predictions are intuitively sensible: the lumped aromatic yield appears to have a positive correlation with both overall φ and cracking gas carbon number. In other words, at more fuel-rich pyrolysis conditions with longer-chain cracking gases the propensity for aromatic formation is enhanced, entirely consistent with expectation. Of course, there are other variables to consider that are not captured by Figure 5-14, such as the degree of unsaturation of the cracking gas. Having the capability to make detailed (and hopefully accurate) models of aromatic formation will aid in future work to identify what are the critical variables dictating PAH growth, perhaps through principal component analysis (PCA). For our current purposes, however, the two variables selected by intuition, overall φ and cracking gas carbon

number, are sufficient to explain why certain pilot plant runs are expected to yield more aromatics than others.

The pilot plant runs predicted to make the most aromatics contain butane (cracking gas carbon number $\approx$ 3.2 and overall $\phi \approx$ 3.1), butene (2 and 3.5) or hexane (6 and 3) in the cracking gas. The butene prediction is particularly illuminating, because during the pilot plant campaign adding 1-butene to the cracking gas caused severe coking in the reactor that necessitated a shutdown. However, the overall ϕ for the specific pilot plant run where severe coking occurred was actually at the lower end of the range in Figure 5-14, contrary to what our predictions would suggest. This is likely due to limitations of our very simple transport model that describes the complex mixing and heat loss processes occurring in the HTP reactor as a series of ideal, perfectly-mixed reactors. Specifically, at lower ϕ the overall heat duty is generally higher, meaning that there is more gas flow in the burner section, which might make mixing in of the cracking gas more difficult. Therefore, although the overall ϕ is lower at higher heat duties, the mixing might be incomplete, creating rich "pockets" of hot cracking gas in the HTP reactor that will tend to make coke. Clearly for a complicated process such as HTP, chemistry is not the only concern, and a parallel effort is underway to model the complex transport phenomenon using computational fluid dynamics (CFD). The coupling between chemistry and transport will be especially important to take into account when modeling scale-up of HTP from a pilot-plant to an industrial reactor. Nonetheless, the model used in this work, which combines a detailed chemical mechanism with simplified transport, is useful for determining what chemical pathways are important in the overall process, and can guide future mechanism reduction necessary for full CFD simulations. Sensitivity analysis on all 71 runs is discussed next, followed by an exploration and discussion of the major decomposition and aromatic-forming pathways of the most sooting run (NG + butane cracking gas, section 5.4.4).

5.4.3   Sensitivity Analysis

Given the wide range of conditions simulated in this work (71 pilot plant runs), it was necessary to develop a standardized approach to quantifying sensitivity for two reasons: 1.) to ensure that simulations can be directly compared with one another, and 2.) to avoid being overwhelmed by data. This standardized approach is described below before presenting sensitivity results.

Using the model described in section 5.3, sensitivity analysis was conducted on the exit concentration of the six major species measured at the pilot plant (C_2H_2, C_2H_4, CO, CO_2, CH_4 and H_2), as well as of four representative aromatic/aromatic precursor species (CPD, benzene, indene and naphthalene). For a PFR, CHEMKIN reports time-integrated sensitivities of species concentrations to reaction rate coefficients. Therefore, sensitivity coefficients at the exit of either PFR2 or PFR3 (Figure 5-6) were used in this analysis, depending on in which PFR the species in question was mostly produced (PFR2 for C_2H_2, C_2H_4, CO, CO_2, CH_4, H_2 and benzene; PFR 3 for CPD, indene and naphthalene). This choice of sensitivity coefficient is equivalent to perturbing each rate coefficient in the mechanism one-by-one, solving the PFR equations for the perturbed mechanism, and measuring the impact on the exit composition. The sensitivity coefficients obtained in this manner were normalized by the maximum concentration of the species of interest along the PFR length. Normalizing by maximum rather than local concentration is preferred in this case, because many of the species (such as C_2H_2, Figure 5-8) have near-zero concentrations near the PFR entrance, which can result in arbitrarily large sensitivity coefficients if local normalization is used.

For each of the ten species, the normalized, integrated sensitivity coefficients were ranked, and the top five from each of the 71 simulations were plotted against each other. The ten resulting sensitivity plots (one for each species) could each include up to 355 unique reactions (71 simulations × 5 top sensitive reactions), but fortunately there was a great deal of overlap between simulations, and the actual plots included a manageable number of reactions. Furthermore, it was clear from these plots that certain reactions distinguish themselves as being extremely sensitive across a wide range of simulated conditions. It is these extremely sensitive reactions that are reported in Table 5-3 above (Mech v1) and Table 5-8 below (Mech v2). As shown, there is significant overlap even amongst the extremely sensitive reactions with respect to the different species, such that there are only a handful of important reactions for NG HTP across all 71 simulations. Subsequently, it is this handful of reactions that are worth deeper, future investigation.

All of the sensitive reactions for small molecules shown in Table 5-3 (#1-4 and 6-8) were previously identified using Mech v1, and their kinetics are all from FFCM-1.[4] The only exception is #6, OH + C_2H_2, for which pressure-dependent effects could be important at the pilot plant conditions, therefore a library of pressure-dependent kinetics for the OH + C_2H_2 system

was used, based on the calculations of Senosiain et al.[3] The effects of sensitive reactions #1-4 and 6-8 are generally straightforward. For example, #1 is a well-skipping reaction that converts a C1 species (methyl radical) to a C2 species (ethyl radical) and a hydrogen. Therefore, CH_4 has a net negative sensitivity to #1, while the C2's (C_2H_2 and C_2H_4) and H_2 have a positive sensitivity to #1. Another important small-molecule reaction is #7, $OH + CO \leftrightarrow H + CO_2$, which mostly runs in reverse as evidenced by the positive sensitivity for CO and negative sensitivities for H_2 and CO_2.

Unlike Mech v1, the sensitive reactions in Mech v2 for aromatics/aromatic precursor (#20-28) are all either elementary (#20, 22, 25, 27 and 28) or well-skipping based on master-equation simulations on an underlying elementary PES (#21, 23, 24, 26).[7] None of the sensitive reactions #20-28 are empirically fitted and their kinetics can all be traced back to reliable sources. #20 and #21 produce CPD *via* vinyl radical + 1,3-butadiene and both come from route F in Table 5-6 (C_6H_9 PES). #22 and #23 are part of the pathway from propargyl radical recombination to benzene (C_6H_6 PES, route C) that was discussed extensively in section 5.3.1.2. As expected, #22 and #23 are sensitive not just for benzene, but for larger aromatic that depend on benzene formation (indene and naphthalene). #24 produces propyne that is later converted to propargyl radical (which can later recombine to form benzene), whereas #25-26 effectively consume propargyl radical by recombination with methyl radical to form a C4 that is eventually converted to either vinylacetylene or diacetylene. Finally #27 converts the adduct of phenyl + propargyl radicals into a radical that can undergo ring-closure to form indene (route H), and similarly #28 "activates" a closed-shell product of phenyl radical + vinylacetylene into a radical than can form naphthalene (route K). From this brief analysis of the most sensitive aromatic-related reactions the general outline of aromatic formation is already clear: benzene is formed through propargyl radical recombination and indene/naphthalene are formed through phenyl radical reaction with propargyl radical/vinylacetylene. ROP analysis of the most sooting run (NG + butane cracking gas) in the following section will confirm this understanding and provide some additional detail.

Table 5-8: Summary of most sensitive reactions for major species using Mech v2. + and – indicate net positive or negative sensitivity. Numbering is consistent with Mech v1 sensitivity results in Table 5-3.

#	Sensitive Reactions	Sensitive for: C_2H_2	C_2H_4	CO	CO_2	H_2	CH_4	CPD	Benzene	Indene	Naphthalene
1	$\dot{C}H_3 + \dot{C}H_3 \Longleftrightarrow \dot{H} + H_3C{-}\dot{C}H_2$	+	+	–	+	+	–				
2	$\dot{H} + HC{\equiv}CH \Longleftrightarrow H\dot{C}{=}CH_2$	+	–	–			+				
3	$\dot{H} + CH_4 \Longleftrightarrow H_2 + \dot{C}H_3$	+	+	–	+	+	–				
6	$\dot{O}H + HC{\equiv}CH \Longleftrightarrow \dot{H} + O{=}C{=}CH_2$	–		+		+	+				
4	$\dot{H} + H_2C{=}CH_2 \Longleftrightarrow H_2 + H\dot{C}{=}CH_2$		–		+					+	
8	$\dot{H} + \dot{C}H_3 \Longleftrightarrow CH_4$		–		+	–	+				
7	$\dot{O}H + CO \Longleftrightarrow \dot{H} + O{=}C{=}O$			+	–	–					
20	$H\dot{C}{=}CH_2 + \;\rlap{—}\diagup \;\Longleftrightarrow\; \rlap{—}\diagup$							+			
21	$\dot{C}H_3 + \;\bigcirc \;\Longleftrightarrow\; \rlap{—}\diagup$							+			
22	structure $\Longleftrightarrow$ structure								+	+	+
23	$HC{=}C{=}CH_2 + HC{=}C{=}CH_2 \Longleftrightarrow$ structure								+	+	+
24	$\dot{C}H_3 + HC{\equiv}CH \Longleftrightarrow \dot{H} + \;\equiv\!{-}$								+		
25	$\dot{H} + {=}\dot{C}\diagup \Longleftrightarrow H_2 + \cdot{=}C\diagup$									–	
26	$\dot{C}H_3 + H\dot{C}{=}C{=}CH_2 \Longleftrightarrow \dot{H} + \cdot{=}C\diagup$									–	
27	$\dot{H} + \;$structure$\; \Longleftrightarrow\;$ structure									+	
28	$\dot{H} + \;$structure$\; \Longleftrightarrow\;$ structure										+

5.4.4 Rate of Production Analysis for Most Sooting Run

Scheme 5-7 summarizes the major predicted decomposition pathways of the butane additive in the most sooting pilot plant run. Butane mostly decomposes to propene, which can either lose a hydrogen and a methyl radical to form C_2H_2, or it can lose three hydrogens to form propargyl radical. As mentioned in the previous section, propargyl radical will mostly recombine with itself to form benzene, which can lose a hydrogen to from phenyl radical. Phenyl radical will mostly add to the acetylene and diacetylene present in high concentration to form closed shell phenylacetylene and phenyldiacetylene (and another hydrogen). Although not shown, a small amount of the phenylacetylene does go on to form naphthalene *via* the hydrogen abstraction acetylene addition pathway (HACA, route G in Table 5-6). Both phenylacetylene and phenyldiacetylene are essentially dead-ends in the current mechanism, consistent with the conclusion reached in many previous PAH studies that HACA alone is insufficient to explain rapid PAH growth.[27] Specifically, if RMG were trained on the phenyl addition/cyclization pathway (PAC) then phenyl radical would have a more expedient route to larger PAH (section 6.3.2). However, given the current limitations of RMG for accurately predicting the thermochemistry of larger polycyclic molecules (section 5.3.1.4), the current mechanism without PAC will have to suffice, and phenylacetylene/phenyldiacetylene are best regarded as proxies for the larger PAH that would actually form.
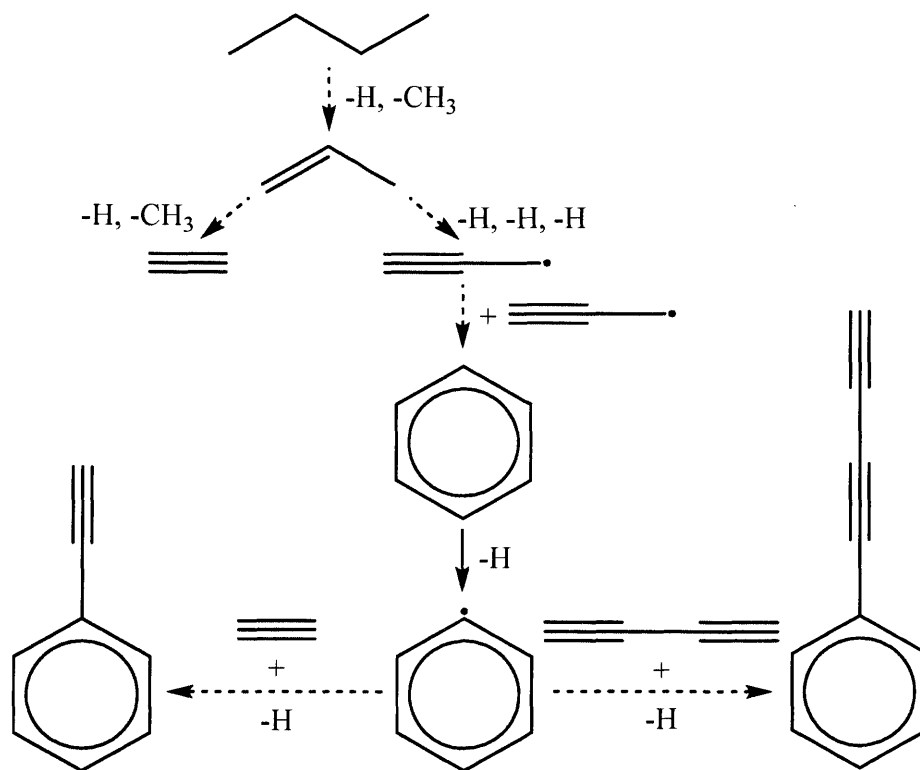
Scheme 5-7: Major predicted decomposition pathways of butane additive to cracking gas.

Scheme 5-8 shows the major routes to indene/naphthalene, both of which are predicted to form in significantly lower concentration than phenylacetylene/phenyldiacetylene. Indene is mostly formed by phenyl + propargyl radical recombination, as suggested by sensitive reaction #27 in Table 5-8, but there is also a minor route to indene through phenyl radical + propene to benzyl radical (partially through the "aromatic-catalyzed" 1,2-hydrogen migration discussed in section 4.2) and subsequent addition to acetylene (route I). Finally, naphthalene is almost exclusively formed through phenyl radical + vinylacetylene (route K), although as mentioned in the preceding paragraph some of the phenylacetylene undergoes HACA (route G).
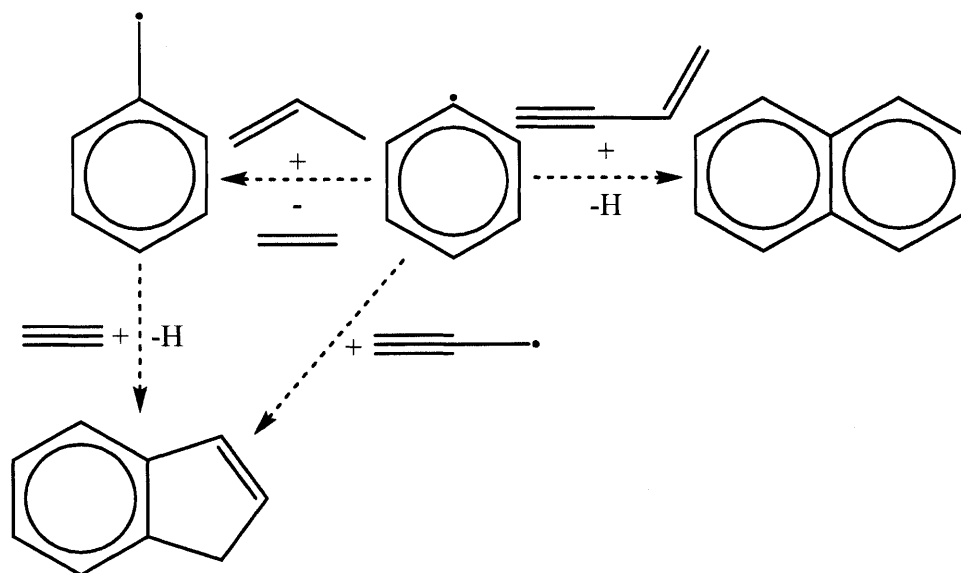
Scheme 5-8: Major predicted routes to indene and naphthalene.

From this analysis, it seems that access to propargyl radical should largely dictate PAH formation. Therefore, one can anticipate the extent of coking for HTP of a certain cracking gas mixture based on how chemically similar the constituents are to propargyl radical. For example, butane, butene and hexane can all easily decompose to propargyl radical, which would explain why our model predicts the highest aromatic yields for runs with those additives. Of course there are other routes to PAH that don't involve propargyl radical at all, such as CPD'yl recombination (route L),[336] so the best option for predicting the sooting tendency of a certain cracking gas is still a tool like RMG.

5.5   Conclusions

A model was developed for high temperature pyrolysis (HTP) of natural gas (NG) and other hydrocarbon additives. The model consists of a detailed chemical mechanism generated by RMG, a network of ideal reactors to simulate a pilot plant reactor and an empirical model for heat loss. The model compares mostly favorably with measurements of methane, hydrogen, acetylene, ethene, carbon monoxide and carbon dioxide made at the exit of the pilot plant reactor for 71 different runs using different cracking gases and heat duties. The model does slightly underpredict methane, which could be explained by the uncertainty in the handful of sensitive reactions dictating the small-molecule chemistry, or the empirical heat loss model. Ethene is also underpredicted whereas acetylene is overpredicted, but the sum of the two, which is of greatest

interest currently, is matched by the model. The model also predicts higher aromatic formation for richer overall conditions and longer-chain hydrocarbon additives. From sensitivity analysis of all 71 runs, and ROP analysis of the most sooting run, the general pathway from small-molecules to C2's to aromatics was elucidated, which highlighted the central role of propargyl radical.

The most exciting part of this work was the enhancement of RMG's ability to predict aromatic chemistry, which was discussed in great detail. The three components of the enhancement were: 1.) inclusion of the propargyl radical recombination pathway to benzene, 2.) inclusion of 14 other aromatic/aromatic precursor forming/consuming pathways, and 3.) a new algorithm for the estimation of bicyclic ring-strain. Following these changes, RMG is now able to model PAH formation up to indene/naphthalene starting from only small, linear molecules. In order for RMG to model higher-PAH formation, more improvements need to be made. Specifically, estimates of ring strain for fused polycyclic molecules need to be more accurate, and missing aromatic chemistry, such as phenyl addition/cyclization (PAC) should be added to the database.

Chapter 6

Recommendations

Over the course of completing this thesis work, I have explored many other research directions besides what was discussed in the previous chapters. Some of these alternative directions were fruitless, but for most of them there was simply insufficient time for further exploration. This concluding chapter summarizes some of the most promising/interesting directions for future research, divided into three categories: reactions systems for future study, improvements to the LAS/PI TOF-MS apparatus and improvements to RMG.

6.1 Reaction Systems for Experimental/Theoretical Study

Considering that the bulk of my PhD work was spent exploring different gas-phase reaction systems experimentally, this is also the area in which I am most qualified to give recommendations. The PES's of some of the proposed systems below are also worth theoretical exploration, as noted.

6.1.1 Continuation of Molecular Weight Growth Experiments

The most obvious future experimental direction (and fastest route to publication) is to continue experiments on molecular weight growth in combustion, i.e., PAH formation. Given that the overall workflow from experiments to applications has been demonstrated in this thesis using phenyl radical + propene as an example (LAS/PI TOF-MS Experiments → Quantitative Model → RMG → Applications), any future work on molecular weight growth chemistry can take the same approach. Of course, as demonstrated by the 1-naphthyl radical + 2-butene thought experiment in section 4.2.4.5, as the chemical reactants get more complicated so too will the distribution of products observed, and it will certainly not be a simple case of "fill-in-the-blank" to apply the ideas established for phenyl radical + propene to another system. Practical issues will also arise, for example if butene isomers are used as excess reagents the PI TOF-MS sensitivity will drop noticeably due to attenuation of both the VUV and molecular beam density.

Regarding specific molecular weight growth systems to probe experimentally, any combination of either phenyl or naphthyl radicals (generated by 266 nm photodissociation of the corresponding iodide precursor) with an unsaturated hydrocarbon (ethene, propene, butene isomers, butadiene and acetylene to start with) would be of value to the field. As was the case for phenyl radical + propene, there has been a boom in recent years in publications exploring many of the reactions listed above (and many others) using either crossed molecular beams (CMB)[10-11, 13, 15-18, 20] or flash pyrolysis reactors,[31-33, 35, 41] usually coupled to some kind of mass spectrometry, but a glaring lack of LFP experiments on the same systems (other than the cavity ring-down spectrometry[8] and MS[43] experiments of Park and Lin). As discussed in Chapter 1, although CMB and flash-pyrolysis experiments can provide both qualitative and quantitative insights for validating theoretical predictions, they are not without limitations, such as a lack of time-resolution, that can be compensated for by complementary LFP experiments. Several of the reactions above have also been initiated in shock-tubes with end-product analysis.[251, 258, 337] Given this literature backdrop, and given that we have recently developed an approach to extracting quantitatively useful information from inherently "dirty" PAH experiments (section 4.2), the time seems ripe for a systematic study of molecular weight growth chemistry with LFP. Experiments with acetylene would be particularly useful because of its central role in PAH growth,[183] but also challenging because of its tendency to oligomerize. Preliminary experiments on phenyl radical + acetylene conducted by Te-Chun Chu and a visiting student Zehao Gou were promising, but due to excessive fragmentation in the PI TOF-MS (section 2.2.1) and rapid diffusion of products out of the MS Sampling region (section 2.2.2) at that time the results were of limited quantitative use. Both experimental issues have since been resolved, as described in Chapter 2, and it would be worthwhile to return to this system, as well as the naphthyl radical version that has already been studied theoretically by our group.[338] Although the chemistry will still be complicated (oligomerization in addition to the usual secondary and side reactions with I atom) there is a good chance that the results can be explained with the help of RMG.

One benefit of continuing to do LAS/PI TOF-MS experiments on molecular weight growth is the potential for greater collaboration within the Green group. Several large, well-funded projects in the group are concerned with alkylaromatic decomposition/growth/oxidation in either fuels or kerogen. LAS/PI TOF-MS experiments on molecular weight growth could become the

"bottom-up" part (e.g., phenyl radical + propene, Scheme 1-1) of a larger program that includes "top-down" pyrolysis experiments (e.g., propylbenzene decomposition) and RMG modeling.[330]

6.1.2   Reactions of Resonantly Stabilized Radicals (RSR's)

Resonantly stabilized radicals (RSR's) such as propargyl, allyl, cyclopentadienyl (CPD'yl) and benzyl radicals can accumulate to sufficiently high concentrations under combustion conditions to undergo self- and cross-radical recombination reactions. Because radical recombinations are inherently exothermic, the singlet adduct formed will have a lot of excess energy to dissipate that can go into otherwise unfavorable isomerizations involving carbenes and diradicals, eventually leading to a very stable aromatic molecule. Well-known examples include propargyl self-recombination to benzene,[207] CPD'yl self-recombination to naphthalene[336] and benzyl + propargyl cross-recombination to naphthalene.[329] Due to its importance, RSR recombination has already been the subject of numerous LFP experiments with either MBMS detection,[339] end product analysis,[22] or both.[23-24]

RSR's can also do more than just recombine with each other, such as adding to an unsaturated, closed-shell molecule present in high concentration, but owing to their low reactivity these reactions are challenging to observe directly by experiment. Recently, Savee et al. were able to directly observe the addition of acetylene to the following sequence of RSR's using LFP with MBMS detection: propargyl, CPD'yl and tropyl (RSR isomer of benzyl) radicals.[340] The sequence was terminated by indene formation. Observing this elusive chemistry required both long reaction times (~40 ms) and high temperatures (800-1000 K), conditions that have only recently become available to us by switching to the compact quartz reactor described in section 2.2.2. Therefore, in theory RSR chemistry other than recombination can now be observed with our LAS and PI TOF-MS apparatus, opening up entirely new avenues of research. However, iodide-containing photolytic precursors will no longer be suitable at these temperatures, due to thermal instability, and different precursors/photolysis wavelengths must be sought.

6.1.3   Oxidation Chemistry

Hydroxyl radical, OH, is the primary driver of oxidation in both combustion[341] and in the daytime atmosphere.[342] There have been innumerable experimental kinetics studies of OH reacting with various species encountered in combustion and the atmosphere, often using either

laser induced fluorescence (LIF) or direct absorbance of OH as sensitive and time-dependent probes. In contrast, there have been far fewer reported measurements of the products of such reactions, for example OH + acetylene, as mentioned at the very beginning of Chapter 1, which is critical to inhibiting PAH formation.[295] The recent re-discovery of acetylacetone (AcAc) as a convenient photolytic precursor of OH radical might facilitate more product branching studies going forward using LFP, especially at higher temperatures.[343] As shown in Scheme 6-1, AcAc undergoes keto-enol tautomerization, with the enolic form favored at T < 800 K owing to hydrogen bonding. The enol has an anomalously large cross section at 266 nm (almost 1×10^{-16} cm^2), and will photodissociate to form two radicals, including OH.[344] The vinylic radical also formed by photodissociation will certainly be reactive as well, but as an oxygenated hydrocarbon its chemistry can be predicted automatically by RMG, as opposed to other reactive photolytic co-products such as I atom that are not currently included in RMG.
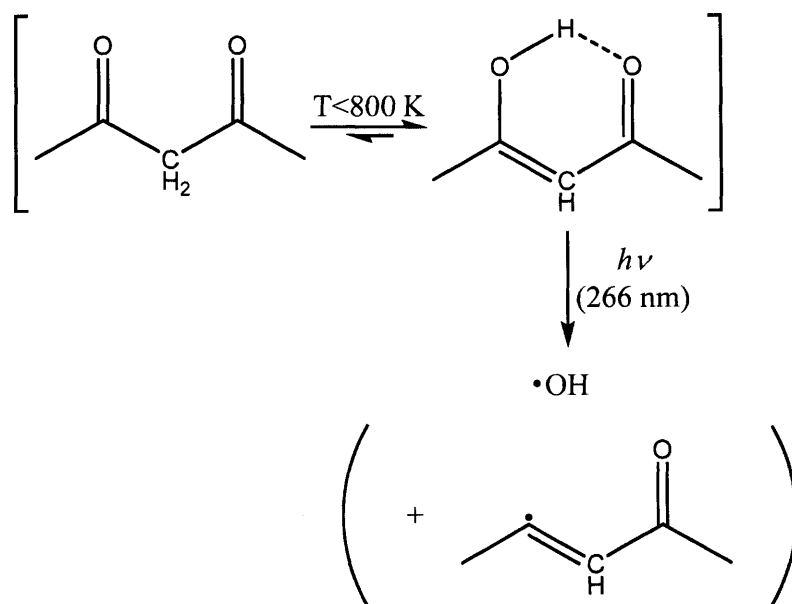
Scheme 6-1: Keto-enol tautomerization of acetylacetone and photodissociation of enolic form.

Although having a convenient photolytic source of OH that can be used up to relatively high temperatures is one of the requirements for product branching measurements, there are other concerns as well. Specifically, can the products even be detected? In the case of OH + acetylene (C_2H_3O PES), Senosiain et al. predicted five main product channels[3]: hydrogen abstraction to form water and ethynyl radical, and radical addition followed by either stabilization to an adduct well, hydrogen-loss to form ketene/ethynol, or methyl-loss to form CO.

Of these eight products, only two can definitely be observed with 10.5 eV PI TOF-MS (ketene and methyl radical), four cannot be observed (water, ethynyl radical, hydrogen atom and CO) and the remaining two have unknown ionization energies (radical adducts and ethynol). Even if only the ratio of ketene to methyl radical could be measured that would be a measurable improvement over the current status of OH + acetylene in the literature. However, methyl radical is quite reactive and is unlikely to persist long-enough for quantitative detection. Therefore, attempting to study OH + acetylene with our current LAS/PI TOF-MS apparatus is unlikely to yield any new insights into this system that has elicited interest for decades,[345] but has so far proved experimentally elusive.

A more fruitful foray into oxidation chemistry might by the analogous OH + *phenyl*acetylene reaction system. The corresponding C_8H_7O PES has been calculated by Dr. Adeel Jamal, and a reduced version is shown in Figure 6-1. All of the elementary pathways on the C_2H_3O PES have C_8H_7O analogues, the products of which are more amenable to PI TOF-MS detection. For example, in place of methyl radical + CO, OH + phenylacetylene will produce benzyl radical + CO, which will be easier to detect owing to the greater stability of benzyl compared to methyl radical. There are also two additional product channels on the C_8H_7O PES that are not equivalent to anything on the C_2H_3O PES: secondary ring-closure to form benzofuran + H and phenyl radical loss to form ketene. All of the bimolecular products of OH + phenylacetylene (including products of hydrogen abstraction not shown) can be detected by 10.5 eV PI TOF-MS, except for water, hydrogen atom and CO. The radical formed from hydrogen-abstraction might be difficult to observe, however, due to possible overlap with phenylacetylene fragments in the MS.
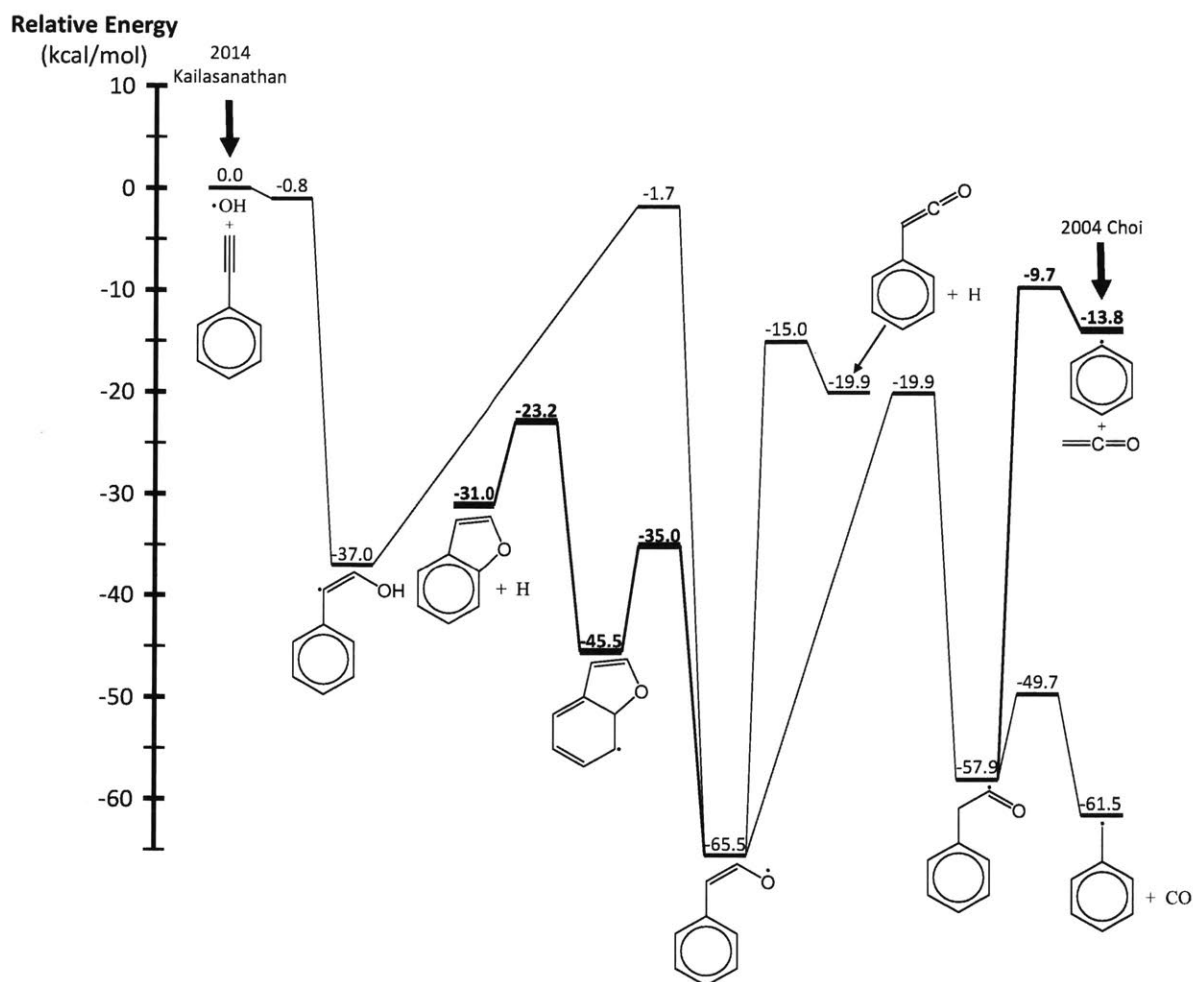
Figure 6-1: Reduced C_8H_7O PES. All energies and geometries were calculated with CBS-QB3 except for entrance channels, which used CCSD(T)-F12/cc-pVDZ-F12//M06/cc-pvtz. Experimental entrance points onto the PES from literature are indicated. All of the elementary reactions shown have analogues on the C_2H_3O PES (OH + acetylene) except for the bolded pathways to benzofuran + H and phenyl radical + ketene.

Aside from parallels to OH + acetylene, OH + phenylacetylene is an interesting chemical system by its own merits. This system first came to our attention while using the aromatic oxidation mechanism of Narayanaswamy et al. to model natural gas pyrolysis.[311] In that mechanism, a collision limited rate for direct conversion of OH + phenylacetylene to benzene + HCCO radical was necessary to match experimental PFR data. The lack of direct experimental data for OH + phenylacetylene led Kailasanathan et al. to measure the overall kinetics using OH LIF.[346] Interestingly, the rate that they measured was more than an order of magnitude faster than OH + acetylene over the same temperature range (~300-400 K).[3] A similar observation was

made in recent measurements of OH + styrene overall kinetics, which is of interest to atmospheric chemistry where styrene is a major anthropogenic emission.[347] These two independent observations of fast reaction between OH and a substituted aromatic suggest that the aromatic ring must be playing a stabilizing role, either through resonance stabilization of the radical or favorable hydrogen bonding. Indeed, as shown in Figure 6-1 the calculated terminal addition barrier for OH + phenylacetylene is ~1 kcal/mol below reactants (there is a Van der Waals complex along the addition pathway), in contrast to OH + acetylene, which has a positive 2 kcal/mol addition barrier. However, using the C_8H_7O PES of Figure 6-1 T,P-dependent rate coefficients were calculated that underpredict the measured OH + phenylacetylene rate by an order of magnitude (Figure 6-2). A submerged barrier for OH + styrene addition was also calculated, although rates were not predicted.[347] More concerning than the underprediction of OH + phenylacetylene kinetics, which is theoretically challenging because of the submerged barrier, is that predictions of overall phenyl radical + ketene kinetics using the same C_8H_7O PES also underpredict experiments by as much as two orders of magnitude (Figure 6-2).[348] The latter discrepancy is surprising because phenyl radical addition to the terminal carbon of ketene proceeds over a positive barrier of ~4 kcal/mol, which should not pose any particular challenge to canonical TST calculations. Only if this addition barrier is lowered by ~2.5 kcal/mol will the predictions match experiments. Choi and Lin made the same finding using G2MS calculations of the single-point energies.[348] Such an adjustment seems large for the level of theory used (CCSD(T)-F12/cc-pVDZ-F12), but is actually consistent with a recent theoretical study on a similarly sized system (di-*tert*-butyl sulfide pyrolysis) that also estimated the true barrier height uncertainty for this level of theory as 2.5 kcal/mol.[349] In any case, even the limited experimental data available on the C_8H_7O PES poses several fundamental questions that more theoretical work might be able to answer: Why is OH + phenylacetylene/styrene so much faster than OH + acetylene? Why does the theory underpredict the entrance rate of OH + phenylacetylene by an order of magnitude? Finally, why is the predicted barrier for phenyl radical + ketene addition so far off?
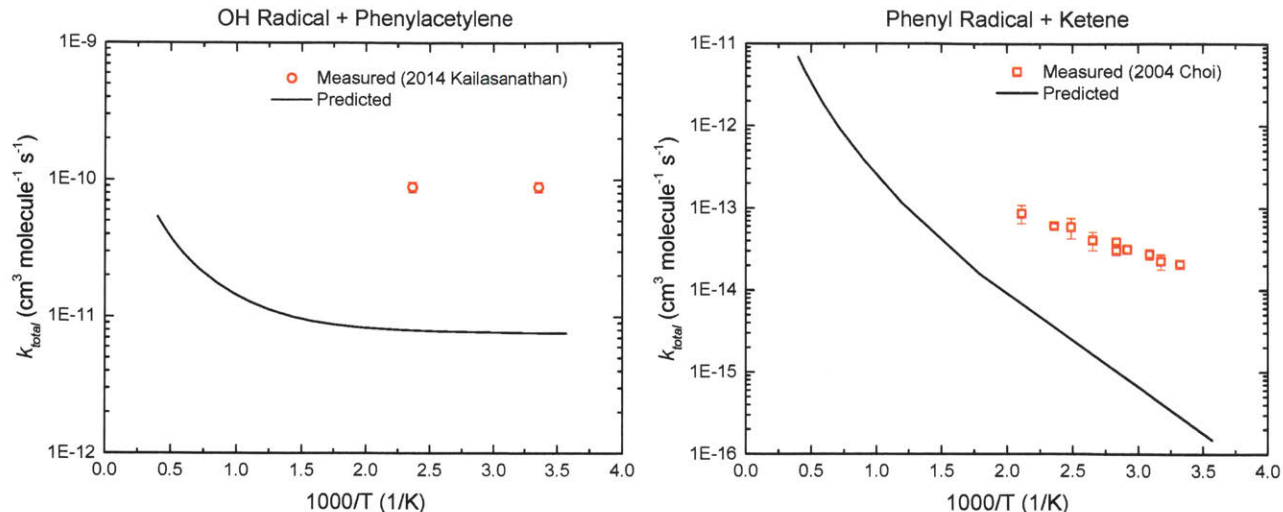
Figure 6-2: Overall kinetics measured for entrance onto C_8H_7O PES from OH radical + phenylacetylene (left),[346] or phenyl radical + ketene (right).[348] Unadjusted predictions of this work are also shown for comparison.

To summarize, OH + phenylacetylene seems to be an interesting chemical system for future theoretical and experimental work, with applications to both inhibition of PAH formation in combustion, and oxidation of antropogenic VOC's in the atmosphere. Experimentally, the C_8H_7O PES is also attractive because it can be easily accessed in two ways: OH + phenylacetylene and phenyl radical + ketene. If the OH route is taken, either 266 nm photolysis of AcAc or 355 nm photolysis of HONO[346] can be used for radical generation. 266 nm photodissociation of either iodobenzene or nitrosobenzene can be used for phenyl radical, as in our previous work. Finally, insights made on the C_8H_7O PES might be extended to OH + acetylene, which has long evaded experimentalists.

6.2   Improvements to LAS and PI TOF-MS Apparatus

As summarized in section 2.3, nearly every aspect of the LAS/PI TOF-MS apparatus could be improved in some quantifiable way (e.g., detection limit, time and mass resolution, T,P-range). Additionally, new features can always be added, such as reactor cooling and end product analyses. Nonetheless, as demonstrated for the phenyl radical + propene system (section 4.2) the current iteration of the apparatus is suitable for its original purpose: accurate and quantitative measurements of overall kinetics and primary product branching. Therefore, my main

recommendation to any future user of this apparatus is to first focus on using it to explore new chemistry, which is why recommendations of interesting chemical systems appeared first in this chapter. As such, the recommendations below for improving the three components of the apparatus (LFP reactor, PI TOF-MS and LAS detection) are either relatively minor in implementation (such as improving the uniformity of the photolysis beam) or peripheral to the main experiment (such as adding reactor cooling and end product analyses, or changing the LAS probe laser) so that experiments and apparatus improvement can largely proceed in parallel, in contrast to a major overhaul that would prohibit simultaneous experiments (such as switching from an LFP to a shock tube reactor).

6.2.1 Improvements to LFP Reactor

The most substantial potential improvement to the LFP reactor is also the least exciting: make the photolysis beam more radially uniform. By doing so, there will be less of a driving force for radial diffusion within the reactor, and ideally the time resolution of PI TOF-MS measurements should approach the theoretical limit of ~10-100 μs due to supersonic sampling. One limited approach to obtaining better photolysis beam profiles is to switch to the 355 nm output of the Nd:YAG laser whenever possible. Krasnoperov and coworkers have claimed photolysis uniformities of ±7% for their 1 atm LFP experiments, where uniform radical concentration in both the axial and radial dimension is critical due to slow diffusion.[56] Perhaps they can offer more concrete advice. Finally, Sheps and coworkers have recently built a "high-P" LFP reactor (used up to 3 atm so far) where sampling occurs at the end of the reactor in line with both the gas flow and the photolysis beam such that effects of radial inhomogeneity are minimized. This approach is not practical for our apparatus, however, if coupling of LAS detection to the PI TOF-MS is still desired.

The other two suggested improvements to the LFP reactor are both new features that could be added: reactor cooling and a trap for the reactor effluent. Because the compact quartz reactor is modular (Figure 2-2) it is foreseeable that at some point there might be at least two interchangeable reactors: a nichrome-wrapped high-T reactor for combustion-relevant experiments, and another reactor for atmospheric experiments that is wrapped with cooling lines through which refrigerant is continuously circulated and temperature controlled, similar to the design of Eskola and Timonen.[81] Regarding an effluent trap, attempts have already been made by Te-Chun Chu to trap stable species under typical experimental conditions for GC/MS analysis.

These preliminary tests were promising, and the lower flow required by the current reactor compared to when the tests were conducted will facilitate trapping even further. Knyazev has recently used such a trap to distinguish the $C_{10}H_8$ isomers of CPD'yl recombination,[24] and can offer advice.

6.2.2   Improvements to PI TOF-MS

The main limitation of the PI TOF-MS itself is the lack of flexibility in ionization energy, which is currently fixed at the ninth harmonic frequency of an Nd:YAG laser (118 nm, 10.5 eV). Atomic resonance lamps (ARL's) have frequently been used in the last thirty years to have some coarse control over ionization energy,[63, 80-81] and they were briefly explored as an alternative photoionization source for our apparatus. There are three common ARL's that are commercially available: xenon fill gas with an MgF_2 window (8.4/9.6 eV), krypton fill with MgF_2 (10.0/10.6) and argon fill with LiF (11.6/11.8 eV).[350] The argon lamp would be especially useful since many small oxygenated hydrocarbons such as formaldehyde, hydrogen peroxide and HO_2 only start to ionize above 11 eV.[351] There would also be advantages to using lower ionization energies, such as 9.6 eV from the xenon lamp, so as to reduce fragmentation (particularly from iodide-containing species) or to have some crude test for the isomeric identity of a given m/z signal.

Another advantage of ARL's compared to our current laser-generated PI source is that ARL's are a continuous ionization source, whereas the Nd:YAG laser can only be flashed as fast as 20 Hz. Therefore, instead of the PI laser defining the fastest rate at which mass spectra can be recorded, if an ARL is used as the continuous ionization source than the extraction plates of the TOF-MS can be pulsed up to 50 kHz, or one mass spectrum every 20 μs. If the data is binned and post-processed intelligently, for every photolysis event (~1 Hz) it is possible to obtain the time-evolution of the mass spectra over the entire ~50 ms residence time in the MS Sampling region with 1000's of individual time point measurements (instead of the ~10 time points that we currently get over the same 50 ms time scale using the pulsed PI laser source). Of course, the mass spectra at each time point will have to be averaged to obtain acceptable signal-to-noise, so multiple photolysis flashes will still be necessary. A simple LabView program was written using the FastFrame feature of the Tektronix DPO7254 oscilloscope to prove that mass spectra could be binned, averaged and stored correctly at a 50 kHz repetition rate.

The main disadvantage of ARL's is their low power output compared to lasers. We attempted to circumvent this issue by using an ellipsoidal waveguide, shown in the CAD

drawing of Figure 6-3 and the ray-tracing simulation of Figure 6-4, to focus the limited lamp output in the ionization region. The waveguide idea grew out of the experiments and simulations of the waveguide used by Blitz et al. for focusing 10.5 eV laser PI radiation in their ionization region (section 2.2.1).[82] According to the simulations, ~75% of the lamp's power should be focused in the ionization region, compared to <1% without a waveguide. However, this simulation models the lamp as an ideal point source that could be located at one of the foci of the ellipse. The simulations showed that even for small ~1mm deviations from the point source assumption the power in the ionization region would drop by two orders of magnitude. Indeed, when the ARL/waveguide combination was tested experimentally, the waveguide only increased the TOF-MS signal marginally compared to experiments without a waveguide.
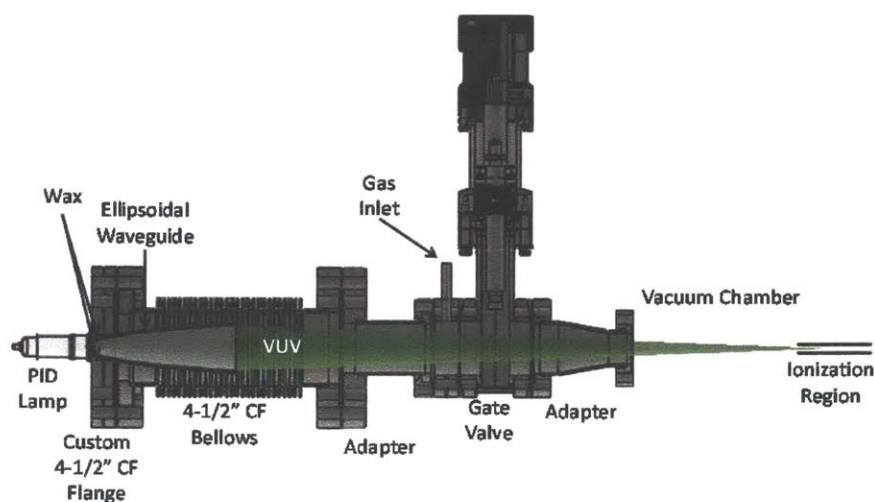
Figure 6-3: CAD drawing of atomic resonance lamp with ellipsoidal waveguide for focusing in the ionization region of TOF-MS.
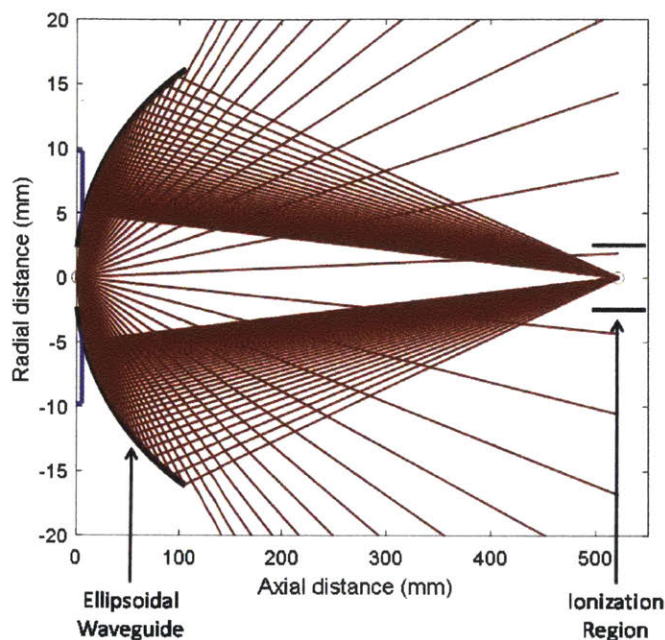
Figure 6-4: Ray tracing simulation results for VUV generation using atomic resonance lamp with ellipsoidal waveguide focusing.

However, TOF-MS signals recorded in subsequent experiments with the ARL ionization source at different distances from the ionization region, z_{ion}, exhibited a $1/z_{ion}^2$ dependence, as expected. At the shortest z_{ion} tested, ~20 cm, the detection limit was ~100 ppm with 10,000 averages (~3 hours of averaging at 1 Hz), therefore if the lamp could be moved as close to the ionization region as possible, ~2 cm, the detection limit should approach ~1 ppm (or ~1 × 10^{11} cm^{-3} of a typical organic molecule in the reactor). This is still a couple of orders of magnitude above the detection limit with laser PI radiation (Table 2-1), thus the prospects for ARL's replacing laser PI generation seem dim. In any case, the lamp cannot currently fit through any of the openings in the vacuum chamber, so in order to place it as close to the ionization region as possible (~2 cm) would require enlarging one of the openings. Fortunately, Dr. Joshua Middaugh designed the apparatus with mobility in mind, so that if such a modification were strongly desired, the entire chamber could be conveniently wheeled to the machine shop.

6.2.3 Improvements to LAS

As mentioned in Chapter 2, the picosecond Ti:Sapphire laser currently used for LAS is interchangeable as long as the Herriott mirrors can still reflect the output wavelength. For

example, the doubled output of a cw ring dye laser operating with either Rhodamine 6G or Kiton Red dye could be used to generate 308 nm UV radiation for selective probing of OH radical.[53-54, 58] Quantum cascade lasers (QCL's) tuned to mid-IR bands of specific molecules/radicals are also becoming more common,[352] and could perhaps be combined with Herriott multiple-pass LAS to selectively probe other important combustion intermediate and products such as HO_2,[353-354] H_2O_2,[355] CO[356] and CO_2.[58] Finally, the 532 nm pump laser was identified by Dr. Ismail as the main source of noise in LAS measurements,[67] and this continues to be the case. Replacing it would improve the LAS detection limit, and hopefully reduce the amount of time spent aligning the Ti:Sapphire laser and doubler in order to obtain a stable output.

6.3 Improvements to RMG

Most of my experience with RMG has been related to PAH chemistry during hydrocarbon cracking. As such, the recommendations below were mostly conceived with that application in mind. However, if some of the issues highlighted below are addressed (e.g., accuracy of cyclic thermochemistry, use of training data), there will undoubtedly be improvements to RMG's predictions of other chemistry far outside of the limited scope of PAH formation.

6.3.1 More Accurate Thermochemistry for Polycyclic Species

Accurate thermochemistry estimates for polycyclic species has long been a challenge for RMG.[357] Until recently, RMG still relied on a group-additive approach using "ring-strain corrections" calculated by Benson,[358] Bozzelli[359] and others. The issue with this approach is that it does not scale well as the number of rings in the molecule increases. Even if one only considers molecules with two rings (bicyclic), taking into account different ring sizes, degrees of unsaturation and heteroatoms, there are too many combinations for the ring-strain of each to be calculated individually. Previous attempts have been made at automating on-the-fly quantum calculations of polycyclic thermochemistry,[360] but have so far been hampered by computational expense. Simple heuristics for estimating polycyclic thermochemistry using RMG's finite database of ring-strain corrections are therefore highly desirable, and Kehang Han recently proposed and validated one such heuristic shown in Scheme 6-2.[333] Essentially, the overall ring-strain of the tricyclic molecule in the example is estimated as the sum of its three bicyclic components, minus the overlapping monocyclics.
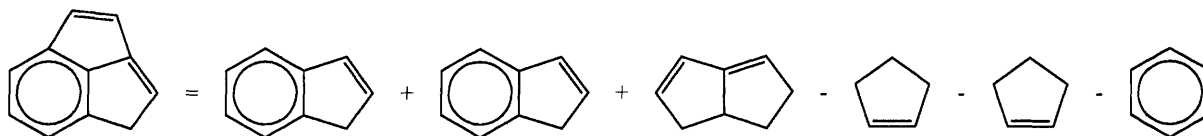
Scheme 6-2: Example of simple heuristic for polycyclic ring-strain estimation used by RMG. In this case, the overall ring-strain is badly underestimated.

While this approach works well for "linear" polycyclics, where atoms are at most shared by two rings, it underestimates the ring-strain of "fused" polycyclics, such as in Scheme 6-2, where there are atoms shared by at least three rings. The example given above is particularly problematic, because all of the constituent bicyclics and monocyclics used by the heuristic have little ring strain, whereas the tricyclic should clearly have a high ring strain. Therefore, in this example the heuristic is not failing due to a lack of data, but rather the underlying formula is not adequate. The end result is that whenever RMG makes indene and acetylene in high concentration (such as in natural gas pyrolysis), it will want to react them together to make the fused tricyclic species shown in Scheme 6-2 because the overall stability of the fused tricyclic is significantly overestimated.

In my observation, the issue outlined above is the main roadblock to using RMG for predictions of PAH formation beyond the 2-ring species indene and naphthalene (e.g., the 4-ring species pyrene, which is often the starting point for models of PAH inception, coagulation and growth[295]). Until the thermochistry of arbitrarily complex polycyclic molecules and radicals can be quickly and accurately estimated, any RMG-generated mechanism for PAH formation will be polluted with unreasonable polycyclic species, which will siphon the major reaction flux from where it should be going (higher order PAH's). While I don't have a specific solution to this nagging problem in the sub-field of automatic mechanism generation, the problematic example in Scheme 6-2 can at least serve as a test case for any future, proposed solution. For example, a "big-data" approach is currently being pursued that attempts to utilize a large dataset of DFT-calculated energies for ~134k molecules.[361] Because this dataset only includes species that are likely to appear in nature, it does not contain the fused tricyclic species in Scheme 6-2. Therefore, any polycyclic thermochemistry heuristic that is fit or "machine-learned" to the dataset should be tested against highly-strained RMG-generated molecules such as the one in Scheme 6-2.

6.3.2   Fill in Missing PAH Chemistry

If a tractable solution to the polycyclic thermochemistry issue described in the previous section can be implemented in RMG, then it will also be worthwhile to update the kinetic database of RMG to reflect the current understanding of PAH chemistry. Specifically, there are three aspects of PAH chemistry that are well known in the combustion field, but unknown to RMG currently: high-barrier cis-trans isomerizations, phenyl addition/cyclization reactions and o-benzyne chemistry.

Figure 6-5 shows an example from literature of a high-barrier (~50 kcal/mol) cis-trans isomerization of a substituted aromatic species.[332] The cause of the high barrier is a loss of conjugation between the aromatic ring and the unsaturated bonds on the side chain during isomerization as the π-orbitals of the TS are no longer overlapping. RMG does not distinguish between cis/trans-isomers, the underlying assumption being that the barrier between the two is small enough that at combustion temperatures they are equilibrated. While this assumption may be adequate for small, unconjugated molecules, it clearly breaks down for bulky, conjugated aromatic molecules.
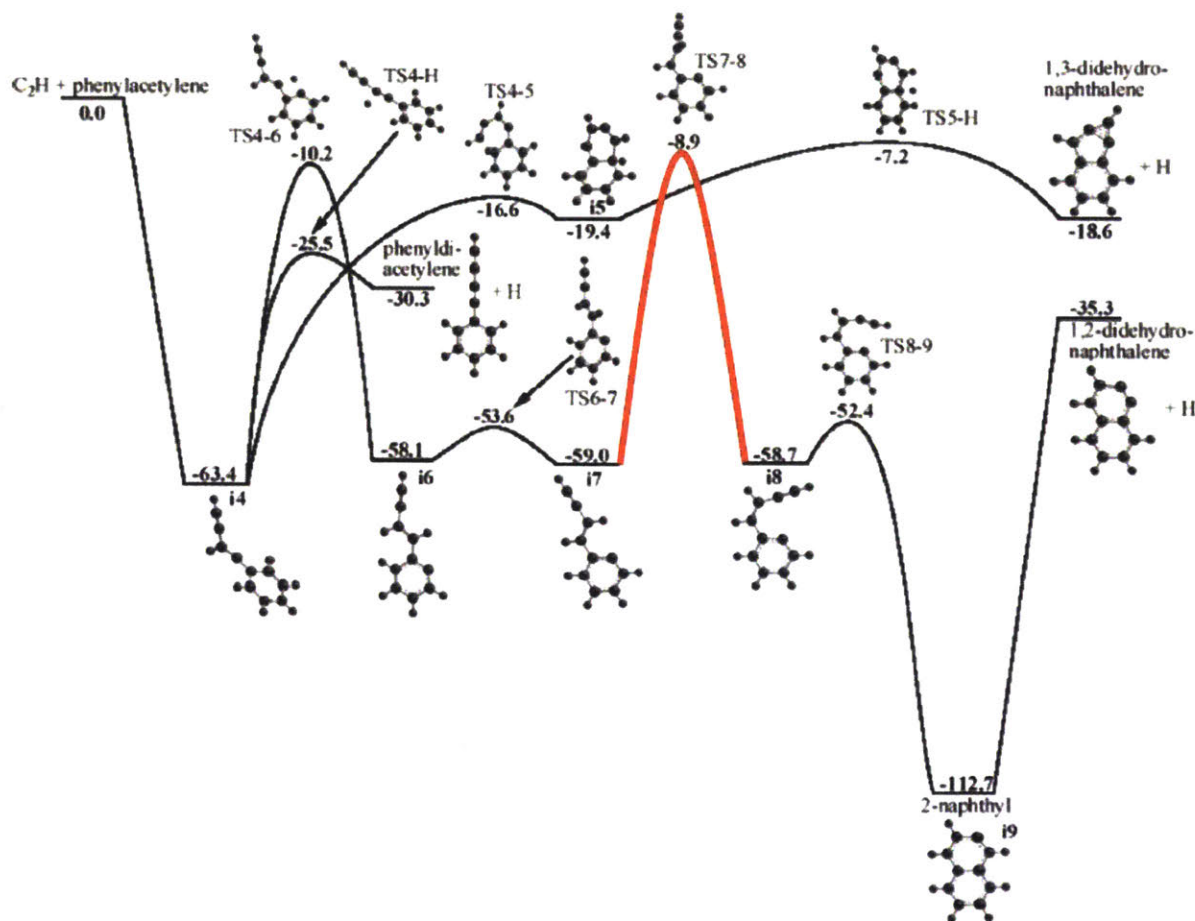
Figure 6-5: Example of a high-barrier aromatic cis-trans isomerization, highlighted in red. Taken for C_8H_7 PES of Mebel et al.[332]

As discussed in section 5.3.1.3, these high high-barrier cis-trans isomerization can actually be the bottleneck of a multi-step process. The specific example given was for phenyl radical + diacetylene, which can easily isomerize to **i6/i7** on the C_8H_7 PES of Figure 6-5, but must then surmount the ~50 kcal barrier to reach **i8**, the cis-isomer of **i7**. Once **i8** is formed, ring-closure to make stable 2-naphthyl radical is facile (followed by hydrogen-abstraction to make naphthalene). Initially, RMG ignored isomerization between **i7** and **i8**, assuming the two to be in equilibrium, and 2-naphthyl radical formation was subsequently overpredicted (as was naphthalene). As a temporary solution, an **i7/i8** → 2-naphthyl radical library reaction was added to RMG with effective kinetics determined by the rate-limiting cis-trans-isomerization. While this approach prevented subsequent RMG mechanisms from forming naphthalene *via* phenyl radical + diacetylene, it is not sustainable. There are many more unsaturated, substituted aromatics that

will have large barriers to cis/trans-isomerization besides the one example given in Figure 6-5, and it is not feasible to manually introduce effective kinetics for all of them. Therefore, a more general solution should be implemented in RMG. Ideally, RMG would be able to distinguish all cis/trans-isomers, but if that proves impractical then at least for aromatic molecules a distinction between cis- and trans- should be made.

The second aspect of PAH chemistry of which RMG is currently ignorant is the recently proposed phenyl addition/cyclization (PAC) pathway (Scheme 6-3).[27] PAC was first proposed by Shukla and Koshi, who observed products of benzene and acetylene co-pyrolysis with MBMS that were separated by intervals of either 26 or 76 amu. The former they attributed to hydrogen abstraction and acetylene addition (HACA)[328] and the latter they attributed to PAC. PAC proceeds in two simple steps: a phenyl radical replaces hydrogen on a stable aromatic molecule, and a new aromatic bond is formed by dehydrocyclization. In this manner, the original aromatic molecule gains two more aromatic rings at once.
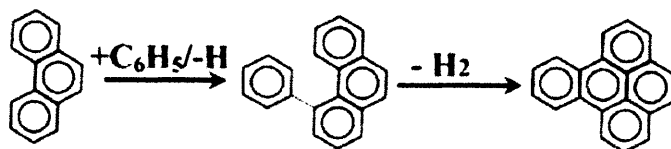
Scheme 6-3: Example of the phenyl addition/cyclization (PAC) pathway. Taken from Shukla and Koshi.[27]

Unlike HACA, which can sometimes terminate growth by forming a five-membered ring (e.g., 1-naphthyl radical + acetylene → acenaphthalene[338]), PAC can proceed indefinitely because "bay" sites for future addition are always maintained. Although RMG can predict the addition and hydrogen-loss steps (the PA part) there is currently not a reaction family for dehydrocylization (C step). More importantly, there is a lack of either measured or predicted kinetic data for such reactions upon which a new reaction family could be built. Nonetheless, the kinetics of some representative dehydrocyclization reactions could be calculated, after which a new reaction family could be created. Given the high concentration of both benzene and phenyl radical predicted in our models of natural gas high temperature pyrolysis, it is expected that once PAC is incorporated into RMG formation of large PAH's will proceed much more rapidly than in current models.

Finally, there have been several experimental and theoretical studies recently that suggest a more prominent role for ortho-benzyne (o-benzyne) in PAH chemistry (Scheme 6-4). First,

decomposition of o-benzyne was implicated as the source of acetylene and vinylacetylene in flash propargyl radical pyrolysis experiments with MBMS detection.[40] Second, owing to its singlet biradical character, o-benzyne can undergo 1,4-cycloaddition with an n-ring aromatic molecule, followed by fragmentation of an acetylene to form an (n+1)-ring aromatic (the overall process is deemed 1,4-CAF). The calculated energetics of 1,4-CAF appear favorable compared to other potential reactions between o-benzyne and a closed-shell aromatic.[362] Because RMG treats o-benzyne as a closed-shell molecule, it is currently unable to capture this interesting and potentially important chemistry.
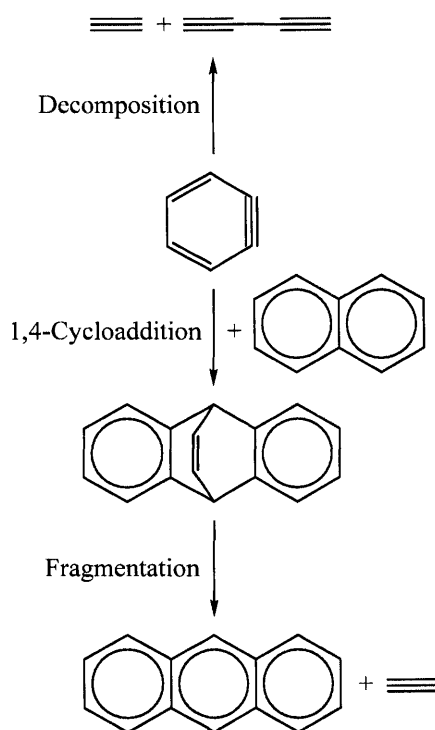
Scheme 6-4: Examples of o-benzyne chemistry relevant to PAH formation.

6.3.3   Better Use of Training Reactions

RMG currently relies on a mix of both training reactions and rate rules to estimate the kinetics of new reactions.[181] However, just because a training reactions exists somewhere in the RMG database does not mean that it is being fully utilized. In fact, as illustrated by the example in Scheme 6-5, much of the subtle, chemical information conveyed by a training reaction is apparently elided by RMG in favor of a simple, "first-order" understanding. The example given is the aromatic-catalyzed 1,2-hydrogen-migration pathway, which was discovered on the C_9H_{11}

PES and added as training reactions to RMG's database. As discussed in section 4.2.4.6, RMG's ability to apply this finding to an analogous system, the $C_{14}H_{15}$ PES of 1-naphthyl radical + 2-butene, was tested with mixed results: although the identical pathway was found (1,2-H-migration catalyzed by the phenyl "active site", magenta pathway in Scheme 6-5), RMG was unable to extrapolate the "aromatic-catalyzed" concept either to a different active site (naphthyl active site) or a different reaction (1,3-hydrogen-migration). Currently, the only recourse to ensure that RMG will find the other three aromatic-catalyzed pathways is to add more specific training reactions, which is time-consuming and antithetical to the automated philosophy of RMG.
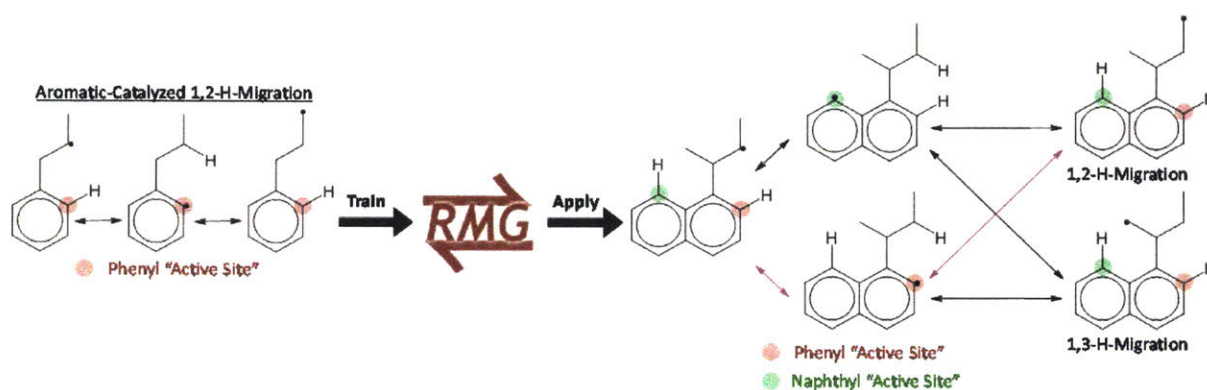
Scheme 6-5: Illustration of how RMG should be able to apply training reactions, using the aromatic-catalyzed 1,2-H-migration as an example. The magenta pathway is the only one found by RMG.

Similar to the example of a polycyclic molecule with poorly estimated thermochemistry in Scheme 6-2, I don't have a specific solution for this shortcoming of RMG, but I hope that the example above can be used as a test of any attempted re-organization of the database. For example, efforts are being made in the Green group to convert all of the training reactions into "fingerprints" that are amenable to machine learning through convolutional neural networks. Hopefully, after such an overhaul of the database the subtler details of the training reactions will no longer be lost in translation.

6.3.4   Incorporate Halogen Chemistry

Currently, RMG is intended for construction of mechanisms that include only carbon, hydrogen, oxygen, nitrogen and sulfur (CHONS) atoms. However, there is no reason that the fundamental concepts behind RMG (flux-based mechanism construction, group-additivity

estimates of thermochemistry and averaging of analogous training reactions/rate rules) can't be extended to other atoms. Specifically, I am advocating for the inclusion of halogen chemistry in RMG because of the interference of photolytically generated iodine (I) atom in our LFP experiments, which required manual construction of a submechanism (section 4.2.4.4.2). Similarly, photolytically-generated chlorine (Cl) atom is often used as the "ignition" source in experimental studies of low-temperature autoignition and must be taken into account in any quantitative model of the observed chemistry.[50]

Beyond the narrow scope of laboratory experiments, there are many other applications where an RMG-like tool for predicting halogen chemistry would be useful. For example: in atmospheric models of the marine boundary layer where chlorine, bromine and iodine all play important and varied roles;[170, 363] in screening commercially-viable CFC replacements;[364] in modeling of nuclear accidents where radioactive iodine leaks into the atmosphere;[365] in low-CO_2 halogen-mediated processes for the partial oxidation of natural gas and alkanes to commodity chemicals;[366-367] and in corrosion prevention.[368]

As demonstrated in section 4.2.4.4.2, there is already a lot of experimental data on halogen chemistry in the literature to draw from that could form the backbone of a kinetic and thermochemistry database in RMG. Where experimental data is lacking, theoretical predictions might be practical and are becoming more common for halogens.[257, 369]

While I hardly expect (or want) all of the recommendations above to be followed verbatim, it is my hope that at least some of them will spark some new ideas, including for myself.

Appendix A

Additional Details for CH₂OO + Alkenes

Criegee Intermediate (CI) Formation Rate Experimental Details

The analytical model from the main text (Eqs. 3-1 to 3-4) is reproduced here for reference.

$$[CH_2OO](t) = \frac{\alpha k_1[O_2][CH_2I]_0}{k_1[O_2] - k_2[Alkene] - k_3} \left(e^{-(k_2[Alkene]+k_3)t} - e^{-k_1[O_2]t} \right)$$

$$[I](t) = \frac{[CH_2I]_0}{k_1[O_2] - k_4} \left([(1 + \alpha)k_1[O_2] - k_4]e^{-k_4 t} - \alpha k_1[O_2]e^{-k_1[O_2]t} \right)$$

$$A_{375}(t) = \sigma_{CH_2OO}(\lambda = 375 \text{ nm})l_{375}[CH_2OO](t) + \text{shift}$$

$$A_I(t) = \sigma_I(\lambda = 1315.246 \text{ nm})l_I[I](t)$$

Table A 1 and Table A 2 summarize the experimental conditions of the CI formation experiment at 298 K, as well as the global and local fit parameters obtained by fitting this data. The uncertainties reported for α, k_1 and σ_{CH_2OO} in Table A 1 are not due to uncertainty in the fitting procedure (because of the high density of data points in a single absorbance trace this number was very small), but rather are due to uncertainties in other parameters, which are discussed next.

Table A 1: Experimental conditions and global fit parameters for 298 K CI formation experiments

	Parameter	Units	Value
Measured	T	K	298 ± 1.3
	P	Torr	25
	FPR[a]	Unitless	7.55
	$[CH_2I_2]$[b c]	molecules cm^{-3}	2.89×10^{14}
	$[O_2]$ Range[c]	molecules cm^{-3}	$0.99\text{-}69.3 \times 10^{15}$
	Photolysis Power	mJ $pulse^{-1}$	92
	l_{375}	Cm	1510 ± 409
	l_I	Cm	73 ± 12
Fit	α	Unitless	0.71 ± 0.07
	k_1	cm^3 $molecule^{-1}$ s^{-1}	$(1.4 \pm 0.1) \times 10^{-12}$
	σ_{CH2OO} (λ=375 nm)	cm^2 $molecule^{-1}$	$(7 +7/\text{-}3.5) \times 10^{-18}$

[a]FPR = Flashes per Refresh
[b]$[CH_2I_2]$ was estimated by using the vapor pressure of CH_2I_2 at 298 K[166]
[c]All concentrations have $\pm10\%$ uncertainty, as discussed in the text

Table A 2: Local fit parameters for 298 K CI formation experiment

[O_2]	Local Fit Parameters			
	$[CH_2I]_0$	k_3	k_4	shift
10^{15} molecules cm^{-3}	10^{12} molecules cm^{-3}	s^{-1}	s^{-1}	Unitless
0.99	2.8	429	131	7.73E-04
4.95	2.7	325	100	7.84E-04
9.9	2.5	328	112	1.50E-03
19.8	2.7	298	117	2.08E-04
29.7	2.6	283	111	7.22E-05
39.6	2.6	297	107	4.12E-06
49.5	2.5	282	141	8.53E-06

In the case of k_1, its final fit value is coupled to whatever $[O_2]$ value was fed to the model because the quantity $k_1[O_2]$ always appears in the analytical model as a single entity. For example, if the value of $[O_2]$ is systematically $1.1 \times$ higher than its model value (i.e., 10% systematic uncertainty), then the final fit value of k_1 will be off by $\frac{1}{1.1} \approx 0.90 \times$ in order to fit the data to within the specified tolerance. Because the mass flow controllers (MFC's) used in this

experiment are calibrated with N_2, a gas correction factor (GCF) is needed when flowing non-N_2 gases. The GCF can introduce a ±5% systematic uncertainty in the flowrate, which in a worst case scenario would cause a ±10% systematic uncertainty in the concentrations because all gases used in this experiment require a GCF (helium, oxygen, ethene, propene and butenes). Therefore, all of the concentrations in this experiment have ±10% uncertainty, including O_2, which causes the uncertainty of k_1 to also be ±10%, as reported here. As discussed in section 3.1, the value for k_1 measured here agrees well with other reported values.

In the case of σ_{CH_2OO} the largest sources of uncertainty are the pathlengths of both the ultraviolet and infrared lasers. The absorbance equations shown above can be rearranged to solve for σ_{CH_2OO} at the time t_1 at which $[CH_2OO] = \alpha[I]_0$ (i.e., when CH_2OO is at its peak concentration) as shown below.

$$\sigma_{CH_2OO} = \sigma_I \frac{A_{375}(t_1)}{\alpha A_I(t=0)} \frac{l_I}{l_{375}}$$

The random uncertainty of σ_{CH_2OO} can be estimated by propagation of uncertainty on the above equation.

$$\frac{\Delta(\sigma_{CH_2OO})}{\sigma_{CH_2OO}} = \sqrt{\frac{\Delta(\sigma_I)^2}{\sigma_I^2} + \frac{\Delta(A_{375}(t_1))^2}{A_{375}(t_1)^2} + \frac{\Delta(A_I(t=0))^2}{A_I(t=0)^2} + \frac{\Delta(\alpha)^2}{\alpha^2} + \frac{\Delta(l_I)^2}{l_I^2} + \frac{\Delta(l_{375})^2}{l_{375}^2}}$$

Both A_{375} and A_I have small relative uncertainties as demonstrated by the good signal to noise observed in Figure 3-1 for both ultraviolet and infrared absorption. The uncertainty of α is estimated as 10% because it is also sensitive to systematic uncertainties in $[O_2]$. That leaves the following contributors to the uncertainty: σ_I, which has a relative uncertainty of 20% as reported by Ha et al.,[78] and l_I and l_{375}, which have 16 and 27% relative uncertainty, respectively, as shown in Table A 1. Combining these uncertainties using the above equation gives the following.

$$\frac{\Delta(\sigma_{CH_2OO})}{\sigma_{CH_2OO}} = 0.37 \approx 0.40$$

Therefore the uncertainty of σ_{CH_2OO} can be estimated as 40%. However, this analysis for σ_{CH_2OO} assumes a perfectly circular and homogeneous photolysis beam that is aligned perfectly coaxially with the reactor and the Herriott multiple pass cell. If deviations from this ideal case are taken into account, our uncertainty is on the order of a factor of 2 or more, which is what we report here.

In addition to measuring σ_{CH_2OO} at $\lambda = 375$ nm we also measured it at 370 and 385 nm over a range of O_2 concentrations to confirm that it increases at shorter wavelengths as Beames et al.[123] and Sheps[122] measured. Figure A 1 compares our measurements on an absolute scale.
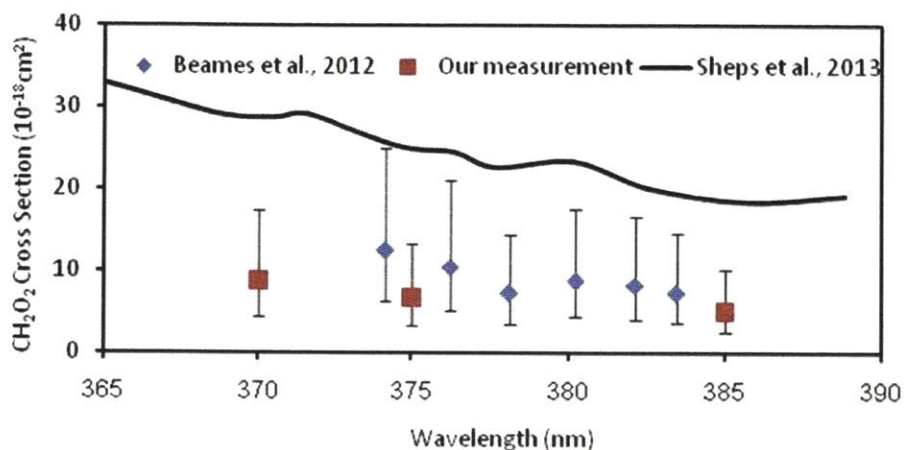
Figure A 1: Comparison between our measured σ_{CH_2OO} value at 370, 375 and 385 nm and the measurements of Beames et al.[123] and Sheps.[122] Error bars on both our measurement and Beames measurement represent a factor of two uncertainty. Uncertainty in Sheps data is 25%.

Our measurements agree quite well with the Beames data, both relatively (same trend with λ) and absolutely. Both our measurement and the Beames measurement differ significantly in an absolute sense, however, from Sheps. Specifically, his measured cross sections are about 3-4 times higher than ours. Because the purpose of the current study is to measure pseudo first order kinetics that don't depend on path lengths and cross sections this discrepancy does not affect the main results presented here. The fidelity of the relative trend is greater than the error bars in Figure A 1 suggest because our measurements were taken within the same week (in the case of the 370 and 385 nm measurements they were taken back to back the same day) during which time the laser alignment was stable. Therefore any systematic uncertainties with regard to the pathlengths will be roughly the same for all three measurements and in a relative sense the wavelength trend is real and not merely noise.

The α reported in Table A 1 is noticeably smaller than that reported in the literature[144-145] (0.71 ± 0.07 as opposed to ~0.90). This might be due to significant multiphoton dissociation of CH_2I_2 to CH_2 because of the high photolysis power used in this experiment. This power was necessary in order to obtain sufficient signal to noise for the single-pass I atom absorption traces. Such a phenomenon would cause the apparent $[CH_2I]_0$ values to be larger than they actually are

due to the presence of more I atoms at the time of photolysis. Hence the fit α value will be lower than it should be in order to fit the second rise of the I atom trace. Note that the fit value of $[CH_2OO]_0(= \alpha[CH_2I])$ should still be correct, regardless of the individual values of α and $[CH_2I]_0$, hence the fit values of σ_{CH_2OO} are unaffected. Furthermore, as will be shown in the following section, it was found that varying the photolysis power by roughly a factor of two did not affect the measured CI + Alkenes rates, therefore the possible occurrence of multi-photon dissociation of CH_2I_2 does not affect our main results. We also found $[CH_2I]_0 \approx 0.01 \times [CH_2I_2]$, providing a useful heuristic for future experiments.

The formation of CI was also verified at 700 K by measuring ultraviolet and infrared absorbance traces over the range of $[O_2]$ shown in Table A 3 and fitting to the same analytical model, the results of which are summarized in both Table A 3 and Table A 4. Sample fits of both the ultraviolet and infrared absorbance traces at this temperature are shown in Figure A 2.

Table A 3: Experimental conditions and global fit parameters for 700 K CI formation experiment

	Parameter	Units	Value
Measured	T	K	700 ± 11
	P	Torr	25
	FPR	Unitless	7.55
	$[CH_2I_2]$	molecules cm^{-3}	2.89×10^{14}
	$[O_2]$ Range	molecules cm^{-3}	$0.99\text{-}69.3 \times 10^{15}$
	Photolysis Power	mJ pulse^{-1}	105
	l_{375}	cm	1150 ± 437
	l_I	cm	57 ± 10
Fit	α	Unitless	0.70 ± 0.07
	k_1	cm^3 molecule^{-1} s^{-1}	$(1.0 \pm 0.1) \times 10^{-12}$
	σ_{CH2OO} (λ=375 nm)	cm^2 molecule^{-1}	$(6 +6/-3) \times 10^{-18}$

Table A 4: Local fit parameters for 700 K CI formation experiment

[O$_2$]	Local Fit Parameters			
10^{15} molecules cm^{-3}	[CH$_2$I]$_0$	k_3	k_4	shift
	10^{12} molecules cm^{-3}	s^{-1}	s^{-1}	Unitless
0.99	9.3	11492	0	1.60E-03
4.95	9.2	11558	221	1.80E-03
9.9	9.1	11695	104	2.10E-03
19.8	9	11602	0	2.70E-03
29.7	9.3	11526	0	3.60E-03
39.6	9.3	11569	2	3.40E-03
49.5	9.1	11546	57	3.20E-03
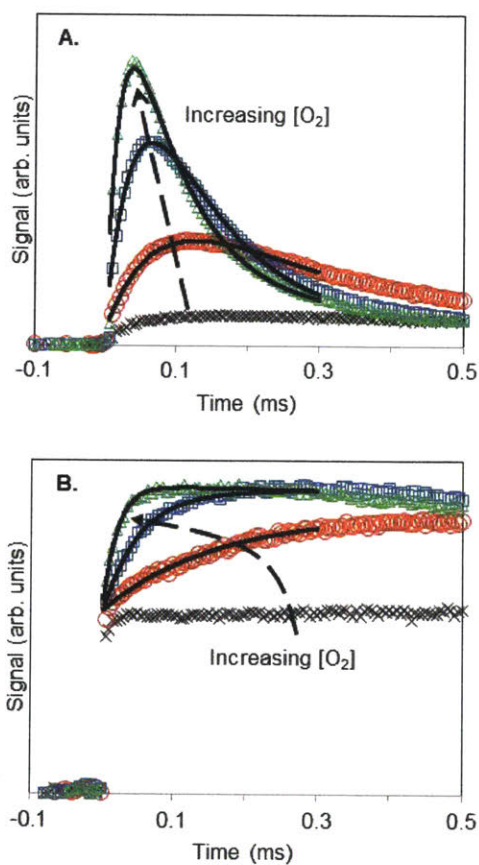
Figure A 2: Measurement of CH$_2$OO formation at 699 K and 25 Torr using ultraviolet absorption of CH$_2$OO at λ = 375 nm (Panel A) and infrared absorption of I atom (Panel B) over the following range of O$_2$ concentrations (units of molecules cm^{-3}): [O$_2$] = 0 (black), 4.9× 10^{15} (red), 20.0 × 10^{15} (blue) and 49.3 × 10^{15} (green). The infrared absorbance trace with no O$_2$ is shifted up. Only every 500th point is shown for clarity. Solid black lines are model fit.

The uncertainties in the global fit parameters were determined in the same manner as at 300 K. There are several interesting differences to note between the 700 and 300 K data. First, as mentioned in section 3.1, k_1 decreases at this elevated temperature consistent with expectation.[146] Second, there is a noticeable amount of absorption at 375 nm in the absence of O_2 that appears to be responsible for the long time baseline offset observed at all values of $[O_2]$. This is likely due to absorption by a species produced by secondary chemistry. Third, at 700 K $[CH_2I]_0 \approx 0.03 \times [CH_2I_2]$, possibly because the higher temperature encourages more CH_2I_2 to photolyze at 355 nm. Finally, k_3, the first order loss of CH_2OO, is almost two orders of magnitude larger at 700 K, while k_4, the first order loss of I atom, hardly changes.

This experiment provides evidence that at 700 K we are still able to probe CH_2OO at 375 nm, although it is far less stable at this temperature as evidenced by the large values of k_3.

CI + Alkenes Experimental Details

The details of the CI + ethene, propene and butene isomer experiments are summarized in **Table A 5**, **Table A 6** and Table A 7, respectively.

Table A 5: CI + ethene experimental details

	T	P	FPR	[O2]	Range of [C$_2$H$_4$]	Approximate [CH$_2$I$_2$]	% Change from Base Case	Approximate Photolysis Power	% Change from Base Case	k$_2$	% Change from Base Case
Units:	K	Torr	Unitless	$x10^{16}$ molecule cm^{-3}	$x10^{17}$ molecule cm^{-3}	$x10^{14}$ molecule cm^{-3}	% Change from Base Case	mJ/pulse	% Change from Base Case	10^{-16} cm^3 molecule^{-1} s^{-1}	% Change from Base Case
Base Case	298 ± 1.3	25	1.27	2.9	0 - 4.15	1.41	-	79	-	6.6 ± 1.1	-
Controls	298 ± 1.3	25	1.23	2.82	0 - 4.0	2.54	80.1	79	0	6.8 ± 1.5	3.3
	298 ± 1.3	25	1.27	2.9	0 - 4.15	1.41	0.0	111	40.51	7.4 ± 1.5	13.0
	298 ± 1.3	25	1.27	2.9	0 - 4.15	1.41	0	50	-36.7	6.7 ± 1.4	2.3
Pressure Dependence	298 ± 1.3	15	1.27	2.9	0 - 4.15	1.41	-	70	-	6.6 ± 1.5	-
	298 ± 1.3	50	1.15	2.9	0 - 8.3	1.41	-	70	-	7.1 ± 1.1	-
Base Case	390 ± 5	25	1	2.95	0 - 3.28	1.44	-	48	-	12.1 ± 1.8	-
Controls	390 ± 5	25	0.98	2.89	0 - 3.21	2.03	41.0	48	0	12.3 ± 1.7	2.1
	390 ± 5	25	1	2.95	0 - 3.28	1.44	0	100	108.3	13.4 ± 2.7	10.9
Base Case	494 ± 5	25	1	2.94	0 - 3.26	1.43	-	53	-	20.5 ± 3.6	-
Controls	494 ± 5	25	0.97	2.89	0 - 3.21	2.01	40.6	53	0	21.7 ± 5.1	5.7
	494 ± 5	25	1	2.94	0 - 3.26	1.43	0	112	111.3	22.1 ± 6.6	7.6

Table A 6: CI + propene experimental details

	T	P	FPR	[O2]	Range of [C$_3$H$_6$]	Approximate [CH$_2$I$_2$]	% Change from Base Case	Approximate Photolysis Power	% Change from Base Case	k$_2$	% Change from Base Case
Units:	K	Torr	Unitless	$x10^{16}$ molecule cm^{-3}	$x10^{17}$ molecule cm^{-3}	$x10^{14}$ molecule cm^{-3}	% Change from Base Case	mJ/pulse	% Change from Base Case	10^{-16} cm^3 molecule^{-1} s^{-1}	% Change from Base Case
Base Case	298 ± 1.3	25	1.27	2.9	0 - 2.5	1.41	-	79	-	17.5 ± 2.6	-
Controls	298 ± 1.3	25	1.23	2.82	0 - 2.41	2.54	80.1	79	0	18.6 ± 3.2	6.0
	298 ± 1.3	25	1.27	2.9	0 - 2.5	1.41	0	111	40.5	17.6 ± 2.5	0.3
Pressure Dependence	298 ± 1.3	10	1.27	2.9	0 - 2.5	1.41	-	70	-	17.9 ± 3.3	-
	298 ± 1.3	50	1.15	2.9	0 - 5.0	1.41	-	70	-	20.4 ± 4.3	-
Base Case	390 ± 5	25	1	2.95	0 - 1.97	1.44	-	51	-	24.9 ± 3.4	-
Controls	390 ± 5	25	0.98	2.89	0 - 1.93	2.03	41.0	51	0	24.7 ± 4.2	-0.7
	390 ± 5	25	1	2.95	0 - 1.97	1.44	0	108	111.8	24.4 ± 3.5	-2.0
Base Case	494 ± 5	25	1	2.94	0 - 1.96	1.43	-	50	-	32.0 ± 4.9	-
Controls	494 ± 5	25	0.97	2.86	0 - 1.91	2.01	40.6	50	0	32.3 ± 4.8	1.1
	494 ± 5	25	1	2.94	0 - 1.96	1.43	0	112	124.0	34.4 ± 6.2	7.6

Table A 7: CI + butene isomers experimental details

	T	P	FPR	[O2]	Range of [C$_4$H$_8$]	Approximate [CH$_2$I$_2$]	Approximate Photolysis Power	k$_2$
Units:	K	Torr	Unitless	$x10^{16}$ molecule cm^{-3}	$x10^{17}$ molecule cm^{-3}	$x10^{14}$ molecule cm^{-3}	mJ/pulse	10^{-16} cm^3 molecule^{-1} s^{-1}
Iso-Butene	298 ± 1.3	25	1.27	2.9	0 - 1.66	1.41	50	14.0 ± 2.6
	390 ± 5	25	1	2.9	0 - 1.64	1.44	50	18.5 ± 3.3
	494 ± 5	25	1	2.9	0 - 1.63	1.43	50	24.2 ± 5.4
	298 ± 1.3	10	1.27	2.9	0 - 1.87	1.41	50	14.8 ± 4.1
	298 ± 1.3	50	1.15	2.9	0 - 2.9	1.41	50	17.1 ± 5.6
1-Butene	298 ± 1.3	25	1.27	2.9	0 - 1.66	1.41	50	15.2 ± 3.0
	390 ± 5	25	1	2.9	0 - 1.64	1.44	50	18.0 ± 2.6
	494 ± 5	25	1	2.9	0 - 1.63	1.43	50	25.8 ± 5.6
	298 ± 1.3	10	1.27	2.9	0 - 1.87	1.41	50	17.6 ± 3.7
	298 ± 1.3	50	1.15	2.9	0 - 2.9	1.41	50	16.4 ± 4.0
2-Butene	298 ± 1.3	25	1.27	2.9	0 - 1.66	1.41	50	6.5 ± 1.8
	390 ± 5	25	1	2.9	0 - .98	1.44	50	7.8 ± 1.8
	494 ± 5	25	1	2.9	0.163 - 1.3	1.44	50	11.4 ± 1.1
	298 ± 1.3	10	1.27	2.9	0 - 1.87	1.41	50	9.1 ± 2.6
	298 ± 1.3	50	1.15	2.9	0 - 2.5	1.41	50	9.4 ± 2.8

As shown, control experiments were conducted for both CI + ethene and CI + propene at every temperature to ensure that increasing photolysis power and precursor concentration did not affect the measured k_2 value out of its error bounds. For the base case measurements two or three replicates were taken at each [Alkene]. k' was measured at five to eight different values of [Alkene] over the range indicated.

The error bounds on k_2 incorporate both random experimental uncertainty, as well as systematic uncertainty in [Alkene] due to the 5% flow inaccuracy of our MFC's for non-N_2 gases discussed in the section above. To summarize: k_2 was obtained with 95% confidence intervals from the slope of the pseudo-first-order decay of CH_2OO, k', versus [Alkene] for both the highest and lowest sets of [Alkene] values. The lowest and highest values of k_2 obtained within the 95% confidence intervals were averaged together to arrive at the values of k_2 reported above, with the uncertainties reflecting the full span of possible k_2 values. Both systematic and random uncertainties were also taken into account when fitting the Arrhenius parameters by obtaining values of A and E_a over the entire range of possible $k_2(T)$ values and then averaging the results.

As an example of how the error bounds on $k_2(T)$, A and E_a were determined, Figure A 3 shows k' versus $[C_2H_4]$ at 298 K for three different sets of $[C_2H_4]$: the base case set assuming the GCF introduces no inaccuracy in the flow rates, and the sets with $\pm 10\%$ systematic offset in $[C_2H_4]$.
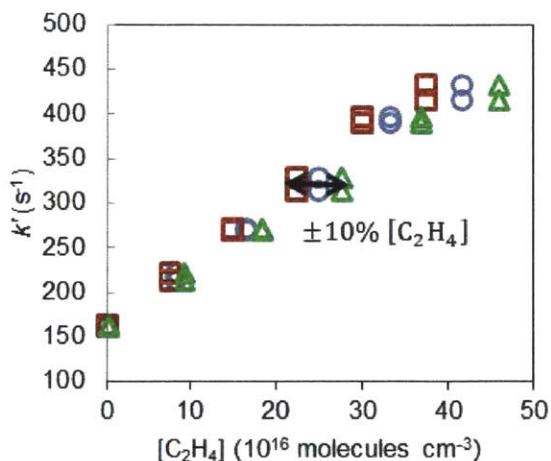
Figure A 3: Sample pseudo-first-order CH_2OO decay rate k' vs. $[C_2H_4]$ demonstrating the effect of $\pm 10\%$ $[C_2H_4]$ uncertainty

A k_2 value with 95% confidence intervals was obtained from the linear fit of each of these sets. The full range of k_2 values in this example (including confidence intervals) is $(0.55 - 0.77) \times 10^{-15} \text{cm}^3\text{molecule}^{-1}\text{s}^{-1}$ and the final value of k_2 reported here is chosen to reflect the entire range: $k_2(298 \text{ K}) = (0.66 \pm 0.11) \times 10^{-15} \text{cm}^3\text{molecule}^{-1}\text{s}^{-1}$. $k_2(T)$ was determined in this manner for every experiment.

To determine A and E_a, the Arrhenius fit was conducted for four extreme cases: all of the $k_2(T)$ values were shifted up or down together by their respective systematic uncertainties and the highest $k_2(T)$ value was set to the upper (lower) extreme of its confidence interval while the lowest $k_2(T)$ value was set to the lower (upper) extreme of its confidence interval to produce an Arrhenius plot with the steepest (shallowest) slope. Table A 8 shows the values of ln(A) and $\frac{E_a}{1000R}$ obtained for these four (two by two) extreme cases.

Table A 8: Range of possible fit Arrhenius parameter for CH_2OO + ethene at 298 K taking into account both random and systematic uncertainty in k_2. Units of A are $\text{cm}^3\text{molecule}^{-1}\text{s}^{-1}$.

	Shifted Down		Shifted Up	
	ln(A)	$E_a/(1000R)$ K^{-1}	ln(A)	$E_a/(1000R)$ K^{-1}
Steepest Slope	-32.53	0.74	-32.33	0.74
Shallowest Slope	-31.96	0.95	-31.76	0.95

The average and standard deviation of the values in Table A 8 was taken to obtain ln(A) = $-(32.1 \pm 0.3)$ and $\frac{E_a}{1000R} = 0.85 \pm 0.1 \text{ K}^{-1}$, or in meaningful units: $A = (11 \pm 5) \times 10^{-15}\text{cm}^3\text{molecule}^{-1}\text{s}^{-1}$ and $E_a = 7000 \pm 900 \frac{J}{\text{mol}}$. These correspond to the values and uncertainties reported in section 3.1.

Attempts were made to measure the rate of CI + alkenes at temperatures above 494 K but as mentioned above we found that CI was less stable above this temperature and there was also a small baseline offset in the 375 nm absorbance traces as shown in Figure A 4 below. Furthermore, even for the maximum propene concentration that could be used at this temperature (red curve in Figure A 4) the change in CH_2OO decay was not very substantial.
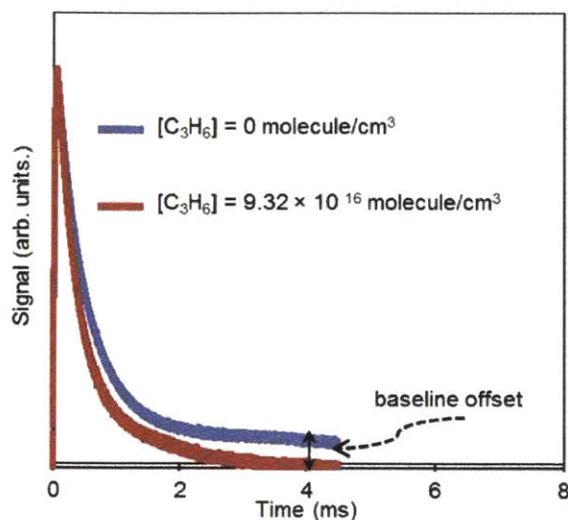
Figure A 4: Decays of CH_2OO absorbance ($\lambda = 375$ nm) at 599 K and 25 Torr in the absence and presence of propene. Without propene there is a clear and reproducible baseline offset as indicated possibly due to absorption by another species. With propene this absorbing species still seems to be there, but it is decaying away on a noticeable time scale.

Probing IO at $\lambda = 427.2$ nm

Figure A 5 shows the short and long time behavior of a typical absorbance trace taken at $\lambda = 427.2$ nm along with a typical $\lambda = 375$ nm trace taken at the same conditions for comparison. At short times the qualitative difference between the traces obtained using different probe wavelengths is clear. Specifically, at $\lambda = 427.2$ nm the absorbance signal continues to increase well past the time at which the $\lambda = 375$ nm trace has reached its maximum. This could be attributable to later formation of IO by processes other than the initial $CH_2I + O_2$ reaction. Also, the signal at $\lambda = 427.2$ nm decays at a slower rate than at $\lambda = 375$ nm, as conveyed in Figure 3-2. It should also be noted that at long times the absorbance signal at $\lambda = 427.2$ nm goes negative, which could simply be due to thermal lensing. However, this behavior was reproducible and insensitive to the multiple-pass probe laser alignment, suggesting that it could be attributable to a real phenomenon. Because of the multiple processes that seem to be occurring at $\lambda = 427.2$ nm (initial IO formation, later secondary IO formation, decay and another phenomenon causing the negative offset) a single exponential fit to the decay portion of the trace does not perfectly match the data, as shown. Nevertheless, such a fit is sufficient to determine if the observed decay increases significantly with increasing propene, as was done here.
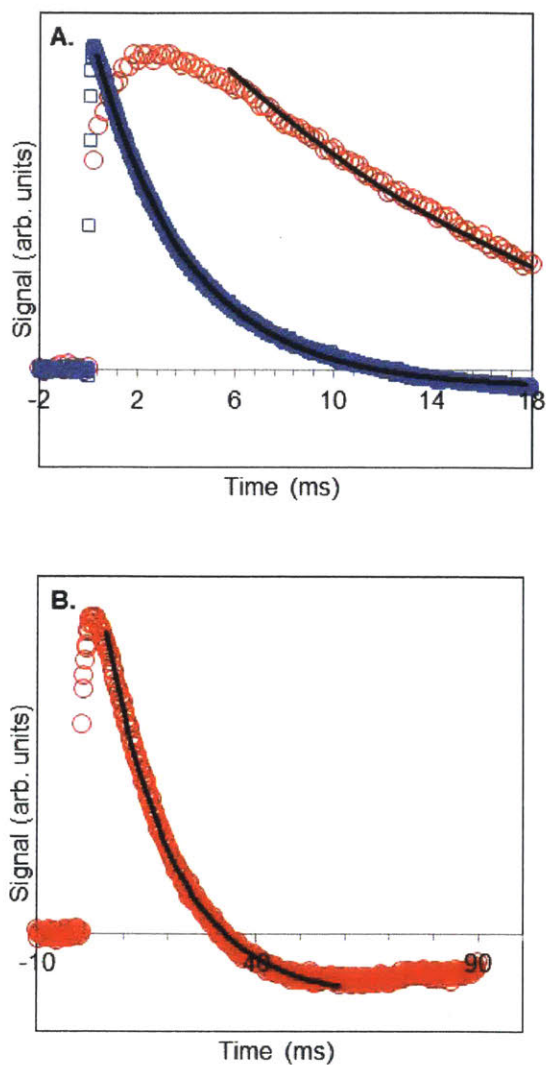
Figure A 5: Panel A shows short time behavior of absorbance traces recorded at the same conditions with $\lambda = 375$ (□) and 427.2 nm (○). Panel B shows long time behavior with $\lambda = 427.2$ nm only. Only every 200th point is shown. Solid black lines are single exponential fits.

To gain further confidence that the signal observed at $\lambda = 427.2$ nm is mostly attributable to IO, the relative absorbance was measured at two nearby wavelengths (Figure A 6). As shown, $\lambda = 427.2$ nm corresponds to a peak in absorbance to within 0.5 nm, consistent with the 4,0 band of IO.[149]
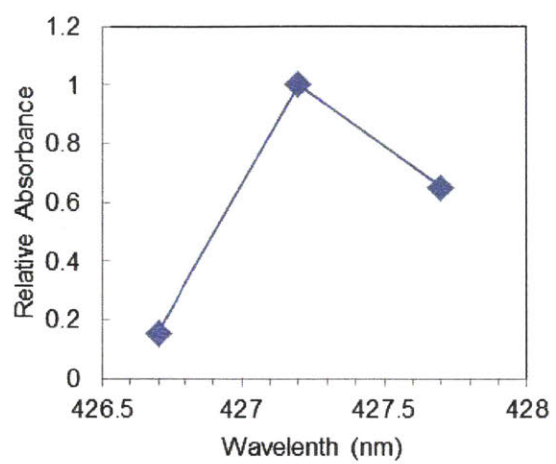
Figure A 6: Relative absorbance measured at wavelengths near the 4,0 band of IO's $A^2\Pi \leftarrow X^2\Pi$ transition.

Appendix B

Additional Details for CH$_2$OO Self-Reaction

Details of Fitting I Atom Growth to Obtain [CH$_2$OO]$_0$

For convenient reference, the equation used to calculate [CH$_2$OO]$_0$ is reproduced here.

$$[CH_2OO]_0 = \frac{A_{I,2}}{\sigma_I(\lambda = 1315.246 \text{ nm})l_I}$$

Using the integrated absorption cross section of the I atom at its F = 3 $^2P_{1/2} \leftarrow$ F = 4 $^2P_{3/2}$ hyperfine atomic transition measured by Ha et al.,[78] as well as the approximate Voigt profile given by Whiting[143] and the empirical broadening parameters measured by Davis et al.[370] in different bath gases to account for collisional and Doppler broadening, we can calculate $\sigma_I(\lambda = 1315.246 \text{ nm})$. For example, at 297 K and in 25 Torr N$_2$, $\sigma_I(\lambda = 1315.246 \text{ nm}) = 2.2 \pm 0.4 \times 10^{-18}$ cm^2 molecule^{-1}. l_I is calculated by measuring the distance between the I atom laser and the center of the photolysis laser beam in Cartesian coordinates (x_{in}, y_{in}) at some point, z_{in}, before the beams enter the reactor and at another point, z_{out}, after the beams exit (x_{out}, y_{out}). The distance between the inlet and outlet points, $z_{tot} = z_{out} - z_{in}$, is also measured as well as the radius of the collimated photolysis laser beam, $r_{photolysis}$, allowing l_I to be calculated by the following equations.

$$l_I = \sqrt{z_{overlap}^2 + r_{overlap}^2}$$

$$z_{overlap} = \frac{2z_{total}\sqrt{r_{photolysis}^2[(x_{in} - x_{out})^2 + (y_{in} - y_{out})^2] - [x_{out}y_{in} - x_{in}y_{out}]^2}}{(x_{in} - x_{out})^2 + (y_{in} - y_{out})^2}$$

$$r_{overlap} = \frac{z_{overlap}}{z_{total}}\sqrt{(x_{out} - x_{in})^2 + (y_{out} - y_{in})^2}$$

The uncertainty in the value of [CH$_2$OO]$_0$ is calculated by propagation of uncertainty.

$$\frac{\Delta([CH_2OO]_0)}{[CH_2OO]_0} = \sqrt{\left[\frac{\Delta(A_{I,2})}{A_{I,2}}\right]^2 + \left[\frac{\Delta(\sigma_I)}{\sigma_I}\right]^2 + \left[\frac{\Delta(l_I)}{l_I}\right]^2}$$

The relative uncertainty in $\Delta A_{I,2}$ is due to uncertainty in the back extrapolation of the fit to t_0 (Figure B 1).
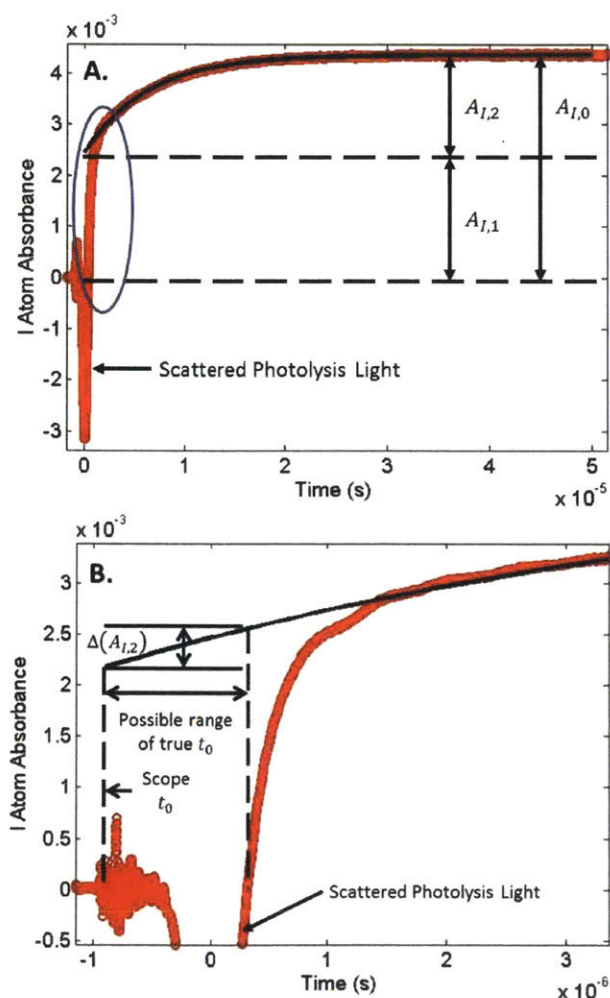
Figure B 1: Representative I atom absorbance trace at 297 K, in 50 Torr He and $[O_2] = 1.1 \times 10^{17}$ cm^{-3} with model fit (black line) to extract value of $[CH_2OO]_0$. **A.** shows the entire fit and **B.** shows only times around t_0 (circled portion of **A.**).

As shown, there is a ~1.25 μs window of possible t_0 values, as defined by the time zero recorded by the oscilloscope (lower t_0 limit, defined by the time when a separate photodiode detects photolysis light) and when the spike from scattered photolysis recorded by the I atom

photodiode has passed (upper t_0 limit). Throughout this work t_0 is defined as the time at which scattered photolysis light measured by the I atom photodiode is recorded on our digital oscilloscope (time at which photolysis spike peaks). This definition eliminates the approximately one microsecond delay introduced by the Stanford Research Systems SR560 low-noise pre-amplifier through which the I atom signal is amplified before being recorded on the oscilloscope (because the I atom laser is only single-pass the pre-amplifier is necessary to obtain sufficient signal-to-noise.). Nonetheless, to be conservative we assume that the true t_0 could be anywhere within this 1.25 μs window, which translates into ~10% relative uncertainty in $A_{I,2}$. Although the pre-amplifier also has a 1 MHz (10% accuracy) low-bandpass filter that broadens the recorded signal at very short time scales (≤ 1 μs), we are fitting for a growth rate with characteristic time, $\tau \left(= \left(k_{growth}[O_2] \right)^{-1} \right)$, that is ~6 μs at its fastest. The oscilloscope itself introduces no additional signal distortion at these fast times, as evidenced by the fact that if the I atom signal is directly routed to the oscilloscope, bypassing the pre-amplifier, the photolysis spike recorded by the I atom photodiode corresponds to the oscilloscope t_0 within nanoseconds, and the spike itself becomes orders of magnitude sharper (rise and fall times on the scale of nanoseconds). The oscilloscope does, however, distort signals with $\tau \geq 65$ ms due to the RC electronics, as discussed in a later section. It should also be noted that this 10% uncertainty in $A_{I,2}$, as well as $A_{I,1}$, results in an ~20% uncertainty in $\alpha \left(= \frac{A_{I,2}}{A_{I,1}} \right)$.

Ha et al. quote 20% relative uncertainty in their measured I atom cross section value, σ_I,[9] which we depend on as our absolute calibration. We determine $\frac{\Delta(l_I)}{l_I} \approx 25\%$ from propagation of uncertainty on the equations for l_I shown above. Combining these three uncertainties using the equation above, the overall uncertainty in our determination of $[CH_2OO]_0$ is 35%.

Details of Fitting "Complex" Model to CH₂OO and I Atom Decay

Table B 1 summarizes the values obtained for the global fit parameters of the "complex" model (k_{self}, k_{CH_2OO+I}, k_{uni} and $k_{uni,I}$) for all of the experiments conducted here. The only local fit parameters (allowed to vary trace to trace) are b and c, which are shift factors for the normalized CH₂OO and I Atom decay fits, respectively, and $[CH_2OO]_0$, which is allowed to vary ±35% from the value measured using I atom absorbance due to the uncertainty of that

measurement as discussed in the previous section. b and c range from 0 to 0.1 and 0.07 to 0.4, respectively.

Table B 1: Fit rate coefficients from "complex" model for all experiments (T=297 K)

Base Case Experiments	k_{self} [a]	k_{CH_2OO+I} [b]	k_{uni} [c, d]	$k_{uni,I}$ [c, e]	Range of $[CH_2OO]_0$ Scaling [f]
P = 25 Torr He	5.0 ± 1.8	8.4×10^{-28}	70	82	-5% to +2%
P = 25 Torr N_2	3.6 ± 1.3	1.6×10^{-20}	180	50	-33% to +30%
P = 50 Torr He	6.1 ± 2.0	3.3×10^{-20}	40	63	-15% to +1%
P = 50 Torr N_2	10.0 ± 3.5	5.2×10^{-12}	0	43	-35% to -18%
P = 100 Torr N_2	5.0 ± 1.8	1.2×10^{-27}	200	38	-35% to +30%
Control Experiments [g]					
Larger Photolysis Beam (1.3 cm)	4.9 ± 1.7	1.3×10^{-20}	170	38	-35% to +35%
Smaller Photolysis Beam (1 cm)	10.9 ± 3.8	5.3×10^{-28}	80	39	-34% to -7%
Single UV Pass	4.8 ± 1.7	1.1×10^{-20}	240	37	-35% to +35%
Double Flashes per Refresh	5.8 ± 2.0	9.1×10^{-13}	50	43	+18% to +35%
Half Flashes per Refresh	5.6 ± 2.0	9.7×10^{-22}	150	80	-14% to +16%

[a] Units of $10^{-11} cm^3$ molecule^{-1} s^{-1}
[b] Units of cm^3 molecule^{-1} s^{-1}
[c] Units of s^{-1}
[d] Typical error bars from uncertainty of fit (one standard deviation) are ±10 s^{-1}.
[e] Error bars from not completely taking into account effect of RC electronics are ±10%.
[f] Constrained to be ±35%
[g] Control experiments were conducted at a total pressure of 50 Torr N_2, except for "Half Flashes per Refresh" experiment, which was in 50 Torr He

There are several important points to note about these fit values. First, the values of k_{self} obtained from the "complex" model and the "simplified" model for a given experiment are within their respective error bars (compare Table B 1 above with Table 3-6). The differences between fit values of the two models is likely due to the fitting procedure itself: in the case of the "complex" model there is much more data that the model has to fit because both CH_2OO and I Atom decays are being used, and there are also more parameters to adjust, whereas for the "simplified" model, only the CH_2OO decay is fit.

Second, all of the fit values for k_{CH_2OO+I} are arbitrarily small, except for the "50 Torr N_2" experiment, which is likely in a local optimum of the sum of least squares. These results indicate that CH_2OO + I is not a significant sink of either CH_2OO or I at our conditions, as discussed in section 3.2.

Finally, $k_{uni,I}$ is essentially constant for all experiments in N_2 but it increases noticeably when the bath gas is switched to He, consistent with decay of I Atom being predominantly due to diffusion out of the beam. Furthermore, in going from 25 Torr He to 50 Torr He, there is a noticeable decrease in $k_{uni,I}$, which again is as expected if diffusion is the main loss process.

To ensure that $CH_2OO + I$ is not occurring significantly, we refit the "50 Torr He" experiment to the "complex" model and constrained k_{CH_2OO+I} to various values as shown in Figure B 2 and summarized in Table B 2. The largest value of k_{CH_2OO+I} used was 5×10^{-11} cm^3 molecule^{-1} s^{-1}, which is on the same order as the theoretical predictions of Su et al. for the same reaction at similar pressures.[164] From Figure B 2 it is clear that if $k_{CH_2OO+I} = 5 \times 10^{-11}$ cm^3 molecule^{-1} s^{-1} the model is not able to fit the data, indicating that this rate coefficient is much too fast. As k_{CH_2OO+I} is decreased below 1.0×10^{-11} cm^3 molecule^{-1} s^{-1} the model is able to capture the data well, but as shown in Table B 2 this is only because all of the values of $[CH_2OO]_0$ are being pushed to their lower limit of -35% and k_{uni} is forced to zero (it should at least be ~ 40 s^{-1} to account for diffusion of CH_2OO out of the beam). Therefore, we put a conservative upper bound of 1.0×10^{-11} cm^3 molecule^{-1} s^{-1} on the rate coefficient of $CH_2OO + I$ at our conditions, which is at least a factor of five lower than the predictions of Su et al.[164]
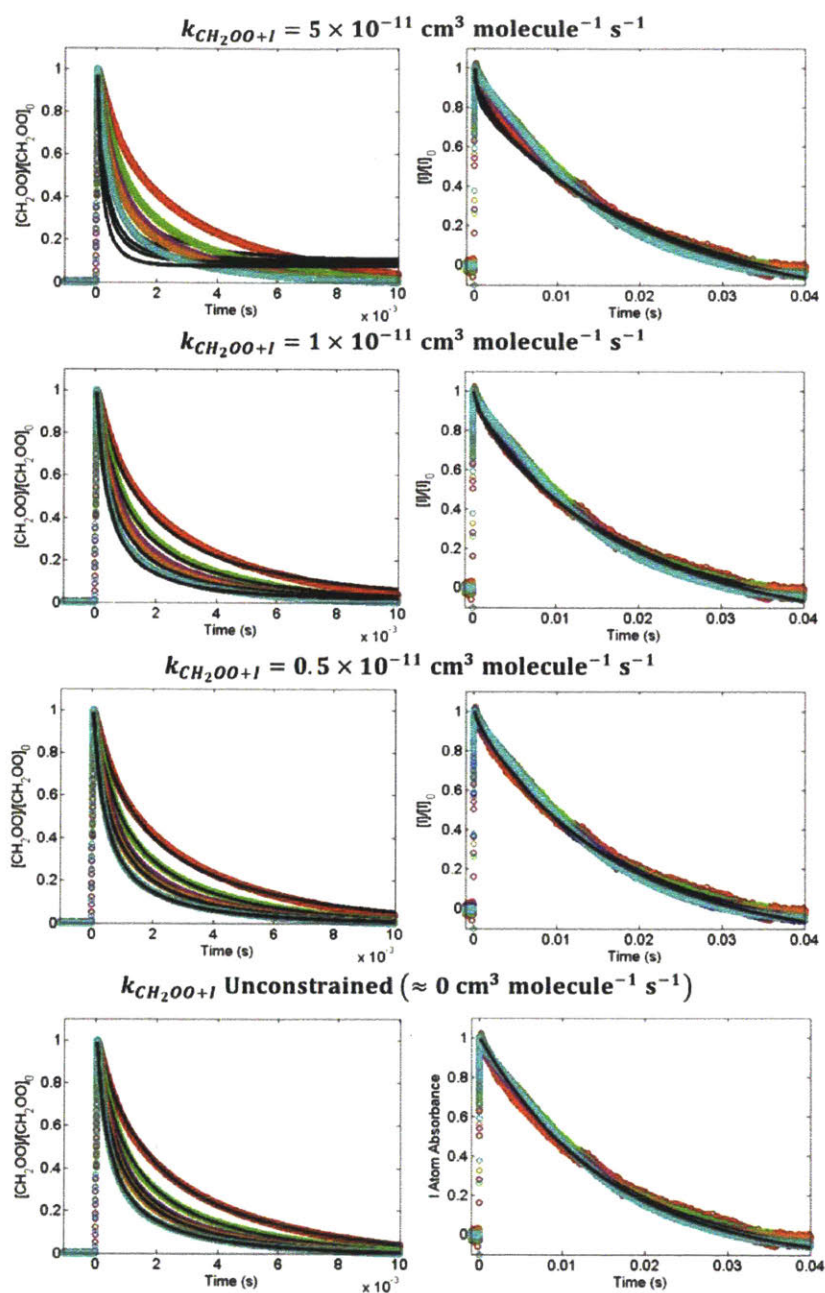
Figure B 2: Measured decays of CH_2OO (left) and I Atom (right) at 297 K and 50 Torr He over a range of $[CH_2OO]_0$ values ($5 - 18 \times 10^{12}$ molecules cm^{-3}). Solid black lines are fits of the "complex" model with k_{CH_2OO+I} constrained to the various values indicated.

Table B 2: Fit rate coefficients from "complex" model for "50 Torr He" experiment for different constrained values of k_{CH_2OO+I}

Lower Bound Constraint on k_{CH_2OO+I}[a]	k_{CH_2OO+I}[a]	k_{self}[a]	k_{uni}[b]	$k_{uni,I}$[b]	Range of $[CH_2OO]_0$ Scaling[c]
> 5.0	5.0	21.3	0	45	-35%
> 1.0	1.0	8.8	0	50	-35%
> 0.8	0.8	8.7	0	52	-35%
> 0.5	0.5	8.7	0	55	-35%
>0.1	0.1	8.7	17	62	-35% to -31%
>0.05	0.05	8.4	30	62	-35% to -28%
>0.01	0.01	8.1	41	63	-35% to -24%
Unconstrained	≈ 0	6.1	40	63	-14% to +1%

[a]Units of $10^{-11} cm^3$ molecule^{-1} s^{-1}
[b]Units of s^{-1}
[c]Constrained to be ±35%

Details of Fitting "Simplified" Model to CH$_2$OO Decay

Another approach to putting an upper bound on k_{CH_2OO+I} is to fit the decay of CH$_2$OO only to the "simplified" kinetic model, where k_{uni} is a local fit parameter. Because this model does not include CH$_2$OO + I, the catch-all first-order decay rate coefficient, k_{uni}, should capture the contribution of this reaction. Figure B 3 shows the fit value of k_{uni} obtained by fitting the "simplified" model to the "50 Torr He" experiment as a function of $[I]_0$.
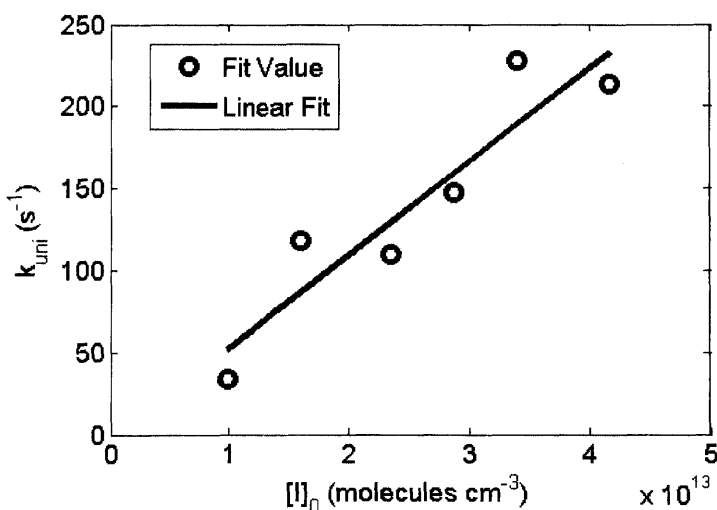
Figure B 3: Fit values of k_{uni} as a function of $[I]_0$ for the "50 Torr He" experiment obtained by fitting data to the "simplified" model.

As shown, k_{uni} does seem to increase linearly with $[I]_0$ with an approximate bimolecular rate coefficient of 0.57×10^{-11} cm^3 molecule^{-1} s^{-1} (slope of the linear fit shown in Figure B

3). This type of pseudo-first-order analysis, where I atom is treated as the excess reagent is possible because on the timescale over which CH_2OO is decaying (~10 ms) the I atom concentration only drops by ~20%, at most (see the decays in Figure B 2 as an example). This same analysis was conducted for the other nine experiments reported here and Table B 3 summarizes the results.

Table B 3: Values of k_{CH_2OO+I} obtained by fitting all experiments to the "simplified" model and measuring the slope of the linear fit of k_{uni} versus $[I]_0$ (pseudo-first-order analysis).

Base Case Experiments	k_{CH_2OO+I} [a, b]
P = 25 Torr He	0.4 ± 0.3
P = 25 Torr N_2	1.0 ± 0.3
P = 50 Torr He	0.6 ± 0.2
P = 50 Torr N_2	0.6 ± 0.4
P = 100 Torr N_2	1.5 ± 0.4
Control Experiments [e]	
Larger Photolysis Beam (1.3 cm)	2.3 ± 0.4
Smaller Photolysis Beam (1 cm)	No Trend Observed
Single UV Pass	1.5 ± 0.6
Double Flashes per Refresh	0.6 ± 0.2
Half Flashes per Refresh	0.6 ± 0.6

[a] Units of $10^{-11} cm^3$ molecule^{-1} s^{-1}
[b] Uncertainty is due to linear fitting procedure (one standard deviation reported)

Fit values of k_{CH_2OO+I} range from $0.4 - 2.3 \times 10^{-11}$ cm^3 molecule^{-1} s^{-1} (ignoring the "Smaller Photolysis Beam" experiment where k_{uni} showed no clear dependence on $[I]_0$). The increasing trend of k_{uni} with $[I]_0$ suggests that much of the apparent first-order decay is due to CH_2OO + I, and our data is broadly consistent with $k_{CH_2OO+I} \approx 0.5 \times 10^{-11}$ cm^3 molecule^{-1} s^{-1} at our conditions. However, for several reasons we cannot unambiguously determine this rate coefficient:

1. Most of the CH_2OO decay is due to the faster self-reaction, which varies with the imperfectly known $[CH_2OO]_0$, so it is difficult to quantify exactly the first order portion of the decay, k_{uni}.

2. Our I atom absorbance signal is noisy because it is only single-pass, so it is hard to perceive the effects of CH_2OO + I on the I atom decay if this reaction is slow.

3. There are other possible explanations for why k_{uni} increases with photolysis energy, for

    example secondary chemistry such as $CH_2OO + CH_2O$. Indeed, the fact that the fit value

    of k_{CH_2OO+I} changes noticeably going from the smallest (1.0 cm) to middle (1.15 cm, all

    base case experiments) to largest (1.3 cm, both the "Larger Photolysis Beam" and "Single

    UV Pass" control experiments) photolysis diameter suggests that there is some other

    phenomenon being captured by k_{CH_2OO+I}.

Although we cannot firmly determine the rate coefficient for $CH_2OO + I$, we can set a firm upper bound based on these results and the "complex" model results discussed in the previous section: $k_{CH_2OO+I} < 1.0 \times 10^{-11}$ cm^3 molecule^{-1} s^{-1}.

   As mentioned in section 3.2, it should not be necessary to fit both the growth and decay of CH_2OO at the same time because the two processes occur on vastly different time scales (~20 μs compared to ≥ 2 ms). To quantitatively show that the production of CH_2OO can essentially be treated as instantaneous when fitting for its long-time decay we have fit the "50 Torr He" experiment to a "simplified" model where $k_{growth}(= 1.4 \pm 0.1 \times 10^{-12}$ cm^3 molecule^{-1} s^{-1}) is included (Figure B 4 below). The fit value of k_{self} obtained in this manner is $5.8 \pm 2 \times 10^{-11}$ cm^3 molecule^{-1} s^{-1}, well within the uncertainty of the value obtained when k_{growth} is not included ($5.4 \pm 1.9 \times 10^{-11}$cm^3 molecule^{-1} s^{-1}), justifying our decision to only fit the decay portion of $[CH_2OO](t)$.
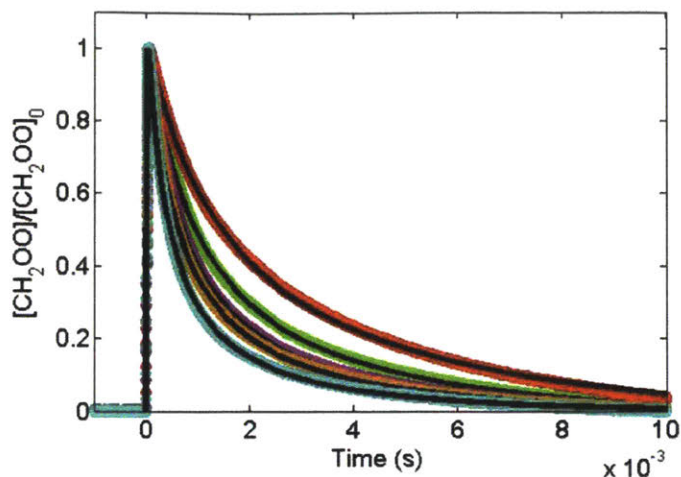
Figure B 4: Representative normalized CH_2OO decays at 297 K and 50 Torr He ("50 Torr He" experiment in Table 3-5, same data as in Figure 3-11). Solid black lines are fits of the "simplified" model with k_{growth} included.

Measuring CH₂OO UV Absorption Cross Section Using Single-Pass Probe

In our previous work we reported a UV absorption cross section of CH_2OO at $\lambda = 375$ nm (wavelength of UV probe laser) that was $\sim 7 \times 10^{-18}$ cm^2 molecule^{-1} (section 3.1.4.1), in reasonable agreement with Beames et al.[123] and in significant disagreement with Sheps.[122] This measurement was conducted using a Herriott multiple-pass alignment of the UV probe laser, which improves the signal to noise of the measurement by a factor of ~ 30, but also introduces significant uncertainty in the probe laser path length, l_{probe}. As mentioned in section 3.2, one of the control experiments we did as part of this work was measuring the UV absorbance of CH_2OO, A_{375}, for a single-pass configuration where both the UV and I atom lasers are following the same optical path through the reactor and hence $l_{probe} = l_I$. In addition to reducing the relative uncertainty in l_{probe} from $\sim 50\%$ to $\sim 35\%$, this overlapping single-pass configuration ensures that both the I Atom and UV lasers encounter the same radical concentrations as they intersect with the photolysis beam. In this configuration, $\sigma_{CH_2OO}(\lambda = 375$ nm$)$ can be calculated by the following equation:

$$\sigma_{CH_2OO}(\lambda = 375 \text{ nm}) = \frac{A_{375,max}}{l_I[CH_2OO]_0}$$

$[CH_2OO]_0$ is quantified by fitting the I Atom absorbance at short times, as detailed in section 3.2. Figure B 5 shows values of $\sigma_{CH_2OO}(\lambda = 375\ nm)$ calculated from the "Single UV Pass" control experiment using the equation above for different values of $[CH_2OO]_0$. The error bars on the measurement represent 35% relative uncertainty.
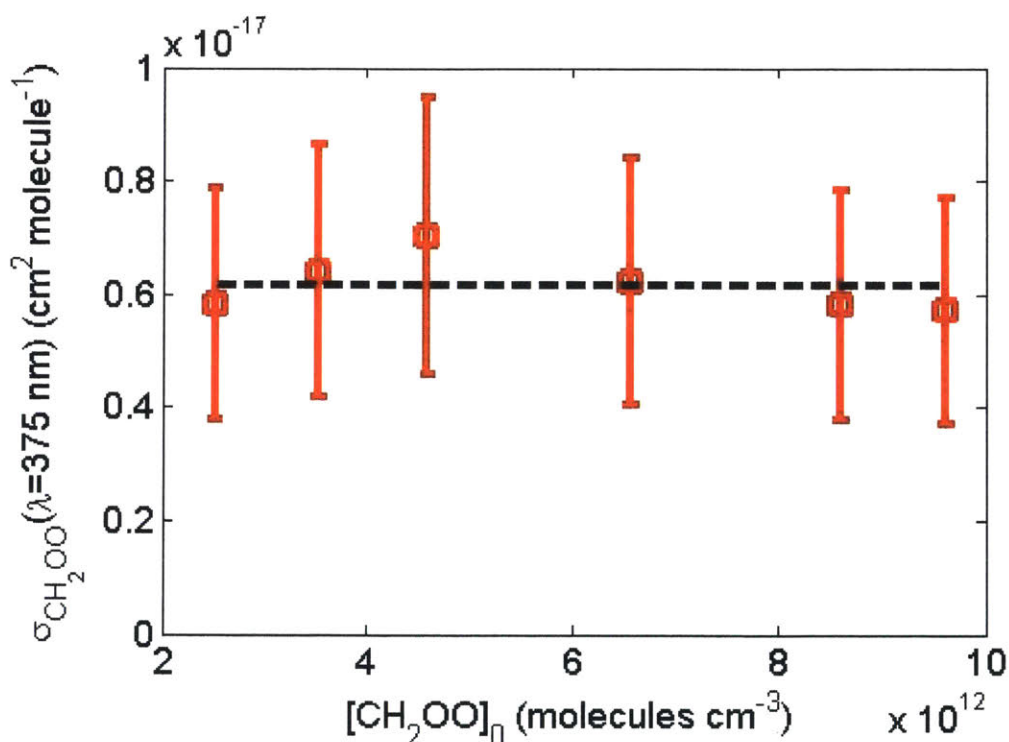
Figure B 5: UV Absorption cross section of CH_2OO at $\lambda = 375$ nm measured at different values of $[CH_2OO]_0$. Dashed black line is an average of the six points. The UV probe laser was in a single-pass alignment for this experiment and overlapping with the single-pass of the I Atom laser ("Single UV Pass Control" experiment in Table 3-5).

Based on the average value of all six measurements (dashed black line in Figure B 5) we report a value of $\sigma_{CH_2OO}(\lambda = 375\ nm) = 6.2 \pm 2.2 \times 10^{-18}\ cm^2\ molecule^{-1}$, in excellent agreement with both our previous measurement,[74] as well as the recent measurement of Ting et al. $(7.7 \pm 0.385 \times 10^{-18}\ cm^2\ molecule^{-1}$ at 375 nm).[165] As mentioned in section 3.2, the agreement in $\sigma_{CH_2OO}(\lambda = 375\ nm)$ values obtained using both a Herriott multiple-pass and single-pass alignment of the UV probe beam provides evidence that the photolysis laser generates a homogeneous mixture of radicals. The agreement between our measurement and

Ting et al. provides evidence that the way in which we are quantifying $[CH_2OO]_0$ is not systematically different from their approach.

Effect of O_2 on I Atom Decay

It was shown in section 3.2 that the long time decay of I atom is insensitive to $[CH_2OO]_0$, $[I]_0$ and $[CH_2I_2]$. Here we report a separate experiment where the decay of I atom was measured over a wide range of oxygen concentrations (Figure B 6).
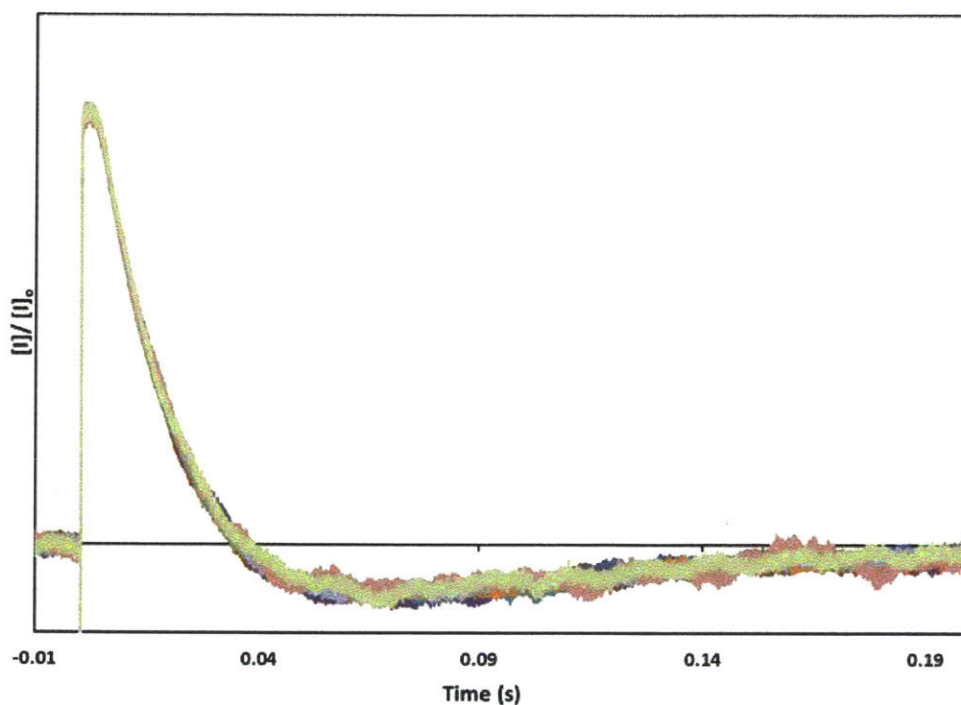
Figure B 6: Normalized decay of I atom at O_2 concentrations ranging from $2.2 - 32.6 \times 10^{16}$ molecules cm^{-3}.

Two observations were made from this experiment. First, the I atom decay is insensitive to $[O_2]$, leaving diffusion out of the beam as its primary loss process as discussed in an earlier section. Second, the I Atom absorbance goes significantly below baseline and then returns to baseline at longer times. We have previously observed this kind of behavior for IO in Figure A 5, another long-lived species. This phenomenon is due to details of the electronics used to amplify and record the signals as discussed in the next section. However, this long-time phenomenon, after all of the CH_2OO had been consumed, does not affect the main conclusion taken from measuring the I Atom decays, which is that $CH_2OO + I$ is not significant at our conditions.

Effect of RC Electronics on I Atom Decay Signal

As mentioned in the previous section, we observed the I Atom signal go below baseline and return to baseline at long-times. We hypothesize this is an effect introduced by the RC electronics. Specifically, because the I Atom signal is AC coupled to the oscilloscope it goes through a series RC circuit, which acts as a high-bandpass filter. There is also a 0.03 Hz high-bandpass filter on the pre-amplifier through which the signal is amplified before being recorded by the oscilloscope, but this filter will only impact signals on much longer time scales (~30 s). To characterize this effect we considered a typical first order decay of I Atom absorbance with time constant, $\tau = \frac{1}{k_{uni,I}}$.

$$A_I = A_{I,0} e^{-\frac{t}{\tau}}$$

$$= -\ln\left(1 + \frac{V_{in}(t)}{V_{ref}}\right)$$

$V_{in}(t)$ is the (negative) transient signal being input to the oscilloscope (proportional to the light intensity detected by the photodiode) and V_{ref} is the absolute value of the maximum signal that could be obtained (corresponding to complete attenuation of the laser beam). $\frac{V_{in}(t)}{V_{ref}} \leq$ $\sim \frac{-20\,mV}{6000\,mV} = -0.003$ and therefore the equation above can be simplified using a Taylor Series.

$$-\frac{V_{in}(t)}{V_{ref}} \approx A_{I,0} e^{-\frac{t}{\tau}}$$

$$V_{in}(t) = -V_{ref} A_{I,0} e^{-\frac{t}{\tau}}$$

$$V_{in}(t) = -V_0 e^{-\frac{t}{\tau}}$$

It can be shown for a series RC circuit, that if $V_{in}(t)$ is defined as the equation above, then the voltage recorded by the oscilloscope ($V_{out}(t)$, which is the voltage across the resistor in the circuit) will exhibit the following transient behavior.

$$-\frac{V_{out}(t)}{V_0} = (1 + c)e^{-\frac{t}{\tau}} - ce^{\frac{t}{RC}}$$

$$c = \frac{\tau}{RC - \tau}$$

RC is the RC time constant of the circuit. At short times relative to RC, $\frac{t}{RC} \approx 0$ and the equation above can be simplified to the following.

$$-\frac{V_{out}(t)}{V_0} = (1 + c)e^{-\frac{t}{\tau}} - c$$

This is essentially the same equation to which $\frac{A_I(t)}{A_{I,0}}$ was fit in the "complex" model where c was treated as a fit parameter. To both test whether this explanation of the transient I Atom behavior is correct and if the simplified equation shown above (and used throughout this work) is sufficient to capture the decay behavior at relatively short times, we fit a typical I Atom decay to the full model above that includes the RC decay (τ and RC are the fit parameters) and the simplified model (τ and b are the fit parameters) as shown in Figure B 7.
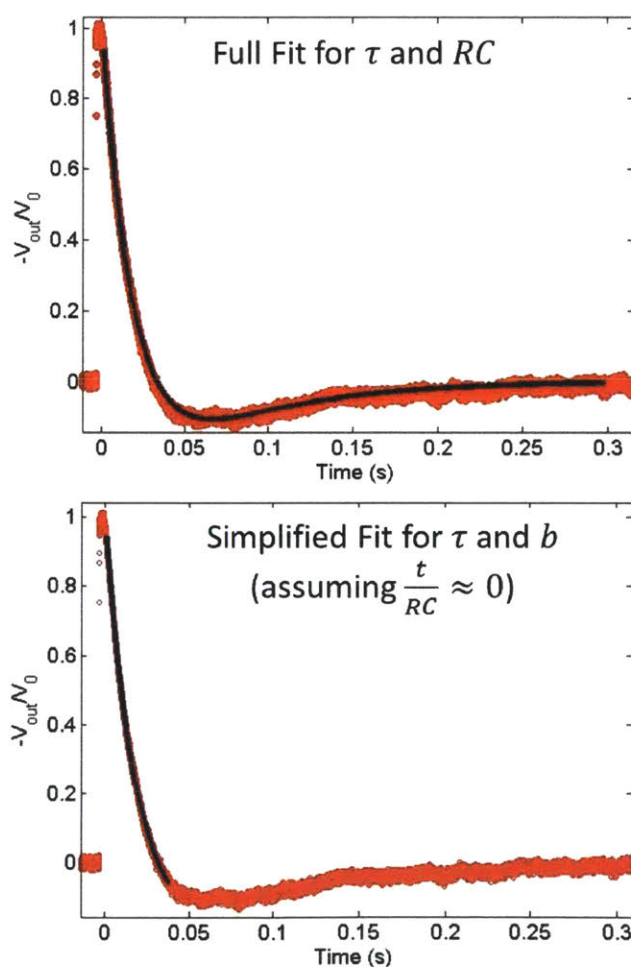
Figure B 7: Fits of a typical I Atom decay to a full model that includes RC decay and a simplified model that assumes this effect is negligible at early time scales.

Judging from the good fit of the full model, this description of the transient I atom signal is reasonable. Furthermore, from the full model fit, $\tau = 0.019$ s $\left(k_{uni,I} = 52 \text{ s}^{-1}\right)$ and RC =

0.065 s, and from the simplified model fit, $\tau = 0.017$ s $\left(k_{uni,I} = 57 \text{ s}^{-1}\right)$ and $b = 0.1991$. Therefore, although the RC and I Atom decay time scales are almost within a factor of three of each other, the simplified model is able to adequately fit for $k_{uni,I}$, which is the quantity of interest, within about 10%. This uncertainty in $k_{uni,I}$ due to not completely taking the RC effect into account for every I atom decay is reflected in Table B 1. The effect of the RC circuit is much less important for the decay of CH_2OO ($\tau \leq \sim 10$ ms), the signal for which is coupled to the oscilloscope in the same manner as the I atom signal and therefore encounters the same circuitry. This is consistent with the fit values of b, the vertical shift factor for the CH_2OO decay, being around four times smaller than the fit values of c.

Linearized Plots of [CH$_2$OO](t)
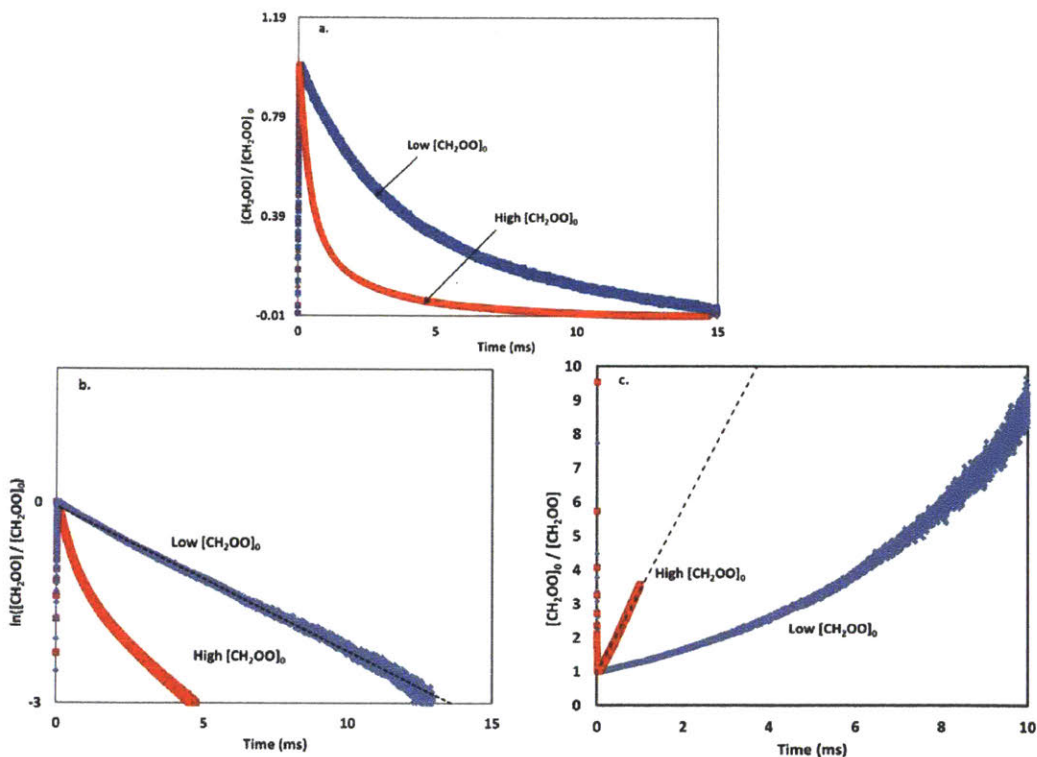
Figure B 8: Representative decays of $[CH_2OO](t)$ at high (red) and low (blue) initial concentrations of CH_2OO ($[CH_2OO]_0 = 18 \times 10^{12}$ and 2×10^{12} molecules cm^{-3} , respectively), plotted in different forms.

Figure B 8a shows representative CH_2OO decays at high and low $[CH_2OO]_0$. At high $[CH_2OO]_0$, $[CH_2OO](t)$ has already dropped substantially within about 1 ms. Figure B 8b is a

linearized first order plot (ln $[CH_2OO]/[CH_2OO]_0$ vs time) of the same data. The low $[CH_2OO]_0$ trace was fit to the following linear equation.

$$\ln\left(\frac{[CH_2OO]}{[CH_2OO]_0}\right) = -k_{uni}t$$

As shown, this fit is good over a long time range (> 10 ms), showing that at low $[CH_2OO]_0$ the decay is dominantly first-order, as expected. The slope of this fit yields an estimated value of $k_{uni} = 216\ s^{-1}$ under the given experimental conditions, which is within the range of k_{uni} values we obtained in our "complex" and "simplified" model fits. In contrast, the high $[CH_2OO]_0$ trace cannot be adequately fit by a simple first order decay.

Figure B 8c is a linearized second order self-reaction plot ($[CH_2OO]_0/[CH_2OO]$ vs time) of the same data. The low $[CH_2OO]_0$ trace was fit to the following linear equation.

$$\frac{[CH_2OO]_0}{[CH_2OO]} = 1 + k't$$

$$k' = 2k_{self}[CH_2OO]_0$$

As expected, the trace at high $[CH_2OO]_0$ manipulated in this manner shows a linear relationship at early times (up to 1ms). The slope of this linear fit, k', can be used to estimate a value of $k_{self} = \frac{k'}{2[CH_2OO]_0} = 6.75 \times 10^{-11}\ cm^3\ molecule^{-1}\ s^{-1}$. This value of k_{self} is within the error bars of our recommended value of ($6.0 \pm 2.1 \times 10^{-11} cm^3\ molecule^{-1}\ s^{-1}$).

Appendix C

Additional Details for CH₂OO + Carbonyls

UV Absorption Experiments at Different T and P

Table C 1 summarizes the conditions of the CH_2OO + CH_3COCH_3/CH_3CHO experiments. In all of our experiments $[O_2]$ was kept constant (6.1×10^{16} molecule cm^{-3}), $[CH_3COCH_3]$ was varied from $1.59 \times 10^{14} - 1.35 \times 10^{15}$ molecule cm^{-3} and $[CH_3CHO]$ was varied from $1.59 \times 10^{14} - 1.11 \times 10^{15}$ molecule cm^{-3}. The number of flashes per refresh was 1.21 and the photolysis beam diameter = 1.15 cm.

Table C 1: Conditions for T- and P- dependence UV absorbance experiments

Base case experiments	T	P	$[CH_2I_2]^a$	Photolysis power
	K	Torr	molecule/cm^3	mJ/ pulse
T-dependence	(298 ± 1.3) to (494 ± 5)	25	1.35×10^{14}	50
P- dependence	(298 ± 1.3) and (444 ± 3)	4 - 50	1.35×10^{14}	50
Control experiments				
Max. Photolysis energy	(298 ± 1.3) and (494 ± 5)	25	1.35×10^{14}	100
double $[CH_2I_2]$	(298 ± 1.3) and (494 ± 5)	25	2.44×10^{14}	50

$^a[CH_2I_2]$ was estimated by using the vapor pressure of CH_2I_2 at 298 K[166]

Two absorbance-control experiments were conducted at 298 and 494 K at constant pressure of 25 Torr, one with double the base case precursor concentration ($[CH_2I_2]$) and the other at maximum photolysis energy (100 mJ/pulse). These control experiments were performed to confirm that no interfering secondary chemistry was being observed under the base case conditions. Traces were also recorded in the absence of O_2 or CH_2I_2 at every temperature to ensure that no CH_2OO radicals are formed except under the normal reactor

conditions (i.e., with both CH_2I_2 and O_2 gases present) and/or that no other species are contributing to the 375 nm absorbance signal. Results of control experiments are shown in Figure C 1.
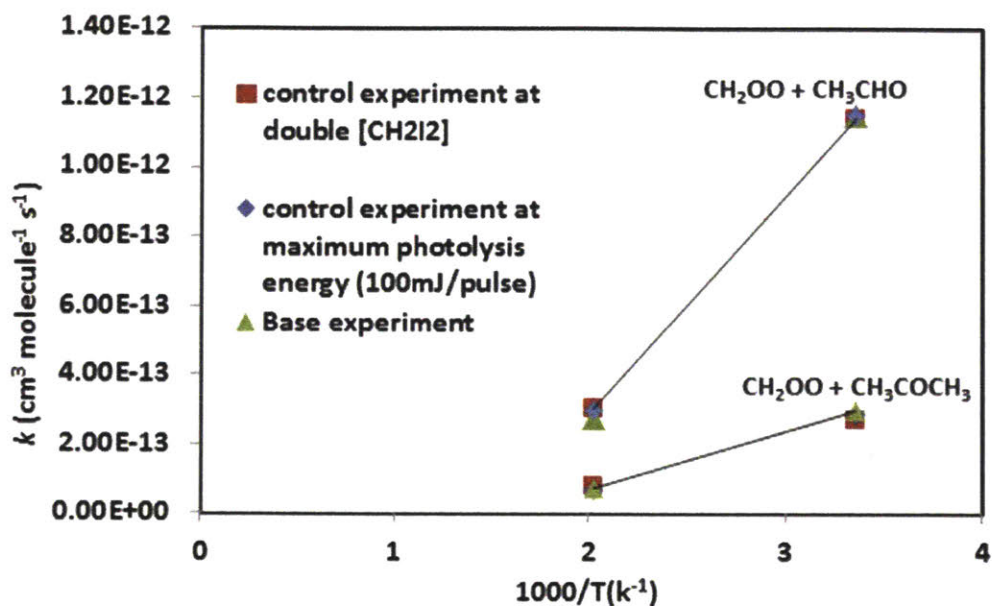
Figure C 1: Control experiments at 298 K and 494 K together with the base experiments for $CH_2OO + CH_3CHO$ (top points) and $CH_2OO + CH_3COCH_3$ (bottom points).

Figure S1 shows example of the control experiments carried out at the double concentration of CH_2I_2 and at maximum laser photolysis energy. As seen in the figure, the control results are consistent with the base condition ($[CH_2I_2] = 1.35 \times 10^{14}$ molecules cm^{-3} and 50 mJ/pulse), implying that the effect of laser energy and precursor concentration on the measured rate coefficients is negligible.

$CH_2OO + CH_3COCH_3$ MS Control Experiments

In addition to $\frac{m}{z} = 46$ amu (the mass of the simplest CI, CH_2OO), we observed four other transient species in our $\frac{m}{z}$ range of interest (0-104 amu) in the "Base Case" mass spectrometry (MS) experiment: $\frac{m}{z} = 31$, 73, 89 and 104 amu. Transient behavior was not discernible at $\frac{m}{z} = 15$ due to overlap with a CH_3COCH_3 fragment. This Base Case refers to the conditions where $CH_2OO + CH_3COCH_3$ is occurring and there is also calibration mixture (cal mix) present

in the reactor to act as an internal standard (Base Case = CH_2I_2 + O_2 + CH_3COCH_3 + cal mix + 355 nm photolysis). Control MS experiments were conducted without CH_3COCH_3, without O_2 and without cal mix to identify which of these transient species are possible products of CH_2OO + CH_3COCH_3. The maximum signal of transient species i, $S_{i,max}$, was normalized by the initial amount of CH_2I present, $[CH_2I]_0$ (obtained from simultaneously recorded I Atom Absorbance), and the average internal standard (benzene) signal during that experiment, $\overline{S}_{benzene}$:

$$\hat{S}_{i,max} = S_{i,max}/([CH_2I]_0\overline{S}_{benzene})$$

Performing this normalization removes the effect of varying CH_2I concentration and MS signal response from experiment to experiment. The ratio of $\hat{S}_{i,max}$, for a given control experiment with the base case experiment was then taken:

$$\frac{\left(\hat{S}_{i,max}\right)_{Control}}{\left(\hat{S}_{i,max}\right)_{Base\ Case}} = \frac{[i]_{max,Control}}{[i]_{max,Base\ Case}}$$

As shown, this ratio is indicative of how much the concentration of transient species, i, changed going from the Base Case to the control experiment. Table C 2 summarizes the results of this analysis for the three control experiments mentioned above. Note that for the "No Cal Mix" control, $\overline{S}_{benzene}$ = 0, so for this experiment we had no internal standard to use and we assumed that the signal response of the MS was the same for this control experiment as for the base case. We believe this is a good assumption because the Base Case and "No Cal Mix" experiments were done back-to-back for this reason, and because the Cal Mix was present in such low concentration ($\sim10^{11}$ molecules cm^{-3} compared to $\sim10^{17}$ molecules cm^{-3} total at the pressure of these experiments, 10 Torr) that the MS signal response should not be affected by removing it anyway.

Table C 2: Results of MS control experiments for CH_2OO + CH_3COCH_3. T = 298 K and P = 10 Torr. For Base Case experiment: $[CH_3COCH_3]$= 1.24×10^{15} molecule cm^{-3}, $[CH_2I_2]$ = 2.44×10^{14}, $[O_2]$ = 6×10^{16} molecule cm^{-3} and [Cal Mix Species] = 1.6×10^{11} molecule cm^{-3}. Each Control experiment was conducted under identical conditions as the Base Case experiment, except for the one change noted.

MS Control Experiment	$\frac{[i]_{max,control}}{[i]_{max,Base\ Case}}$ for $\frac{m}{z}$ =			
	31 amu	73 amu	89 amu	104 amu
No Acetone	1.0 ± 0.4	1.3 ± 0.5	0	0
No O_2	1.1 ± 0.4	1.1 ± 0.4	0	0
No Cal Mix.	0.17 ± 0.06	1.7 ± 0.6	1.0 ± 0.4	1.1 ± 0.7

There are several important things to note about these results. First, the species at $\frac{m}{z}$ = 89 and 104 amu only appear when both acetone and O_2 are present and their maximum concentrations are not affected by the presence of Cal Mix. Therefore, we conclude that these two species are products of CH_2OO + CH_3COCH_3, consistent with what Taatjes et al. have observed.[120] Second, the species at $\frac{m}{z}$ = 31 and 73 amu are present at the same maximum concentration regardless of whether acetone or O_2 are present. Therefore $\frac{m}{z}$ = 31 and 73 amu cannot be products of CH_2OO + CH_3COCH_3. Finally, the maximum concentration of $\frac{m}{z}$ = 31 decreases substantially without Cal Mix present, indicating that how much $\frac{m}{z}$ = 31 is being formed depends on one of the Cal Mix species being present. At the same time that the maximum concentration of $\frac{m}{z}$ = 31 decreases with no Cal Mix, the maximum concentration of $\frac{m}{z}$ = 73 increases, likely because whatever channels are producing $\frac{m}{z}$ = 31 and $\frac{m}{z}$ = 73 amu are competing for CH_2I. Therefore, if the rate for the $\frac{m}{z}$ = 31 producing channel decrease, there is more CH_2I available to form $\frac{m}{z}$ = 73 amu. We think that $\frac{m}{z}$ = 73 is produced by a side reaction involving a contaminant in our reactor, which previous to the current Criegee Intermediate studies has been used for studies on the vinyl and allyl radical.

Quantifying Pressure-Dependent Product Yields for CH_2OO + CH_3COCH_3

The kinetic model from section 3.3.3.4 is reproduced here for reference.

$$CH_2OO + CH_3COCH_3 \xrightarrow{k_2} \text{Products} \xrightarrow{\beta_{89}} \text{Product which forms } \frac{m}{z} = 89$$

$$\xrightarrow{\beta_{104}} \frac{m}{z} = 104 \text{ Product (SOZ)}$$

$$\xrightarrow{\beta_{46}} HCOOH + CH_3COCH_3$$

$$CH_2OO \xrightarrow{k_4} \text{Products}$$

$$2\,CH_2OO \xrightarrow{k_{self}} \text{Products}$$
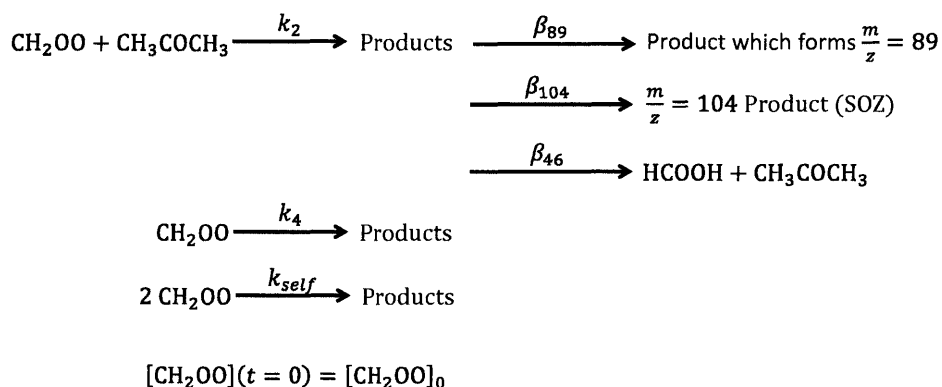
$$[CH_2OO](t = 0) = [CH_2OO]_0$$

Scheme C 1: General kinetic model for $CH_2OO + CH_3COCH_3$

Assuming that CH_3COCH_3 is present in excess, the analytical expressions for $[CH_2OO](t)$ and the steady state concentration of the CH_2OO + Acetone products, $[Products]_{CI+Acetone}$ ($t \rightarrow \infty$), based on the kinetic model above are the following:

$$[CH_2OO](t) = \frac{(k_2[CH_3COCH_3] + k_4)[CH_2OO]_0}{(k_2[CH_3COCH_3] + k_4 + 2k_{self}[CH_2OO]_0)e^{(k_2[CH_3COCH_3]+k_4)t} - 2k_{self}[CH_2OO]_0}$$

$$\left[\, Products_{(CI+Acetone)}\right](t \rightarrow \infty)$$

$$= \frac{k_2[CH_3COCH_3]}{2k_{self}} \ln\left(\frac{k_2[CH_3COCH_3] + k_4 + 2k_{self}[CH_2OO]_0}{k_2[CH_3COCH_3] + k_4}\right)$$

The time dependence of CH_2OO and the steady state concentration of the products of its reaction with CH_3COCH_3 depend on many parameters: $[CH_2OO]_0$, k_2, k_{self} and k_4. k_2 is known from the UV absorbance experiments also reported in this work. The experiments to quantify the other parameters are discussed below.

The initial concentration of CH_2OO, $[CH_2OO]_0$, in the above equation can be quantified from transient I atom absorbance assuming that $[CH_2I]_0 = [I]_0$. A narrow linewidth low-noise continuous-wave diode laser was used to generate an infrared beam tuned to the ($F = 3\ ^2P_{1/2} \leftarrow F = 4\ ^2P_{3/2}$) I atom atomic transition.[127] The infrared path lengths for I atom absorption were in the range of $50 - 70$ cm. Both ultraviolet and single-pass infrared absorbance traces were averaged over 500 acquisitions and recorded simultaneously.

We have previously shown that the I atom absorbance, A_I, may be fit adequately to the following equations (section 3.1.4.1).

$$[I](t) = \frac{[CH_2I]_0}{k_1[O_2] - k_5} \left([(1+\alpha)k_1[O_2] - k_5]e^{-k_5t} - \alpha k_1[O_2]e^{-k_1[O_2]t} \right)$$

$$A_I(t) = \sigma_I(\lambda = 1315.246 \text{ nm})l_I[I](t)$$

Where α is the branching fraction of $CH_2I + O_2$ to CH_2OO, k_1 is the total rate of that reaction, k_5 is the first order loss rate of I atom due to various processes, $\sigma_I(\lambda)$ is the known absorption cross section of I atom for a given hyperfine transition and l_I is the measured path length of the I atom laser. In these equations, α and k_1 are global fit parameters and k_5 and $[CH_2I]_0$ are local fit parameter (i.e. a different value of each is fit for every trace). The quantity $\alpha[CH_2I]_0$ is equal to $[CH_2OO]_0$. A representative fit to an I atom trace is shown in Figure C 2.
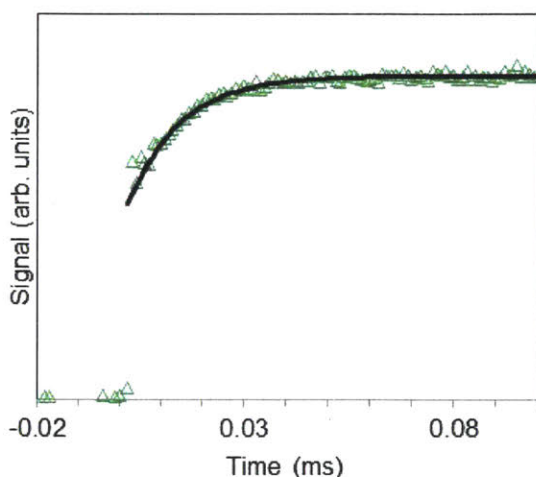
Figure C 2: Representative I atom trace at 298 K, 10 Torr and $[O_2] = 6.0 \times 10^{16}$ cm^{-3} with model fit to extract value of $[CH_2OO]_0$. Only every 100th point is shown.

The growth in I Atom absorbance shown in Figure C 2, A_I, corresponds to the sum of the initial photolytic production of I, and the production of I by the reaction $CH_2I + O_2 \rightarrow CH_2OO + I$ with rate $k_1 (= 1.4 \pm 0.1 \times 10^{-12}$ cm^3 molecule^{-1} s^{-1}).[74, 146] The amount of I Atom produced by the second process, $[I]_0$, can be captured and is equal to the amount of $[CH_2OO]$ formed.

The equation for $[Products]_{CI+Acetone}$ $(t \rightarrow \infty)$, also depends on k_{self} and k_4. Until recently, k_{self} had not previously been experimentally measured, although Vereecken et al.[126] had predicted a value of $k_{self} \approx 3.8 \times 10^{-11}$ cm^3 molecule^{-1}cm^{-1} using quantum calculations and TST. Just prior to the current work, our group was successfully able to experimentally measure k_{self} using UV absorption.[75] We measured $k_{self} = 6.2 \pm 2.2 \times 10^{-11}$ cm^3 molecule^{-1}cm^{-1}, in good agreement with Vereecken et al. and

later experimental measurements by Ting et al.[168] and Chhantyal-Pun et al.[169] We used this value of k_{self} in all calculations here.

The value of k_4, which includes diffusion out of the sampling volume, could change significantly if the experimental apparatus is modified. This study was conducted over the course of a few days, however, during which time the reactor was kept as static as possible. Therefore, for a given pressure and temperature, we expect this value to be roughly the same for all of the results reported here.

In order to obtain values for k_4 at 10, 25 and 50 Torr (temperature is always 298 K), the decay of $\frac{m}{z} = 46$ measured by TOF-MS, $S_{46}(t)$, was recorded under conditions where CH_2OO is formed (ie, $CH_2I_2 + O_2 + 355$ nm photolysis) both with and without CH_3COCH_3. $S_{46}(t)$ was then normalized and fit to the expression for $\frac{[CH_2OO](t)}{[CH_2OO]_0}$ above. k_4 was used as fit parameter for traces taken at the same pressure while k_2 and k_{self} were fixed to the values measured with UV absorbance earlier. Representative fits to normalized $S_{46}(t)$ with and without acetone and the fitted values obtained for k_4 are given in Figure C 3 and Table C 3, respectively.
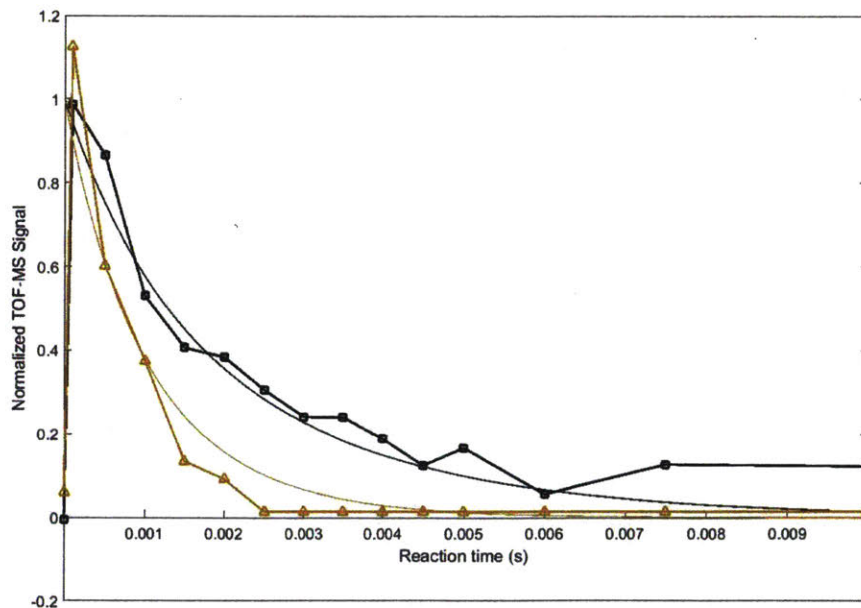
Figure C 3: Representative normalized decay of $\frac{m}{z} = 46$ measured by TOF-MS at 298 K, 50 Torr, $[O_2] = 6.0 \times 10^{16} cm^{-3}$ and $[CH_3COCH_3] = 0$ (black squares) and 1.24×10^{15} cm^{-3} (orange triangles). Thin lines are fits to the kinetic model given in Scheme C 1.

Table C 3: Values obtained for k_4 at 298 K and different pressures.

Pressure (Torr)	$k_4(s^{-1})$
10	230
25	470
50	320

With values of k_2, k_{self} and k_4 known at 10, 25 and 50 Torr, it is possible to calculate $[Products_{CI+Acetone}](t \rightarrow \infty)$ at those conditions for a given $[CH_2OO]_0$ and $[CH_3COCH_3]$.

The steady state concentrations of the $\frac{m}{z} = 89$ and 104 amu product species are related to $[Products_{(CI+Acetone)}](t \rightarrow \infty)$ through their respective branching fractions, β_i, by the following equations.

$$\left[\frac{m}{z} = 89\,amu\right](t \rightarrow \infty) = \beta_{89}\left[\,Products_{(CI+Acetone)}\right](t \rightarrow \infty)$$

$$\left[\frac{m}{z} = 104\,amu\right](t \rightarrow \infty) = \beta_{104}[Products_{CI+Acetone}](t \rightarrow \infty)$$

The general relationship between the PI TOF-MS signal due to a species i, S_i, (measured as integrated peak area) and its concentration is the following.

$$S_i = FR_i\sigma_i(E)[i]$$

Where F is the instrument response factor, R_i is the mass discrimination factor and $\sigma_i(E)$ is the photoionization cross-section of species i at energy E. Accordingly, the steady-state PI TOF-MS signals for $\frac{m}{z} = 89$ amu and $\frac{m}{z} = 104$ amu can be expressed as follows.

$$S_{89}(t \rightarrow \infty) = FR_{89}\sigma_{89}(E = 10.5\,eV)\left[\frac{m}{z} = 89\,amu\right](t \rightarrow \infty)$$

$$S_{104}(t \rightarrow \infty) = FR_{104}\sigma_{104}(E = 10.5\,eV)\left[\frac{m}{z} = 104\,amu\right](t \rightarrow \infty)$$

Or

$$S_{89}(t \rightarrow \infty) = FR_{89}\sigma_{89}(E = 10.5\,eV)\beta_{89}\left[Products_{(CI+Acetone)}\right](t \rightarrow \infty)$$

$$S_{104}(t \rightarrow \infty) = FR_{104}\sigma_{104}(E = 10.5\,eV)\beta_{104}\left[Products_{(CI+Acetone)}\right](t \rightarrow \infty)$$

In all of our PI TOF-MS experiments, a small amount of a gas mixture with known composition was simultaneously flowed in the reactor to act as an internal standard. The concentrations of

calibration mixture species are small so as not to interfere with the chemistry ($\sim 10^{11}$ cm^{-3}) and known to within 15% based on the reactor conditions. The mixture contains 100 ppm of each of the following species: methylamine (31 amu), propene (42 amu), 1,3-butadiene (54 amu), propanol (60 amu) , furan (68 amu) , benzene (78 amu) , cyclohexane (84 amu) , toluene(92 amu) and heptane (100 amu).

Taking the ratio of $S_{89}(t \to \infty)$ or $S_{104}(t \to \infty)$, to the average PI TOF-MS signal from any of the calibration mixture species, $\overline{S}_{calmix,j}$, results in the following.

$$\frac{S_{89}(t \to \infty)}{\overline{S}_{calmix,j}} = \frac{FR_{89}\sigma_{89}(E = 10.5 \text{ eV})\beta_{89}[Products_{(CI+Acetone)}](t \to \infty)}{FR_{calmix,j}\sigma_{calmix,j}(E = 10.5 \text{ eV})[calmix,j]}$$

$$\frac{S_{104}(t \to \infty)}{\overline{S}_{calmix,j}} = \frac{FR_{104}\sigma_{104}(E = 10.5 \text{ eV})\beta_{104}[Products_{(CI+Acetone)}](t \to \infty)}{FR_{calmix,j}\sigma_{calmix,j}(E = 10.5 \text{ eV})[calmix,j]}$$

F cancels out because it is a constant. For our apparatus we have found the mass discrimination factor to have very weak or no dependence on mass. Therefore the ratio of R values also becomes one.

$$\frac{S_{89}(t \to \infty)}{\overline{S}_{calmix,j}} = \beta_{89} \frac{\sigma_{89}(E = 10.5 \text{ eV})}{\sigma_{calmix,j}(E = 10.5 \text{ eV})} \frac{[Products_{(CI+Acetone)}](t \to \infty)}{[calmix,j]}$$

$$\frac{S_{104}(t \to \infty)}{\overline{S}_{calmix,j}} = \beta_{104} \frac{\sigma_{104}(E = 10.5 \text{ eV})}{\sigma_{calmix,j}(E = 10.5 \text{ eV})} \frac{[Products_{(CI+Acetone)}](t \to \infty)}{[calmix,j]}$$

These equations can be rearranged for, $\sigma_{89}\beta_{89}$ and $\sigma_{104}\beta_{104}$.

$$\sigma_{89}\beta_{89} = \sigma_{calmix,j}(E = 10.5 \text{ eV}) \frac{S_{89}(t \to \infty)}{\overline{S}_{calmix,j}} \frac{[calmix,i]}{[Products_{(CI+Acetone)}](t \to \infty)}$$

$$\sigma_{104}\beta_{104} = \sigma_{calmix,j}(E = 10.5 \text{ eV}) \frac{S_{104}(t \to \infty)}{\overline{S}_{calmix,j}} \frac{[calmix,i]}{[Products_{(CI+Acetone)}](t \to \infty)}$$

The quantity $\sigma_i\beta_i$, where i = 89 or 104, cannot be separated because σ_i is not known. If, however, we assume that σ_i is independent of pressure, then we can ratio the measured value of $\sigma_i\beta_i$ at one pressure, $(\sigma_i\beta_i)_{P1}$, to another pressure, $(\sigma_i\beta_i)_{P2}$ and cancel out the σ_i values.

$$\frac{(\sigma_i\beta_i)_{P1}}{(\sigma_i\beta_i)_{P2}} = \frac{(\beta_i)_{P1}}{(\beta_i)_{P2}}$$

Furthermore, if we assume that $\sigma_{calmix,j}$ and σ_i are pressure independent:

$$\frac{(\beta_i)_{P1}}{(\beta_i)_{P2}} = \frac{\left(\frac{S_i(t \to \infty)}{\overline{S}_{calmix,i}} \frac{[calmix, i]}{[Products_{(CI+Acetone)}](t \to \infty)} \right)_{P1}}{\left(\frac{S_i(t \to \infty)}{\overline{S}_{calmix,i}} \frac{[calmix, i]}{[Products_{(CI+Acetone)}](t \to \infty)} \right)_{P2}}$$

This equation was given in section 3.3.3.4. In this manner, the relative pressure dependent yield of both $\frac{m}{z} = 89$ and $\frac{m}{z} = 104$ can be computed.

Note that, of the nine species present in the calibration mix, only benzene is a suitable internal standard. Of the other eight, propene and 1,3-butadiene overlap with acetone fragment signals in the mass spectrum, methylamine and propanol are not thermally stable, furan and heptane have low signal (relatively small cross sections), and the concentrations of toluene and cyclohexane have decreased below 100 ppm over the lifetime of the gas cylinder. The stable benzene signal used as an internal standard is shown in Figure C 4.
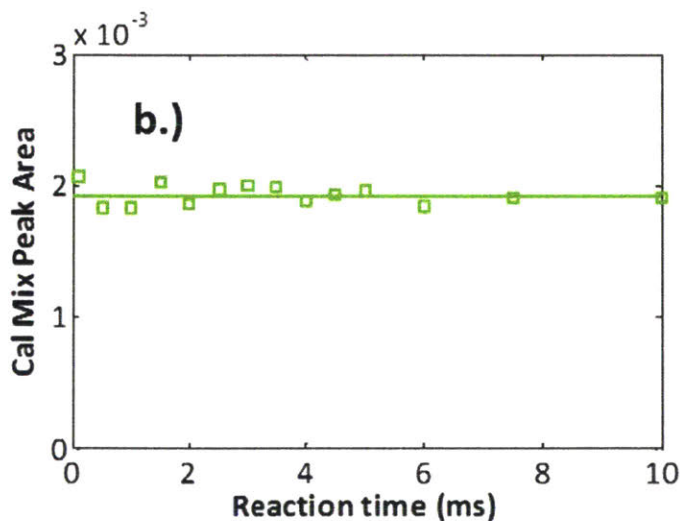
Figure C 4: TOF-MS signal of the internal benzene standard at 298 K, 10 Torr, $[O_2] = 5.95 \times 10^{16} cm^{-3}$ and $[CH_3COCH_3] = 1.24 \times 10^{15} cm^{-3}$ recorded simultaneously as the product signals shown in Figure 3-17. The line is an average values of the stable benzene signal, $\overline{S}_{calmix,benzene}$.

Figure C 5 shows the measured values of $\frac{(\beta_i)_{P_1}}{(\beta_i)_{P_2}}$ for $\frac{m}{z} = 104$ amu as a function of pressure. The TOF-MS signal for this species was too low to discern a trend with respect to pressure (S_{104} too small).
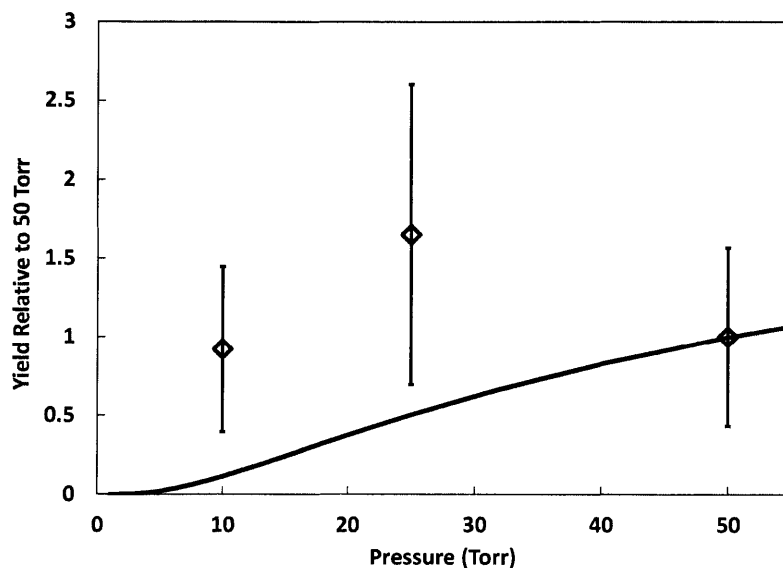
Figure C 5: Relative yield of $\frac{m}{z} = 104$ amu product from $CH_2OO + CH_3COCH_3$ normalized to the 50 Torr measurement $\left(\frac{(\beta_{104})_{P=X\,Torr}}{(\beta_{104})_{P=50\,Torr}}\right)$ at 298 K (markers) compared to predicted relative yield of SOZ at the same conditions from Jalan et al.[128] (line).

Theoretical Calculations Details

Figure C 6 shows the lack of sensitivity to $k_{outer}^{P=\infty}$ exhibited by $k_{observable}^{P=0}$ and $k_{observable}^{P=\infty}$. Figure C 7 shows the logarithm of the various contributions to the ratio of inner TS to reactant partition functions, $\frac{Q_{TS,inner}}{Q_{reactants}}$, in the expression for $k_{TST}(T)$ below:

$$k_{TST}(T) = \frac{k_B T}{h}\left(\frac{Q_{TS,inner}}{Q_{reactants}}\right) \times \exp\left(-\frac{\left[E_0^{TS,inner} - E_0^{reactants}\right]}{RT}\right)$$

$$\log_{10}\left(\frac{Q_{TS,inner}}{Q_{reactants}}\right)$$

$$= \log_{10}\left(\frac{Q_{TS,inner}}{Q_{reactants}}\right)_{rot} + \log_{10}\left(\frac{Q_{TS,inner}}{Q_{reactants}}\right)_{vib} + \log_{10}\left(\frac{Q_{TS,inner}}{Q_{reactants}}\right)_{trans}$$

$$+ \log_{10}\left(\frac{Q_{TS,inner}}{Q_{reactants}}\right)_{hindered\ rotor} + \log_{10}\left(\frac{Q_{TS,inner}}{Q_{reactants}}\right)_{optical\ isomers}$$
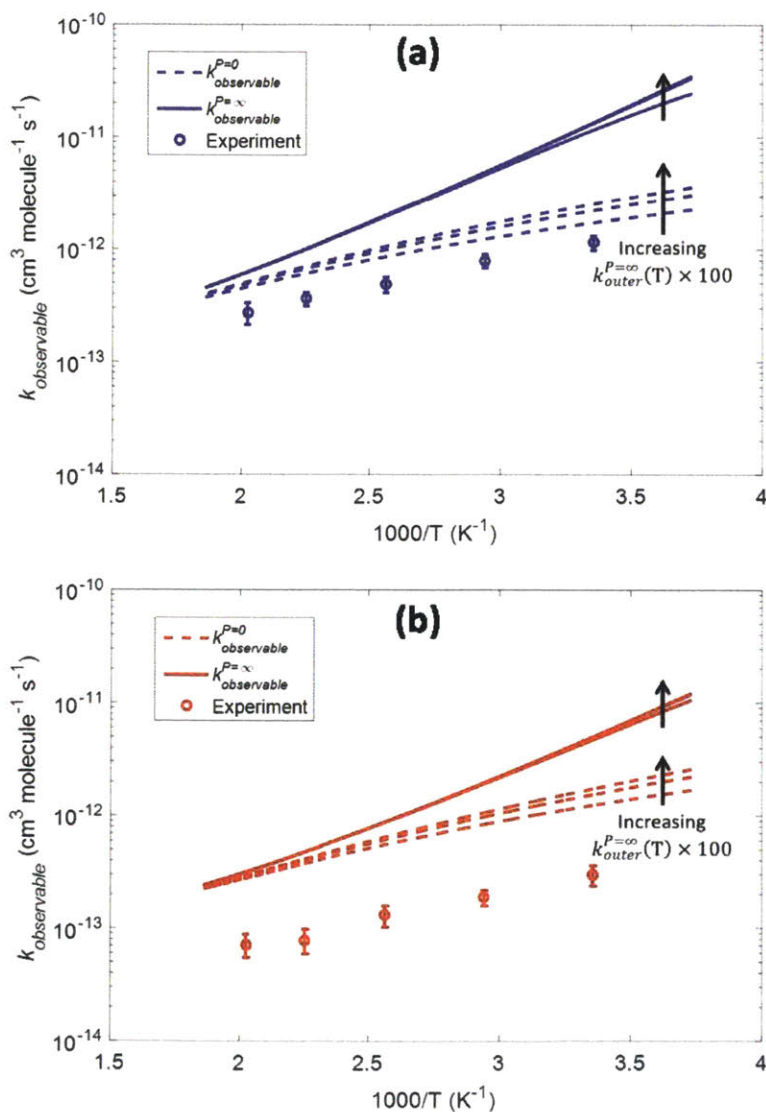
Figure C 6: Predicted T-dependence of $k_{observable}^{P=0}$ and $k_{observable}^{P=\infty}$ over a range of $k_{outer}^{P=\infty}$ for **(a)** $CH_2OO + CH_3CHO$ and **(b)** $CH_2OO + CH_3COCH_3$.
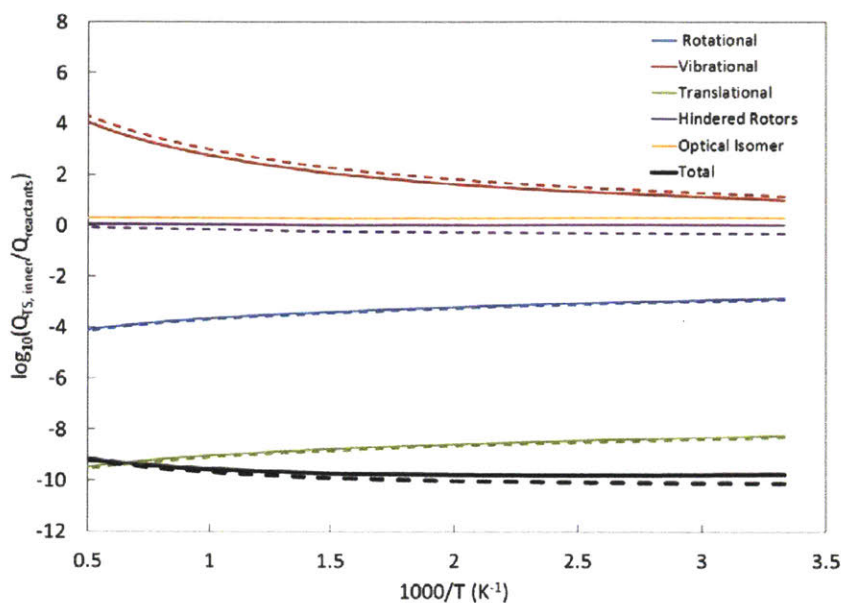
Figure C 7: Different contributions to the ratio $Q_{TS,inner}/Q_{reactants}$ in the TST expression for the high-P limit k, demonstrating the dominance of the vibrational term at higher temperatures. Solid lines are for $CH_2OO + CH_3CHO$ and dashed lines are for $CH_2OO + CH_3COCH_3$.

Comparison of Predictions with HCHO Yield Measurements of Stone et al.

Using HCHO laser-induced fluorescence (LIF), Stone et al. quantified yields of HCHO from $CH_2OO + CH_3CHO$ at 295 K in 25 to 300 Torr of mostly N_2 bath gas.[55] They observed that the yield decreased significantly with increasing pressure and by fitting their data to a Stern-Volmer equation they were able to estimate an HCHO yield of 88% at 4 Torr and 4% at 730 Torr (in N_2). At first glance, these measurements seem to be inconsistent with our own predictions of the $CH_2OO + CH_3CHO$ product distribution, wherein the low-pressure HCHO yield at room temperature is ~25%, and the remaining ~75% is attributable to $HCOOH + CH_3CHO$ (see Figure 3-21 and Figure C 8). However, this discrepancy can be explained by uncertainties in both the measurements of Stone et al. and our predictions.
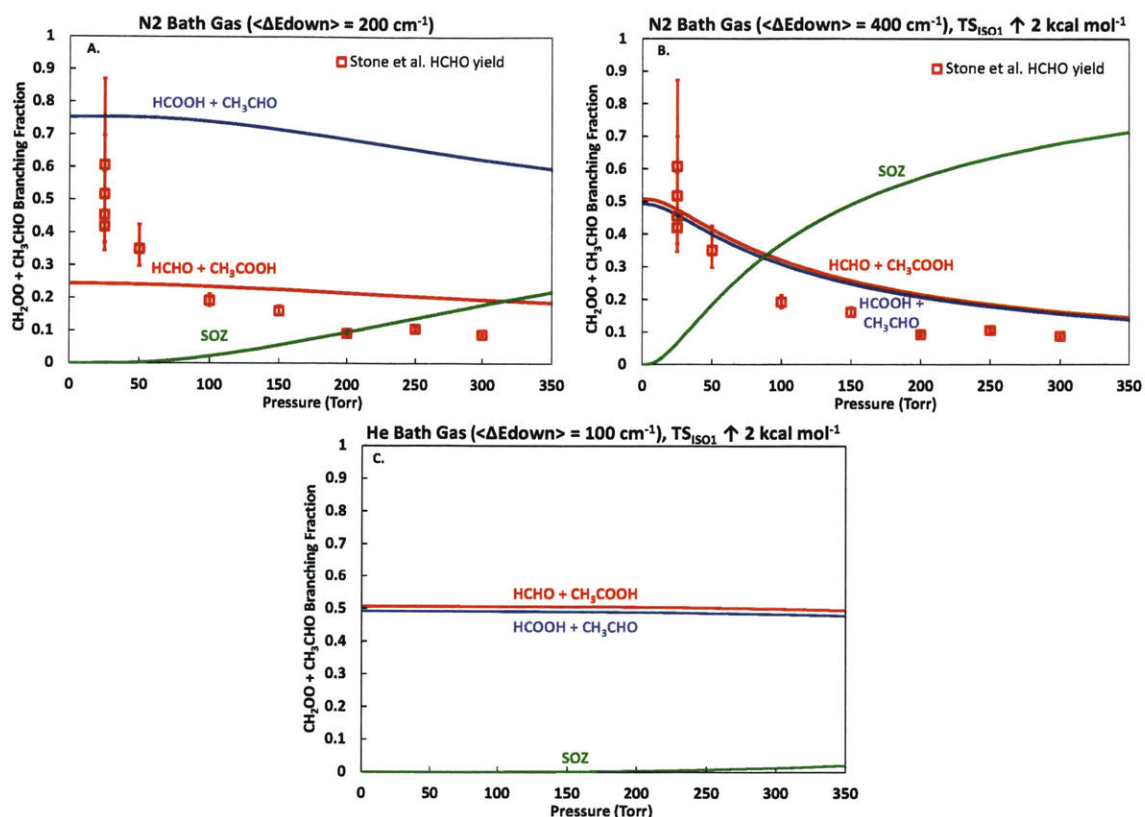
Figure C 8: Comparison between HCHO yield measured by Stone et al.,[55] and our predictions using the methodology of Jalan et al.[128] with the modifications indicated.

First, in order to obtain the estimates of the HCHO yield above, Stone et al. forced the intercept of their Stern-Volmer plot to equal 1.0, which is tantamount to assuming that in the low-P limit, HCHO is the only product. The authors report that without this assumption, the intercept of the fit is 1.19 ± 0.39, which corresponds to low-pressure HCHO yields in the range of 63-100%. The remainder of the yield can be attributed to the HCOOH + CH$_3$CHO product channel, consistent with our predictions and also with the PI TOF-MS measurements of Taatjes et al., where HCHO, CH$_3$COOH and HCOOH were all observed as products of CH$_2$OO + CH$_3$CHO in 4 Torr He.[120]

Second, as demonstrated by Jalan et al., the predicted product branching is quite sensitive to certain transition state energies, as well as the energy transfer model.[128] It was previously shown that the yield of HCHO versus HCOOH is predominantly controlled by the energies of the transition states labelled TS$_{ISO1}$ and TS$_{ISO2}$, which are only separated by 1.6 kcal mol^{-1}. For the purpose of quantitative comparison with Stone et al., we have increased TS$_{ISO1}$ until our low-

pressure predictions are in good agreement with their 25 Torr measurements (Figure C 8b). An increase of 2 kcal mol^{-1} was necessary, which is reasonable given the level of theory used (RCCSD(T)-F12a/VTZ-F12//B3LYP/MG3S) and also considering that in reality it is the combined uncertainty of TS$_{ISO1}$ and TS$_{ISO2}$ (as well as TS$_{D3}$ possibly) that leads to the observed discrepancy.

In order to capture the pressure dependence of the yield measured by Stone et al., we also increased $< \Delta E_{down} >$ for an N$_2$ bath gas from 200 cm^{-1} to 400 cm^{-1} (Figure C 8b). Although Jalan et al. used the former value for their original predictions in an N$_2$ bath gas (taken from an *ab initio* study of monomethylhydrazine, CH$_3$NHNH$_2$, decomposition in N$_2$[371]), the latter value also has precedence in the literature (toluene in N$_2$, for example[207]). Even with this large adjustment, however, our predicted decrease in HCHO yield with pressure is not as steep as Stone et al.'s measurement. This might be explained by underestimated uncertainty in the higher-pressure measurements of Stone et al., where the presence of CH$_2$IOO complicates their analysis. Furthermore, the scatter in the data at the lowest pressure (25 Torr) suggests that the real uncertainty in the yield at a given pressure is larger than what is indicated by the error bars on an individual measurement.

Finally, as a consistency check, we calculated the product branching at our experimental conditions (4-100 Torr He bath gas) using the modified PES (TS$_{ISO1}$ increased by 2 kcal mol^{-1}). Figure C 8c shows that even up to 100 Torr the branching to SOZ is negligible, consistent with the lack of SOZ observed by either us or Taatjes et al. at these conditions.

Appendix D

Additional Details for Vinyl Radical + 1,3-Butadiene

Photolysis of 1,3-Butadiene

During each absorbance experiment, a trace was recorded at the maximum $[1,3 - C_4H_6]$ ($= 5 \times 10^{16}$ molecules cm^{-3}) without C_2H_3I present (and hence no C_2H_3 either). The purpose of these traces was to photolyze $1,3 - C_4H_6$ by itself and check for any photoproducts that absorb at $\lambda = 423.2\, nm$. Figure D 1 shows one such representative trace, with the corresponding trace recorded in the presence of C_2H_3 also shown for comparison. As described in the main text, if $[1,3 - C_4H_6]$, the photolysis power and temperature are all high enough, we have observed absorbance at 423.2 nm which we attribute to propargyl radical, C_3H_3 produced by $1,3 - C_4H_6$ photodissociation.[231] In all of the absorbance experiments reported here, however, even at the maximum $[1,3 - C_4H_6]$, photolysis power and temperature there is no 423.2 nm absorbance discernible from the noise when $1,3 - C_4H_6$ is photolyzed by itself, just as shown in Figure D 1.
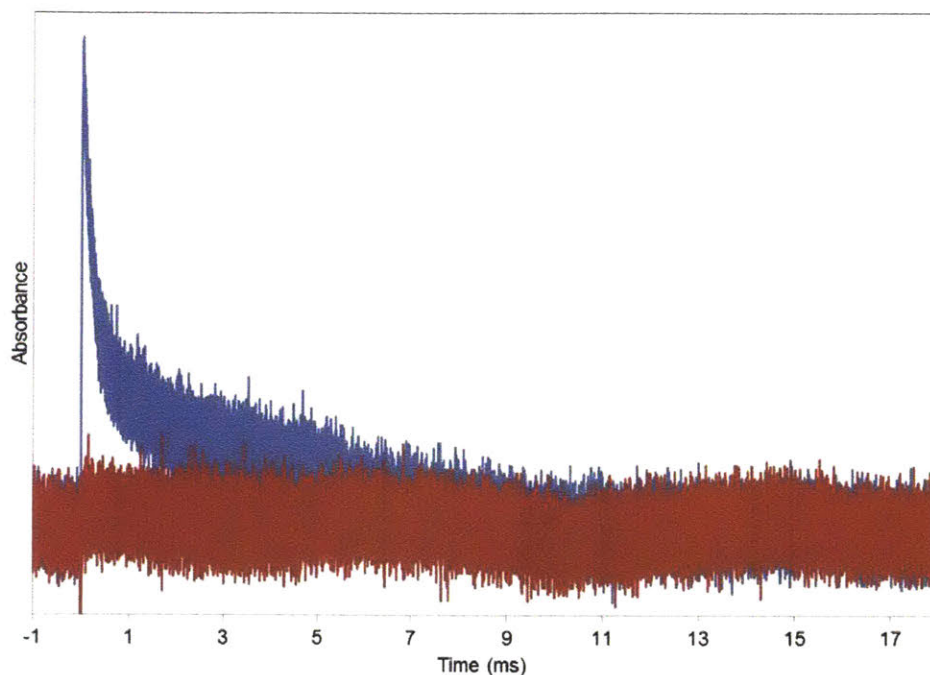
Figure D 1: Comparison of 423.2 nm absorbance traces at identical conditions (494 K, 100 Torr, 15 mJ pulse^{-1} photolysis energy and $1,3 - [C_4H_6] = 5 \times 10^{16}$ molecules cm^{-3}) except for the presence (blue) or absence (red) of C_2H_3I ($[C_2H_3I] = 2.4 \times 10^{14}$ molecules cm^{-3}).

Summary of Fit Parameters to Absorbance Data

Table D 1 and Table D 2 summarize all of the fit parameters obtained for both the Low- and High-T models. Quoted error bars include both fitting uncertainty, which is quite small due to the high density of points in an absorbance trace, and systematic uncertainty due to the ~10% uncertainty in $[1,3 - C_4H_6]$ as described in our previous work.[74] The fit values of b deserve special attention and are discussed in the next section.

Table D 1: Summary of fit parameters for Low-T absorbance experiments.

T (K)	P (Torr)	Photolysis Energy (mJ/pulse)	$[C_2H_3I]$ (10^{14} molecule/cm^3)	Number of traces	k_1 (10^{-14} cm^3 molecule^{-1}s^{-1})	k_2 (s^{-1})
297	4	15	2.4	9	1.7 ± 0.17	297 ± 0.5
297	25	15	2.4	9	1.9 ± 0.20	243 ± 0.4
297	25	30	1.2	6	2.1 ± 0.22	245 ± 0.4
297	50	15	2.4	9	2.1 ± 0.21	251 ± 0.4
297	100	15	2.4	9	2.3 ± 0.23	220 ± 0.3
340	25	15	2.4	9	3.2 ± 0.32	222 ± 0.3

Table D 2: Summary of fit parameters for High-T absorbance experiments.

T (K)	P (Torr)	Photolysis Energy (mJ/pulse)	$[C_2H_3I]$ (10^{14} molecule/cm^3)	Number of traces	k_1 (10^{-14} cm^3 molecule^{-1}s^{-1})	k_2 (s^{-1})	k_3 (s^{-1})	b
390	25	15	2.4	9	6.5 ± 0.69	294 ± 0.4	461 ± 4.1	0.257 ± 0.002
444	25	15	2.4	9	7.4 ± 0.79	255 ± 0.4	408 ± 3.7	0.268 ± 0.002
494	4	15	2.4	8	14.2 ± 1.5	381 ± 0.8	360 ± 2.1	0.403 ± 0.001
494	25	15	2.4	9	9.5 ± 1.0	255 ± 0.4	239 ± 1.3	0.336 ± 0.001
494	25	30	1.2	6	10.0 ± 1.1	260 ± 0.4	203 ± 1.1	0.359 ± 0.001
494	100	15	2.4	9	10.9 ± 1.1	306 ± 0.4	277 ± 1.3	0.299 ± 0.001

Interpretation of "b" Fit Parameter

As shown in section 4.1.4.2, b is a lumped fit parameter that has the following definition.

$$b = \frac{\alpha_{n-C_6H_9} \sigma_{n-C_6H_9}(423.2 \text{ nm})}{\sigma_{C_2H_3}(423.2 \text{ nm})}$$

For the conditions of our absorbance experiments $\alpha_{n-C_6H_9} \approx 1$ (the title reaction proceeds entirely to $n - C_6H_9$). Therefore the following should be true.

$$b = \frac{\sigma_{n-C_6H_9}}{\sigma_{C_2H_3}}(423.2 \text{ nm})$$

Unfortunately, $\sigma_{n-C_6H_9}(423.2 \text{ nm})$ is not known, so we cannot exactly verify the equality above. We can make the approximation, however, that the absolute absorption cross section of the allylic product, $n - C_6H_9$, is similar to that of allyl radical, C_3H_5.

$$b \approx \frac{\sigma_{C_3H_5}}{\sigma_{C_2H_3}}(423.2 \text{ nm})$$

We have measured the cross sections of both vinyl and allyl radical at 423.2 nm as a function of temperature and pressure using the same approach as Ismail et al.[96] The only difference between our approaches is that we measured the path length of the Iodine Atom laser more accurately as described previously.[74] Because only the ratio of cross sections is of interest, there is a large cancellation of errors (i.e., uncertainties in path lengths and the cross section of the Iodine Atom $F = 3\ ^2P_{1/2} \leftarrow F = 4\ ^2P_{3/2}$ transition cancel out), and the uncertainty of the ratio is very small. Figure D 2 compares fit b values at 25 Torr and 15 mJ pulse^{-1} photolysis energy to $\frac{\sigma_{C_3H_5}}{\sigma_{C_2H_3}}(423.2 \text{ nm})$ as a function of temperature. Given the coarseness of our approximation $\left(\sigma_{n-C_6H_9} \approx \sigma_{C_3H_5}\right)$, the agreement between the two quantities is remarkable. This agreement gives credibility to both our High-T model, as well as the conclusion that $\alpha_{n-C_6H_9} \approx 1$.
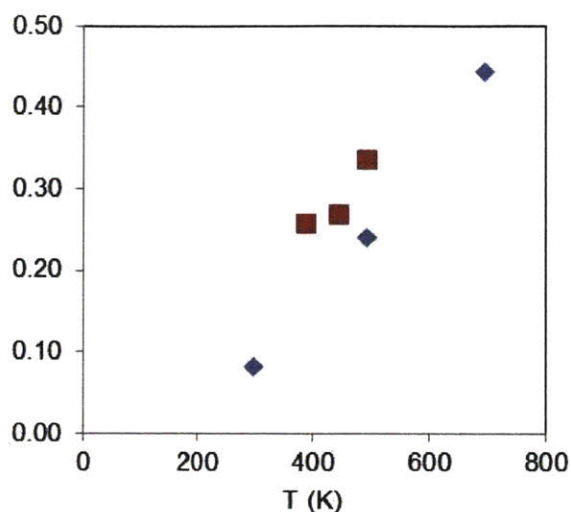
Figure D 2: Comparison of fit b parameters from High-T model (red squares) and measured ratio of allyl to vinyl radical cross sections at $\lambda = 423.2$ nm, $\frac{\sigma_{C_3H_5}}{\sigma_{C_2H_3}}$ (blue diamonds). P = 25 Torr for all measurements and all b values were obtained at a 15 mJ pulse^{-1} photolysis energy.

Alternative Absorbance Models

In addition to the Low-T model presented in section 4.1.4.2 (hereafter referred to as the "Global 1st Order Model") we considered two other models, described below, to fit the absorbance decays obtained at T < 390 K.

a. Global 1st Order + Self-Reaction Model

The only difference between this model and the Global 1st Order Model is the inclusion of vinyl radical self-reaction:

$$2C_2H_3 \xrightarrow{k_{self}} \text{Products} \tag{R4}$$

The time-dependent behavior of vinyl radical is then described by the following equation.

$$\frac{[C_2H_3](t)}{[C_2H_3]_0} = \frac{k_1[1,3-C_4H_6]+k_2}{(k_1[1,3-C_4H_6]+k_2+2k_{self}[C_2H_3]_0)e^{(k_1[1,3-C_4H_6]+k_2)t}-2k_{self}[C_2H_3]_0} \tag{D-1}$$

The measured absorbance is related to the equation above through Eqs. 4-4 and 4-5.

In this model, just as in the Global 1st Order Model, k_1 and k_2 are the only fit parameters. Values of $k_{self}\left(= 1.2 \times 10^{-11}e^{\frac{400}{T}} \text{ cm}^3 \text{ molecule}^{-1} \text{ s}^{-1}\right)$ are taken from the 300-700 K and 20 Torr measurements of Ismail et al.[96] $[C_2H_3]_0$ was determined for each experiment using the absorbance of 423.2 nm at t = 0 (time of photolysis flash), A_0, the pathlength of the visible

probe laser, l_{probe} (= 2000 ± 600 cm), and the temperature/pressure dependent absorption cross section of the vinyl radical at this wavelength, $\sigma_{C_2H_3}$ (λ = 423.2 nm) (Table D 3).

$$[C_2H_3]_0 = \frac{A_0}{\sigma_{C_2H_3}(\lambda=423.2\ nm)l_{probe}} \qquad (D\text{-}2)$$

$\sigma_{C_2H_3}$ (λ = 423.2 nm) was quantified in a separate set of experiments using the same method as Ismail[96] (i.e., $[C_2H_3]_0$ was initially quantified by probing the $F = 3\ ^2P_{1/2} \leftarrow F = 2\ ^2P_{3/2}$ transition of photolytically co-produced I Atom and assuming $[C_2H_3]_0 = [I]_0$) with the exception that the pathlength of the I Atom laser, l_I, was determined in a more accurate manner.[75] Despite this difference our measurement at 297 K and 25 Torr (0.29 ± 0.12 cm^2 molecule^{-1}) and Ismail's at 293 K and 20 Torr (0.18 ± 0.04 cm^2 molecule^{-1}) have overlapping uncertainties. The major contributors to our large uncertainty are the laser pathlengths, l_{probe} and l_I, and the cross section of I atom, σ_I. The values of $[C_2H_3]_0$ obtained using this approach are given in Table 4-1 and are $\sim 1 - 2 \times 10^{12}$ molecules cm^{-3}.

Table D 3: Temperature and pressure dependent vinyl radical absorption cross section, $\sigma_{C_2H_3}$ at 423.2 nm. Units are 10^{-18} cm^2 molecule^{-1}.

Pressure (Torr):	Temperature (K): 297	390	494
4	0.30 ± 0.15	-	0.21 ± 0.08
25	0.29 ± 0.12	0.25 ± 0.11	0.21 ± 0.09
50	0.35 ± 0.16	-	-
100	0.52 ± 0.24	-	0.28 ± 0.15

Including vinyl radical self-reaction in the Global 1st Order Model had no effect on the quality of the fits to the absorbance data. Fit values of k_1 and k_2 obtained for all experiments at T < 390 K using this model are summarized in Figure D 4 and Figure D 5, respectively, and compared against the other two models considered. k_1 is unaffected by the inclusion of self-reaction in the model, while k_2 decreased from $\sim 250\ s^{-1}$ to $\sim 150\ s^{-1}$. Clearly self-reaction is a non-negligible sink of vinyl radicals in the absence of 1,3-butadiene, but because the goal of this work is to measure k_1 we chose not to include self-reaction in the Global 1st Order Model described in the main text for the sake of simplicity. We did not consider the impact of self-reaction at T ≥ 390 K (High-T) because the negative temperature dependence of k_{self} will render this reaction even less important at higher temperatures.

b. Local 1ˢᵗ Order Model

In this model, absorbance traces were fit to the same first order equations as the Global 1st Order Model, but rather than fitting single "Global" values of k_1 and k_2 to all 6-9 traces at different $[1,3 - C_4H_9]$, a "Local" value of $k'(= k_1[1,3 - C_4H_6] + k_2)$ was fit to each decay individually. k_1 and k_2 were then extracted from the slope and intercept, respectively, of k' versus $[1,3 - C_4H_6]$ (Figure D 3). The resulting k_1 and k_2 values are shown in Figure D 4 and Figure D 5. Within the uncertainty, k_1 is the same whether a Global or Local fit is used and k_2 is also the same in almost every case. We prefer the Global fit, however, by virtue of a reduced number of fit parameters (2 as compared to x, where x is the number of traces recorded at different $[1,3 - C_4H_6]$), which translates into a noticeably reduced uncertainty in both k_1 and k_2.
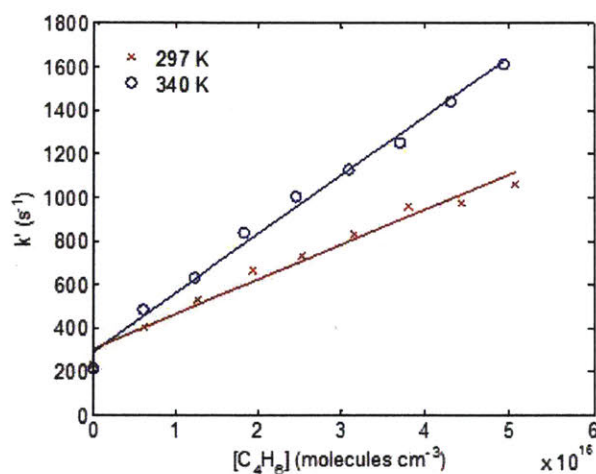
Figure D 3: Representative linear dependence of local pseudo-first-order rate coefficients, k', on $[1,3 - C_4H_6]$.
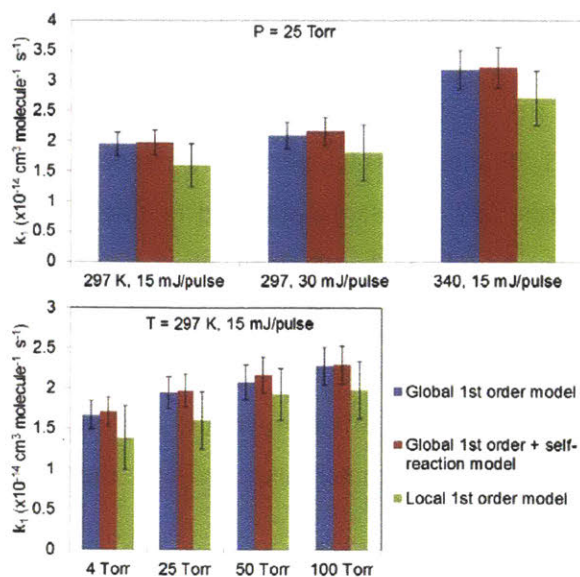
Figure D 4: Comparison of fit k_1 values obtained using different models.
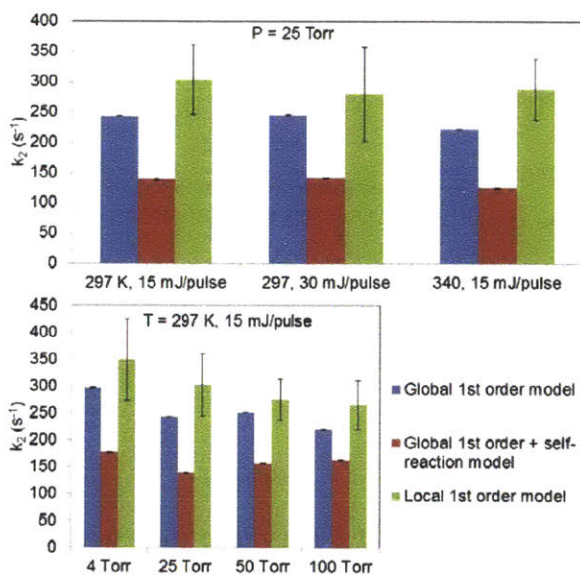
Figure D 5: Comparison of fit k_2 values obtained using different models.

Comparison of Vinyl/Phenyl Radical + 1,3-Butadiene/Acetylene Addition Rates

Figure D 6 compares the measured temperature dependence of the vinyl + 1,3-butadiene addition rate coefficient from 297 to 494 K obtained in this work to the analogous radical addition rate coefficients for phenyl + 1,3-butadiene, vinyl + acetylene and phenyl + acetylene over the same temperature range (all rate coefficients are in the high-pressure limit) from Ismail et al.,[236] Miller et al.[196] and Tokmakov et al.,[237] respectively. All three literature k's were obtained from experiments conducted in this temperature range (or in the case of Miller et al., theoretical predictions were scaled to match experimental measurements) so this is a fair comparison without any extrapolation.
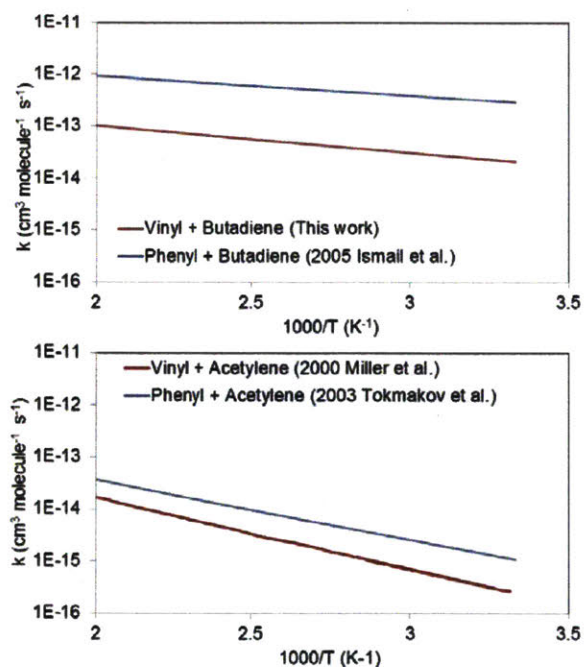
Figure D 6: Arrhenius plots of vinyl + 1,3-butadiene (this work), phenyl + 1,3-butadiene,[236] vinyl + acetylene[196] and phenyl + acetylene[237] from 300 to 500 K.

Summary of PI TOF-MS Experiments

Figure D 7 is representative of the full mass spectrum obtained in the presence of 1,3-C_4H_6 and C_2H_3I (helium bath gas) without photolysis (stable species only). The spectrum has been smoothed and baseline corrected. Some of the large peaks have been truncated due to signal saturation. Although relatively "soft" 10.5 eV photoionization was employed in this work, there is still significant fragmentation of species present in high concentration (i.e., 1,3-C_4H_6 and

C_2H_3I). Much of this fragmentation was later reduced by improvements to VUV generation (section 2.2.1). Unfortunately, large daughter ion signal at $\frac{m}{z} = 27$ amu from both 1,3-C_4H_6 and C_2H_3I obscure any small transient behavior due to vinyl radical, C_2H_3. Similarly, fragmentation of 1,3-C_4H_6 at 39 amu blocks any small propargyl radical signal from 1,3-butadiene photodissociation. The spectrum is relatively clean, however, in the range of 60-150 amu, which encompasses the observed products of C_2H_3 + 1,3-C_4H_6 (80 and 81 amu), some of the species in a calibration mixture used as an internal standard (84 and 100 amu) and I atom (127 amu). The only significant stable signals in that range are from the 1,3-butadiene dimer and its daughter ions, impurities in the vinyl iodide (THF and vinyl bromide), small fragment signals of vinyl iodide at 127 and 128 amu, and an unidentified impurity in the 1,3-butadiene at 142 amu. The presence of a small helium signal suggests other ionization sources besides 10.5 eV photoionization, but by careful alignment of the photoionization laser before every TOF-MS experiment this effect can be minimized to the acceptably low level shown in Figure D 7. The helium signal was later completely eliminated from the TOF-MS following the improvements of section 2.2.1.
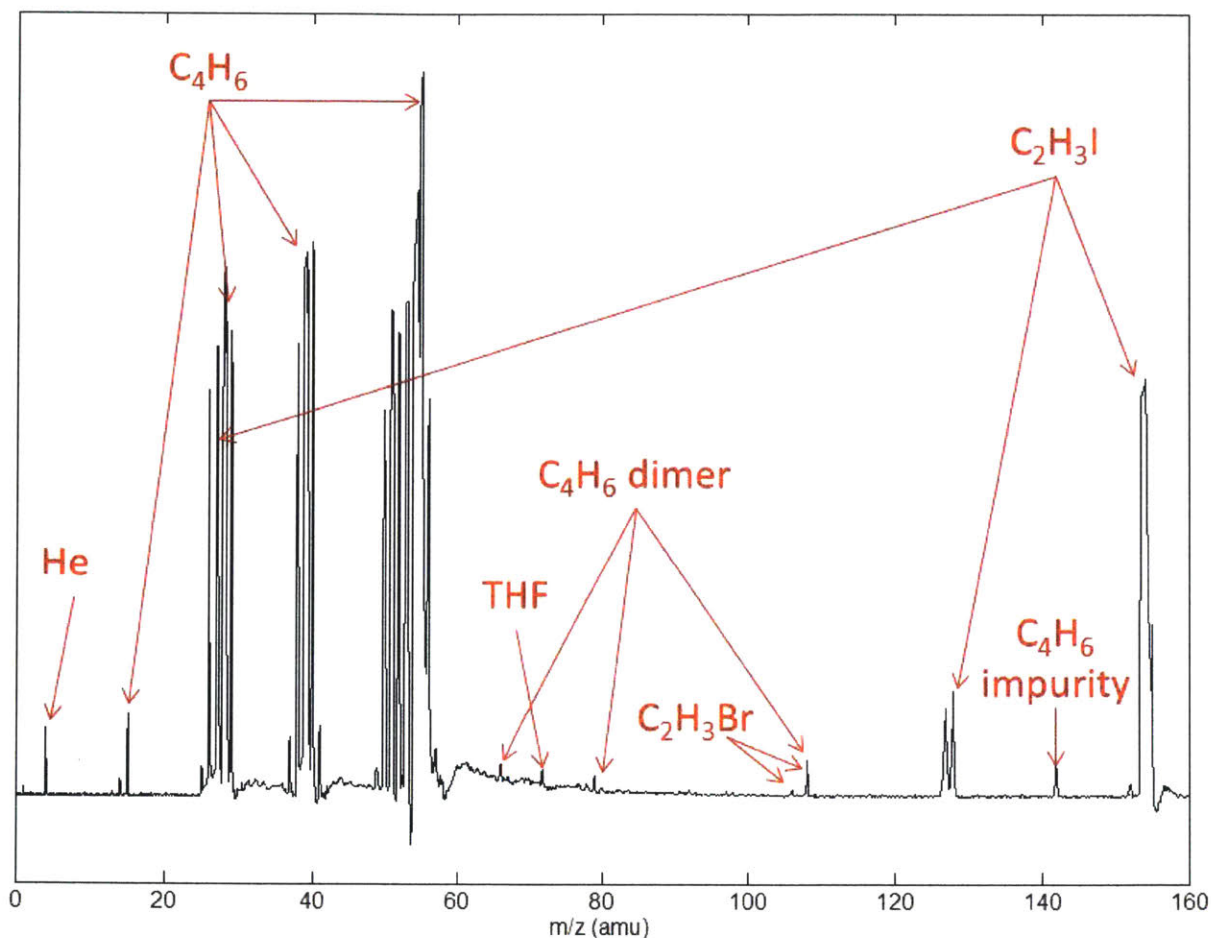
Figure D 7: Representative mass spectrum of C_2H_3I and $1,3$-C_4H_6 without photolysis.

Table 4-2 of the main text summarizes all of the PI TOF-MS experiments conducted for this work. At each T and P condition there is one "Base Case" experiment and then several "Control" experiments. The control experiments with C_2H_3 only and $1,3 - C_4H_6$ only are particularly important as they displayed no transient behavior at $\frac{m}{z} = 79, 80$ or 81 amu, allowing us to identify these species as possible products of $C_2H_3 + 1,3 - C_4H_6$. Figure D 8 shows the transient mass spectra obtained in the 25 Torr and 297 K "Base Case" experiment. As mentioned in section 4.1.4.3, the signal to noise at this temperature is lower than at 500 K (Figure 4-6) because of the lower production rate, and hence overall concentration, of 81 amu product. This lower signal to noise is also the reason why both a larger $[C_2H_3I]$ and photolysis power were needed at 297 K, as shown in Table 4-2.
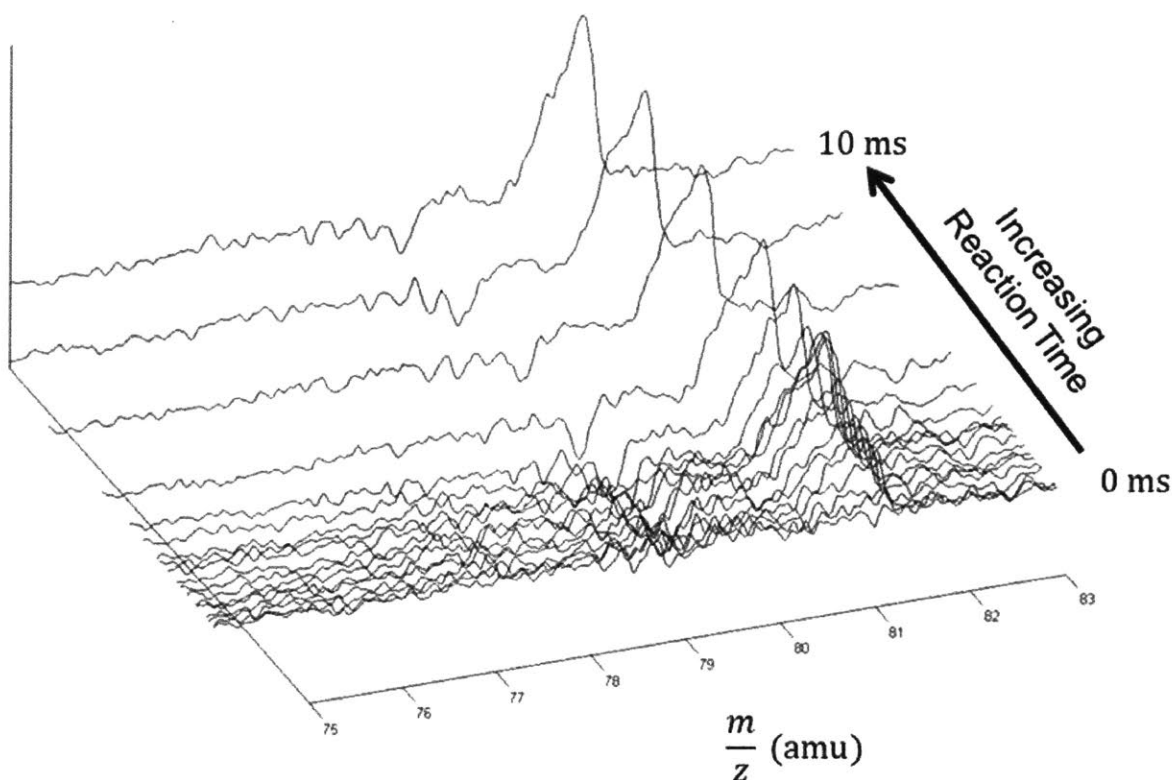
Figure D 8: Transient mass spectra obtained under conditions where $C_2H_3 + 1,3 - C_4H_6$ can occur (297 K, 25 Torr, $[C_2H_3I] = 2.5 \times 10^{14}$ and $[1,3 - C_4H_6] = 1.2 \times 10^{16}$ molecules cm^{-3}, 297 K "Base Case" experiment). The spectrum acquired at a reaction time of -0.20 ms was subtracted from all subsequent spectra so that only transient changes are observed. Other than the I Atom signal at m/z=127 amu no other section of the mass spectrum displayed time-dependent behavior. The spectra were also smoothed and baseline corrected.

The purpose of the remaining control experiments at 25 Torr and 494 K was to determine if both the 79 and 81 amu species were products of the title reaction. For example, if 81 amu is a product of $C_2H_3 + 1,3 - C_4H_6$ as expected, and secondary chemistry is producing something at 79 amu, then by more than doubling the Flashes per Refresh (FPR), which has the effect of enhancing secondary chemistry, the ratio of 79 to 81 amu PI TOF-MS signal should increase noticeably. This is not what was observed, however, for any of the control experiments, as shown in Figure D 9.
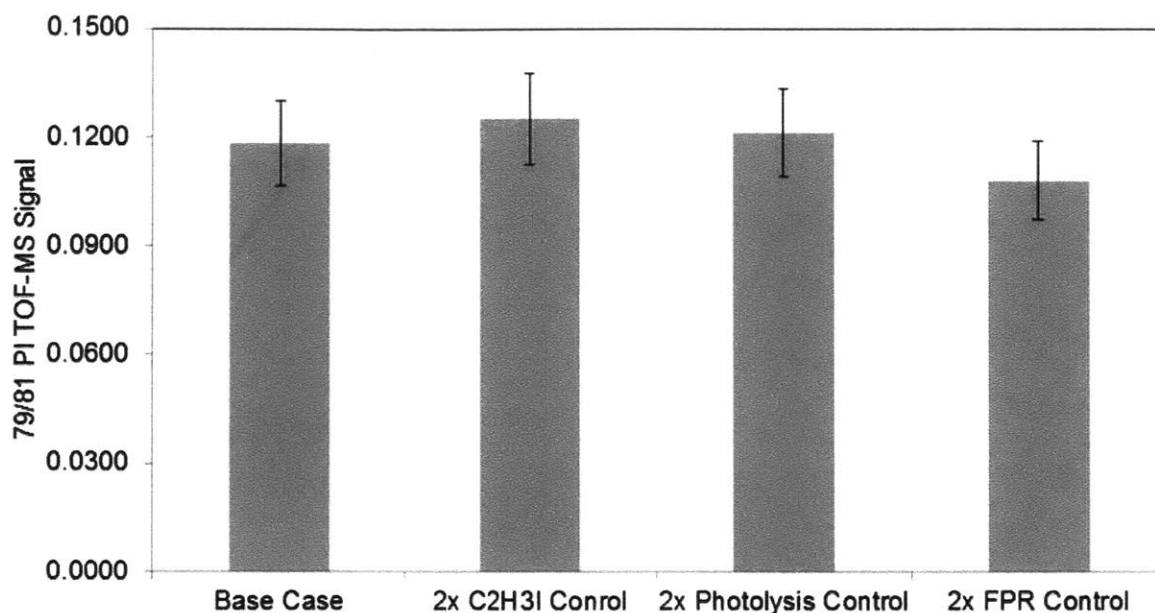
Figure D 9: Ratio of steady state m/z=79 to 81 amu PI TOF-MS signals (integrated peak areas) at 494 K and 25 Torr for various control experiments.

However, we did notice one significant difference between the 79 and 81 amu signals, which is that they display noticeably different time-dependence (Figure D 10). This same result was obtained for all four of the 25 Torr and 494 K experiments where $C_2H_3 + 1,3 - C_4H_6$ occurs. Therefore, 79 is not from dissociative ionization of 81. From previous literature measurements, we know it is also not a daughter ion of either cyclohexadiene isomer.[238-239] One conceivable reaction that could produce a species with a 79 amu mass is H-abstraction from cyclohexadiene. However, the low concentration of cyclohexadiene produced from $C_2H_3 + 1,3 - C_4H_6$ compared to the abundance of 1,3-butadiene present makes this pathway seem unlikely.

Reaction between C_2H_3 with vinylacetylene, C_4H_4, would also produce an adduct with formula C_6H_7 and mass 79 amu. Vinylacetylene is not a large impurity in the purchased butadiene ($\leq$ 10 ppm from Gas Chromatographic, GC, analysis), therefore it might be produced in the reactor by photodissociation of 1,3-butadiene (along with H_2 as a coproduct), as observed by Lockyear et al. and others at shorter wavelengths.[232, 372-373] Unfortunately, we cannot discern if there is an increase in the TOF-MS signal at m/z=52 amu (C_4H_4) following photolysis because of significant dissociative ionization of the large 1,3-butadiene signal at that m/z value. If C_4H_4

is being formed photolytically from $1,3 - C_4H_6$, then based on the insensitivity of our measured k_1 to photolysis power, we can conclude that our measurement of the overall rate is unaffected by this phenomenon. Furthermore, it is not possible for $C_2H_3 + C_4H_4$ to produce species with masses 80 and 81 amu (other than ^{13}C isomers, which will have negligibly small concentrations). Therefore, our TOF-MS measurements of m/z=80 and 81 amu would be unaffected by $C_2H_3 + C_4H_4$.
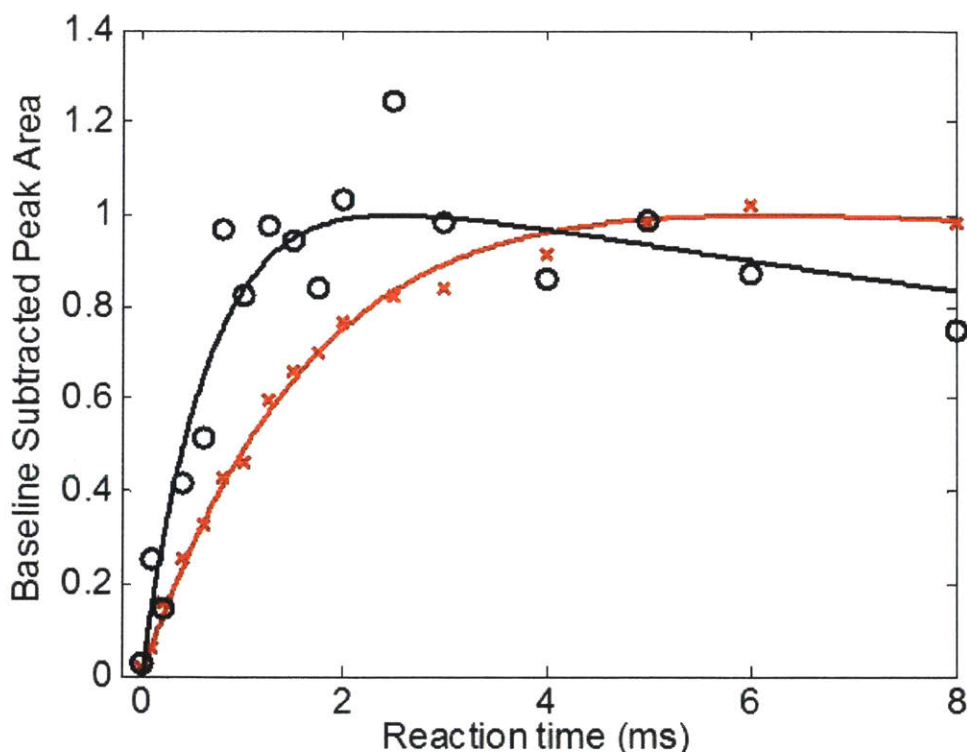
Figure D 10: Comparison of time-dependent behavior for normalized m/z=79 (black circles) and 81 amu (red crosses) PI TOF-MS signals in 25 Torr and 494 K "Base Case" experiment. Solid lines are biexponential fits to the data.

Further complicating our interpretation of the 79 amu species is the fact that 79 amu is a daughter ion of the butadiene dimer. Although the dimer is only ~0.1% of the purchased butadiene as confirmed by GC analysis, this low concentration of dimer in the reactor ($\sim 10^{13}$ molecules cm^{-3}) is comparable to the concentrations of radicals and products that are of interest to us ($\sim 10^{12}$ molecules cm^{-3}). Therefore, fluctuations in the dimer concentrations, as measured by the parent ion signal at 108 amu, are correlated with fluctuations in the daughter ion signal at 79 amu that are of the same magnitude as the changes in signal we are trying to

observe. We attempted to minimize such fluctuations in dimer concentration by keeping the butadiene cylinder in an ice bath during experiments and verifying with TOF-MS that the 108 amu signal is stable as a function of time before beginning experiments.

We are unable to definitively identify the origin of the 79 amu species at this time. Perhaps PI TOF-MS experiments using tunable ionization energy could provide critical insight. Nonetheless, whatever side reaction is responsible for producing the species at 79 amu, will not impact the three main experimental results presented in this work:

1. Measured values of k_1.

2. Observation that at 25 Torr the dominant product of $C_2H_3 + 1,3 - C_4H_6$ is $n - C_6H_9$.

3. Quantification of branching fraction to cyclohexadiene isomers at 4 Torr, assuming that 80 amu signal of cyclohexadiene is not being diverted to 79 amu either by dissociative ionization or reaction. Both of these assumptions are justified above.

The TOF-MS experiments at 700 K deserve special attention. Besides the increased propargyl absorbance, the TOF-MS data also provides evidence for enhanced 1,3-butadiene photodissociation at this elevated temperature. Table D 4 summarizes the nine transient species observed in the 700 K, 4 Torr Base Case experiment. Of these nine species, only 79, 80 and 81 amu disappear when vinyl iodide is removed. The other six are present in the same amount when only $1,3 - C_4H_6$ is photolyzed, suggesting that they are products of $1,3 - C_4H_6$ photodissociation and subsequent reactions of the propargyl and methyl radicals. For example, the signal at 15 amu is clearly attributable to methyl radical, while that at 78 amu is likely from propargyl radical recombination. The purpose of the "No Cal Mix" control experiments will be explained in the next section.

Table D 4: Summary of observations from control experiments at 700 K.

	Transient Species Observed (amu):								
	15	66	69	77	78	79	80	81	91
C_2H_3 Required?	No	No	No	No	No	**Yes**	**Yes**	**Yes**	No
Cal Mix Required?	No	No	No	No	No	No	No	No	No

Quantifying α_{c-C6H8}

As discussed in the previous section, the species at m/z=80 and 81 amu are the only clear products of $C_2H_3 + 1,3 - C_4H_6$ that we observed using PI TOF-MS. Based on our predictions of the product branching, Figure 4-9, we assumed that at all of the conditions of our experiment the transient 80 and 81 amu TOF-MS signals were entirely attributable to the 1,3-/1,4-cyclohexadiene isomers, $c - C_6H_8$, and the linear, allylic adduct, $n - C_6H_9$, respectively. Because the photoionization cross section, $\sigma_{PI}(E = 10.5 \text{ eV})$, is not known for $n - C_6H_9$, we cannot currently quantify the branching to this channel, which we expect to be dominant at our conditions. However, $\sigma_{PI}(E = 10.5 \text{ eV})$ is known for both cyclohexadiene isomers (27.63 ± 5.5 for 1,3-[238] and 25 ± 6.3 MB for 1,4-[239]), allowing us to quantify the summed branching fraction to these channels, $\alpha_{c-C_6H_8}$. TOF-MS signal at 80 amu was only observed for experiments conducted at 4 Torr ($T = 494, 599$ and 700 K), so we limit our discussion here to those experiments. This section explains the steps in experimentally quantifying $\alpha_{c-C_6H_8}$.

Reactions R1, R2 and R4 are reproduced below for convenience, with the addition of an explicit channel for $c - C_6H_8 + H$ that wasn't included before.

$$C_2H_3 + 1,3 - C_4H_6 \xrightarrow{\alpha_{n-C_6H_9}k_1} n - C_6H_9 \tag{R1a}$$

$$C_2H_3 + 1,3 - C_4H_6 \xrightarrow{\alpha_{c-C_6H_8}k_1} c - C_6H_8 + H \tag{R1b}$$

$$C_2H_3 + 1,3 - C_4H_6 \xrightarrow{(1-\alpha_{n-C_6H_9}-\alpha_{c-C_6H_8})k_1} \text{Other Products} \tag{R1c}$$

$$C_2H_3 \xrightarrow{k_2} \text{Products} \tag{R2}$$

$$2C_2H_3 \xrightarrow{k_{self}} \text{Products} \tag{R4}$$
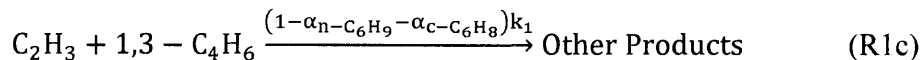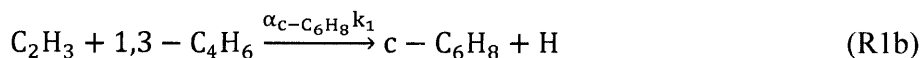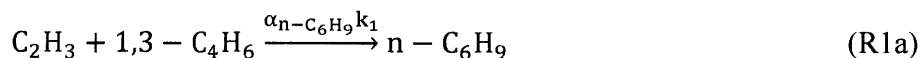
This model includes vinyl self-reaction but ignores all other possible radical-radical reactions (i.e. cross radical reactions), which is justified by the low radical concentrations used in all experiments ($[C_2H_3]_0 = 1 - 2 \times 10^{12}$ molecules cm^{-3} for all experiments at 4 Torr with one exception). This model also ignores $C_2H_3 + C_4H_4$, where C_4H_4 is derived from 1,3-butadiene photodissociation as discussed in the previous section, because $[C_4H_4] \ll [C_4H_6]$, at least by two orders of magnitude based on the cross section of $1,3 - C_4H_6$ near 266 nm alone.[374] The analytical solution for the maximum amount of cyclohexadine, $[c - C_6H_8]_{max}$, approached as $t \rightarrow \infty$ is shown below.

$$[c - C_6H_8]_{max} = \frac{\alpha_{c-C_6H_8} k_1 [1,3-C_4H_6]}{2k_{self}} \ln\left(\frac{k_1[1,3-C_4H_6]+k_2+2k_{self}[C_2H_3]_0}{k_1[1,3-C_4H_6]+k_2}\right) \tag{D-3}$$

The above can then be rearranged for the quantity of interest.

$$\alpha_{c-C_6H_8} = \frac{\frac{2k_{self}[c-C_6H_8]_{max}}{k_1[1,3-C_4H_6]}}{\ln\left(\frac{k_1[1,3-C_4H_6]+k_2+2k_{self}[C_2H_3]_0}{k_1[1,3-C_4H_6]+k_2}\right)} \tag{D-4}$$

Each term in the above equation is known experimentally. Values of k_1 are known from our experimental Arrhenius fit (Figure 4-4). Based on our predictions of the overall rate, it should be possible to accurately extrapolate this simple fit to 599 and 700 K where measurements of k_1 could not be conducted due to 1,3-butadiene photodissociation. k_{self} values are taken from Ismail et al.[96] k_2 values were obtained by fits of Eq. D-1 to 423.2 nm absorbance measurements of $[C_2H_3](t)$ in the absence of $1,3 - C_4H_6$. $[1,3 - C_4H_6]$ is known to within 10% uncertainty from the T and P of the reactor, as well as the relative flow rates of the mass flow controllers (MFC's). $[C_2H_3]_0$ was measured by simultaneously probing the $F = 3\ ^2P_{1/2} \leftarrow F = 4\ ^2P_{3/2}$ atomic transition of I atom following the same method described by Ismail et al.[96] However, we use a different method than Ismail et al. to quantify the pathlength of the continuous wave I atom laser, l_I, as described in an earlier work.[75] Furthermore, 1,3-butadiene was used as the quenching gas to bring excited I atom back to the ground state as opposed to oxygen or ethylene. I atom is a photolytic co-product of vinyl iodide, C_2H_3I, photodissociation along with vinyl radical. Therefore, by measuring $[I]_0$ and assuming $[C_2H_3]_0 = [I]_0$ we can determine $[C_2H_3]_0 \pm 50\%$. This large error bound is primarily due to uncertainty in the pathlength of the continuous wave I atom laser, l_I, ($\pm 30\%$) and the absolute Doppler and collision-broadened I atom cross section, σ_I ($\pm 20\%$).[78] The only remaining quantity needed to determine $\alpha_{c-C_6H_8}$ is $[c - C_6H_8]_{max}$, which can be obtained from the TOF-MS data as explained below.

For some species i, its TOF-MS signal, S_i, is proportional to its concentration, [i], as shown below.

$$S_i = FR_i \sigma_{PI,i}(E)[i] \tag{D-5}$$

The proportionality constant includes the instrument response factor, F, the mass discrimination factor, R_i and the photoionization cross section of species i at ionization energy E, $\sigma_{PI,i}(E)$. In our case, a calibration gas containing nine species (propene, methylamine, 1,3-butadiene,

propanol, furan, benzene, cyclohexane, toluene and heptane) was simultaneously present in the reactor during TOF-MS experiments when $C_2H_3 + 1,3 - C_4H_6$ was occurring. The concentration of each calibration gas species was very small ($1.8 \pm 0.2 \times 10^{11}$ molecules cm^{-3}) to prevent any interference with the chemistry. Of these nine species, only two of them were suitable internal standards for this reaction because their masses did not overlap with any other large, stable signals: cyclohexane and heptane. As shown in Table 4-2 and Table D 4, control experiments were conducted in the absence of the calibration gas mixture (referred to hereafter as "cal mix") as confirmation of two assumptions: 1.) The cal mix does not affect the measured amounts of transient species, i.e. 80 and 81 amu, and 2.) In the absence of cal mix, there is no signal at the masses of the internal standards cyclohexane (84 amu) or heptane (100 amu). The ratio between the maximum $c - C_6H_8$ signal, $S_{c-C_6H_8,max}$, and the average signal for cal mix species i, $\bar{S}_{calmix,i}$, is shown below.

$$\frac{S_{c-C_6H_8,max}}{\bar{S}_{calmix,i}} = \left(\frac{FR_{c-C_6H_8}}{FR_{calmix,i}}\right)\left(\frac{\sigma_{PI,c-C_6H_8}(E=10.5\text{ eV})}{\sigma_{PI,calmix,i}(E=10.5\text{ eV})}\right)\left(\frac{[c-C_6H_8]_{max}}{[calmix,I]}\right) \qquad \text{(D-6)}$$

In this equation, F is a constant and cancels out of the ratio. Furthermore, for this apparatus we have observed the mass discrimination factor to have negligible mass dependence in our range.[68] Therefore R also cancels out and the ratio simplifies to the following.

$$\frac{S_{c-C_6H_8,max}}{\bar{S}_{calmix,i}} = \left(\frac{\sigma_{PI,c-C_6H_8}(E=10.5\text{ eV})}{\sigma_{PI,calmix,i}(E=10.5\text{ eV})}\right)\left(\frac{[c-C_6H_8]_{max}}{[calmix,i]}\right) \qquad \text{(D-7)}$$

This equation is rearranged for the quantity of interest.

$$[c-C_6H_8]_{max} = [calmix, i]\left(\frac{S_{c-C_6H_8,max}}{\bar{S}_{calmix,i}}\right)\left(\frac{\sigma_{PI,calmix,i}(E=10.5\text{ eV})}{\sigma_{PI,c-C_6H_8}(E=10.5\text{ eV})}\right) \qquad \text{(D-8)}$$

All of the terms in Eq. D-8 are known experimentally. [calmix, i] is known from the reactor conditions. The photoionization cross sections for the internal standards cyclohexane and heptane at the relevant ionization energy are known from literature ($21.3^{[84]}$ and 9.9 MB,[266] respectively, both with $\pm 20\%$ uncertainty). $\sigma_{PI,c-C_6H_8}(E = 10.5$ eV) is also known for both cyclohexadiene isomers from literature, as mentioned earlier. $S_{c-C_6H_8,max}$ and $\bar{S}_{calmix,i}$ are obtained from the TOF-MS data as shown in Figure D 11. $S_{c-C_6H_8,max}$ is taken as the maximum of a biexponential fit to the integrated $\frac{m}{z} = 80$ peak area as a function of reaction time and

$\bar{S}_{calmix,i}$ is simply the average of the integrated cal mix species i peak area over the same reaction time. Clearly, the 80 amu signal is not at steady state because it continues to decrease after it reaches a maximum. However, the difference in time scales between the growth of 80 amu and its decay are sufficiently separated to allow us to approximate the maximum value as what the steady state value would be in the absence of any decay phenomenon. The error due to this approximation is certainly within the large error bars of our measurement reported later. We attribute this decay of what should be a chemically stable species (cyclohexadiene) to fast diffusion out of the TOF-MS sampling volume at the low pressure conditions of these experiments (4 Torr). For comparison, the growth and decay of C_6H_9 at 81 amu during the same experiment is also shown in Figure D 11. From the biexponential fits to the TOF-MS signals both species have a characteristic decay rate of $40 \pm 20 \text{ s}^{-1}$ (error bounds are 95% confidence intervals of fit). The fact that both species decay at the same rate is indicative of the chemical stability of the C_6H_9 isomer (likely it is the resonantly stabilized $n - C_6H_9$ isomer), which apparently diffuses faster than it reacts at these conditions.
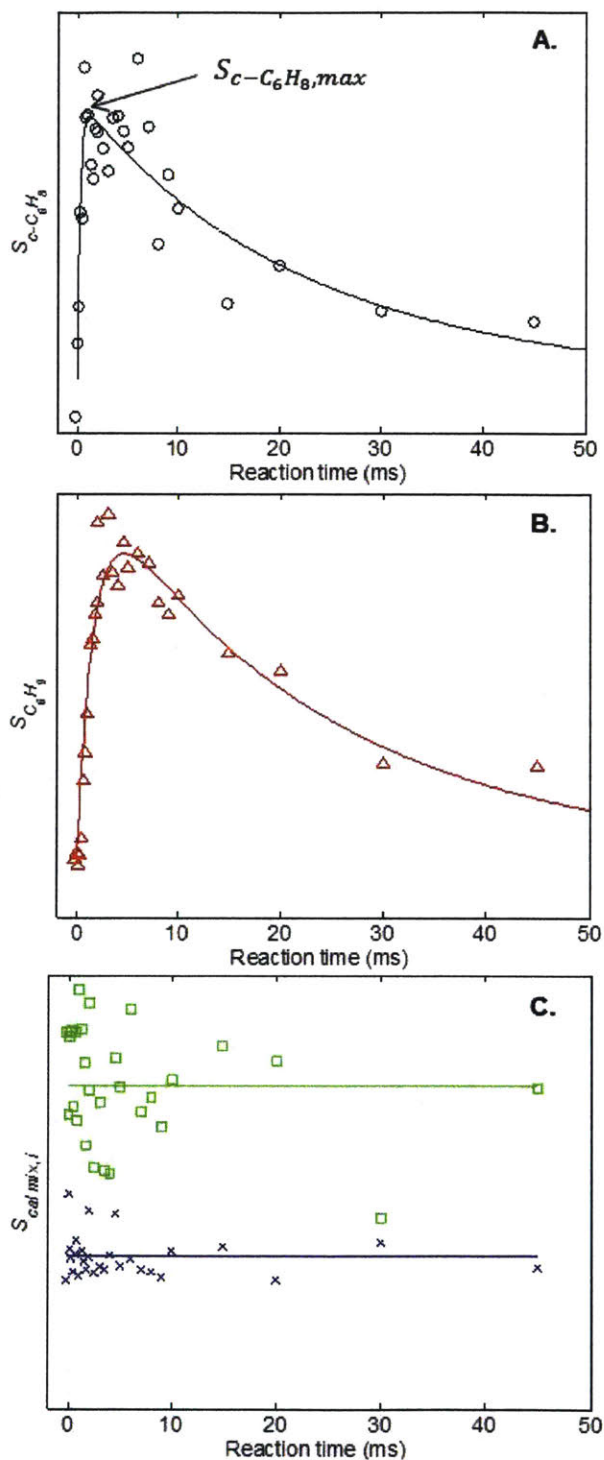
Figure D 11: Simultaneously measured TOF-MS signals at 494 K and 4 Torr for **A.** m/z=80 amu ($c - C_6H_8$), **B.** m/z=81 amu ($n - C_6H_9$) and **C.** cyclohexane (green squares) and heptane (blue crosses). The lines in **A.** and **B.** are biexponential fits to the data, while the lines in **C.** are average values, $\overline{S}_{calmix,i}$.

357

The initial concentrations of I atom and methyl radical, $[I]_0$ and $[CH_3]_0$, can also be quantified from their respective TOF-MS signals using an analogous form of Eq. D-8 and the recently measured values of $\sigma_{PI,i}(E = 10.5\ eV)$ for both species (74^{+33}_{-23} for I atom,[268] and 5.7 ± 0.67 for methyl radical MB[375]). Their initial TOF-MS signals, $S_{I,0}$ and $S_{CH_3,0}$, were obtained by fitting an exponential decay and back-extrapolating to $t = 0$, as shown in Figure D 12 and Figure D 13. Back-extrapolation is necessary due to the finite rise times of both I atom and CH$_3$ (species that are produced essentially instantaneously by photolysis) caused by molecular beam sampling effects that have been discussed extensively elsewhere.[65, 110-111] Transient signal at 15 amu was only observed at 700 K, where 1,3-butadiene photodissociation is more favorable compared to lower temperatures. Therefore, at all other temperatures only a conservative upper bound estimate of $[CH_3]_0 < 0.3 \times 10^{12}$ molecules cm^{-3} could be asserted based on the sensitivity of the TOF-MS and the relatively small photoionization cross section of CH$_3$.
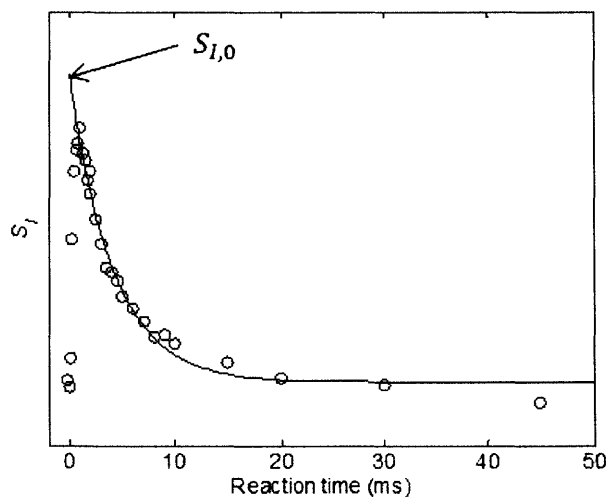
Figure D 12: TOF-MS signals at 494 K and 4 Torr for m/z = 127 amu (I Atom). The line is an exponential fit to the decay portion of the data.
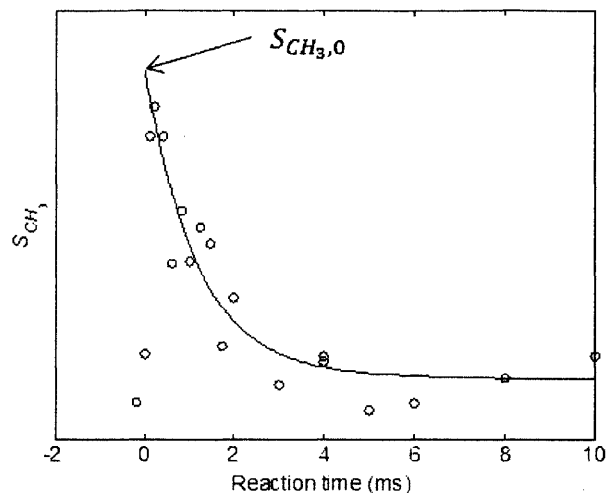
Figure D 13: TOF-MS signals at 700 K and 4 Torr for $\frac{m}{z} = 15$ amu (CH_3 radical). The line is an exponential fit to the decay portion of the data.

Once $[c - C_6H_8]_{max}$ is known for a given experiment, $\alpha_{c-C_6H_8}$ can be computed using Eq. D-4. Table D 5 summarizes the inputs to Eq. D-4 (along with uncertainties) for all of the experiments to measure $\alpha_{c-C_6H_8}$ reported here, as well as the final values of $\alpha_{c-C_6H_8}$, which are plotted in Figure 4-7. The final quoted error bars on $\alpha_{c-C_6H_8}$ are based on propagation of uncertainty and include the range of possible values if either the 1,3- or the 1,4-isomer is 100% dominant (because the cross sections of the two isomers are so close, this contribution to the uncertainty is very small).

Table D 5: Summary of $\alpha_{c-C_6H_8}$ calculation at 4 Torr

T (K)	PDMS coated?	[1,3-C₄H₆][1] (10^{16} molecule/cm³)	$x_{1,3-C_4H_6}$[2]	Photolysis Energy (mJ/pulse)	Photolysis diameter (cm)	k_1 (10^{-14} cm³ molecule⁻¹s⁻¹)	k_2 (s⁻¹)	$[I]_0$[3] (10^{12} molecule/cm³)	$[I]_0$[4] (10^{12} molecule/cm³)	$[CH_3]_0$[4] (10^{12} molecule/cm³)	$[c-C_6H_8]_{max}$[4] (10^{12} molecule/cm³)	$\alpha_{c-C_6H_8}$
494	No	1.2	0.156	30	1.2	10.1 ± 0.2	0 −210	1.6 ± 0.6	0.45 ± 0.2	< 0.3	0.05 ± 0.02	0.04 ± 0.02
494	Yes	1.2	0.156	30	1.2	10.1 ± 0.2	0 −194	1.6 ± 0.8	1.3 ± 0.7	< 0.3	0.06 ± 0.03	0.04 ± 0.03
494	Yes	1.2	0.156	30	1.5	10.1 ± 0.2	0 −113	1.2 ± 0.7	1.0 ± 0.5	< 0.3	0.04 ± 0.02	0.04 ± 0.03
494	Yes	1.2	0.156	80	1.2	10.1 ± 0.2	0 −229	3.6 ± 1.6	3.5 ± 2.0	< 0.3	0.14 ± 0.06	0.05 ± 0.03
599	No	1.2	0.19	30	1.2	15.3 ± 0.3	0 −236	1.9 ± 0.8	0.6 ± 0.3	< 0.3	0.12 ± 0.04	0.07 ± 0.04
700	No	1.2	0.222	30	1.2	20.4 ± 0.4	0 −530	1.4 ± 0.7	0.4 ± 0.2	1.0 ± 0.5	0.14 ± 0.05	0.12 ± 0.08
700	No	0.6	0.111	30	1.2	20.4 ± 0.4	0 −530	1.4 ± 0.7	0.6 ± 0.3	0.5 ± 0.3	0.09 ± 0.04	0.09 ± 0.06

[1] Uncertainty in [1,3-C₆H₆] is 10% due to uncertainty in MFC calibration
[2] Mole fraction of 1,3 − C₄H₆
[3] Obtained from simultaneous measurements of I Atom absorbance. This value of [I]₀ was assumed to equal [C₂H₃]₀ in analysis.
[4] Obtained from TOF-MS as detailed in the text

A range of k_2 values is given in Table D 5 where the upper limit represents the value measured by the multiple-pass absorbance. This is because a large component, if not most, of the k_2 value measured using absorbance is due to diffusion of vinyl out of the probe beam area. The time scale of this diffusion will depend on the geometry of the Herriott multiple-pass alignment, which is totally unrelated to the time scale of diffusion out of the sampling region for the TOF-MS. We therefore estimate that the "real" k_2 for the TOF-MS measurement is somewhere between 0 s^{-1} and the k_2 value measured by absorbance. This assumption is validated by the time scale of decay observed for transient TOF-MS signals such as $\frac{m}{z} = 80$ and 81 amu shown in Figure D 11, which have decay time constants of 40 s^{-1}.

As expected, the branching to the chemically activated cyclohexadiene channel increases as a function of temperature. The agreement between $\alpha_{c-C_6H_8}$ values measured at 700 K and different $[1,3 - C_4H_6]$ provides further confidence in our results and analysis. As discussed in the main text, these measurements are within the large uncertainty of the predictions. One important contributor to the prediction uncertainty is the value of $\langle \Delta E_d \rangle_{300}$, which our results suggest needs to be increased from the value recommended by Jasper et al. for methane in helium bath gas.[376] This might be partially explained by the experimental presence of a significant mole fraction of $1,3 - C_4H_6$ (as much as 0.22) for the 4 Torr experiments, as shown in Table D 5. Unfortunately, this concentration of $1,3 - C_4H_6$ is needed to produce enough cyclohexadiene for TOF-MS detection.

To allay concerns regarding unaccounted loss of vinyl radical to the stainless steel wall of the reactor (which would cause a systematic deviation in our measured values of $\alpha_{c-C_6H_8}$) additional experiments were conducted at 500 K and 4 Torr after coating the inside of the reactor with polydimethylsiloxane (PDMS). As shown in Table D 5, coating the reactor clearly had an effect on $[I]_0$ measured using TOF-MS, bringing those values into much closer agreement with $[I]_0$ measured by I Atom absorbance. This point is most clearly illustrated by the parity plot of Figure D 14. This result suggests that prior to coating the reactor, I atom was being lost to the walls. Coating with PDMS appears to have eliminated this issue.
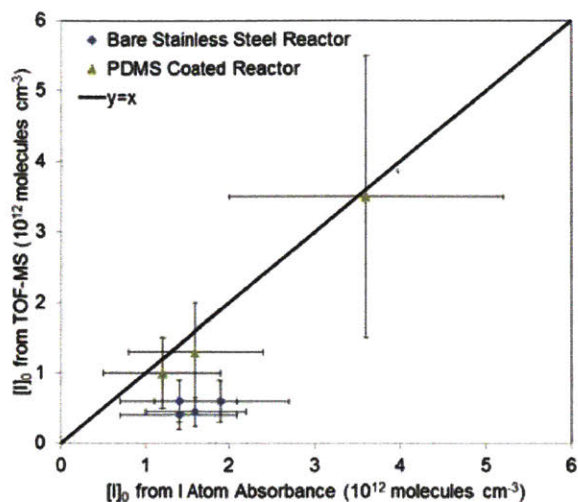
Figure D 14: Parity plot of $[I]_0$ measured using I Atom Absorbance and TOF-MS.

Despite the dramatic increase in $[I]_0$ measured using TOF-MS, coating had no effect on the quantification of $\alpha_{c-C_6H_8}$. Furthermore, we also enlarged the photolysis beam diameter from 1.2 to 1.5 cm in order to submerge more of the TOF-MS sampling cone in the photolyzed region and to also shorten the distance between the edge of the photolyzed region and the reactor walls. Enlargement of the photolysis beam also induced no change in $\alpha_{c-C_6H_8}$. All of this suggests wall reactions are not consuming a significant portion of the vinyl radical pool, even when the reactor surface is bare stainless steel. This could be due to the unique geometry of our apparatus, where only the small tip of the sampling cone is in direct contact with the photolyzed region, or perhaps because loss to the walls is already captured by our large range of k_2 values.

Appendix E

Additional Details for Phenyl Radical + Propene

Experimental Procedure for Quantifying PICS

10.5 eV photoionization cross sections (PICS) were quantified by flowing both a controlled but imprecisely known concentration of species i, and a known concentration of the calibration gas mixture (calmix, consisting of 100 ppm propene, 1,3-butadiene, furan, benzene, cyclohexane, toluene and heptane) through the quartz flow reactor while recording PI TOF-MS signal, S. A portion of the gas mixture was trapped at the inlet of the reactor by a pneumatically controlled sample loop, and the relative concentration, C, of i to calmix in the mixture was quantified using Gas Chromatography (GC)/MS. PICS for species i, σ_i, could then be quantified using one of the calmix species as an internal standard:

$$\sigma_i = \sigma_{calmix} \times \left(\frac{S_i}{S_{calmix}}\right) \times \left(\frac{C_{calmix}}{C_i}\right)$$

PICS were quantified in this manner for different concentration ratios and for i = hexane, styrene and 3-phenylpropene. At each concentration ratio three replicate measurements were taken (both GC/MS and PI TOF-MS measurements were repeated). Average PICS with 95% confidence intervals are reported in Figure E 1, Figure E 2 and Figure E 3 below, using either toluene or heptane as the internal standard. The measured PICS for both hexane[266] and styrene[265] are in good agreement with literature, which is encouraging, especially considering that the absolute PICS of hexane and styrene differ by about an order of magnitude. Most importantly, the measured PICS for 3-phenylpropene is 38.8 ± 7.0 MB (no literature value available for comparison), which seems reasonable given that many of the other closed-shell aromatic-containing compounds in Table 4-8 have PICS ~30-40 MB.
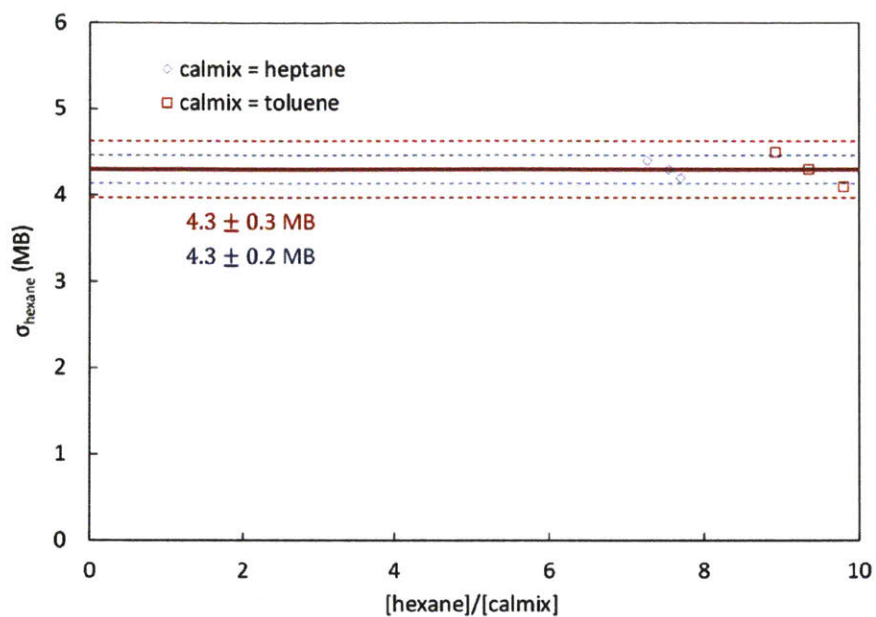
Figure E 1: Quantification of hexane 10.5 eV PICS. Literature value is 4.5±0.7.[266]
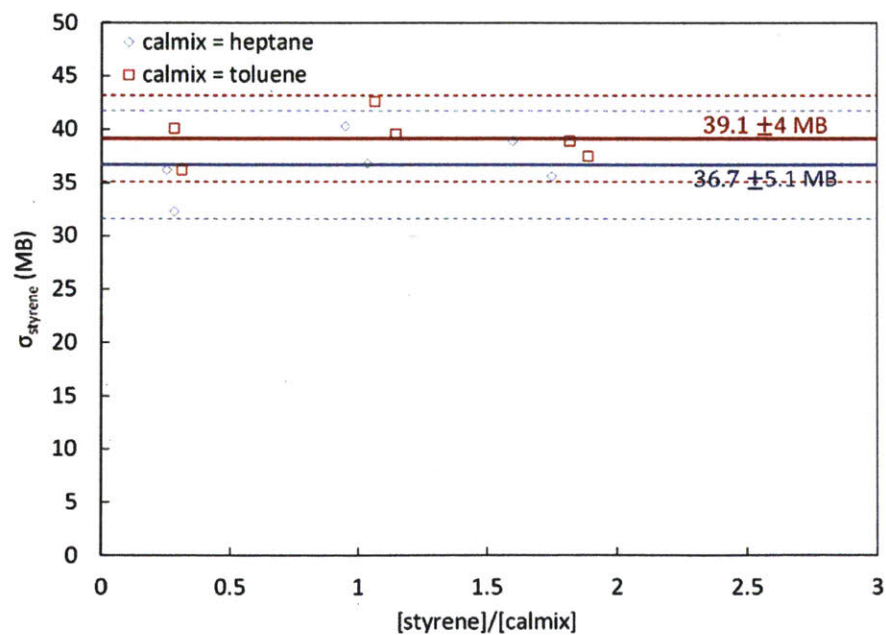
Figure E 2: Quantification of styrene 10.5 eV PICS. Literature value is 42.9±4.3.[265]
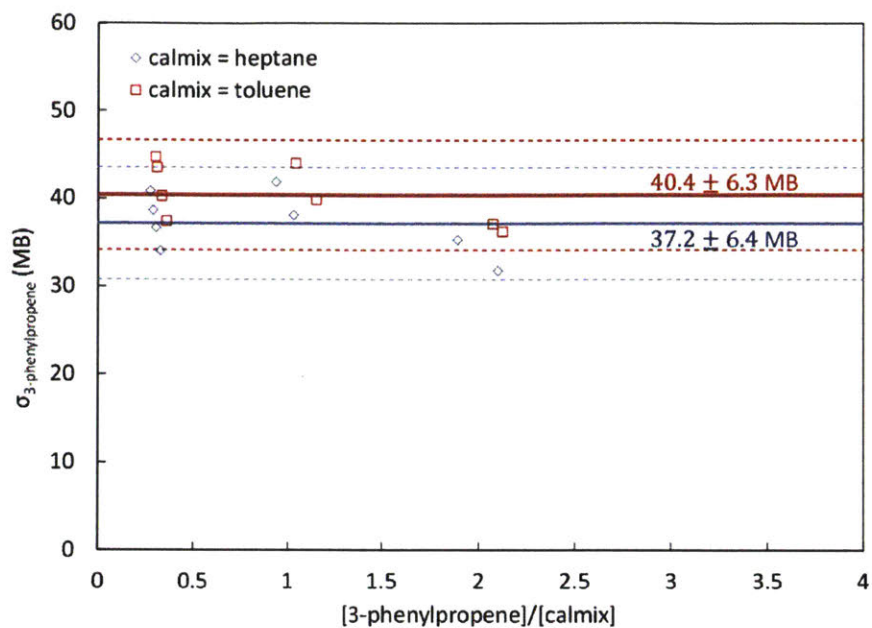
Figure E 3: Quantification of 3-phenylpropene 10.5 eV PICS.

While this experimental procedure for quantifying PICS seems to work well for stable molecules with relatively strong CC and CH bonds, for heavier molecules with weaker bonds it is expected that wall-effects and thermal decomposition will make precise concentration measurements more difficult. For example, attempts to quantify PICS for nitrosobenzene, C_6H_5NO, were less successful, likely because of both adsorption of C_6H_5NO on the walls of the sampling loop, and thermolysis of the weak C-N bond upon heating of the loop to encourage desorption.

Measured Fragmentation Patterns
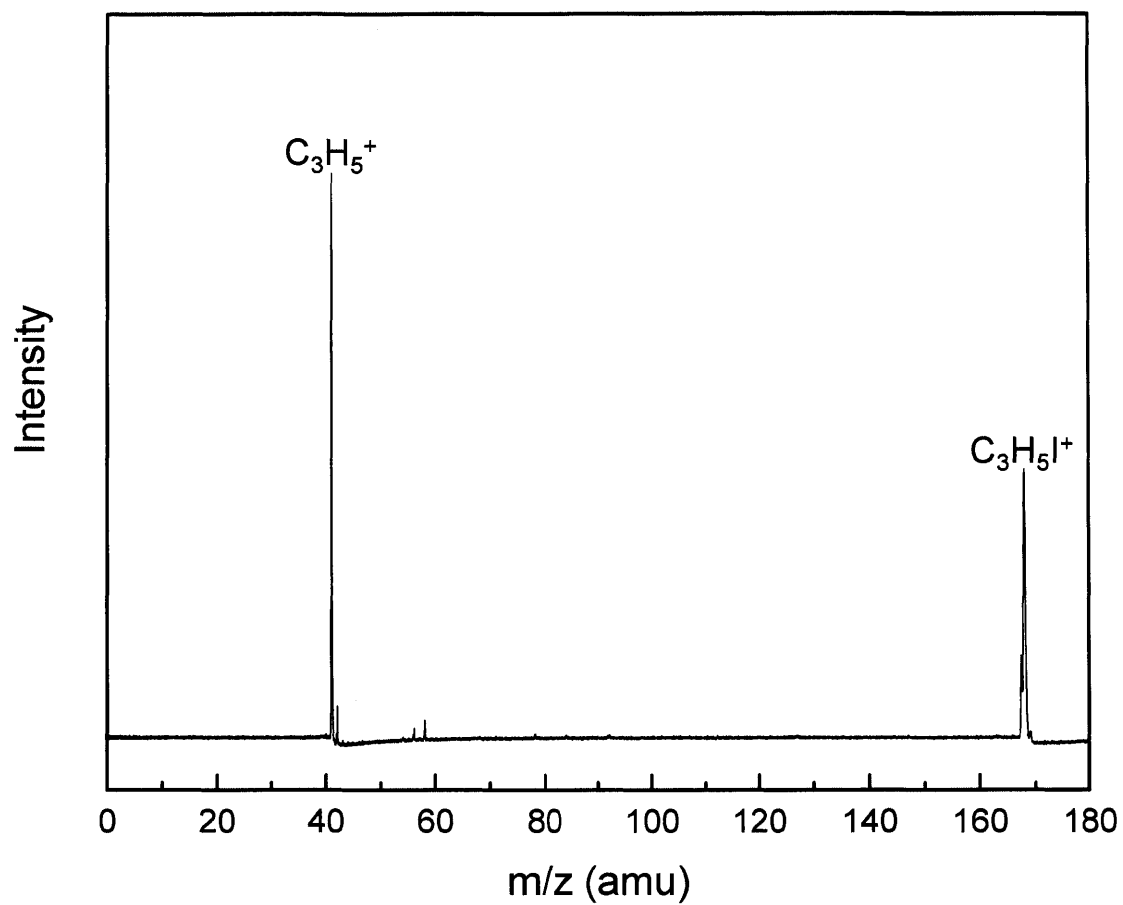
Figure E 4: Measured fragmentation pattern of C_3H_5I at 10.5 eV displaying signals at m/z = 168 ($C_3H_5I^+$ parent ion) and 41 amu ($C_3H_5^+$ daughter ion). Signal at 58 amu is from acetone impurity.
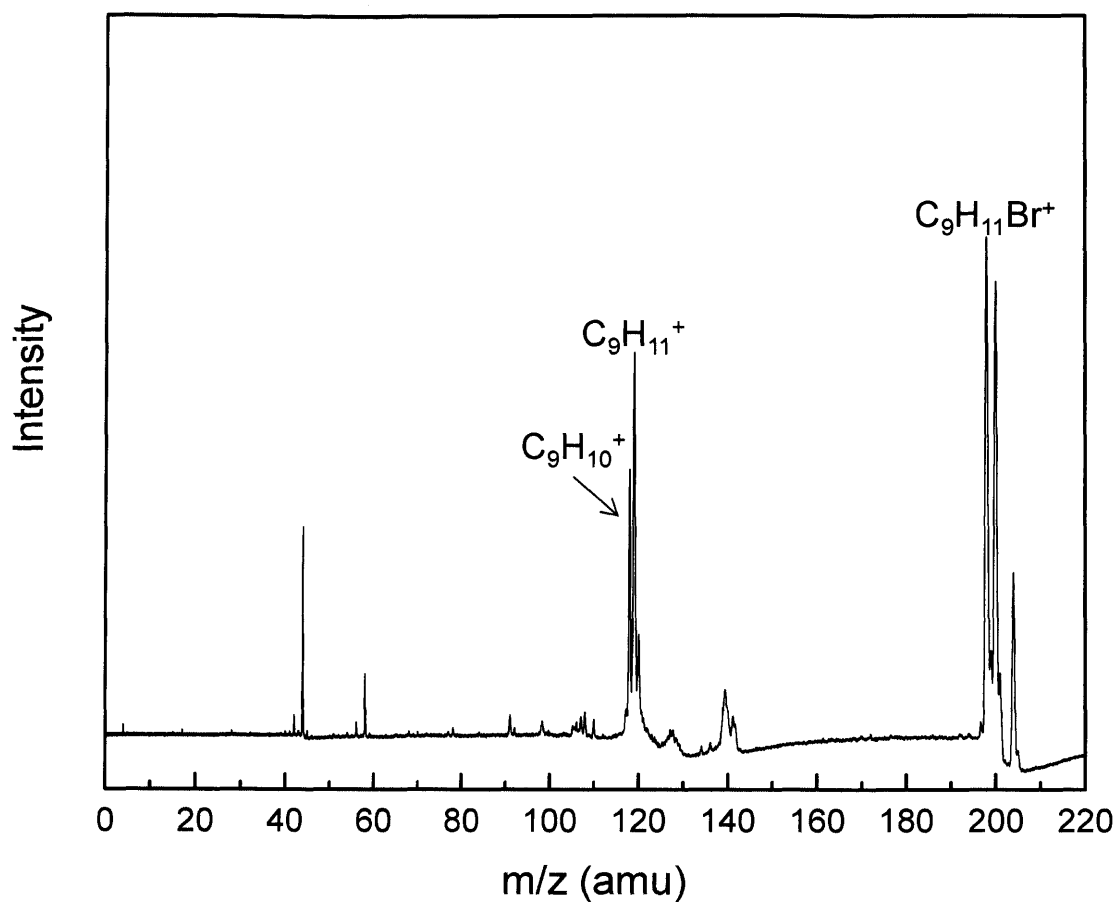
Figure E 5: Measured fragmentation pattern of i1-Br at 10.5 eV displaying signals at m/z = 198/200 (^{79}Br/^{81}Br isotopologues of $C_9H_{11}Br^+$ parent ion), 119 ($C_9H_{11}^+$ daughter ion) and 118 amu ($C_9H_{10}^+$ daughter ion). Signals at 58 and 204 amu are from acetone and iodobenzene impurities, respectively. Source of 44 amu signal is unkown.

Predicted Methyl Radical MBMS Profiles

Figure E 6 shows predicted methyl radical, CH_3, time profiles for MBMS at 600 and 700 K. CH_3 is a coproduct of styrene from $C_6H_5 + C_3H_6$, which is the major product channel at 700 K. However, even though the concentration of CH_3 in the reactor should be relatively high we were unable to detect it with MBMS for the three reasons mentioned in section 4.2.4.4.7: low MBMS signal due to mass discrimination factor and small PICS, overlap with a C_3H_6 fragment and lack of a CH_3 wall reaction in the model. At 600 K, the maximum predicted MS signal is ~0.003 (units of flight-time integrated signal area), whereas the smallest signals detected were ~0.001. At 700 K, the predicted CH_3 signal has increased ~3× due to more styrene production,

and should be distinguishable from the noise. However, at both temperatures the model predicts CH_3 to persist over the full 45 ms measurement time, which is not reasonable given that phenyl radical decays within ~10 ms largely due to wall reactions. Therefore, if CH_3 wall reaction were included in the model, the maximum predicted CH_3 MBMS signal in Figure E 6 would drop significantly, likely below the MBMS detection limit. However, in the absence of any measurable CH_3 signal on which to base k_{wall} for CH_3, no value was fit.

CH₃ Radical
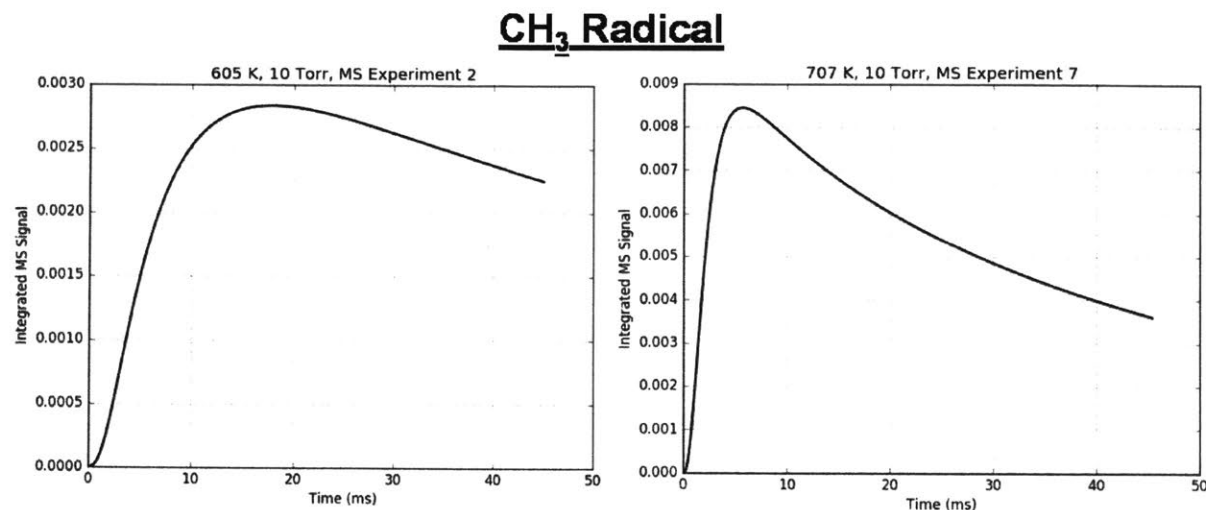
Figure E 6: Predicted time profile for methyl radical, CH_3, in MBMS at 600 (left) and 700 K (right).

MBMS Profiles without Propene

Figure E 7 summarizes the results of Experiment #1, which was conducted without C_3H_6. There are several noteworthy observations. Most obviously, the model does not match most of the MBMS measurements. In fact, of the six m/z's where transient behavior was observed, only 154 amu, biphenyl, has good agreement between the model and measurements. The other five m/z signals are all influenced by the walls in some way that is not described by our gas-phase model. Specifically, phenyl radical, C_6H_5, at m/z=77 amu is being rapidly converted to benzene, C_6H_6, at 78 amu, much faster than can be explained by gas-phase chemistry. Although the model does predict some C_6H_6 formation through self-disproportionation between two C_6H_5 radicals, it is not nearly enough to explain the large and rapidly-appearing 78 amu signal. Hydrogen (H)-abstraction from the iodobenzene precursor, C_6H_5I, is not included in the model but is expected to be slow at our experimental conditions owing to the strength of a phenylic C-H bond.[264] If C_6H_6 was being formed purely in the gas phase, then the time constant of its growth should

match the time constant of both C_6H_5 decay and biphenyl growth, which it clear does not. Similarly, I atom at 127 amu somehow gains a hydrogen atom, H, to form HI at 128 amu, although the time-scale is longer than C_6H_6 formation. I atom also recombines with itself to form molecular iodine, I_2, at 254 amu in much higher concentration than predicted by the model, which uses a recommended P-dependent rate for $2I (+ M) \rightarrow I_2 (+M)$ in a helium bath gas that is very slow at our conditions.[167]

Figure E 7: Summary of all time profiles measured (markers) with MBMS in Experiment 1 (600 K, 10 Torr, no propene). Lines are model results. Simultaneously recorded 505.3 nm absorbance is also shown with model comparison.

The proposed mechanism for most of these unexpected observations involves an Eley-Rideal type of heterogeneous reaction on the quartz reactor walls between a gas-phase radical and an adsorbed H atom (denoted H-wall):

$$C_6H_5/I \,(g) + H - wall \rightarrow C_6H_6/HI(g)$$
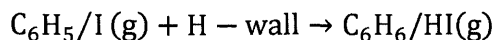
H atom might have adsorbed on and saturated the walls from previous experiments. The reaction above is essentially an H-abstraction between the wall and gas-phase C_6H_5/I, similar to what has been observed between gas-phase fluorine atoms and deuterium adsorbed on various surfaces (including quartz).[102] The mechanism for I_2 formation is probably different, but also likely involves the walls. For example, ro-vibrationally excited I_2 formed immediately after I atom recombination might be stabilized by the walls much more than by the helium bath gas, which is an inefficient collision partner.

If the proposed mechanism for $C_6H_6/HI/I_2$ formation above is correct, then by adding a sufficient amount of an excess reagent (e.g., C_3H_6) wall catalysis might be suppressed in favor of fast gas-phase chemistry (e.g., $C_6H_5 + C_3H_6$ and subsequent product formation). This was the approach taken here, where primary product branching was measured at three different propene concentrations ("low", "medium" and "high") that vary by 4× in order to verify insensitivity to $[C_3H_6]$, and therefore insensitivity to wall catalysis as well. Comparing Experiments #2-5 (600 K) and #7-9 (700 K), the primary product branching does appear to be largely insensitive to $[C_3H_6]$, confirming that wall catalysis is not influencing the main results of this work.

Although we have found a way to sidestep the effects of wall catalysis in the current work, efforts should continue to be made to reduce the effects further. Specifically, we found the geometry of the sampling pinhole to be quite critical to preventing wall catalysis, as quantified by the ratio of maximum 78 to 77 amu signal without C_3H_6. As shown in Figure E 7, the 78:77 ratio is currently ~1 using the "funnel-shaped" pinhole geometry of Wyatt et al.[72] Similar experiments with a straight pinhole (essentially a 300 micron diameter tube through the 2.5 mm thick reactor walls) resulted in ratios ~10:1, likely due to enhanced contact between radicals and the walls during sampling. Efforts to reduce wall catalysis even further should first focus on the pinhole. The reactor was also treated with boric acid following the procedure of Krasnoperov et al.,[103] but the resulting boron oxide (B_2O_3) coating was found to have negligible effect on the wall catalysis shown in Figure E 7. A better coating would have only strong C-F bonds exposed,

such as in Teflon or Halocarbon wax, but neither of these coatings are suitable at the temperatures of interest to us (>600 K).

Returning to the results shown in Figure E 7, although the maximum C_6H_5 concentration is overpredicted by the model by ~2×, the sum of measured C_6H_5 and C_6H_6 signals is much closer to the model, effectively closing the mass balance. A k_{wall} of 100 s^{-1} for C_6H_5 was found to fit both the time scale of the 77 amu decay from MBMS (~10 ms) and the 505.3 nm absorbance decay adequately. No k_{wall} was fit for I atom, because it was not found to be necessary to match the experiments with C_3H_6 (Figure 4-25, for example).

Experiment #6 (700 K, 10 Torr, summarized in Figure E 8) was also conducted without C_3H_6, and all of the commentary regarding Experiment #1 still applies. The only feature of Experiment #6 worth additional comment is that compared to #1 there appears to be less HI formation. This could be due to the higher temperature driving desorption of H atoms from the walls,[277] or it might simply be due to the fact that chronologically #6 was actually run before #1 when the reactor was freshly-cleaned and B_2O_3 coated. Also unlike Experiment #1, no I_2 was measured.

Hydrocarbons

Iodide-Containing Species
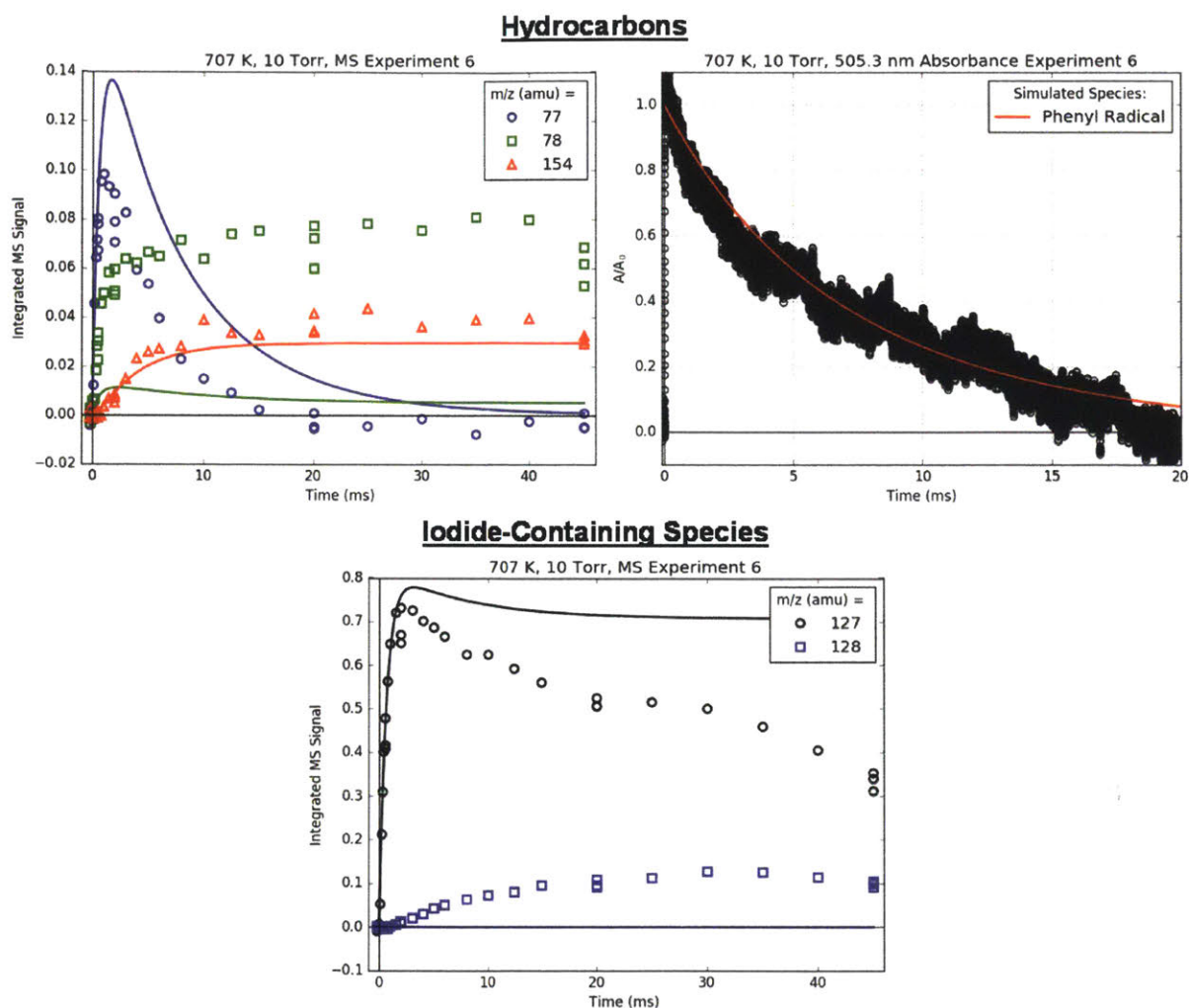
Figure E 8: Summary of all time profiles measured (markers) with MBMS in Experiment 6 (700 K, 10 Torr, no propene). Lines are model results. Simultaneously recorded 505.3 nm absorbance is also shown with model comparison.

MBMS Profiles at Higher Pressures

25 Torr

Experiment #13 (summarized in Figure E 9, Figure E 10 and Figure E 11) is identical to #7 (and #15) except that the pressure is higher: 25 instead of 10 (or 50) Torr. Experiment #13 exhibits the worst agreement between the measured and predicted primary product branching at 700 K. Specifically, 91, 118 and 119 amu are all underpredicted by ~2×. However, all of these products have relatively low concentrations compared to the major product, styrene, at 104 amu, which is described well by the model.

There are several other concerning features of Experiment #13. First, there is a clear baseline shift in the 505.3 nm absorbance that might indicate C_6H_5OO formation, which could explain some of the other discrepancies with the model. Second, although the steady-state 104 amu signal matches the model well, the measured time-dependence is slower than the model. As discussed in section 4.2.4.4.5 this is due to slower diffusion at higher-P inhibiting MBMS sampling. The delayed growth at 104 amu (and other time-dependent m/z's) becomes even more pronounced at higher-P (#15), consistent with this explanation. Figure E 11 shows all of the primary product profiles normalized by the instantaneous styrene/104 amu signal, such that transport delays should largely cancel out. As shown, the ratio of styrene to any of the other primary products is essentially flat as a function of reaction time after the first few milliseconds, confirming that although the absolute signals are distorted by transport effect, the ratios between products at any given time are still reliable. Finally, the iodide containing species exhibit contradictory behavior as a function of P. The large signal at 168 amu from C_3H_5I has disappeared when increasing P from 10 (Figure 4-29) to 25 Torr (Figure E 10), while the signals at the parent m/z of the other two iodide-containing species, CH_3I and **i1**-I at 142 and 248 amu, respectively, have increased. The latter behavior is consistent with P-dependent kinetics, while the former is contradictory. As already mentioned in section 4.2.4.5, this might indicate that C_3H_5I is actually formed on the walls instead of in the gas-phase.
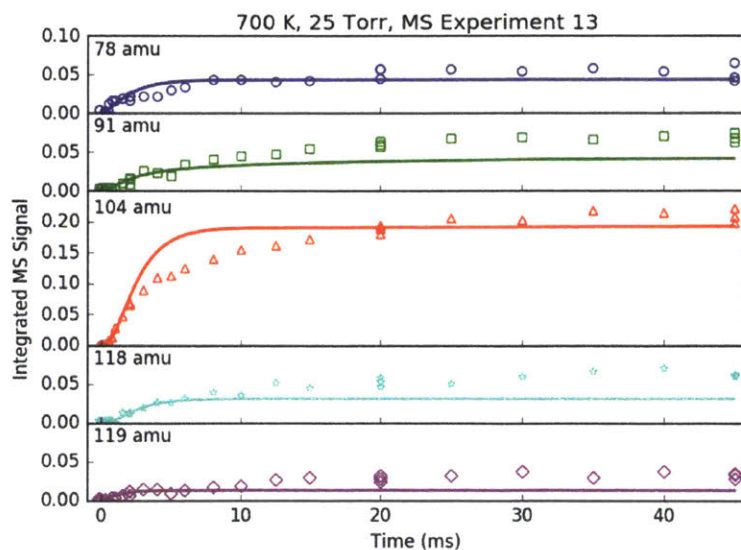
Figure E 9: Time profiles of primary phenyl radical + propene products measured (markers) with MBMS in Experiment 13 (700 K, 25 Torr, "Low" propene). Lines are model results.
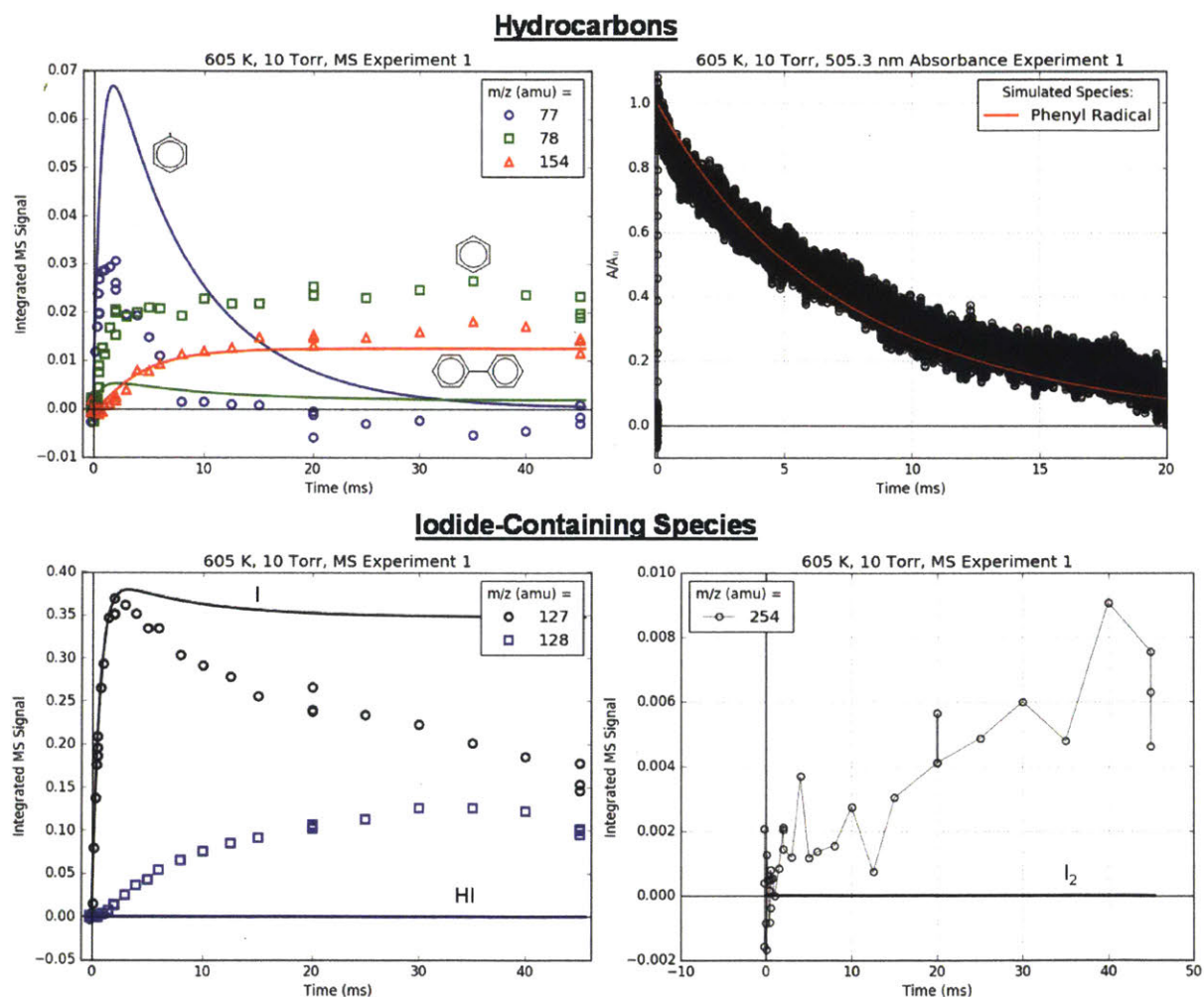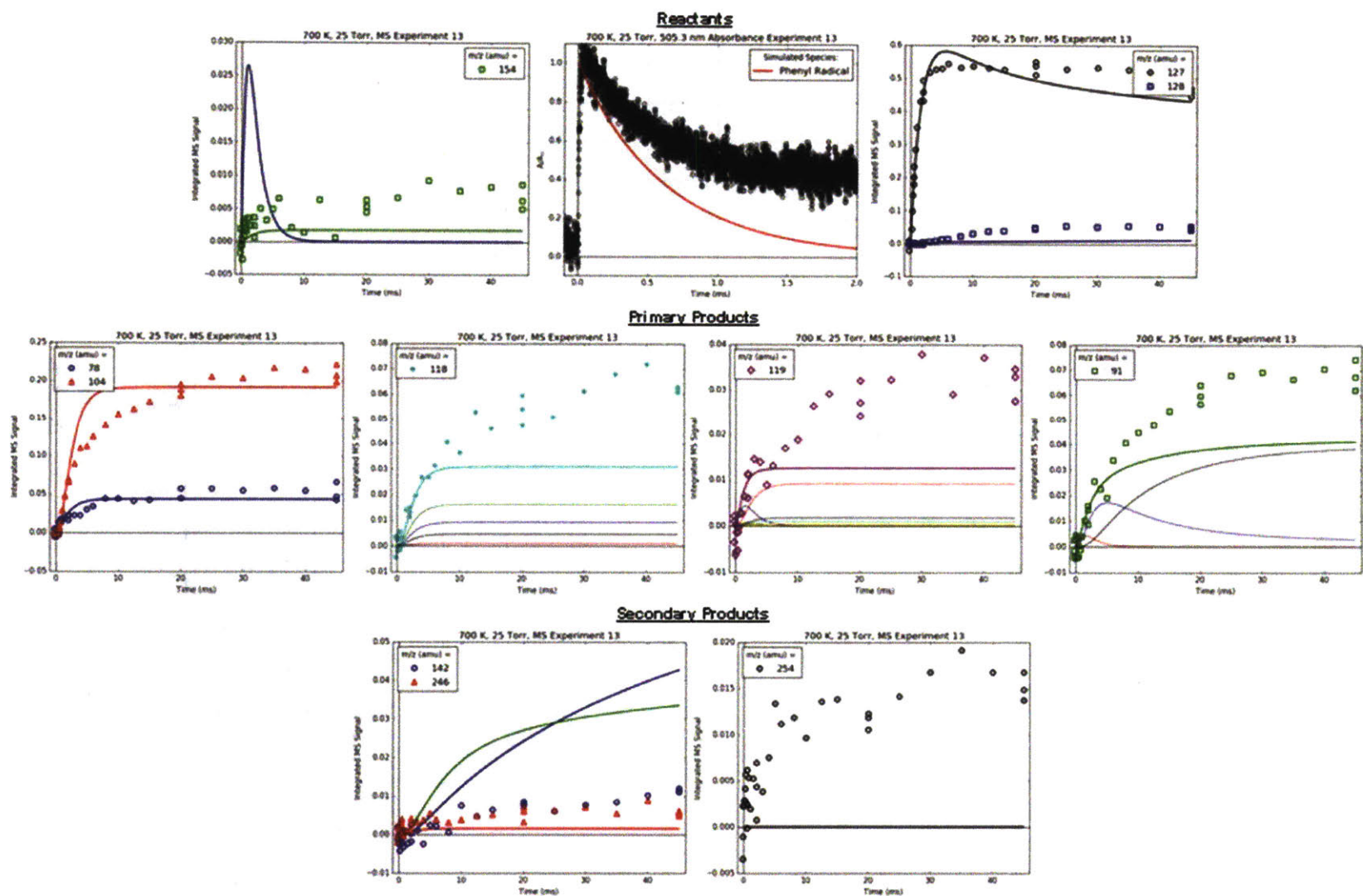
Figure E 10: Summary of all time profiles measured (markers) with MBMS in Experiment 13 (700 K, 25 Torr, "Low" propene). Lines are model results. Simultaneously recorded 505.3 nm absorbance is also shown with model comparison.
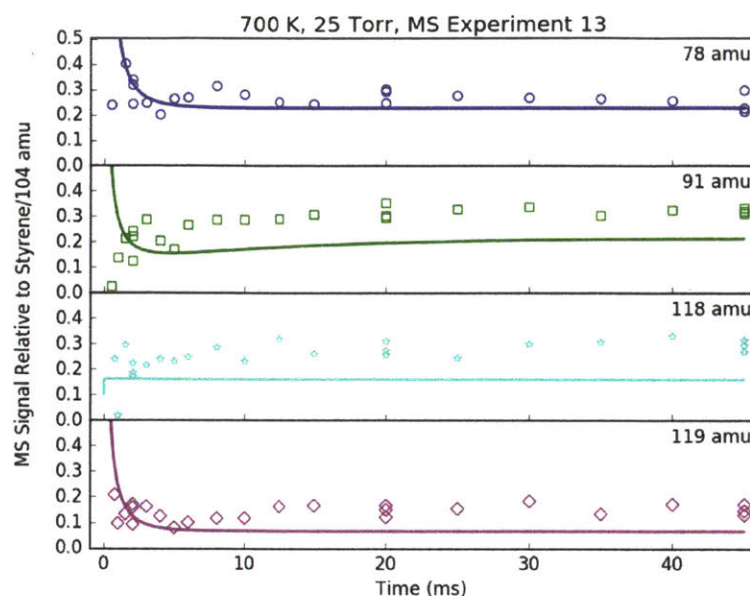
Figure E 11: Time profiles of primary phenyl radical + propene products measured (markers) with MBMS in Experiment 13 (700 K, 25 Torr, "Low" propene). Lines are model results. Both measured and modeled results are plotted relative to the 104 amu/styrene signal at each time point.

50 Torr

Experiment #15 (summarized in Figure E 12, Figure E 13 and Figure E 14) is identical to #7 (and #15) except that the pressure is higher: 50 instead of 10 (or 25) Torr. Figure E 12 is shown in section 4.2.4.3 and is reproduced here for convenience. All of the P-dependent trends highlighted for Experiment #13 continue for #15: the time-scale for primary product growth is noticeably slower (and in disagreement with the simple transport model), more CH_3I is observed experimentally (and in closer agreement with the model) and C_3H_5I is still absent. Most importantly, the steady state product branching matches the model satisfactorily, in agreement with the prediction made in Figure 4-12 that at our experimental conditions the product branching would have negligible P-dependence. Figure E 14 shows the instantaneous primary product ratios (relative to styrene/104 amu) such that transport delays largely canceled out. Just as was observed at 25 Torr (Figure E 11), the product ratios are essentially flat after the first few milliseconds, in contrast to the absolute product signals shown in Figure E 12 and Figure E 13 that require ~30 ms to reach steady state. Furthermore, the model matches these ratios well, as expected, again supporting the predicted lack of P-dependence.
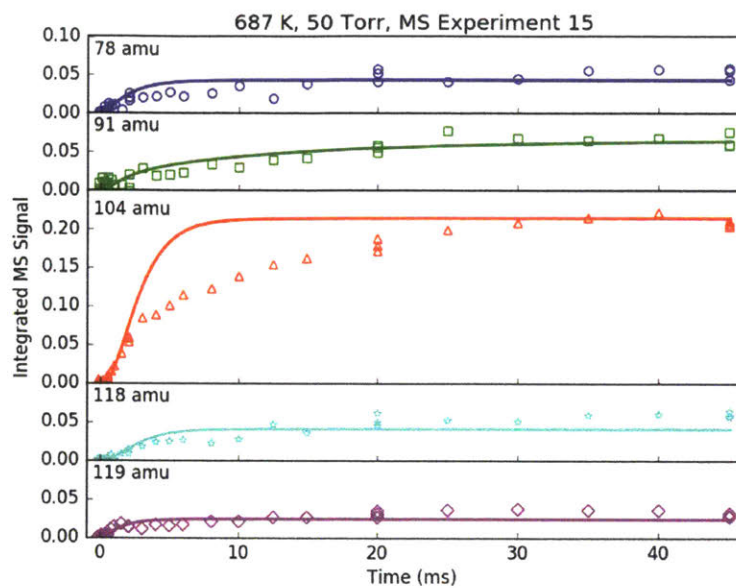
Figure E 12: Time profiles of primary phenyl radical + propene products measured (markers) with MBMS in Experiment 15 (700 K, 50 Torr, "Low" propene). Lines are model results.
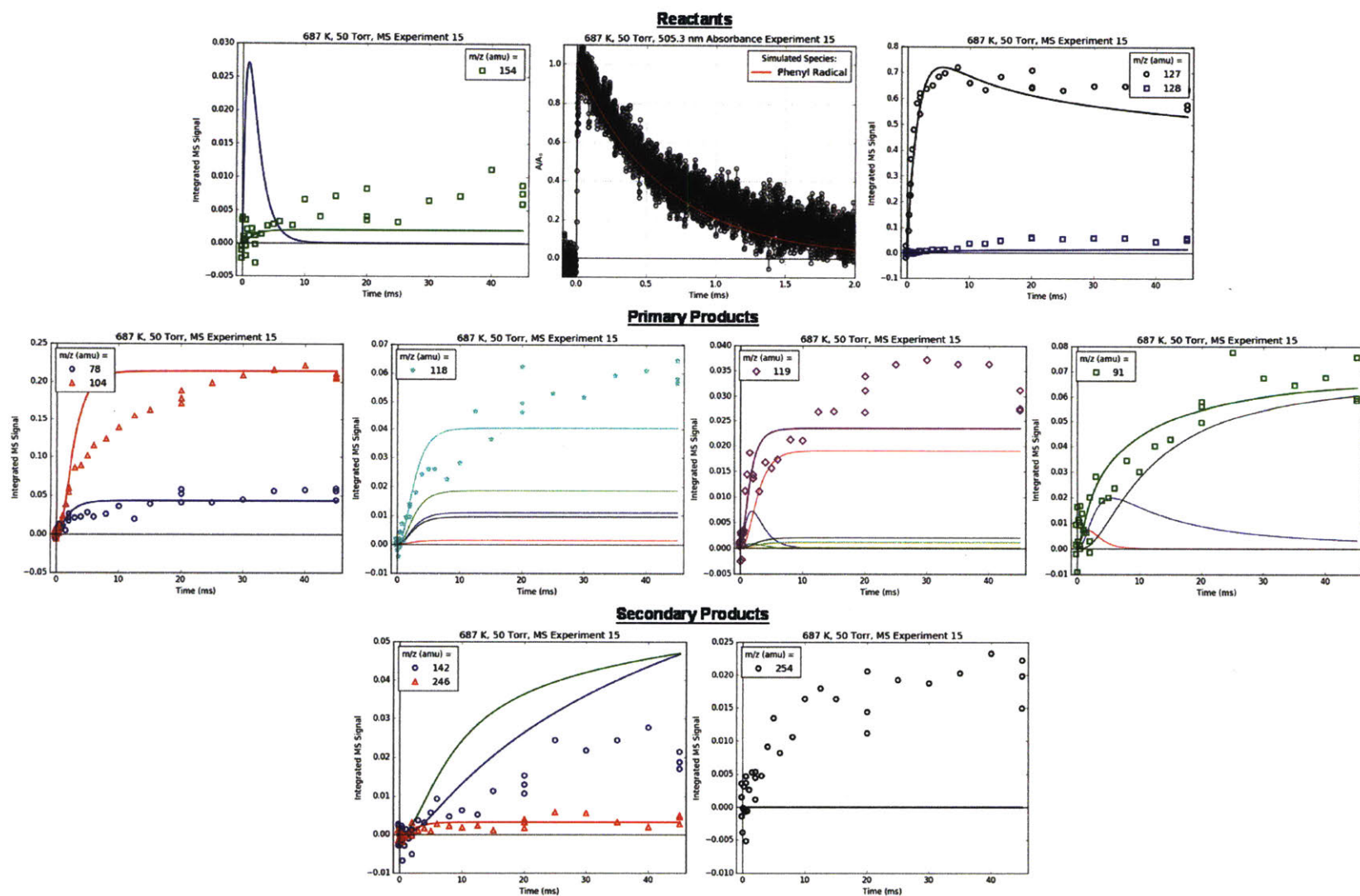
Figure E 13: Summary of all time profiles measured (markers) with MBMS in Experiment 15 (700 K, 50 Torr, "Low" propene). Lines are model results. Simultaneously recorded 505.3 nm absorbance is also shown with model comparison.
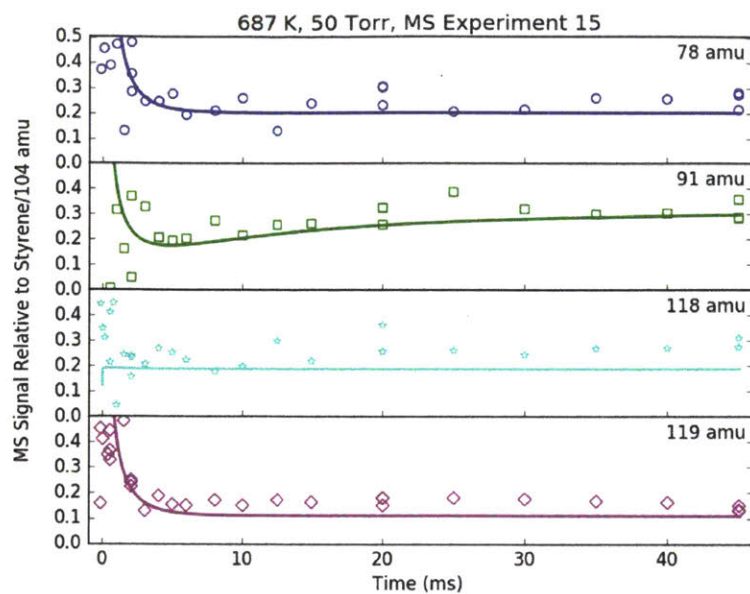
Figure E 14: Time profiles of primary phenyl radical + propene products measured (markers) with MBMS in Experiment 15 (700 K, 50 Torr, "Low" propene). Lines are model results. Both measured and modeled results are plotted relative to the 104 amu/styrene signal at each time point.

Measured 505.3, 447.7 and 408.4 nm Absorbance
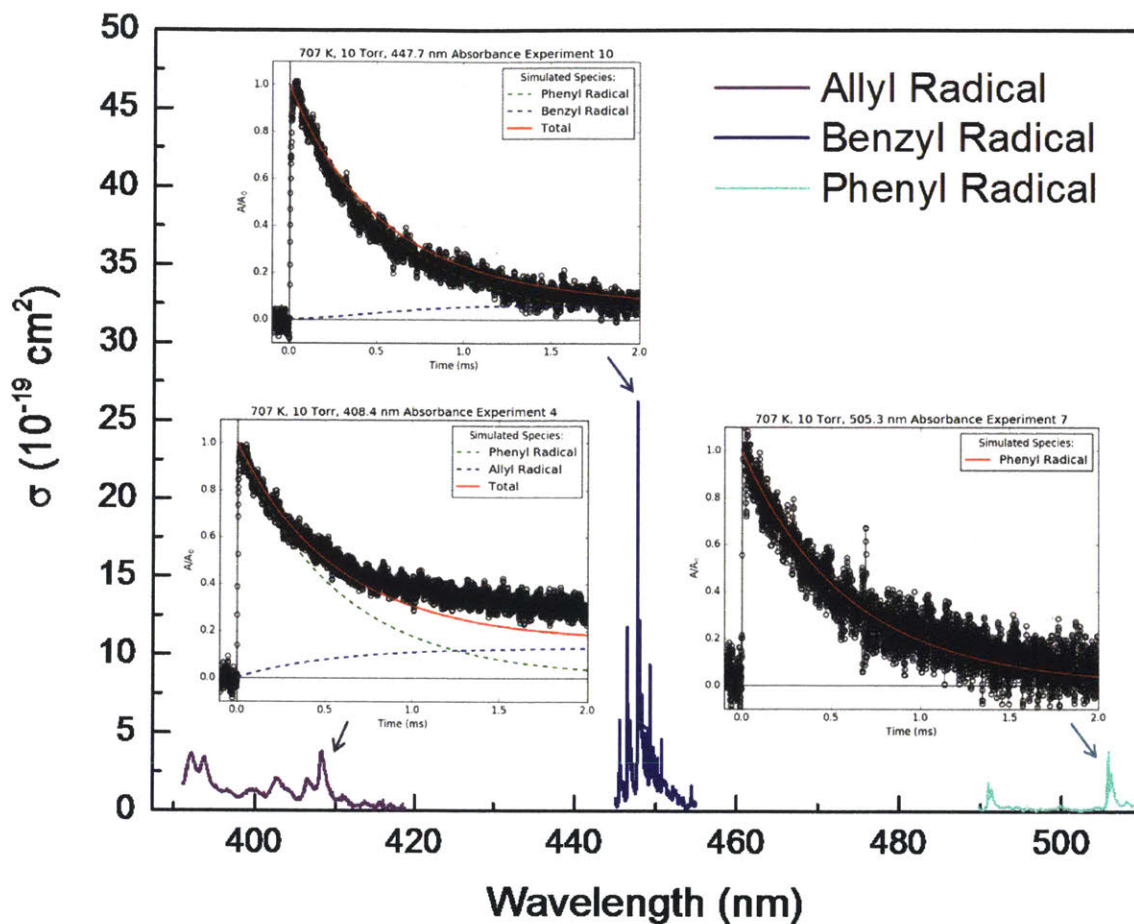
Figure E 15: Room temperature visible absorbance spectra measured by Tonokura *et al.* for allyl,[233] benzyl[248] and phenyl[105] radicals. Insets show representative absorbance traces (markers are measured and lines are modelled) measured in this work at the different wavelengths indicated and otherwise identical conditions (707 K, 10 Torr, $[C_3H_6] = 7.5 \times 10^{15}$ cdm^{-3}). Identical to Figure 4-30, except the recombination reaction between C_3H_5 and I atom ($C_3H_5 + I \rightarrow C_3H_5I$) has been removed from the model.

Appendix F

NG HTP RMG Mechanism Development
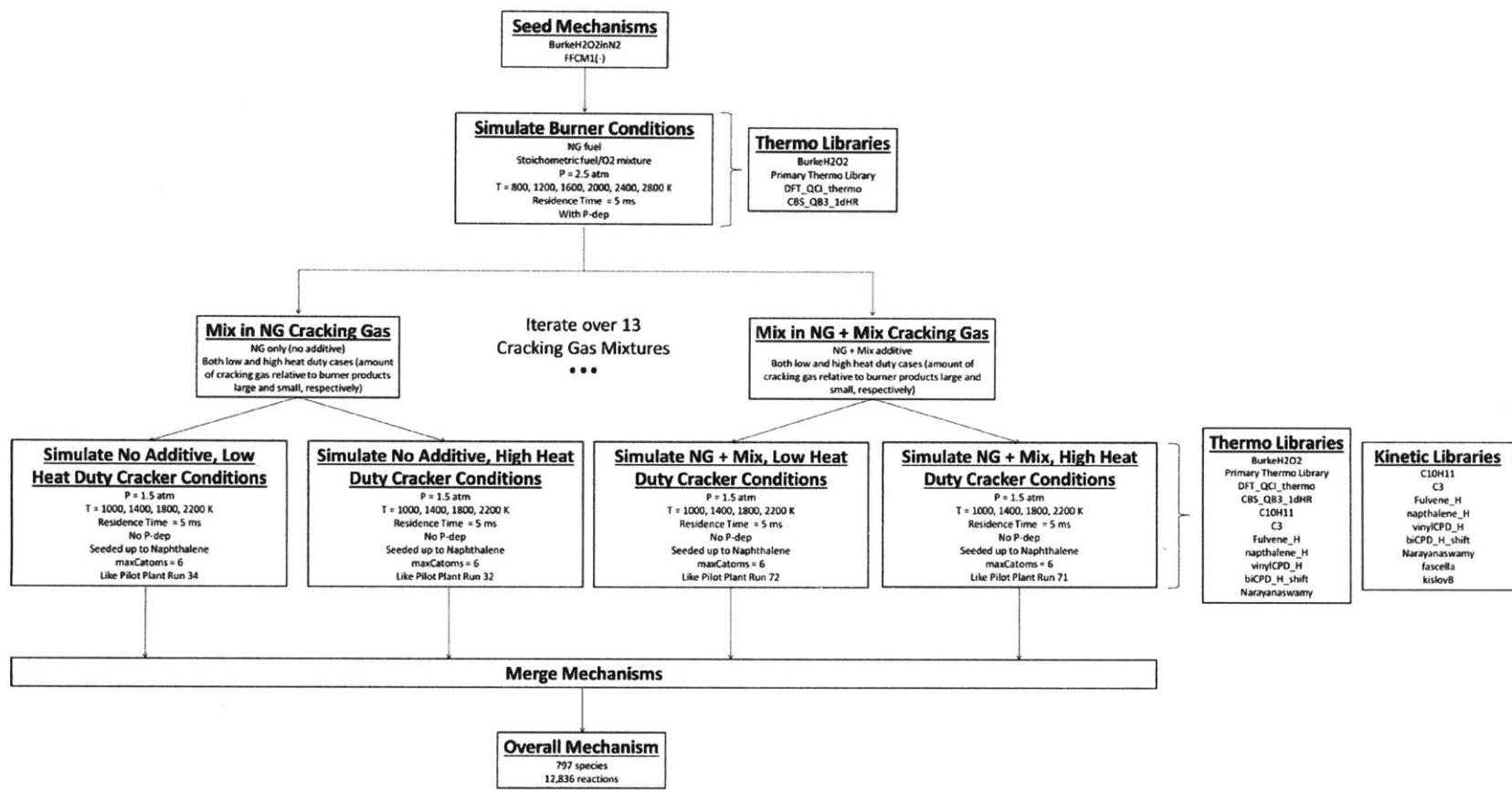
Figure F 1: Detailed flow diagram for RMG Mech v1 development for NG HTP.
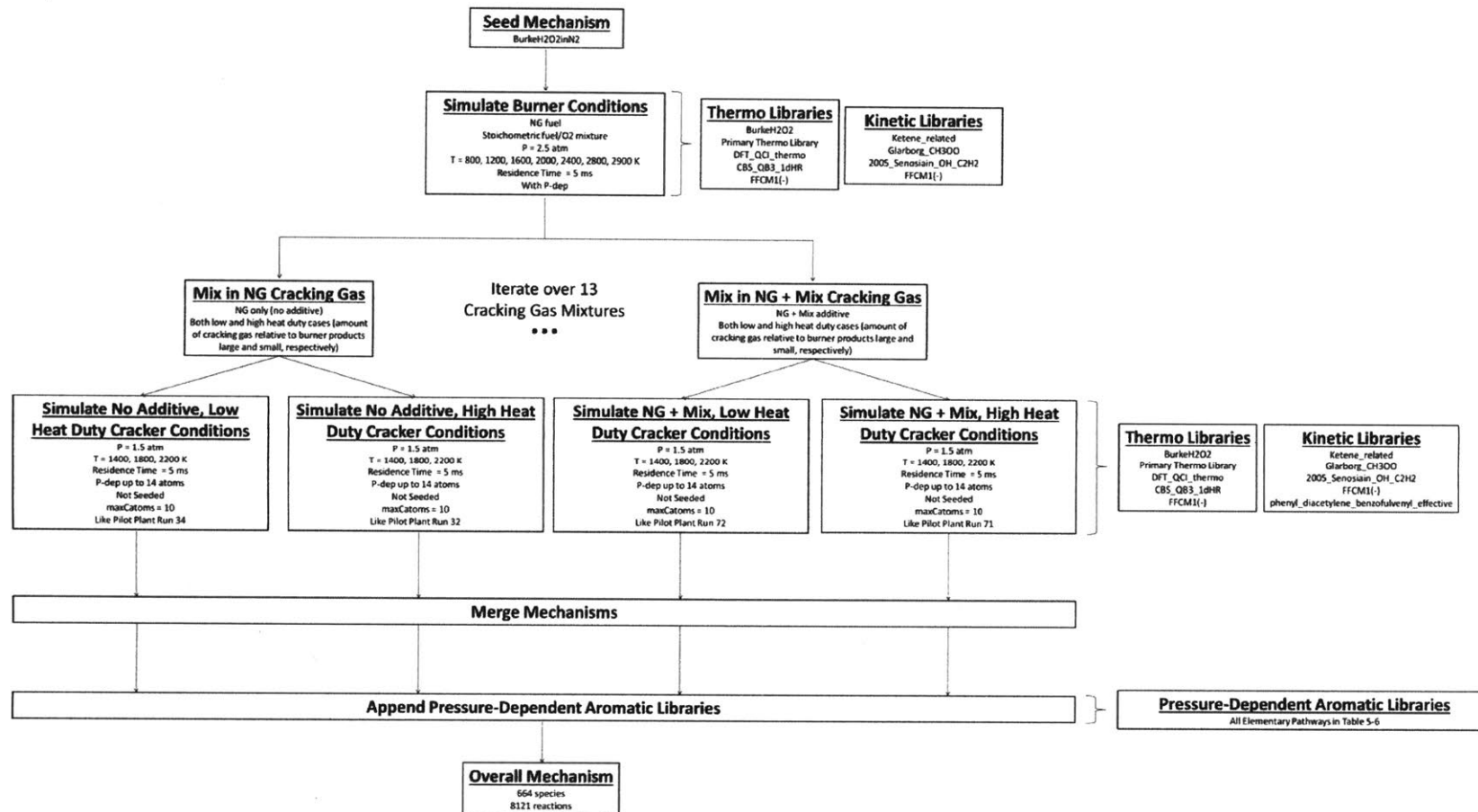
Figure F 2: Detailed flow diagram for RMG Mech v2 development for NG HTP.

References

1. Manion, J. A.; Huie, R. E.; Levin, R. D.; Burgess Jr., D. R.; Orkin, V. L.; Tsang, W.; McGivern, W. S.; Hudgens, J. W.; Knyazev, V. D.; Atkinson, D. B.; Chai, E.; Tereza, A. M.; Lin, C.-Y.; Allison, T. C.; Mallard, W. G.; Westley, F.; Herron, J. T.; Hampson, R. F.; Frizzel, D. H. NIST Chemical Kinetics Database, NIST Standard Reference Database 17. http://kinetics.nist.gov/.

2. Miller, J. A.; Klippenstein, S. J., Master Equation Methods in Gas Phase Chemical Kinetics. *J. Phys. Chem. A* **2006,** *110*, 10528-10544.

3. Senosiain, J. P.; Klippenstein, S. J.; Miller, J. A., The Reaction of Acetylene with Hydroxyl Radicals. *J. Phys. Chem. A* **2005,** *109*, 6045-6055.

4. Smith, G. P.; Tao, Y.; Wang, H. Foundational Fuel Chemistry Model Version 1.0 (FFCM-1). http://nanoenergy.stanford.edu/ffcm1.

5. Tseng, C.-M.; Choi, Y. M.; Huang, C.-L.; Ni, C.-K.; Lee, Y. T.; Lin, M. C., Photodissociation of Nitrosobenzene and Decomposition of Phenyl Radical. *J. Phys. Chem. A* **2004,** *108*, 7928-7935.

6. Sage, A. G.; Oliver, T. A. A.; Murdock, D.; Crow, M. B.; Ritchie, G. A. D.; Harvey, J. N.; Ashfold, M. N. R., nσ* and πσ excited states in aryl halide photochemistry: a comprehensive study of the UV photodissociation dynamics of iodobenzene. *Phys. Chem. Chem. Phys.* **2011,** *13*, 8075-8093.

7. Allen, J. W.; Goldsmith, C. F.; Green, W. H., Automatic Estimation of Pressure-Dependent Rate Coefficients. *Phys. Chem. Chem. Phys.* **2012,** *14*, 1131-1155.

8. Park, J.; Nam, G. J.; Tokmakov, I. V.; Lin, M. C., Experimental and Theoretical Studies of the Phenyl Radical Reaction with Propene. *J. Phys. Chem. A* **2006,** *110*, 8729-8735.

9. Kislov, V. V.; Mebel, A. M.; Aguilera-Iparraguirre, J.; Green, W. H., Reaction of Phenyl Radical with Propylene as a Possible Source of Indene and Other Polycyclic Aromatic Hydrocarbons: An Ab Initio/RRKM-ME Study. *J. Phys. Chem. A* **2012,** *116*, 4176-4191.

10. Gu, X.; Zhang, F.; Guo, Y.; Kaiser, R. I., Crossed-Molecular-Beam Study on the Formation of Phenylacetylene from Phenyl Radicals and Acetylene. *Angewandte Chemie International Edition* **2007,** *46*, 6866-6869.

11. Zhang, F.; Gu, X.; Guo, Y.; Kaiser, R. I., Reaction Dynamics of Phenyl Radicals (C6H5) with Propylene (CH3CHCH2) and Its Deuterated Isotopologues. *J. Phys. Chem. A* **2008,** *112*, 3284-3290.

12. Albert, D. R.; Davis, H. F., Collision Complex Lifetimes in the Reaction C6H5 + O2 → C6H5O + O. *J. Phys. Chem. Lett.* **2010,** *1*, 1107-1111.

13. Kaiser, R. I.; Parker, D. S. N.; Goswami, M.; Zhang, F.; Kislov, V. V.; Mebel, A. M.; Aguilera-Iparraguirre, J.; Green, W. H., Crossed beam reaction of phenyl and D5-phenyl radicals with propene and deuterated counterparts-competing atomic hydrogen and methyl loss pathways. *Phys. Chem. Chem. Phys.* **2012,** *14*, 720-729.

14. Parker, D. S. N.; Zhang, F.; Kaiser, R. I., Phenoxy Radical (C6H5O) Formation under Single Collision Conditions from Reaction of the Phenyl Radical (C6H5, X2A1) with Molecular Oxygen (O2, X3 Σ g-): The Final Chapter? *J. Phys. Chem. A* **2011,** *115*, 11515-11518.

15. Parker, D. S. N.; Zhang, F.; Kim, Y. S.; Kaiser, R. I.; Landera, A.; Mebel, A. M., On the formation of phenyldiacetylene (C6H5CCCCH) and D5-phenyldiacetylene

(C6D5CCCCH) studied under single collision conditions. *Phys. Chem. Chem. Phys.* **2012**, *14*, 2997-3003.

16. Parker, D. S. N.; Zhang, F.; Kim, Y. S.; Kaiser, R. I.; Landera, A.; Kislov, V. V.; Mebel, A. M.; Tielens, A. G. G. M., Low temperature formation of naphthalene and its role in the synthesis of PAHs (Polycyclic Aromatic Hydrocarbons) in the interstellar medium. *Proceedings of the National Academy of Sciences* **2012**, *109*, 53-58.

17. Kaiser, R. I.; Parker, D. S. N.; Zhang, F.; Landera, A.; Kislov, V. V.; Mebel, A. M., PAH Formation under Single Collision Conditions: Reaction of Phenyl Radical and 1,3-Butadiene to Form 1,4-Dihydronaphthalene. *J. Phys. Chem. A* **2012**, *116*, 4248-4258.

18. Albert, D. R.; Todt, M. A.; Davis, H. F., Crossed Molecular Beams Studies of Phenyl Radical Reactions with Propene and trans-2-Butene. *J. Phys. Chem. A* **2013**, *117*, 13967-13975.

19. Vanuzzo, G.; Balucani, N.; Leonori, F.; Stranges, D.; Nevrly, V.; Falcinelli, S.; Bergeat, A.; Casavecchia, P.; Cavallotti, C., Reaction Dynamics of O(3P) + Propyne: I. Primary Products, Branching Ratios, and Role of Intersystem Crossing from Crossed Molecular Beam Experiments. *J. Phys. Chem. A* **2016**, *120*, 4603-4618.

20. Thomas, A. M.; Lucas, M.; Yang, T.; Kaiser, R. I.; Fuentes, L.; Belisario-Lara, D.; Mebel, A. M., A Free-Radical Pathway to Hydrogenated Phenanthrene in Molecular Clouds—Low Temperature Growth of Polycyclic Aromatic Hydrocarbons. *ChemPhysChem* **2017**, *18*, 1971-1976.

21. Ratliff, B. J.; Alligood, B. W.; Butler, L. J.; Lee, S.-H.; Lin, J. J.-M., Product Branching from the CH2CH2OH Radical Intermediate of the OH + Ethene Reaction. *J. Phys. Chem. A* **2011**, *115*, 9097-9110.

22. Fahr, A.; Nayak, A., Kinetics and products of propargyl (C3H3) radical self-reactions and propargyl-methyl cross-combination reactions. *Int. J. Chem. Kinet.* **2000**, *32*, 118-124.

23. Shafir, E. V.; Slagle, I. R.; Knyazev, V. D., Kinetics and Products of the Self-Reaction of Propargyl Radicals. *J. Phys. Chem. A* **2003**, *107*, 8893-8903.

24. Knyazev, V. D.; Popov, K. V., Kinetics of the Self Reaction of Cyclopentadienyl Radicals. *J. Phys. Chem. A* **2015**, *119*, 7418-7429.

25. Morin, J.; Bedjanian, Y., Reaction of O(3P) with C2H4: Yield of the Reaction Products as a Function of Temperature. *J. Phys. Chem. A* **2016**, *120*, 9063-9070.

26. Stein, S. E.; Walker, J. A.; Suryan, M. M.; Fahr, A., A new path to benzene in flames. *Symp. (Int.) Combust.* **1991**, *23*, 85-90.

27. Shukla, B.; Koshi, M., A highly efficient growth mechanism of polycyclic aromatic hydrocarbons. *Phys. Chem. Chem. Phys.* **2010**, *12*, 2427-2437.

28. Shukla, B.; Tsuchiya, K.; Koshi, M., Novel Products from C6H5 + C6H6/C6H5 Reactions. *J. Phys. Chem. A* **2011**, *115*, 5284-5293.

29. Yuan, W.; Li, Y.; Dagaut, P.; Wang, Y.; Wang, Z.; Qi, F., A comprehensive experimental and kinetic modeling study of n-propylbenzene combustion. *Combust. Flame* **2017**, *186*, 178-192.

30. Weber, K. H.; Lemieux, J. M.; Zhang, J., Flash Pyrolysis of Ethyl, n-Propyl, and Isopropyl Iodides as Monitored by Supersonic Expansion Vacuum Ultraviolet Photoionization Time-of-Flight Mass Spectrometry. *J. Phys. Chem. A* **2009**, *113*, 583-591.

31. Zhang, F.; Kaiser, R. I.; Golan, A.; Ahmed, M.; Hansen, N., A VUV Photoionization Study of the Combustion-Relevant Reaction of the Phenyl Radical (C6H5) with

Propylene (C3H6) in a High Temperature Chemical Reactor. *J. Phys. Chem. A* **2012**, *116*, 3541-3546.

32. Golan, A.; Ahmed, M.; Mebel, A. M.; Kaiser, R. I., A VUV photoionization study of the multichannel reaction of phenyl radicals with 1,3-butadiene under combustion relevant conditions. *Phys. Chem. Chem. Phys.* **2013**, *15*, 341-347.

33. Parker, D. S. N.; Kaiser, R. I.; Troy, T. P.; Ahmed, M., Hydrogen Abstraction/Acetylene Addition Revealed. *Angewandte Chemie International Edition* **2014**, *53*, 7740-7744.

34. Parker, D. S. N.; Kaiser, R. I.; Troy, T. P.; Kostko, O.; Ahmed, M.; Mebel, A. M., Toward the Oxidation of the Phenyl Radical and Prevention of PAH Formation in Combustion Systems. *J. Phys. Chem. A* **2015**, *119*, 7145-7154.

35. Parker, D. S. N.; Kaiser, R. I.; Bandyopadhyay, B.; Kostko, O.; Troy, T. P.; Ahmed, M., Unexpected Chemistry from the Reaction of Naphthyl and Acetylene at Combustion-Like Temperatures. *Angewandte Chemie International Edition* **2015**, *54*, 5421-5424.

36. Urness, K. N.; Guan, Q.; Troy, T. P.; Ahmed, M.; Daily, J. W.; Ellison, G. B.; Simmie, J. M., Pyrolysis Pathways of the Furanic Ether 2-Methoxyfuran. *J. Phys. Chem. A* **2015**, *119*, 9962-9977.

37. Parker, D. S. N.; Kaiser, R. I.; Kostko, O.; Ahmed, M., Selective Formation of Indene through the Reaction of Benzyl Radicals with Acetylene. *ChemPhysChem* **2015**, *16*, 2091-2093.

38. Buckingham, G. T.; Ormond, T. K.; Porterfield, J. P.; Hemberger, P.; Kostko, O.; Ahmed, M.; Robichaud, D. J.; Nimlos, M. R.; Daily, J. W.; Ellison, G. B., The thermal decomposition of the benzyl radical in a heated micro-reactor. I. Experimental findings. *J. Chem. Phys.* **2015**, *142*, 044307.

39. Constantinidis, P.; Schmitt, H. C.; Fischer, I.; Yan, B.; Rijs, A. M., Formation of polycyclic aromatic hydrocarbons from bimolecular reactions of phenyl radicals at high temperatures. *Phys. Chem. Chem. Phys.* **2015**, *17*, 29064-29071.

40. Constantinidis, P.; Hirsch, F.; Fischer, I.; Dey, A.; Rijs, A. M., Products of the Propargyl Self-Reaction at High Temperatures Investigated by IR/UV Ion Dip Spectroscopy. *J. Phys. Chem. A* **2017**, *121*, 181-191.

41. Yang, T.; Troy, T. P.; Xu, B.; Kostko, O.; Ahmed, M.; Mebel, A. M.; Kaiser, R. I., Hydrogen-Abstraction/Acetylene-Addition Exposed. *Angewandte Chemie International Edition* **2016**, *55*, 14983-14987.

42. Vasiliou, A. K.; Hu, H.; Cowell, T. W.; Whitman, J. C.; Porterfield, J.; Parish, C. A., Modeling Oil Shale Pyrolysis: High-Temperature Unimolecular Decomposition Pathways for Thiophene. *J. Phys. Chem. A* **2017**, *121*, 7655-7666.

43. Park, J.; Lin, M. C., Kinetics for the Recombination of Phenyl Radicals. *J. Phys. Chem. A* **1997**, *101*, 14-18.

44. Savee, J. D.; Welz, O.; Taatjes, C. A.; Osborn, D. L., New mechanistic insights to the O(3P) + propene reaction from multiplexed photoionization mass spectrometry. *Phys. Chem. Chem. Phys.* **2012**, *14*, 10410-10423.

45. Lockyear, J. F.; Welz, O.; Savee, J. D.; Goulay, F.; Trevitt, A. J.; Taatjes, C. A.; Osborn, D. L.; Leone, S. R., Isomer Specific Product Detection in the Reaction of CH with Acrolein. *J. Phys. Chem. A* **2013**, *117*, 11013-11026.

46. Welz, O.; Burke, M. P.; Antonov, I. O.; Goldsmith, C. F.; Savee, J. D.; Osborn, D. L.; Taatjes, C. A.; Klippenstein, S. J.; Sheps, L., New Insights into Low-Temperature

Oxidation of Propane from Synchrotron Photoionization Mass Spectrometry and Multiscale Informatics Modeling. *J. Phys. Chem. A* **2015**, *119*, 7116-7129.

47. Muller, G.; Scheer, A.; Osborn, D. L.; Taatjes, C. A.; Meloni, G., Low Temperature Chlorine-Initiated Oxidation of Small-Chain Methyl Esters: Quantification of Chain-Terminating HO2-Elimination Channels. *J. Phys. Chem. A* **2016**, *120*, 1677-1690.

48. Antonov, I. O.; Zádor, J.; Rotavera, B.; Papajak, E.; Osborn, D. L.; Taatjes, C. A.; Sheps, L., Pressure-Dependent Competition among Reaction Pathways from First- and Second-O2 Additions in the Low-Temperature Oxidation of Tetrahydrofuran. *J. Phys. Chem. A* **2016**, *120*, 6582-6595.

49. Bourgalais, J.; Spencer, M.; Osborn, D. L.; Goulay, F.; Le Picard, S. D., Reactions of Atomic Carbon with Butene Isomers: Implications for Molecular Growth in Carbon-Rich Environments. *J. Phys. Chem. A* **2016**, *120*, 9138-9150.

50. Eskola, A. J.; Antonov, I. O.; Sheps, L.; Savee, J. D.; Osborn, D. L.; Taatjes, C. A., Time-resolved measurements of product formation in the low-temperature (550-675 K) oxidation of neopentane: a probe to investigate chain-branching mechanism. *Phys. Chem. Chem. Phys.* **2017**, *19*, 13731-13745.

51. Dürrstein, S. H.; Aghsaee, M.; Jerig, L.; Fikri, M.; Schulz, C., A shock tube with a high-repetition-rate time-of-flight mass spectrometer for investigations of complex reaction systems. *Rev. Sci. Instrum.* **2011**, *82*, 084103.

52. Alquaity, A. B. S.; Giri, B. R.; Lo, J. M. H.; Farooq, A., High-Temperature Experimental and Theoretical Study of the Unimolecular Dissociation of 1,3,5-Trioxane. *J. Phys. Chem. A* **2015**, *119*, 6594-6601.

53. Petway, S. V.; Ismail, H.; Green, W. H.; Estupiñán, E. G.; Jusinski, L. E.; Taatjes, C. A., Measurements and Automated Mechanism Generation Modeling of OH Production in Photolytically Initiated Oxidation of the Neopentyl Radical. *J. Phys. Chem. A* **2007**, *111*, 3891-3900.

54. Knepp, A. M.; Meloni, G.; Jusinski, L. E.; Taatjes, C. A.; Cavallotti, C.; Klippenstein, S. J., Theory, measurements, and modeling of OH and HO2 formation in the reaction of cyclohexyl radicals with O2. *Phys. Chem. Chem. Phys.* **2007**, *9*, 4315-4331.

55. Stone, D.; Blitz, M.; Daubney, L.; Howes, N. U. M.; Seakins, P., Kinetics of CH2OO reactions with SO2, NO2, NO, H2O and CH3CHO as a function of pressure. *Phys. Chem. Chem. Phys.* **2013**,

56. Yan, C.; Kocevska, S.; Krasnoperov, L. N., Kinetics of the Reaction of CH3O2 Radicals with OH Studied over the 292–526 K Temperature Range. *J. Phys. Chem. A* **2016**, *120*, 6111-6121.

57. Frank, P.; Herzler, J.; Just, T.; Wahl, C., High-temperature reactions of phenyl oxidation. *Symp. (Int.) Combust.* **1994**, *25*, 833-840.

58. Nasir, E. F.; Farooq, A., A Shock-Tube Study of the CO + OH Reaction Near the Low-Pressure Limit. *J. Phys. Chem. A* **2016**, *120*, 3924-3928.

59. Zabeti, S.; Fikri, M.; Schulz, C., Reaction-time-resolved measurements of laser-induced fluorescence in a shock tube with a single laser pulse. *Rev. Sci. Instrum.* **2017**, *88*, 115105.

60. Gu, X.; Kaiser, R. I., Reaction Dynamics of Phenyl Radicals in Extreme Environments: A Crossed Molecular Beam Study. *Acc. Chem. Res.* **2009**, *42*, 290-302.

61. Mebel, A. M.; Landera, A.; Kaiser, R. I., Formation Mechanisms of Naphthalene and Indene: From the Interstellar Medium to Combustion Flames. *J. Phys. Chem. A* **2017**, *121*, 901-926.

62. Guan, Q.; Urness, K. N.; Ormond, T. K.; David, D. E.; Barney Ellison, G.; Daily, J. W., The properties of a micro-reactor for the study of the unimolecular decomposition of large molecules. *Int. Rev. Phys. Chem.* **2014**, *33*, 447-487.

63. Slagle, I. R.; Gutman, D., Kinetics of polyatomic free radicals produced by laser photolysis. 5. Study of the equilibrium methyl + oxygen .dblarw. CH3O2 between 421 and 538 K. *J. Am. Chem. Soc.* **1985**, *107*, 5342-5347.

64. Osborn, D. L.; Zou, P.; Johnsen, H.; Hayden, C. C.; Taatjes, C. A.; Knyazev, V. D.; North, S. W.; Peterka, D. S.; Ahmed, M.; Leone, S. R., The multiplexed chemical kinetic photoionization mass spectrometer: A new approach to isomer-resolved chemical kinetics. *Rev. Sci. Instrum.* **2008**, *79*, -.

65. Baeza-Romero, M. T.; Blitz, M. A.; Goddard, A.; Seakins, P. W., Time-of-flight mass spectrometry for time-resolved measurements: Some developments and applications. *Int. J. Chem. Kinet.* **2012**, *44*, 532-545.

66. Wang, Z.; Zhang, L.; Zhang, F., Kinetics of Homoallylic/Homobenzylic Rearrangement Reactions under Combustion Conditions. *J. Phys. Chem. A* **2014**, *118*, 6741-6748.

67. Ismail, H. Addition and Recombination Reactions of Unsaturated Radicals Using a Novel Laser Kinetics Spectrometer. Massachusetts Institute of Technology, Cambridge, 2008.

68. Middaugh, J. E. The Study of Bimolecular Radical Reactions using a Novel Time-Resolved Photoionization Time-of-Flight Mass Spectrometry and Laser Absorption Spectrometry Apparatus. PhD, Massachusetts Institute of Technology, Cambridge, 2014.

69. Herriott, D.; Kogelnik, H.; Kompfner, R., Off-Axis Paths in Spherical Mirror Interferometers. *Appl. Opt.* **1964**, *3*, 523-526.

70. Trutna, W. R.; Byer, R. L., Multiple-pass Raman gain cell. *Appl. Opt.* **1980**, *19*, 301-312.

71. Pilgrim, J. S.; Jennings, R. T.; Taatjes, C. A., Temperature controlled multiple pass absorption cell for gas phase chemical kinetics studies. *Rev. Sci. Instrum.* **1997**, *68*, 1875-1878.

72. Wyatt, J. R.; Decorpo, J. J.; McDowell, M. V.; Saalfeld, F. E., Sampling of flow systems at atmospheric pressure. *International Journal of Mass Spectrometry and Ion Physics* **1975**, *16*, 33-38.

73. Kumaran, S. S.; Su, M. C.; Michael, J. V., Thermal decomposition of iodobenzene using I-atom absorption. *Chem. Phys. Lett.* **1997**, *269*, 99-106.

74. Buras, Z. J.; Elsamra, R. M. I.; Jalan, A.; Middaugh, J. E.; Green, W. H., Direct Kinetic Measurements of Reactions between the Simplest Criegee Intermediate CH2OO and Alkenes. *J. Phys. Chem. A* **2014**, *118*, 1997-2006.

75. Buras, Z. J.; Elsamra, R. M. I.; Green, W. H., Direct Determination of the Simplest Criegee Intermediate (CH2OO) Self Reaction Rate. *J. Phys. Chem. Lett.* **2014**, *5*, 2224-2228.

76. Elsamra, R. M. I.; Jalan, A.; Buras, Z. J.; Middaugh, J. E.; Green, W. H., Temperature- and Pressure-Dependent Kinetics of CH2OO + CH3COCH3 and CH2OO + CH3CHO: Direct Measurements and Theoretical Analysis. *Int. J. Chem. Kinet.* **2016**, *48*, 474-488.

77. Buras, Z. J.; Dames, E. E.; Merchant, S. S.; Liu, G.; Elsamra, R. M. I.; Green, W. H., Kinetics and Products of Vinyl + 1,3-Butadiene, a Potential Route to Benzene. *J. Phys. Chem. A* **2015**, *119*, 7325-7338.

78. Ha, T.-K.; He, Y.; Pochert, J.; Quack, M.; Ranz, R.; Seyfang, G.; Thanopoulos, I., Absolute Integrated Band Strength and Magnetic Dipole Transition Moments in the 2P3/2 → 2P1/2 Fine Structure (with Hyperfine Structure) Transition of the Iodine Atom: Experiment and Theory. *Ber. Bunsen-Ges. Phys. Chem.* **1995**, *99*, 384-392.

79. Slagle, I. R.; Yamada, F.; Gutman, D., Kinetics of free radicals produced by infrared multiphoton-induced decompositions. 1. Reactions of allyl radicals with nitrogen dioxide and bromine. *J. Am. Chem. Soc.* **1981**, *103*, 149-153.

80. Fockenberg, C.; Bernstein, H. J.; Hall, G. E.; Muckerman, J. T.; Preses, J. M.; Sears, T. J.; Weston, R. E., Repetitively sampled time-of-flight mass spectrometry for gas-phase kinetics studies. *Rev. Sci. Instrum.* **1999**, *70*, 3259-3264.

81. Eskola, A. J.; Timonen, R. S., Kinetics of the reactions of vinyl radicals with molecular oxygen and chlorine at temperatures 200-362 K. *Phys. Chem. Chem. Phys.* **2003**, *5*, 2557-2561.

82. Blitz, M. A.; Goddard, A.; Ingham, T.; Pilling, M. J., Time-of-flight mass spectrometry for time-resolved measurements. *Rev. Sci. Instrum.* **2007**, *78*, -.

83. Van Bramer, S.; Johnston, M., Tunable, coherent vacuum ultraviolet radiation for photoionization mass spectrometry. *Appl. Spectrosc.* **1992**, *46*, 255-261.

84. Cool, T. A.; Wang, J.; Nakajima, K.; Taatjes, C. A.; McLlroy, A., Photoionization Cross Sections for Reaction Intermediates in Hydrocarbon Combustion. *Int. J. Mass Spectrom.* **2005**, *247*, 18-27.

85. Lockyer, N. P.; Vickerman, J. C., Single photon ionisation mass spectrometry using laser-generated vacuum ultraviolet photons. *Laser Chem.* **1997**, *17*, 139-160.

86. Shi, Y. J.; Consta, S.; Das, A. K.; Mallik, B.; Lacey, D.; Lipson, R. H., A 118 nm vacuum ultraviolet laser/time-of-flight mass spectroscopic study of methanol and ethanol clusters in the vapor phase. *J. Chem. Phys.* **2002**, *116*, 6990-6999.

87. Hollenstein, U.; Palm, H.; Merkt, F., A broadly tunable extreme ultraviolet laser source with a 0.008 cm−1 bandwidth. *Rev. Sci. Instrum.* **2000**, *71*, 4023-4028.

88. Shukla, B.; Susa, A.; Miyoshi, A.; Koshi, M., In Situ Direct Sampling Mass Spectrometric Study on Formation of Polycyclic Aromatic Hydrocarbons in Toluene Pyrolysis. *J. Phys. Chem. A* **2007**, *111*, 8308-8324.

89. Tonokura, K.; Kanno, N.; Yamamoto, Y.; Yamada, H., Development of a compact laser-based single photon ionization time-of-flight mass spectrometer. *Int. J. Mass Spectrom.* **2010**, *290*, 9-13.

90. Williams, M. W.; Arakawa, E. T., Optical properties of crystalline MgF2 from 115 nm to 400 nm. *Appl. Opt.* **1979**, *18*, 1477-1478.

91. Weissler, G. L.; Samson, J. A. R.; Ogawa, M.; Cook, G. R., Photoionization Analysis by Mass Spectroscopy. *J. Opt. Soc. Am.* **1959**, *49*, 338-349.

92. Shuman, N. S.; Ochieng, M. A.; Sztáray, B.; Baer, T., TPEPICO Spectroscopy of Vinyl Chloride and Vinyl Iodide: Neutral and Ionic Heats of Formation and Bond Energies. *J. Phys. Chem. A* **2008**, *112*, 5647-5652.

93. Ismail, H.; Goldsmith, C. F.; Abel, P. R.; Howe, P.-T.; Fahr, A.; Halpern, J. B.; Jusinski, L. E.; Georgievskii, Y.; Taatjes, C. A.; Green, W. H., Pressure and Temperature Dependence of the Reaction of Vinyl Radical with Ethylene. *J. Phys. Chem. A* **2007**, *111*, 6843-6851.

94. Goldsmith, C. F.; Ismail, H.; Abel, P. R.; Green, W. H., Pressure and Temperature Dependence of the Reaction of Vinyl Radical with Alkenes II: Measured Rates and

Predicted Product Distributions for Vinyl + Propene. *Proc. Combust. Inst.* **2009**, *32*, 139-148.

95.   Goldsmith, C. F.; Ismail, H.; Green, W. H., Pressure and Temperature Dependence of the Reaction of Vinyl Radical with Alkenes III: Measured Rates and Predicted Product Distributions for Vinyl + Butene. *J. Phys. Chem. A* **2009**, *113*, 13357-13371.

96.   Ismail, H.; Abel, P. R.; Green, W. H.; Fahr, A.; Jusinski, L. E.; Knepp, A. M.; Zádor, J.; Meloni, G.; Selby, T. M.; Osborn, D. L.; Taatjes, C. A., Temperature-Dependent Kinetics of the Vinyl Radical (C2H3) Self-Reaction. *J. Phys. Chem. A* **2009**, *113*, 1278-1286.

97.   Delone, N. B.; Krainov, V. P., *Multiphoton Processes in Atoms*. 2nd ed.; Springer: 2000.

98.   Hecht, E., *Optics*. Addison-Wesley: 2002.

99.   Hidaka, T., Extremely low-loss hollow core waveguide for VUV light. *Opt. Commun.* **1982**, *44*, 90-93.

100.   Davis, D.; Braun, W., Intense Vacuum Ultraviolet Atomic Line Sources. *Appl. Opt.* **1968**, *7*, 2071-2074.

101.   Xu, H.; Pratt, S. T., Photodissociation of Methyl Iodide via Selected Vibrational Levels of the B̃ (2E3/2)6s Rydberg State. *J. Phys. Chem. A* **2015**, *119*, 7548-7558.

102.   Greer, F.; Fraser, D.; Coburn, J. W.; Graves, D. B., Fundamental beam studies of deuterium and fluorine radical reaction kinetics on surfaces. *Journal of Vacuum Science & Technology B* **2003**, *21*, 1391-1402.

103.   Krasnoperov, L. N.; Niiranen, J. T.; Gutman, D.; Melius, C. F.; Allendorf, M. D., Kinetics and thermochemistry of Si(CH3)3 + NO reaction: direct determination of a Si-N bond energy. *J. Phys. Chem.* **1995**, *99*, 14347-14358.

104.   Fuller, E. N.; Schettler, P. D.; Giddings, J. C., New method for prediction of binary gas-phase diffusion coefficients. *Industrial & Engineering Chemistry* **1966**, *58*, 18-27.

105.   Tonokura, K.; Norikane, Y.; Koshi, M.; Nakano, Y.; Nakamichi, S.; Goto, M.; Hashimoto, S.; Kawasaki, M.; Sulbaek Andersen, M. P.; Hurley, M. D.; Wallington, T. J., Cavity Ring-down Study of the Visible Absorption Spectrum of the Phenyl Radical and Kinetics of Its Reactions with Cl, Br, Cl2, and O2. *J. Phys. Chem. A* **2002**, *106*, 5908-5917.

106.   Goldsmith, C. F. Predicting Combustion Properties of Hydrocarbon Fuel Mixtures. Massachussetts Institute of Technology, Cambridge, 2010.

107.   Sveum, N. E.; Goncher, S. J.; Neumark, D. M., Determination of absolute photoionization cross sections of the phenyl radical. *Phys. Chem. Chem. Phys.* **2006**, *8*, 592-598.

108.   Morse, M. D., 2 - Supersonic Beam Sources. In *Experimental Methods in the Physical Sciences*, Dunning, F. B.; Hulet, R. G., Eds. Academic Press: 1996; Vol. 29, pp 21-47.

109.   Tranter, R. S.; Klippenstein, S. J.; Harding, L. B.; Giri, B. R.; Yang, X.; Kiefer, J. H., Experimental and Theoretical Investigation of the Self-Reaction of Phenyl Radicals. *J. Phys. Chem. A* **2010**, *114*, 8240-8261.

110.   Moore, S. B.; Carr, R. W., Molecular velocity distribution effects in kinetic studies by time-resolved mass spectrometry. *International Journal of Mass Spectrometry and Ion Physics* **1977**, *24*, 161-171.

111.   Taatjes, C. A., How does the molecular velocity distribution affect kinetics measurements by time-resolved mass spectrometry? *Int. J. Chem. Kinet.* **2007**, *39*, 565-570.

112. McManus, J. B.; Zahniser, M. S.; Nelson, D. D., Dual quantum cascade laser trace gas instrument with astigmatic Herriott cell at high pass number. *Appl. Opt.* **2011,** *50,* A74-A85.

113. Vereecken, L.; Francisco, J. S., Theoretical studies of atmospheric reaction mechanisms in the troposphere. *Chem. Soc. Rev.* **2012,** *41,* 6259-6293.

114. Harrison, R. M.; Yin, J.; Tilling, R. M.; Cai, X.; Seakins, P. W.; Hopkins, J. R.; Lansley, D. L.; Lewis, A. C.; Hunter, M. C.; Heard, D. E.; Carpenter, L. J.; Creasey, D. J.; Lee, J. D.; Pilling, M. J.; Carslaw, N.; Emmerson, K. M.; Redington, A.; Derwent, R. G.; Ryall, D.; Mills, G.; Penkett, S. A., Measurement and modelling of air pollution and atmospheric chemistry in the U.K. West Midlands conurbation: Overview of the PUMA Consortium project. *Sci. Total Environ.* **2006,** *360,* 5-25.

115. Leather, K. E.; McGillen, M. R.; Cooke, M. C.; Utembe, S. R.; Archibald, A. T.; Jenkin, M. E.; Derwent, R. G.; Shallcross, D. E.; Percival, C. J., Acid-yield measurements of the gas-phase ozonolysis of ethene as a function of humidity using Chemical Ionisation Mass Spectrometry (CIMS). *Atmos. Chem. Phys.* **2012,** *12,* 469-479.

116. Cox, R. A.; Penkett, S. A., Aerosol formation from sulphur dioxide in the presence of ozone and olefinic hydrocarbons. *J. Chem. Soc., Faraday Trans.* **1972,** *68,* 1735-1753.

117. Criegee, R.; Wenner, G., Die Ozonisierung des 9,10-Oktalins. *Justus Liebigs Annalen der Chemie* **1949,** *564,* 9-15.

118. Welz, O.; Savee, J. D.; Osborn, D. L.; Vasu, S. S.; Percival, C. J.; Shallcross, D. E.; Taatjes, C. A., Direct Kinetic Measurements of Criegee Intermediate (CH2OO) Formed by Reaction of CH2I with O-2. *Science* **2012,** *335,* 204-207.

119. Taatjes, C. A.; Shallcross, D. E.; Percival, C. J., Research frontiers in the chemistry of Criegee intermediates and tropospheric ozonolysis. *Phys. Chem. Chem. Phys.* **2014,**

120. Taatjes, C. A.; Welz, O.; Eskola, A. J.; Savee, J. D.; Osborn, D. L.; Lee, E. P. F.; Dyke, J. M.; Mok, D. W. K.; Shallcross, D. E.; Percival, C. J., Direct measurement of Criegee intermediate (CH2OO) reactions with acetone, acetaldehyde, and hexafluoroacetone. *Phys. Chem. Chem. Phys.* **2012,** *14,* 10391-10400.

121. Liu, Y.; Bayes, K. D.; Sander, S. P., Measuring Rate Constants for Reactions of the Simplest Criegee Intermediate (CH2OO) by Monitoring the OH Radical. *J. Phys. Chem. A* **2014,**

122. Sheps, L., Absolute Ultraviolet Absorption Spectrum of a Criegee Intermediate CH2OO. *J. Phys. Chem. Lett.* **2013,** 4201-4205.

123. Beames, J. M.; Liu, F.; Lu, L.; Lester, M. I., Ultraviolet Spectrum and Photochemistry of the Simplest Criegee Intermediate CH2OO. *J. Am. Chem. Soc.* **2012,** *134,* 20045-20048.

124. Lee, E. P. F.; Mok, D. K. W.; Shallcross, D. E.; Percival, C. J.; Osborn, D. L.; Taatjes, C. A.; Dyke, J. M., Spectroscopy of the Simplest Criegee Intermediate CH2OO: Simulation of the First Bands in Its Electronic and Photoelectron Spectra. *Chem.--Eur. J.* **2012,** *18,* 12411-12423.

125. Crehuet, R.; Anglada, J. M.; Cremer, D.; Bofill, J. M., Reaction Modes of Carbonyl Oxide, Dioxirane, and Methylenebis(oxy) with Ethylene: A New Reaction Mechanism. *J. Phys. Chem. A* **2002,** *106,* 3917-3929.

126. Vereecken, L.; Harder, H.; Novelli, A., The reactions of Criegee intermediates with alkenes, ozone, and carbonyl oxides. *Phys. Chem. Chem. Phys.* **2014,** *16,* 4039-4049.

127. Baughcum, S. L.; Leone, S. R., Photofragmentation infrared emission studies of vibrationally excited free radicals CH3 and CH2I. *J. Chem. Phys.* **1980,** *72,* 6531-6545.

128. Jalan, A.; Allen, J. W.; Green, W. H., Chemically activated formation of organic acids in reactions of the Criegee intermediate with aldehydes and ketones. *Phys. Chem. Chem. Phys.* **2013,** *15,* 16841-16852.

129. Lynch, B. J.; Zhao, Y.; Truhlar, D. G., Effectiveness of Diffuse Basis Functions for Calculating Relative Energies by Density Functional Theory. *J. Phys. Chem. A* **2003,** *107,* 1384-1388.

130. Clark, T.; Chandrasekhar, J.; Spitznagel, G. W.; Schleyer, P. V., Efficient diffuse function-augmented basis sets for anion calculations. III. The 3-21+G basis set for the first-row elements, Li-F. *J. Comput. Chem.* **1983,** *4,* 294-301.

131. Frisch, M. J.; Pople, J. A.; Binkley, J. S., Self-consistent molecular-orbital methods. 25. Supplementary functions for gaussian-basis sets. *J. Chem. Phys.* **1984,** *80,* 3265-3269.

132. Frisch, M. J.; Trucks, G. W.; Schlegel, H. B.; Scuseria, G. E.; Robb, M. A.; Cheeseman, J. R.; Montgomery, J. A.; Vreven, T.; Kudin, K. N.; Burant, J. C.; Millam, J. M.; Iyengar, S. S.; Tomasi, J.; Barone, V.; Mennucci, B.; Cossi, M.; Scalmani, G.; Rega, N.; Petersson, G. A.; Nakatsuji, H.; Hada, M.; Ehara, M.; Toyota, K.; Fukuda, R.; Hasegawa, J.; Ishida, M.; Nakajima, T.; Honda, Y.; Kitao, O.; Nakai, H.; Klene, M.; Li, X.; Knox, J. E.; Hratchian, H. P.; Cross, J. B.; Bakken, V.; Adamo, C.; Jaramillo, J.; Gomperts, R.; Stratmann, R. E.; Yazyev, O.; Austin, A. J.; Cammi, R.; Pomelli, C.; Ochterski, J. W.; Ayala, P. Y.; Morokuma, K.; Voth, G. A.; Salvador, P.; Dannenberg, J. J.; Zakrzewski, V. G.; Dapprich, S.; Daniels, A. D.; Strain, M. C.; Farkas, O.; Malick, D. K.; Rabuck, A. D.; Raghavachari, K.; Foresman, J. B.; Ortiz, J. V.; Cui, Q.; Baboul, A. G.; Clifford, S.; Cioslowski, J.; Stefanov, B. B.; Liu, G.; Liashenko, A.; Piskorz, P.; Komaromi, I.; Martin, R. L.; Fox, D. J.; Keith, T.; Laham, A.; Peng, C. Y.; Nanayakkara, A.; Challacombe, M.; Gill, P. M. W.; Johnson, B.; Chen, W.; Wong, M. W.; Gonzalez, C.; Pople, J. A. *Gaussian 03, Revision C.02,* 2003.

133. Adler, T. B.; Knizia, G.; Werner, H. J., A simple and efficient CCSD(T)-F12 approximation. *J. Chem. Phys.* **2007,** *127,*

134. Adler, T. B.; Werner, H. J., Local explicitly correlated coupled-cluster methods: Efficient removal of the basis set incompleteness and domain errors. *J. Chem. Phys.* **2009,** *130,*

135. Adler, T. B.; Werner, H. J.; Manby, F. R., Local explicitly correlated second-order perturbation theory for the accurate treatment of large molecules. *J. Chem. Phys.* **2009,** *130,*

136. Aguilera-Iparraguirre, J.; Boese, A. D.; Klopper, W.; Ruscic, B., Accurate ab initio computation of thermochemical data for C3Hx (x=0,...,4) species. *Chem. Phys.* **2008,** *346,* 56-68.

137. Aguilera-Iparraguirre, J.; Curran, H. J.; Klopper, W.; Simmie, J. M., Accurate benchmark calculation of the reaction barrier height for hydrogen abstraction by the hydroperoxyl radical from methane. Implications for C(n)H(2n+2) where n = 2 -> 4. *J. Phys. Chem. A* **2008,** *112,* 7047-7054.

138. Knizia, G.; Adler, T. B.; Werner, H. J., Simplified CCSD(T)-F12 methods: Theory and benchmarks. *J. Chem. Phys.* **2009,** *130,*

139. Noga, J.; Kutzelnigg, W., Coupled-cluster theory that takes care of the correlation cusp by inclusion of linear terms in the interelectronic coordinates. *J. Chem. Phys.* **1994,** *101,* 7738-7762.

140. Peterson, K. A.; Adler, T. B.; Werner, H. J., Systematically convergent basis sets for explicitly correlated wavefunctions: The atoms H, He, B-Ne, and Al-Ar. *J. Chem. Phys.* **2008**, *128*,

141. MOLPRO, v.; Werner, H.-J.; Knowles, P. J.; Knizia, G.; Manby, F. R.; Schütz, M.; Celani, P.; Korona, T.; Lindh, R.; Mitrushenkov, A.; Rauhut, G.; Shamasundar, K. R.; Adler, T. B.; Amos, R. D.; Bernhardsson, A.; Berning, A.; Cooper, D. L.; Deegan, M. J. O.; Dobbyn, A. J.; Eckert, F.; Goll, E.; Hampel, C.; Hesselmann, A.; Hetzer, G.; Hrenar, T.; Jansen, G.; Köppl, C.; Liu, Y.; Lloyd, A. W.; Mata, R. A.; May, A. J.; McNicholas, S. J.; Meyer, W.; Mura, M. E.; Nicklass, A.; O'Neill, D. P.; Palmieri, P.; Pflüger, K.; Pitzer, R.; Reiher, M.; Shiozaki, T.; Stoll, H.; Stone, A. J.; Tarroni, R.; Thorsteinsson, T.; Wang, M.; A. Wolf; see; http://www.molpro.net.

142. Sharma, S.; Harper, M. H.; Green, W. H. *CanTherm*, 2010.

143. Whiting, E. E., An empirical approximation to the Voigt profile. *J. Quant. Spectrosc. Radiat. Transfer* **1968**, *8*, 1379-1384.

144. Huang, H.; Rotavera, B.; Eskola, A. J.; Taatjes, C. A., Correction to "Pressure-Dependent I Atom Yield in the Reaction of CH2I with O2 Shows a Remarkable Apparent Third-Body Efficiency for O2". *J. Phys. Chem. Lett.* **2013**, *4*, 3824-3824.

145. Stone, D.; Blitz, M.; Daubney, L.; Ingham, T.; Seakins, P., CH2OO Criegee biradical yields following photolysis of CH2I2 in O2. *Phys. Chem. Chem. Phys.* **2013**, *15*, 19119-19124.

146. Eskola, A. J.; Wojcik-Pastuszka, D.; Ratajczak, E.; Timonen, R. S., Kinetics of the reactions of CH2Br and CH2I radicals with molecular oxygen at atmospheric temperatures. *Phys. Chem. Chem. Phys.* **2006**, *8*, 1416-1424.

147. Meller, R.; Moortgat, G. K., Temperature dependence of the absorption cross sections of formaldehyde between 223 and 323 K in the wavelength range 225–375 nm. *J. Geophys. Res., [Atmos.]* **2000**, *105*, 7089-7101.

148. Tucceri, M. E.; Holscher, D.; Rodriguez, A.; Dillon, T. J.; Crowley, J. N., Absorption cross section and photolysis of OIO. *Phys. Chem. Chem. Phys.* **2006**, *8*, 834-846.

149. Dillon, T. J.; Tucceri, M. E.; Hölscher, D.; Crowley, J. N., Absorption cross-section of IO at 427.2 nm and 298 K. *J. Photochem. Photobiol., A* **2005**, *176*, 3-14.

150. Gadzhiev, O. B.; Ignatov, S. K.; Krisyuk, B. E.; Maiorov, A. V.; Gangopadhyay, S.; Masunov, A. E., Quantum Chemical Study of the Initial Step of Ozone Addition to the Double Bond of Ethylene. *J. Phys. Chem. A* **2012**, *116*, 10420-10434.

151. Wheeler, S. E.; Ess, D. H.; Houk, K. N., Thinking Out of the Black Box: Accurate Barrier Heights of 1,3-Dipolar Cycloadditions of Ozone with Acetylene and Ethylene. *J. Phys. Chem. A* **2008**, *112*, 1798-1807.

152. Harding, L. B.; Klippenstein, S. J.; Jasper, A. W., Ab initio methods for reactive potential surfaces. *Phys. Chem. Chem. Phys.* **2007**, *9*, 4055-4070.

153. Truhlar, D. G.; Garrett, B. C., Variational transition-state theory. *Acc. Chem. Res.* **1980**, *13*, 440-448.

154. Villa, J.; Truhlar, D. G., Variational transition state theory without the minimum-energy path. *Theor Chem Acta* **1997**, *97*, 317-323.

155. Lonneman, W. A.; Seila, R. L.; Meeks, S. A., Non-methane organic composition in the Lincoln Tunnel. *Environ. Sci. Technol.* **1986**, *20*, 790-796.

156. Zweidinger, R. B.; Sigsby, J. E.; Tejada, S. B.; Stump, F. D.; Dropkin, D. L.; Ray, W. D.; Duncan, J. W., Detailed hydrocarbon and aldehyde mobile source emissions from roadway studies. *Environ. Sci. Technol.* **1988,** *22,* 956-962.

157. Sawada, S.; Totsuka, T., Natural and anthropogenic sources and fate of atmospheric ethylene. *Atmos. Environ.* **1986,** *20,* 821-832.

158. Singh, H. B.; Zimmerman, P. R., Atmospheric Distribution and Sources of Nonmethane Hydrocarbons. In *Gaseous Pollutants: Characterization and Cycling*, Nriagu, J. O., Ed. John Wiley: New York, 1992; pp 177-235.

159. Percival, C. J.; Welz, O.; Eskola, A. J.; Savee, J. D.; Osborn, D. L.; Topping, D. O.; Lowe, D.; Utembe, S. R.; Bacak, A.; M c Figgans, G.; Cooke, M. C.; Xiao, P.; Archibald, A. T.; Jenkin, M. E.; Derwent, R. G.; Riipinen, I.; Mok, D. W. K.; Lee, E. P. F.; Dyke, J. M.; Taatjes, C. A.; Shallcross, D. E., Regional and global impacts of Criegee intermediates on atmospheric sulphuric acid concentrations and first steps of aerosol formation. *Faraday Discuss.* **2013,** *165,* 45-73.

160. Lewis, A. C.; Carslaw, N.; Marriott, P. J.; Kinghorn, R. M.; Morrison, P.; Lee, A. L.; Bartle, K. D.; Pilling, M. J., A larger pool of ozone-forming carbon compounds in urban atmospheres. *Nature* **2000,** *405,* 778-781.

161. Beachell Harold, C.; Nemphos Spero, P., Oxidative Degradation of Polymers in Presence of Ozone. In *OZONE CHEMISTRY AND TECHNOLOGY*, AMERICAN CHEMICAL SOCIETY: 1959; Vol. 21, pp 168-175.

162. Giurginca, M.; Zaharescu, T.; Meghea, A., Degradation of ethylene-propylene elastomers in the presence of ozone. *Polym. Degrad. Stab.* **1995,** *50,* 45-48.

163. Taatjes, C. A.; Shallcross, D. E.; Percival, C. J., Research frontiers in the chemistry of Criegee intermediates and tropospheric ozonolysis. *Phys. Chem. Chem. Phys.* **2014,** *16,* 1704-1718.

164. Su, Y.-T.; Lin, H.-Y.; Putikam, R.; Matsui, H.; Lin, M. C.; Lee, Y.-P., Extremely rapid self-reaction of the simplest Criegee intermediate CH2OO and its implications in atmospheric chemistry. *Nat Chem* **2014,** *6,* 477-483.

165. Ting, W.-L.; Chen, Y.-H.; Chao, W.; Smith, M. C.; Lin, J. J., The UV Absorption Spectrum of the Simplest Criegee Intermediate CH2OO. *Phys. Chem. Chem. Phys.* **2014,** *16,* 10438-10443.

166. CRC Handbook of Chemistry and Physics. In *Physical Constants of Organic Compounds* [Online] 89 ed.; Lide, D. R., Ed. CRC Press/Taylor and Francis: Boca Raton, FL, 2009.

167. Baulch, D. L.; Duxbury, J.; Grant, S. J.; Montague, D. C., Evaluated kinetic data for high temperature reactions. Volume 4 Homogeneous gas phase reactions of halogen- and cyanide- containing species. *Journal of Physical and Chemical Reference Data* **1981,** *10,*

168. Ting, W.-L.; Chang, C.-H.; Lee, Y.-F.; Matsui, H.; Lee, Y.-P.; Lin, J. J.-M., Detailed mechanism of the CH2I + O2 reaction: Yield and self-reaction of the simplest Criegee intermediate CH2OO. *J. Chem. Phys.* **2014,** *141,* 104308.

169. Chhantyal-Pun, R.; Davey, A.; Shallcross, D. E.; Percival, C. J.; Orr-Ewing, A. J., A kinetic study of the CH2OO Criegee intermediate self-reaction, reaction with SO2 and unimolecular reaction using cavity ring-down spectroscopy. *Phys. Chem. Chem. Phys.* **2015,** *17,* 3617-3626.

170. Saiz-Lopez, A.; Plane, J. M. C.; Baker, A. R.; Carpenter, L. J.; von Glasow, R.; Gómez Martín, J. C.; McFiggans, G.; Saunders, R. W., Atmospheric Chemistry of Iodine. *Chemical Reviews* **2012**, *112*, 1773-1804.

171. Neeb, P.; Horie, O.; Moortgat, G. K., The Ethene–Ozone Reaction in the Gas Phase. *J. Phys. Chem. A* **1998**, *102*, 6778-6785.

172. Vereecken, L.; Harder, H.; Novelli, A., The reaction of Criegee intermediates with NO, RO2, and SO2, and their fate in the atmosphere. *Phys. Chem. Chem. Phys.* **2012**, *14*, 14682-14695.

173. Mauldin III, R. L.; Berndt, T.; Sipilä, M.; Paasonen, P.; Petäjä, T.; Kim, S.; Kurtén, T.; Stratmann, F.; Kerminen, V. M.; Kulmala, M., A new atmospherically relevant oxidant of sulphur dioxide. *Nature* **2012**, *488*, 193.

174. Lewis, T. R.; Blitz, M. A.; Heard, D. E.; Seakins, P. W., Direct evidence for a substantive reaction between the Criegee intermediate, CH2OO, and the water vapour dimer. *Phys. Chem. Chem. Phys.* **2015**, *17*, 4859-4863.

175. Horie, O.; Schafer, C.; Moortgat, G. K., High reactivity of hexafluoro acetone toward Criegee intermediates in the gas-phase ozonolysis of simple alkenes. *Int. J. Chem. Kinet.* **1999**, *31*, 261-269.

176. Berndt, T.; Kaethner, R.; Voigtlander, J.; Stratmann, F.; Pfeifle, M.; Reichle, P.; Sipila, M.; Kulmala, M.; Olzmann, M., Kinetics of the unimolecular reaction of CH2OO and the bimolecular reactions with the water monomer, acetaldehyde and acetone under atmospheric conditions. *Phys. Chem. Chem. Phys.* **2015**, *17*, 19862-19873.

177. Aplincourt, P.; Ruiz-Lopez, M. F., Theoretical study of formic acid anhydride formation from carbonyl oxide in the atmosphere. *J. Phys. Chem. A* **2000**, *104*, 380-388.

178. Aplincourt, P.; Ruiz-Lopez, M. F., Theoretical investigation of reaction mechanisms for carboxylic acid formation in the atmosphere. *J. Am. Chem. Soc.* **2000**, *122*, 8990-8997.

179. Yang, D. L.; Yu, T.; Wang, N. S.; Lin, M. C., CN radical reactions with selected olefins in the temperature range of 174–740 K. *Chem. Phys.* **1992**, *160*, 317-325.

180. Traeger, J. C., Heat of formation for the formyl cation by photoionization mass spectrometry. *Int. J. Mass Spectrom. Ion Processes* **1985**, *66*, 271-282.

181. Gao, C. W.; Allen, J. W.; Green, W. H.; West, R. H., Reaction Mechanism Generator: Automatic construction of chemical kinetic mechanisms. *Comput. Phys. Commun.* **2016**, *203*, 212-225.

182. Georgievskii, Y.; Klippenstein, S. J., Long-range transition state theory. *J. Chem. Phys.* **2005**, *122*, 194103.

183. Richter, H.; Howard, J. B., Formation of Polycyclic Aromatic Hydrocarbons and their Growth to Soot—a Review of Chemical Reaction Pathways. *Prog. Energy Combust. Sci.* **2000**, *26*, 565-608.

184. Dockery, D. W.; Pope, C. A.; Xu, X.; Spengler, J. D.; Ware, J. H.; Fay, M. E.; Ferris, B. G.; Speizer, F. E., An Association between Air Pollution and Mortality in Six U.S. Cities. *N. Engl. J. Med.* **1993**, *329*, 1753-1759.

185. Jacobson, M. Z., Strong Radiative Heating Due to the Mixing State of Black Carbon in Atmospheric Aerosols. *Nature* **2001**, *409*, 695-697.

186. Hansen, J.; Nazarenko, L., Soot Climate Forcing via Snow and Ice Albedos. *Proc. Natl. Acad. Sci. U. S. A.* **2004**, *101*, 423-428.

187. Penner, J. E.; Zhang, S. Y.; Chuang, C. C., Soot and Smoke Aerosol May not Warm Climate. *J. Geophys. Res., [Atmos.]* **2003**, *108*, 4657.

188. McEnally, C. S.; Pfefferle, L. D.; Atakan, B.; Kohse-Höinghaus, K., Studies of Aromatic Hydrocarbon Formation Mechanisms in Flames: Progress Towards Closing the Fuel Gap. *Prog. Energy Combust. Sci.* **2006**, *32*, 247-294.

189. Wang, H., Formation of Nascent Soot and Other Condensed-Phase Materials in Flames. *Proc. Combust. Inst.* **2011**, *33*, 41-67.

190. Gomez, A.; Sidebotham, G.; Glassman, I., Sooting Behavior in Temperature-Controlled Laminar Diffusion Flames. *Combust. Flame* **1984**, *58*, 45-57.

191. Glassman, I., Soot Formation in Combustion Processes. *Symp. (Int.) Combust.* **1989**, *22*, 295-311.

192. Frenklach, M.; Wang, H., Detailed Modeling of Soot Particle Nucleation and Growth. *Symp. (Int.) Combust.* **1991**, *23*, 1559-1566.

193. Cole, J. A.; Bittner, J. D.; Longwell, J. P.; Howard, J. B., Formation Mechanisms of Aromatic Compounds in Aliphatic Flames. *Combust. Flame* **1984**, *56*, 51-70.

194. Westmoreland, P. R.; Dean, A. M.; Howard, J. B.; Longwell, J. P., Forming Benzene in Flames by Chemically Activated Isomerization. *J. Phys. Chem.* **1989**, *93*, 8171-8180.

195. Miller, J. A.; Melius, C. F., Kinetic and Thermodynamic Issues in the Formation of Aromatic Compounds in Flames of Aliphatic Fuels. *Combust. Flame* **1992**, *91*, 21-39.

196. Miller, J. A.; Klippenstein, S. J.; Robertson, S. H., A Theoretical Analysis of the Reaction between Vinyl and Acetylene: Quantum Chemistry and Solution of the Master Equation. *J. Phys. Chem. A* **2000**, *104*, 7525-7536.

197. Senosiain, J. P.; Miller, J. A., The Reaction of n- and i-C4H5 Radicals with Acetylene†. *J. Phys. Chem. A* **2007**, *111*, 3740-3747.

198. Ebert, K. H.; Ederer, H. J.; Stabel, U., Modeling Studies of the Homogeneous Formation of Aromatic Compounds in the Thermal Decomposition of n-Hexane. *Ber. Bunsen-Ges. Phys. Chem.* **1983**, *87*, 1036-1039.

199. Weissman, M.; Benson, S. W., Pyrolysis of Methyl Chloride, a Pathway in the Chlorine-Catalyzed Polymerization of Methane. *Int. J. Chem. Kinet.* **1984**, *16*, 307-333.

200. Lindstedt, R. P.; Skevis, G., Benene Formation Chemistry in Premixed 1,3-Butadiene Flames. *Symp. (Int.) Combust.* **1996**, *26*, 703-709.

201. Goldaniga, A.; Faravelli, T.; Ranzi, E., The Kinetic Modeling of Soot Precursors in a Butadiene Flame. *Combust. Flame* **2000**, *122*, 350-358.

202. Cavallotti, C.; Rota, R.; Carrà, S., Quantum Chemistry Computation of Rate Constants for Reactions Involved in the First Aromatic Ring Formation. *J. Phys. Chem. A* **2002**, *106*, 7769-7778.

203. Cavallotti, C.; Fascella, S.; Rota, R.; Carrà, S., A Quantum Chemistry Study of the Formation of PAH and Soot Precursors through Butadiene Reactions. *Combust. Sci. Technol.* **2004**, *176*, 705-720.

204. Gueniche, H. A.; Glaude, P. A.; Fournet, R.; Battin-Leclerc, F., Rich Premixed Laminar Methane Flames Doped by Light Unsaturated Hydrocarbons: II. 1,3-Butadiene. *Combust. Flame* **2007**, *151*, 245-261.

205. Xu, C.; Al Shoaibi, A. S.; Wang, C.; Carstensen, H.-H.; Dean, A. M., Kinetic Modeling of Ethane Pyrolysis at High Conversion. *J. Phys. Chem. A* **2011**, *115*, 10470-10490.

206. Melius, C. F.; Colvin, M. E.; Marinov, N. M.; Pit, W. J.; Senkan, S. M., Reaction Mechanisms in Aromatic Hydrocarbon Formation Involving the C5H5 Cyclopentadienyl Moiety. *Symp. (Int.) Combust.* **1996**, *26*, 685-692.

207. Miller, J. A.; Klippenstein, S. J., The Recombination of Propargyl Radicals and Other Reactions on a C6H6 Potential. *J. Phys. Chem. A* **2003**, *107*, 7783-7799.

208. Georgievskii, Y.; Miller, J. A.; Klippenstein, S. J., Association Rate Constants for Reactions between Resonance-Stabilized Radicals: C3H3 + C3H3, C3H3 + C3H5, and C3H5 + C3H5. *Phys. Chem. Chem. Phys.* **2007**, *9*, 4259-4268.

209. Dean, A. M., Detailed Kinetic Modeling of Autocatalysis in Methane Pyrolysis. *J. Phys. Chem.* **1990**, *94*, 1432-1439.

210. Mebel, A. M.; Kislov, V. V., Can the C5H5 + C5H5 → C10H10 → C10H9 + H/C10H8 + H2 Reaction Produce Naphthalene? An Ab Initio/RRKM Study. *J. Phys. Chem. A* **2009**, *113*, 9825-9833.

211. Ellis, R. J.; Frey, H. M., The Thermal Unimolecular Isomerisation of Bicyclo[3,1,0]hex-2-ene and Decomposition of Cyclohexa-1,4-diene. *J. Chem. Soc. A* **1966**, 553-556.

212. Benson, S. W.; Shaw, R., Kinetics and Mechanism of the Pyrolysis of 1,4-Cyclohexadiene. *Trans. Faraday Soc.* **1967**, *63*, 985-992.

213. Alfassi, Z. B.; Benson, S. W.; Golden, D. M., Very low pressure pyrolysis of 1,3-cyclohexadiene. Orbital symmetry nonallowed reaction. *J. Am. Chem. Soc.* **1973**, *95*, 4784-4788.

214. Gulati, S. K.; Walker, R. W., Addition of Cyclohexane to Slowly Reacting H2-O2 Mixtures at 480 [degree]C. *J. Chem. Soc., Faraday Trans. 2* **1989**, *85*, 1799-1812.

215. Kumar, A.; Chowdhury, P. K.; Rama Rao, K. V. S.; Mittal, J. P., Real-Time Observation of Concerted Benzene Formation in the Infrared Multiphoton Dissociation of 1,4-Cyclohexadiene. *Chem. Phys. Lett.* **1991**, *182*, 165-170.

216. Dayma, G.; Glaude, P. A.; Fournet, R.; Battin-Leclerc, F., Experimental and Modeling Study of the Oxidation of Cyclohexene. *Int. J. Chem. Kinet.* **2003**, *35*, 273-285.

217. Li, W.; Law, M. E.; Westmoreland, P. R.; Kasper, T.; Hansen, N.; Kohse-Höinghaus, K., Multiple Benzene-Formation Paths in a Fuel-Rich Cyclohexane Flame. *Combust. Flame* **2011**, *158*, 2077-2089.

218. Hansen, N.; Miller, J. A.; Kasper, T.; Kohse-Höinghaus, K.; Westmoreland, P. R.; Wang, J.; Cool, T. A., Benzene Formation in Premixed Fuel-Rich 1,3-Butadiene Flames. *Proc. Combust. Inst.* **2009**, *32*, 623-630.

219. Kostina, S. A.; Shestov, A. A.; Knyazev, V. D., Kinetics of the Reaction of the CCl2 Biradical with Molecular Chlorine. *J. Phys. Chem. A* **2003**, *107*, 10292-10295.

220. Werner, H.-J.; Knowles, P. J.; Knizia, G.; Manby, F. R.; Schütz, M., Molpro: a general-purpose quantum chemistry program package. *Wiley Interdisciplinary Reviews: Computational Molecular Science* **2012**, *2*, 242-253.

221. Zhao, Y.; Truhlar, D. G., Exploring the Limit of Accuracy of the Global Hybrid Meta Density Functional for Main-Group Thermochemistry, Kinetics, and Noncovalent Interactions. *J. Chem. Theory Comput.* **2008**, *4*, 1849-1868.

222. Shao, Y.; Molnar, L. F.; Jung, Y.; Kussmann, J.; Ochsenfeld, C.; Brown, S. T.; Gilbert, A. T. B.; Slipchenko, L. V.; Levchenko, S. V.; O'Neill, D. P.; DiStasio Jr, R. A.; Lochan, R. C.; Wang, T.; Beran, G. J. O.; Besley, N. A.; Herbert, J. M.; Yeh Lin, C.; Van Voorhis, T.; Hung Chien, S.; Sodt, A.; Steele, R. P.; Rassolov, V. A.; Maslen, P. E.; Korambath, P. P.; Adamson, R. D.; Austin, B.; Baker, J.; Byrd, E. F. C.; Dachsel, H.; Doerksen, R. J.; Dreuw, A.; Dunietz, B. D.; Dutoi, A. D.; Furlani, T. R.; Gwaltney, S. R.; Heyden, A.; Hirata, S.; Hsu, C.-P.; Kedziora, G.; Khalliulin, R. Z.; Klunzinger, P.; Lee, A. M.; Lee, M. S.; Liang, W.; Lotan, I.; Nair, N.; Peters, B.; Proynov, E. I.; Pieniazek, P.

A.; Min Rhee, Y.; Ritchie, J.; Rosta, E.; David Sherrill, C.; Simmonett, A. C.; Subotnik, J. E.; Lee Woodcock Iii, H.; Zhang, W.; Bell, A. T.; Chakraborty, A. K.; Chipman, D. M.; Keil, F. J.; Warshel, A.; Hehre, W. J.; Schaefer Iii, H. F.; Kong, J.; Krylov, A. I.; Gill, P. M. W.; Head-Gordon, M., Advances in Methods and Algorithms in a Modern Quantum Chemistry Program Package. *Phys. Chem. Chem. Phys.* **2006**, *8*, 3172-3191.

223. Alecu, I. M.; Zheng, J.; Zhao, Y.; Truhlar, D. G., Computational Thermochemistry: Scale Factor Databases and Scale Factors for Vibrational Frequencies Obtained from Electronic Model Chemistries. *J. Chem. Theory Comput.* **2010**, *6*, 2872-2887.

224. Boese, A. D.; Martin, J. M. L., Development of Density Functionals for Thermochemical Kinetics. *J. Chem. Phys.* **2004**, *121*, 3405-3416.

225. East, A. L. L.; Radom, L., Ab Initio Statistical Thermodynamical Models for the Computation of Third-Law Entropies. *J. Chem. Phys.* **1997**, *106*, 6655-6674.

226. Eckart, C., The Penetration of a Potential Barrier by Electrons. *Phys. Rev.* **1930**, *35*, 1303-1309.

227. Jasper, A. W.; Miller, J. A., Theoretical Unimolecular Kinetics for CH4 + M ⇄ CH3 + H + M in Eight Baths, M = He, Ne, Ar, Kr, H2, N2, CO, and CH4. *J. Phys. Chem. A* **2011**, *115*, 6438-6455.

228. Poling, B. E.; Prausnitz, J. M.; O' Connell, J. P., *The Properties of Gases and Liquids*. 5th ed.; McGraw-Hill, Inc.: New York, 2001.

229. Welty, J. R.; Wicks, C. E.; Wilson, R. E.; Rorrer, G. L., *Fundamentals of Momentum, Heat, and Mass Transfer*. John Wiley & Sons: 2001.

230. Harper, M. R.; Van Geem, K. M.; Pyl, S. P.; Marin, G. B.; Green, W. H., Comprehensive Reaction Mechanism for n-Butanol Pyrolysis and Combustion. *Combust. Flame* **2011**, *158*, 16-41.

231. Newby, J. J.; Stearns, J. A.; Liu, C.-P.; Zwier, T. S., Photochemical and Discharge-Driven Pathways to Aromatic Products from 1,3-Butadiene. *J. Phys. Chem. A* **2007**, *111*, 10914-10927.

232. Lockyear, J. F.; Fournier, M.; Sims, I. R.; Guillemin, J.-C.; Taatjes, C. A.; Osborn, D. L.; Leone, S. R., Formation of fulvene in the reaction of C2H with 1,3-butadiene. *Int. J. Mass Spectrom.* **2015**, *378*, 232-245.

233. Tonokura, K.; Koshi, M., Absorption Spectrum and Cross Sections of the Allyl Radical Measured Using Cavity Ring-Down Spectroscopy: The Ã ← X̃ Band. *J. Phys. Chem. A* **2000**, *104*, 8456-8461.

234. Zou, P.; Strecker, K. E.; Ramirez-Serrano, J.; Jusinski, L. E.; Taatjes, C. A.; Osborn, D. L., Ultraviolet photodissociation of vinyl iodide: understanding the halogen dependence of photodissociation mechanisms in vinyl halides. *Phys. Chem. Chem. Phys.* **2008**, *10*, 713-728.

235. Shahu, M.; Yang, C.-H.; Pibel, C. D.; McIlroy, A.; Taatjes, C. A.; Halpern, J. B., Vinyl Radical Visible Spectroscopy and Excited State Dynamics. *J. Chem. Phys.* **2002**, *116*, 8343-8352.

236. Ismail, H.; Park, J.; Wong, B. M.; Green Jr, W. H.; Lin, M. C., A theoretical and experimental kinetic study of phenyl radical addition to butadiene. *Proc. Combust. Inst.* **2005**, *30*, 1049-1056.

237. Tokmakov, I. V.; Lin, M. C., Reaction of Phenyl Radicals with Acetylene: Quantum Chemical Investigation of the Mechanism and Master Equation Analysis of the Kinetics. *J. Am. Chem. Soc.* **2003**, *125*, 11397-11408.

238. Wang, J.; Yang, B.; Cool, T. A.; Hansen, N.; Kasper, T., Near-Threshold Absolute Photoionization Cross-Sections of Some Reaction Intermediates in Combustion. *Int. J. Mass Spectrom.* **2008**, *269*, 210-220.

239. Kanno, N.; Tonokura, K., Vacuum Ultraviolet Photoionization Mass Spectra and Cross-Sections for Volatile Organic Compounds at 10.5 eV. *Appl. Spectrosc.* **2007**, *61*, 896-902.

240. Hippler, H.; Troe, J.; Wendelken, H. J., Collisional Deactivation of Vibrationally Highly Excited Polyatomic Molecules. II. Direct Observations for Excited Toluene. *J. Chem. Phys.* **1983**, *78*, 6709-6717.

241. Gilbert, R. G.; Smith, S. C., *Theory of Unimolecular and Recombination Reactions.* Blackwell Scientific Publications: London, 1990.

242. Mebel, A. M.; Georgievskii, Y.; Jasper, A. W.; Klippenstein, S. J., Pressure-dependent rate constants for PAH growth: formation of indene and its conversion to naphthalene. *Faraday Discuss.* **2016**, *195*, 637-670.

243. Hefter, H. J.; Hecht, T. A.; Hammond, G. S., Radical attack on propylene as studied by electron spin resonance. *J. Am. Chem. Soc.* **1972**, *94*, 2793-2797.

244. Yu, T.; Lin, M. C., Kinetics of the C6H5 + O2 Reaction at Low Temperatures. *J. Am. Chem. Soc.* **1994**, *116*, 9571-9576.

245. NIST Precomputed vibrational scaling factors. http://cccbdb.nist.gov/vibscalejust.asp.

246. Jasper, A. W.; Oana, C. M.; Miller, J. A., "Third-Body" collision efficiencies for combustion modeling: Hydrocarbons in atomic and diatomic baths. *Proc. Combust. Inst.* **2015**, *35*, 197-204.

247. CHEMKIN-PRO 15131. 2013; p. CHEMKIN software is distributed by ANSYS.

248. Tonokura, K.; Koshi, M., Cavity Ring-Down Spectroscopy of the Benzyl Radical. *J. Phys. Chem. A* **2003**, *107*, 4457-4461.

249. Yaws, C. L. Yaws' Critical Property Data for Chemical Engineers and Chemists. http://app.knovel.com/hotlink/toc/id:kpYCPDCECD/yaws-critical-property/yaws-critical-property.

250. Bradley, G. M.; Strauss, H. L., Infrared studies of nitrosobenzene. *J. Phys. Chem.* **1975**, *79*, 1953-1957.

251. Comandini, A.; Malewicki, T.; Brezinsky, K., Chemistry of Polycyclic Aromatic Hydrocarbons Formation from Phenyl Radical Pyrolysis and Reaction of Phenyl and Acetylene. *J. Phys. Chem. A* **2012**, *116*, 2409-2434.

252. Brand, U.; Hippler, H.; Lindemann, L.; Troe, J., Carbon-carbon and carbon-hydrogen bond splits of laser-excited aromatic molecules. 1. Specific and thermally averaged rate constants. *J. Phys. Chem.* **1990**, *94*, 6305-6316.

253. Harding, L. B.; Klippenstein, S. J.; Georgievskii, Y., On the Combination Reactions of Hydrogen Atoms with Resonance-Stabilized Hydrocarbon Radicals. *J. Phys. Chem. A* **2007**, *111*, 3789-3801.

254. Benson, S. W., *Thermochemical kinetics: methods for the estimation of thermochemical data and rate parameters.* Wiley: 1976.

255. Hunter, T. F.; Kristjansson, K. S., Optoacoustic method of measuring reaction rates of the radicals CH3, CD3, C2H5 and CH2I with I and I2. *J. Chem. Soc., Faraday Trans. 2* **1982**, *78*, 2067-2076.

256. Guercione, J. A.; Wijnen, M. H. J., Recombination and Disproportionation Reactions of Iodine Atoms and Ethyl Radicals. *J. Chem. Phys.* **1963**, *38*, 1-3.

257. Gao, Y.; Fessel, K.; McLeod, C.; Marshall, P., A kinetic study of the reaction of atomic hydrogen with iodobenzene. *Chem. Phys. Lett.* **2008,** *451,* 8-13.

258. Lifshitz, A.; Tamburu, C.; Dubnikova, F., Reactions of 1-Naphthyl Radicals with Ethylene. Single Pulse Shock Tube Experiments, Quantum Chemical, Transition State Theory, and Multiwell Calculations. *J. Phys. Chem. A* **2008,** *112,* 925-933.

259. Mulenko, S., The application of an intracavity laser spectroscopy method for elementary processes study in gas-phase reactions. *Rev. Roum. Phys* **1987,** *32,* 173.

260. Jenkin, M. E.; Murrells, T. P.; Shalliker, S. J.; Hayman, G. D., Kinetics and product study of the self-reactions of allyl and allyl peroxy radicals at 296 K. *J. Chem. Soc., Faraday Trans.* **1993,** *89,* 433-446.

261. Mueller-Markgraf, W.; Troe, J., Thermal decomposition of benzyl iodide and of benzyl radicals in shock waves. *J. Phys. Chem.* **1988,** *92,* 4899-4905.

262. Golden, D. M.; Rodgers, A. S.; Benson, S. W., The Kinetics and Mechanism of the Reaction I2 + C3H6 $\rightarrow\leftarrow$ C3H5I + HI and the Heat of Formation of the Allyl Radical1. *J. Am. Chem. Soc.* **1966,** *88,* 3196-3198.

263. Ruscic, B.; Bross, D. H. Active Thermochemical Tables (ATcT) values based on ver. 1.122 of the Thermochemical Network. ATcT.anl.gov.

264. Blanksby, S. J.; Ellison, G. B., Bond Dissociation Energies of Organic Molecules. *Acc. Chem. Res.* **2003,** *36,* 255-263.

265. Zhou, Z.; Xie, M.; Wang, Z.; Qi, F., Determination of Absolute Photoionization Cross-Sections of Aromatics and Aromatic Derivatives. *Rapid Commun. Mass Spectrom.* **2009,** *23,* 3994-4002.

266. Zhou, Z.; Zhang, L.; Xie, M.; Wang, Z.; Chen, D.; Qi, F., Determination of Absolute Photoionization Cross-Sections of Alkanes and Cyclo-Alkanes. *Rapid Commun. Mass Spectrom.* **2010,** *24,* 1335-1342.

267. Yang, B.; Wang, J.; Cool, T. A.; Hansen, N.; Skeen, S.; Osborn, D. L., Absolute photoionization cross-sections of some combustion intermediates. *Int. J. Mass Spectrom.* **2012,** *309,* 118-128.

268. Gans, B.; Mendes, L. A. V.; Boyé-Péronne, S.; Douin, S.; Garcia, G.; Soldi-Lose, H.; de Miranda, B. K. C.; Alcaraz, C.; Carrasco, N.; Pernot, P.; Gauyacq, D., Determination of the Absolute Photoionization Cross Sections of CH3 and I Produced from a Pyrolysis Source, by Combined Synchrotron and Vacuum Ultraviolet Laser Studies. *J. Phys. Chem. A* **2010,** *114,* 3237-3246.

269. Robinson, J. C.; Sveum, N. E.; Neumark, D. M., Determination of absolute photoionization cross sections for isomers of C3H5: allyl and 2-propenyl radicals. *Chem. Phys. Lett.* **2004,** *383,* 601-605.

270. Dyakov, Y. A.; Hsu, W. H.; Ni, C.-K.; Tsai, W.-C.; Hu, W.-P., Photodissociation dynamics of benzyl alcohol at 193 nm. *J. Chem. Phys.* **2012,** *137,* 064314.

271. Bobeldijk, M.; van der Zande, W. J.; Kistemaker, P. G., Simple models for the calculation of photoionization and electron impact ionization cross sections of polyatomic molecules. *Chem. Phys.* **1994,** *179,* 125-130.

272. Xu, H.; Pratt, S. T., Photoionization Cross Section of the Propargyl Radical and Some General Ideas for Estimating Radical Cross Sections. *J. Phys. Chem. A* **2013,** *117,* 9331-9342.

273. Traeger, J. C.; Kompe, B. M., Threshold C7H+7 formation from the benzyl halides by photoionization mass spectrometry. *Int. J. Mass Spectrom. Ion Processes* **1990**, *101*, 111-120.

274. Tang, W.; Tranter, R. S.; Brezinsky, K., Isomeric Product Distributions from the Self-Reaction of Propargyl Radicals. *J. Phys. Chem. A* **2005**, *109*, 6056-6065.

275. Taatjes, C. A.; Osborn, D. L.; Selby, T. M.; Meloni, G.; Fan, H.; Pratt, S. T., Absolute Photoionization Cross-Section of the Methyl Radical. *J. Phys. Chem. A* **2008**, *112*, 9336-9343.

276. Deakin, J. J.; Husain, D., Electronically excited iodine atoms, I(5p52P1/2). A kinetic study of collisional quenching by time-resolved atomic absorption, at λ = 206.23 nm. *J. Chem. Soc., Faraday Trans. 2* **1972**, *68*, 41-47.

277. Kota, G. P.; Coburn, J. W.; Graves, D. B., Heterogeneous recombination of atomic bromine and fluorine. *Journal of Vacuum Science & Technology A* **1999**, *17*, 282-290.

278. Berkowitz, J.; Greene, J. P.; Cho, H.; Ruscić, B., The ionization potentials of CH4 and CD4. *J. Chem. Phys.* **1987**, *86*, 674-676.

279. Williams, B. A.; Cool, T. A., Two - photon spectroscopy of Rydberg states of jet - cooled C2H4 and C2D4. *J. Chem. Phys.* **1991**, *94*, 6358-6366.

280. Luo, Y.-R.; Pacey, P. D., Effects of alkyl substitution on ionization energies of alkanes and haloalkanes and on heats of formation of their molecular cations Part 2.* Alkanes and chloro-, bromo- and iodoalkanes. *Int. J. Mass Spectrom. Ion Processes* **1992**, *112*, 63-77.

281. Matsugi, A.; Miyoshi, A., Kinetics of the self-reactions of benzyl and o-xylyl radicals studied by cavity ring-down spectroscopy. *Chem. Phys. Lett.* **2012**, *521*, 26-30.

282. Wallington, T. J.; Egsgaard, H.; Nielsen, O. J.; Platz, J.; Sehested, J.; Stein, T., UV-visible spectrum of the phenyl radical and kinetics of its reaction with NO in the gas phase. *Chem. Phys. Lett.* **1998**, *290*, 363-370.

283. Siirola, J. J., The impact of shale gas in the chemical industry. *AIChE J.* **2014**, *60*, 810-819.

284. Mohr, S. H.; Evans, G. M., Long term forecasting of natural gas production. *Energy Policy* **2011**, *39*, 5550-5560.

285. Cao, S.; Wang, D.; Wang, T., Simulation of partial oxidation of natural gas with detailed chemistry: Influence of addition of H2, C2H6 and C3H8. *Chem. Eng. Sci.* **2010**, *65*, 2608-2618.

286. Lin, Y.; Abdelghani, M. Process For The Production Of Ethylene From Natural Gas With Heat Integration. 2010.

287. Berger, R. J.; Marin, G. B., Investigation of Gas-Phase Reactions and Ignition Delay Occurring at Conditions Typical for Partial Oxidation of Methane to Synthesis Gas. *Ind. Eng. Chem. Res.* **1999**, *38*, 2582-2592.

288. Howard, W. B. Production of acetylene. 1966.

289. Nikolaus, P.; Rudolf, W.; Werner, F., Process for cracking hydrocarbons. 1966;

290. Zhang, Q.; Wang, J.; Wang, T., Enhancing the Acetylene Yield from Methane by Decoupling Oxidation and Pyrolysis Reactions: A Comparison with the Partial Oxidation Process. *Ind. Eng. Chem. Res.* **2016**, *55*, 8383-8394.

291. Al-Hamamre, Z.; Voß, S.; Trimis, D., Hydrogen production by thermal partial oxidation of hydrocarbon fuels in porous media based reformer. *Int. J. Hydrogen Energy* **2009**, *34*, 827-832.

292. Liu, Y.; Wang, T., Analysis of the Autoignition Process under the Industrial Partial Oxidation Conditions Using Detailed Kinetic Modeling. *Ind. Eng. Chem. Res.* **2011**, *50*, 6009-6016.

293. Li, X.; Dai, Z.; Guo, Q.; Liang, Q.; Wang, F., Experimental and numerical study of MILD combustion in a bench-scale natural gas partial oxidation gasifier. *Fuel* **2017**, *193*, 197-205.

294. Köhler, M.; Oßwald, P.; Xu, H.; Kathrotia, T.; Hasse, C.; Riedel, U., Speciation data for fuel-rich methane oxy-combustion and reforming under prototypical partial oxidation conditions. *Chem. Eng. Sci.* **2016**, *139*, 249-260.

295. Skjøth-Rasmussen, M. S.; Glarborg, P.; Østberg, M.; Johannessen, J. T.; Livbjerg, H.; Jensen, A. D.; Christensen, T. S., Formation of polycyclic aromatic hydrocarbons and soot in fuel-rich oxidation of methane in a laminar flow reactor. *Combust. Flame* **2004**, *136*, 91-128.

296. Glarborg, P.; Bentzen, L. L. B., Chemical Effects of a High CO2 Concentration in Oxy-Fuel Combustion of Methane. *Energy Fuels* **2008**, *22*, 291-296.

297. Li, C. e.; Burke, N.; Gerdes, K.; Patel, J., The undiluted, non-catalytic partial oxidation of methane in a flow tube reactor – An experimental study using indirect induction heating. *Fuel* **2013**, *109*, 409-416.

298. Li, Q.; Wang, T.; Liu, Y.; Wang, D., Experimental study and kinetics modeling of partial oxidation reactions in heavily sooting laminar premixed methane flames. *Chemical Engineering Journal* **2012**, *207-208*, 235-244.

299. Watanabe, H.; Arai, F.; Okazaki, K., Role of CO2 in the CH4 oxidation and H2 formation during fuel-rich combustion in O2/CO2 environments. *Combust. Flame* **2013**, *160*, 2375-2385.

300. Turbiez, A.; El Bakali, A.; Pauwels, J. F.; Rida, A.; Meunier, P., Experimental study of a low pressure stoichiometric premixed methane, methane/ethane, methane/ethane/propane and synthetic natural gas flames. *Fuel* **2004**, *83*, 933-941.

301. Stelzner, B.; Weis, C.; Habisreuther, P.; Zarzalis, N.; Trimis, D., Super-adiabatic flame temperatures in premixed methane flames: A comparison between oxy-fuel and conventional air combustion. *Fuel* **2017**, *201*, 148-155.

302. Ktalkherman, M. G.; Namyatov, I. G., Pyrolysis of hydrocarbons in a heat-carrier flow with fast mixing of the components. *Combustion, Explosion, and Shock Waves* **2008**, *44*, 529-534.

303. Ktalkherman, M.; Namyatov, I.; Emel'kin, V., High-Temperature Pyrolysis of Liquified Petroleum Gases in the Fast-Mixing Reactor. In *International Journal of Chemical Reactor Engineering*, 2011; Vol. 9,

304. Ktalkherman, M. G.; Namyatov, I. G.; Emel'kim, V. A.; Lomanovich, K. A., High-selective pyrolysis of naphtha in the fast-mixing reactor. *Fuel Process. Technol.* **2013**, *106*, 48-54.

305. Smith, G. P.; Golden, D. M.; Frenklach, M.; Moriarty, N. W.; Eiteneer, B.; Goldenberg, M.; Bowman, C. T.; Hanson, R. K.; Song, S.; Gardiner, J., W. C.; Lissianski, V. V.; Qin, Z. GRI-Mech 3.0. http://www.me.berkeley.edu/gri_mech/.

306. Hughes, K. J.; Turányi, T.; Clague, A. R.; Pilling, M. J., Development and testing of a comprehensive chemical mechanism for the oxidation of methane. *Int. J. Chem. Kinet.* **2001**, *33*, 513-538.

307. Petersen, E. L.; Davidson, D. F.; Hanson, R. K., Kinetics modeling of shock-induced ignition in low-dilution CH4/O2 mixtures at high pressures and intermediate temperatures. *Combust. Flame* **1999,** *117,* 272-290.

308. Konnov, A. A.; Zhu, J. N.; Bromly, J. H.; Zhang, D.-K., Noncatalytic partial oxidation of methane into syngas over a wide temperature range. *Combust. Sci. Technol.* **2004,** *176,* 1093-1116.

309. Healy, D.; Curran, H. J.; Simmie, J. M.; Kalitan, D. M.; Zinner, C. M.; Barrett, A. B.; Petersen, E. L.; Bourque, G., Methane/ethane/propane mixture oxidation at high pressures and at high, intermediate and low temperatures. *Combust. Flame* **2008,** *155,* 441-448.

310. Bourque, G.; Healy, D.; Curran, H.; Zinner, C.; Kalitan, D.; de Vries, J.; Aul, C.; Petersen, E., Ignition and Flame Speed Kinetics of Two Natural Gas Blends With High Levels of Heavier Hydrocarbons. *Journal of Engineering for Gas Turbines and Power* **2009,** *132,* 021504-021504-11.

311. Narayanaswamy, K.; Blanquart, G.; Pitsch, H., A consistent chemical mechanism for oxidation of substituted aromatic species. *Combust. Flame* **2010,** *157,* 1879-1898.

312. Blanquart, G.; Pepiot-Desjardins, P.; Pitsch, H., Chemical mechanism for high temperature combustion of engine relevant fuels with emphasis on soot precursors. *Combust. Flame* **2009,** *156,* 588-607.

313. Wang, H.; You, X.; Joshi, A. V.; Davis, S. G.; Laskin, A.; Egolfopoulos, F.; Law, C. K., USC Mech Version II. High-Temperature Combustion Reaction Model of H2/CO/C1-C4 Compounds. **May 2007,**

314. Benson, S. W., *Thermochemical Kinetics.* John Wiley and Sons: New York, 1968.

315. Burke, M. P.; Chaos, M.; Ju, Y.; Dryer, F. L.; Klippenstein, S. J., Comprehensive H2/O2 kinetic model for high-pressure combustion. *Int. J. Chem. Kinet.* **2012,** *44,* 444-474.

316. Goldsmith, C. F.; Magoon, G. R.; Green, W. H., Database of Small Molecule Thermochemistry for Combustion. *J. Phys. Chem. A* **2012,** *116,* 9033-9057.

317. Stewart, P. H.; Larson, C. W.; Golden, D. M., Pressure and temperature dependence of reactions proceeding via a bound complex. 2. Application to 2CH3 $\rightarrow$ C2H5 + H. *Combust. Flame* **1989,** *75,* 25-31.

318. Joshi, A. V.; Wang, H., Master equation modeling of wide range temperature and pressure dependence of CO + OH $\rightarrow$ products. *Int. J. Chem. Kinet.* **2006,** *38,* 57-73.

319. Knyazev, V. D.; Slagle, I. R., Kinetics of the Reaction between Propargyl Radical and Acetylene. *J. Phys. Chem. A* **2002,** *106,* 5613-5617.

320. Roy, K. Kinetische Untersuchung zur Hochtemperaturpyrolyse und -oxidation von Cyclopentadien und Cyclopentadienyl mit Hilfe der Stosswellentechnik. Stuttgart University, Germany, 1999.

321. Sharma, S.; Green Jr, W. H., Computed Rate Coefficients and Product Yields for c-C5H5 + CH3 -$\rightarrow$ Products. *J. Phys. Chem. A* **2009,** *113,* 8871-8882.

322. Kislov, V. V.; Mebel, A. M., Ab Initio G3-type/Statistical Theory Study of the Formation of Indene in Combustion Flames. I. Pathways Involving Benzene and Phenyl Radical. *J. Phys. Chem. A* **2007,** *111,* 3922-3931.

323. Aguilera-Iparraguirre, J.; Klopper, W., Density Functional Theory Study of the Formation of Naphthalene and Phenanthrene from Reactions of Phenyl with Vinyl- and Phenylacetylene. *J. Chem. Theory Comput.* **2007,** *3,* 139-145.

324. Kislov, V. V.; Islamova, N. I.; Kolker, A. M.; Lin, S. H.; Mebel, A. M., Hydrogen Abstraction Acetylene Addition and Diels–Alder Mechanisms of PAH Formation: A Detailed Study Using First Principles Calculations. *J. Chem. Theory Comput.* **2005**, *1*, 908-924.

325. Woodcock, H. L.; Moran, D.; Brooks, B. R.; Schleyer, P. v. R.; Schaefer, H. F., Carbene Stabilization by Aryl Substituents. Is Bigger Better? *J. Am. Chem. Soc.* **2007**, *129*, 3763-3770.

326. Merchant, S. S. Molecules to Engines: Combustion Chemistry of Alcohols and their Application to Advanced Engines. MIT, Cambridge, 2015.

327. Wang, K.; Villano, S. M.; Dean, A. M., Reactions of allylic radicals that impact molecular weight growth kinetics. *Phys. Chem. Chem. Phys.* **2015**, *17*, 6255-6273.

328. Mebel, A. M.; Georgievskii, Y.; Jasper, A. W.; Klippenstein, S. J., Temperature- and pressure-dependent rate coefficients for the HACA pathways from benzene to naphthalene. *Proc. Combust. Inst.* **2017**, *36*, 919-926.

329. Matsugi, A.; Miyoshi, A., Computational study on the recombination reaction between benzyl and propargyl radicals. *Int. J. Chem. Kinet.* **2012**, *44*, 206-218.

330. Carr, A. G.; Class, C. A.; Lai, L.; Kida, Y.; Monrose, T.; Green, W. H., Supercritical Water Treatment of Crude Oil and Hexylbenzene: An Experimental and Mechanistic Study on Alkylbenzene Decomposition. *Energy Fuels* **2015**, *29*, 5290-5302.

331. Djokic, M. R.; Van Geem, K. M.; Cavallotti, C.; Frassoldati, A.; Ranzi, E.; Marin, G. B., An experimental and kinetic modeling study of cyclopentadiene pyrolysis: First growth of polycyclic aromatic hydrocarbons. *Combust. Flame* **2014**, *161*, 2739-2751.

332. Mebel, A. M.; Kislov, V. V.; Kaiser, R. I., Photoinduced Mechanism of Formation and Growth of Polycyclic Aromatic Hydrocarbons in Low-Temperature Environments via Successive Ethynyl Radical Additions. *J. Am. Chem. Soc.* **2008**, *130*, 13618-13629.

333. Han, K.; Jamal, A.; Grambow, C.; Buras, Z. J.; Green Jr, W. H., An Extended Group Additivity Method for Polycyclic Thermochemistry Estimation. *Submitted*,

334. Sieder, E. N.; Tate, G. E., Heat Transfer and Pressure Drop of Liquids in Tubes. *Industrial & Engineering Chemistry* **1936**, *28*, 1429-1435.

335. Bird, R. B.; Stewart, W. E.; Lightfoot, E. N., *Transport Phenomena*. 2nd ed.; John Wiley & Sons, Inc.: New York, 2006.

336. Long, A. E.; Merchant, S. S.; Vandeputte, A. G.; Carstensen, H.-H.; Vervust, A. J.; Marin, G. B.; Van Geem, K. M.; Green, W. H., Pressure dependent kinetic analysis of pathways to naphthalene from cyclopentadienyl recombination. *Combust. Flame* **2018**, *187*, 247-256.

337. Lifshitz, A.; Tamburu, C.; Dubnikova, F., Reactions of 1-Naphthyl Radicals with Acetylene. Single-Pulse Shock Tube Experiments and Quantum Chemical Calculations. Differences and Similarities in the Reaction with Ethylene. *J. Phys. Chem. A* **2009**, *113*, 10446-10451.

338. Richter, H.; Mazyar, O. A.; Sumathi, R.; Green, W. H.; Howard, J. B.; Bozzelli, J. W., Detailed Kinetic Study of the Growth of Small Polycyclic Aromatic Hydrocarbons. 1. 1-Naphthyl + Ethyne. *J. Phys. Chem. A* **2001**, *105*, 1561-1573.

339. Selby, T. M.; Meloni, G.; Goulay, F.; Leone, S. R.; Fahr, A.; Taatjes, C. A.; Osborn, D. L., Synchrotron Photoionization Mass Spectrometry Measurements of Kinetics and Product Formation in the Allyl Radical (H_2CCHCH_2) Self-Reaction. *J. Phys. Chem. A* **2008**, *112*, 9366-9373.

340.   Savee, J. D.; Selby, T. M.; Welz, O.; Taatjes, C. A.; Osborn, D. L., Time- and Isomer-Resolved Measurements of Sequential Addition of Acetylene to the Propargyl Radical. *J. Phys. Chem. Lett.* **2015,** *6*, 4153-4158.

341.   Merchant, S. S.; Goldsmith, C. F.; Vandeputte, A. G.; Burke, M. P.; Klippenstein, S. J.; Green, W. H., Understanding low-temperature first-stage ignition delay: Propane. *Combust. Flame* **2015,** *162*, 3658-3673.

342.   Heard, D. E., Atmospheric field measurements of the hydroxyl radical using laser-induced fluorescence spectroscopy. *Annu. Rev. Phys. Chem.* **2006,** *57*, 191-216.

343.   Antonov, I. O.; Kwok, J.; Zádor, J.; Sheps, L., A Combined Experimental and Theoretical Study of the Reaction OH + 2-Butene in the 400–800 K Temperature Range. *J. Phys. Chem. A* **2015,** *119*, 7742-7752.

344.   Messaadia, L.; El Dib, G.; Ferhati, A.; Chakir, A., UV–visible spectra and gas-phase rate coefficients for the reaction of 2,3-pentanedione and 2,4-pentanedione with OH radicals. *Chem. Phys. Lett.* **2015,** *626*, 73-79.

345.   Troe, J., The Polanyi Lecture. The colourful world of complex-forming bimolecular reactions. *J. Chem. Soc., Faraday Trans.* **1994,** *90*, 2303-2317.

346.   Abhinavam Kailasanathan, R. K.; Thapa, J.; Goulay, F., Kinetic Study of the OH Radical Reaction with Phenylacetylene. *J. Phys. Chem. A* **2014,** *118*, 7732-7741.

347.   Cho, J.; Roueintan, M.; Li, Z., Kinetic and Dynamic Investigations of OH Reaction with Styrene. *J. Phys. Chem. A* **2014,** *118*, 9460-9470.

348.   Choi, Y. M.; Lin, M. C., Kinetics and Mechanisms for the Reactions of Phenyl Radical with Ketene and its Deuterated Isotopomer: An Experimental and Theoretical Study. *ChemPhysChem* **2004,** *5*, 225-232.

349.   Class, C. A.; Liu, M.; Vandeputte, A. G.; Green, W. H., Automatic mechanism generation for pyrolysis of di-tert-butyl sulfide. *Phys. Chem. Chem. Phys.* **2016,** *18*, 21651-21658.

350.   Kanofsky, J. R.; Lucas, D.; Pruss, F.; Gutman, D., Direct identification of the reactive channels in the reactions of oxygen atoms and hydroxyl radicals with acetylene and methylacetylene. *J. Phys. Chem.* **1974,** *78*, 311-316.

351.   Dodson, L. G.; Shen, L.; Savee, J. D.; Eddingsaas, N. C.; Welz, O.; Taatjes, C. A.; Osborn, D. L.; Sander, S. P.; Okumura, M., VUV Photoionization Cross Sections of HO2, H2O2, and H2CO. *J. Phys. Chem. A* **2015,** *119*, 1279-1291.

352.   Hanson, R. K.; Davidson, D. F., Recent advances in laser absorption and shock tube methods for studies of combustion chemistry. *Prog. Energy Combust. Sci.* **2014,** *44*, 103-114.

353.   Sakamoto, Y.; Tonokura, K., Measurements of the Absorption Line Strength of Hydroperoxyl Radical in the v 3 Band using a Continuous Wave Quantum Cascade Laser. *J. Phys. Chem. A* **2012,** *116*, 215-222.

354.   Brumfield, B.; Sun, W.; Ju, Y.; Wysocki, G., Direct In Situ Quantification of HO2 from a Flow Reactor. *J. Phys. Chem. Lett.* **2013,** *4*, 872-876.

355.   Sajid, M. B.; Es-sebbar, E.; Javed, T.; Fittschen, C.; Farooq, A., Measurement of the Rate of Hydrogen Peroxide Thermal Decomposition in a Shock Tube Using Quantum Cascade Laser Absorption Near 7.7 μ m. *Int. J. Chem. Kinet.* **2014,** *46*, 275-284.

356.   Nasir, E. F.; Farooq, A., Time-resolved temperature measurements in a rapid compression machine using quantum cascade laser absorption in the intrapulse mode. *Proc. Combust. Inst.* **2017,** *36*, 4453-4460.

357. Yu, J. Estimation Method for the Thermochemical Properties of Polycylcic Aromatic Molecules. Massachusetts Institute of Technology, Cambridge, 2005.

358. Benson, S. W.; Cruickshank, F. R.; Golden, D. M.; Haugen, G. R.; O'Neal, H. E.; Rodgers, A. S.; Shaw, R.; Walsh, R., Additivity rules for the estimation of thermochemical properties. *Chemical Reviews* **1969**, *69*, 279-324.

359. Lay, T. H.; Yamada, T.; Tsai, P.-L.; Bozzelli, J. W., Thermodynamic Parameters and Group Additivity Ring Corrections for Three- to Six-Membered Oxygen Heterocyclic Hydrocarbons. *J. Phys. Chem. A* **1997**, *101*, 2471-2477.

360. Magoon, G. R. Automated Reaction Mechanism Generation: Improving Accuracy and Broadening Scope. MIT, Cambridge, 2012.

361. Ramakrishnan, R.; Dral, P. O.; Rupp, M.; von Lilienfeld, O. A., Quantum chemistry structures and properties of 134 kilo molecules. **2014**, *1*, 140022.

362. Comandini, A.; Abid, S.; Chaumeix, N., Polycyclic Aromatic Hydrocarbon Growth by Diradical Cycloaddition/Fragmentation. *J. Phys. Chem. A* **2017**, *121*, 5921-5931.

363. Finlayson-Pitts, B. J., Halogens in the Troposphere. *Anal. Chem.* **2010**, *82*, 770-776.

364. Tirtowidjojo, M. M.; Au-Yeung, P. H.; Chakraborty, D.; Eiffler, J.; Groenewald, H.; Hirsekorn, K. F.; Kokott, M.; Kruper, W. J.; Luebbe, T. U.; Meemann, H. Processes for the production of chlorinated and/or fluorinated propenes and higher alkenes. 2013.

365. Dickinson, S.; Auvinen, A.; Ammar, Y.; Bosland, L.; Clément, B.; Funke, F.; Glowa, G.; Kärkelä, T.; Powers, D. A.; Tietze, S.; Weber, G.; Zhang, S., Experimental and modelling studies of iodine oxide formation and aerosol behaviour relevant to nuclear reactor accidents. *Ann. Nucl. Energy* **2014**, *74*, 200-207.

366. McFarland, E., Unconventional Chemistry for Unconventional Natural Gas. *Science* **2012**, *338*, 340-342.

367. Upham, D. C.; Gordon, M. J.; Metiu, H.; McFarland, E. W., Halogen-Mediated Oxidative Dehydrogenation of Propane Using Iodine or Molten Lithium Iodide. *Catal. Lett.* **2016**, *146*, 744-754.

368. Lauterbach, A.; Uber, G., Iodine and Iodine Compounds. In *Kirk-Othmer Encyclopedia of Chemical Technology*, John Wiley & Sons, Inc.: 2000.

369. Khanniche, S.; Louis, F.; Cantrel, L.; Černušák, I., A Density Functional Theory and ab Initio Investigation of the Oxidation Reaction of CO by IO Radicals. *J. Phys. Chem. A* **2016**, *120*, 1737-1749.

370. Davis, S. J.; Mulhall, P. A.; Bachman, M.; Kessler, W. J.; Keating, P. B., Measurements of Pressure-Broadening Coefficients for the F' = 3 ← F' ' = 4 Hyperfine Line of the 2P1/2 ← 2P3/2 Transition in Atomic Iodine. *J. Phys. Chem. A* **2002**, *106*, 8323-8327.

371. Zhang, P.; Klippenstein, S. J.; Sun, H.; Law, C. K., Ab initio kinetics for the decomposition of monomethylhydrazine (CH3NHNH2). *Proc. Combust. Inst.* **2011**, *33*, 425-432.

372. Collin, G. J.; Deslauriers, H.; De Mare, G. R.; Poirier, R. A., The 213.8-nm Photochemistry of Gaseous 1,3-Butadiene and the Structure of Some C3H3 Radicals. *J. Phys. Chem.* **1990**, *94*, 134-141.

373. Robinson, J. C.; Harris, S. A.; Sun, W.; Sveum, N. E.; Neumark, D. M., Photofragment Translational Spectroscopy of 1,3-Butadiene and 1,3-Butadiene-1,1,4,4-d4 at 193 nm. *J. Am. Chem. Soc.* **2002**, *124*, 10211-10224.

374. Fahr, A.; Nayak, A. K., Temperature Dependent Ultraviolet Absorption Cross Sections of 1,3-Butadiene and Butadiyne. *Chem. Phys.* **1994**, *189*, 725-731.

375.   Savee, J. D.; Soorkia, S.; Welz, O.; Selby, T. M.; Taatjes, C. A.; Osborn, D. L., Absolute photoionization cross-section of the propargyl radical. *J. Chem. Phys.* **2012,** *136*, 134307.

376.   Jasper, A. W.; Miller, J. A., Theoretical Unimolecular Kinetics for CH4 + M $\rightleftarrows$ CH3 + H + M in Eight Baths, M = He, Ne, Ar, Kr, H2, N2, CO, and CH4. *J. Phys. Chem. A* **2011,** *115*, 6438-6455.